A Discrete Approach to Modelling Helicopter Blade Sailing

by

Alanna Wall

A Dissertation submitted to
the Faculty of Graduate Studies and Research
in partial fulfilment of
the requirements for the degree of
Doctor of Philosophy

Ottawa-Carleton Institute for
Mechanical and Aerospace Engineering

Department of Mechanical and Aerospace Engineering
Carleton University
Ottawa, Ontario, Canada
January 2009

Your file Votre référence
ISBN: 978-0-494-47494-5
Our file Notre référence
ISBN: 978-0-494-47494-5

Abstract

Blade sailing is an aeroelastic phenomenon which can occur during the engage and disengage phases of shipboard operations. This phenomenon is characterized by large blade deflections which are known to occur mainly at low rotor rotational speeds in high wind and sea conditions. Proper examination of this phenomenon requires adequate modelling of many contributing factors, including system dynamics, ship motion, airwake modelling, and aerodynamics. The research encompassed in this thesis sought to achieve a greater understanding of the factors that affect the blade sailing phenomenon through numerical modelling of the system as a whole.

Novel models for system dynamics and ship airwake were developed under this research programme. The dynamic model is comprised of a series of rigid segments, which allows the analyst to completely define the parameters of the system, including number of blades and blade segments. The model also allows the inclusion of coupled stiffness terms, and a method for calculating the equivalent lumped stiffnesses from continuous coupled stiffness distributions. The numerical model was shown to capture non-linear, coupled, flexible beam bending behaviour through validation against published experimental data and analytical models.

The airwake model is based on experimental data, and incorporates changing mean and turbulent flow characteristics over the flight deck in space, time, and with ship deck roll angle. The experimental research showed that ship motion changes the airwake significantly. A novel approach to the modelling of spatially- and temporally-correlated turbulence was developed, which recreates the time history of turbulent velocity fluctuations as experienced by a specific point on the rotating blade.

Using these and previously developed models for ship motion and for blade aerodynamics, a comprehensive model of the system was developed and validated in combined blade sailing-like conditions through experiment. The results of the experiment support the claims that the developed numerical tools capture the important aspects of the blade sailing environment, and that the interplay between the contributors to blade sailing motion is very complex.

The goals of this research, to study the contributors to the blade sailing phenomenon, and to develop validated modelling tools for this purpose, were achieved through this research.

This thesis is dedicated to my sisters

Emily Wall and Caitlin Wall

who are two strong, intelligent, free, and wonderful women.

Acknowledgments

Ten years in university! It's been fun, wonderful, difficult, and fulfilling. My first thanks go to my supervisors - I feel fortunate to have had the opportunity to work with these fine and brilliant gentlemen over the past five years. Prof. Robert Langlois, this research project started with you - I came to Carleton because I wanted to work under your supervision. The Applied Dynamics Laboratory is a great place because of your technical expertise, and also your vision and ability to network. Thanks for providing me with a wonderful academic opportunity, for being there for me and for understanding and sharing my love of the outdoors. Prof. Fred Afagh, I feel fortunate to have benefited from your perspective and experience in things related to dynamics. Thanks for your meticulousness, your negotiating skills, your sense of humour, and for your wonderful outlook on life. You have been a role model to me in these things. Dr. Steve Zan, you completed the technical picture with your experience in experimental aerodynamics. Thanks for encouraging me to take advantage of the facilities, the expertise, and the enthusiasm at NRC, and for making those things available to me. NRC is a place I have come to love very much. To all three of you - for hours spent, pages read, meetings attended, questions answered, opinions voiced - I extend my sincerest gratitude.

Thanks are due to Dr. Guy Larose, who was, in many ways, an adoptive supervisor to me: you helped and supported me beyond the call of duty on so many occasions. Thanks so much for being a friend and role model. Also to Fadil Khouli, my Ph.D. colleague and the other half of the blade sailing equation: you have inspired me, challenged me, listened to me, helped me, and been a friend to me. You are a talented researcher and I hope we will continue to collaborate.

At the National Research Council of Canada, many hands and minds assisted me in many different aspects of the project. Without Keith Jowsey, Brian Jahraus, Paul Penna, Bernard Tanguay, Rick Lee, Norman Ball, Brian McAuliffe, Mazen Sabbagh, Harold Rook, Francine Baptista, Lorrie Greer, Eric Parron, Pierre Gravelle, Keith Hansen, Steve Totolo, Youseff Mebarki... and all the instrumentation and tunnel crew at NRC M2, there would be no thesis.

On the technical side, thanks are due to: Indal Technologies, Inc, for allowing the use of their wind tunnel models; Agusta-Westland Helicopters for providing helicopter property information; Maj. Chris Brown, from 424 Transport and Rescue Canadian Forces Squadron in 8th Wing from Trenton, ON, Canada, for facilitating field testing on a 424 Squadron helicopter; Dr. E. Smith of Pennsylvania State University and Dr. J. Keller for providing experimental and numerical results; and Prof. Angelo Mingarelli, from Carleton University in Ottawa, ON, Canada, for mathematical consultation.

The research project was supported both financially and actively by the Carleton University Applied Dynamics Laboratory and the Department of Mechanical and Aerospace Engineering, the Natural Sciences and Engineering Research Council of Canada, Defense Research and Development Canada (Atlantic), the National Research Council or Canada Institute for Aerospace Research (NRC-IAR), and Zonta International.

On a more personal note, this thesis would not have been possible without the support of wonderful family and friends - I am very lucky. I thank my parents, Sarah Hambleton and Denis Wall, for being role models, (both in life and in academia), for believing in me, for loving me, and for encouraging me to take on the world. Mum and Dad, you are the reason I am here today - in more ways than one.

There are three important women who have stood by me, encouraged me, and inspired me. Elaine Greidanus, you have taught me so much about myself, about life and about love. Andréane Lafreniére, you have the biggest heart. I am so glad we got to go through grad school together. Sherry Stevenson, you inspire me daily, and call me to be more than I am. I can't wait to see what wonderful things you will do with your life. I love the three of you more than I can say.

Finally, Graham Ashford, you have been a source of incredible support. Thanks for the many much needed distractions. Thanks to David Heerema and the climbing crew for keeping me sane and in shape, and to Annick D'Auteuil, Sean McTavish, Simon Jones, Terje Andersen, Calvin Rans, Travis Martin, and all the grads in ME3284 and in ME 3129, for the laughs, the exchange of ideas, and for making this a great experience.

Table of Contents

List of Tables

List of Figures

List of Symbols

The reader is encouraged the consult the body text, Sections 3.1, 4.1, 4.2 and B.1 for descriptions of the nomenclature in context, including the subscripting procedure.

A - Fourier transforms of signal a

A - amplitude of a components of a Fourier series

A - coordinate systems used in examples

a - functional constant

a - velocity record used in examples

a - geometrical constant defined in Reference [1]

a - acceleration

B - Fourier transforms of signal b

B - coordinate systems used in examples

$B_{(i,n)}$ - coordinate system of the $(i,n)^{th}$ blade segment

b - functional constant

b - velocity record used in examples

C - chordwise force

C - aerodynamic force coefficient

C_{l_α} - lift curve slope

c,$[\mathbf{c}]$ - damping, or damping matrix

c - chord length

c - functional constant

D - drag force

D - characteristic length for similarity relationships

d - width of blade segment or aerodynamic section

d - functional constant

Δd - correlation point spacing

e - hinge offset from rotor rotational axis

f - frequency

f, $\{\mathbf{f}\}$ - force, or force vector

f^* - reduced frequency

G - global coordinate system

g - acceleration due to gravity

H - helicopter coordinate system

$H_{1/3}$ - significant wave height

i - turbulence intensity

J - mass moment of inertia

K - modified Bessel functions of the second kind

k - wave number

k - reduced frequency

k,$[\mathbf{k}]$ - stiffness, or stiffness matrix

L - length scale of turbulence

L - lift force

M - aerodynamics moment

M - applied segment moment

$M_{\mathbf{damping}}$ - applied moment at each segment joint due to damping

m, $[\mathbf{M}]$ - mass, or mass matrix

N - number of Fourier series frequency components

N - normal force

N - lead-lag moment

n_s - number of rotor blade segments

n_b - number of rotor blades

n_b - number of rotor blades

n_d - number of statistical records

n_{dof} - number of system degrees of freedom

o - structural offset Bryan angles

Q - non-conservative contributions to Lagrange's Equation

q, $\{\mathbf{q}\}$ - generalized coordinate, or generalized coordinate vector

R - rotor coordinate system

R - correlation functions

R - rotor radius

$[\mathbf{R}]$ - rotation matrix

r_{hinge} - root hinge pin radius

r,$\{\mathbf{r}\}$ - position, or position vector

S - ship coordinate system

S - power spectral density

S - sample equation to demonstrate embedded sum differentiation rule

S - size scaling factor between model and full scale

$\hat{S}$ - statistical estimate of power spectral density

T - system kinetic energy

T - length of a statistical record

T - mean wave period

T_o - peak wave period

t - time

t_{r1} - rotor engagement time

t_{r2} - time rotor starts to disengage

t_{r3} - time rotor finishes disengaging

U (kg m^2/s^2) - system potential energy

$\bar{U}$ - time-averaged local velocity

U_{free} - reference flow velocity

U - time-averaged velocity component along the x axis expressed in global coordinates

U_b - elastic energy of the blade

u_1 - unit vector along the x axis of the relevant coordinate system

u_2 - unit vector along the y axis of the relevant coordinate system

u_2 - lateral deflection of the beam reference line

u_3 - unit vector along the z axis of the relevant coordinate system

u_3 - vertical deflections of the beam reference line

u - unsteady velocity component expressed in global coordinates

V - velocity

V - time-averaged velocity component along the y axis expressed in global coordinates

V - characteristic velocity for similarity relationships

v - geometrical constant defined in Reference [1]

v - unsteady velocity component expressed in global coordinates

W - time-averaged velocity component along the z axis expressed in global coordinates

w - unsteady velocity component expressed in global coordinates

X - global displacement along the x axis of the subscripted coordinate system

Y - global displacement along the y axis of the subscripted coordinate system

Z - global displacement along the z axis of the subscripted coordinate system

$\Delta\bar{y}$ - correlation point spacing projected in the direction of the local time-averaged velocity

$\alpha\epsilon^{2/3}$ - (Kolmogorov constant)(rate of viscous dissipation of kinetic energy)$^{2/3}$

α - angle of attack

α_a - stall angle

β - blade flap angle

γ - root coherence

ϵ - Bryan angle

$\{\bar{\epsilon}\}$ - beam curvature vector

ε_1, ε_2 - Bryan angles to define the rotations axis of the rotor

θ - root hinge displacement angle

θ_1 - blade twist

θ_{roll}, θ_{pitch}, θ_{yaw} - Bryan angles of the subscripted coordinate system

θ_x, θ_y, θ_z - rotation angles projected along the x, y, z axes of the blade coordinate systems for spring force calculation

μ - time-averaged flow velocity component

μ - coefficient of friction in the blade root hinge pin

ν - normalized time-averaged flow velocity component

π - numerical value of π

ρ - air density

ρ - correlation coefficient

σ - standard deviation of flow velocity component

σ - rotor azimuth angle

τ - temporal correlation point spacing

τ - Bryan angle about the y axis of each blade segment

ϕ - Bryan angle about the x axis of each blade segment

ϕ - phase angle for velocity signal coherence

χ - damping filter value to accommodate application only during droop and flap stop impacts

ψ - phase angle

ψ - phase angles of the components of a Fourier series

ψ - Bryan angle about the z axis of each blade segment

ψ^2 - mean square value of a statistical record

Ω - maximum rotor rotation speed

ω - frequency component of a Fourier series

ω - frequency

$\{\omega\}$ - angular velocity vector

AFS - Advancing Fourier Series

AMT - Arbitrary Motion Theorem

BCL - Blade Clearance Limit

BCS - Blade Clearance Scale

CFD - Computational Fluid Dynamics

ESDU - Engineering Sciences Data Unit

IMSL - International Mathematics and Statistics Library

LE - Leading Edge

NR - Normal Rotational speed for a helicopter rotor

NRC - National Research Council of Canada

PCT - Perfectly Correlated Turbulence

PLE - Pre-Leading Edge (ship deck location)

PTE - Post-Trailing Edge (ship deck location)

SHOL - Ship Helicopter Operational Limits

STC - Spatially and Temporally Correlated turbulence

TE - Trailing Edge

Chapter 1

Introduction

Blade sailing is an aeroelastic phenomenon that can occur during the engage and disengage phases of shipboard helicopter operation. While the rotor is turning at normal operating speed, centrifugal force stiffens the blades. During engage and disengage, however, the blades transition through a range of speeds where the centrifugal stiffening is potentially low compared to the excitation from aerodynamics and ship motion. These can lead to large blade deflections, which can cause tailboom or tunnel strike, a condition in which the blades come into contact with the fuselage of the helicopter causing structural damage, danger to crew performing on-deck tasks, and high internal blade loads. These large blade deflections have been labeled blade sailing, and they are believed to stem from the interaction of a number of dynamic and aerodynamic factors. This research seeks to understand and model the blade sailing phenomenon.

1.1 Motivation and Context

Shipboard helicopter operations are an important part of national defense and of modern search and rescue. Since the first shipboard helicopter landing in 1943, the study of all phases of shipboard operations by researchers, helicopter manufacturers, and helicopter operators alike has been taking place. Shipboard operations have since become routine, even though the practice carries inherent risk. Helicopters are required to land on moving ship decks, often with small landing areas, and often in high seas. Turbulent airwake,

moving landing references and the potential for poor visibility all make shipboard landings extremely difficult.

During a typical Canadian Forces helicopter landing, the helicopter approaches the ship from port/stern, positions itself laterally alongside the landing point, and traverses laterally into high hover above the deck. Shipboard landing in elevated seas and on-deck securing is enabled by the Helicopter Hauldown and Rapid Securing Device (HHRSD). A messenger cable from the helicopter is manually connected to the Recovery Assist (RA) cable, which is used to guide the helicopter to the deck. Assisted by another trained pilot on the deck [called the landing signals officer (LSO)], the pilot of the landing aircraft transitions into low hover, and during a period of lesser ship motion known as quiescence, lands. The helicopter is immediately secured to the deck by the Rapid Securing Device (RSD) system. The rotor blades are then disengaged and the helicopter is manoeuvered into the ship's hangar.

Due to the complexity of the shipboard environment, helicopter operations are governed by Ship Helicopter Operational Limits (SHOLs), which define the allowable conditions for helicopter operations and are determined mainly by practical testing during sea trials [1]. These limits are established separately for each ship-helicopter combination, and take into account many factors including pilot workload, helicopter control input limits, and the likelihood of severe blade deflections. At each phase of operations, different challenges and factors must be considered to ensure the safety of the flight crew and the on-deck crew. In this study, the rotor engage and disengage phases of operations are of interest from a flight safety point of view, in that they can occasionally give rise to blade sailing.

1.2 Definition of Blade Sailing

Some blade deflection is expected during normal helicopter operations, therefore not all downward blade deflections are cause for concern. A specific definition allowing a clear distinction between safe and dangerous blade deflections does not exist. Indeed, this distinction depends on the geometry of the helicopter, including droop stop angle, blade flexibility, and the height of the helicopter fuselage. The purpose of this research is not to categorize blade

Table 1.1: Blade Clearance Scale [1].

BCS #	Clearance
1	0.584 m
2	0.203 - 0.584 m
3	0.127 - 0.203 m
4	0 - 0.127 m

deflections as either safe or unsafe, but to provide tools to evaluate this on a case-by-case basis. Still, the following pieces of information should help the reader to put the magnitude of blade deflections in context.

- In 1985, the standard United States sea trial procedure involved measuring the blade-to-airframe clearance with a series of frangible pegs [1]. At that time, danger of fuselage strike during engage and disengage was measured on the Blade Clearance Scale, given in Table 1.1, where increasing BCS number indicates increasing risk.
- Flexible beam bending cannot be properly evaluated using linear models for elastic tip deflections greater than 15% of the blade length (1.35 m for a 9 m blade) [2]. Blade sailing deflections can exceed this.
- The study of blade sailing primarily considers total blade tip deflection, which includes both elastic blade deflection and rigid body motion due to hub articulation.

1.3 The Blade Sailing Environment

Blade sailing is commonly observed in the shipboard environment, although cases have also been documented on offshore platforms [3]. Shipboard helicopter operations take place on large ships, such as the Landing Helicopter Assault (LHA) ship and also on small aviation-compatible ships, such as frigates. In Canada, shipboard helicopter operations take place on Halifax class frigates or Iroquois class destroyers. Examples of some typical ships for helicopter operations are shown in Figure 1.1.

Figure 1.1: HMCS Regina (Halifax Class Frigate, Canada) left, and USS Saipan (Amphibious assault ship, LHA-2, USA) right [online source: wikipedia, 2008].

A variety of helicopters have been employed in the shipboard environment over the years, including: the SH-60 Sea Hawk, perhaps the most widely used; the CH-46 Sea Knight and the CH-47 Chinook, used by the United States starting in the 1960s; the Sea King, slightly different versions of which have been used in Canada (CH-124), the United States (SH-3), and the United Kingdom (WS-61); the Lynx; the SH-2 Seasprite; and the AS365 Dauphin. The Sea Knight is equivalent to the now retired Canadian Labrador (CH-113). Figure 1.2 shows photographs of some common shipboard helicopters.

Since the 1960s, Sea King helicopters have been used in Canada for maritime operations. The Maritime Helicopter Project is currently underway to replace Canada's maritime helicopter fleet with the CH-148 Cyclone, Sikorsky's maritime variant of the H-92 Superhawk. Canada also uses the Augusta-Westland CH-149 Cormorant, which replaced the Labrador, for search and rescue operations. In Canada, search and rescue vehicles do not currently operate in the shipboard environment.

The typical shipboard environment, as shown in Figure 1.3, is a possible blade sailing site. Blade sailing in the shipboard environment can be attributed to the following important contributors:

- helicopter and blade dynamic properties, including hub configuration;
- ship motion; and
- aerodynamic environment.

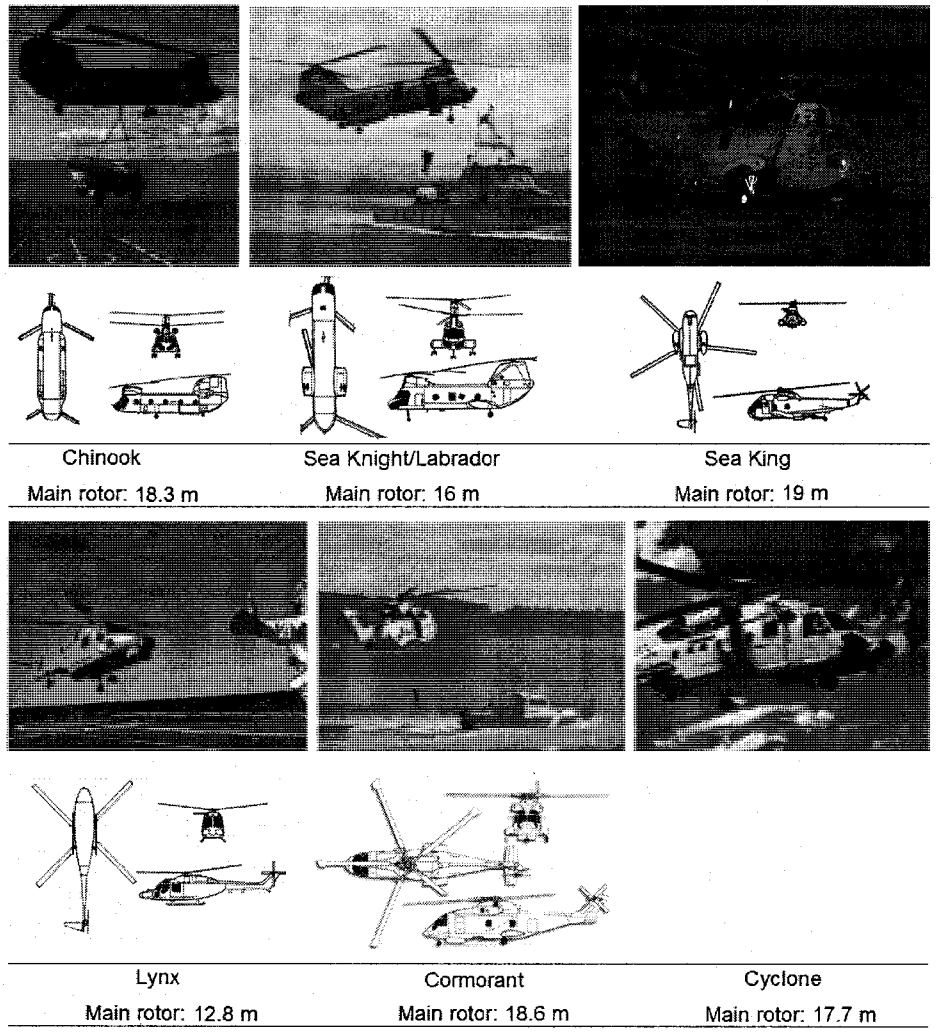

Figure 1.2: Some maritime helicopters in use [online source: wikipedia, 2008].

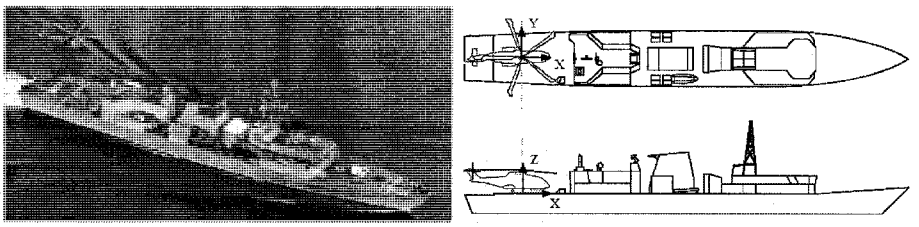

Figure 1.3: Typical environment for shipboard helicopter operations.

These three contributors are the important areas of focus in the research encompassed in this thesis, and are referred to many times throughout this document. Operational considerations, including pilot inputs and engage/disengage rotor speed profiles, also play a role but are included in the other three contributors.

Chapter 2

Literature and Subject Review

The shipboard helicopter environment, during all phases of operation, has been the focus of much research. These works often consider safety [4], operational limits (SHOLs) [5], or the suitability of different types of helicopters to the shipboard environment [6]. The study of blade sailing has an element of each of these considerations.

In this chapter, relevant literature is given for each contributing factor individually: dynamics, ship motion, and aerodynamics. These sections show that each contributing factor is itself a large and current research field. The current state of blade sailing study is then discussed.

2.1 Dynamics

The equations of motion for dynamic systems can be formulated using a number of methods [7]. The Newton-Euler equations, an example of technical mechanics, and Lagrange's formulation, an example of analytical mechanics, are the two most common methods of developing dynamic equations of motion. Newton-Euler is most suited to problems where constraint forces are known and internal forces are of direct interest. Lagrange's Equation,

$$\frac{d}{dt}\left(\frac{\partial T}{\partial \dot{q}_\nu}\right) - \frac{\partial T}{\partial q_\nu} + \frac{\partial U}{\partial q_\nu} = Q_\nu \tag{2.1}$$

uses generalized coordinates, q_ν, and is developed from the expressions for the scalar quantities kinetic energy, T, and potential energy, U, and non-conservative work, Q_ν. This

formulation efficiently yields the equations for complex systems, but does not yield directly internal forces.

Many other dynamic formulations exist, including D'Alembert's principle, which involves using the principle of virtual work to analyze moving bodies; Hamilton's principle, which is often used for continuous systems; and Gibbs-Appell equations, which are often used for non-holonomic systems. The characteristics of the dynamic system being modelled and the desired output govern the dynamic formulation that best suits the problem.

For blade sailing, the dynamic formulation could include beam/blade flexibility, hub configuration, helicopter suspension, aerodynamics load input, and ship motion. The details of each are here discussed.

2.1.1 Blade and Beam Dynamics

Helicopter rotor blades are flexible bodies, which can deflect in a number of ways. Flap is defined as the deflection and deformation of the blade out of the plane of rotation; lead lag is defined as the deflection and deformation of the blade in the plane of rotation. Torsion or twist is the rotation of the blade about its longitudinal axis and extension is the deformation of the blade along its longitudinal axis. The cross section of helicopter blades can also undergo deformation.

The dynamic modelling of flexible helicopter rotor blades is an active field; it has been approached from a wide variety of fundamental directions over the past 50 years [9]. Rigid blade models with articulated flap hinges have been widely employed, as have models based on linearized elastic beam theory. With increasing computer power, the complexity of rotor analysis has also increased. Hodges et al. have been developing analytical non-linear flexible beam models that are valid to second order, and allow for much more versatility in beam modelling than traditional continuous analytical solutions [10]. Finite element analysis [11, 12] has also been widely applied, and is especially applicable to the complex hub configuration of helicopter rotors. Many publications in the field of continuous beam and blade dynamic modelling contain analytical or experimental data that can be used to validate other models.

Another philosophical approach to dynamic modelling exists: the idea that the behaviour of continuously flexible systems can be accurately modelled using a series of rigid bodies connected by flexible elements. This approach lends itself to relatively simple, closed-form equations of motion that are easily and quickly handled by numerical solvers. No linearizing assumptions, other than the assumption of lumped deformation characteristics, are required to achieve solvability.

The rigid body approach is seen as a compromise between accuracy and solution speed compared to continuous beam models. While a continuous beam model might more accurately reflect the physics of the system, a model in which the blades are represented as a series of rigid blade segments connected by rotational springs can be used to evaluate the blade response with excellent accuracy, and with potentially decreased solution times. The rigid-segment modelling approach is not known to have been used previously in the blade sailing context.

The rigid-segment approach is supported by the work of Huston, who has applied the rigid-body approach to a long slender beam undergoing extensional vibration [12]. This work shows agreement within five percent for the first three natural frequencies when ten rigid segments were used and for the first seven when 30 segments were used. Not surprisingly, the solution accuracy increases with segment number.

Langlois and Anderson examined a simple beam and cart problem using the rigid segment approach, finite element approach, and a flexible multibody formulation [13]. Although they noted the potential difficulty in arriving at optimal parameters for the rigid segment model, the results among the methods show good agreement, especially for the beam fundamental frequency.

Work by Haering incorporates both axial and bending flexibility into a lumped parameter model that is intended for the modelling of beams undergoing large deflections [14]. A cantilever beam attached to a rotating reference frame was modelled using a beam with four degrees of freedom: two extensional and two rotational. This lumped parameter model had two segments. The model results were compared to results for a closed-form solution for large beam deflections, where the lumped parameter model captured the trends of the

closed-form solution with increasing accuracy for two segments compared to one segment. Results from the model were also compared to those for a non-cartesian non-linear continuous beam model, where the results showed excellent agreement. With this study, Haering also used the lumped parameter model to provide insight into the important modelling considerations in the development of his continuous model.

2.1.2 Hub Dynamics

The configuration of a helicopter hub contributes significantly to the blade dynamics. Teetering rotors, always two bladed, are not presently in use in the shipboard environment. Multi-bladed rotors can be categorized as either semi-rigid, where the blades are connected to the rotor hub by structural elements with finite stiffness, or articulated, where the blades are connected to the hub by hinges, often in the lead-lag direction as well as in flap. A schematic of the hub configuration for the CH-47 Chinook is shown in Figure 2.1. This rotor is articulated.

Depending on whether the helicopter being modelled has semi-rigid or articulated rotor blades, the blade root modelling requirements change. If the blades are semi-rigid, they can be approximated by a cantilever beam-type model. Articulated blades have low or no stiffness at the root. For this reason, they are supported at low rotational speeds by droop stops that keep the blades from collapsing due to gravity. At operational speeds, centrifugal effects keep the blades from sagging due to their weight, and thus the stops are often retracted. Flap stops prevent the blade from excessive upward flapping during engage and disengage, and also retract and extend at an appropriate rotational speed. The lead/lag stops, often hydraulic or elastomeric dampers, similarly restrict blade motion outside a given acceptable range of motion; however their modelling is simplified by the fact that they do not extend or retract during operation. Large blade deflections have been shown to occur in high wind conditions for both articulated and semi-rigid rotors. However, the deflections experienced by articulated rotors are often larger owing to the fact that larger kinetic and potential energies are exchanged when a hinged blade falls onto the droop stop.

The pitch of each blade at the root is controlled by pitch links, which are connected to

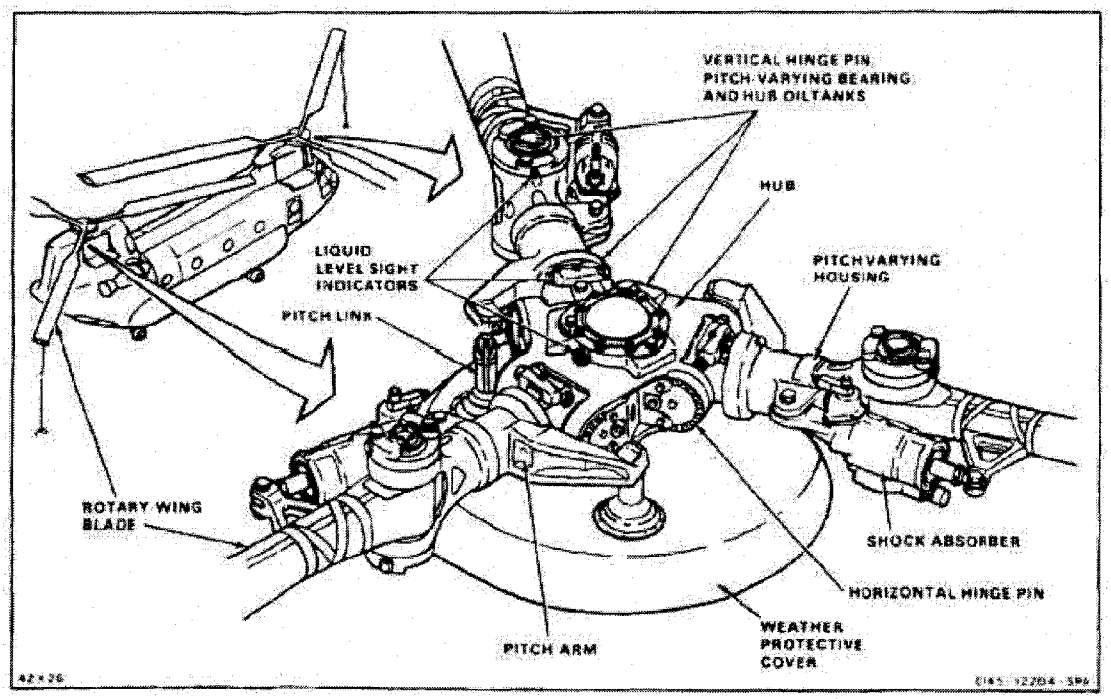

Figure 2.1: Typical articulated rotor hub: CH-47 Chinook [15].

the swash plate, directly controlled by the pilot. In this way, blade pitch at the root is not strictly a dynamic degree of freedom, although the linkage stiffness may be of interest and the pilot inputs may be modelled numerically.

The geometry of the rotor hub, including hinges and stops, is an important part of modelling the blade sailing phenomenon. Their treatment in other blade sailing studies is discussed in Section 2.4.

2.1.3 Helicopter Suspension

Vehicle suspension systems are intended to isolate the occupants and cargo from shock and vibration [16]. They usually consist of vertical suspension elements, such as oleos or struts, and tires which have stiffness characteristics in three orthogonal directions.

For shipboard helicopters, suspension systems come into play during landing, taxiing, and on-deck manoeuvring. They have also been shown to contribute to dynamic blade

phenomena, such as ground resonance, in which the lead/lag motion of the blades are coupled through the helicopter suspension. As such, suspension should be considered in a model used for the evaluation of on-deck blade dynamic phenomena, such as blade sailing.

Suspension elements can be modelled as linear stiffness and damping elements, or with more complicated models to capture their non-linear characteristics [17].

2.2 Ship Motion

The movement of the ship in six degrees of freedom has been identified as one of the possible contributing factors to the blade sailing phenomenon. The motion of a ship in a given seaway depends on a number of parameters: the direction, amplitude and frequencies of the approaching waves, and the geometry and inertial properties of the ship itself. Sea waves are complicated, involving the interaction of wave components traveling in different directions, and are time varying [18]. The characteristics of the sea are often expressed by the point wave spectrum, which is the statistical representation of the amplitudes of waves of different frequencies as seen from a single inertial point on the surface of the ocean. This representation does not include directional or time varying effects (from a statistical point of view), but allows an expression of the state of the sea. The concept of sea state is used to describe the roughness of the sea. Table 2.1 shows a summary of the classification of sea state [19].

Assuming statistically invariant sea conditions, ship motion can be simulated using statistical methods and the concept of linear superposition. The typical shape of a wave spectrum varies depending on the geographical location being simulated, and several spectral expressions have been developed, involving different experimental data and different modelling parameters. For instance, the Bretschneider spectrum, $S_{\text{Bretschneider}}$, given as a function of wave frequency, ω, is used to model open seas, and depends on the significant wave height, $H_{1/3}$, and mean wave period, T. It is given by [20]

$$S_{\text{Bretschneider}}(\omega) = \frac{A}{\omega^5} e^{\left(\frac{-B}{\omega^4}\right)} \tag{2.2}$$

Table 2.1: NATO sea state numeral table for the open ocean (North Atlantic) [19].

		Significant Wave Height (m)		Sustained Wind Speed (Knots)	
Sea State	Description	Range	Mean	Range	Mean
0-1	Smooth	0-0.1	0.06	0-6	3
2	Slight	0.1-0.5	0.3	7-10	8.5
3	Moderate	0.5-1.25	0.88	11-16	13.5
4	Rough	1.25-2.5	1.88	17-21	19
5	Very rough	2.5-4	3.25	22-27	24.5
6	High	4-6	5	28-47	37.5
7	Very high	6-9	7.5	48-55	51.5
8	Mountainous	9-14	11.5	56-63	59.5
>8		>14	>14	>63	>63

in $m^2/(rad/s)$, where

$$A = 172.75\frac{H_{1/3}}{T^4} \tag{2.3}$$

and

$$B = \frac{691}{T^4} \tag{2.4}$$

The JONSWAP spectrum, S_{JONSWAP}, describes waves in more protected bodies of water, and is given by

$$S_{\text{JONSWAP}}(\omega) = .658\ C\ S_{\text{Bretschneider}}(\omega) \tag{2.5}$$

where

$$C = 3.3^J \tag{2.6}$$

$$J = e^{\left(\frac{-1}{2\gamma^2}\left(\frac{\omega T_o}{2\pi}-1\right)^2\right)} \tag{2.7}$$

and

$$\gamma = \begin{cases} 0.07 & \text{if } \omega \leq \frac{2\pi}{T_o} \\ 0.09 & \text{if } \omega > \frac{2\pi}{T_o} \end{cases} \tag{2.8}$$

where T_o is the peak wave period.

Simulation of ship motion is computed using a linear frequency domain method applied in the time domain. This requires the calculation of the ship response in six degrees of freedom to waves of unit amplitude. These spectra are called Response Amplitude Operators (RAO). Each of six rigid-body ship motions: surge, sway, heave, roll, pitch, and yaw, are considered independently. RAOs are calculated using the program ShipMo7, developed at Defense Research and Development Canada, Atlantic [21].

The relevant wave spectrum, Bretschneider, JONSWAP, or other, is multiplied by the RAOs for each of six ship degrees of freedom. This calculation typically includes ship translation, which shifts the wave frequencies to encounter frequencies, which are relative to the ship. This process gives a frequency-domain representation of the ship motion for all degrees of freedom at the ship's centre of rotation. The motion can then be expressed at any point on the ship through appropriate transformations.

The displacement, r, of ship motion for each ship degree of freedom, k, is determined computationally by summing sine waves of different frequencies using [20]

$$r_k = \sum_{j=1}^{40} (A_{k,j} \sin(\omega_{k,j} t + \psi_{k,j})) \tag{2.9}$$

where $A_{k,j}$, $\omega_{k,j}$, and $\psi_{k,j}$ are the amplitude, encounter frequency, and phase for the kth ship degree of freedom and the jth frequency component. The velocity of each degree of freedom can be calculated similarly, by differentiating Equation 2.9 with respect to time, t.

$$\dot{r}_k = \sum_{j=1}^{40} (A_{k,j} \omega_{k,j} \cos(\omega_{k,j} t + \psi_{k,j})) \tag{2.10}$$

While the corresponding amplitudes can be obtained directly from the response spectrum, care must be taken when selecting the phase angles and frequencies. Phase angles are given by the sum of two components. The first is a random component, which is different for each frequency component, but consistent across the six degrees of freedom. The random component preserves the relative independence of each frequency component. The second phase component allows proper correlation between degrees of freedom. The

frequency spacing between each frequency component is also randomized. This greatly increases the time over which non-repeating motion can be simulated [22, 23]. Typically 40 to 50 frequency components are included in ship motion simulation.

Representative ship motions at the flight deck of a Canadian patrol frigate in sea state 5 (4 m significant wave height, 45° relative wave direction, 25 kn ship speed) are shown in Figure 2.2. This ship has a length of 134 metres, a width of 16 metres, and an approximate displacement of 4700 tonnes.

2.3 Aerodynamic Environment

The aerodynamic environment for blade sailing, called the ship airwake, has historically been considered an important contributor to blade sailing. This environment is complex, owing to the interplay between many different factors: the atmospheric boundary layer, including the relative angle between the mean wind and the ship deck; the ship geometry, which leads to flow separation; and ship motion. The airwake is characterized by regions of forward flow, regions of recirculation and reattachment, and spatially-changing turbulence characteristics.

Perfect modelling of the shipboard aerodynamic environment would take each of these into account; in practice, modelling is often simplified to achieve acceptable fidelity with the resources at hand.

2.3.1 Flowfields

The velocity characteristics of flowfields are often measured by recording a time history of velocity at one or more spatial locations. For statistically stationary flows, the steady, or time-averaged, and unsteady, or turbulent, properties can be evaluated using statistical tools for the analysis of random data. In fluid dynamic experiments, flow velocity is sampled over a finite time, T, at finite frequency, Δf. These sampled signals are then separated into records that are used to estimate the theoretical statistical properties of the flow at the measurement point. In order for flow velocity records to be evaluated using statistical

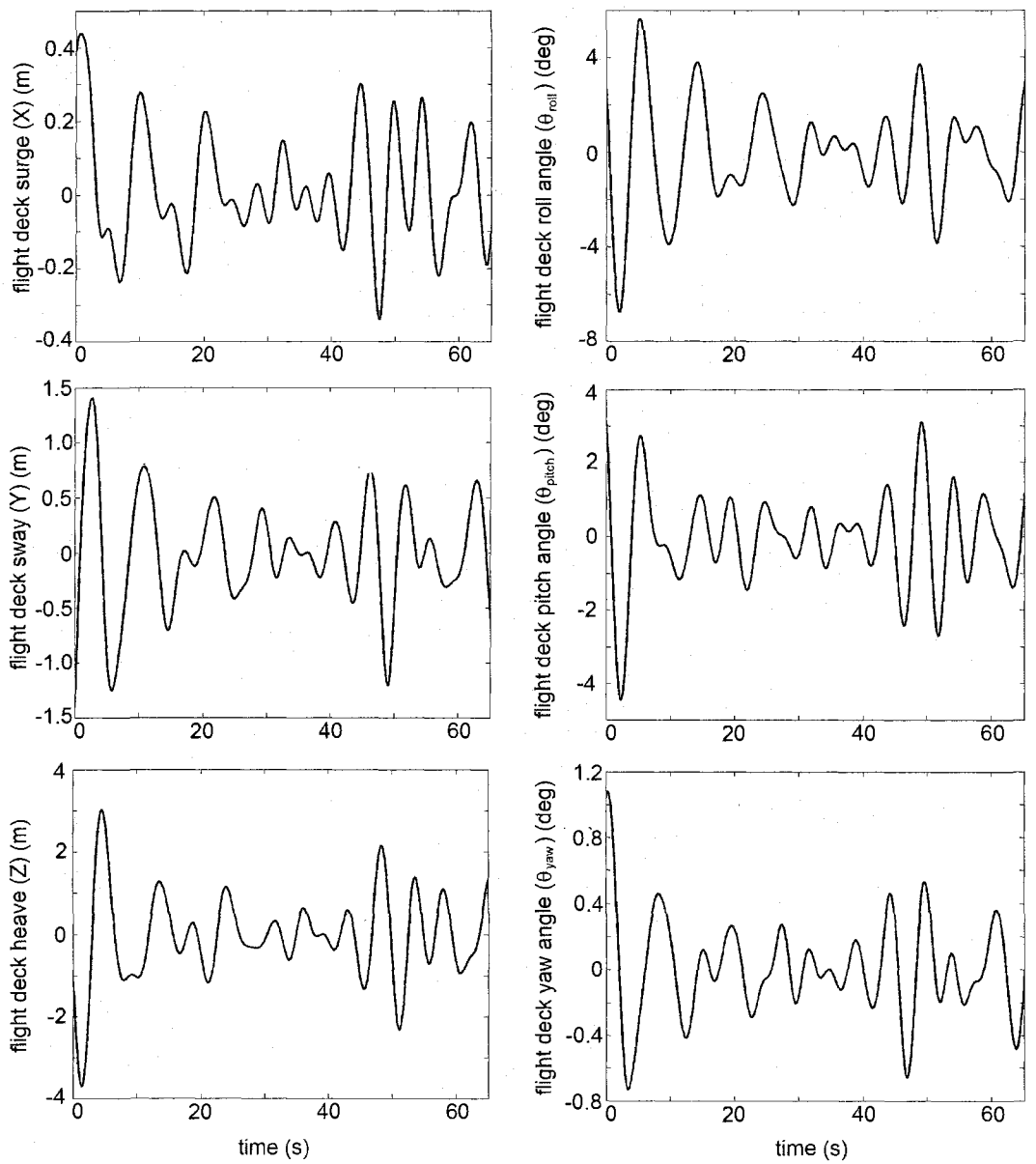

Figure 2.2: Typical frigate motion, sea state 5.

methods, some characteristics of the phenomenon need to be satisfied.

Stationarity: is satisfied if the statistical properties of the phenomenon (such as mean value and auto-correlation function) can be calculated by computing the averages of these values calculated over a set of sample records.

Ergodicity: is satisfied if the statistical properties of the phenomenon can be calculated by computing the properties over each sample record.

Normality: is satisfied if velocity fluctuations in real flow follow a Gaussian distribution. This characteristic is reflected in real flow.

The characteristics of any flowfield are given by three important statistical quantities, all of which can change depending on the location in the flowfield for which they are being evaluated. These quantities are:

- the mean speed in three orthogonal directions;
- the auto-spectra of turbulence in three orthogonal directions; and
- the cross-correlation tensor.

Two additional properties, which can be obtained from those above, are also used to characterize flow. They are:

- standard deviation of speed in three orthogonal directions (turbulence intensity); and
- length scales of turbulence.

A flowfield is modelled accurately when the important characteristics above are reproduced. While the steady component of flow velocity, due to its invariability with time, is easily given by a look-up table or function with spatial dependance, the unsteady component presents a much greater challenge. The quintessential goal for flowfield modelling involves achieving spatial and temporal correlation of turbulence, which means that the model exhibits the correct unsteady flow characteristics at a given spatial point, relative to

every other point in the flowfield with time. Some common assumptions can be employed to facilitate correlated flow field modelling [24].

Homogeneity: is the assumption that the statistical properties of the flow field do not depend on location. In the context of surface boundary layer flows, vertical homogeneity is not considered a valid assumption.

Isotropy: occurs in a flow field when the turbulence characteristics are independent of direction. In the Earth's surface boundary layer, this assumption is considered valid in horizontal directions only.

Neutrality: is satisfied when the effects of temperature do not significantly affect the boundary layer.

Frozen turbulence assumption: (also called Taylor's hypothesis) states that turbulent structures can be taken to convect with the freestream wind velocity and that the deformation of the structures with time can be neglected. This assumption is valid when the mean flow speed is much greater than the fluctuating component, and has been shown to apply for wavelengths of less than 300 m in the atmospheric boundary layer [25].

2.3.2 Flowfield Modelling

Several different methods have been employed in the literature to achieve spatially- and temporally-correlated turbulence modelling. Computational Fluid Dynamics (CFD) numerically solves a gridded flowfield based on the Navier-Stokes equations, the form of which depends on the CFD formulation. While many CFD solutions capture time-averaged effects only, significant recent advancements in computing power have made unsteady solvers possible. The CFD approach is quickly becoming an inexpensive alternative to experiment for studying flow characteristics. In literature, CFD has been used to successfully capture many aspects of the wind-over-deck flow of ships.

CFD, however, does have some limitations, especially the computational time involved with solving fully correlated turbulent flows. The flowfield research discussed in this thesis was approached from an experimental point of view for a number of reasons. Through the collaboration with the National Research Council of Canada, significant facility and human resources were available for experimental studies. Additionally, experimental flowfield results are useful in the community of CFD for flow validation. While CFD could be part of future work on the blade sailing phenomenon, it was not used for the research documented herein; and hence is not discussed further.

Analytical models have been developed for the simulation of spatially and temporally correlated flow. J. Mann modified the von Kármán spectral tensor [26] to include the shearing effect present in the atmospheric boundary layer. Using atmospheric spectra from several sources including the Engineering Sciences Data Unit (ESDU) [27], the spectral tensor model was shown to capture the main characteristics of atmospheric turbulence [28]. The spectral tensor model has also been expanded to include the effects of complex terrain including changes in surface roughness and hills [29].

The discrete-grid method [30] is an efficient method for calculating the correlated flowfield time history. It calls on the theory of linear multi-input/multi-output systems [31]. The flowfield is gridded into a series of discrete points at which a statistically consistent velocity signal can be calculated by summing the correlated contributions from every grid point in the flowfield on the grid point of interest. The time domain contributions are calculated by convoluting an appropriate transfer function by a string of random numbers generated at each grid point. Although the desired quantities exist in the time domain, frequency domain analysis is required to find the transfer functions. The details of this process can be found in References [30] and [32].

2.3.3 Ship Airwake

The complexities of the ship airwake contribute significantly to shipboard helicopter operations, including the blade sailing phenomenon. In his detailed overview of the current state of aerodynamic helicopter-ship modelling and simulation, S. Zan discussed the successes

and areas of improvement for airwake simulation [33].

The National Research Council of Canada has been involved in issues relating to the ship-helicopter dynamic interface for many years. In 1983, K. Cooper published an experimental study that examined flow characteristics over the flight deck of several proposed flight deck configurations at several proposed landing locations [34]. Starting in the 1990s, Zan conducted extensive research focussing on the ship airwake by studying the topology of the flow behind a typical frigate shape [35]. Under this research project, hot wire anemometers were used to characterize the unsteady flowfield behind a 1:50 scale Canadian Patrol Frigate model with wind relative to the longitudinal axis of the ship at 0° and 12°. The impact on the airwake of a Close In Weapons System (CIWS) located in the aft starboard corner of the hangar was studied by modifying the ship model. For the 0° wind direction, downward flow velocities over most of the flight deck were observed; these were attributed to the flow moving around the hangar face. The flow exhibited symmetric characteristics about the ship centreline without the CIWS, and antisymmetric flow with the CIWS.

The wind tunnel data was validated against full-scale sea trial data and CFD results for similar ships. The CFD results give the correct flow trends compared with the wind tunnel measurements, but with higher velocity gradients.

Other airwake studies completed at the National Research Council of Canada involved the development of a correlated unsteady airwake in the rotor disc plane and the calculation of the resulting forces on the rotor [30]; and the characterization of helicopter fuselage loads in a typical frigate airwake in the context of pilot workload [36, 37].

Over the past 20 years, J. Val Healey of the United States Naval Postgraduate School has studied the prospects for modelling the airwake aspect of the ship helicopter interface, in addition to his work on modelling the atmospheric boundary layer and ship motion. In a paper published in 1989, Val Healey identifies the following four items as critical to airwake simulation [38]:

- the incoming atmospheric boundary layer, complete with turbulence;
- the wind/ship speed ratio;

- the relative wind direction; and
- the ship motion.

That study detailed flow visualization experiments done over the flight deck of a model ship. A research program in which the airwake profile behind many different model ships was to be mapped was explained. Results from a following phase of that study, including more flow visualization and some quantitative measurements were published in 1992. These results included three-axis hot-wire measurements taken as the probe was flown along a typical flight path [39].

Over the flight deck of a typical frigate-like ship, Rhoades and Val Healey identified four distinct regions. The first is the outer region, which is characterized by relatively smooth flow. This flow is separated from the inner turbulent and recirculating regions by shear layers, whose locations relative to the flight deck depend on the relative direction of the incoming wind to the ship. The three inner flow regions result in flow separation from the aft edges of the hangar and the port and starboard edges of the deck. They conclude that overall, the aerodynamic conditions over the flight deck of typical frigates are unfavourable for helicopter operations [40].

The Technical Cooperation Program (TTCP) is a joint defence research and development program that was started in the 1950's, and currently consists of a partnership between Canada, USA, UK, Australia, and New Zealand. Under the auspices of this program, an effort to study the ship airwake and create CFD validation data was undertaken. A simplified and common ship model geometry was used by all parties to standardize the results.

Wakefield, Newman (who has studied blade sailing extensively), and Wilson [41] have examined the flow around this standardized ship experimentally, using flow visualization and oil flow, as well as CFD. They have shown good agreement between the time-averaged experimental and computational results, where CFD predicted most, but not all, of the important flow characteristics. They extended their research to include the downwash flow from a helicopter rotor using the computational tools, and have examined the effect on the airwake itself. Further computational studies of the flow over the simplified shape have

been done in Canada [42], Australia [43] and in the United States [44].

The studies mentioned above are by no means an exhaustive list on the subject of airwake research, and are in addition to the studies done by Newman et al. for the specific purpose of modelling blade sailing, which are discussed in detail in Section 2.4. These references contain qualitative and quantitative data regarding the characteristics of airwakes for a variety of ship yaw angles. The details of these characteristics are not individually discussed, since they vary depending on the type of ship. However, the results lead to the following conclusions about ship airwakes. Airwake flows are:

- highly turbulent, involving separation, shear layers and reverse flow;
- dependent on wind direction, strength, surface boundary layer, and ship motion, all of which can vary;
- not necessarily stationary; and
- anisotropic and non-homogeneous.

Clearly the airwake environment is changing and complex, and that its perfect recreation in a simulation environment is a phenomenal challenge.

Beam winds, where the freestream wind approaches the ship perpendicular (or almost perpendicular) to its longitudinal axis, are known to create an environment where blade sailing has been reported. In beam wind conditions, up and down drafts are generated over the flight deck as the wind flows over the ship. The vertical wind component excites the slowly turning blades in a cyclic manner, and the loads are especially severe if the blade tips travel beyond the edge of the deck as is often the case with frigate-sized ships. The ship deck also induces turbulence, the effect of which on blade response is currently uncharacterized.

The motion of the ship is known to affect the unsteady nature of the airwake environment. For example, in beam winds, the ship roll angle affects the size and shape of the separation bubble that exists near the surface of the deck. For large, but realistic, roll angles away from the wind, the rotor disc plane can pass through the shear layer produced by the ship deck separation bubble.

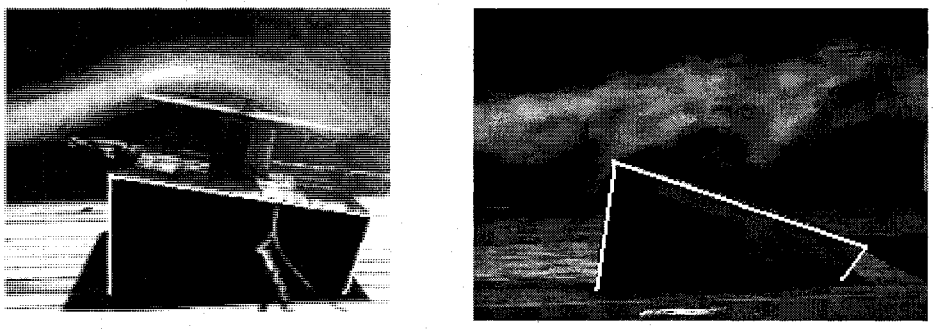

Figure 2.3: Flow visualization experiments on a representative frigate flight deck shape (left: rotor turning, deck roll angle -10° [45]; right: no rotor, deck roll angle -20°).

Flow visualization experiments, completed at the National Research Council of Canada and shown in Figure 2.3, show the characteristic wind in the rotor disc plane generated in beam wind conditions, and the importance of ship roll angle.

2.3.4 Aerodynamic Forces

Aerodynamic models attempt to describe the forces generated by the interaction between the airwake model and the helicopter blade and body. The aerodynamic forces are affected by the blade cross-section, blade velocity relative to the wind, blade location in the flow, unsteady effects, dynamic stall and reattachment, and tip effects. In the blade sailing context, all angles of attack are possible, therefore, appropriate airfoil coefficients must be available for any relative wind direction.

Many aerodynamic force models exist. In general, the aerodynamic lift, L, drag, D, and moment, M, given in blade coordinates for angle of attack, α are given respectively by

$$L = \frac{1}{2}\rho V^2 C_l(\alpha) cd \tag{2.11}$$

$$D = \frac{1}{2}\rho V^2 C_d(\alpha) cd \tag{2.12}$$

and

$$M = \frac{1}{2}\rho V^2 C_m(\alpha) c^2 d \tag{2.13}$$

where ρ is the air density, V is the relative air velocity, c is the chord length, and d is the width of the section. The coefficients, C_l, C_d, and C_m, can also depend on Mach number, however this dependance is not considered in this research since blade sailing Mach numbers are below 0.3 and the flow can therefore be considered incompressible.

The coefficients can be determined in a number of different ways. For quasi-steady modelling, the airfoil coefficients are measured at static angles of attack and tabulated. For the NACA 0012 airfoil, which is commonly used in helicopter research, the steady coefficients have been measured and published [46, 47]. The coefficient curves for the NACA 0012 airfoil have also been expressed in functional form [48]. Unsteady aerodynamic effects on the force coefficients are often modelled using thin airfoil theory.

Unsteady aerodynamic effects are considered to be important when the reduced frequency of airfoil oscillations relative to the wind speed is above 0.05. The reduced frequency, k, is given by

$$k = \frac{\omega c}{2V} \tag{2.14}$$

where ω is the frequency of airfoil oscillation, V is the relative wind speed, and c is the airfoil chord length.

Unsteady effects have been extensively studied, and a variety of different models are available in literature, including Theodorsen's theory and Sears' theory [49]. Many of these models are based on potential flow and thin airfoil theory, have been developed in the frequency domain, and capture only certain types of unsteady motion. For example, some models include pitch and/or plunge of the airfoil, but do not allow for variations in the relative airflow. There are two families of aerodynamic models that give aerodynamic forces at each timestep, allowing for arbitrary airfoil motions and variations in the relative flow.

An indicial method, dubbed the Arbitrary Motion Theorem (AMT), has been developed by J. Leishman and his colleagues. This model considers arbitrary fluctuations in the freestream velocity and the angle of attack using Duhamel superposition [50]. The model has been expanded to include compressibility effects [51]. Non-circulatory terms, due to vertical airfoil accelerations and the rate of change of angle of attack, are contained within this model. The AMT method couples naturally with a semi-empirical dynamic stall model, which incorporates the understanding of physical mechanisms and fitted parameters [52]. The dynamic stall model incorporates leading edge and trailing edge stalls. The fitted parameters for a NACA 012 airfoil are given in Reference [53]. The model provides an indication as to whether the airfoil has stalled, including dynamic effects; appropriate modifications to the aerodynamic coefficients; and criteria for flow reattachment.

Another family of unsteady aerodynamics models has been developed by D. Peters and his colleagues [54, 55, 56]. These models also allow for arbitrary motions in the time domain. They also allow for the easy inclusion of a variety of inflow models, which have been developed extensively by the same authors, a feature which is useful for helicopter rotors operating at full speed.

Since validated and published models exist for the calculation of aerodynamic forces, these were modified only slightly, as discussed in Appendix A.1, for the work contained herein.

2.4 Blade Sailing Modelling Initiatives

Over the past 25 years, the blade sailing phenomenon has been widely studied [57]. Although blade sailing occurrences were documented much earlier, publicly available research on blade sailing began in the 1980's. In addition to many single-publication studies, two comprehensive multi-year multi-publication research programmes have been conducted on the blade sailing phenomenon: one at the University of Southampton, and one at Pennsylvania State University. This section reviews them, in chronological order.

2.4.1 Early Research

A study published in 1964 by P. F. Leone [58] modelled blade and droop stop impacts, and compared theoretical and experimental blade bending during droop stop impacts. Another study, examined the likelihood of blade-to-blade impacts on coaxial helicopter rotors on ship decks, also including stop impacts and blade flexibility [59]. Both of these studies were limited by the computing power that was available for their simulation. The blade dynamic models consider beam bending only in the linear range.

2.4.2 University of Southampton

D. W. Hurst and S. J. Newman began to publish open literature on the topic of blade sailing in 1985 [60]. With this first study, they examined several different aspects of the blade sailing environment, and identified the following effects as important in the blade sailing context [61]:

- blade elasticity (in flap primarily and also in torsion);
- centrifugal forces due to rotor rotation;
- blade dynamics, including Coriolis and gyroscopic accelerations;
- gravitational effects;
- rotor hub motion;
- blade cyclic and collective inputs;
- ship motion; and
- aerodynamic forces,

where the first six items belong under the umbrella of dynamics. In the same study, airwake tests over the flight deck of a Royal Fleet Auxiliary ship and $1/120^{th}$ scale model were completed, in order to investigate the effect of relative wind direction and ship super structure on the characteristics of the flow. Time history flow measurements were taken with golf ball

anemometers over the full scale deck and with hot-wire anemometers in the wind tunnel. The results of the comparison of these two experiments show that wind tunnel tests can be used to estimate the trends in both steady and turbulent flow over the flight deck, as influenced by the bluff body presence of the ship. This airwake study did not include the effect of the body of the helicopter on the airwake, an assumption that is deemed to be valid over the majority of the rotor disc plane. A dynamic blade model that was used to calculate blade deflections during engage and disengage was also developed.

Newman continued the research with a subsequent publication in 1990 [62] that describes the dynamic model in depth. The semi-rigid rotor of a Lynx helicopter was modelled using modal superposition. The model uses four modes in the flapwise direction only, and includes the effects of centrifugal force due to rotor rotation, gravity, and a degree of torsional deflection that can be added to each flapping mode. The solution was advanced numerically through time using a fourth-order Runge-Kutta integrator. A representative rotor engage profile given by a hyperbolic tangent function was assumed, based on the idea that constant torque is applied and rotor drag varies as the square of speed. The disengage profile was generated assuming the rotor decelerates due to aerodynamic drag and friction before the brake is applied.

A separated flow model was used to include the possibility of large and reverse flow angles of attack in the calculation of aerodynamic forces. While experimental airwake data were also used to generate results, Newman observed that the up- and downdrafts created with a wind direction of 90° relative to the longitudinal axis of the ship (beam winds) were significant for causing upward and downward blade excursions at low rotational speeds. This is called "the cliff edge effect". As such, Newman proposed some simplified airwake models, which involved superimposing an up- and downdraft profile over a simple horizontal flow profile in the rotor disc plane. These simplified profiles are shown in Figure 2.4. They were intended to be numerically efficient while capturing the important time-averaged flow effects in beam wind conditions.

Newman further advanced his blade sailing study to include examining the effect of blade articulation on the phenomenon [63]. He modified his model to include flap and

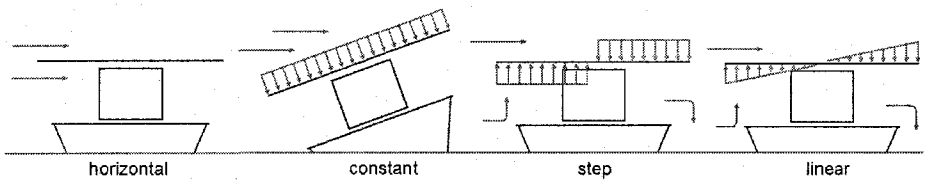

Figure 2.4: Deterministic airwake models proposed by Newman.

droop stops, represented by linear springs that were applied at a short distance from the articulated flap hinge when the stop contact angle is exceeded. In this study, it was shown that the interaction between blade kinetic energy and blade flexibility is important for determining the maximum deflection the blade will achieve when it impacts the stops. By increasing the number of modes included in the simulation from one to four, the transfer of kinetic energy to potential energy in each mode was demonstrated. This work also included the comparison of simulated and experimental blade deflection results for a full scale Puma helicopter during rotor engage and disengage. This validation showed that the main characteristics of the blade response were reproduced in the simulation. The effect of sinusoidally varying ship roll, with a period of 10 seconds and an amplitude of 7.5°, on the flow in the rotor disc was included.

In 1995, Newman conducted a validation experiment to compare hinge angle results from his simulation with the measured value from an experimental rotor placed in a wind tunnel [64]. The tests were conducted on a Kalt-Cyclone model, which is a teetering two-bladed rotor. Some tests were conducted with both blades; others were conducted with one blade removed and replaced with a counterbalance weight in order to isolate the articulated flapping behaviour of one blade. The rotor was engaged with constant acceleration, held at full speed, and then disengaged with constant acceleration. The model was attached to a ship deck model approximating the size and cross-sectional shape of a Rover Class Royal Fleet Auxilliary ship with a Westland Lynx helicopter. This deck was used to approximate the airwake profile above this ship in beam winds.

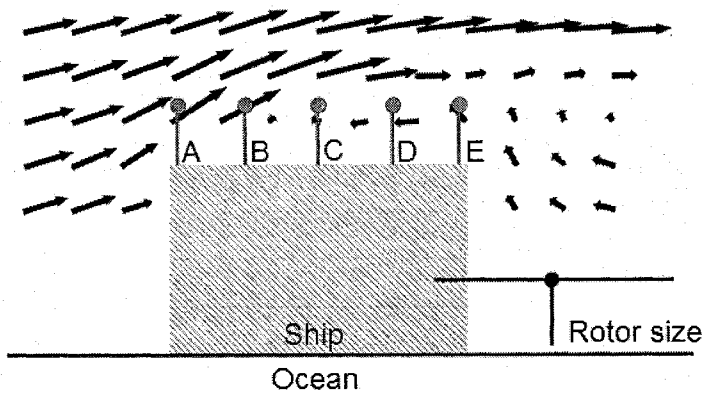

Figure 2.5: Experimental (scaled) airwake test results [64].

In addition to rotor tests, laser doppler anemometer measurements were taken of the airwake in the plane of the ship deck cross-section. The results, illustrated in Figure 2.5, showed two important airwake characteristics. First, updrafts are created at the windward deck edge as the wind flows over the ship structure. At the leading edge, the flow exhibits velocities comparable to the freestream, if at an angle. Along the deck, the flow slows and transitions to a turbulent separation bubble, which includes slow, turbulent, and reversing flows. The transition between the separation bubble and the horizontal freestream above the bubble is a shear layer.

The tests were conducted with the rotor stationed at various deck positions laterally, as shown in Figure 2.5. Centred at position A, the rotor sees mainly updrafts in "clean" air, at position B and to some extent C, the rotor spins through the shear layer, and at positions D, and E, the rotor lies mainly in turbulent and reversing flow. For this reason, the largest blade deflections were observed for position B, then A, and then C. Positions D and E exhibited comparatively small blade deflections.

The following conclusions about blade sailing result from the studies completed by Newman.

- The largest blade deflections are observed at low rotor speeds, in the range of about

4% to 14% NR.

- Articulated blades exhibit larger maximum blade deflections than semi-rigid rotors due to droop stop impacts.
- In high-wind conditions (50 - 60 kn), Lynx and Sea King blades can undergo deflections large enough to cause tailboom strike.
- Wind tunnel scale model tests to measure airwake can be taken as representative of the airwake on an equivalent full-scale ship.
- Beam winds are a significant direction for blade sailing, and the beam wind airwake over a simple ship deck is characterized by a shear layer and recirculation zone.
- The position of the helicopter on the flight deck affects the magnitude of blade deflections, and also the type of aerodynamic modelling that is appropriate.

Recently, Jones, working with Newman, investigated the use of a trailing-edge flap to control the blade sailing phenomenon [65]. Using the dynamic model described above and another, in which the flap and droop stops were modelled as pin-type, they showed that trailing edge flaps can be effective at reducing the deflections and bending moments associated with the blade sailing phenomenon.

2.4.3 Pennsylvania State University

Another major study of the blade sailing phenomenon was started in the 1990s at Pennsylvania State University by E. C. Smith, J. A. Keller and W. P. Geyer Jr. This study builds on the groundwork laid by Newman, and further explores modelling techniques and the contributors to blade deflection.

The characteristics, validations, and resulting studies are covered in References [48, 66, 67, 68]. The dynamic model is a linear finite element model, which includes flap and torsional blade flexibility. It has one blade, semi-rigid or articulated, connected to a helicopter that sits on the deck of a ship undergoing six degrees of representative ship motion. The

ship motion effect influences only the aerodynamics but not the system inertia. The method accommodates many system features and blade properties that could vary as a function of blade radius, including inertial properties, elastic properties, centre of gravity and quarter chord offset, pre-twist and pitch link flexibility. The model includes droop and flap stops, modelled as variable stiffness rotational springs applied at the articulated hinge joint. The contribution of each system component: blade strain energy, blade kinetic energy, pitch link stiffness, droop stop stiffness, and aerodynamic loads, are incorporated into the equations of motion using Hamilton's principle. The blade is then discretized by the finite element method, where flap deformations are represented by cubic shape functions and torsional deformations are given by quadratic shape functions. The simulation was advanced through time using a fourth-order Runge-Kutta integrator. Due to the stiff nature of the problem when the beam comes into contact with the droop and flap stops, a modal swapping technique was used.

The simulation developed under this study includes Newman's suggested deterministic airwake models, and blade element calculation of aerodynamic forces with unsteady effects and dynamic stall. Two rotor engage and disengage profiles, as used in this research, are shown in Figure 2.6.

In 1996 [67], the dynamic model was modified to include flap stops and flap damping. Validation cases were run to compare the simulated blade deflections with the experimental results at model scale generated in Reference [64]. The results agreed best for deck location A, which is expected given that the deterministic airwake models do not model the flow properly inside the deck separation bubble. The results for deck position A also showed differences when the unsteady model was used and compared with the quasi-steady aerodynamic model. The blade natural frequency with rotor speed response was also validated, using experimental data.

In this same study, the H-46 Sea Knight was modelled and some parametric studies were completed to understand the effects of certain contributors on the maximum downward tip deflection. A short description of each study and the general conclusions are presented herein below.

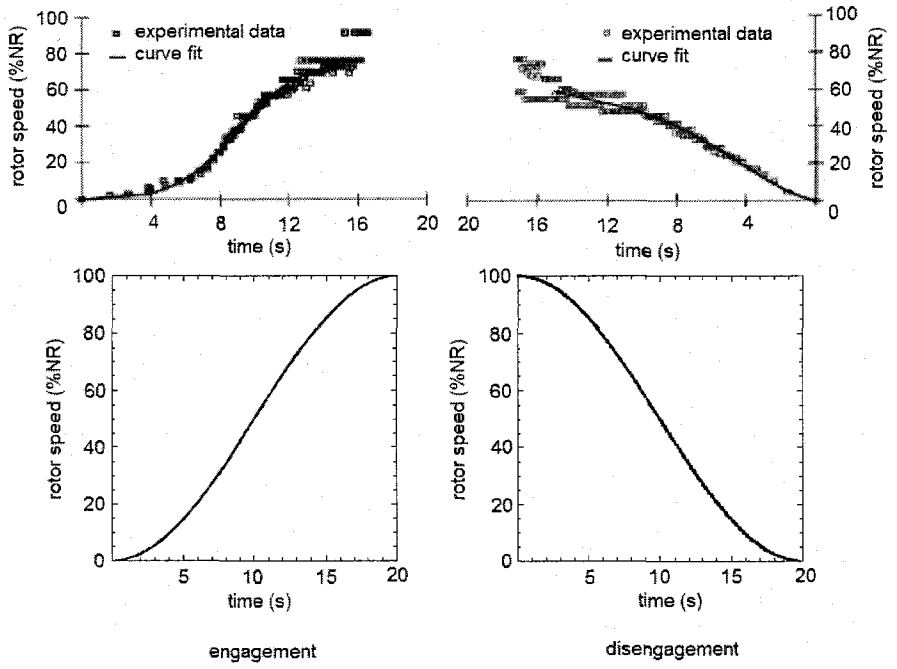

Figure 2.6: Measured (top) and assumed (bottom) rotor engage and disengage profiles [48].

Flap Damping Study: investigated the maximum downward blade tip deflection predicted when a rotational damper was applied at the flap hinge. A variety of damping values and stop contact angles were examined. It was shown that larger blade deflections are generated by undamped blades for larger stop contact angles, and that the dampers were also more effective for larger stop contact angles.

Start Azimuth Angle Study: investigated the effect of the starting azimuthal angle relative to the wind direction on the azimuth at which the largest downward blade deflection was observed. This study showed that engaging with wind approaching the aft of the ship (100 - 260 degrees relative to the ship centre line) ensures the azimuth of maximum downward deflection does not occur over the helicopter fuselage. This result is independent of starting azimuthal angle.

Engage Envelope Study: investigated the impact of control inputs on the envelope for safe engage operations based on the conditions for safe engagement as laid out by

the American Navy. It was shown that a lateral cyclic input of 2° reduces the safe operation zone by 20.7%, and thus demonstrates the sensitivity of the safe engage envelope to minor changes in control inputs.

Rotor Profile Study: investigated the sensitivity of maximum downward tip deflection to engagement speed and disengagement brake application. The study showed that faster profiles lead to a lower possibility of tunnel strike, and that the maximum downward blade tip deflection is insensitive to the speed at which the rotor brake is applied during disengage.

Aerodynamic Model Study: investigated the maximum downward tip deflection predicted using the quasi-steady and unsteady aerodynamic models with and without blade torsion for the uniform and linear deterministic models. This study showed that similar tip deflections were predicted with all models, but that differences became more pronounced at higher wind speeds.

Ship Motion Study: investigated the effect of changing ship roll amplitude and period on the magnitude of maximum downward blade tip deflection. This study showed that the tip deflection was sensitive to the roll amplitude, in its effect on the airflow relative to the rotor disc, but not to the period at which the rolling motion occurs.

In 1999, Smith and Keller improved their airwake model using a CFD code called PUMA (Parallel Unstructured Maritime Aerodynamics) [69], and examined the rotor deflections at two locations on the flight deck. These were then compared with results for horizontal flow only and for a linear deterministic airwake model, both of which are shown in Figure 2.4. They showed that the simple deterministic airwake distributions led to under-predictions in the tip deflections by as much as half, when compared to deflections generated using the computationally generated airwake.

In this work, the practice of increasing the blade collective for rotor speeds less than 20% NR was examined in its effectiveness as a blade sailing control procedure. Here, increasing the collective has the effect of coupling the structural flap and lead-lag stiffnesses

such that the blade is stiffer in the vertical direction. This practice was shown to decrease predicted blade deflections, but not the structural moments.

Also in 1999, Keller and Smith conducted a validation experiment to examine the behaviour of a Froude-scaled model of an H-46 blade during non-rotating droop stop impacts from drop tests [70, 71]. This work gives blade hinge angle, tip deflection, and strain values during the drop test, and has proven to be an important source of validation for beam and droop stop behaviour. The work in this paper also examined the importance of non-linear beam modelling. The non-linear terms were shown to influence the results by 4% for the cases given in the paper.

Smith and Keller have also been involved in expanding blade sailing research for use with gimballed rotors, which are short and highly twisted [72], such as those found on the V-22 Osprey. They have looked into controlling the blade deflection in gimballed rotors using swash plate actuation [73].

2.4.4 Georgia Institute of Technology

In 2001, C. L. Bottasso and O. A. Bauchau demonstrated the applicability of their multibody modelling techniques to the blade sailing phenomenon [74]. Their model was constructed from a library of pre-validated finite element-based flexible bodies, which allowed the assembly of many rotor and hub configurations and components, with the possibility of modelling the complexities of the hub linkages and control components. Their element library includes a variety of joint options for interconnecting the bodies, and they discussed modelling droop and flap stops from the point of view of contacting bodies.

They have validated their model against data published by Keller, Geyer, and Smith [70, 68]. They also simulated engage and disengage sequences, and showed the interplay between droop stop impacts and large downward blade deflections.

2.4.5 Advanced Rotorcraft Technology, Inc.

H. Kang, C. He, and D. Carico have approached the blade sailing issue from yet another direction [75]. They modelled the ship-helicopter-rotor system using a commercial software package, FLIGHTLAB, which allows the combination of available finite element body types. FLIGHTLAB, developed by Advanced Rotorcraft Technology, Inc., also has a built-in aerodynamics model that includes a wide variety of aerodynamic effects. Unsteady and quasi-steady blade element models were used to compute the airloads while the Peters and He [55, 56] finite state dynamic wake model was selected for modelling the rotor wake. Their model configuration includes droop and flap stop modelling, with stop extension and retraction; landing gear models, which allow flexible contact between the ship deck and the helicopter; and representative ship motion, which affects the inertial response of the helicopter blades.

The FLIGHTLAB simulation was interfaced with CFD ship airwake data that gave non-uniform and unsteady airflow as a function of ship position over the flight deck. The solution of the combined system is solved numerically through time.

This study involved simulating the validation tests that Newman published in Reference [64]. The agreement is good. They then modelled an H-60 helicopter operating from the deck of a Landing Helicopter Assault ship, and examined the effect of deck location, ship motion, and ship motion period on the blade dynamic response and landing gear compression during blade engage.

The following conclusions were drawn from this study.

- Landing gear flexibility combined with ship motion effects affect the magnitude of blade downward deflections during engage sequences.
- Shorter ship motion periods tend to increase the amplitude of blade response.
- Deck location affects the blade sailing phenomenon.

2.4.6 Applied Dynamics Laboratory, Carleton University

The blade sailing phenomenon has been studied in the Applied Dynamics Laboratory at Carleton University, and is the subject of this thesis. The research programme encompassed herein had two objectives:

1. to study the contributors to the blade sailing phenomenon individually and collectively; and

2. to develop validated modelling tools for this purpose.

The contributors have been studied using a series of numerical models, which are shown schematically in Figure 2.7. The research is based on the following claims, which are supported by the literature review.

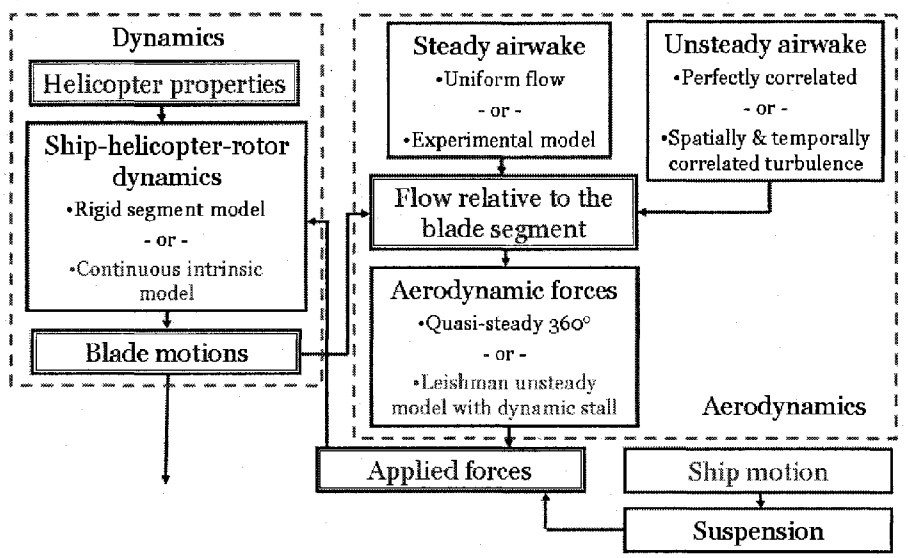

Figure 2.7: Flow-chart of numerical models used in this research programme (dashes box - group of models; single solid box - numerical model; double solid box - simulation quantity).

- Rigid-segment dynamic models have the potential to model flexible systems well, provided an adequate number of segments are used. They can be used to model non-linear dynamic systems using closed-form equations.

- Scaled experimental methods are an efficient and accurate way to examine the time-averaged and unsteady characteristics of a typical ship airwake in beam winds.
- Models for representative ship motion and helicopter blade aerodynamics exist, and shall therefore be employed in this research without further development.
- The combination of non-linear dynamics, representative ship motion, and representative ship deck aerodynamics, including turbulence and the effect of ship motion on the airwake, are critical for the complete study of the blade sailing phenomenon.

The research objectives have been met, and the details are covered in the subsequent chapters of this thesis.

Dynamics Modelling: covers the development of a versatile rigid-segment ship-helicopter-rotor dynamic model and discusses the validation of the components of the dynamic model (Chapter 3).

Airwake Modelling: covers the development of an airwake model for a typical frigate in beam winds using experimentally obtained data, including both steady and unsteady components, and the effect of ship motion (Chapter 4).

Experimental Validation: details the experimental exploration of the combined effects of dynamics, ship motion, and aerodynamics using a Froude scaled two-bladed rotor model and discusses the validation of the developed tools using the gathered data (Chapter 5).

Blade Sailing Results: shows some blade deflection results for a typical maritime helicopter in blade sailing conditions (Chapter 6).

Some of the work has already been published or presented. These publications are listed here.

Reference [76]: lays out the basics of the research programme, including initial development of models for each contributor.

Reference [77]: discusses the effect of ship motion on the quasi-steady component of the ship airwake in beam winds, as shown by experimental data.

Reference [32]: gives an overview of the contributing factors to blade sailing, focussing on experimental results for turbulent correlation and ideas for modelling spatially and temporally correlated turbulence.

Reference [78]: describes the challenges of the dynamic formulation for a planar case and includes initial study of the effect of ship motion on blade behaviour.

Reference [79]: expands the methodology given in [78] into 3D, describes the model components, and gives dynamic validation cases.

Reference [80]: discusses the validation experiment and gives experimental results.

The relevant content of these publications are either referred to or reproduced in the subsequent chapters of this thesis.

This blade sailing research project is part of a comprehensive research program in the Applied Dynamics Laboratory at Carleton University focussed on shipboard helicopter operation. So far, two theses have focussed on blade sailing. One is this work, which focussed on modelling and identification of the blade sailing phenomenon. The second has been conducted in parallel by another Ph.D. candidate, F. Khouli, with a focus on structural modelling, continuous beam modelling, and blade sailing control strategies. Some of the publications representing the collaborative work that has been carried out under this complimentary research programme are listed here.

Reference [81]: deals with the calculation of stiffness properties for composite rotor blade.

Reference [82]: discusses an efficient numerical solver for use with a continuous non-linear beam model.

Reference [83]: investigates the authority of active twist for blade sailing control in the airwake environment.

Table 2.2: Summary of the modelling approaches of blade sailing initiatives.

Study	Dynamics	Ship Motion	Airwake	Turbulence
Southampton	Modal superposition	Sinusoidal, aero effects only	Experimental/ simplified	None
Pennsylvania State	Linear finite element	Sinusoidal, aero effects only	Simplified/ CFD	Simple
Georgia Tech	Finite element multi-body	None	Simplified	None
Advanced Rotorcraft	FLIGHTLAB modal	Representative	CFD	None
Carleton/ NRC	**Non-linear rigid-segment**	**Representative, aero and inertial**	**Experimental**	**Experimental correlated**
Carleton	Continuous non-linear	Representative, aero and inertial	Experimental	Experimental simple

Reference [84]: discusses blade sailing control strategies and shows results in the form of SHOLs.

The main components of all the blade sailing studies, including the current research programmes at Carleton, are summarized in Table 2.2. The research covered by this thesis is shown in bold. The table highlights the important aspects of blade sailing modelling: dynamics, ship motion, and aerodynamics, which each study addresses in some fashion. However, the research programmes at Carleton University are currently the only studies that have included the combination of non-linear dynamics, representative ship motion, and representative ship deck aerodynamics, including turbulence and the effect of ship motion on the airwake.

Chapter 3

Dynamics Modelling

In an effort to model the dynamic and aerodynamic interactions of helicopter blades in a sailing state, a rigid body approach was employed. Fundamentally, this approach draws on the idea that a flexible continuous system can be modelled using a system of discrete rigid bodies and flexible elements, provided that the properties assigned to the discrete system are representative of the real system, and that an adequate number of appropriate degrees of freedom are included. The approach supports incorporation of geometric non-linearities and modal coupling.

As with any modelling exercise, the ship-helicopter-rotor model used in this research is intended to model carefully the effects that are important while optimizing engineering and computing time associated with using the developed model. The rigid body model was designed according to the priorities summarized in the following statements, which deal specifically with the system dynamics.

- Blade flap is the motion of greatest concern, since it is the primary motion in blade sailing. Torsion, to the extent that it affects aerodynamic loads and thus flap is also of concern. This includes flap-twist coupling. Lead/lag, while included in the model, is of lesser concern.

- The small angle assumption for blade flap deformation is invalid since blade sailing deflections can be severe. If the local orientation angles of each blade segment are small, then a linear approximation of each local transformation matrix could be used

while maintaining the overall ability of the model to capture large displacements. This approximation was not utilized in order to avoid the modelling restriction that the number of rigid segments be sufficient to maintain each local angle in the linear range.

- Blade sailing occurs at low rotor speeds exhibiting mainly rigid body and first elastic mode vibration of the rotor blades. Those behaviours prevalent in the range of 0.1 to 3 Hz are carefully included, whereas those acting at greater than 10 Hz have been deemed to be of lesser concern.
- Blade extension flexibility was not modelled, as the extension is minimal at low rotor speeds.
- Model flexibility, in the sense that all system properties are user-defined, is of utmost importance. Efforts were made to allow a wide range of options and operating conditions.
- Time-domain results are desired.

3.1 Nomenclature and Definitions

Before describing the model, it is prudent to address some nomenclature that will be used throughout the dynamic analysis.

3.1.1 Matrix and Vector Notation

The model is composed of a series of rigid bodies whose locations and orientations are expressed by a series of vectors, defined in one of a number of reference frames. The relative orientations of reference frames are defined by Bryan angles, which are a specific set of Euler angles defined by rotations around the (x, y, z) axes of the previous coordinate systems respectively [85]. The quantity $\{\mathbf{r}_{a_B}\}$ is the position of point a defined in coordinate system B. If the subscript a identifies the coordinate system A, then the vector refers to the origin of coordinate system A in B. The quantity $\{\omega_{A_B}\}$ gives the angular velocities of the body in local coordinates. Bryan angles for reference frame A in frame B are defined

herein by the notation $\{\varepsilon_{A_B}\}$. First, second, and third vector components are respectively indicated with bracket notation, as for example, $\varepsilon_{A_B}(1)$, $\varepsilon_{A_B}(2)$, and $\varepsilon_{A_B}(3)$.

Transformation matrices are of the form $[\mathbf{R}_{AB}]$ and refer to a rotational transformation from the A coordinate system to the B coordinate system. Transformation matrices are functions of the Bryan angles between reference frames A and B as

$$[\mathbf{R}_{AB}(\{\varepsilon_{A_B}\})] = \tag{3.1}$$

$$\begin{bmatrix} \cos\varepsilon_{A_B}(2)\cos\varepsilon_{A_B}(3) & -\cos\varepsilon_{A_B}(2)\sin\varepsilon_{A_B}(3) & \sin\varepsilon_{A_B}(2) \\ \cos\varepsilon_{A_B}(1)\sin\varepsilon_{A_B}(3)+ & \cos\varepsilon_{A_B}(1)\cos\varepsilon_{A_B}(3)- & -\sin\varepsilon_{A_B}(1)\cos\varepsilon_{A_B}(2) \\ \sin\varepsilon_{A_B}(1)\sin\varepsilon_{A_B}(2)\cos\varepsilon_{A_B}(3) & \sin\varepsilon_{A_B}(1)\sin\varepsilon_{A_B}(2)\sin\varepsilon_{A_B}(3) & \\ \sin\varepsilon_{A_B}(1)\sin\varepsilon_{A_B}(3)- & \sin\varepsilon_{A_B}(1)\cos\varepsilon_{A_B}(3)+ & \cos\varepsilon_{A_B}(1)\cos\varepsilon_{A_B}(2) \\ \cos\varepsilon_{A_B}(1)\sin\varepsilon_{A_B}(2)\cos\varepsilon_{A_B}(3) & \cos\varepsilon_{A_B}(1)\sin\varepsilon_{A_B}(2)\sin\varepsilon_{A_B}(3) & \end{bmatrix}$$

The local angular velocity vector, $\{\omega_{A_B}\}$, can be calculated from the matrix $[\mathbf{R}_{\omega A}]$ using

$$\{\omega_{A_B}\} = [\mathbf{R}_{\omega A}(\varepsilon_{A_B})]\,\{\dot{\varepsilon}_{A_B}\} \tag{3.2}$$

which is also a function of the local Bryan angles,

$$[\mathbf{R}_{\omega A}(\{\varepsilon_{A_B}\})] = \begin{bmatrix} \cos\varepsilon_{A_B}(2)\cos\varepsilon_{A_B}(3) & \sin\varepsilon_{A_B}(3) & 0 \\ -\cos\varepsilon_{A_B}(2)\sin\varepsilon_{A_B}(3) & \cos\varepsilon_{A_B}(3) & 0 \\ \sin\varepsilon_{A_B}(2) & 0 & 1 \end{bmatrix} \tag{3.3}$$

As a final definition, unit vectors u_1 through u_3, defined as

$$\{\mathbf{u}_1\} = \begin{Bmatrix} 1 \\ 0 \\ 0 \end{Bmatrix}, \quad \{\mathbf{u}_2\} = \begin{Bmatrix} 0 \\ 1 \\ 0 \end{Bmatrix}, \quad \{\mathbf{u}_3\} = \begin{Bmatrix} 0 \\ 0 \\ 1 \end{Bmatrix} \tag{3.4}$$

are used in the dynamic equations.

3.1.2 Coordinate Systems and System Definition

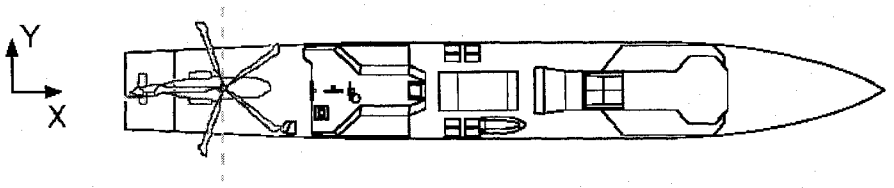

Figure 3.1: Ship-helicopter-rotor system being modelled.

The mathematical model developed for this study could represent the ship-helicopter-rotor system shown in Figure 3.1. For this system, the helicopter is modelled as a single rigid body with the exception of the rotor blades, which are each divided into a series of rigid segments that are inter-connected by three-dimensional rotational springs. These rotational springs allow blade flexibility in the torsion, flap and lead/lag directions. Ship motion acts on the helicopter body through a suspension system model, and the ship airwake acts on the blade segments through an aerodynamic model. This dynamic model was first developed in the planar case, as shown in Figure 3.2, and then expanded into three dimensions.

Each blade segment is defined with properties $m_{(i,n)}$, the segment mass that is assumed concentrated at the mass centre of the segment, $\{\mathbf{r}_{b_{(i,n)_{B_{(i,n)}}}}\}$; and $[J_{b(i,n)_{B_{(i,n)}}}]$, the segment rotational inertia matrix about its centre of mass in the local reference frame. Each blade segment is connected to the last at point $\{\mathbf{r}_{B_{(i,n)_{B_{(i,n)}}}}\}$ in the coordinate system of the preceding segment with a rotational element of stiffness matrix, $[\mathbf{k}_{(i,n)}]$, and viscous rotational

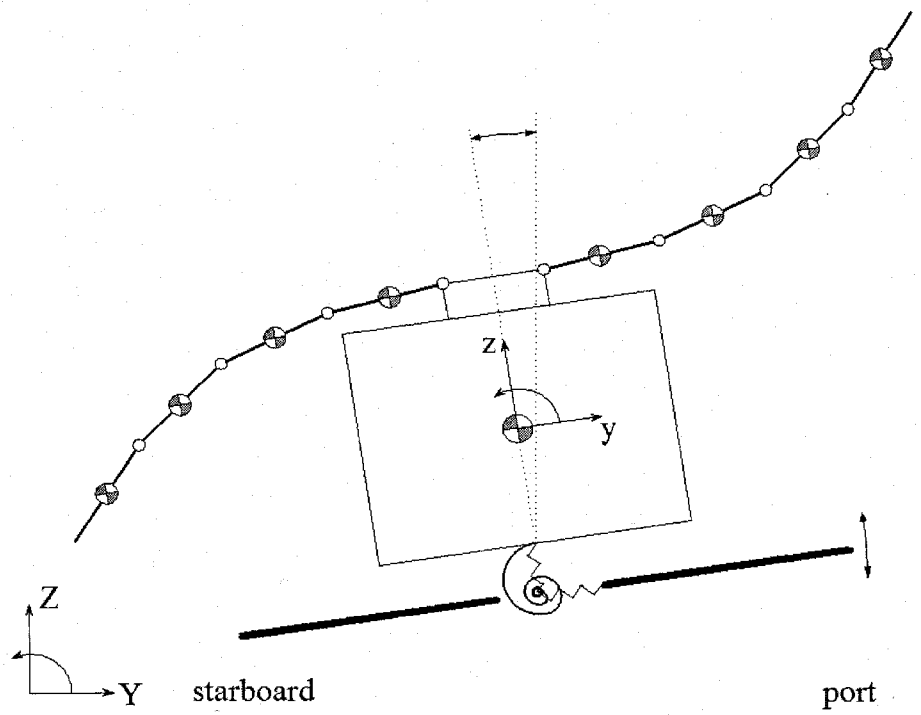

Figure 3.2: Schematic representation of planar ship-helicopter-rotor model.

damping coefficient matrix, $[\mathbf{c}_{(i,n)}]$. The subscripts (i, n) indicate that the quantity is specified for the ith segment on the nth blade, and that each $(i, n)^{\text{th}}$ quantity can be defined separately from the others. Since the properties can be individually assigned to each segment, they can be tuned to approximate closely any continuous and generally non-uniform rotor blade. As with variable finite element gridding, shorter segments can be used in areas of higher flexibility, while longer segments can be used in stiffer areas. The total number of segments and the individual geometrical and inertial properties of the blade segments are completely definable.

A number of different coordinate systems are employed in the model to keep track of the motion of each body. Figure 3.3 shows the approximate locations of the coordinate systems in use.

The global or inertial coordinate system, G, exists at the centre of the flight deck when

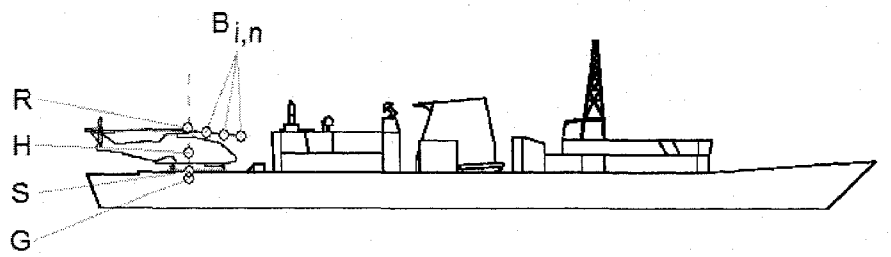

Figure 3.3: Dynamic model coordinate systems.

all ship motions, except for constant speed horizontal (X) translation, are zero. The global or inertial frame of reference translates with the ship at constant speed. All dynamic equations are ultimately expressed in the global frame of reference, and all quantities are transformed into global coordinates using appropriate transformations.

The ship frame of reference, S, is defined in the global coordinate system. The origin of the reference frame is located at the centre of the flight deck. The position of the ship frame is given by the ship motion algorithm and is in the form (surge, sway, heave), given by

$$\{\mathbf{r}_{S_G}\} = \begin{Bmatrix} X_S \\ Y_S \\ Z_S \end{Bmatrix} \tag{3.5}$$

where these are the relative displacements of the centre of the flight deck with respect to the global coordinate system. The orientation of the ship is given by the Bryan angles

$$\{\varepsilon_{S_G}\} = \begin{Bmatrix} \theta_{S_{roll}} \\ \theta_{S_{pitch}} \\ \theta_{S_{yaw}} \end{Bmatrix} \tag{3.6}$$

which are assumed equal to the orientations determined individually from Equation 2.9.

This assumption is inherent in linear ship motion theory, which is widely used. It is valid if only one rotation angle is expected to be large at a time [21]. If there is no ship motion, then the ship and global coordinate systems are coincident.

The helicopter coordinate system, H, is also defined relative to the global system. The coordinate system has its origin at the helicopter centre of mass, and this position is defined by a position vector

$$\{\mathbf{r}_{H_G}\} = \begin{Bmatrix} X_H \\ Y_H \\ Z_H \end{Bmatrix} \tag{3.7}$$

in global coordinates that tracks the position of the helicopter centre of mass. The orientation is given by Bryan angles

$$\{\varepsilon_{H_G}\} = \begin{Bmatrix} \theta_{H_{roll}} \\ \theta_{H_{pitch}} \\ \theta_{H_{yaw}} \end{Bmatrix} \tag{3.8}$$

The rotor frame of reference, R, is a coordinate system that defines the axis of the rotor disc and allows the blades to turn together. It is defined in the helicopter frame of reference, and the origin is located at the centre of the rotor hub in line with the plane of the blades. The position of the origin, $\{\mathbf{r}_{R_H}\}$, is fixed. The first two Bryan angles, ε_1 and ε_2, allow the axis of rotor rotation to be different from the z axis of the helicopter. These angles are defined by the geometry of the aircraft and are fixed. The final Bryan angle, σ, allows the rotor hub to be turned in a manner that is representative of the engage or disengage profiles of the helicopter. The magnitude, velocity, and acceleration of this quantity are defined in

the model, and are functions of time as given by

$$\{\varepsilon_{R_H}\} = \begin{Bmatrix} \varepsilon_1 \\ \varepsilon_2 \\ \sigma(t) \end{Bmatrix} \tag{3.9}$$

The blade reference frames, $B_{(i,n)}$, are defined in the rotor reference frame, R, if $i = 1$, or in the previous blade segment reference frame, $B_{i-1,n}$, where i represents the blade segment number starting with 1 at the inboard segment. Each blade reference frame origin is located at the joint where the segment attaches to the frame of reference in which its coordinate system is defined. The discrete elastic joint origin should be defined such that it is coincident with the local shear centre of the blade. The position vectors of each subsequent segment reference frame are defined independently and in three-dimensional space. Thus, the elastic axes and the joints need not lie along a straight axial line, and the joints do not need to be equidistant. The number of discrete segments is defined by the analyst.

Since the blade segments are rigid, the position vectors to the origins of each subsequent reference frame, $\{\mathbf{r}_{B_{(1,n)_R}}\}$ and $\{\mathbf{r}_{B_{(i,n)_{B_{(i-1,n)}}}}\}$, are fixed. The segments are, however, allowed to rotate relative to one another in three degrees of freedom at each joint. Each blade reference frame has a set of Bryan angles that track blade bending, lead-lag, and torsion in time. The Bryan angles that define the orientation of each segment are

$$\left\{\varepsilon_{B(i,n)_{B(i-1,n)}}\right\} = \begin{Bmatrix} \phi_{B(i,n)} \\ \tau_{B(i,n)} \\ \psi_{B(i,n)} \end{Bmatrix} \tag{3.10}$$

The rigid blade segment coordinate systems, $B_{\text{rigid}(i,n)}$, define the undeflected shape of the blade. They are defined in the previous coordinate system, like the systems $B_{(i,n)}$;

however they are based on the Bryan angles

$$\left\{\varepsilon_{o_{B(i,n)}}\right\} = \left\{\begin{array}{c} o_{x(i,n)} \\ \\ o_{y(i,n)} \\ \\ o_{z(i,n)} \end{array}\right\} \tag{3.11}$$

which are the "zero" Bryan angles for the $(i,n)^{\text{th}}$ segment. These coordinate systems are used to calculate the correct spring energy for a given deformation, since the spring energy is defined to be zero when the coordinate system $B_{(i,n)}$ is coincident with $B_{\text{rigid}(i,n)}$. At the hinge joint, the coordinate system $B_{\text{rigid}(i,n)}$ is also used to define the directions of the flap and/or lead/lag hinges, which are coincident with the rigid y and z axes if the blade is articulated. The coordinate system is used to resolve the component of hinge force acting in the plane perpendicular to the hinge axis.

The axial extension is known to be a dynamic variable of important consideration for flexible bodies rotating at high velocities. In addition to small axial displacements that can affect the final blade tip location, the axial extension is known to change slightly the torsional rigidity of blades. Axial extension can also be coupled with torsion and other blade motions in composite beams thus modifying the aerodynamic angle of attack for high rotor speeds. Discrete axial flexibility could be included in a similar manner as the rotational flexibility, as shown in Reference [14], without rendering the equations of motion unsolvable. Since the blade sailing phenomenon is believed to occur at low rotational speeds [less that 50% normal operating speed (NR)], and axial forces vary with the square of rotational speed, the axial extension effects are believed to be insignificant. Axial extension has therefore not been included in the current version of the dynamic model.

3.1.3 Degrees of Freedoms

The number of degrees of freedom, n_{dof}, required to completely define the helicopter motion is given by

$$n_{\text{dof}} = 6 + n_b(3n_s - 1) \tag{3.12}$$

where the constant 6 accounts for the translational and rotational degrees of freedom of the helicopter body, and n_s and n_b are the number of blade segments and the number of blades respectively. Each blade has three degrees of freedom per blade segment: torsion, flap, and lead/lag, with the exception of the first joint, which only has two degrees of freedom. This is because the "torsion" at the first joint is defined by the collective and cyclic inputs, which allow the pilot to control the blade root angle. The position portion of the state vector for the system is

$$\begin{aligned}[X_H\ Y_H\ Z_H\ \theta_{H_{roll}}\ \theta_{H_{pitch}}\ \theta_{H_{yaw}}\ \phi_{B(2,1)}\ \phi_{B(3,1)}\ \cdots\ \phi_{B(i,1)}\ \phi_{B(2,2)}\ \cdots \\ \phi_{B(i,n)}\ \tau_{B(1,1)}\ \tau_{B(2,1)}\ \cdots\ \tau_{B(i,n)}\ \psi_{B(1,1)}\ \cdots\ \psi_{B(i,n)}]\end{aligned} \tag{3.13}$$

The cyclic and collective angles are defined as functions of time in the model. Ship motion, $[X_S\ Y_S\ Z_S\ \theta_{S_{roll}}\ \theta_{S_{pitch}}\ \theta_{S_{yaw}}]$, rotor rotation, σ, and hub-adjacent blade segment torsion angle, $[\phi_{B(1,1)}\ \cdots\ \phi_{B(1,n)}]$, are also predetermined functions of time and as a result do not have associated degrees of freedom.

3.1.4 Joint Nomenclature

The blades are composed of a series of connected rigid segments, and the flexible interface between these segments are referred to as "joints". The first joint is the interface between the rotor hub and the first segment. This joint is referred to as the "root". If the helicopter rotor being modelled is of the articulated type, then the root joint is modelled as a hinge. Semi-rigid rotors have flexible root joints, but they do not have hinges.

3.2 Equations of Motion: General Form

The equations of motion for the ship-helicopter-rotor system were derived using Lagrange's Equation, given in Equation 2.1, where T is the system kinetic energy and U is the system potential energy. The left side of the equations contains all the conservative contributions to the system dynamics. The non-conservative contributions are part of Q_ν, which is the generalized non-conservative applied force associated with the νth degree of freedom. The resulting system of equations can be distilled into the matrix form of Newton's second law,

$$[\mathbf{M}]\{\ddot{\mathbf{q}}\} = \{\mathbf{f}\} \tag{3.14}$$

where the vector $\{\ddot{\mathbf{q}}\}$ contains the accelerations associated with each configuration coordinate. The equivalent mass matrix [78] is

$$[\mathbf{M}] = \tag{3.15}$$

$$\begin{bmatrix} \frac{\partial}{\partial \ddot{q}_1}\left(\frac{d}{dt}\left(\frac{\partial T}{\partial \dot{q}_1}\right)\right) & \cdots & \frac{\partial}{\partial \ddot{q}_{n_{\text{dof}}}}\left(\frac{d}{dt}\left(\frac{\partial T}{\partial \dot{q}_1}\right)\right) \\ \vdots & \ddots & \vdots \\ \frac{\partial}{\partial \ddot{q}_1}\left(\frac{d}{dt}\left(\frac{\partial T}{\partial \dot{q}_{n_{\text{dof}}}}\right)\right) & \cdots & \frac{\partial}{\partial \ddot{q}_{n_{\text{dof}}}}\left(\frac{d}{dt}\left(\frac{\partial T}{\partial \dot{q}_{n_{\text{dof}}}}\right)\right) \end{bmatrix}$$

where the inner most derivative in each element is taken with respect to the velocity of the degree of freedom associated with the row, the second derivative is taken with respect to time, and the outermost derivative is taken with respect to the acceleration of the degree of freedom associated with the column.

The equivalent force vector is

$$\{\mathbf{f}\} = \begin{Bmatrix} Q_1 - \epsilon_1 \\ \vdots \\ Q_{n_{\text{dof}}} - \epsilon_{n_{\text{dof}}} \end{Bmatrix} \tag{3.16}$$

where the terms contained in ϵ_ν come from all the terms on the left-hand side of Lagrange's Equation that do not depend on the second derivative of any configuration coordinate and thus are not a part of the equivalent mass matrix. These contributions are largely the results of potential energy and of centripetal and Coriolis forces from the geometric non-linearities preserved in the kinetic energy expressions. The terms in Q_ν come from the non-conservative contributions contained on the right hand side of Lagrange's Equation.

Both $[\mathbf{M}]$ and $\{\mathbf{f}\}$, which were extracted from Lagrange's equation symbolically, depend on known quantities $\{\mathbf{q}\}$ and $\{\dot{\mathbf{q}}\}$, the configuration coordinates and their derivatives (velocities). They are thus easily reevaluated at each time step. The equations can then be converted to a set of first order differential equations and the dynamic solution can be advanced numerically through time by an appropriate numerical integrator. The appropriate type of integrator varies depending on the numerical stiffness of the system once it has been defined with specific system properties. Explicit integrators, such as Runge-Kutta methods [86], handle non-stiff systems efficiently. Implicit integrators are more appropriate for stiffer systems. Both have been used in this research.

3.3 Equations of Motion: Conservative Contributions

The definition of the system energy expressions is the first step toward applying Lagrange's Equation. The subsequent steps involve the derivation of long and complex expressions of derivatives with respect to various degrees of freedom and time. The kinetic and potential energy expressions are separated into parts to facilitate organization. The kinetic energy is split into four parts,

$$T = T_1 + T_2 + T_3 + T_4 \tag{3.17}$$

where the translational energy of the helicopter body is given by

$$T_1 = \frac{1}{2} m_H \left(\{\dot{\mathbf{r}}_{H_G}\} \cdot \{\dot{\mathbf{r}}_{H_G}\} \right) \tag{3.18}$$

which is also expressed as

$$T_1 = \frac{1}{2} m_H \left(\left(\{\mathbf{u}_1\}^T \{\dot{\mathbf{r}}_{H_G}\} \right)^2 + \left(\{\mathbf{u}_2\}^T \{\dot{\mathbf{r}}_{H_G}\} \right)^2 + \left(\{\mathbf{u}_3\}^T \{\dot{\mathbf{r}}_{H_G}\} \right)^2 \right) \tag{3.19}$$

to facilitate the derivative-taking that is part of the application of Lagrange's equation. The rotational energy of the helicopter body is

$$T_2 = \frac{1}{2} \{\omega_{H_G}\}^T [\mathbf{J}_{H_G}] \{\omega_{H_G}\} \tag{3.20}$$

the translational energy of the blade segments is

$$T_3 = \tag{3.21}$$

$$\sum_{n=1}^{n_b} \sum_{i=1}^{n_s} \frac{1}{2} m_{b_{(i,n)}} \left(\left(\{\mathbf{u}_1\}^T \left\{ \dot{\mathbf{r}}_{b_{(i,n)_G}} \right\} \right)^2 + \left(\{\mathbf{u}_2\}^T \left\{ \dot{\mathbf{r}}_{b_{(i,n)_G}} \right\} \right)^2 + \left(\{\mathbf{u}_3\}^T \left\{ \dot{\mathbf{r}}_{b_{(i,n)_G}} \right\} \right)^2 \right)$$

and the rotational energy of the blade segments is

$$T_4 = \sum_{n=1}^{n_b} \sum_{i=1}^{n_s} \frac{1}{2} \left\{ \omega_{b_{(i,n)_G}} \right\}^T \left[\mathbf{J}_{b_{(i,n)_G}} \right] \left\{ \omega_{b_{(i,n)_G}} \right\} \tag{3.22}$$

where

$$[\mathbf{J}_{H_G}] = [\mathbf{R}_{HG}] [\mathbf{J}_{H_H}] \tag{3.23}$$

is the inertia matrix of the helicopter body defined in the global reference frame and

$$\left[\mathbf{J}_{b_{(i,n)_G}} \right] = [\mathbf{R}_{HG}] \left[\mathbf{R}_{RH(n)} \right] \prod_{j=1}^{i} \left[\mathbf{R}_{B_{(j,n)} B_{(j-1,n)}} \right] \left[\mathbf{J}_{b_{(i,n)_{B_{(i,n)}}}} \right] \tag{3.24}$$

is the inertia matrix of the $(i,n)^{th}$ blade segment defined in the global reference frame.

The potential energy is given in three parts,

$$U = U_1 + U_2 + U_3 \tag{3.25}$$

where the gravitational potential energy of the helicopter body is

$$U_1 = g m_H \left(\{\mathbf{u}_3\}^T \{\mathbf{r}_{H_G}\} \right) \tag{3.26}$$

the gravitational potential energy of the blade segments is

$$U_2 = \sum_{n=1}^{n_b} \sum_{i=1}^{n_s} \left(g m_{b_{(i,n)}} \left(\{\mathbf{u}_3\}^T \left\{ \mathbf{r}_{B_{(k,n)_G}} \right\} \right) \right) \tag{3.27}$$

and the potential energy of the flexible connecting elements is

$$U_3 = U_{3_{flap}} + U_{3_{leadlag}} + \sum_{n=1}^{n_b} \sum_{i=2}^{n_s} \frac{1}{2} \left\{\theta_{(i,n)}\right\}^T \left[\mathbf{k}_{(i,n)}\right] \left\{\theta_{(i,n)}\right\} \tag{3.28}$$

where the details of U_3 are given in Section 3.3.2.

3.3.1 Derivation of General Conservative Expressions

Equations 3.19 through 3.27 depend on the globally defined positions and velocities of each rigid body. The global position and orientation of the helicopter body is given by Equation 3.7 and

$$\left\{\omega_{H_G}\right\} = \left[\mathbf{R}_{HG}\right]\left[\mathbf{R}_{\omega H}\right] \begin{Bmatrix} \dot{\theta}_{H_{roll}} \\ \dot{\theta}_{H_{pitch}} \\ \dot{\theta}_{H_{yaw}} \end{Bmatrix} = \left[\mathbf{R}_{HG}\right]\left[\mathbf{R}_{\omega H}\right]\left\{\dot{\varepsilon}_{H_G}\right\} \tag{3.29}$$

respectively.

The global position and angular velocity of the $(i,n)^{\text{th}}$ blade segment is given by

$$\left\{\mathbf{r}_{b_{(i,n)_G}}\right\} = \left\{\mathbf{r}_{H_G}\right\} + \left[\mathbf{R}_{HG}\right]\left\{\mathbf{r}_{R_H}\right\} + \sum_{k=0}^{i-1} \tag{3.30}$$

$$\left(\left[\mathbf{R}_{HG}\right]\left[\mathbf{R}_{RH(n)}\right] \prod_{j=1}^{k} \left[\mathbf{R}_{B_{(j,n)}B_{(j-1,n)}}\right] \left\{\mathbf{r}_{B_{(k,n)_{B_{(k-1,n)}}}}\right\}\right) +$$

$$\left[\mathbf{R}_{HG}\right]\left[\mathbf{R}_{RH(n)}\right] \prod_{j=1}^{i} \left[\mathbf{R}_{B_{(j,n)}B_{(j-1,n)}}\right] \left\{\mathbf{r}_{b_{(i,n)_{B_{(i,n)}}}}\right\}$$

and

$$\left\{\omega_{b_{(i,n)_G}}\right\} = \left[\mathbf{R}_{HG}\right]\left[\mathbf{R}_{\omega H}\right]\left\{\dot{\varepsilon}_{H_G}\right\} + \tag{3.31}$$

$$\left[\mathbf{R}_{HG}\right]\left[\mathbf{R}_{RH(n)}\right]\left[\mathbf{R}_{\omega R(n)}\right]\left\{\dot{\varepsilon}_{R_H}\right\} +$$

$$\sum_{k=1}^{i} \left(\left[\mathbf{R}_{HG}\right]\left[\mathbf{R}_{RH(n)}\right] \prod_{j=1}^{k} \left[\mathbf{R}_{B_{(j,n)}B_{(j-1,n)}}\right] \left[\mathbf{R}_{\omega B(k,n)}\right] \left\{\dot{\varepsilon}_{B(i,n)_{B_{(j-1,n)}}}\right\}\right)$$

respectively.

The expressions contain characteristic cascading sums and products that vary in size with blade and segment number. The derivation of the differentiated terms in Lagrange's equation has proven challenging owing to the variability of the equations, however a procedure has now been defined [78]. The procedure, initially defined using the two-bladed planar model shown in Figure 3.2, is described first; its expansion into three dimensions is addressed second.

The following equation, the expression for the kinetic energy arising from the horizonal component of velocity of the port blade for the planar model, is used to demonstrate the method of general differentiation. It is given by [78]

$$T_{X(1)} = \frac{1}{2}\sum_{i=1}^{n_s} m_{(i,1)} \tag{3.32}$$

$$\left(\left(\dot{Y}_H - v\,\dot{\theta}\,\sin\left(\theta + a\right) - \sum_{k=1}^{i}\left(\sin\left(\theta + \sum_{j=1}^{k}\phi_{(j,1)}\right)\right)\right.\right.$$

$$\left(\dot{\theta} + \sum_{j=1}^{k}\dot{\phi}_{(j,1)}\right) d_{(k,1)}$$

$$\left.\left. + \frac{1}{2}\left(\sin\left(\theta + \sum_{j=1}^{i}\phi_{(j,1)}\right)\right)\left(\dot{\theta} + \sum_{j=1}^{i}\dot{\phi}_{(j,1)}\right) d_{(i,1)}\right)^2\right)$$

where the planar orientation of the helicopter body is given by θ and the flap orientations of the blade segments are given by $\phi_{(i,1)}$. The length of each blade segment is given by $d_{(i,1)}$, and the centre of mass is assumed to act half way along the segment length. The quantity Y_H describes the horizontal position of the helicopter centre of mass, the quantity $(v\sin\left(\theta + a\right))$ gives the horizontal distance from the helicopter centre of mass to the blade attachment point, and a and v are geometrical constants defined in Reference [78].

One characteristic of this equation is three layers of embedded sums. The innermost layer, with index j, comes from the fact that the position and orientation of each blade segment depends on the angle of that segment and all others inboard of it. This cascading angle effect appears frequently in the kinetic and potential energy expressions, as well as in the final equations of motion. The middle layer, with index k, comes from the fact that

the velocity of each segment is the sum of that body's velocity relative to the other bodies plus the other bodies' velocities. The outermost layer, with index i, results from the fact that the energy from each segment must be summed to obtain a complete expression.

The challenge in differentiation arises from the fact that n_s, which is both the upper summation limit on the first sum and the number of segments in the port blade, is unknown. This means that all three layers of embedded sums are not defined including the innermost angle summation, which contains the degree of freedom $\phi_{l,1}$, with respect to which the derivative is required.

If both n_s and the index l with respect to which the derivative is required are selected prior to differentiation, then all three layers of sums become finite and defined, and the derivatives can easily be taken using a symbolic mathematics package such as Maple [87]. However, for a general solution, these quantities must remain unknown. It is impossible, then, for the software to evaluate $\frac{\partial Tx}{\partial \phi_{l,1}}$ because there is no way to indicate that $\phi_{l,1}$ is simply any one of the $(\phi_{j,1})$s. To this end, a rule for differentiating the expressions by hand was developed.

The problem lies in differentiating

$$S_2 = \sum_{j=1}^{i} \phi_{(j,n)} \tag{3.33}$$

with respect to an arbitrary $\phi_{(l,n)}$. By inspection, the derivative is

$$\frac{\partial S_2}{\partial \phi_{(l,n)}} = 1 \tag{3.34}$$

Furthermore, the derivative of

$$S_3 = \sum_{i=1}^{n_s} \sum_{j=1}^{i} \phi_{(j,n)} \tag{3.35}$$

is

$$\frac{\partial S_3}{\partial \phi_{(l,n)}} = \sum_{i=l}^{n_s} 1 = (n_s - l + 1) \tag{3.36}$$

which is perhaps less intuitive, since the lower index on the summation must be changed to l to obtain the correct expression. This is because any inner sums differentiated for $i < l$ do not contain the important quantity $\phi_{l,n}$, and therefore do not contribute to the final sum.

This phenomenon can be generalized in the following rule,

$$\frac{\partial}{\partial \phi_{(l_2,n)}} \left(\sum_{i=l_1}^{n_s} G_i \right) = \sum_{i=l_{max}}^{n_s} \frac{\partial G_i}{\partial \phi_{(l_2,n)}} \tag{3.37}$$

$$\text{where } l_{max} = \begin{cases} \max(l_1, l_2) & \text{if } G_i \text{ contains } \sum_{j=1}^{i} \phi_{(j,n)} \\ l_1 & \text{otherwise} \end{cases}$$

which shows how the indices of embedded sums must be updated depending on the form of G_i. As is consistent with the rules of differentiation, the chain rule applies when differentiating G_i.

This rule can be illustrated with the example

$$S_4 = \sum_{k=1}^{i} \left(d_{(i,n)} \sum_{j=1}^{k} \phi_{(j,n)} \right) \tag{3.38}$$

If $i = 3$,

$$\begin{aligned} S_4 = d_{(1,n)}(\phi_{(1,n)}) + d_{(2,n)}(\phi_{(1,n)} + \phi_{(2,n)}) \\ + d_{(3,n)}(\phi_{(1,n)} + \phi_{(2,n)} + \phi_{(3,n)}) \end{aligned} \tag{3.39}$$

The derivative with respect to the second angle is

$$\frac{\partial S_4}{\partial \phi_{(2,n)}} = d_{(2,n)} + d_{(3,n)} = \sum_{k=2}^{i} d_{(i,n)} \tag{3.40}$$

which can also be obtained from Equation 3.37.

Applying the rule shown, the derivative of Equation 3.32 with respect to any blade segment angle, is given by

$$\frac{\partial T_{X(1)}}{\partial \dot{\phi}_{(l,1)}} = \sum_{i=l}^{n_s} m_{(i,1)} \tag{3.41}$$

$$\left(\left(\dot{Y}_H - v\dot{\theta}\sin(\theta+a) - \sum_{k=1}^{i}\left(\sin\left(\theta+\sum_{j=1}^{k}\phi_{(j,1)}\right)\right)\right.\right.$$
$$\left(\dot{\theta}+\sum_{j=1}^{i}\dot{\phi}_{(j,1)}\right)d_{(k,1)}$$
$$\left.+\frac{1}{2}\left(\sin\left(\theta+\sum_{j=1}^{i}\phi_{(j,1)}\right)\right)\left(\dot{\theta}+\sum_{j=1}^{i}\dot{\phi}_{(j,1)}\right)d_{(i,1)}\right)$$
$$\left(-\sum_{i=l}^{i}\left(\sin\left(\theta+\sum_{j=1}^{i}\phi_{(j,1)}\right)\right)d_{(k,1)}\right.$$
$$\left.\left.+\frac{1}{2}\left(\sin\left(\theta+\sum_{j=1}^{i}\phi_{(j,1)}\right)\right)d_{(i,1)}\right)\right)$$

The extension of this method from the planar to the three-dimensional case is illustrated using the kinetic energy arising from the horizontal (X) component of velocity associated with the masses of the blade segments of blade n.

The kinetic energy expression for the three-dimensional case is given by

$$T_{X(n)} = \frac{1}{2}\sum_{i=1}^{n_s} m_{(i,n)}\left(\begin{bmatrix}1 & 0 & 0\end{bmatrix}\left\{\dot{\mathbf{r}}_{b_{(i,n)_G}}\right\}\right)^2 \tag{3.42}$$

where

$$\left\{\dot{\mathbf{r}}_{b_{(i,n)_G}}\right\} = \{\dot{\mathbf{r}}_{H_G}\} + \left[\dot{\mathbf{R}}_{HG}\right]\{\mathbf{r}_{R_H}\} + \sum_{k=1}^{i-1}$$
$$\left(\left[\dot{\mathbf{R}}_{HG}\right]\left[\mathbf{R}_{RH(n)}\right]\prod_{j=1}^{k}\left[\mathbf{R}_{B_{(j,n)}B_{(j-1,n)}}\right]\left\{\mathbf{r}_{B_{(k,n)}B_{(k-1,n)}}\right\}\right.$$
$$+\left[\mathbf{R}_{HG}\right]\left[\dot{\mathbf{R}}_{RH(n)}\right]\prod_{j=1}^{k}\left[\mathbf{R}_{B_{(j,n)}B_{(j-1,n)}}\right]\left\{\mathbf{r}_{B_{(k,n)}B_{(k-1,n)}}\right\}$$
$$+\sum_{h=1}^{k}\left[\mathbf{R}_{HG}\right]\left[\mathbf{R}_{RH(n)}\right]\left(\prod_{\alpha=1}^{h-1}\left[\mathbf{R}_{B_{(\alpha,n)}B_{(\alpha-1,n)}}\right]\right)$$
$$\left[\dot{\mathbf{R}}_{B_{(h,n)}B_{(h-1,n)}}\right]\left(\prod_{\beta=h+1}^{k}\left[\mathbf{R}_{B_{(\beta,n)}B_{(\beta-1,n)}}\right]\right)\left\{\mathbf{r}_{B_{(k,n)}B_{(k-1,n)}}\right\}\Bigg)$$
$$+\left[\dot{\mathbf{R}}_{HG}\right]\left[\mathbf{R}_{RH(n)}\right]\prod_{j=1}^{i}\left[\mathbf{R}_{B_{(j,n)}B_{(j-1,n)}}\right]\left\{\mathbf{r}_{b_{(i,n)}B_{(i,n)}}\right\}$$

$$+ [\mathbf{R}_{HG}] \left[\dot{\mathbf{R}}_{RH(n)}\right] \prod_{j=1}^{i} \left[\mathbf{R}_{B_{(j,n)}B_{(j-1,n)}}\right] \left\{\mathbf{r}_{b_{(i,n)}B_{(i,n)}}\right\}$$

$$+ \sum_{h=1}^{i} [\mathbf{R}_{HG}] \left[\mathbf{R}_{RH(n)}\right] \left(\prod_{\alpha=1}^{h-1} \left[\mathbf{R}_{B_{(\alpha,n)}B_{(\alpha-1,n)}}\right]\right)$$

$$\left[\dot{\mathbf{R}}_{B_{(h,n)}B_{(h-1,n)}}\right] \left(\prod_{\beta=h+1}^{k} \left[\mathbf{R}_{B_{(\beta,n)}B_{(\beta-1,n)}}\right]\right) \left\{\mathbf{r}_{b_{(i,n)}B_{(i,n)}}\right\}$$

where the rotational matrix $\left[\mathbf{R}_{B_{(1,n)}B_{(0,n)}}\right]$ given inside the product operators is equivalent to $\left[\mathbf{R}_{B_{(1,n)}R}\right]$.

The indices i and k represent the summation of equivalent phenomena in both Equations 3.32 and 3.42, and are subject to the index replacement rule shown in Equation 3.37. The summation of cascading angles, given by index j in Equation 3.32, which is responsible for causing the index replacement rule, appears in a slightly different form in Equation 3.42. In the three-dimensional case, the expressions for blade position, velocity, and angular velocity are derived in vector form and are given in the global coordinate system through a series of cascading matrix transformations, which are given by the product operator, also in index j.

Two cases that result from the extension of the procedure into three dimensions are worth mentioning. First, when the energy expressions are differentiated with respect to time, an additional summation appears, shown in Equation. 3.42)in index h. This results from the fact that the product rule must be applied to all the matrices in the cascading matrix product, since all depend on the variable time. When differentiating with respect to configuration coordinates or their derivatives as with Lagrange's equation, the differentiation quantity appears in only one matrix in each product and therefore the extra summation does not result. The product indices α and β result from the same phenomenon, and simply allow the cascading rotational matrix, to which the time derivative is applied, to be advanced from one index to the next.

Second, a complete expression of the kinetic energy resulting from the horizontal component of velocity requires that this quantity be summed over the total number of blades present in the system (given as an index in n). The index replacement rule does not apply

to this summation index since the degrees of freedom for each blade are independent and differentiation with respect to any one of them will result in zero components for all blades except the one of interest.

The derivation of all the required expressions for Lagrange's Equation can be arrived at straightforwardly provided care is taken to ensure that the index replacement rule is applied only when necessary based on the logic given in Reference [78]. The rule given in Equation 3.37 was used to generate, by hand, the mass matrix, $[\mathbf{M}]$, and the conservative parts of the forcing vector, $\{\mathbf{f}\}$.

3.3.2 Segment Joint Potential Energy

The potential energy of the flexible elements, given in Equation 3.28, is not subject to the cascading sums or products that are characteristic of Equations 3.19 through 3.27. This is because the spring forces are based only on the relative motion of two adjacent coordinate systems. Structural coupling can be preserved by employing a fully-populated stiffness matrix, such that the potential energy of each joint is given by

$$U_{(i,n)} = \frac{1}{2} \left\{\theta_{(i,n)}\right\}^T \left[\mathbf{k}_{(i,n)}\right] \left\{\theta_{(i,n)}\right\} \tag{3.43}$$

where

$$\left\{\theta_{(i,n)}\right\} = \begin{Bmatrix} \theta_{x(i,n)} \\ \theta_{y(i,n)} \\ \theta_{z(i,n)} \end{Bmatrix} \tag{3.44}$$

Since the Bryan angles that define the motion at each joint do not explicitly give the displacements of the individual joint springs, the projected rotation angles must be calculated to find the individual linear spring forces about each axis.

The components of $\left\{\theta_{(i,n)}\right\}$ are projected angles given by

$$\theta_{x(i,n)} = \tag{3.45}$$

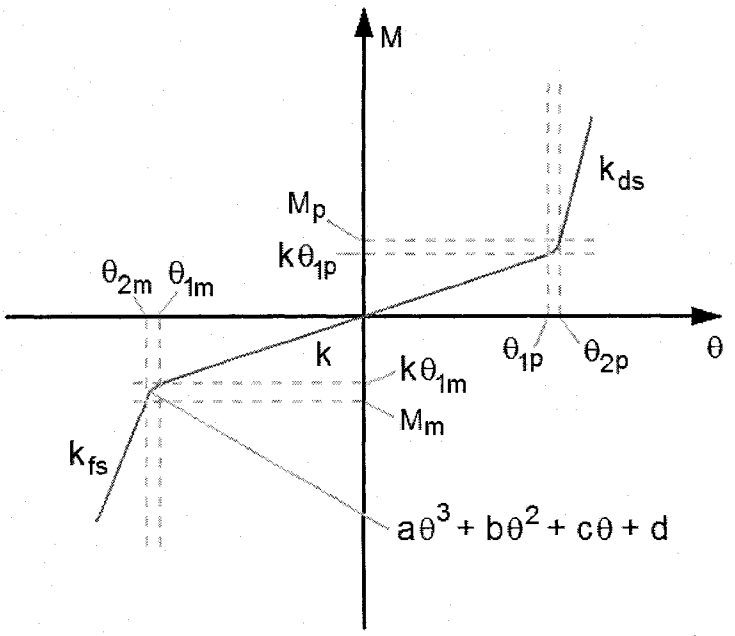

Figure 3.4: General stiffness curve for blade root springs.

$$\left(\frac{\{\mathbf{u}_2\}^T\,[\mathbf{R}_{B_{(i-1,n)}B_{\text{rigid}(i,n)}}][\mathbf{R}_{B_{(i,n)}B_{(i-1,n)}}]\,\{\mathbf{u}_3\}}{\{\mathbf{u}_3\}^T\,[\mathbf{R}_{B_{(i-1,n)}B_{\text{rigid}(i,n)}}][\mathbf{R}_{B_{(i,n)}B_{(i-1,n)}}]\,\{\mathbf{u}_3\}}\right)$$

$$\theta_{y(i,n)} = \tag{3.46}$$

$$\left(\frac{\{\mathbf{u}_1\}^T\,[\mathbf{R}_{B_{(i-1,n)}B_{\text{rigid}(i,n)}}][\mathbf{R}_{B_{(i,n)}B_{(i-1,n)}}]\,\{\mathbf{u}_3\}}{\{\mathbf{u}_3\}^T\,[\mathbf{R}_{B_{(i-1,n)}B_{\text{rigid}(i,n)}}][\mathbf{R}_{B_{(i,n)}B_{(i-1,n)}}]\,\{\mathbf{u}_3\}}\right)$$

and

$$\theta_{z(i,n)} = \tag{3.47}$$

$$\left(\frac{\{\mathbf{u}_2\}^T\,[\mathbf{R}_{B_{(i-1,n)}B_{\text{rigid}(i,n)}}][\mathbf{R}_{B_{(i,n)}B_{(i-1,n)}}]\,\{\mathbf{u}_1\}}{\{\mathbf{u}_1\}^T\,[\mathbf{R}_{B_{(i-1,n)}B_{\text{rigid}(i,n)}}][\mathbf{R}_{B_{(i,n)}B_{(i-1,n)}}]\,\{\mathbf{u}_1\}}\right)$$

The blade motion limits, droop and flap stops and lead/lag dampers, are modelled using additional rotational springs and dampers at the blade root when the angle of blade displacement at the root exceeds the stop contact angle. The stiffness curve for these elements is shown in Figure 3.4 where the subscript m refers to quantities in the range of negative θ values. The subscript p refers to quantities in the positive range of θ. The

negative and positive properties can be defined separately. The quantities k, k_{fs} and k_{ds} refer to the joint stiffness, flap stop stiffness, and droop stop stiffness respectively. For the lead/lag stops, k_{fs} refers to the stiffness of the stop when the joint angle is negative, and so on. While the root hinge joint can be assigned a stiffness value as per the figure, it is usually set to zero since the hinges do not exhibit spring characteristics between the stop regions.

The discontinuity between the stopping element and the hinge stiffness is smoothed with a cubic smoothing function where the coefficients are a, b, c, and d. The values θ_{1m} and θ_{1p} are the stop contact angles in the negative and positive angular directions respectively. The values θ_{2m}, θ_{2p}, M_m, and M_p are selected so that the curve fit occurs over a small angle and the shape of the curve does not include inflection points.

The extension and retraction of droop and flap stops presents some interesting modelling challenges. For instance, they retract and extend at a given rotational speed, however, they cannot extend or retract if the blade is in contact with the stop when the retraction threshold speed is reached. In addition, the extension and retraction is assumed to occurs over some measurable time and the blade might come into contact with the stop during the process. The applied moment in the hinge joint is assumed to vary linearly between the stop stiffness and hinge stiffness values during the extension and retraction process.

For use in Lagrange's Equation, the potential energy expression for the variable flap

spring element, $U_{3_{flap}}$, is

$$U_{3_{flap}(1,n)} = \begin{cases} M_{m_{\text{flap}}}\theta + \frac{1}{2}k_{fs_{\text{flap}}}\theta^2 - k_{fs_{\text{flap}}}\theta_{2m_{\text{flap}}}\theta + C_1 \\ \quad \text{if } -\infty < \theta \leq \theta_{2\text{m}_{\text{flap}}} \text{ and } \omega < \omega_{\text{fs}} \\ \\ \frac{1}{4}a_m\theta^4 + \frac{1}{3}b_m\theta^3 + \frac{1}{2}c_m\theta^2 + d_m\theta + C_2 \\ \quad \text{if } \theta_{2\text{m}_{\text{flap}}} < \theta \leq \theta_{1\text{m}_{\text{flap}}} \text{ and } \omega < \omega_{\text{fs}} \\ \\ \frac{1}{2}k\theta^2 + C_3 \\ \quad \text{if } \theta_{1\text{m}_{\text{flap}}} < \theta \leq \theta_{1\text{p}_{\text{flap}}} \text{ or } \omega > (\omega_{\text{ds}} \text{ or } \omega_{\text{fs}}) \\ \\ \frac{1}{4}a_p\theta^4 + \frac{1}{3}b_p\theta^3 + \frac{1}{2}c_p\theta^2 + d_p\theta + C_4 \\ \quad \text{if } \theta_{1\text{p}_{\text{flap}}} < \theta \leq \theta_{2\text{p}_{\text{flap}}} \text{ and } \omega < \omega_{\text{ds}} \\ \\ M_{p_{\text{flap}}}\theta + \frac{1}{2}k_{ds_{\text{flap}}}\theta^2 - k_{ds_{\text{flap}}}\theta_{2p_{\text{flap}}}\theta + C_5 \\ \quad \text{if } \theta_{2\text{p}_{\text{flap}}} < \theta \leq \infty \text{ and } \omega < \omega_{\text{ds}} \end{cases} \tag{3.48}$$

and $U_{3_{leadlag}}$ is given by the same equation except that the subscript "flap" is replaced with "leadlag". Due to differentiation, the constants C_1 through C_5 do not appear in the equations of motion. The polynomial coefficients a_m, b_m, a_p, b_p, etc. are the negative and positive angle equivalents of the coefficients shown in Fig. 3.4. The quantities ω, ω_{ds} and ω_{fs} refer to the rotor speed and the stop retraction speed for the droop and flap stops respectively. In the case of the lead/lag stops, the conditions on ω do not apply since they do not retract and extend.

3.4 Equations of Motion: Non-conservative Contributions

Non-conservative contributions consist of all system influences that cannot be expressed as conservative kinetic or potential energy. If the applied force, $\{\mathbf{f}\}$, and location of force application, $\{\mathbf{r}_{f_G}\}$, at a given instant are known, then the non-conservative terms in Lagrange's Equation can be calculated as

$$Q_\nu = \{\mathbf{f}\} \cdot \frac{\partial\{\mathbf{r}_{f_G}\}}{\partial q_\nu} \tag{3.49}$$

The simulation currently includes non-conservative contributions from ship motion as applied through the helicopter suspension system, articulated hinge friction, flexible element damping, and aerodynamics.

3.4.1 Ship Motion and Suspension

Once the ship motion has been determined, as described in Section 2.2, the suspension forces on the helicopter body can be calculated. Any number of suspension points can exist, with specifiable geometry and characteristic properties. In the helicopter coordinate system, the vertical suspension stiffness comes largely from the oleo or other equivalent vertical suspension element. The horizontal stiffnesses come from the behaviour of the tire. The current model assumes that the tires cannot slide, roll, or lift off the deck.

The suspension stiffness and damping force vector components, respectively, are assumed to be quadratically related to suspension displacement and velocity in the helicopter frame of reference as given by

$$f_{\text{suspension}_k} = -(a_k\Delta\ |\Delta| + b_k\Delta) \tag{3.50}$$

and

$$f_{\text{suspension}_c} = -(a_c\dot{\Delta}\ |\dot{\Delta}| + b_c\dot{\Delta}) \tag{3.51}$$

where the equations apply to each orthogonal force direction, k, in the helicopter frame of reference. The quantity Δ is the component of suspension displacement in the relevant

direction, and the constants, a_k, b_k, a_c, and b_c define the properties of the stiffness and damping elements for the same coordinate direction. For linear springs, only the b terms need be non-zero.

The location of application of the forces should be clarified. The true point of application is the deflected suspension contact point. However, since the suspension motions are not defined as system degrees of freedom, the force application points are approximated as the undeflected suspension contact point.

3.4.2 Articulated Hinge Friction

In articulated blades, the friction that exists in the blade root hinge is an important part of the model. An articulated rotor may consist of a flap hinge and a lead/lag hinge. The frictional moment due to hinge friction is given as

$$M_{\text{friction}} = f_{\text{friction}} r_{\text{hinge}} \tag{3.52}$$

about the (y) and (z) axes of the local rigid coordinate system of the first blade segment. The quantity f_{friction} is the friction force acting between the sliding surfaces of the hinge, and r_{hinge} is the radius of the hinge pin. Friction force is a discontinuous function, where the maximum static or sliding friction available depends on the coefficients of friction, μ_s or μ_d respectively, and on hinge surface normal force, f_{hinge}. A continuous approximation can be achieved using a modified friction function, which includes the Schilling friction model [88]. The frictional force is

$$\begin{aligned} f_{\text{friction}} = \text{sign(V)} \Big(& \text{B}_\text{d} \left(1 - \text{e}^{(-(\eta_{\text{hinge}}|\text{V}|)}\right) \\ & + (B_s - B_d)\text{e}^{\left(-\frac{|\text{V}|}{\varepsilon_{\text{hinge}}}\right)} \Big) \end{aligned} \tag{3.53}$$

where $B_d = \mu_d f_{\text{hinge}}$, $B_s = \mu_s f_{\text{hinge}}$, and V is the relative sliding velocity in the hinge joint, which can be calculated as the hinge relative rotational velocity multiplied by r_{hinge}. The values of $\varepsilon_{\text{hinge}}$ and η_{hinge} scale the smoothing components of the modified functions. The quantity $\varepsilon_{\text{hinge}}$ is a small positive velocity, such as 0.001 m/s, which represents the time

constant of the smoothing exponential decay from the static peak of the friction function to the sliding friction component. The smaller the velocity, the more representative the continuous approximation. A value of $\eta_{\text{hinge}} = \frac{1}{0.02\varepsilon_{\text{hinge}}}$ provides good smoothing through zero velocity without largely affecting the magnitude of the static friction peak.

Since the equations of motion were derived using Lagrange's method, the reaction forces in the joint are not available unless specifically calculated. The reaction forces in each hinge joint are calculated using a method suggested by Kane [89]. This method assumes an additional translational degree of freedom in the hinge joint, which are the directions of the reaction forces desired, and then sums the inertial and active forces to zero. The unknown quantity in this summation is the reaction force vector.

The reaction force vector at the articulated root hinge joint, $\left\{\mathbf{f}_{\text{hinge(n)}}\right\}$ associated with blade n as derived using this method is

$$\left\{\mathbf{f}_{\text{hinge(n)}}\right\} = \sum_{i=1}^{n_s} \left(m_{(i,n)} \left\{\mathbf{a}_{(i,n)}\right\} - m_{(i,n)} \begin{Bmatrix} 0 \\ 0 \\ -g \end{Bmatrix} - \left\{\mathbf{f}_{\text{applied(i,n)}}\right\} \right) \tag{3.54}$$

where $\left\{\mathbf{f}_{\text{applied(i,n)}}\right\}$ contains the sum of all non-conservative externally applied forces. The appropriate normal force, $f_{\text{hinge(n)}}$ for use in each hinge friction calculation is the magnitude of the reaction vector that projects onto the plane perpendicular to the axis of the hinge joint of interest. The accelerations, $\left\{\mathbf{a}_{(i,n)}\right\}$, are calculated using the acceleration values at the previous timestep.

3.4.3 Blade Joint Damping

The blade segment damping consists of a number of possible components, depending on the blades being modelled. The following rotational viscous damping terms can be independently defined:

- the structural damping associated with the outboard blade joints;
- the root joint damping, having a damping value consistent with a semi-rigid joint or a hinge; and
- additional damping associated with the flap/droop and lead/lag stops, applied when the blade root angle is in the applicable range and the stops are extended.

In order that the damping of the motion stops be applied only in the angular range over which the stops act, the damping force is multiplied by the filter, χ, which has a value of one in the angular range of the stop and zero otherwise. A smoothing function, with the same transitional angles as for the stop stiffness profile, is used to eliminate the discontinuity that occurs when the stops are impacted.

The damping moment about one hinge due to the corresponding motion stops is therefore calculated by applying the filter value using

$$M_{\text{damping}_{\text{flap}}} = \begin{cases} -\chi c_{fs}\dot{\theta} \\ \quad \text{if } \theta < 0 \text{ and } \omega \leq \omega_{\text{fs}} \\ \\ -\chi c_{ds}\dot{\theta} \\ \quad \text{if } \theta > 0 \text{ and } \omega \leq \omega_{\text{ds}} \end{cases} \tag{3.55}$$

where c_{fs} and c_{ds} are the damping coefficients of the flap and droop stops, respectively. If the stop retraction threshold speeds, ω_{fs} and ω_{ds}, have been exceeded, then the damping moments due to stops are not applied. In this case, the damping moment is calculated as defined for the hinge itself as

$$M_{\text{damping}} = -c_{(i,n)}\dot{\theta}_{(i,n)} \tag{3.56}$$

The logical routines used to scale the flap and droop stop damping during extension and retraction as well as the logic used to initiate extension and retraction is the same as that used for the droop and flap stop stiffnesses.

3.4.4 System Proportional Damping

The model contains a proportional damping feature, also called Rayleigh damping, which allows the user to employ a linearized proportional damping relationship

$$[\mathbf{C}_{\text{linear}}] = a[\mathbf{M}_{\text{linear}}] + b[\mathbf{K}_{\text{linear}}] \tag{3.57}$$

where the constants a and b are defined by the analyst. In the proportional damping model, the linear mass and stiffness matrices $[\mathbf{M}_{\text{linear}}]$ and $[\mathbf{K}_{\text{linear}}]$ are calculated about any analyst-specified operating point such that $[\mathbf{C}_{\text{linear}}]$ remains constant throughout the simulation.

In the model, the analyst has the option to toggle proportional damping on and off, or apply proportional damping to certain degrees of freedom and not to others. This is done by zeroing the unwanted columns and rows in the linearized proportional damping matrix. Proportional damping can be applied in addition to other forms of damping available in the model; if multiple damping sources exist, the effects are additive.

3.4.5 Aerodynamic Forces

The aerodynamic model calculates airloads based on the relative instantaneous wind velocity, which depends on the airwake and on the motion of the blades. In the blade sailing context, all angles of attack are possible, therefore, airfoil coefficients must be available for any relative wind direction. For the purposes of this research, two aerodynamic models have been selected. The first is a quasi-steady model, based strictly on published steady coefficients. The second includes unsteady effects and dynamic stall. Both aerodynamic force models are executed in the following manner at each timestep for each blade segment.

1. The motion of the blade segment at the 3/4 chord point is calculated.
2. The wind velocity at the 3/4 chord point is calculated using an airwake model.
3. The total relative velocity and angle of attack are calculated.
4. An aerodynamic force model is used to calculate aerodynamic coefficients.

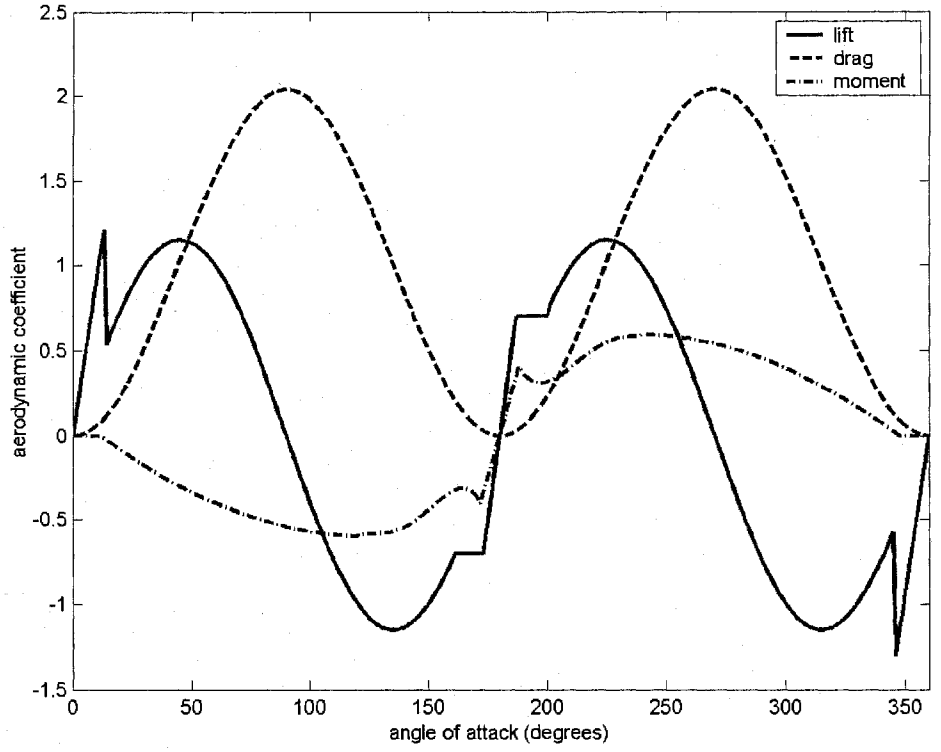

Figure 3.5: Aerodynamic coefficients for quasi-steady aerodynamics model of NACA 0012 airfoil.

5. The aerodynamic forces are calculated using Equations 2.11 through 2.13. These are applied at the 1/4 chord point.

6. The equivalent force and moments applied at the centre of mass are computed.

7. The contributions to Lagrange's equation are calculated using Equation 3.49.

Quasi-steady Model

For the NACA 0012 airfoil, the steady coefficients have been measured and published [46]. The aerodynamic coefficients, particularly lift, are dependent on airfoil shape in the attached flow region. However, after stall they are much more insensitive. They are also relatively insensitive to changes in Reynolds number, in the range of full scale blade sailing, and to

airfoil roughness [47]. The coefficients, as a function of angle of attack, for the NACA 0012 are shown in Figure 3.5 and are given in functional form modified from [48] as

$$C_l = \tag{3.58}$$

$$\begin{cases} C_{l_\alpha}\alpha & \alpha < \alpha_a \\ 1.15\sin(2\alpha) & \alpha_a \leq \alpha < 161^\circ \\ -0.7 & 161^\circ \leq \alpha < 173^\circ \\ 0.1(\alpha - 180^\circ) & 173^\circ \leq \alpha < 187^\circ \\ 0.7 & 187 \leq \alpha < 201^\circ \\ 1.15\sin(2\alpha) & 201^\circ \leq \alpha < (360^\circ - \alpha_a) \\ C_{l_\alpha}(360 - \alpha) & (360^\circ - \alpha_a) \leq \alpha \end{cases}$$

$$C_d = 1.02 - 1.02\cos(2\alpha) \tag{3.59}$$

$$C_m = \tag{3.60}$$

$$\begin{cases} 0 & \alpha < 12^\circ \\ 4.69e^{-5}\alpha^2 - 1.17e^{-2}\alpha + 0.133 & 12^\circ \leq \alpha < 120^\circ \\ 4.23e^{-7}\alpha^4 + 2.36e^{-4}\alpha^3 - 4.92e^{-2}\alpha^2 + 4.52\alpha - 155.5 & 120^\circ \leq \alpha < 172^\circ \\ 0.05(\alpha - 180.0) & 172^\circ \leq \alpha < 188^\circ \\ 2.16e^{-7}\alpha^4 - 1.96e^{-4}\alpha^3 + 6.64e^{-2}\alpha^2 - 9.96\alpha + 556.8 & 188^\circ \leq \alpha < 240^\circ \\ -4.69e^{-5}\alpha^2 + 2.20e^{-2}\alpha - 1.98 & 240^\circ \leq \alpha < 348^\circ \\ 0 & 348^\circ \leq \alpha \end{cases}$$

For airfoils other than the NACA 0012, the attached flow lift curve slope, C_{l_α}, and stall angle, α_a, are changed to reflect the properties of the appropriate airfoil, and the stalled airfoil behaviour is assumed to remain the same.

Unsteady Model

The unsteady model used in this research consists of three integrated models: attached flow, separated flow, and dynamic stall. The indicial arbitrary motion theorem (AMT) method without compressibility effects, is used for attached flow. The AMT method was chosen over other options for three reasons. First, it allows for variations in the flow as well as in airfoil motion. Second, it allows the response to arbitrary motions in the time domain to be calculated in a time-marching manner. Third, it interfaces well with a dynamic stall model by the same author, which is the second model component. For separated flow, the coefficients are calculated using the modified quasi-steady model. The dynamic stall model provides modifications to the calculated coefficients and indicates when the airfoil is in a state of stall, or when the flow is unattached. This model is complex in its execution; the details are covered in Appendix A.1.

3.5 Blade Motion Coupling

There are several sources of blade motion coupling that should be included in any helicopter blade model in order to correctly capture blade response to a variety of conditions. The rigid-segment model captures all these coupling sources either through a fully populated stiffness matrix, or because the equations of motion have not been linearized.

Dynamic Coupling: arises from out-of-plane gyroscopic motion captured by the dynamics in the equations of motion.

Inertial Coupling: occurs if the blade mass centre axis is offset from the torsional elastic axis. As the rotor turns, the centrifugal force that is generated will result in blade deflections. Similarly, flap and lead lag can lead to coupled torsional motion about

the elastic axis.

Structural Coupling: results from a blade shear centre that is offset from the torsional elastic axis. It can occur in isotropic and composite blades.

Composite-structural Coupling: occurs as a result of the composite fibres in the lay-up of a composite rotor blade.

Twist Coupling: results because coupling properties of the blade can change with radius if a built-in twist angle is present.

3.6 Property Determination

Several options exist for determining the equivalent discrete stiffness properties of flexible systems; the most appropriate one for a given situation depends on the information available.

3.6.1 Property Tuning

This method involves tuning the blade response by comparing the rigid segment results with experimental (or some other known) results. Depending on the available information, the researcher may have to make some assumptions about the model, and combine these with the available data to arrive at a complete set of properties. The tuning method often requires iteration and more than one set of data such that the properties can be tuned to one set and then validated against another.

3.6.2 Deflection/Load Case Fit

If a certain deflection shape resulting from a known load case exists, then the individual joint stiffnesses can be calculated by matching the deflections at each joint to the known profile given the same load case. The Bernoulli-Euler beam equation gives a straightforward way to estimate a deflected shape for a simple load case such as a tip force or a uniformly distributed blade weight. Linear cantilever beam theory also provides a convenient way of estimating the stiffness of a continuous uniform blade if the natural frequencies are known.

Langlois and Anderson [13] suggest the following specific approaches to calculating the stiffnesses at each joint based on a specific load case, deflection profile, or dynamic response information.

- The simplest approach involves making all stiffnesses equal, and determining the parameter that will give the correct static deflection at the beam tip for a given applied load.
- A similar approach involves equal stiffnesses that permit the matching of the fundamental frequencies of the simulated and theoretical beam.
- An extension involves solving for individual stiffness values that match the eigenvalues of the problem. This also allows the optimum number of segments to be determined.

3.6.3 Direct Method

If detailed continuous stiffness distributions for the blade are available, then the discrete joint stiffnesses can be calculated directly. Much research is currently being conducted regarding the calculation of coupled stiffness matrices for helicopter rotor blades [81], especially in composite blade applications, where the coupled components are known to be significant. One typical formulation considers the blade energy per unit length, $\frac{U_b}{L}$ stored in a deflected beam as

$$\frac{U_b}{L} = \frac{1}{2} \{\bar{\epsilon}\}^T [\mathbf{k}_b] \{\bar{\epsilon}\} \tag{3.61}$$

where

$$\{\bar{\epsilon}\} = \begin{Bmatrix} \theta_1' \\ u_3'' \\ u_2'' \end{Bmatrix} \tag{3.62}$$

The quantity θ_1 is the blade twist, and u_2 and u_3 are deflections of the beam reference line laterally and vertically, respectively.

Here, $\{\bar{\epsilon}\}$ contains the curvatures in torsion, flap, and lead/lag respectively. These represent the rate of change of displacement angle. Equation 3.61 is compared to Equation 3.44, where $\left\{\theta_{(i,n)}\right\}$ is a measure of the change in angle across a joint, an effective curvature. By considering a beam segment of length $L = l_{(i,n)}$ and the definition of a derivative, it can be justified that

$$\{\bar{\epsilon}\} \simeq \frac{\left\{\theta_{(i,n)}\right\}}{l_{(i,n)}} \tag{3.63}$$

By substitution, it can then be shown that the discrete stiffnesses are simply the continuous stiffnesses divided by the length of the segment over which they act.

$$[k_{(i,n)}] = \frac{[k_b]}{l_{(i,n)}} \tag{3.64}$$

The accuracy of the approximation is good, provided the curvature does not change significantly along the length of each individual blade segment. This can be managed by the user by careful selection of segment length based on the geometry, properties, and other model conditions. The direct method was validated using the property tuning approach previously detailed.

3.6.4 Property Finding Example

The time history of blade tip deflection for an actual non-rotating blade on a typical maritime helicopter was captured on video. Based on the frequency and logarithmic decrement exhibited in the video, an effective stiffness and damping for an equivalent isotropic uniform beam can be estimated. If a model of this helicopter is desired, then one of the following blade models could be developed.

Case 1: If the blade resting on the droop stops is assumed to be a cantilever with no initial hinge angle, and the total blade mass is known, then the blade can be sectioned into segments of equal length, equal mass, and equal stiffness and damping properties then can be tuned to achieve similar tip response.

Case 2: If the blade resting on the droop stops is assumed to be a cantilever with no initial hinge angle, and the mass distribution as a function of radius is available, then

the blade can be sectioned into segments with appropriate masses and the appropriate stiffness and damping properties can be found using the deflection/load fit for a cantilever beam subject to gravity and its own weight. Figure 3.6 shows the experimental data compared to the simulation results for a hingeless blade approximated by different numbers of blade segments. In this case, the blade behaviour is well modelled with three or more rigid segments.

Case 3: If the droop stops are modelled using the hinge and droop stop model described above and the mass distribution as a function of radius is available, then a different set of equivalent stiffnesses can be achieved using the deflection/load fit.

Table 3.1 shows first natural frequency and static deflection results for the test blade in flap modelled using Bernoulli-Euler beam theory and the three test cases. Case 1 and the Bernoulli-Euler beam theory frequencies are similar because both assume uniform beam properties. Cases 2 and 3 allow variable mass and stiffness properties, and therefore agree with the experimental results, which also include variable mass and stiffness. This validation case begins to show the suitability of the discrete approach for modelling beams with variable properties.

3.7 Model Validation

In the blade sailing context, the behaviour of the blade in bending, especially in flap, is of specific interest. A wide variety of continuous blade and beam bending models exist, and the performance of the rigid-segment model was validated against these and experimental data in order to show the appropriateness of the rigid-segment model for simulating blade behaviour.

A number of classical solutions to the rotor dynamics problem have been used to validate the dynamic model. The simulated results used in this validation procedure were solved using a fourth/fifth order Runge-Kutta-Fehlberg explicit integrator.

Table 3.1: Summary of results for bending vibration cases.

	stiffness	mass	freq (rad/s)	static Δ (m)
model case 1	discrete, uniform	discrete, uniform	7.07	0.307
Bernoulli-Euler beam	continuous, uniform	continuous, uniform	7.06	0.305
model case 2	discrete, variable	discrete, variable	7.11	0.305
model case 3	discrete, variable	discrete, variable	7.11	0.305
experiment	continuous, variable	continuous, variable	7.11	0.305

3.7.1 Large Deflections

Since blade sailing can involve large deflections, a model that captures bending of a geometrically linear beam is insufficient. The static flap deflections of a uniform isotropic beam with a vertical load applied at the tip are shown in Fig. 3.7. Ten identical rigid segments were used to model the beam, and the results are compared to published results [2]. The rigid segment results agree well with the published values.

The large deflections in a dynamics sense were also validated, this time using a uniform isotropic beam undergoing spin-up from rest to a constant rotational speed in the horizontal plane. The beam is extremely flexible in the lead-lag direction, and since the model applies no damping, it oscillates as a result of the initial rotational acceleration. The number of segments required to achieve numerical convergence was examined, and six segments was selected as a good compromise between solution accuracy and solution speed.

The properties of the originally defined continuous beam are given in Table 3.2. The corresponding properties for the six-segment rigid body mode are given in Table 3.3. The

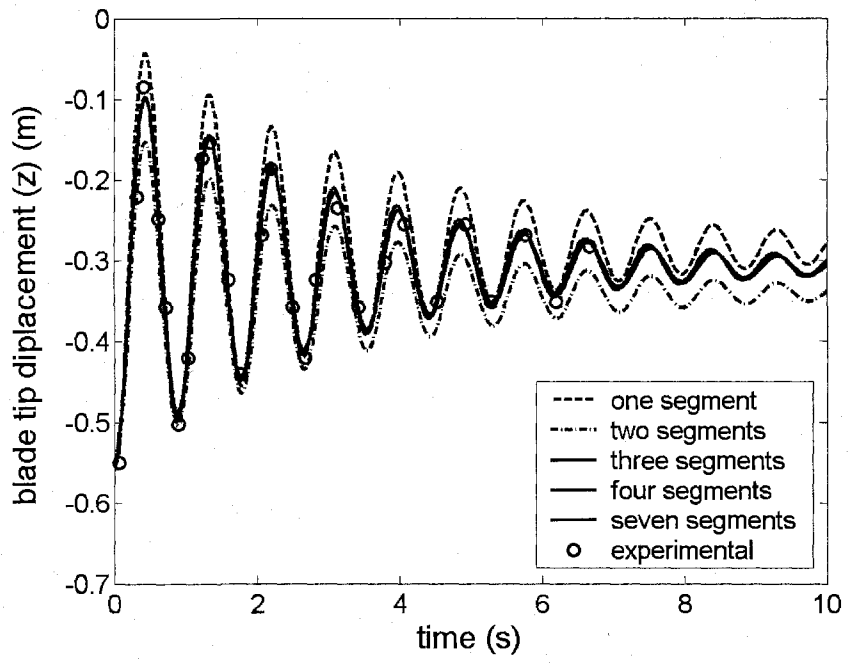

Figure 3.6: Full scale blade response in flap to a pull test (hingeless blade with varying number of segments).

beam spin-up profile defined for a spin-up time of $t_{r1} = 1$ second is given by

$$\dot{\sigma}(t) = \begin{cases} \Omega\left[6t^5 - 15t^4 + 10t^3\right] & 0 \leq t \leq t_{r1} \\ \Omega & t > t_{r1} \end{cases} \tag{3.65}$$

The time-history of beam tip deflection for a six-segment beam shows a satisfactory agreement, within 4%, with the non-linear finite element solutions [90, 91] in Figure 3.8.

3.7.2 Droop Stop Drop Test

The behaviour of the blade interacting with the droop and flap stops is important for the blade sailing of articulated blades. If the blades come into contact with the stops with significant kinetic energy, then it is transferred to potential energy, and the blades can undergo large deflections. The behaviour of the blades when they come into contact with

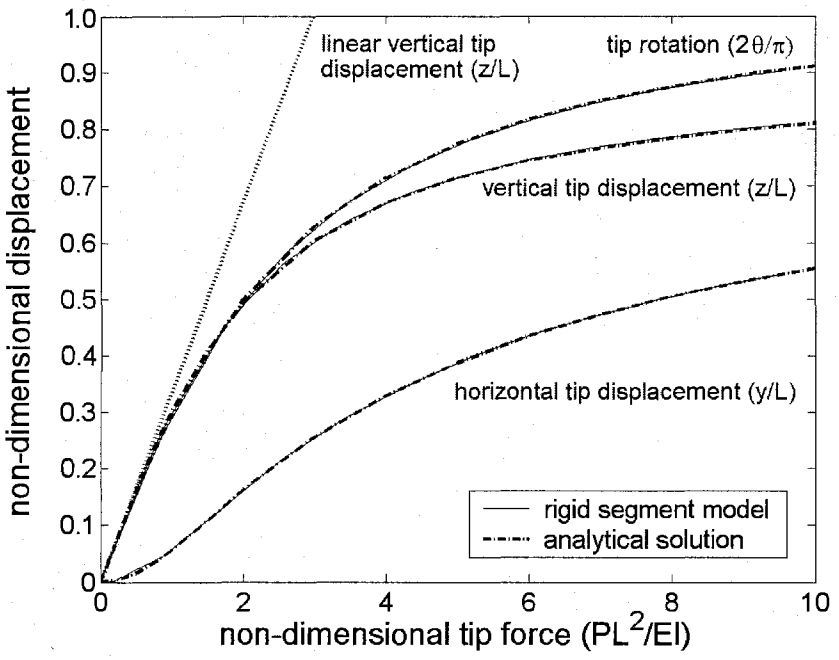

Figure 3.7: Large bending tip deflections due to static tip force (ten segments).

the stops has been validated against experimental results [70], where the details of the experimental blade can be found in Reference [71], and the corresponding segment model properties are given in Table 3.4.

Figures 3.9 and 3.10 show the tip deflection and the hinge angle respectively compared with the published experimental data. The rigid segment model captures the general shape, magnitudes, and frequencies of the major blade response characteristics. Similar differences between numerical and experimental results are shown in Reference [13].

3.7.3 Inertial Coupling

The definable properties of the model allow for the mass centres to be offset from the elastic axis, which is along the x axis of the blade segment in question. This causes a structural coupling of the natural frequencies of vibration such that most natural modes will contain both a bending and torsional component.

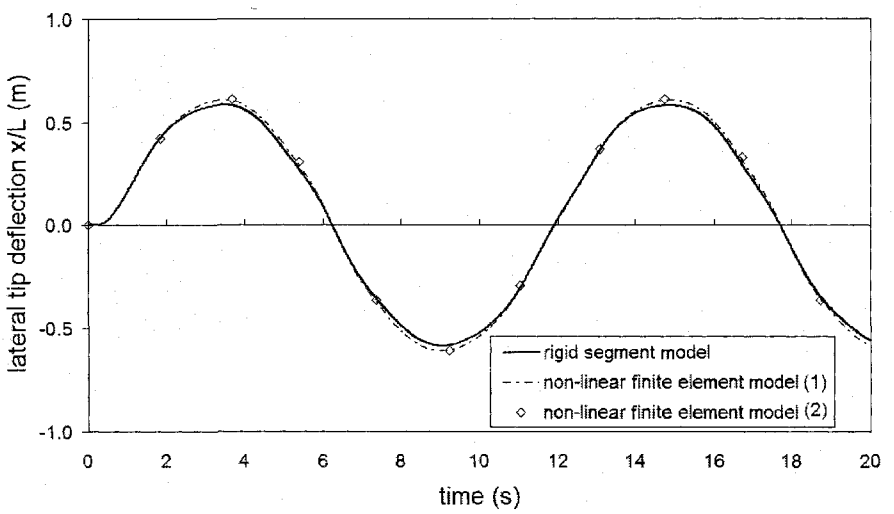

Figure 3.8: Beam spin-up validation (finite element results from (1):[90],(2):[91]).

The inertial coupling between flap and torsion can be shown by solving for the coupled natural frequencies of an isotropic beam with a swept tip [10, 92]. Lead-lag is also coupled in that the system is rotated at constant speed in the plane of the sweep angle and the beam achieves a steady-state deflection in the lead-lag sense for swept tip angles different from zero.

The first three bending-torsion coupled modes for the beam turning at 8.3 Hz are shown in Figure 3.11. The rigid segment model agrees with the published data to within 12% (1 Hz) for the fundamental mode and within 5% (2 Hz) for the second and third modes. This under-prediction can likely be rectified by careful tuning of the root stiffnesses. For the results shown in the Figure, a rule-of-thumb approach was applied, in which the root stiffness is 2.15 times the calculated value for the other joints, provided the beam is uniform and the segment lengths are consistent. This rule was determined by trial and error, and varies somewhat depending on the number of segments being used. The segment properties are given Table 3.5.

Table 3.2: Continuous beam spin-up parameters.

parameter	value	units
beam density ρ	2690	kg/m^3
beam stiffness E	$6.89x10^9$	N/m^2
beam length L	30.5	m
cross-section area A	$9.30x10^{-2}$	m^2
cross-section inertia I	$7.20x10^{-4}$	m^4
final rotor speed Ω	$\pi/10.0$	rad/s
engagement time t_{r1}	1.00	s

Table 3.3: Beam properties used for dynamic large deflection validation.

segment	1	2 - 6
mass (kg)	1272	1272
length (m)	5.08	5.08
lead/lag stiffness (Nm/rad)	$2.1x10^6$	$9.8x10^5$
lead/lag inertia (kgm^2)	2738	2738

3.7.4 Fan Plot

The bending frequencies of rotating blades are known to increase with rotational speed, as a result of the centrifugal forces acting on the blade. An assumed mode solution to Lagrange's equation for a continuous uniform isotropic beam is used to validate this capability of the rigid segment model [93]. Figure 3.12 shows a fan plot that includes the rigid body and first elastic flapping modes of a blade with six rigid segments. The segment properties are given in Table 3.6. Satisfactory agreement, within 1 rad/s, is shown between the rigid segment solution and the Lagrangian solution.

3.7.5 Dynamic (Gyroscopic) Coupling

Classical helicopter theory textbooks discuss blade motion coupling that occurs between flap and lead/lag due to the Coriolis coupling when the blade is rotating at a constant

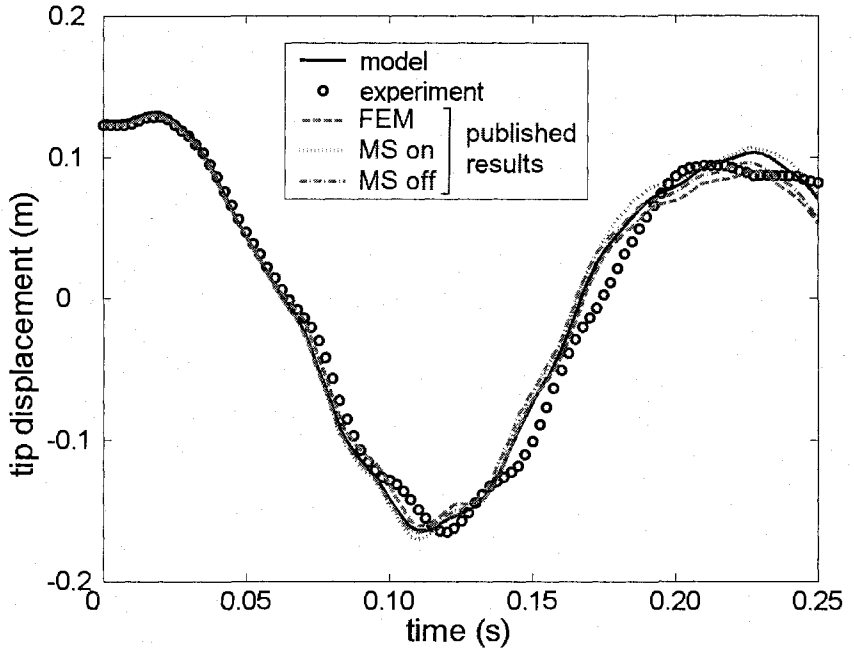

Figure 3.9: Droop stop test blade tip deflection (MS: modal swapping; experimental data and published results from Reference [70]).

speed. Articulated rotors allow this coupled motion since motion about the lead/lag hinge and the bending hinge are essentially unrestrained. A simplified set of equations of motion is solved to give the moment at the lead/lag hinge that would be required to restrain the motion of a rigid articulated blade in lead/lag [93]. This moment is

$$N = -2J_{yr}\Omega\dot{\beta}\sin\beta \tag{3.66}$$

where N is the moment about the lead lag (z) axis, J_{yr} is the moment of inertia about the flap (y) axis through the joint instead of the centre of gravity, Ω is the rotational speed of the hub (constant), and β is the flap angle. Figure 3.13 shows that the application of an equal and opposite moment N restrains the lead/lag motions to zero as soon as the initial transient response is removed with light damping.

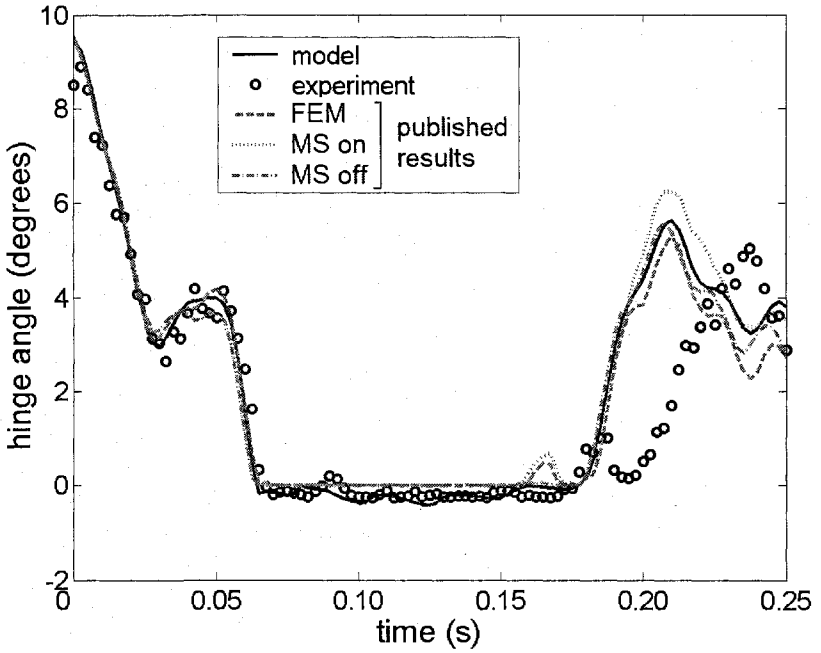

Figure 3.10: Droop stop test flap hinge angle (experimental data and published results from Reference [70]).

3.7.6 Hinge Offset

The offset between the axis of rotation and the flap and lead-lag hinge axes also has an effect on the coupled flap and lead lag frequencies of a rigid rotor blade. For a hinge offset e and total rotor radius R, the corresponding flap and lead-lag frequencies are [94]

$$\omega_{\text{flap}} = \Omega\sqrt{1 + \frac{3e}{2(R-e)}} \tag{3.67}$$

and

$$\omega_{\text{leadlag}} = \Omega\sqrt{\frac{3e}{2(R-e)}} \tag{3.68}$$

Several tests were run with a blade with the properties given in Table 3.7 at rotor speeds of 2 and 6 Hz. The theoretical and model results are shown in Figures 3.14. The agreement is excellent over a wide range of hinge offset to blade length ratios, indicating that the model

Table 3.4: Blade properties used for droop stop validation.

segment	1	2 - 5	6
mass (kg)	.75	0.05	0.05
length (m)	.15	.2	.05
flap stiffness (Nm/rad)	hinged with stops	36.5	36.5
flap inertia (kgm^2)	.0014	.000167	.0000104

captures the hinge offset affect.

3.7.7 Propeller Moment

Pre-twisted helicopter blades are subject to the propeller moment while turning. This is defined as the tendency for the blades to twist such that the principle axis of highest moment of inertia is perpendicular to the plane of rotation; that is so that the airfoil cross-sections lie flat in the rotor disc. This phenomena is a form of inertial coupling, and was observed in simulation results designed to validate this blade behaviour.

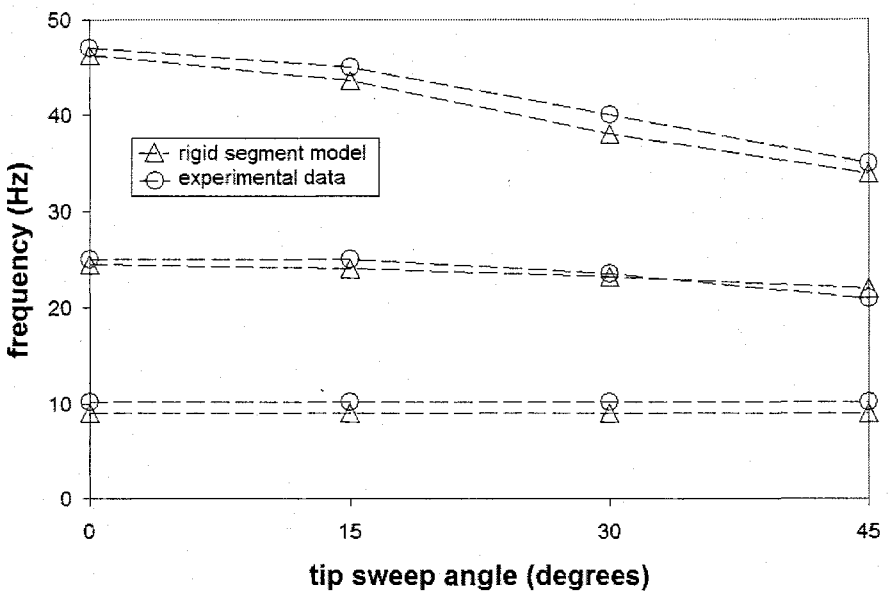

Figure 3.11: First three flap-coupled frequencies for swept tip beam (experimental data from Reference [92]).

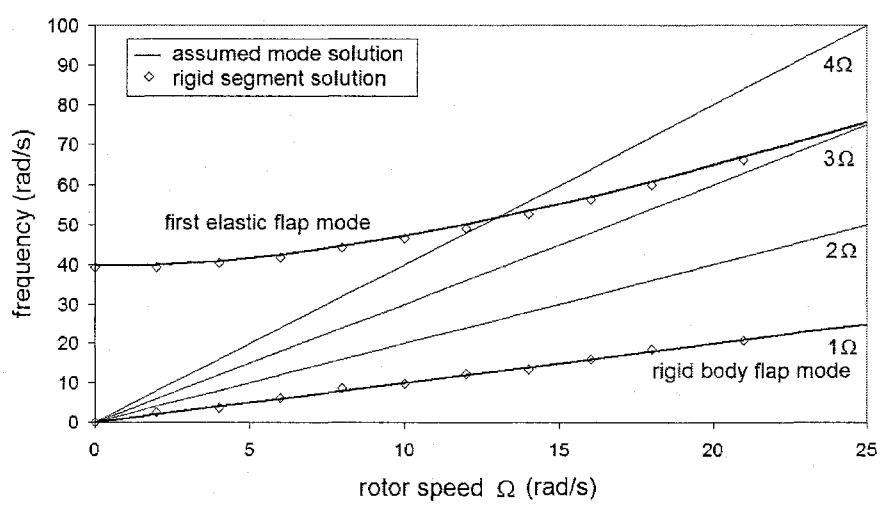

Figure 3.12: Variation in flapping frequencies with rotor speed.

Table 3.5: Blade properties used for swept tip validation.

segment	1	2 - 4	5
mass (kg)	0.0218	0.0218	0.016616
length (m)	.2	.2	0.1524
twist stiffness (Nm/rad)	-	4.4775	5.876
flap stiffness (Nm/rad)	6.816	3.169	4.15925
lead/lag stiffness (Nm/rad)	1717.3	798.4	1047.
twist inertia (kgm^2)	.000117	.000117	.00000089
flap inertia (kgm^2)	0.000073	0.000073	0.000032
lead/lag stiffness (kgm^2)	0.000073	0.000073	0.000032
lag offset angle (degrees)	0	0	variable (tip angle)

Table 3.6: Blade properties used for fan plot validation.

segment	1	2 - 6
mass (kg)	23.14	23.14
length (m)	1.44	1.44
flap stiffness (Nm/rad)	0	4.0×10^5
flap inertia (kgm^2)	4.	4.

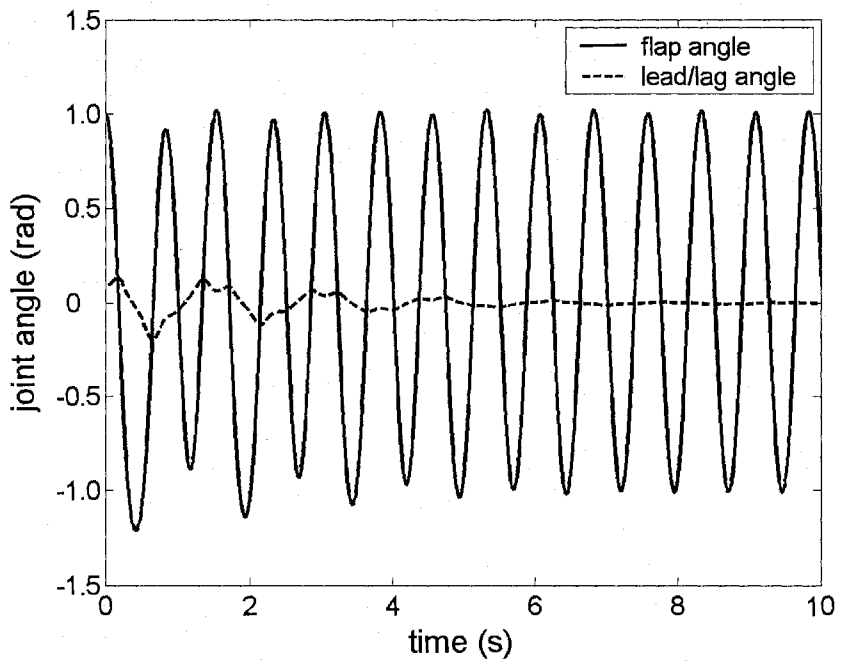

Figure 3.13: Lead/lag motion restrained by Bramwell moment.

Table 3.7: Blade properties for hinge offset validation case.

property	value
mass (kg)	1.0
radius (m)	5.0

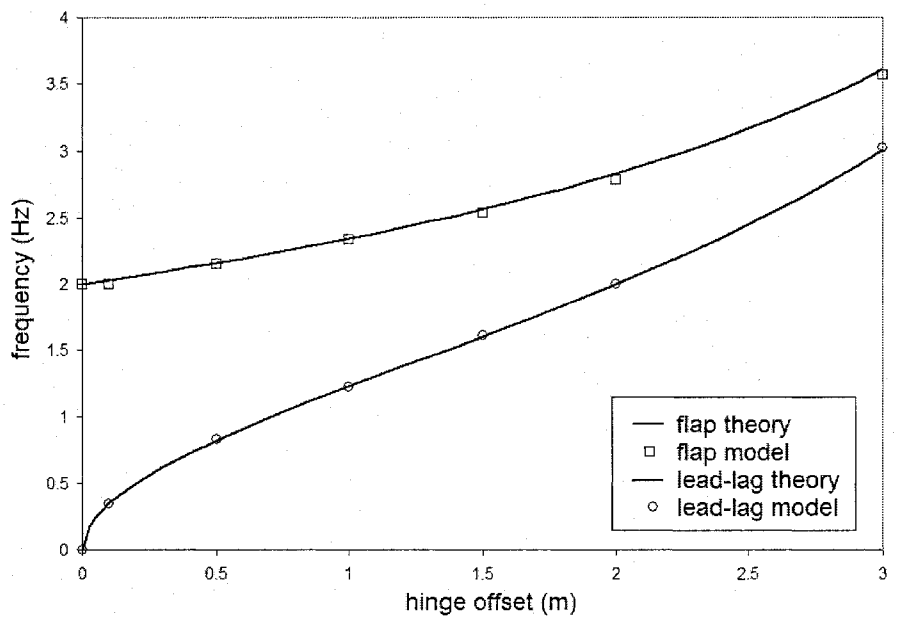

(a) rotor speed of 2 Hz.

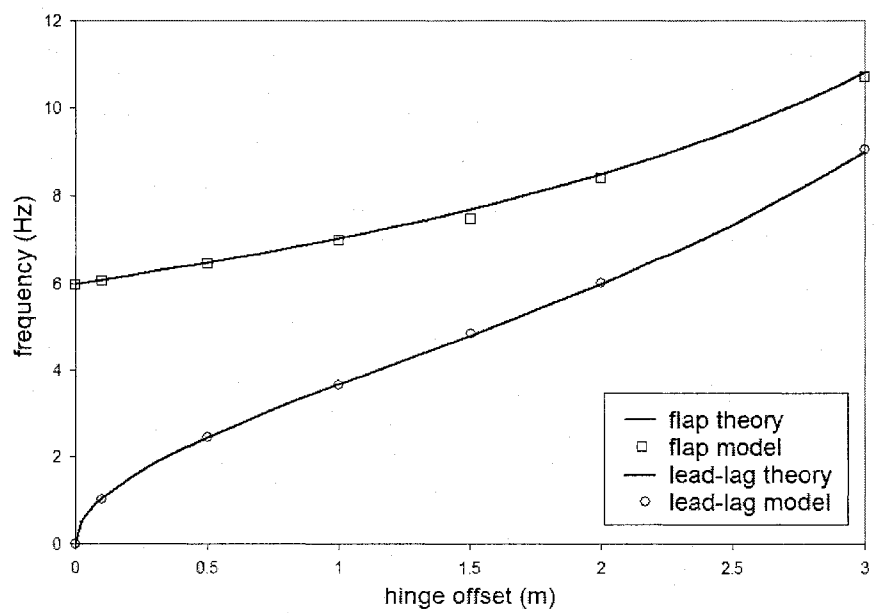

(b) rotor speed of 6 Hz.

Figure 3.14: Flap and lead lag response frequencies for varying hinge offset.

3.8 Simulation Software

The theory presented in this chapter has been implemented into simulation software that calculates the time history of blade response to simulated engage or disengage conditions. The software has been dubbed SHREDS (Shipboard Helicopter Rotor Engage/Disengage Simulation), and is written in Fortran. Appendix B is user manual that contains the details required to successfully simulate a ship-helicopter-rotor system with SHREDS.

3.8.1 Simulation Verification

An extensive code verification process was undertaken to ensure expected code behaviour and correct equation coding. It is impractical to show detailed results for each verification case; therefore the verification procedure is described in general.

Once a complete set of general dynamic equations were derived, a sample set of equations for a three-bladed-three-segmented system was derived from the energy expressions using Maple [87]. Unique variable values were assigned to each blade property. The Calculation Level Three values, as shown in Figure B.1, generated by the simulation were compared with those generated by the verification calculations. The symmetry of the mass matrix, and the final generation of the system of equations with only the active degrees of freedom was also verified. In all cases, the expressions were equal, indicating that the differentiation rule given by Equations 3.37 works for every expression encountered in this study.

Additionally, the correct operation of the simulation execution options, as given in Section B.2, were verified. This process included, but was not limited to, the functions listed here:

- different rotor engage profiles;
- suspension system operation;
- suspension system with rotor turning and with ship motion;
- ship motion without suspension flexibility;

- ship motion with some ship motion degrees not applied;
- activation and deactivation of blade root stops;
- correct stiffness calculation during stop impacts;
- switching of droop and flap stops;
- collective and cyclic pitch profiles;
- linear matrix calculation and eigenvalue calculation;
- proportional damping;
- off-diagonal coupling terms; and
- hinge force calculation.

Through many verification procedures and many validation cases, the simulation code has been shown to function as expected.

Chapter 4

Airwake Modelling

The ship airwake represents an important contribution to the blade sailing phenomenon; investigation of the characteristics of the frigate airwake have been addressed under this research program. The goals of the airwake modelling portion of this research are:

- to study the steady and unsteady flow characteristics over the flight deck of a typical frigate in beam winds;
- to examine the effect of ship roll angle on the flow;
- to consider spatial and temporal flow correlations; and
- to develop representative airwake models based on the gathered data.

The airwake research was conducted experimentally, using the wind tunnels, equipment, and other facilities available at the Aerodynamics Laboratory of the National Research Council of Canada. The experiments conducted to achieve these goals were governed by the following limitations in scope.

- The airwake environment being modelled is above a typical frigate with a typical maritime helicopter. Data was taken to encompass a rotor disc plane for this typical configuration, as shown in Figure 4.1.
- Turbulent energy in the range of 0.1 to 3 Hz is carefully modelled since this is the range of first flapping and rotor rotation frequencies. Energy at greater than 10 Hz

was deemed to be of lesser concern since only higher flexible blade modes, which do not significantly contribute to blade sailing, will be excited at this level.

- The effect of the helicopter fuselage and rotor were not considered to affect significantly the airwake encountered by the rotor. This is considered acceptable since an engaging rotor operates at slow speeds and low pitch angles, which leads to little induced flow across the disc. At high winds where blade sailing occurs, the rotor operates at large advance ratios that tend to remove tip vortices from the flow field before the next blade encounters them. At large negative deck roll angle (positive roll is defined when the deck is tilted into wind), the rotor disc intersects the shear layer and the flow may be more affected by the presence of the blades. However, deck roll rarely achieves such high levels, even in high sea states; therefore the independence of the wind from the helicopter itself is maintained in the modelling in this research.

- The flow is considered planar in the plane shown in Figure 4.1, which cuts laterally and vertically across the flight deck. Flow along the flight deck, or parallel to the longitudinal axis of the ship is assumed to be negligible. As such, hangar effects are not included. This approximation allows the sensitivity of the flow and blade phenomena to ship roll to be examined.

- Earth's surface boundary layer effects have been shown to affect the ship airwake [33] and are therefore included in the experimental setup.

The experiment was separated into two components. Experiment A was used to find the time-averaged flow field characteristics as a function of location over the ship and ship roll angle. Experiment A also examined turbulence intensity, but not spectral characteristics. The results of Experiment A are referred to as the "steady" characteristics of the airwake. Experiment B was used to study flow spectra and correlations above the flight deck. Results from Experiment B are referred to as the "unsteady" characteristics of the airwake. The two experiments, although conducted separately, used the same equipment and measurement techniques. The details of the equipment, procedure, uncertainty analysis, and data

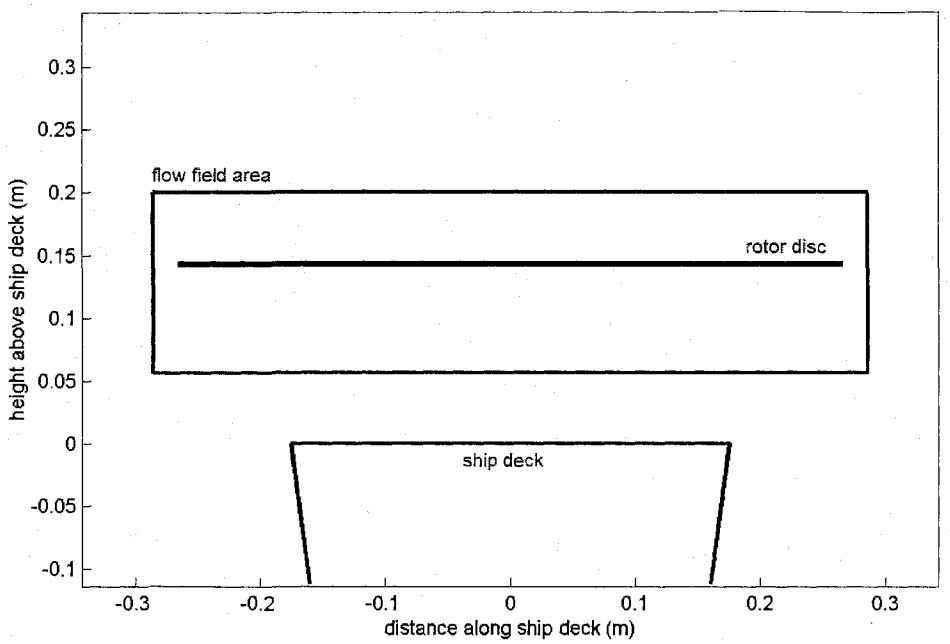

Figure 4.1: Schematic representation of the flowfield area in ship reference frame.

reduction can be found in Appendix C.

This chapter explains the results of the airwake experiment, draws some conclusions about the flowfield itself, and discusses the numerical models that have been developed from the data for use with the blade sailing simulation. The flowfield models have the following characteristics.

- The experiments were conducted at 1:35 scale.
- The modelled flowfield extends from 2 to 7 m full scale (0.057 to 0.2 m model scale) above the ship deck, and is 20 m (0.57 m model scale) wide (streamwise). The typical rotor is assumed to be 9.3 m (0.27 m model scale) in radius with the rotor hub at 5 m (0.14 m model scale) above the ship deck.

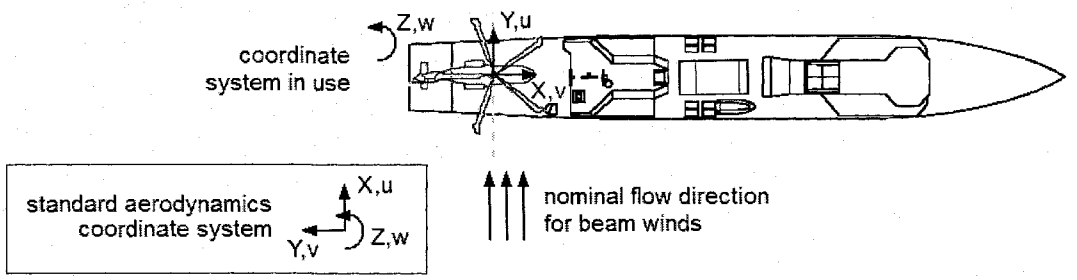

Figure 4.2: Beam winds and associated aerodynamic coordinate systems.

4.1 Coordinate systems

Using the coordinate systems defined in Section 3.1.2 for the ship-helicopter-rotor system, and the fact that this research focuses on beam winds, the freestream flow approaches the ship from the $-Y$ direction, as shown in Figure 4.2. This does not conform to the standard coordinate system definition for fluid dynamics, which assigns the freestream flow direction the axis X, and its flow velocity the symbol u. To maintain consistency, the global coordinate system defined for system dynamics is used for the discussion of the airwake experiment also. Therefore, the freestream flow has a magnitude of u in the Y direction, where lateral variations in the flow have a magnitude of v in the X direction, and vertical variations have a magnitude w in the Z direction. Figure 4.2 shows the aerodynamic coordinate system definition. For the inertial coordinate system, the origin is at the centre of the flight deck when all ship motions, except for constant forward velocity, are zero. For the ship coordinate system, the origin stays fixed to the centre of the flight deck. In the context of these experiments, the ship coordinate system includes the effect of ship deck roll angle.

4.2 Background

Using an experimental approach, a measured record of flow velocity fluctuations at a single point have the form $(V + v(t), U + u(t), W + w(t))$ where the capital letters represent the

mean, or steady components and the small letters represent the turbulent, fluctuating, or unsteady components. The mean component, μ_i of flow is often normalized by some reference flow velocity, U_{free}, as

$$\nu_i = \frac{\mu_i}{U_{\text{free}}} \tag{4.1}$$

where i could be u, v, or w. The turbulence intensity is a measure of the turbulent energy in the flow as

$$i_i = \frac{\sigma_i}{U_{free}} \tag{4.2}$$

where σ_i is the standard deviation (root mean square) of the turbulent signal $i = u$, v, or w.

The single-sided auto-spectrum of turbulence is defined based on the Fourier transform, $A(f)$, of the time history of flow velocity, $a(t)$, in a single orthogonal direction at a single point in the flow. It is given by

$$S_{aa}(f) = \lim_{T \to \infty} \frac{2}{T} E\left[|A_k\left(f, T\right)|^2\right] \tag{4.3}$$

where there are k records of the process, each with length in time T, and the notation E refers to the expected value. For discretely sampled finite time records, the auto-spectrum can be calculated practically as

$$\hat{S}_{aa}(f) = \frac{2}{n_d T} \sum_{k=1}^{n_d} \left[|A_k\left(f, T\right)|^2\right] \tag{4.4}$$

where n_d is the number of records and the area under the auto-spectrum function

$$\int_0^\infty S_{aa}(f) df = \psi_a^2 = \sigma_a^2 + \mu_a^2 \tag{4.5}$$

is the mean square value of the signal, or the square of the standard deviation (variance) plus the square of the mean value.

Cross-correlations are also important for flow modelling. The flow velocities at two points are related by the correlations that exist between them. The quantity $B(f)$ is the

Fourier transform of the flow velocity signal $b(t)$ at the same or some other point in space for the same or some other orthogonal direction, compared with the point for signal $a(t)$. Points a and b are separated from one another in space by the vector $\Delta d = (\Delta x, \Delta y, \Delta z)$. The cross-spectral density function between the two velocity signals $a(t)$ and $b(t)$ can be found using

$$\hat{S}_{ab}(f) = \frac{2}{n_d T} \sum_{k=1}^{n_d} \left[A_k^*(f,T)\, B_k(f,T) \right] \tag{4.6}$$

for discretely sampled velocity signals, where the star notation refers to the complex conjugate. The root coherence (square root of the coherence) is defined as

$$\gamma_{ab} = \frac{|\hat{S}_{ab}(f)|}{\sqrt{\hat{S}_{aa}(f)\hat{S}_{bb}(f)}} \tag{4.7}$$

and gives a measure of the correlation of the frequency components between the two signals in magnitude and phase. A coherence value of 1 for any particular frequency component indicates perfect correlation.

The auto- and cross-correlations can also be calculated as Fourier transforms of the correlation functions, which are given by

$$R_{aa}(\tau) = \lim_{T\to\infty} \frac{1}{T} \int_0^T a(t)a(t+\tau)dt \tag{4.8}$$

and

$$R_{ab}(\tau) = \lim_{T\to\infty} \frac{1}{T} \int_0^T a(t)b(t+\tau)dt \tag{4.9}$$

For samples $a(t)$ placed downstream from $b(t)$, the correlation function will show a maximum at time shift τ corresponding to the time required for turbulent structures to convect from point a to b provided Taylor's hypothesis is valid.

Using this assumption, the phase angle, $\phi(f)$, between the real and imaginary components of the cross-spectra, $S_{ab}(f)$ for points a and b separated in the local streamwise

direction by distance $\Delta\bar{y}$, which is the projection of Δd in the direction of $\bar{U}$, is given by

$$\phi(f) = \frac{2\pi f \Delta\bar{y}}{\bar{U}} \tag{4.10}$$

where $\bar{U}$ is the local streamwise velocity and f is the frequency vector in Hz. Negative phase angle of signal $b(t)$ with respect to signal $a(t)$ indicates that point a experiences the signal first, as a result of being upstream, of point b.

The correlation coefficient function, $\rho_{ab}(\tau)$, is a normalized version of the correlation function and is given by

$$\rho_{ab}(\tau) = \frac{R_{ab}(\tau) - \mu_a\mu_b}{\sqrt{[R_{aa}(0) - \mu_a^2][R_{bb}(0) - \mu_b^2]}} \tag{4.11}$$

where the value of $|\rho_{ab}(\tau)| \leq 1$. This parameter gives another way of measuring the correlation of the signal pairs.

For isotropic, homogeneous flow, a spectral tensor exists, with components $R_{ij}(\Delta d, \tau)$, where i and j are two of u, v, and w, separated by the vector Δd in space, and shifted by τ in time. The components of the spectral tensor are given by the cross-correlation function [95]

$$R_{ij}(\Delta d, \tau) = \frac{1}{T-\tau}\int_0^{T-\tau} a_i(0,t)b_j(\Delta d, t+\tau)dt \tag{4.12}$$

where the Fourier transform of each component in the tensor yields the corresponding cross-spectrum.

The integral length scale of turbulence is a measure that gives an indication of the dominant eddy size in the flow. Integral length scales are defined as

$$L_i^j = \int_0^\infty R_{ii}(r_j)dr_j \tag{4.13}$$

where $j = x$, y, or z and $i = v$, u, or w, respectively. For flow in the atmospheric boundary layer, the values of L_u^x, L_v^x, and L_w^x are of greatest interest. For isotropic turbulence, they are related to one another by the relationship $L_u^x = 2L_{v,w}^x$.

4.2.1 Modelling Flow in the Atmospheric Boundary Layer

The unsteady statistical characteristics of the boundary layer flow can be evaluated from measured time-histories; they can also be estimated from an appropriate model. Many models for the auto-spectra atmospheric boundary layer exist [96, 24, 97, 28], as do many models for coherence and cross-correlations [96, 98, 99]. The von Kármán spectra, while developed for isotropic flows, has several features that make them an attractive modelling tool.

- They contain expressions for auto-spectra and coherence.
- They are based on physical parameters, wave number, k; length scale, L; rate of dissipation of viscous energy, ϵ; the Komolgorov constant, α; and separation distance, Δd.
- They display correct asymptotic behaviour in the coherence expressions as the wave number approaches zero for probe separation distances that are significant compared to the size of the integral length scale.
- They exhibit the correct -5/3 slope in the inertial subrange, which can contain turbulent energy at frequencies that are relevant for blade sailing..

The von Kármán auto-spectra are expressed as [28]

$$S_u(k) = \frac{9}{55}\alpha\epsilon^{2/3}\frac{1}{(L^{-2}+k^2)^{5/6}} \tag{4.14}$$

for the streamwise fluctuations and

$$S_{v,w}(k) = \frac{3}{110}\alpha\epsilon^{2/3}\frac{(3L^{-2}+8k^2)}{(L^{-2}+k^2)^{11/6}} \tag{4.15}$$

for lateral and vertical. In these expressions, k is the wave number, given by $k = 2\pi f/U$, which depends on the frequency vector in Hz, f; ϵ is the rate of viscous dissipation of kinetic energy; and α is the Komolgorov constant. For isotropic flow, the length scale, L is the same in both expressions.

The von Kármán model for the root coherence, γ is given by three equations that give the characteristics of streamwise turbulence, u, and lateral turbulence, v, and vertical turbulence, w, respectively [99].

$$\gamma_u(k) = \frac{2}{\Gamma(\frac{5}{6})}\left(\frac{\lambda}{2}\right)^{\frac{5}{6}}\left\{K_{\frac{5}{6}}(\lambda) - \frac{1}{2}\lambda K_{\frac{1}{6}}(\lambda)\right\} \tag{4.16}$$

$$\gamma_v(k) = \frac{2}{\Gamma(\frac{5}{6})}\left(\frac{\lambda}{2}\right)^{\frac{5}{6}}\left\{K_{\frac{5}{6}}(\lambda) + \frac{3(\Delta dk)^2}{3\lambda^2 + 5(\Delta dk)^2}\lambda K_{\frac{1}{6}}(\lambda)\right\} \tag{4.17}$$

$$\gamma_w(k) = \frac{2}{\Gamma(\frac{5}{6})}\left(\frac{\lambda}{2}\right)^{\frac{5}{6}}\left\{K_{\frac{5}{6}}(\lambda) - \frac{3(\frac{\Delta d}{L_w})^2}{3\lambda^2 + 5(\Delta dk)^2}\lambda K_{\frac{1}{6}}(\lambda)\right\} \tag{4.18}$$

$$\lambda = (\Delta d^2 k^2 + \frac{\Delta d^2}{L_i^2})^{\frac{1}{2}} \tag{4.19}$$

where k is again the wave number, λ is the von Kármán constant as given in Equation 4.19, and K represents the modified Bessel function of the second kind. The root coherence can be fully defined by the quantities Δd, the point spacing, L, the local length scale, and k. Since Δd and k are known for a given set of points, only the parameter L_i, where the i refers to the coordinate direction being considered, requires determination. This value can be found as a function of space in the flowfield by fitting the experimental data. The von Kármán models were derived to apply to isotropic flows without streamwise spacing and phase shift between the velocity signals.

The integral length scales calculated for the root coherence functions are related to the length scale L in von Kármán's auto-spectra by $L = \frac{4}{3}L_u = \frac{8}{3}L_{v,w}$. For non-isotropic turbulence, the individual spectral models may still be valid, however the length scales may not be related in this manner.

4.3 Planar Quasi-steady Airwake

The planar quasi-steady airwake model is based on the data collected in airwake experiment A. As described in Appendix C, the data collected over seven ship deck models at different roll angles was interpolated onto a regular grid. Contour plots showing the variation of flowfield parameters with ship roll angle are given in Figures 4.3 to 4.9. The data shown are: the normalized wind speed in the horizontal and vertical directions relative to the ship deck, ν_u and ν_w respectively; the angle of the flow relative to the ship deck, where horizontal flow has zero angle; and horizontal and vertical turbulence intensity, i_u and i_w respectively. The original data point locations and ship deck angle are given in the small frame to the left of the flow angle frame.

The steady airwake data allows a number of important conclusions to be drawn about the nature of the the flow. Roll angle significantly changes the flowfield. Of specific interest is the variation in the vertical component of mean velocity, which varies from values in the range of -0.2 times freestream for a 20° deck to values in the range of 0.5 times freestream for the -20° deck. This is significant as the vertical component of velocity is believed to contribute significantly to the blade sailing phenomenon.

For negative ship roll angles, the turbulence intensity increases across the ship deck. A turbulence intensity level above 0.33 indicates the onset of recirculating flow for normally distributed velocity fluctuations, based on a three-standard deviation argument. The hot-film sensors used in this experiment cannot differentiate flow direction and therefore overestimate flow velocity and underestimate turbulence intensity in reversing flows. In the time-averaged data shown here, flow velocity in the reversing flow region is taken to be 0 m/s, where the reverse flow region is identified by horizontal turbulence intensity levels above 0.33. The recirculation region can be seen in Figures 4.3 through 4.9 as the area where the flow properties are equal to zero. The size of the recirculation bubble grows with negative roll angle.

Flow visualizations were completed over the -20° deck using a smoke wand for a wind tunnel flow speed of 2.7 m/s. A time history of 1.2 s of flow are shown in Figure 4.10; one

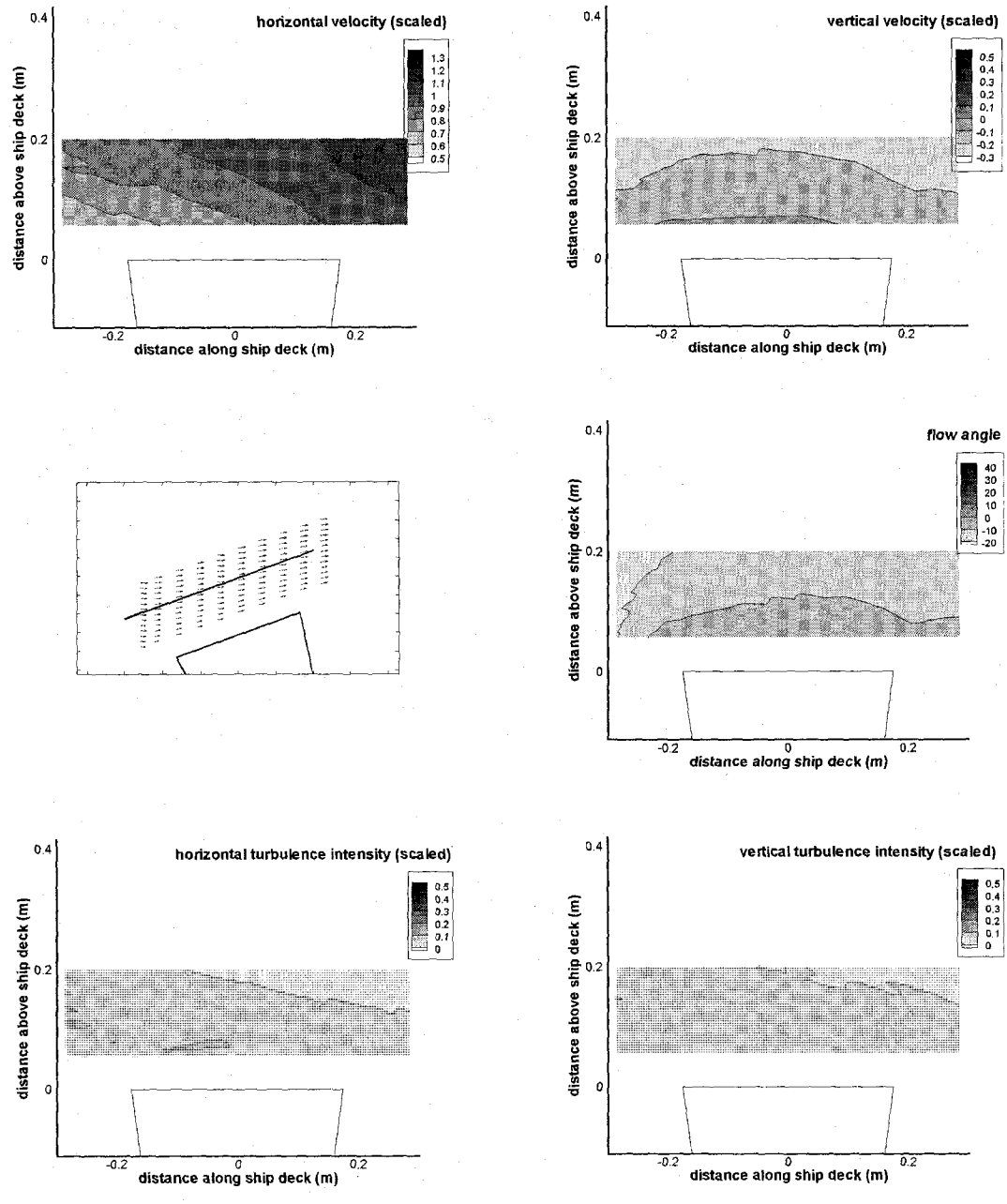

Figure 4.3: Flowfield results of Experiment A for 20° ship deck.

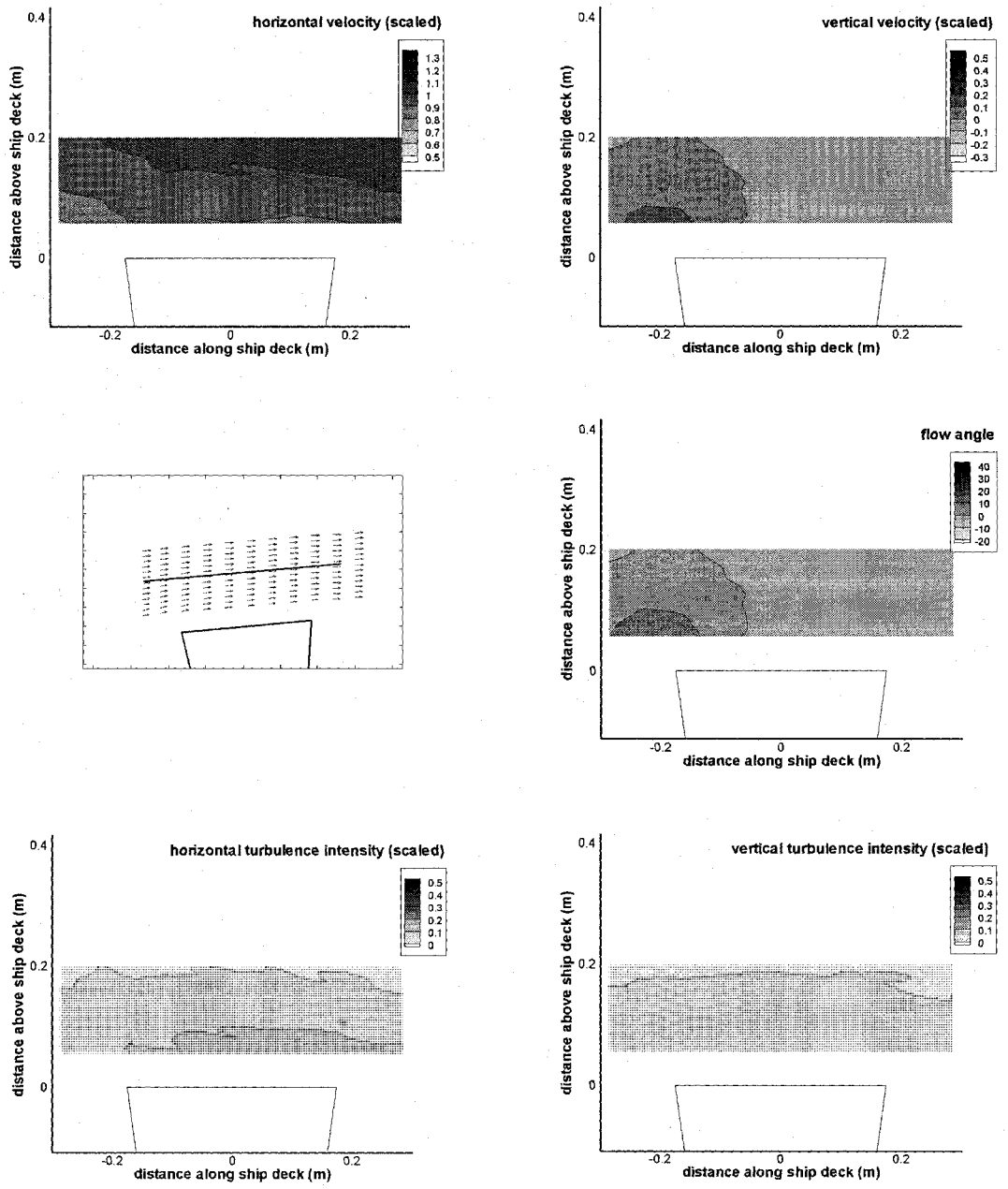

Figure 4.4: Flowfield results of Experiment A for 5° ship deck.

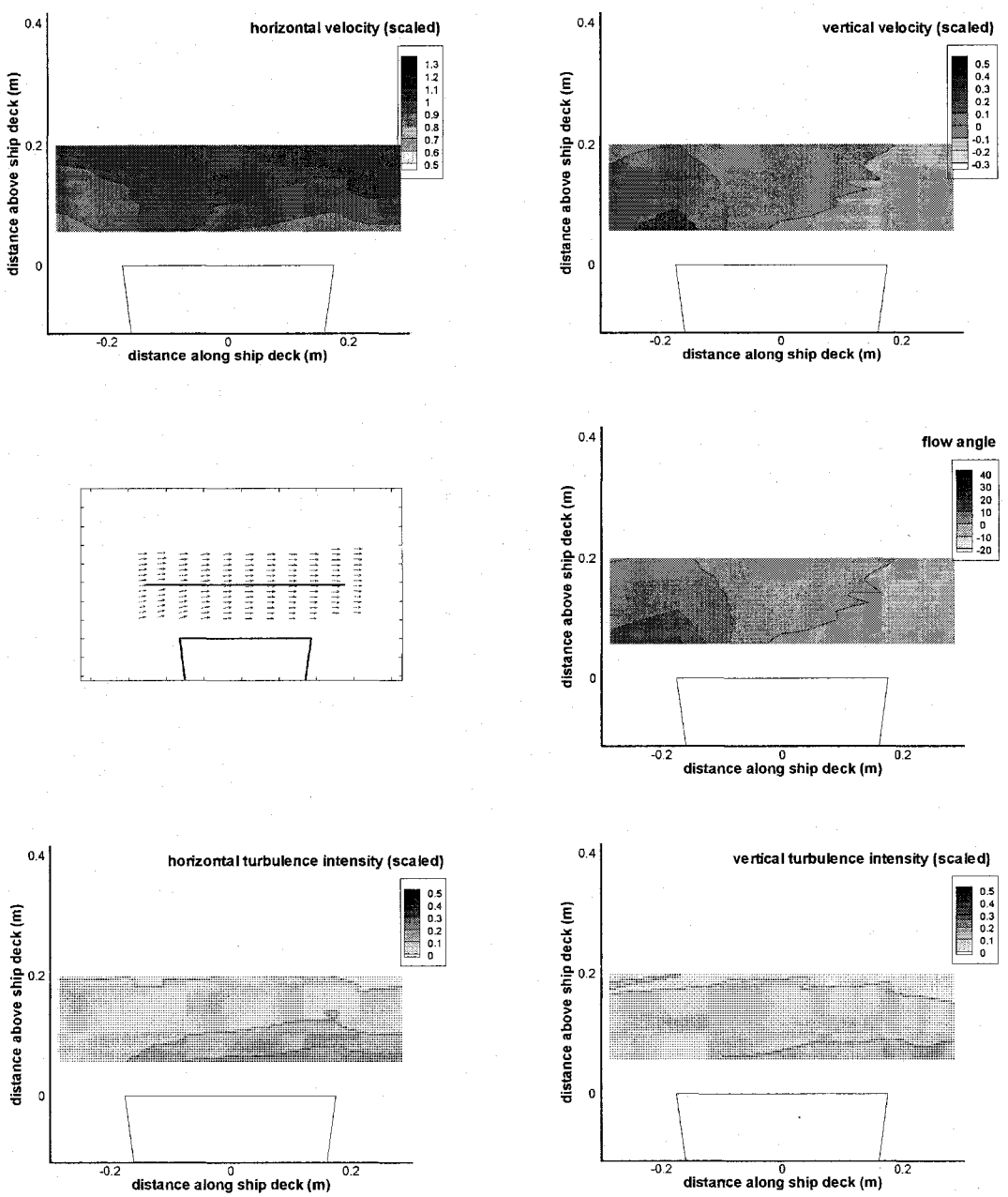

Figure 4.5: Flowfield results of Experiment A for 0° ship deck.

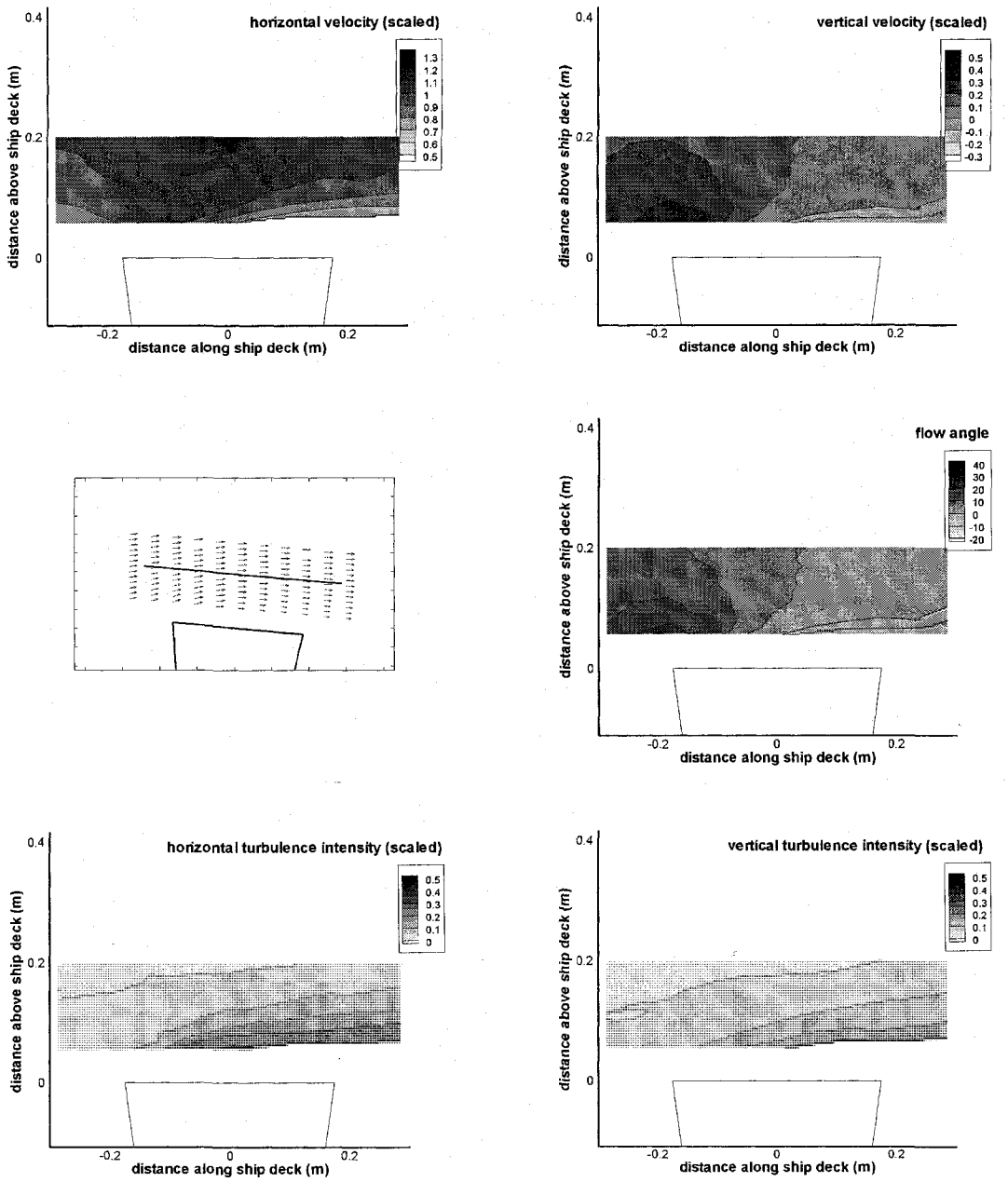

Figure 4.6: Flowfield results of Experiment A for -5° ship deck.

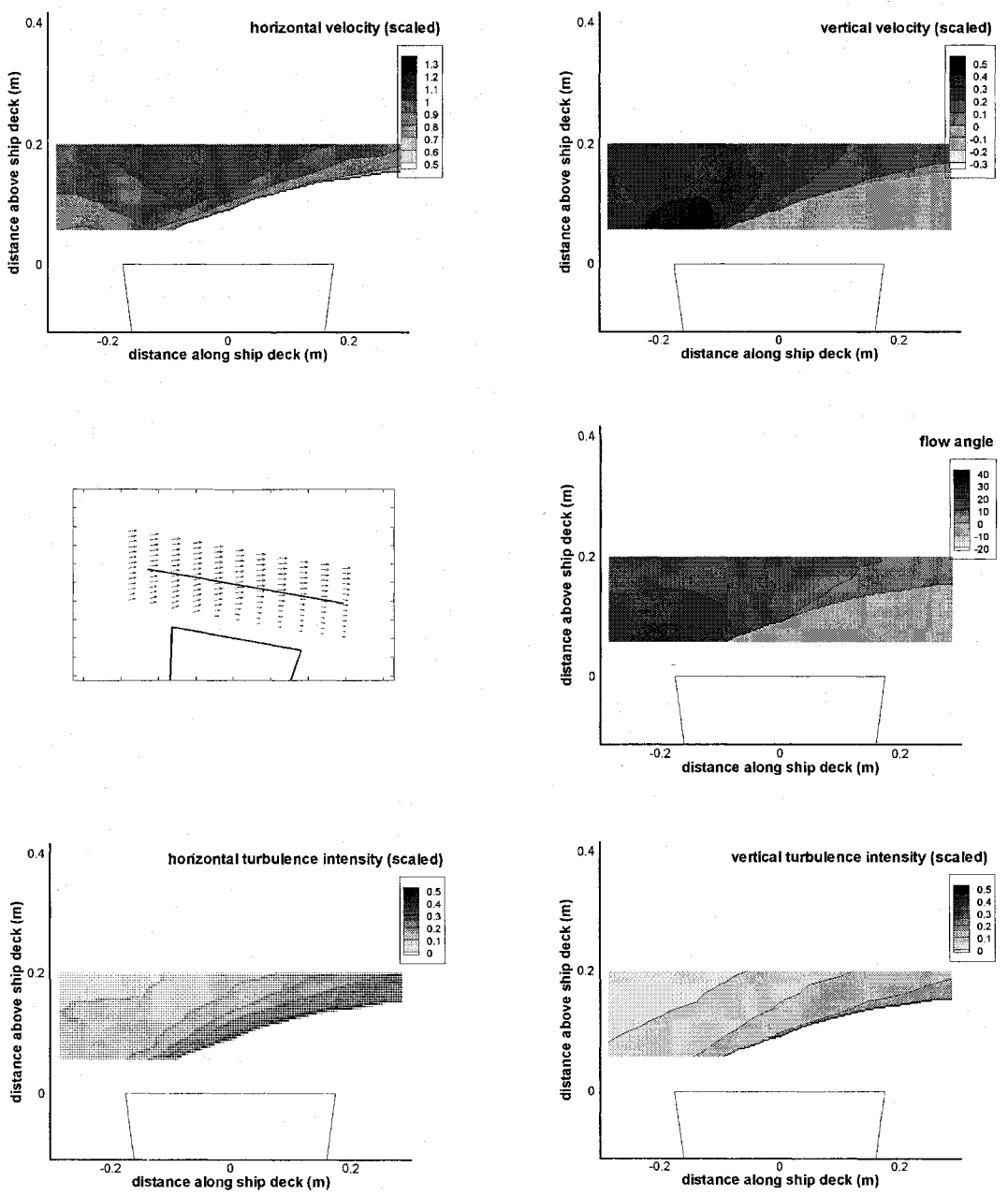

Figure 4.7: Flowfield results of Experiment A for -10° ship deck.

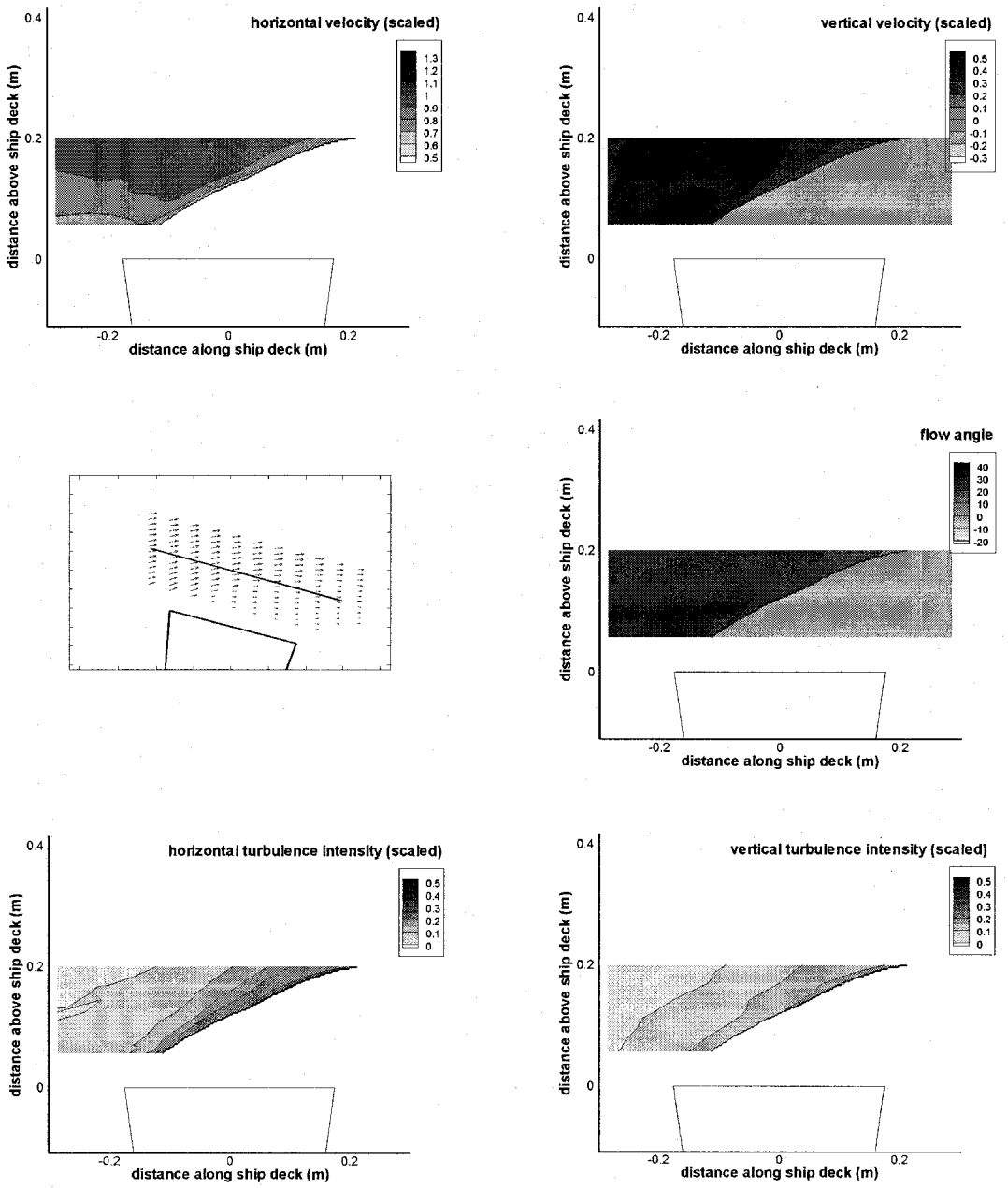

Figure 4.8: Flowfield results of Experiment A for -15° ship deck.

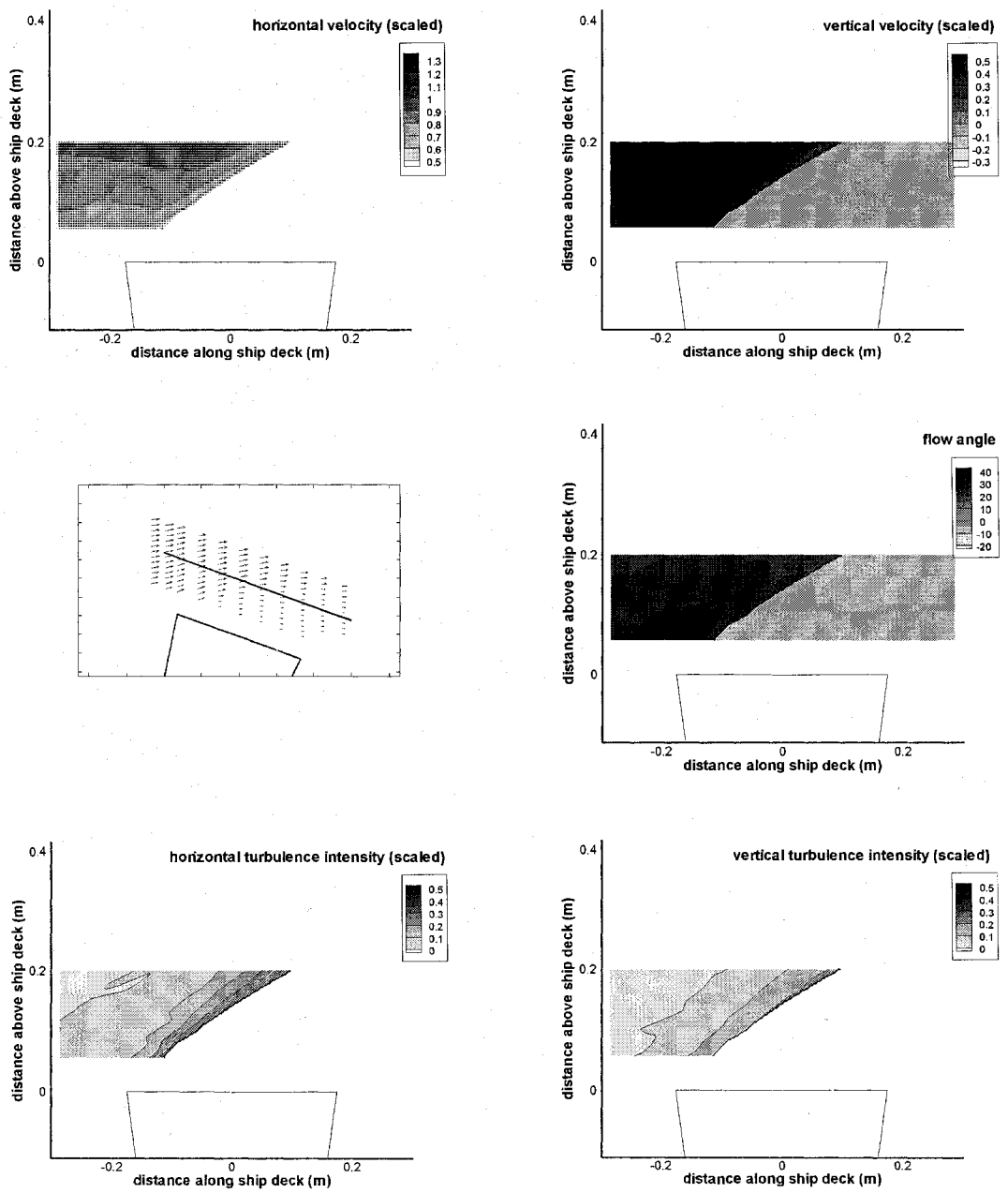

Figure 4.9: Flowfield results of Experiment A for -20° ship deck.

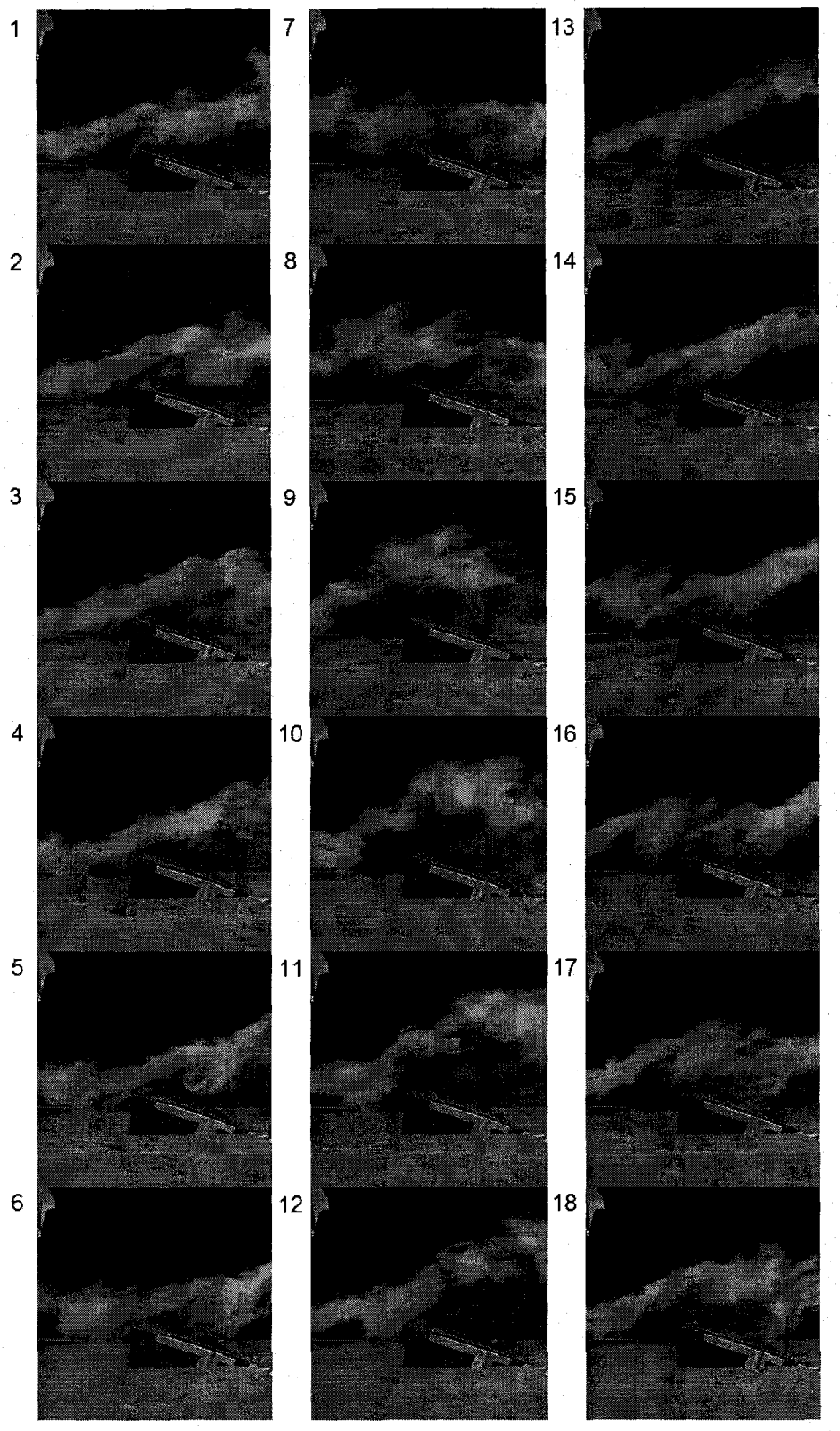

Figure 4.10: Flow visualization over -20° ship deck (1/15 s between images).

second is given by 15 frames. Frame 5 clearly shows a vortex developing over the deck, which is later shed (frame 6, 7, 8). A low frequency flapping motion of the shear layer can be observed by examining the frames in sequence.

At wind speeds that are high enough to induce blade sailing, the reduced frequency of the deck is very low. Therefore the variations in airwake with roll angle can be taken as quasi-steady.

4.3.1 Time-averaged Airwake Model

The quasi-steady airwake model that was developed consists of a look-up table gridded in space above the flight deck and as a function of roll angle, which gives the horizontal and vertical velocity and turbulence intensity at a specified location above the ship deck, in ship coordinates. This model was developed by directly interpolating the collected data onto a regular grid.

4.3.2 Validation

In an effort to determine the consistency of the steady airwake model, the steady statistics from Experiment B were compared against the statistics for the equivalent point in space as calculated by the interpolation algorithm developed from the data from Experiment A. Based on the error analysis discussed in Section C.6, the mean statistics for Experiment B are expected to exhibit higher uncertainty than those from experiment A.

Of the total number of collected data points in Experiment B, 156 pairs fell within the flow field area over the 0° deck and 76 fell within the flowfield area above the -20° deck. Table 4.1 shows the percentage of these points that agree with the time-averaged model to within 5% and 10% for both decks. For the 0° deck, almost all the statistics agree to within 10 %. The -20° deck exhibits higher differences owing to the fact that the flowfield characteristics change much more quickly above the -20° deck.

The points with differences exceeding 10%, for any quantity, are shown in Figure 4.11. The largest differences occur where the velocities gradients are high. These differences are attributed largely to the uncertainty in probe positions.

Table 4.1: Steady statistics verification.

deck angle		0°	-20°
total points		156	76
points with < 5 % difference	ν_u	47 %	21 %
	ν_w	99 %	47 %
	i_u	100 %	68 %
	i_w	100 %	96 %
points with < 10 % difference	ν_u	97 %	74 %
	ν_w	100 %	80 %
	i_u	100 %	96 %
	i_w	100 %	97 %
all points - maximum difference	ν_u	11 %	60 %
	ν_w	6 %	21 %
	i_u	4 %	42 %
	i_w	2 %	25 %
all points - minimum difference	ν_u	0 %	0 %
	ν_w	0 %	0 %
	i_u	0 %	0 %
	i_w	0 %	0 %
all points - average difference	ν_u	5 %	9 %
	ν_w	2 %	6 %
	i_u	2 %	5 %
	i_w	1 %	2 %

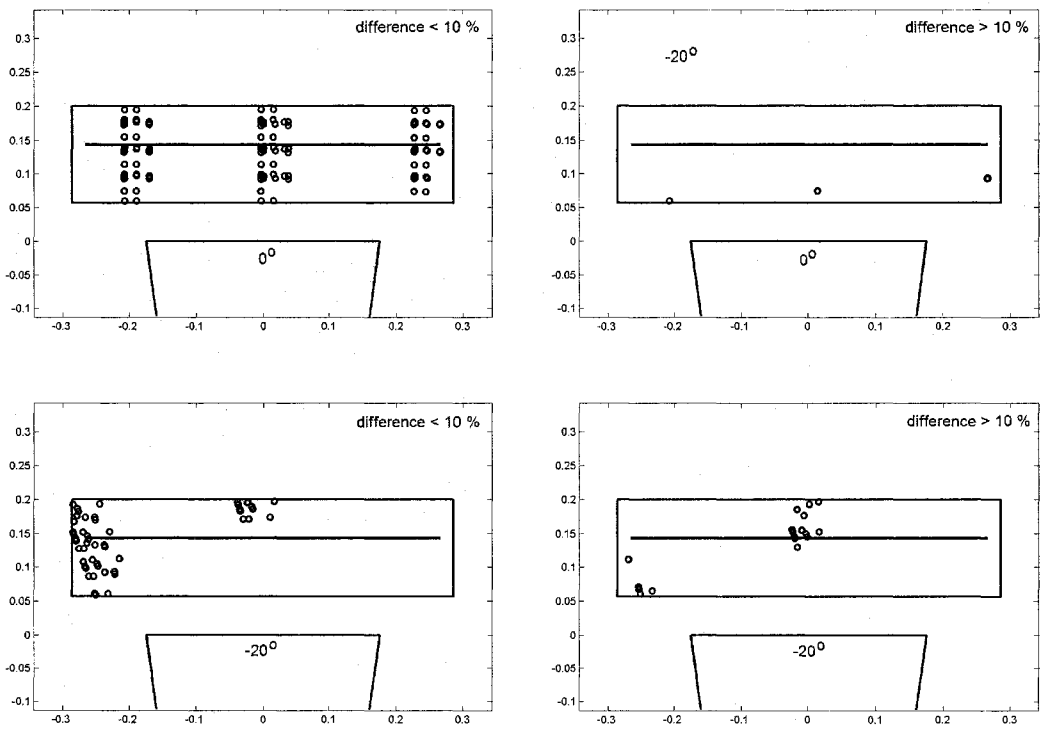

Figure 4.11: Points with measured differences (any quantity) greater than (right) and less than (left) 10 %.

4.4 Correlated Turbulent Airwake

The turbulent airwake model is based on the data collected in airwake Experiment B, as discussed in Appendix C. The goal of this phase was to use experimental data to reproduce, as closely as possible, the auto- and cross-correlation characteristics of the flowfield. This analysis was completed by studying the correlations between many pairs of simultaneously-collected velocity records. The turbulence characteristic experiment was conducted according to the following procedure.

1. An appropriate basic correlation distance was determined through preliminary testing and analysis. This distance was selected such that significant flow correlations could be captured with a reasonable number of measurements (Section 4.4.2).

2. Once a basic separation distance was identified, then a reasonable number of reference flow points and correlation spacings was identified. Pairs of velocity data were taken at each reference point for each correlation spacing (Section 4.4.3).

3. The correlations were examined, and a method for generalizing the correlations across the flowfield for any correlation spacing was developed. This model was intended to capture the changing nature of auto-spectral and correlation characteristics in the flowfield (Section 4.4.4).

4. Using the above spectral model from 3, the spatially- and temporally-correlated flowfield is reconstructed for use in time-history blade sailing simulations (Section 4.4.5).

4.4.1 Spacing Nomenclature

Before proceeding with a discussion of the measured correlations, some nomenclature used to differentiate the measurement pairs is defined. Each pair of points is defined by five characteristics.

Spacing direction: gives the direction of the probe spacing in ship coordinates. The spacing designations are indicated using capital letters that are consistent with the

coordinate system described in Section 4.1. The measured spacings are X and Z, which are spacings along the respective axes in ship coordinates; XY, which is a diagonal spacing at 45° in the horizontal plane; and ZYU and ZYD, which are the upward and downward 45° spacings in the flowfield plane. Figure 4.12 shows the point spacings, which were selected to represent a regular square or diamond grid in space. The streamwise Y spacing cannot be measured since the downstream probe would sit in the wake of the upstream probe.

Spacing distance: is given in mm at model scale. For diagonal spacings, the spacing distance represents the projected spacing along each axis rather than the actual diagonal spacing. This results in a rectangular grid of measured data.

Horizontal measurement location: is also called the "y value". It is given as a designation that indicates the position relative to the deck. The designations TE and LE refer to the trailing (or leeward) edge and leading (or windward) edge, respectively, as shown in Figures 4.13 and 4.14. Data taken at these y locations were used to determine the basic spacing. The designations PLE, M, and PTE refer to pre-leading edge, middle, and post-trailing edge, respectively, as shown in Figures 4.15(a) and 4.15(b). These data make up the main data set.

Vertical measurement location: is also called the "z value". It is given by a number between 1 and 5, where nominal station 1 is closest to the deck.

Deck angle: is either 0° or -20°, depending on the deck roll angle over which the data was taken.

4.4.2 Preparatory Results

In order to determine a suitable basic correlation distance, the correlation coefficient for probe spacings in the X, Z, and XY directions were calculated for a variety of spacing distances between 5 mm and 127 mm. The correlation coefficients are shown in Figures 4.13 and 4.14. Using this data, a nominal probe separation of 18 mm was selected. This distance

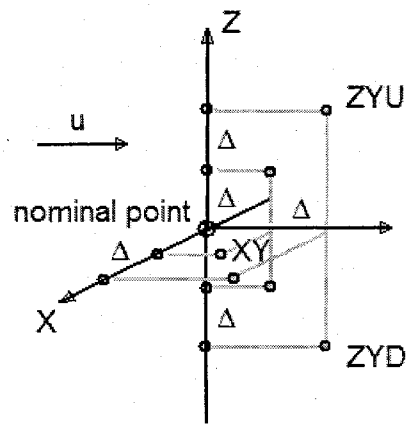

Figure 4.12: Spacings for data point pairs (nominal + another point at some spacing).

was selected for two reasons. Primarily, this distance gives correlation coefficients in the range of 0.8, and twice this distance leads to correlations in the range of 0.6. Spacings at higher multiples of this basic distance, lead to correlation coefficients that are typically less than 0.4, suggesting strongly uncorrelated flow. The correlation distances of approximately 18 mm and 36 mm can be achieved easily with the probe holding equipment, which has discrete probe stations.

4.4.3 Data collection

The main data were collected using a nominal probe spacing of 18 mm, and at the spacing combinations given in Table 4.2. These spacings give a diamond grid for probe spacings up to 35 mm. Pairs of velocity records were collected at each nominal point above the ship deck for a deck angle of 0°, as shown in Figure 4.15(a), and at each nominal point over the -20° deck as shown in Figure 4.15(b).

Figures C.9 to C.50 show the calculated root coherence and phase angle for each set of data points that were collected. Each page shows five correlation pairs, where the horizontal root coherence, vertical root coherence, horizontal phase angle and vertical phase angle are given in each column. In these figures, the frequency axis has been scaled by the freestream velocity.

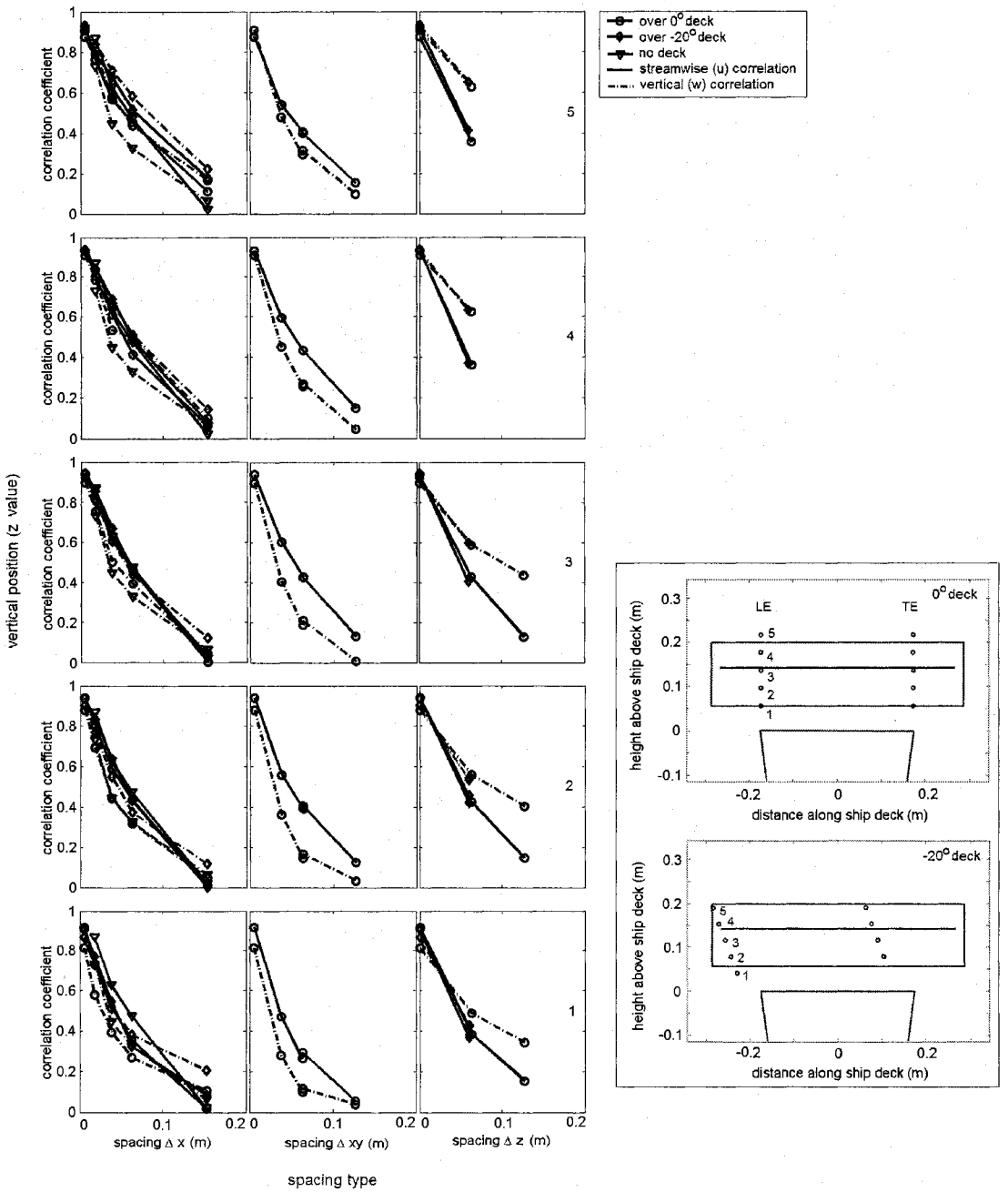

Figure 4.13: Correlation coefficients over windward deck edge.

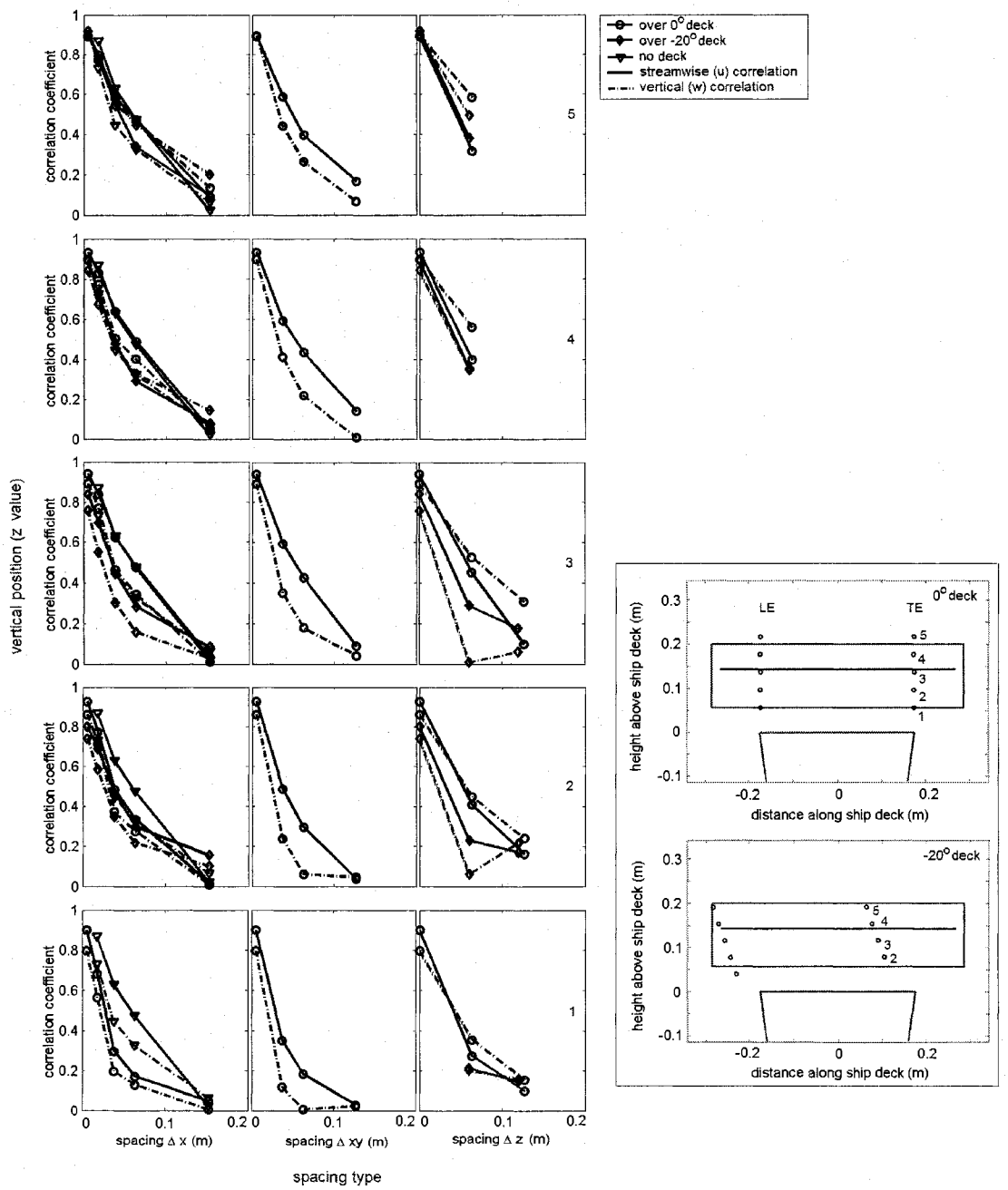

Figure 4.14: Correlation coefficients over leeward deck edge.

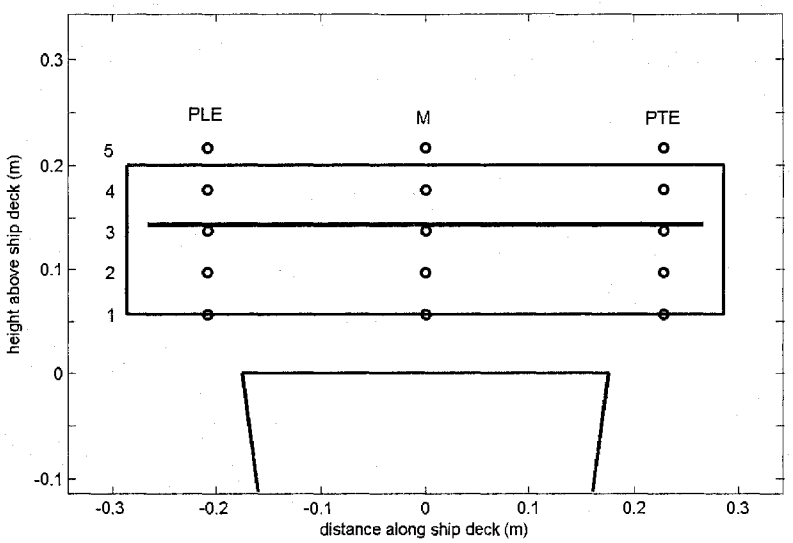

(a) above 0° ship deck

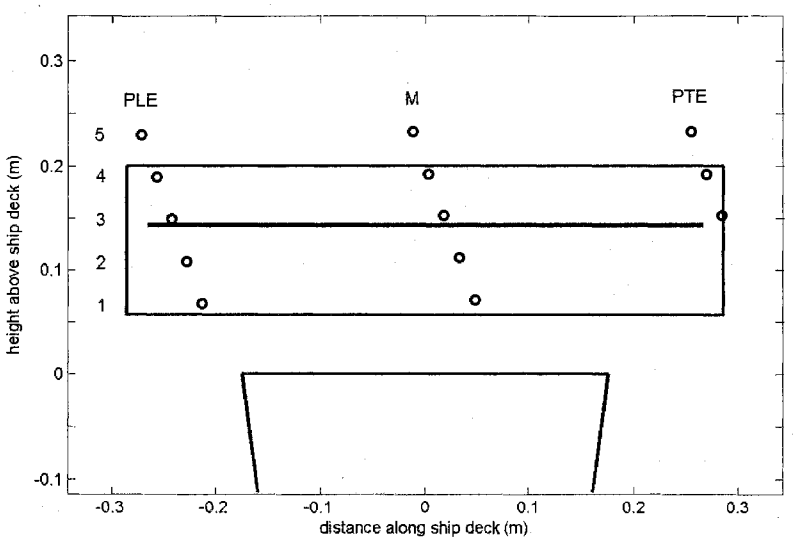

(b) above -20° ship deck

Figure 4.15: Nominal data collection points for unsteady data.

Table 4.2: Probe spacings (ship coordinates) for final data collection.

Designation	Δx (mm)	Δy (mm)	Δz (mm)
X3	35	0	0
XY1	18	18	0
XY3	35	35	0
Z3	0	0	3
ZYU1	0	18	18
ZYU3	0	35	35
ZYD1	0	18	18
ZYD3	0	35	35

4.4.4 Statistical Airwake Model

For the analysis of unsteady characteristics, both the velocity records and the model scale frequencies are scaled to reflect a dynamically similar system with a freestream velocity of unity as

$$\nu + u_n(t) = \frac{U + u(t)}{U_{\text{free}}} \tag{4.20}$$

$$f_n = \frac{f}{U_{\text{free}}} \tag{4.21}$$

where the subscript n refers to the normalized quantity. The corresponding normalized wave number is then

$$k_n = \frac{2\pi f}{\bar{U}_n} \tag{4.22}$$

where

$$\bar{U}_n = \sqrt{\nu_u^2 + \nu_w^2} \tag{4.23}$$

The auto-spectra and coherences are then modelled using the von Kármán relationships.

Data Synthesis

The von Kármán auto-spectra, given in Equations 4.14 and 4.15, were used to represent the data taken during Experiment B. The fitting parameters are L and $\alpha\epsilon^{2/3}$, which are expected to be the same for all three spectral directions if the turbulence is isotropic and homogeneous. Relaxing this restriction leads to four fitting parameters for horizontal and vertical turbulence. They are L_{uauto}, L_{wauto}, $\alpha\epsilon_u^{2/3}$, and $\alpha\epsilon_w^{2/3}$, as shown in

$$S_{u_n}(k_n) = \frac{9}{55}\alpha\epsilon_u^{2/3}\frac{1}{(L_{uauto}^{-2} + k_n^2)^{5/6}} \tag{4.24}$$

for the streamwise fluctuations and

$$S_{v_n,w_n}(k_n) = \frac{3}{110}\alpha\epsilon_w^{2/3}\frac{(3L_{wauto}^{-2} + 8k_n^2)}{(L^{-2} + k_n^2)^{11/6}} \tag{4.25}$$

for lateral and vertical fluctuations.

Figure 4.16 shows samples of the measured and fitted normalized auto-spectra. The fitting parameters are displayed on the figure frames. The quality of the measured spectra and the fitted spectra is representative of the data set; therefore only this sample is given. The distribution of fitting parameters for the auto spectra is given in Figures 4.17 and 4.18 for each deck angle.

The coherence functions, given in Equations 4.16 and 4.18, are modified for use with the normalized data as

$$\gamma_{u_n}(k_n) = \frac{2}{\Gamma(\frac{5}{6})}\left(\frac{\lambda}{2}\right)^{\frac{5}{6}}\left\{K_{\frac{5}{6}}(\lambda) - \frac{1}{2}\lambda K_{\frac{1}{6}}(\lambda)\right\} \tag{4.26}$$

$$\gamma_{w_n}(k_n) = \frac{2}{\Gamma(\frac{5}{6})}\left(\frac{\lambda}{2}\right)^{\frac{5}{6}}\left\{K_{\frac{5}{6}}(\lambda) - \frac{3(\frac{\Delta d}{L_w})^2}{3\lambda^2 + 5(\Delta dk)^2}\lambda K_{\frac{1}{6}}(\lambda)\right\} \tag{4.27}$$

$$\lambda = (\Delta d^2 k_n^2 + \frac{\Delta d^2}{L_i^2})^{\frac{1}{2}} \tag{4.28}$$

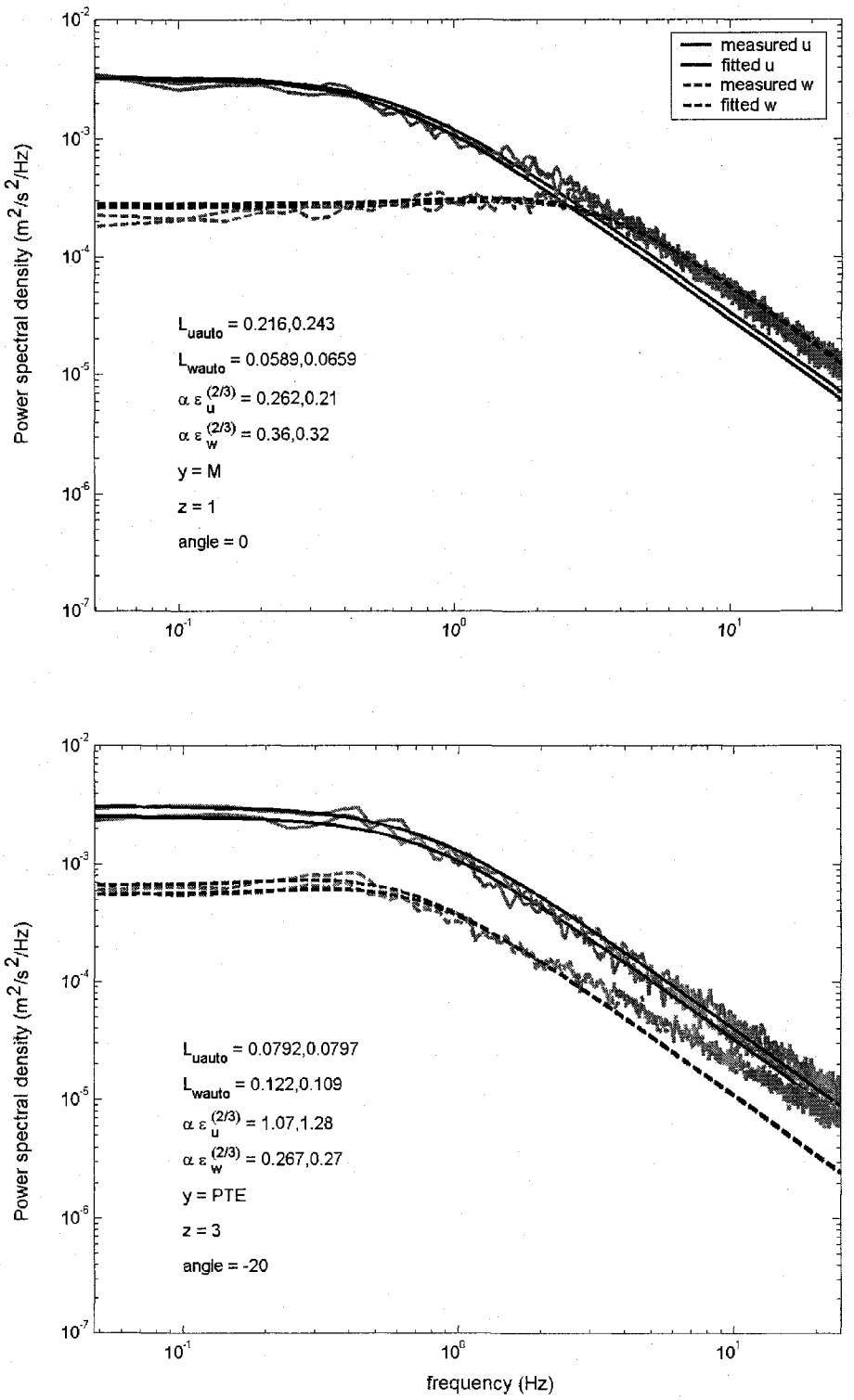

Figure 4.16: Sample horizontal and vertical velocity auto-spectra for pairs of collected points.

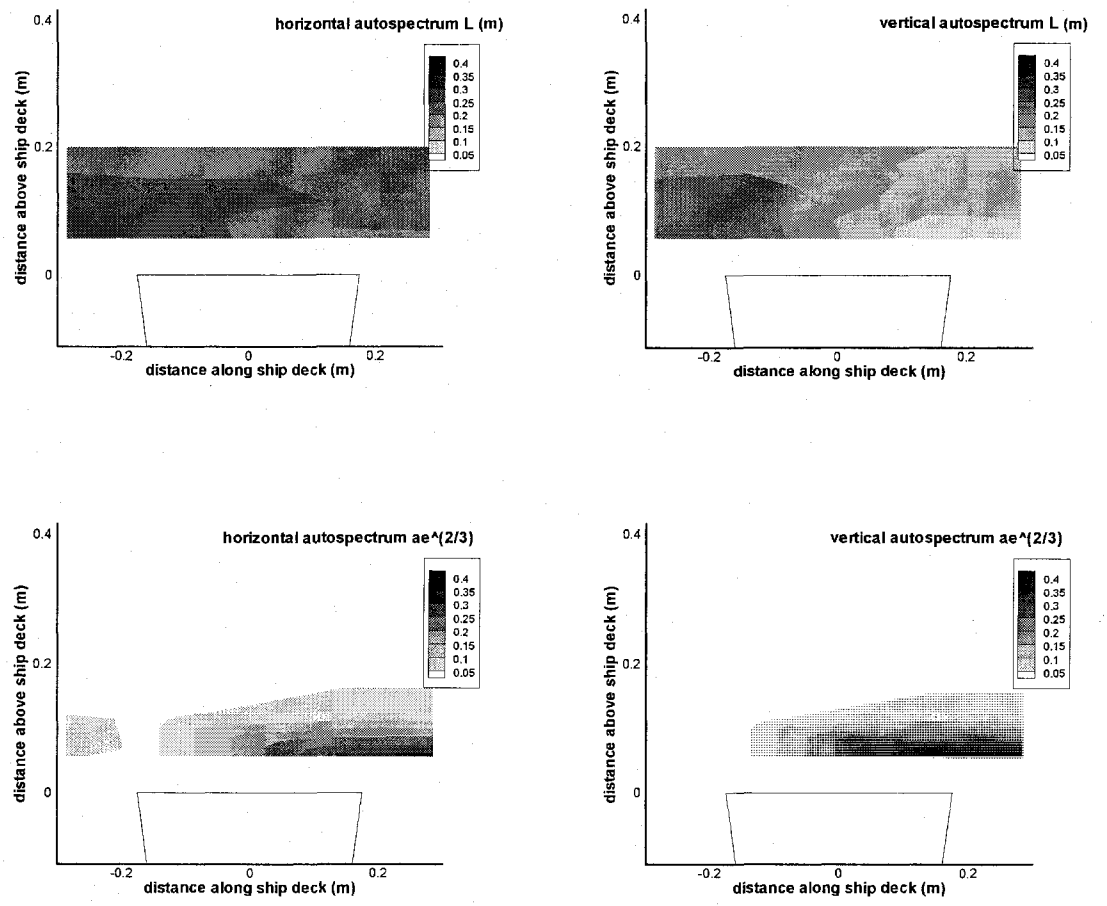

Figure 4.17: Fitting parameters for auto-spectra (0° deck).

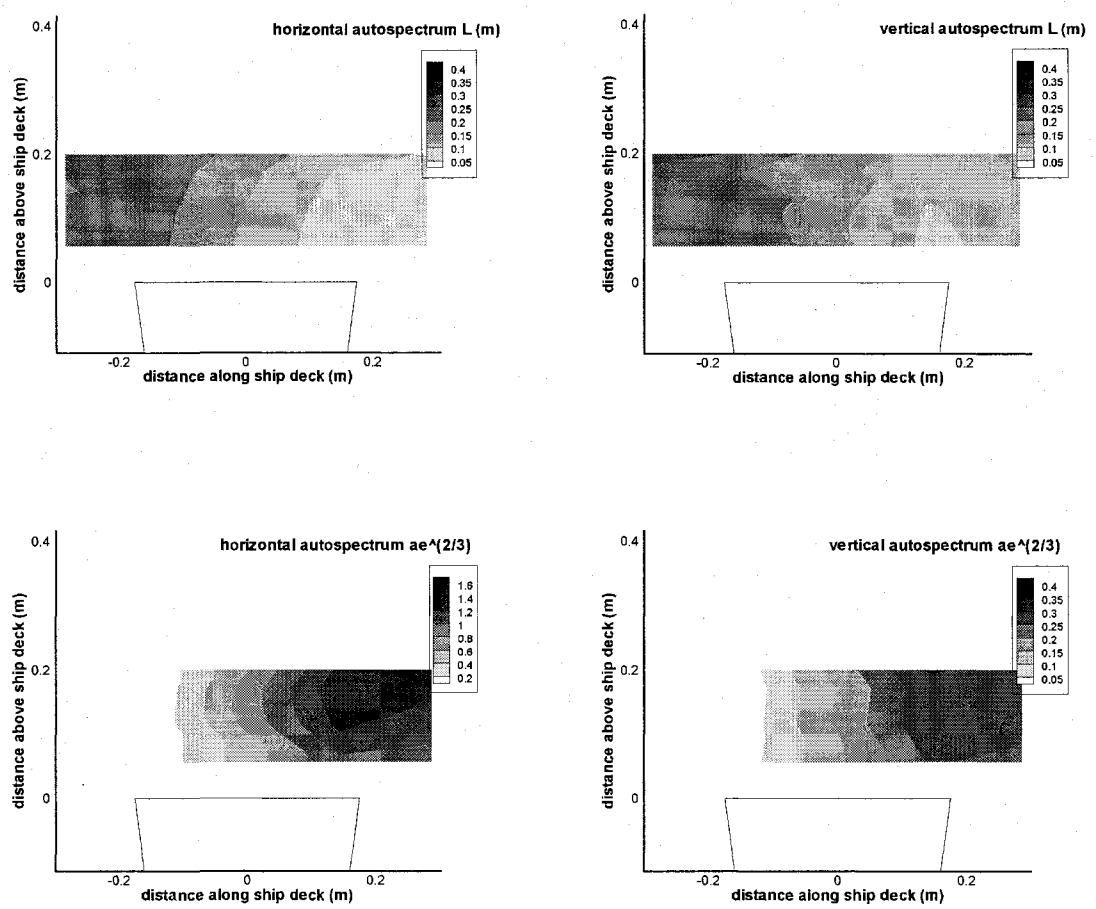

Figure 4.18: Fitting parameters for auto-spectra (-20° deck; data shown in deck reference frame).

The coherence fitting parameters are L_u and L_w. Using the known probe spacing, Δd, which is the probe spacing projected onto the plane perpendicular to the direction of the local mean velocity, $\bar{U}_n$, and wave number, k, based on the normalized local mean velocity, $\bar{U}_n$, the length scales for best agreement at the lowest frequencies or wave numbers were calculated. These are printed on the figures for the coherence data in Figures C.9 to C.50, which show the quality of the coherence modelling given by von Kármán equations.

Results from Experiment B were used to generate the fitted coefficients to calculate the von Kármán coherence functions as a function of position over the flight deck for deck roll angles of 0° and -20°. Figures 4.19 to 4.25 show the variation of coherence fitting parameters with position above the flight deck. These figures are created from an interpolation of the gathered data into a regular grid, which is employed in the correlated turbulence model. Length scales for the same spacing direction at different spacing distances should yield the same fitted length scale. This trend is generally exhibited in the data.

The frequency range at full scale of highest correlation was calculated as

$$f_{\text{full}} = \frac{f_{\text{model}}}{S} \tag{4.29}$$

where S is the scaling factor. This relationship comes from reduced frequency similarity. The reduced frequency, f^*, is given by

$$f^* = \frac{fD}{V} \tag{4.30}$$

where D is a characteristic length and V is a characteristic velocity, assumed to be the freestream at 9 m/s for both model and full scale. In the collected data, coherence values below 0.4 are exhibited for frequencies above approximately 2 - 4 Hz full scale, depending on the turbulence level in the flow. For highly turbulent flows, such as those over the trailing edge of the -20° deck, the flow is essentially uncorrelated above 0.5 Hz full scale, even for probe spacings of 18 mm (0.63 m full scale).

The phase angles were modelled using Equation 4.10, but applied with some special considerations. At coherence values below 0.4, the turbulence is assumed uncorrelated; at

this level, the phase angles are generated randomly. Also, in areas of changing velocity profile, such as the planetary boundary layer, vertical phase lag has also been observed as a result of the fact that eddies moving through regions of higher velocity will convect more quickly than those moving through regions of lower velocity. Using a concept called the shear slope [100], which can be taken as 0 in uniform flow and 1 in the atmospheric boundary layer below 80 m, the phase shift due to changes in velocity has the same form as Equation 4.10 except that $\Delta\bar{y}$ is substituted for $\Delta\bar{z}$, which is the vertical probe spacing perpendicular to the local mean speed. Based on the data collected, this additional shift improves, for the horizonal correlations only, the quality of the phase model for points with vertical probe spacing.

Therefore, the phase model that best represents the data collected in Experiment B is

$$\phi_u(f) = \frac{2\pi f(\Delta\bar{y} + \Delta\bar{z})}{\bar{U}} \tag{4.31}$$

$$\phi_w(f) = \frac{2\pi f \Delta\bar{y}}{\bar{U}} \tag{4.32}$$

The correlation model that has been developed using the von Kármán relationships and the frozen turbulence assumption was intended to capture the general correlation trends that are present in planar flow over a typical frigate deck in beam winds. The developed model does this well, especially considering a large number of interpolations and simplifications.

Combined Statistical Airwake Model

The steady and unsteady airwake models are combined to give a representation of the statistical properties of any two points in the flowfield. For a given pair of points, a and b, in space, the x, y, and z position of each, the deck roll angle, $\theta_{S_{roll}}$, and the freestream velocity, U_{free} are input to the airwake model. The steady model is used to give the normalized mean velocities, ν_u and ν_w, and the turbulence intensities, i_u and i_w at each point and also at the mid point.

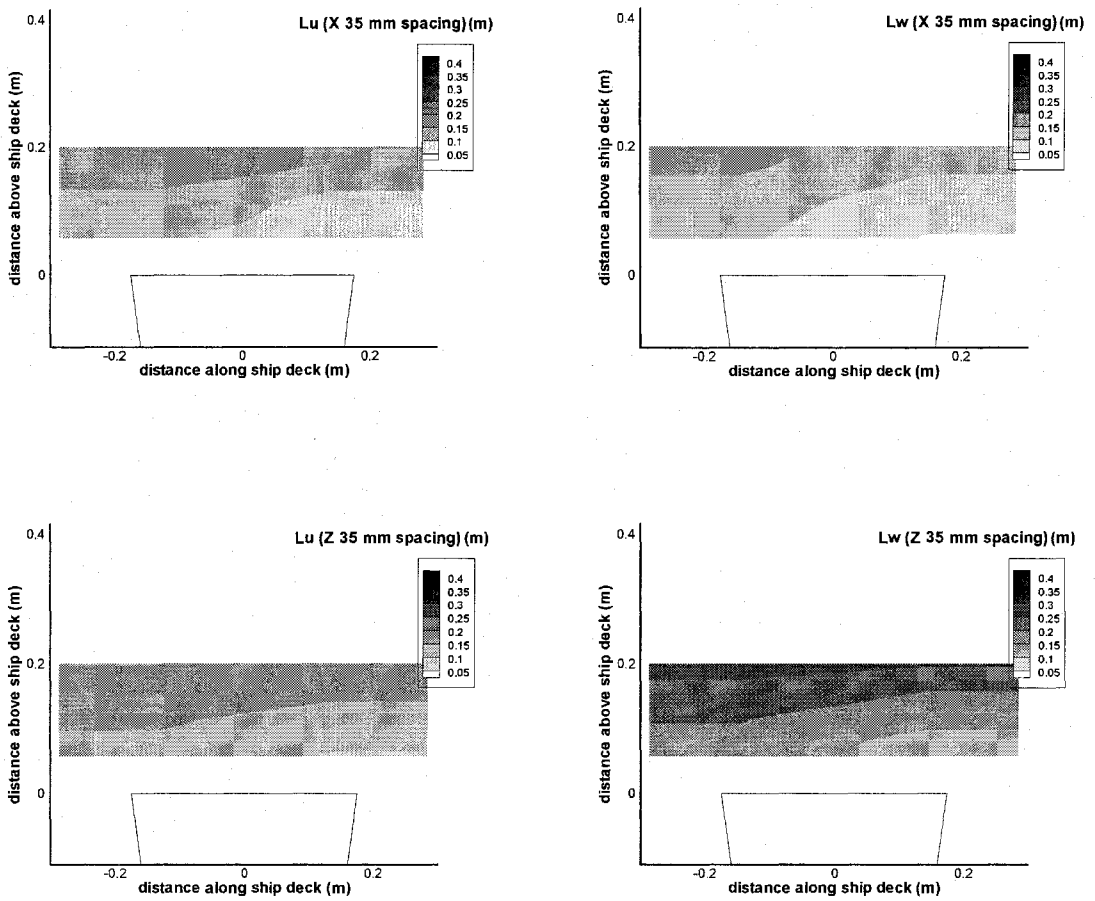

Figure 4.19: Fitting parameters for coherence with X and Z spacings (0° deck).

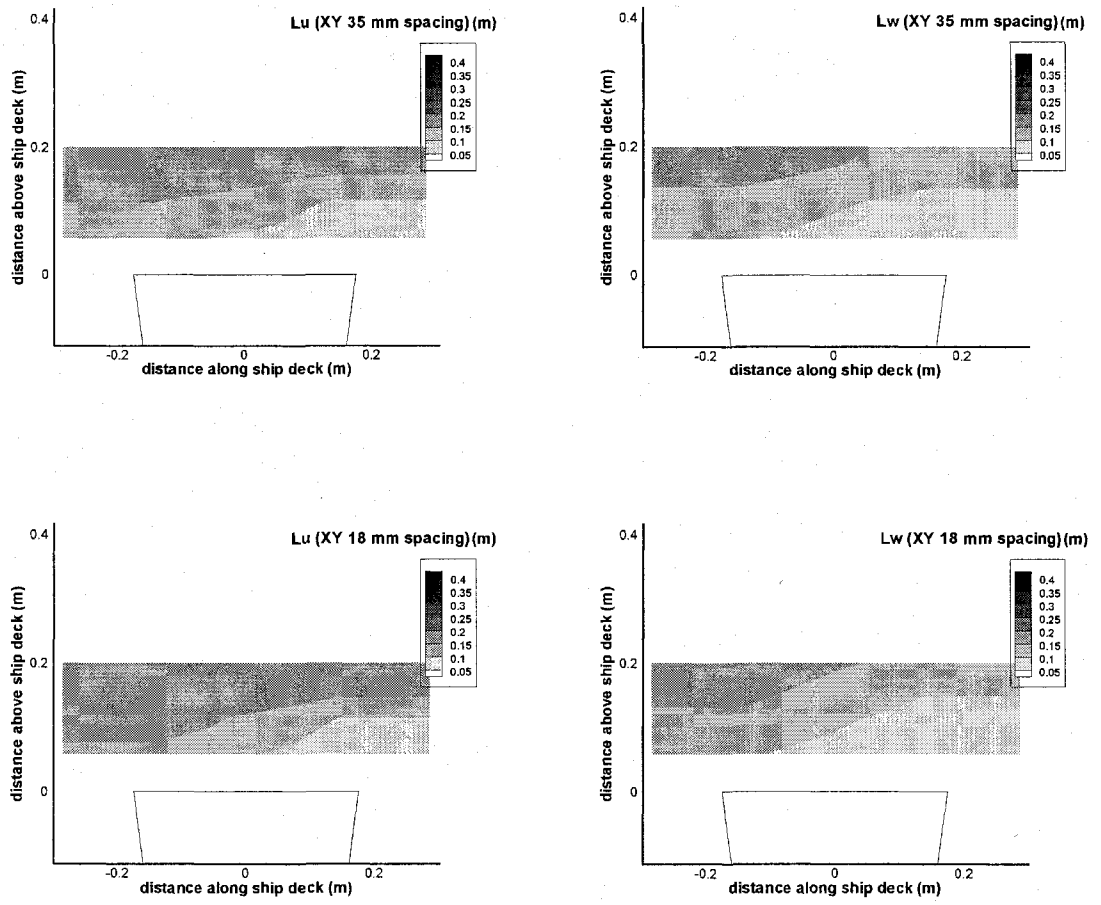

Figure 4.20: Fitting parameters for coherence with XY spacing (0° deck).

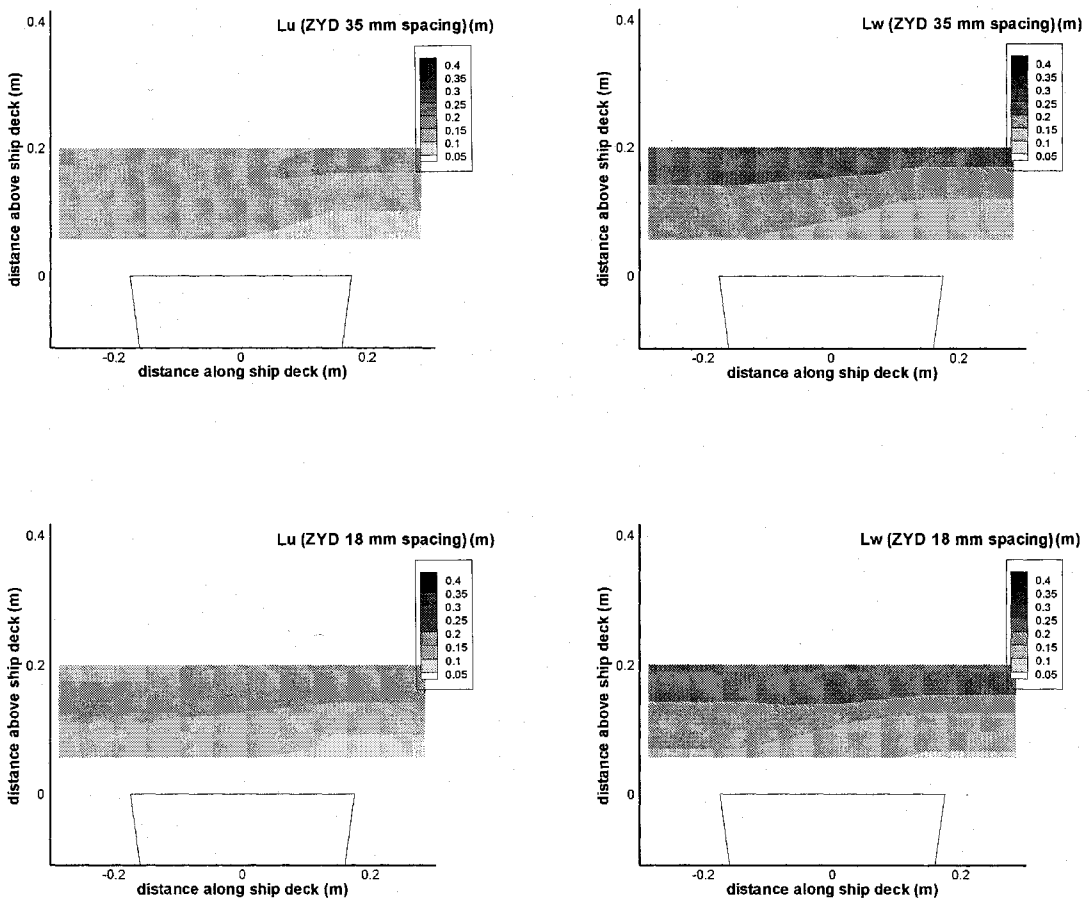

Figure 4.21: Fitting parameters for coherence with ZYD spacing (0° deck).

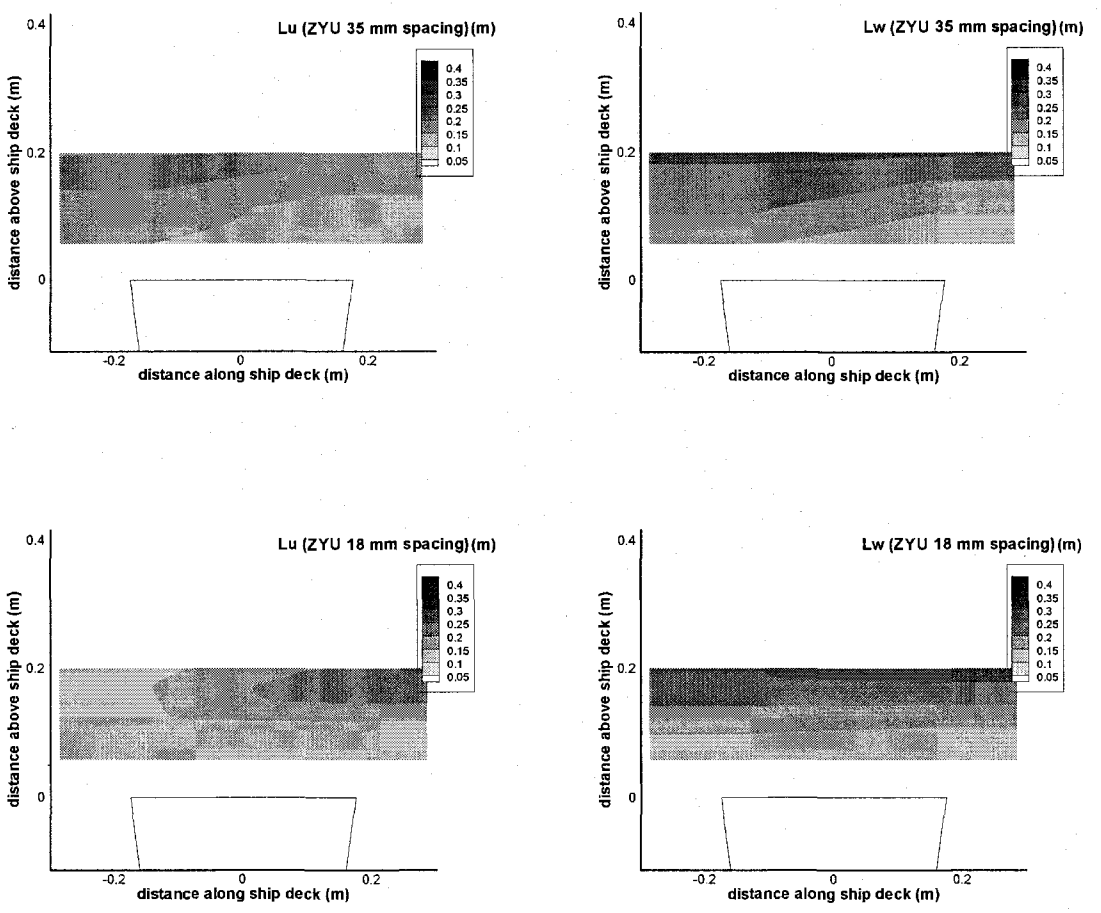

Figure 4.22: Fitting parameters for coherence with ZYU spacing (0° deck).

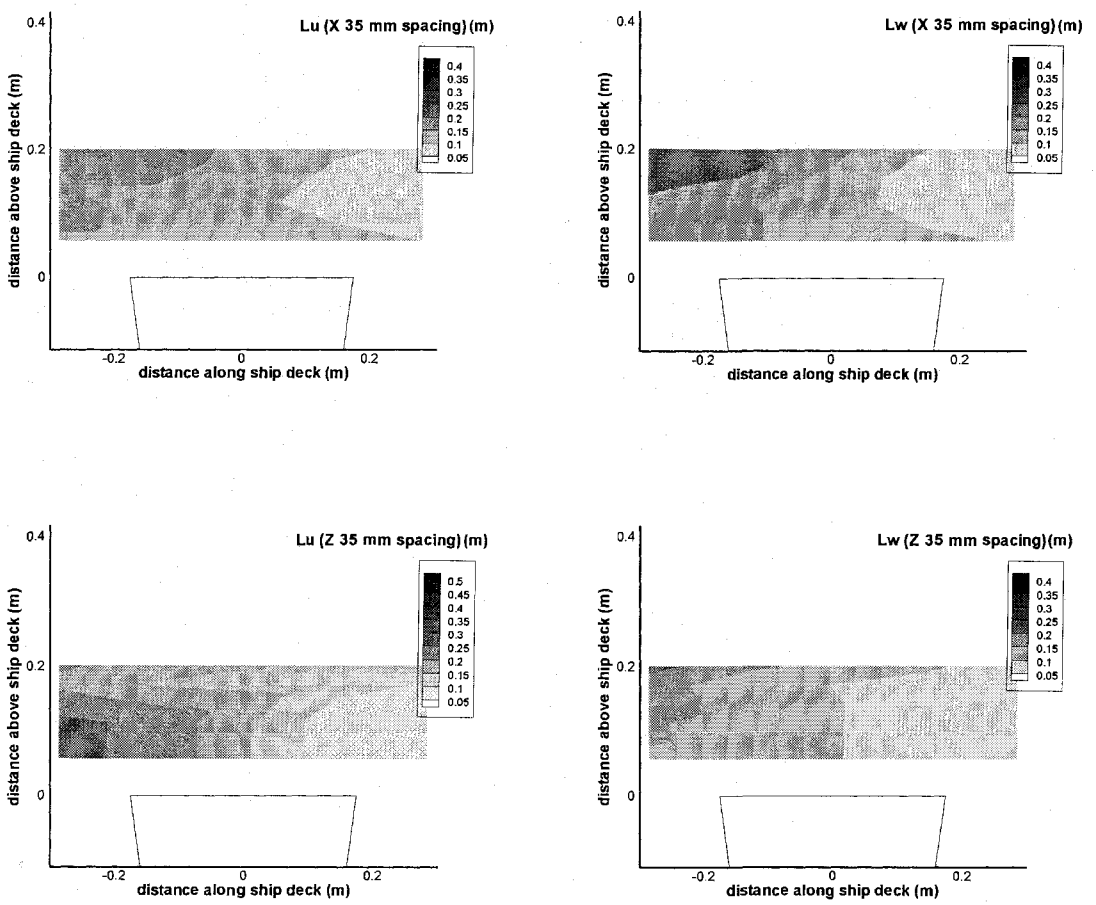

Figure 4.23: Fitting parameters for coherence with X and Z spacings (-20° deck; data shown in deck reference frame).

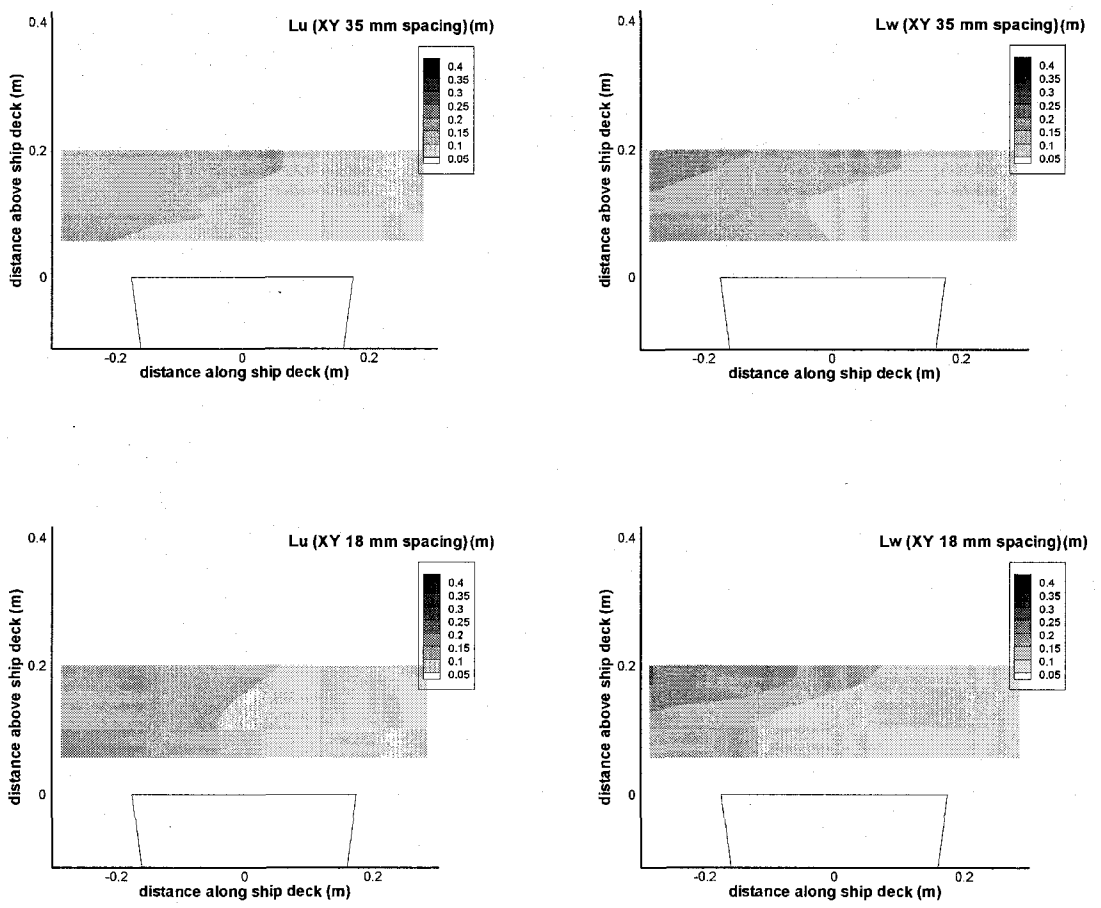

Figure 4.24: Fitting parameters for coherence with XY spacing (-20° deck; data shown in deck reference frame).

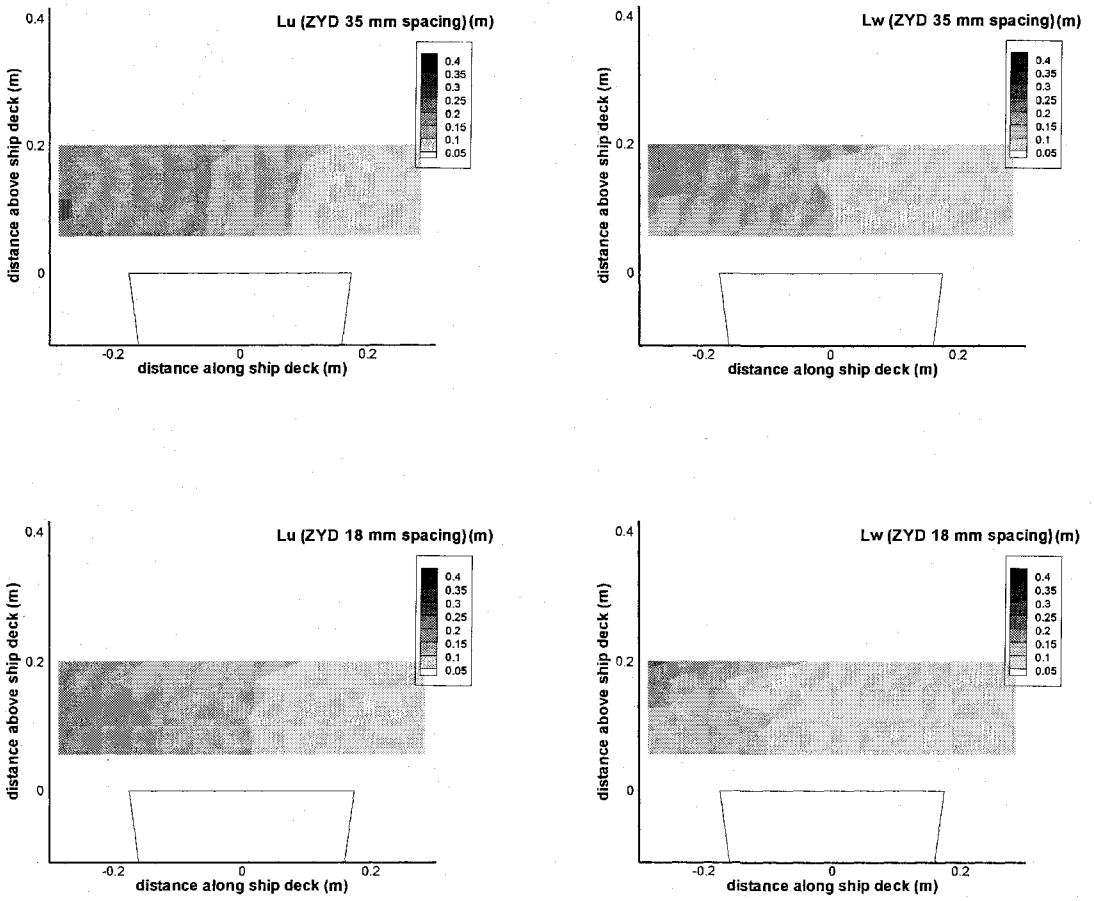

Figure 4.25: Fitting parameters for coherence with ZYD spacing (-20° deck; data shown in deck reference frame).

$$U_i = U_{\text{free}}\nu_{u_i} \tag{4.33}$$

$$W_i = U_{\text{free}}\nu_{w_i} \tag{4.34}$$

$$\sigma_{u_i} = U_{\text{free}}i_{u_i} \tag{4.35}$$

$$\sigma_{w_i} = U_{\text{free}}i_{w_i} \tag{4.36}$$

where the variable i is a for point a, b for point b, or m for the midpoint.

A set of frequencies, f, in Hz, that span the frequency range of interest at an appropriate frequency spacing is generated, and the scale of the airwake being modelled relative to the experimental model (deck width of 350 mm) is specified as D.

In order to calculate the auto-spectra, the equivalent normalized frequencies are calculated using

$$f_n = \frac{fD}{U_{\text{free}}} \tag{4.37}$$

and the wave number vector is calculated using Equation 4.22.

The fitting parameters $\alpha\epsilon_u^{2/3}$, L_{uauto}, $\alpha\epsilon_w^{2/3}$ and L_{wauto} are extracted from the unsteady model, and the normalized auto-spectra can be calculated using Equations 4.24 and 4.25. The auto-spectra are then scaled for size and freestream velocity with

$$S_u = S_{u_n}\frac{U_{\text{free}}^2}{D}\frac{\sigma_u^2}{\sigma_{u_n}^2} \tag{4.38}$$

$$S_w = S_{w_n}\frac{U_{\text{free}}^2}{D}\frac{\sigma_w^2}{\sigma_{w_n}^2} \tag{4.39}$$

which also contains a correction so that the spectrum exhibits the turbulence intensity given by the steady model. This correction is not strictly required, but allows the intensity values from Experiment A, which is believed to have had much better accuracy, to be reflected.

In order to generate the correlations between points a and b, the root coherence fitting parameters L_u and L_w are first extracted from the models. The root coherence functions are then calculated with Equations 4.26 and 4.27. Using the calculated auto spectrum, and

root coherence, the magnitude of the cross-spectrum between points a and b, S_{ab}, can be calculated as

$$|S_{ab}|^2 = \gamma^2_{ab_n}(S_{aa}S_{bb}) \tag{4.40}$$

where S_{aa} and S_{bb} are the auto-spectra. The phase angles are generated using Equations 4.31 and 4.32. All the final spectra are given relative to the original frequencies, f.

4.4.5 Airwake Model Application in Time-domain Simulation

The ultimate goal of the airwake modelling portion of this research is to recreate representative time histories of flow velocity that are correlated in space and in time. Section 4.4.4 shows how the spectral characteristics of the flow between any two points can be calculated. This is an important capability, which facilitates the exploration of methods for reconstructing the time histories.

The unsteady airwake model was originally intended to be modelled after the discrete-grid method described in Reference [30] and Section 2.3.2. However, during execution, a number of challenges were discovered. First, in order for the frequency domain transfer functions to be obtained, the spectral matrix must be linearly consistent in order to yield results that make physical sense. Since the matrix is populated with auto- and cross-spectral approximations from the von Kármán correlation model, the correlations may not be exact representations of consistent correlations for large numbers of points. This leads to accumulated error in the reconstructed velocities and a flowfield that is not representative. The second challenge arises from the fact that the coherent velocities are calculated at discrete locations. If the point for which the velocity is desired is between grid points, then the velocity must be interpolated. This interpolation leads to a less representative auto-spectrum at the interpolated point. Figure 4.26 shows this change in spectral representation at interpolated points.

While this method is theoretically convenient and efficient, some problems with its application led to a search for an alternative method.

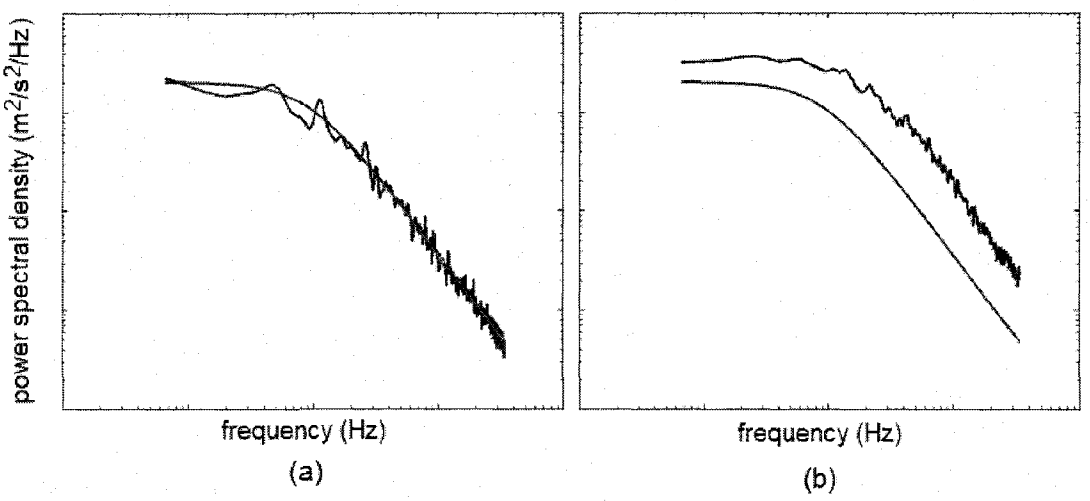

Figure 4.26: Auto-spectrum reconstruction (smooth - target; wavy - reconstructed; (a) at grid point; (b) at interpolated point).

Advancing Fourier Series (AFS) Method

This method traces the motion of a point through time and space, relating each subsequent velocity signal to the last through the appropriate correlation. The method is based on the Fourier series time history approximation where the time history of velocity can be expressed as

$$v_i = \sum_{j=1}^{N} (A_{i,j} \cos(\omega_{i,j} t + \psi_{i,j})) \tag{4.41}$$

where $\omega_{i,j}$ are the N frequency components that are evenly spaced at a given frequency spacing, Δf, and $\psi_{i,j}$ are the phase angles of each frequency. $A_{i,j}$ are the Fourier coefficients given by

$$A_{i,j} = \sqrt{2 S_{ii,j} \Delta f} \tag{4.42}$$

where $S_{ii,j}$ is the magnitude of the target auto-spectrum at point i for frequency component j.

The process tracks a blade point of importance for dynamic and aerodynamic reasons, perhaps point A, as shown in Figure 4.27. The auto-spectrum of this point at location 1,

2, 3, or any other, can be calculated as per the correlation model. The time history of flow velocity of that point can be calculated using Equation 4.41. The velocity at the initial location of the point is given by v_1. The amplitudes of each frequency component are given by

$$A_{1,j} = \sqrt{2S_{11,j}\Delta f} \tag{4.43}$$

As the blade rotates through the flow field, its next location is calculated at time intervals governed by the simulation time step. A correctly correlated velocity signal at the next blade location is then desired. At the new location, an auto-spectrum can be calculated, as well, the cross-spectrum between the two points can be determined. The velocity signal at the second location can be considered to be the sum of two velocity signals. The first is the component of velocity that is correlated with the velocity signal at the previous time step, v_{2_1} and the second is the component that is not correlated, v_{2_2}. As shown in Figure 4.28, the velocity signal at point two is thus the sum of two Fourier series.

By comparing the definitions of Fourier series coefficients and cross-spectra in terms of the Fourier transforms, it can be shown that

$$A_{2_1,j} = \frac{2|S_{12,j}|\Delta f}{A_{1,j}} \tag{4.44}$$

where $|S_{12,j}|$ is the magnitude of the cross-spectrum between the correlated locations, and

$$\psi_{2_1,j} = \psi_{1,j} + \psi_{12,j} \tag{4.45}$$

where $\psi_{12,j}$ is the correlated phase shift between the signals via the frozen turbulence assumption. The correlated series is calculated at the same frequencies as the original signal; the number of frequency components, N, is identical.

Unless the two signals are perfectly correlated, v_{2_1} does not contain all the power that is required in v_2. In order to maintain the auto-spectrum of velocity at the second location, a second Fourier series must be added to the first. In order to maintain the cross-spectrum

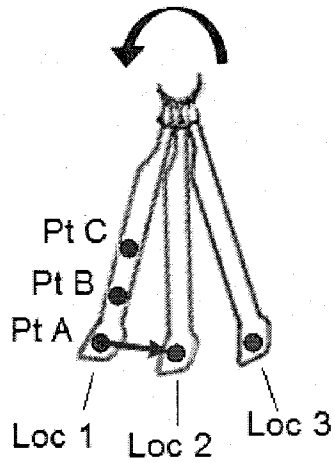

Figure 4.27: Points on the blade are tracked as they advance through space and time.

magnitude, the additional signal must not contribute to the correlations. Thus, the uncorrelated series must contain frequency components that are different from the correlated signal. This can be achieved by including a different number of frequency components, N, in the second series. The appropriate amplitudes for each frequency component can be calculated as

$$A_{2_2,j} = \sqrt{2(S_{22,j} - \frac{|S_{12,j}|^2}{S_{11,j}})\Delta f_2} \tag{4.46}$$

where the term in brackets is the expression of the auto-spectrum of the uncorrelated signal, which is calculated by subtracting the auto-spectrum of the correlated signal from the total target spectrum at the location of interest. The frequency spacing Δf_2 must be different than the spacing used for the correlated and original series. The phase angles are random.

Figure 4.29 shows the target and actual spectral results for location 1 and location 2 reconstructed using the advancing Fourier series method. Overall, the reconstructed results reproduce the original data well. The oscillations in the auto-spectral results are caused by the fact that discrete frequency components are used to reconstruct the velocity signals. Since the reconstructed results are ultimately used in their time-domain form, slight variations at the frequency level are not expected to appreciably change their validity.

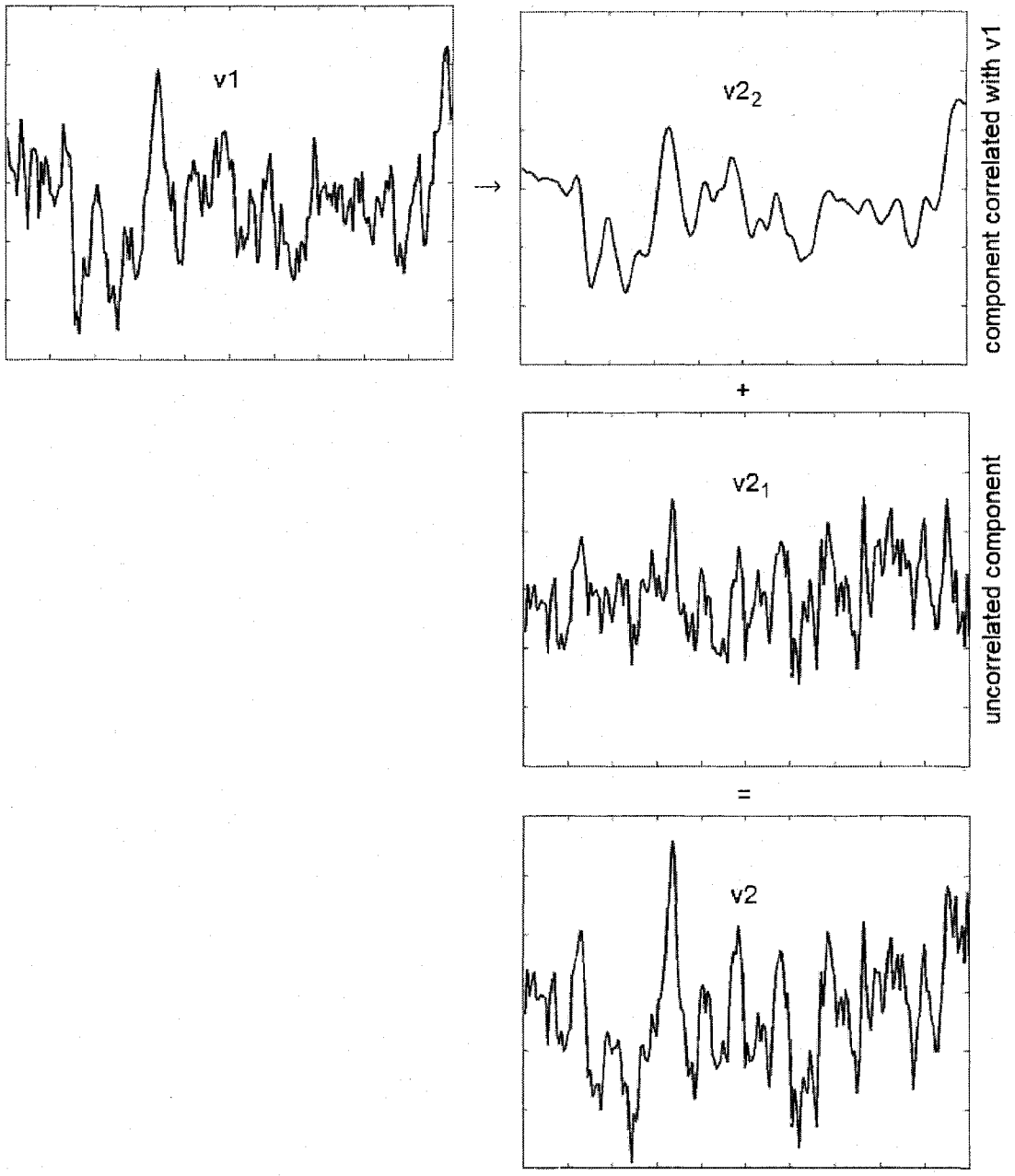

Figure 4.28: Sample velocity signal for locations 1 and 2.

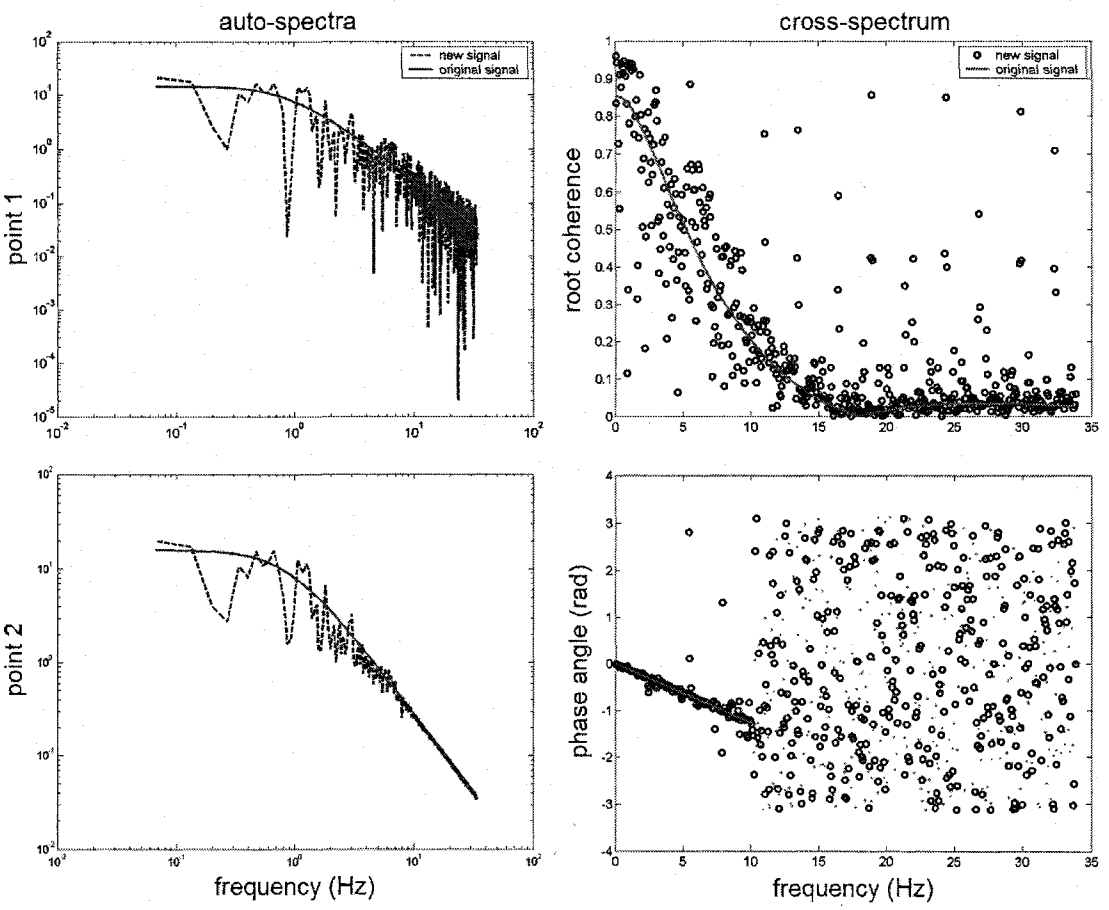

Figure 4.29: Sample statistical results for regenerated point 2 velocity.

If the third location is considered, following the same logic, the velocity signal would be the sum of three Fourier series, two comprising the correlated component from location 2, which is itself the sum of two Fourier series and a third comprising the new uncorrelated component. This leads to an increasing simulation memory requirement with the number of simulation time steps, and is thus undesirable. However, if the velocity signal at location 2 can be expressed as a single Fourier series, then the third signal would be the sum of only two series and only the previous and current set of Fourier coefficients needs to be stored in memory in order to propagate the velocity signal.

If the Fourier transform of the second velocity signal is taken, then the magnitudes and phase angles required to recreate the first part of the signal at location 2 can be extracted. The signal is recreated for the number of velocity points corresponding to the length of the Fourier transform. Therefore, the correlation between location 1 and location 3 is lost after the time corresponding to the length of the Fourier transform.

The length of the Fourier transform dictates how long the advancing reconstructed signals are correlated to the initial signal. This can be tuned to match the correlation characteristics in the flow. For example, consider that the flow has a total correlation coefficient less than 0.3 for point spacings of about 3.5 m full scale and higher, and that a typical Fourier transform length is 1024 data points. If the sampling rate is 67 Hz, then the time equivalent length of the Fourier transform is about 15 s. The blade for the typical helicopter being simulated would have to be rotating at less than 0.004 Hz for the flow at the tip to be expected to be physically correlated after 15 s.

This method could be expanded to include correlated fluctuations along the blade. In Figure 4.27, consider the velocity signal of point A at location 1 on the blade. The next blade segment inboard, point B, has a velocity signal that is correlated to the signal at point A in space in the same way that location 1 is correlated to location 2 in space and time. Point C is correlated to B again as location 3 is correlated to 2. In this way, a representative velocity at all the blade segments can be calculated relative to the first one for any time step. However, at the next time step, this method only allows the correlated propagation of a single signal through time. Thus the signal at each blade segment could be propagated

forward in time without maintaining spatial correlation with one another, or the tip velocity could be propagated through time and the spatial correlation with the spanwise segments recreated at each time step. In this way, the temporal correlation between the signals at the segments other than the tip segment would be lost but the instantaneous spatial correlation between them maintained.

The advancing Fourier series method allows the application of the von Kármán correlation models between any two points separated by space and/or time in the flow field. No interpolation is necessary to arrive at the flow point of interest. The method also has disadvantages. A Fourier transform must be calculated at each simulation time step with a significant impact on simulation speed. Additionally, propagated correlations can only be found between pairs of points rather than grids of multiple points that are known to be mutually correlated. This means that the spanwise elements on any blade cannot be mutually correlated with one another in space and in time, and that individual blades cannot travel through the same turbulent structure. Since the dynamics of the blades are mainly independent, with the exception of small coupled motions communicated through the helicopter suspension and rotor shaft, this limitation is not believed to be of significance between blades.

The algorithm for the implementation and a validation example for the Advancing Fourier Series method is contained in Appendix A.2.

Chapter 5

Experimental Validation

Validation, the process of assessing a model's applicability in reality, is a critical component of simulation development. Section 3.7 discusses the validation of the simulation components using analytical methods and previously published data. However, the validation of the blade response in combined sailing-like conditions cannot be obtained through literature or analytical means. To this end, an experiment was designed in order to gather experimental data to compare with equivalent simulated results.

This chapter details the major design considerations and the test parameters of the validation experiment, as well as the resulting simulation validation. Further design details, the specifics of experimental execution, the data reduction procedure, and results can be found in Appendix D.

5.1 Experimental Design

The validation experiment allowed the measurement of large blade deflections in sailing-like conditions by combining the effects that contribute to blade sailing. The governing design goals of the experiment were:

1. to expose a representative rotor system to ship motion and/or aerodynamic effects while engaging and disengaging;

2. to measure the deflection profile along flexible blades undergoing large deflections;

and

3. to design the system such that the properties were easily measured or calculated.

The second goal, calling for large deflections, was important for two reasons. First, the dynamic models are geometrically nonlinear, and are therefore capable of simulating blade bending beyond the linear range. The validation of this capability was desired. Second, large deflections are more easily measured.

To meet the goals of the experiment, a scaled two-bladed rotor was designed with elastic and hinge flexibility in the flap direction. The hinge motion was restricted by neoprene bumpers, which behave like flap and droop stops without extension and retraction. The beam is stiff in both torsion and lead-lag and does not have pre-twist.

The experiment was conducted in two phases in order to capture both aerodynamic and ship motion effects.

Phase 1: was conducted in the 2 m x 3 m low-speed wind tunnel in the Aerodynamics Laboratory at the National Research Council of Canada. The details of this experimental phase can be found in Section 5.1.3 and Appendix D.

Phase 2: was conducted on the Stewart motion platform facility in the Applied Dynamics Laboratory at Carleton University. The details of this experimental phase can be found in Section 5.1.4 and Appendix D.

5.1.1 Experimental Scaling

For scaled experiments, the length scale, S, is normally determined by the size of the available facilities. Since the blade sailing phenomenon is known to occur at low rotational speeds, frequency effects in the airwake, rotor rotation, and blade structure are believed to be important. For his reason, Froude similarity was selected to guide the design of the experimental model. The Froude number, Fr, is

$$Fr = \frac{V^2}{gD} \tag{5.1}$$

Table 5.1: Experimental scaling parameters

Parameter	Scale
Length	S
Velocity	$\sqrt{S}$
Time	$\sqrt{S}$
Frequency	$\frac{1}{\sqrt{S}}$
Mass	S^3
Froude number	1
Lock number	1
Reduced frequency	1

where g is acceleration due to gravity, and V and D are the characteristic velocity and length, respectively. It represents the ratio between inertial forces and gravitational forces. Froude number scaling is traditionally used in aeroelastic, stability, and control applications.

Reduced frequency, which captures the relationship between the rotor rotational speed and the frequency of the incoming turbulent vortices, is also important for blade sailing. The reduced frequency, f^* is given by [101]

$$f^* = \frac{fD}{V} \tag{5.2}$$

where f is the frequency of interest. Reduced frequency similarity is maintained through Froude number scaling, which gives velocity, time, and frequency scaling factors as given in Table 5.1.

A third scaling parameter, the Lock number, L, is given by

$$L = \frac{\rho a_o c D^4}{I_b} \tag{5.3}$$

where ρ is the air density, a_o is the lift-curve slope of the airfoil, c is the blade chord, and I_b is the flap moment of inertia about the flap hinge. This parameter scales the ratio of aerodynamics forces to the flap inertia of the blade. The result of this scaling factor is that the blade mass scales by S^3.

Table 5.2: Important scaled properties of the rotor system.

Property	Full Scale	Strict Model Scale	Actual Model Scale
Blade length (m)	9.3	0.78	0.82
Ship deck width (m)	12.25	1.02	1
Rotor height (m)	5	0.42	0.44
Chord length (m)	0.6	0.05	0.05
Wind speed (m/s)	15	4.3	4.3
Ship deck angle (deg)	0/-20	0/-20	0/-20
Blade mass (kg)	250	0.145	0.137
Static tip deflection (m)	0.3	0.025	0.12
Droop stop angle (deg)	2	2	8
Flap stop angle (deg)	2	2	6.3
First flap frequency (rad/s)	1.13	3.91	1.04

5.1.2 Physical model

The experiment was designed to represent a typical maritime helicopter operating off the deck of a typical frigate. Considering the size of the wind tunnel, a model scale of 1:12 was selected. Most model parameters are approximately Froude scaled, as shown in Table 5.2. However, the blade flapping frequencies and stop angles were adjusted to ensure large blade deflections would be observed. For this reason, the experimental results are not meant as a study of blade sailing conditions; rather the validated simulation tools are intended for these studies.

A scaled rotor model and accompanying experimental environment was designed and constructed to meet the experimental goals; this model is shown in Figure 5.1. The experimental environments for Phases 1 and 2 are shown on the left. The wind tunnel photo was taken from the end of the test section looking upstream. In this figure, the rotor model is mounted on the -20° deck and a grid to generate the time-averaged properties of the

atmospheric boundary layer is in place at the entrance to the test section. Figure 5.1 also shows individual components of the rotor model and highlights some important features.

As is commonly done with scaled aeroelastic modelling, the blade stiffness is derived from an aluminum spine while the aerodynamic properties were provided by segmented NACA 64A010 airfoil shapes that were mounted over the spine. The airfoil segments were 2.54 cm long and separated by a gap of 1 mm. They were machined in two halves from RenShape, a polyurethane foam, and glued together over the spine. A picture of the blades with and without segments can be seen in the Figure 5.2. A schematic of the blade cross-section can be seen in Figure 5.3

The blades were hinged to the hub by a custom hinge with ball bearings. Between the hub and the hinge, an interfacing piece allows the blade pitch to be set at a constant pitch angle between -10° and 10° in increments of 2°. The neoprene bumpers, which were selected to act as flap and droop stop elements, have a non-linear stiffness curve as shown in Figure 5.4. The rotor model was designed to be easily disassembled and reassembled.

5.1.3 Phase 1: Wind Tunnel

Phase 1 was intended to expose the rotor to representative aerodynamic loading for a typical frigate in beam winds. This phase was used to collect validation data

- at 2 static ship deck roll angles;
- at a variety of wind speeds with a representative boundary layer profile;
- for an engage/disengage profile with 2 final rotor speeds;
- for a variety of rotor engage and disengage times; and
- at a variety of blade pitch angles.

These parameters were selected in order to vary the amount of aerodynamic loading, and to vary the centrifugal stiffening including the time over which the stiffening was increased. These parameters represent a number of the important parameters that can affect full scale shipboard engage and disengage.

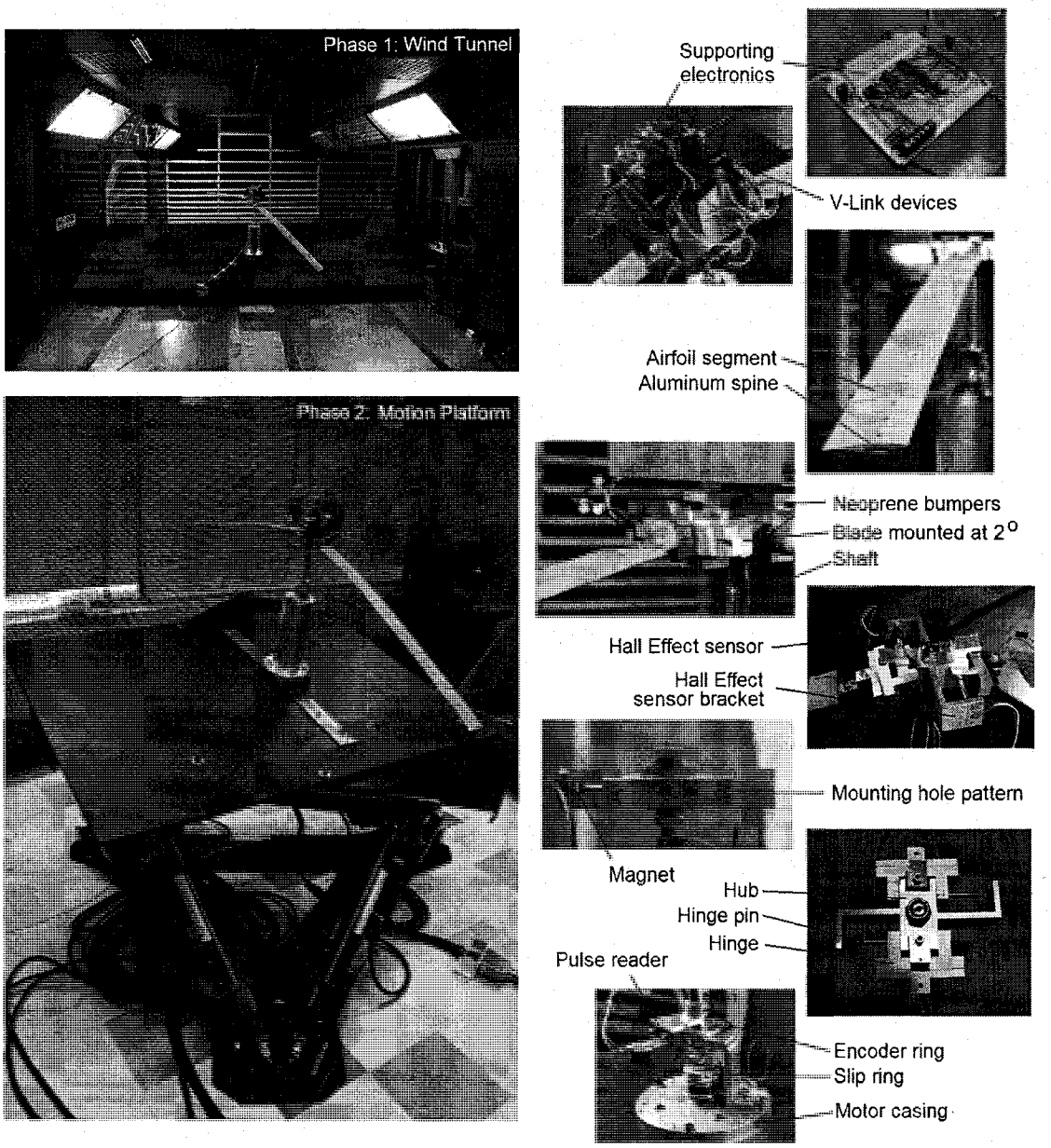

Figure 5.1: Experimental rotor system.

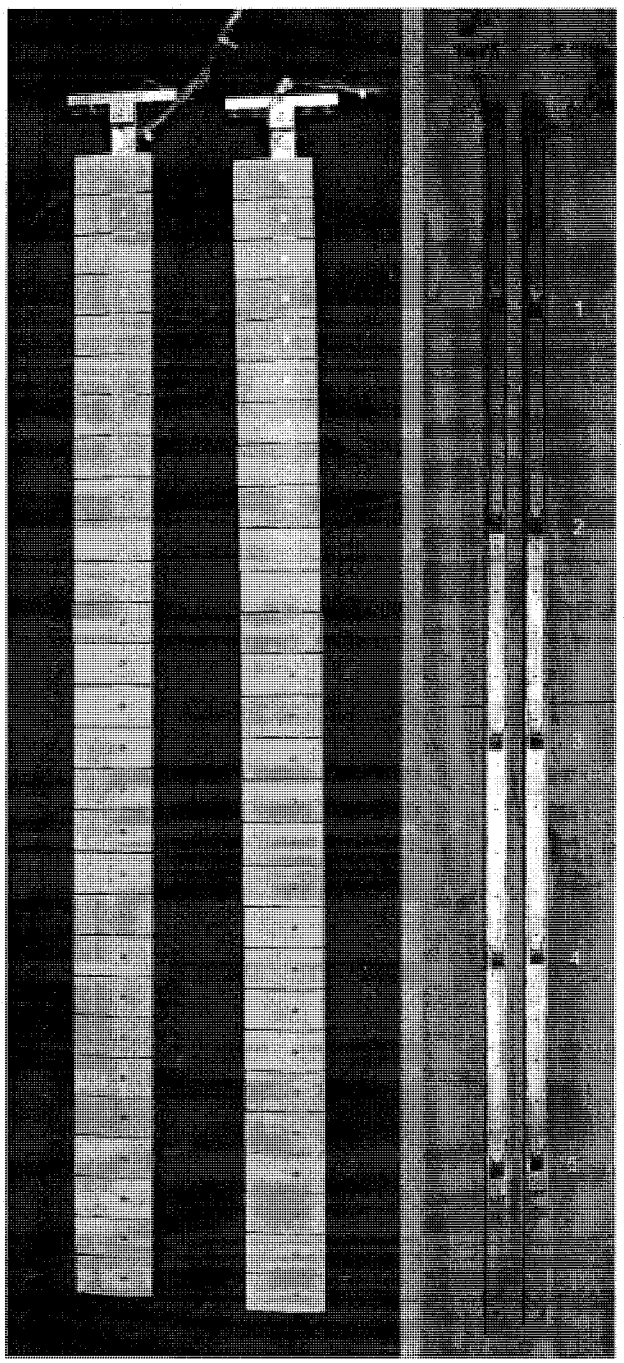

Figure 5.2: Blade construction.

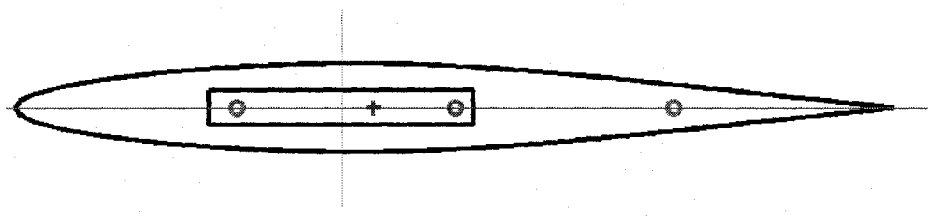

Figure 5.3: Experimental blade cross section with NACA 64A010 airfoil and aluminum beam core [centre of gravity (+) and the 1/4, 1/2, and 3/4 chord points (o) marked].

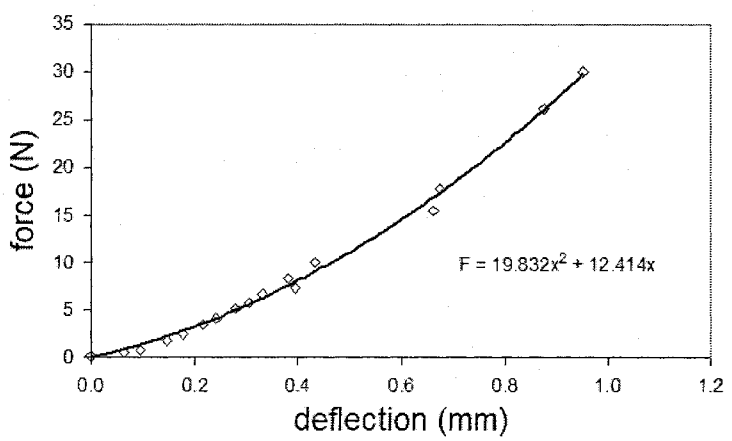

Figure 5.4: Stiffness curve for neoprene bumpers.

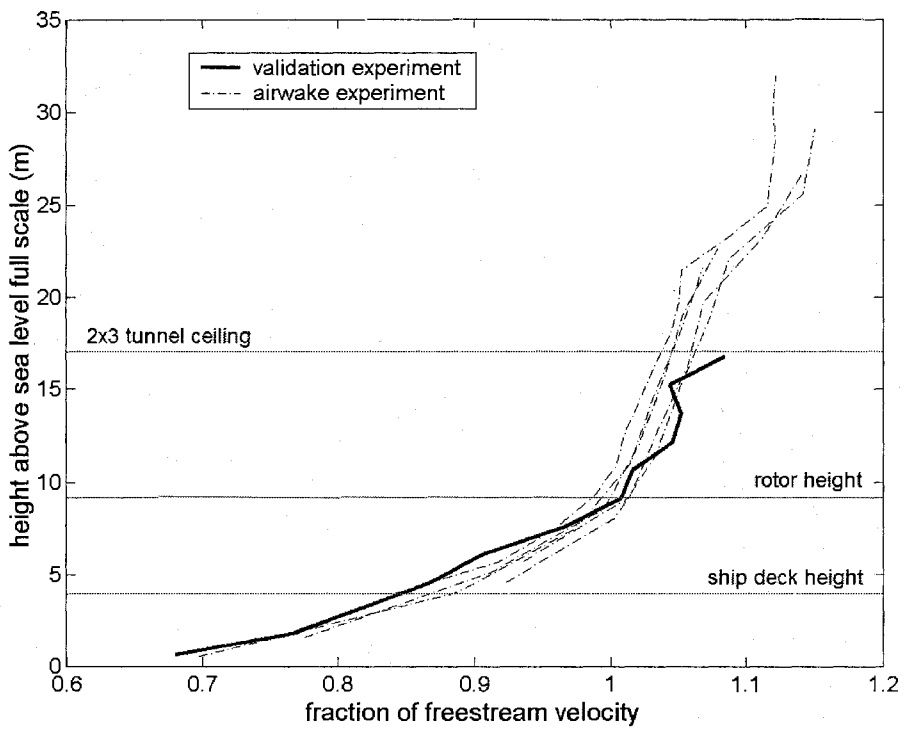

Figure 5.5: Reproduced boundary layer.

Aerodynamics

The experimental aerodynamic environment was designed to achieve appropriate estimation of the aerodynamic loads using the two components of aerodynamic modelling: airwake and aerodynamics.

The validation data was intended to be compared to simulation runs that use the airwake model described in Chapter 4. As such, it was important that the airwake environment in the wind tunnel be similar to that measured during the airwake experiment. The two key components of the airwake experiment were the deck models, which have the cross-section of a typical frigate at different roll angles, and the boundary layer grid, which provides an incoming flow profile that increases in speed with altitude.

In order to reproduce the airwake described by the airwake model, the ship deck models at 0° and -20° roll angle and the boundary layer grid were both scaled up from the earlier airwake experiment, which was conducted at 1:35 scale, to the validation experiment, which was conducted at 1:12 scale. The scaled ship deck models were constructed to span the tunnel to give approximately planar flow. The new boundary layer grid was successful in producing a similar steady boundary layer profile in the region of the ship deck and rotor, as shown in Figure 5.5.

The approximate model and full-scale aerodynamic properties at 33% full rotor speed are given in Table 5.3. The experimental airfoil Reynolds numbers are expected to be in the range below 100 000; in this range, the NACA 0012 airfoil, which is often used for rotorcraft studies, behaves in a non-linear manner. The NACA 64A010 airfoil was selected for the scaled model since it is known to give relatively consistent attached-flow lifting characteristics in the Reynolds number range of 30 000 to 100 000 [102]. Figure 5.6 shows a typical lift-curve for the airfoil at the extremes of this range. Examination of the published data for this airfoil shows that the slope is not strictly linear and indicates a lifting deficiency in the range around 0°. This is attributed to the development of laminar separation bubbles near the sharp leading edge of the airfoil for small angles of attack. Since this airfoil characteristic leads to early transition even for smooth airfoils, the roughness of

Table 5.3: System properties at 33% full rotor speed.

Property	Full Scale	Model Scale
Run-up time (s)	7	2
Run-down time (s)	7	2
Rotor speed (rad/s)	7	22
Wind speed (m/s)	15	4.3
Tip speed (m/s)		
Advancing blade	79	49
Retreating blade	21	12
Tip Reynolds number		
Advancing blade	2.6×10^6	7.0×10^4
Retreating blade	1.6×10^6	4.1×10^4
Tip Mach number		
Advancing blade	0.23	0.06
Retreating blade	0.15	0.04
Tip reduced frequency		
Advancing blade	0.011	0.017
Retreating blade	0.012	0.021

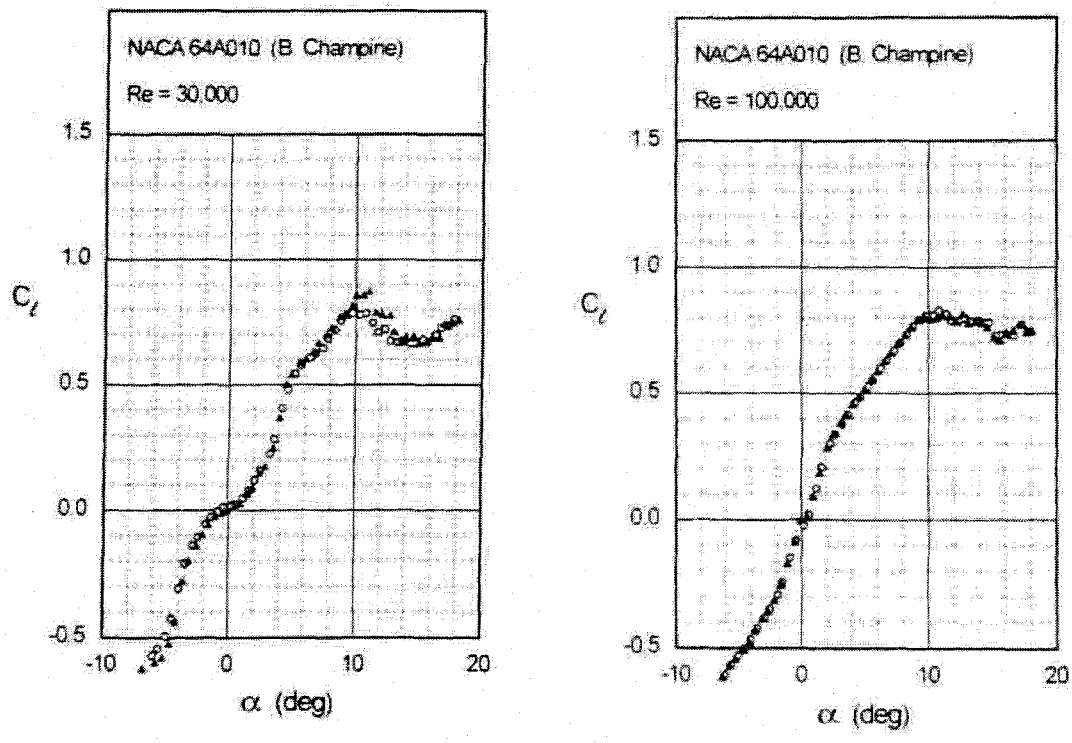

Figure 5.6: Lift curve slope for NACA 64A010 airfoil [102].

the RenShape material is not expected to change appreciably the maximum lift coefficient or the slope of the lift-curve. The roughness may have the effect of smoothing the non-linearity in the lift-curve slope; however since airfoil characterization tests were not conducted this has not been verified. Never the less, a linear approximation for the airfoil lift-curve slope in the attached region is expected to give reasonable results in the blade sailing context.

While efforts were made to allow accurate aerodynamic force estimation, the inherent assumptions in the modelling procedure and inherent imperfections in the experimental apparatus likely lead to some discrepancy between the actual aerodynamic forces applied to the rotor and the forces estimated in the simulation.

Data Collection

An experimental test matrix was constructed using the range of test properties shown in Table 5.4, in order to expose the blade to moderate and severe sailing-like conditions.

Table 5.4: Range of test parameters for Phase 1.

Property						
Wind speed (m/s)	4	6	8			
Max rotor speed (rad/s)	21					
Pitch angle (deg)	-8	-4	0	4	6	8
Ship deck angle (deg)	-20	0				
Engage/disengage time (s)	2	4	8	12	15	

Additionally, for each combination of ship deck, pitch angle, and wind speed, a data set was taken for a maximum rotor speed of 7 rad/s with an engage and disengage time of 4 seconds. The purpose of these test points was to keep the rotor in the sailing range for the duration of the test, rather than to transition through it with an engagement profile. Data points were also taken for some parameter combinations without wind, and for other combinations without the ship deck. A total of 248 sets of data were taken, plus additional calibration runs, drop test runs, and runs to record the non-rotating blades' response to the turbulence in the flow.

5.1.4 Phase 2: Motion Platform

Phase 2 was intended to expose the rotor to representative ship motion, and to aerodynamics of the blades turning through still air. This phase was used to collect validation data

- during sinusoidal platform roll at a variety of roll amplitudes and frequencies;
- during representative six-degree-of-freedom ship motion in 4 m seas;
- for a variety of final rotor speeds (both constant and as part of an engage/disengage profile);
- for two rotor engage/disengage times; and
- at a variety of blade pitch angles.

These parameters were selected in order to vary the frequencies and amplitudes of ship deck roll, the amount of aerodynamic loading, and to vary the centrifugal stiffening including the time over which the stiffening was increased. These parameters represent a number of the important parameters that can affect full scale shipboard engage and disengage.

The motion platform experiment was conducted in three parts.

Part I: examined the blade response during constant sinusoidal roll motion at a constant rotor rotational speed. The roll frequencies were selected to include representative scaled frigate roll (dominant frequency of 0.3 Hz) and representative scaled frigate pitch (dominant frequency of 0.6 Hz). Rotor speeds were selected to cover the first third of scaled normal operating speeds (0 - 20 rad/s).

Part II: examined the blade response during engage and disengage with representative scaled ship motion.

Part III: examined the blade response at slow, constant (3.5 rad/s) rotor rotational speed during representative ship motion.

Ship Motion

The ship motion time histories were generated based on the procedure laid out in Section 2.2. Six motion files, which give a range of motion types within the motion limits of the platform, are listed in Table 5.5. The motion files were scaled in time and in magnitude according to the model scale of 1:12 and the scaling laws given in Table 5.1.

In order to remain within the velocity limits of the motion platform, the heave motions were reduced in magnitude by an additional scaling factor of 2.5.

Data Collection

An experimental test matrix was constructed from the range of test parameters shown in Tables 5.6 through 5.8. A data set was taken for each combination of the parameters. During Part I, data was also collected for a platform roll amplitude of 15° at a frequency of 0.25 Hz for blade pitch angles of 0° and 4°.

Table 5.5: Ship motion files.

motion file	wave height (m)	wave direction (deg)	ship speed (kn)
1	4	0	10
2	4	0	25
3	4	45	10
4	4	45	25
5	4	90	10
6	4	90	25

Table 5.6: Range of test parameters for Phase 2, Part I.

Property									
Platform roll amplitude (deg)	5								
Platform roll frequency (Hz)	0	0.25	0.35	0.45	0.55	0.65	0.75	0.85	0.95
Max rotor speed (rad/s)	0	3.49	6.98	10.47	13.96	17.45	20.94		
Pitch angle (deg)	-8	-4	0	4	8				

Table 5.7: Range of test parameters for Phase 2, Part II.

Property					
Significant wave height (m)	4				
Wave approach angle (deg)	0	45	90		
Ship speed (kts)	10	25			
Max rotor speed (rad/s)	21				
Pitch angle (deg)	-8	-4	0	4	8
Engage/disengage time (s)	4	8			

Table 5.8: Range of test parameters for Phase 3, Part III.

Property			
Significant wave height (m)	4		
Wave approach angle (deg)	0	45	90
Ship speed (kts)	10	25	
Max rotor speed (rad/s)	3.5		
Pitch angle (deg)	-4	0	8

5.2 Experimental Results

The measured quantities obtained from each experimental run, using the instrumentation described in Section D.1.1, are

- rotor shaft encoder voltage;
- flap hinge sensor voltage; and
- blade strain profile.

During post-processing, these were converted to the resulting desired quantities, which are

- elastic blade tip deflection;
- hinge angle; and
- total blade tip deflection.

Details of the instrumentation and data reduction procedure can be found in Appendix D.

To illustrate the quality of data gathered during the experiment, sample results for a moderate wind tunnel test case are shown in Figure 5.7. The operational conditions for this case are

- maximum rotor speed: 20.94 rad/s;
- blade pitch angle: 6°;

- tunnel speed at rotor height: 5.83 m/s;
- ship deck angle: 0°; and
- engage/disengage time: 8 s.

Figure 5.7(a) shows the encoder output voltage, the hinge angle converted to degrees, and the strains measured by each gauge, overlayed. This data is processed to give the blade tip deflections, which are given in Figure 5.7(b). The lower trace shows the blade tip deflection due to elastic deformation only, while the upper trace shows the tip deflection including hinge motion.

The primary result of the validation experiment is a collection of validation cases, which are compared to equivalent simulation results. In addition, the experiments have also confirmed that the blade sailing phenomenon is complex, and depends on a large number of operating parameters. The magnitude of blade deflection depends significantly on ship deck angle, wind speed, engage time, blade pitch angle, azimuthal blade position with respect to the wind, and ship motion. The specifics of the experimental results and some conclusions can be found in Appendix D.5.

5.3 Validation Results

Using the experimental data gathered during the validation experiment, it was possible to demonstrate the validity of the blade sailing simulation for modelling flexible rotor systems in complex environments.

5.3.1 Model Properties and Tuning

The experimental rotor was modelled using eight blade segments, as shown in Figure 5.8: one for the hinge piece, one for the mating piece, which allows blade pitch angles to be introduced, and six along the length of the flexible aluminum spine. The interfaces between segments 2/3 and 3/4 are assumed rigid since these parts of the model are significantly stiffer than the aluminum spine. The assumption of zero flexibility at the root of a cantilever beam

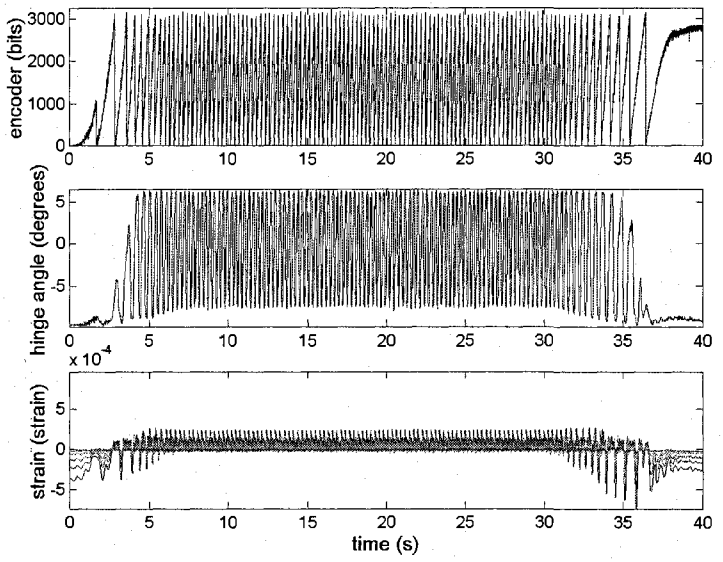

(a) Collected data: encoder voltage, hinge angle, blade strains

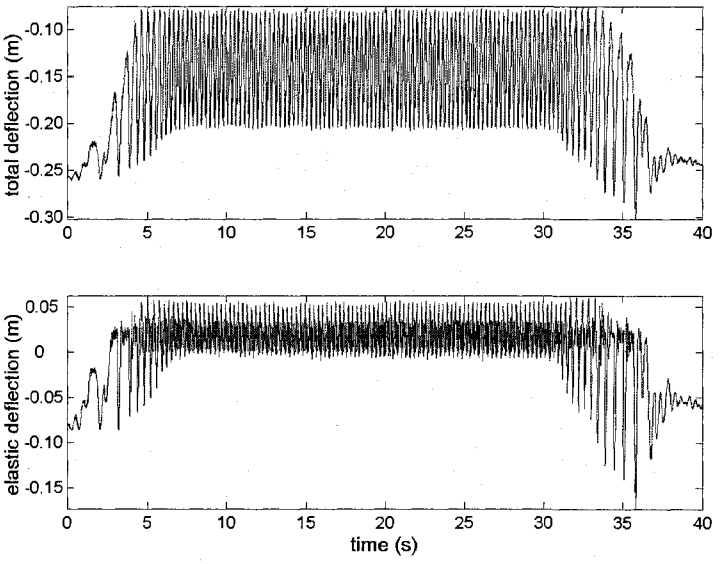

(b) Results: elastic blade tip and total blade tip deformation

Figure 5.7: Experimental data.

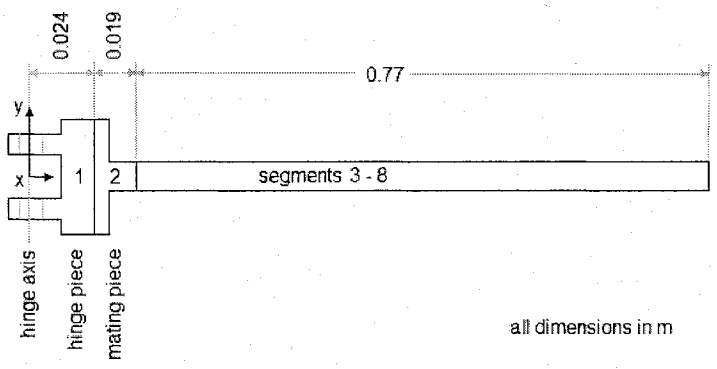

Figure 5.8: Diagram of structural blade model.

was employed here. The torsional and lead/lag flexibilities of the blades and the helicopter suspension were frozen during all validation experimental runs, which were solved using the Adams-Moulton method in the IMSL Fortran implicit integrator, DIVPAG [103].

Some properties, such as those involving distances and weights, were measured directly. The stiffness properties were calculated from the known properties of aluminum and the beam cross-section. The blade damping, and droop stop stiffness and contact angle were selected through parameter tuning, as described in Section 3.6.1, by comparing the simulation results with a blade drop test. The tip displacement and hinge angle results for both the experimental and simulated drop test are shown in Figure 5.9. The simulated rotor properties are given in Tables 5.9 and 5.10. These properties were used to calculate all the validation simulation results given in this thesis.

5.3.2 Interpreting Graphical Results

For the graphical results shown in this section, the simulation results are always given by the solid black line; the experimental results are given by the dashed black line.

Experimental Uncertainty

Some challenges encountered during data collection affected the uncertainty in the experimental results. Their effects are listed here. Descriptions of the challenges themselves are given in Section D.4.

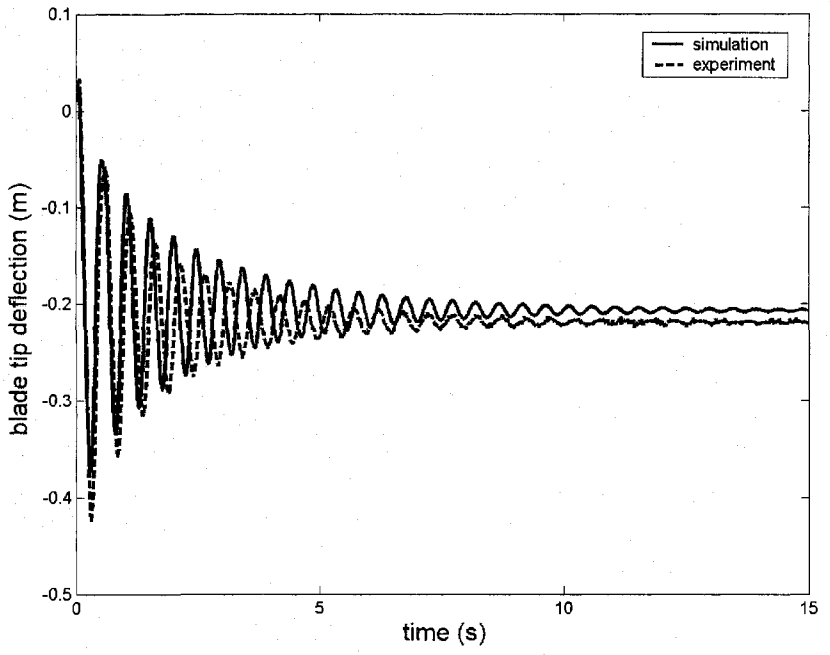

(a) blade tip deflection

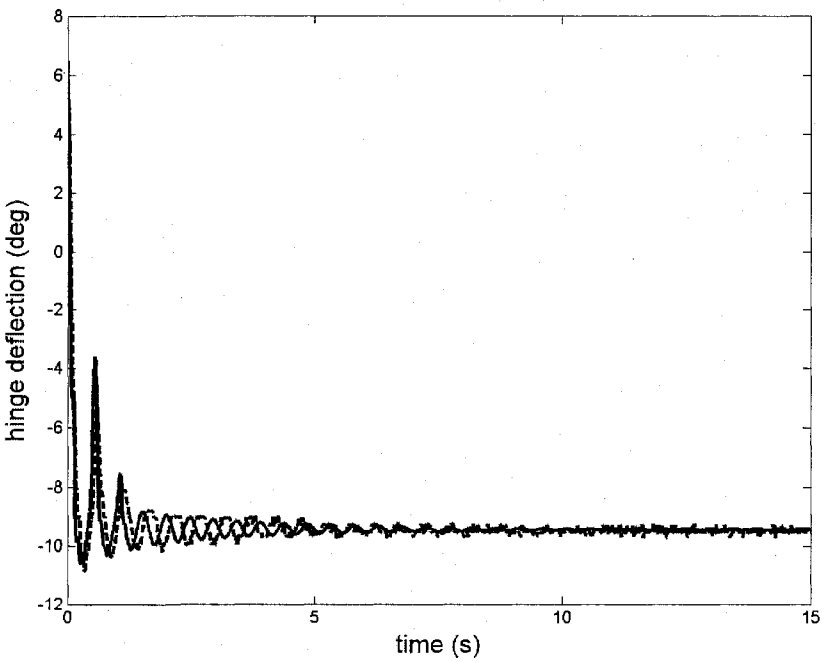

(b) hinge angle

Figure 5.9: Blade drop test for fitting properties (solid: simulation; dashed: experiment).

Table 5.9: Blade segment properties

property	units	segment 1	segment 2	segment 3	segments 4 - 8
flexible segment?		yes	no	no	yes
pitch change?		no	yes	no	no
segment properties					
mass	(kg)	0.0463	0.0252	0.0228	0.0228
length	(m)	0.024	0.019	0.126	0.126
mass centre (x)	(m)	0.0134	0.0058	0.063	0.063
mass centre (y)	(m)	0	0	-0.00183	-0.00183
geometric centre (x)	(m)	0.0134	0.0058	0.063	0.063
geometric centre (y)	(m)	0	0	-0.0065	-0.0065
chord	(m)	0	0	0.05	0.05
flap stiffness	(Nm/rad)	0	0	4.9055	4.9055
flap damping	(Nm/rad s)	0	0	0.02	0.02
moments of inertia					
torsional	(g m^2)	0.19	0.008	0.0001	0.0001
flap	(g m^2)	0.005	0.001	0.0303	0.0303
lead/lag	(g m^2)	0.022	0.008	0.001	0.001

Table 5.10: Root hinge properties

property	units	value
starting azimuth angle	(rad)	1.5708/4.7124
hinge offset	(m)	0.02
droop stop contact angle range	(rad)	0.1537 - 0.1527
flap stop contact angle range	(rad)	-0.1144 - -0.1134
force at stop contact	(N)	0.03
droop stop stiffness	(Nm/rad)	48.4
droop stop damping	(Nm/rad s)	0.1
flap stop stiffness	(Nm/rad)	48.4
flap stop stiffness	(Nm/rad s)	0.1
flap hinge friction coefficient		0.1
radius of hinge pin	(m)	0.009525

Voltage regulation: results in an uncertainty in hinge angle of 1.2°.

Variable bumper stiffness: results in a lower bumper contact angle in the simulation data as the engage proceeds. This is because the physical bumper expands over time to its unloaded, uncompressed height.

Wireless packet drop: results in sporadic phase shifting, which appears as an increase in the frequency, in the experimental data from Phase 1. The tendency over time for the simulation and experimental data to lose alignment is a result of this.

Motor control drift: results in uncertainty as to the actual time that disengagement was initiated by the motor. This uncertainty is the reason disengage deflection time-histories were not presented for the wind tunnel data.

The experimental model exhibits real-world characteristics, but also imperfections that present various modelling challenges, and contribute to a degree of uncertainty between the experimental and numerical results.

The numerical airwake model is based on data that do not include the presence of the spinning rotor or helicopter body. In the experiment, the airwake is affected by the presence of the blades, the motor tube, and the data system. This difference is expected to be small, since the influence of the motor tube and data system is restricted to a small range of azimuthal angles, and since the wind speed is high enough to sweep away blade tip vortices.

The numerical aerodynamics models are based on published coefficients. Although the airfoil segments were machined for a good representation of the airfoil, some differences exist. The spaces between the blade segments are expected to decrease the lift coefficient of the real blade with respect to the published values. The spaces are the consequence of the aeroelastic modelling approach that was used; segmented aerodynamic shapes are a typical method in aeroelastic modelling. Additionally, the blade segments exhibit some variation in shape as a result of their mounting on the blade. These variations change the airfoil camber slightly.

Also, the numerical aerodynamics models are based on idealizations, such as the quasi-steady assumption, or thin airfoil theory. These assumptions allow the use of simple, effective models for the calculation of aerodynamic force. However, the presence of these assumptions is likely to affect the agreement of numerical and experimental results to some degree.

The experimental model exhibited small motions in the mechanical joints, including lead-lag motion of the blades and small shaft vibration. The numerical model did not include these motions. However, the magnitude, while visible to the eye, is believed small enough not to affect significantly the simulated results.

Finally, the numerical dynamics model is based on experience and engineering judgement as to the specific blade segment configuration, and property calculation and tuning as discussed in Section 5.3.1. Still, the possibility exists that further property tuning, or a slightly different blade segment configuration, could lead to a more representative model.

The same set of properties were used to calculate all the results shown in this chapter. This demonstrates a certain robustness to the method, because the properties were determined very easily, and the results of the experimental validation procedure demonstrate

relative consistency.

5.3.3 Phase 1: Wind Tunnel

The wind tunnel validation experiments were used to examine the transient behaviour during blade engagement using the dynamic, airwake and aerodynamics tools that have been developed.

The volume of validation data collected during the validation experiment makes the inclusion of every case impossible. Therefore the validation presented here seeks to show typical results of mild, moderate, and severe sample cases with the focus on the total blade tip deflections of blade 2.

Aerodynamic Model Comparison

The relative quality of the quasi-steady and the unsteady aerodynamic models are shown using a mild and a severe validation case. These cases, along with their experimental parameters are shown in Figure 5.10.

The unsteady model can improve the simulation of blade response, as shown from 4-10 s in Figure 5.10(b), or degrade it, as shown from 0-2 s in Figure 5.10(a). This indicates that the unsteady aerodynamic model captures some, but not all, realistic aerodynamic effects that are present in the experiment. The inconsistencies are likely caused by the dynamic stall modelling. At very low rotational speeds, the blade stalls every rotation due to high angles of attack from the deck updrafts. However, at higher speeds, the resultant angle of attack is much lower and attached flow is maintained, even though the blade undergoes large deflections. The validation results suggest that the attached flow unsteady model is better than the quasi-steady, but that the associated dynamic stall negates this improvement at low rotational speeds.

Given that the unsteady model does not universally improve blade results, especially at very low rotational speeds, the quasi-steady model is currently recommended.

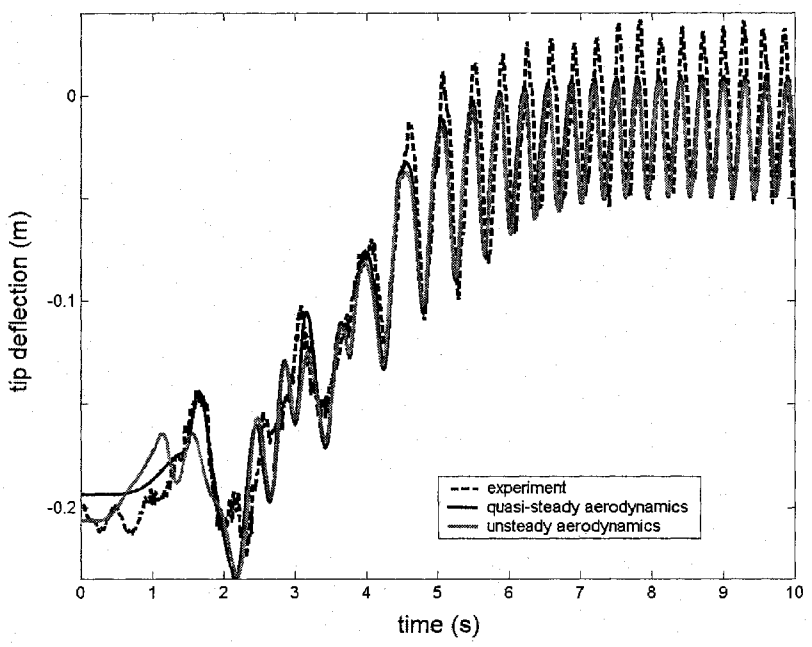

(a) for 0° deck angle, 0° blade pitch, 8.07 m/s wind speed

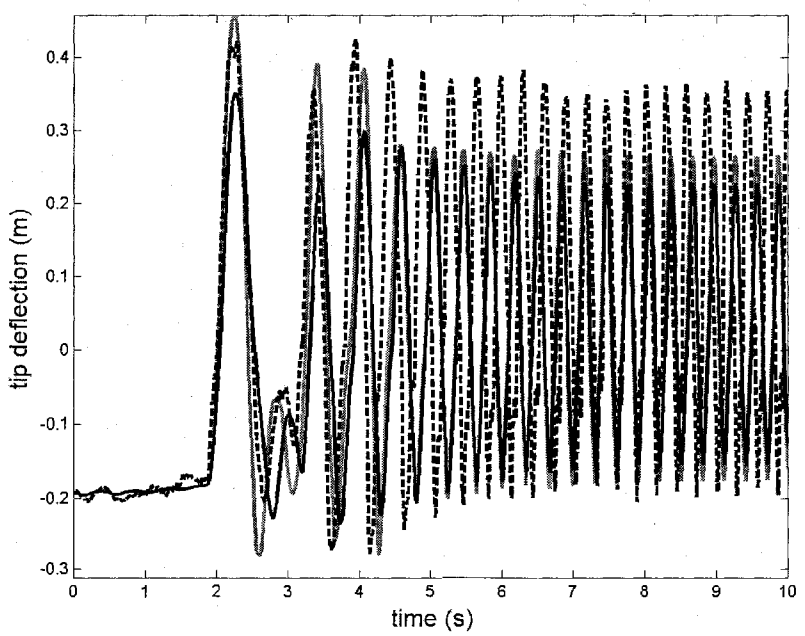

(b) for -20° deck angle, 8° blade pitch, 8.63 m/s wind speed

Figure 5.10: Blade deflection with different aerodynamic models.

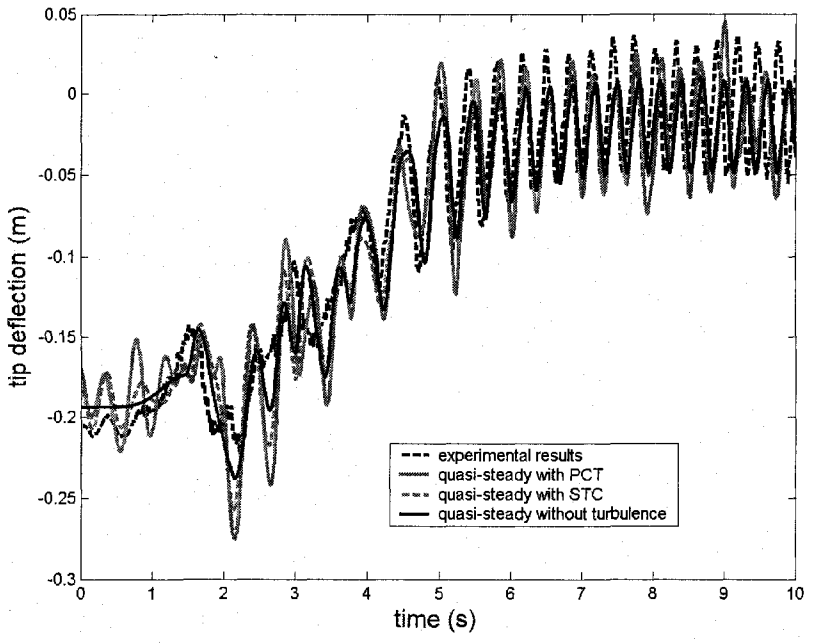

Figure 5.11: Blade deflection with different turbulence models for 0° deck angle, 0° blade pitch, 8.07 m/s wind speed.

Turbulence Model Comparison

In order to examine the effect of turbulence on the simulated results, some cases were run with the perfectly correlated turbulence model (PCT), with the spatially- and temporally-correlated turbulence model (STC) given by the Advancing Fourier Series method, and without turbulence. The first 10 seconds of a sample case are shown in Figure 5.11. A relatively mild case was selected in order that severe dynamic effects due to the mean airwake not overshadow the differences in turbulence modelling. Additionally, turbulence is not included in the modelling of the separation bubble over the -20° ship deck; therefore results shown here are for a 0° ship deck case.

Both turbulence models induce some random variation in the blade tip deflection, which is the expected result of turbulence modelling. The perfectly correlated model significantly over-predicts the blade tip deflection where the spatially- and temporally-correlated model appears to add a reasonable amount of variation in blade tip deflection.

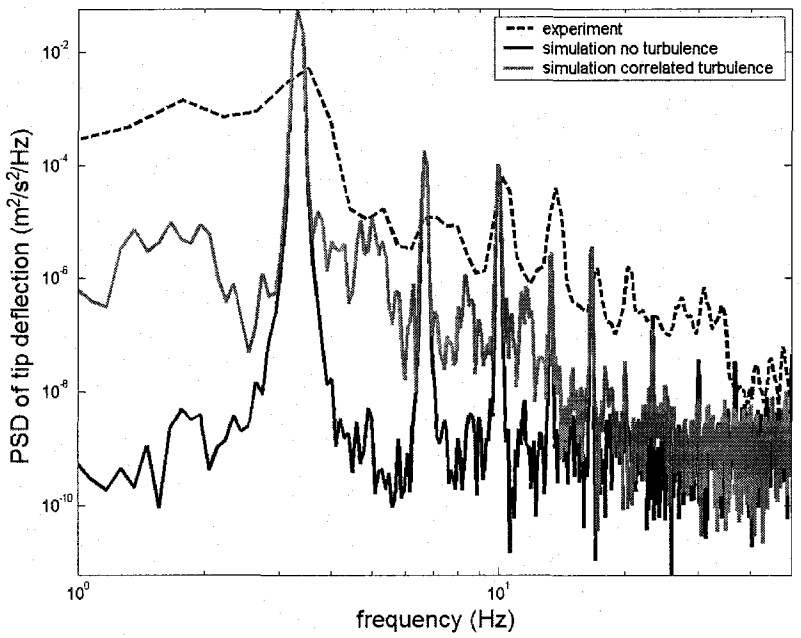

Figure 5.12: Frequency response of the blade rotating at steady state for different turbulence models.

The spatially- and temporally-correlated turbulence model was also validated in the frequency domain using the steady-rotation portion of the rotor profile. Figure 5.12 shows the spectrum of tip deflection after engagement for a moderate deflection case with 0° deck angle, 4° blade pitch, and 7.97 m/s wind speed. In the figure, the structural resonant frequencies are consistent between the three cases. As expected, the application of correlated turbulence improves the simulation results, especially at frequencies in between the structural resonant frequencies.

Given that the difference in predicted blade deflection magnitude with and without turbulence modelling is similar, the simulation time of each method is worth considering. Using a sample case run on a single Intel 1.83 GHz processor with 1 GB of RAM, 15 seconds of blade tip simulation with 12 active degrees of freedom were solved in:

- 27 minutes without turbulence;
- 34 minutes with perfectly correlated turbulence (PCT); and

- 94 minutes with spatially- and temporally-correlated turbulence (STC) via the advancing Fourier series method.

This indicates that adequate simulation is achieved for reduced solution times without turbulence modelling. Still, the application of spatially- and temporally-correlated turbulence improves simulation fidelity in general.

Quasi-steady Comparison

In order to show the relative validation case agreement over a wide range of experimental properties, results for 38 cases with an engagement time of 8 s are presented. The simulation results were calculated using the quasi-steady aerodynamics model, since this model tends to show better agreement at very low rotational speeds. No turbulence was included, since the specific phase angles of each turbulent frequency during experimental data collection are unknown.

Time history plots of the first 10 seconds of blade tip deflection are shown in Appendix D.6, and good agreement between experimental and simulated results is shown throughout the data. Careful examination of each data set shows that the major transient features are captured in the simulations. The extrema of both blade tip deflection and hinge angle over the first 10 seconds of each engage are shown in Figures 5.13 and 5.14. These figures show data for both blades (blade 1 in black, blade 2 in grey). The difference between experimental and simulation results is on average 0.3 m for tip deflection and 0.8° for hinge angle, with the maximum difference being 0.14 m and 3°. In general, the experimental results show higher deflections, suggesting that the simulation aerodynamics do not provide large enough wind loads.

The mean and root mean square of both blade tip deflections and hinge angles for the steady rotation (after 8 s) portion of each validation case are shown in Figures 5.15 and 5.16. In these figures, the results show improved agreement for larger wind velocities, indicating that the underestimated wind loading occurs mainly during the transient portion of each run. The most severe steady-state blade deflections are observed for positive pitch angles

over the -20° ship deck. During these cases, the blades encounter the stop bumpers every rotation. Since the modelled bumper contact angle does not adjust dynamically during the run, the simulated results show lower hinge angles and blade tip deflections than do the experimental results. This could likely be fixed using a more complex bumper modelling technique that allows the bumper to expand when unloaded during engage.

5.3.4 Phase 2: Motion Platform

The motion platform experiments were also used to validate the simulation tools. From experiment Part I, the blade response to uniform sinusoidal platform motion is shown in Figure 5.17. The trends are well reproduced, and the blade tip deflections agrees to within 2 cm.

From experiment Part II, examples of blade deflection time history due to engage/disengage with representative ship motion is shown in Figure 5.18. The trends and amplitudes are well captured by the simulation tools, especially for -4°, 0°, and 4°. The results for these pitch angles are typical of Figure 5.18(a). For the results at -8° and 8°, the simulated magnitudes are higher than those recorded during the experiment. Figure 5.19, which shows the root mean square of blade deflection during the steady rotation portion of the engagement profile, shows this trend as well. This seems to point to an inadequacy in the aerodynamic modelling for higher pitch angles in certain flow conditions.

The frequency domain results for the same two example cases are shown in Figure 5.20. These results suggest that the deflection overprediction occurs in the frequency band centred at 1.5 Hz, and that at the other frequencies, the agreement is better.

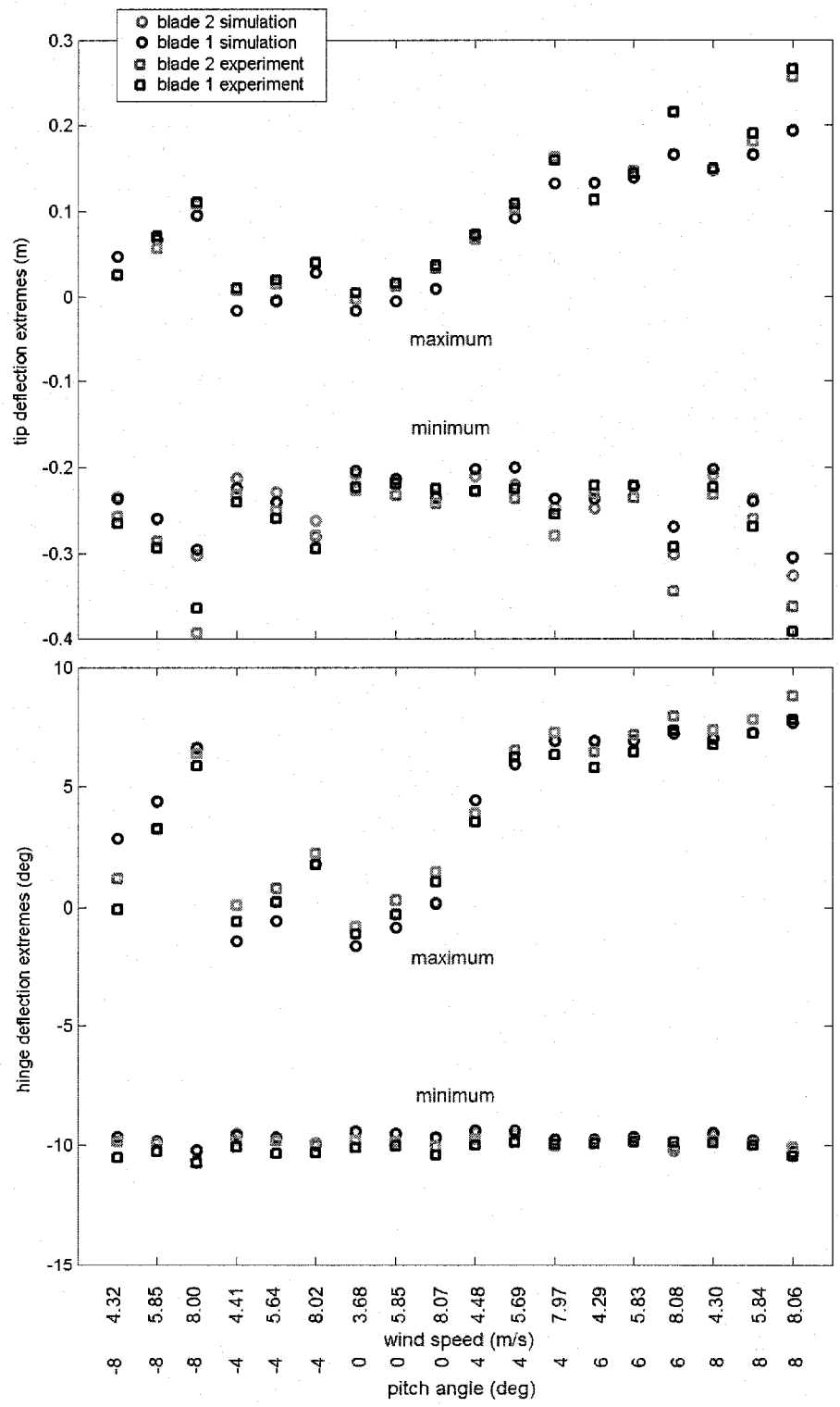

Figure 5.13: Maximum and minimum for first 10 s of validation cases with 8 s engage time on 0° ship deck.

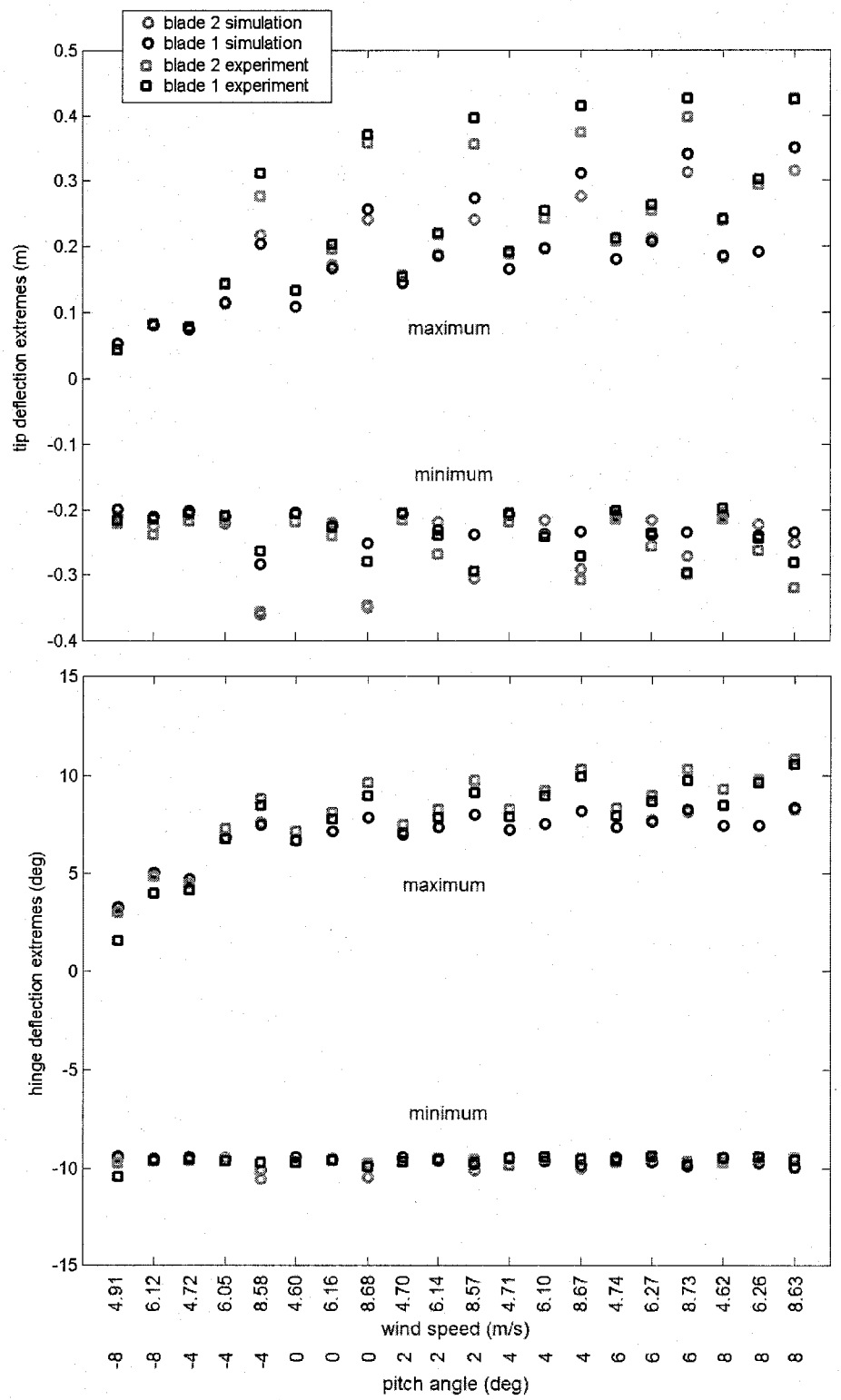

Figure 5.14: Maximum and minimum for first 10 s of validation cases with 8 s engage time on -20° ship deck.

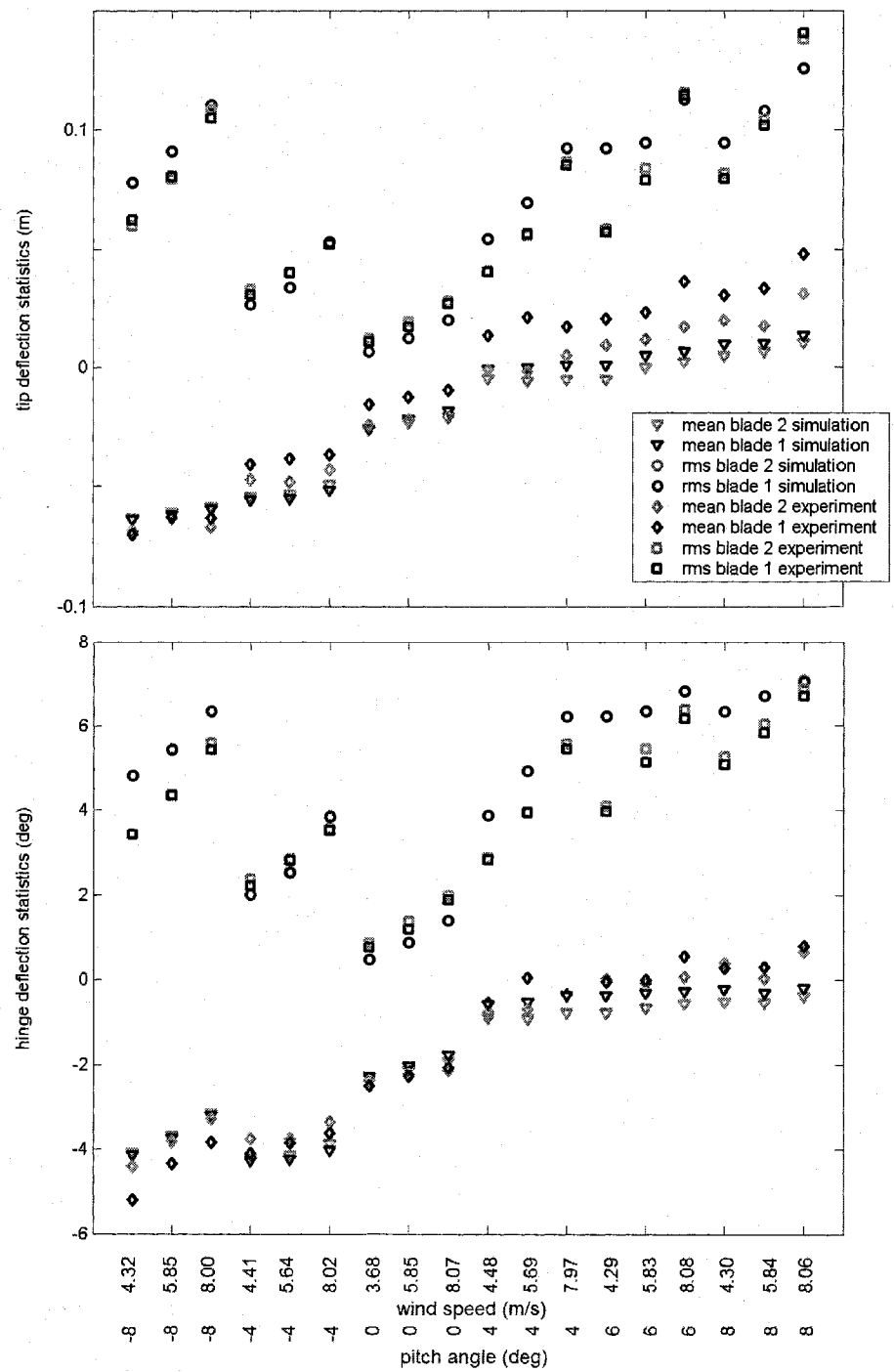

Figure 5.15: Mean and rms of blade deflection at full rotor speed for validation cases with 8 s engage time on 0° ship deck.

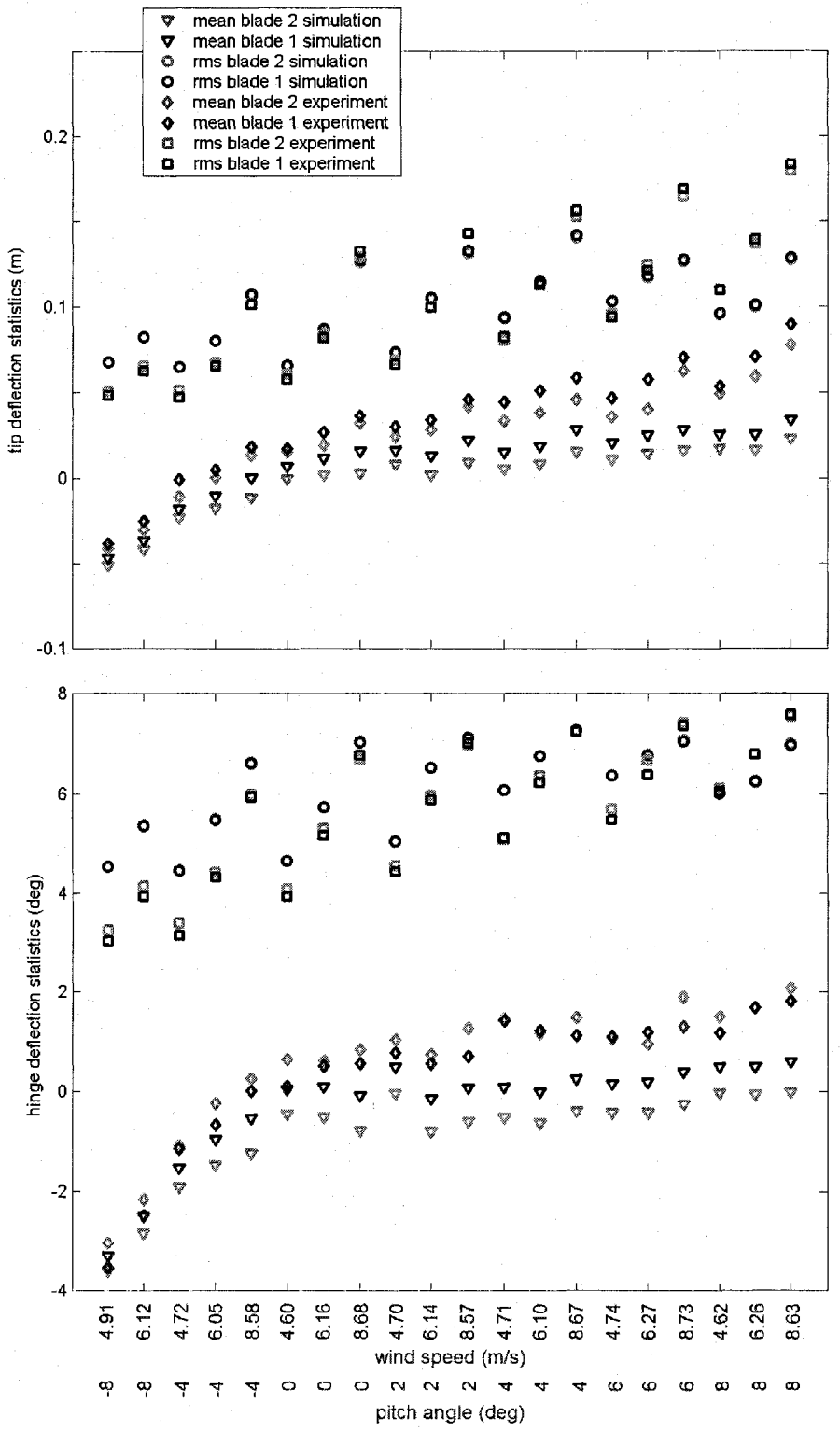

Figure 5.16: Mean and rms of blade deflection at full rotor speed for validation cases with 8 s engage time on -20° ship deck.

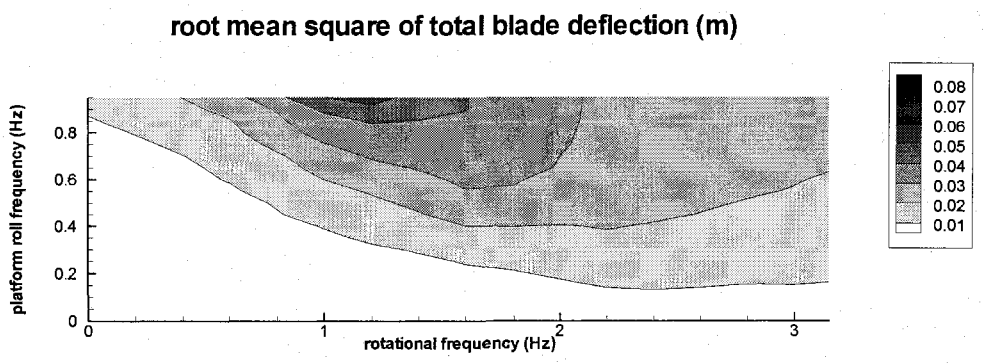

(a) experimental results

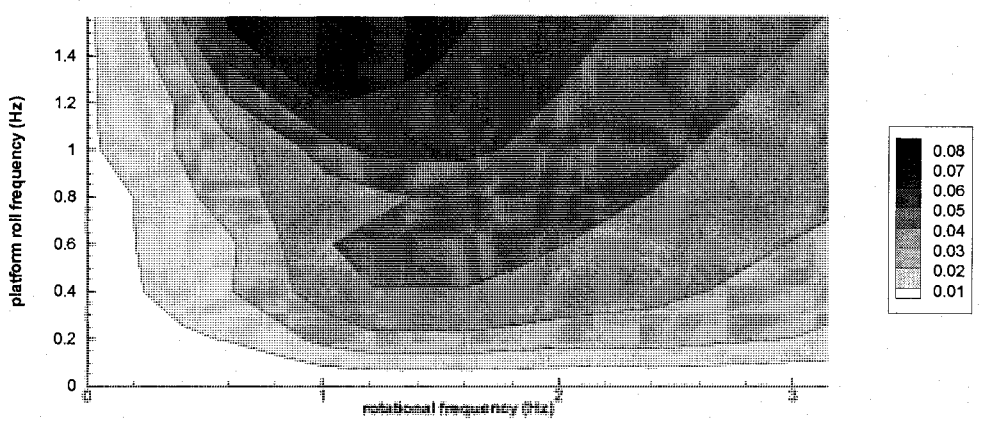

(b) simulation results

Figure 5.17: Blade deflections for motion platform tests with sinusoidal motion for 0° blade pitch.

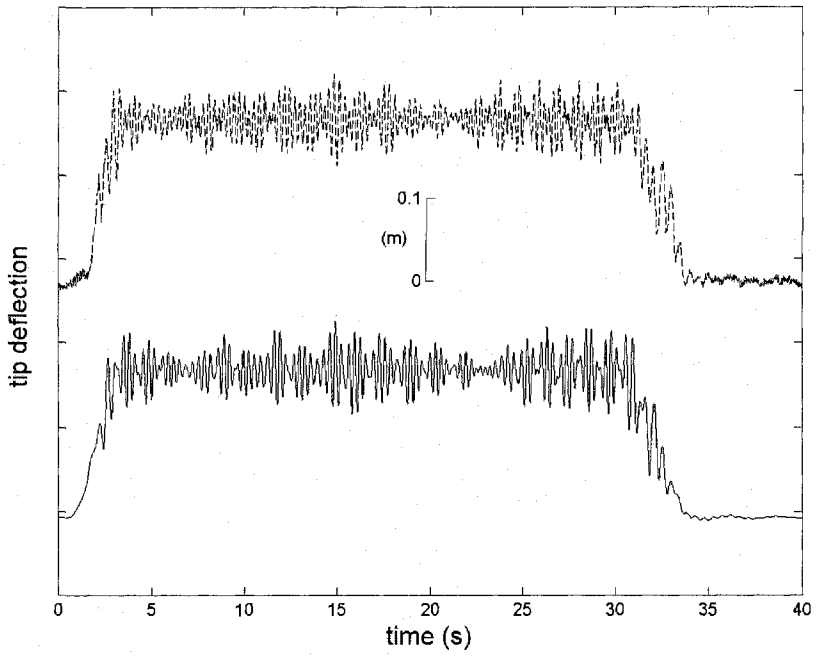

(a) 0° pitch angle

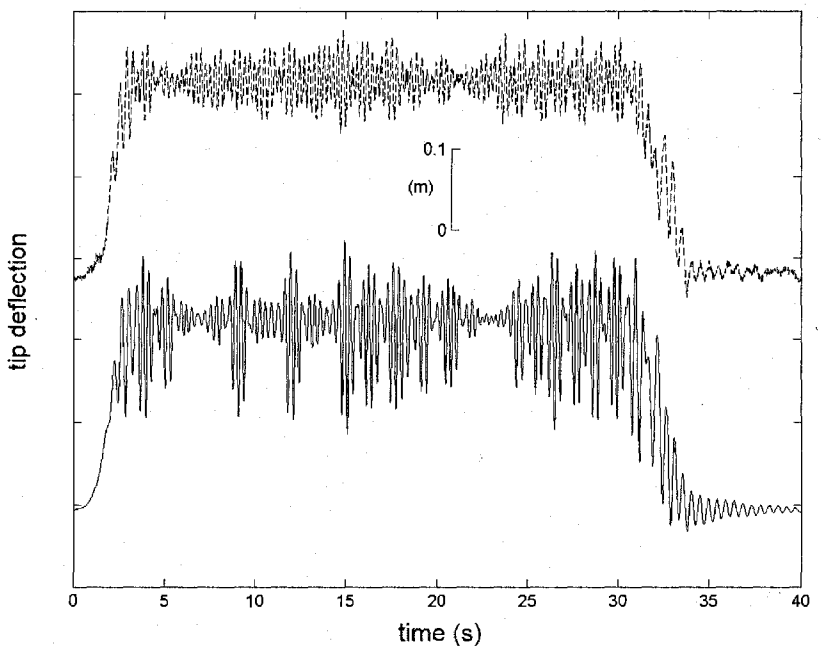

(b) 8° pitch angle

Figure 5.18: Time history of blade response for ship motion file 3, with 4 second engage/disengage time. The traces have been offset vertically for clarity.

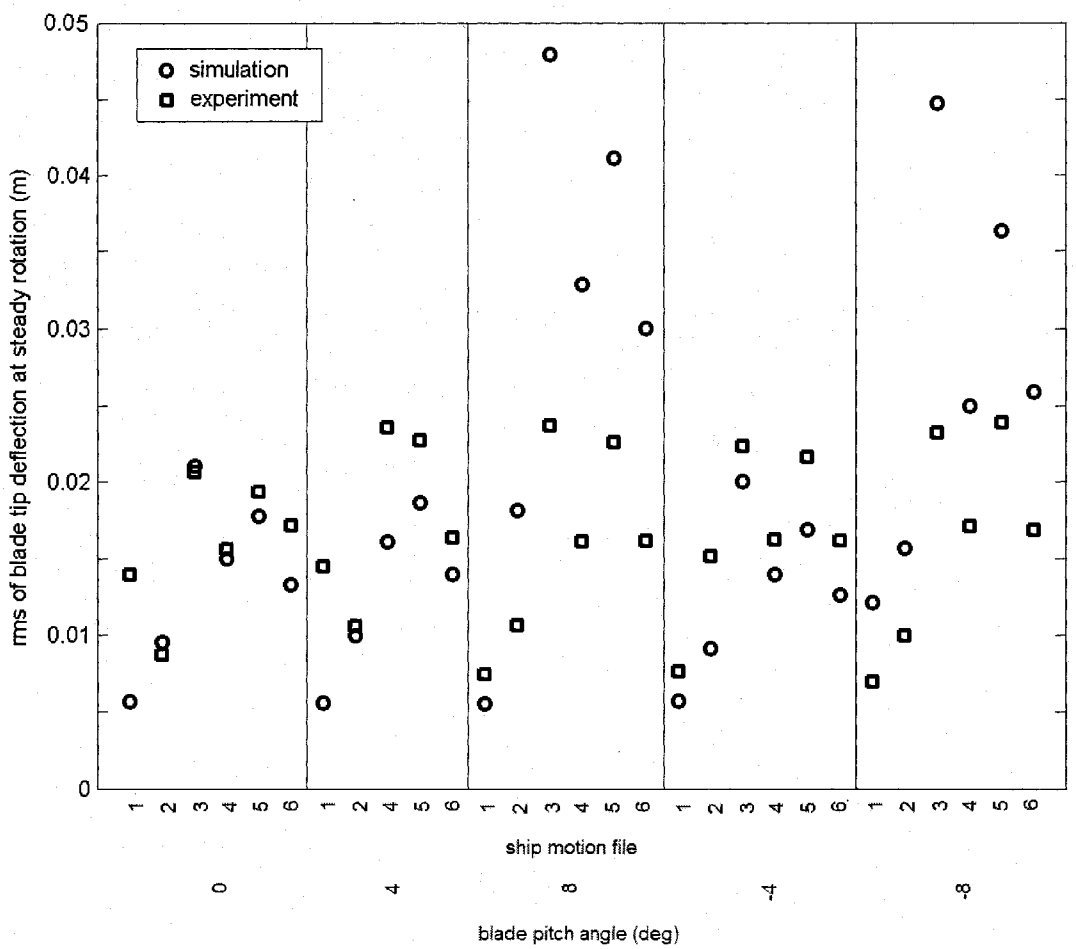

Figure 5.19: RMS of blade deflection during constant rotation for varying experimental properties (ship motion file in Table 5.5).

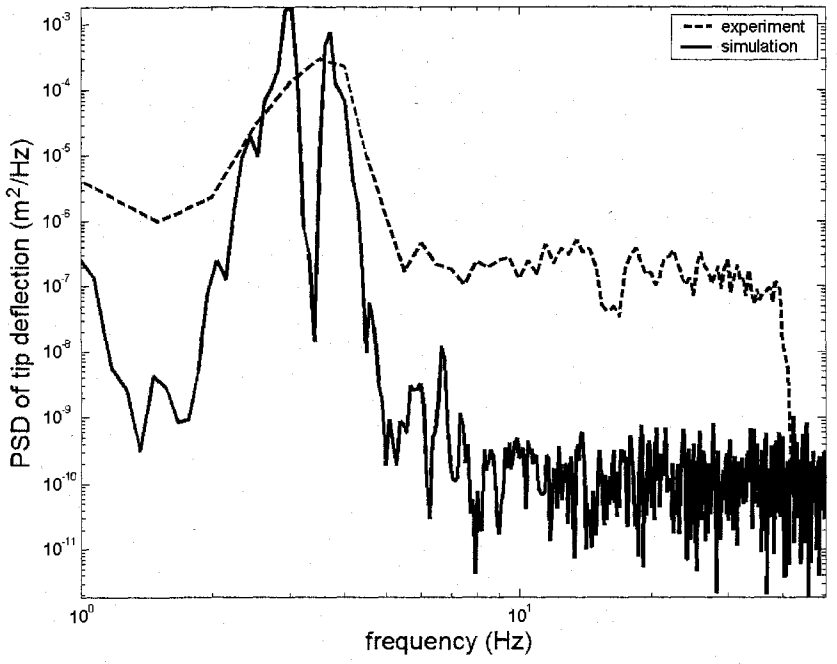

(a) 0° pitch angle

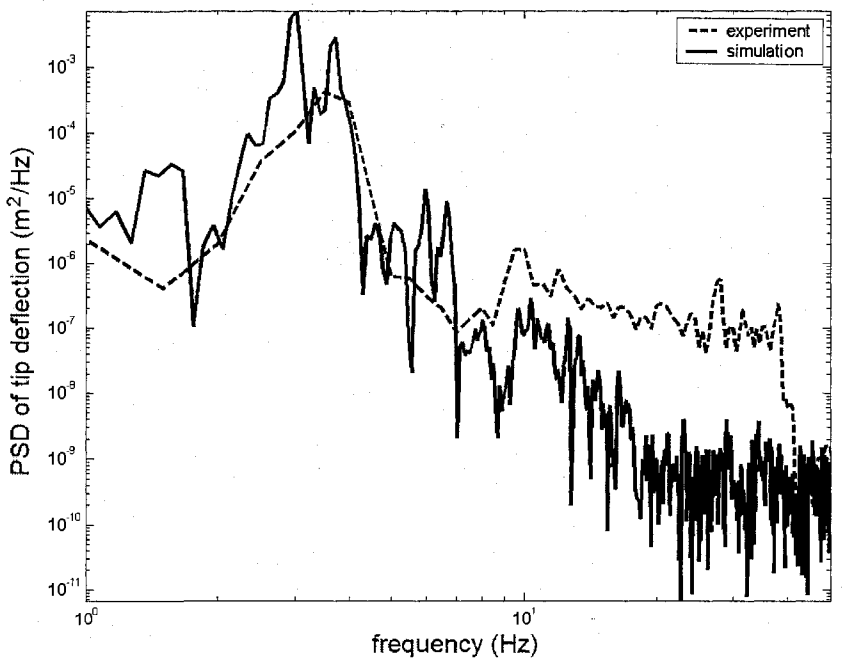

(b) 8° pitch angle

Figure 5.20: Frequency results of blade response for ship motion file 3, with 4 second engage/disengage time.

Chapter 6

Blade Sailing Results

The numerical tools developed in this research are intended for predicting the blade sailing response of shipboard helicopters. Ideally, helicopters are tested on a case-by-case basis, such that the operating conditions and design parameters can be specified carefully. The best long-term application for the numerical tools developed here is for pre-sea trial prediction and parametric studies, since the individual effects from the contributors to the blade sailing phenomenon are difficult to generalize.

The numerical tools, however, can also be used to show the general response trends to varying operational parameters. This chapter demonstrates the applicability and functionality of the numerical tools at full scale. Using a typical shipboard helicopter configuration, sample engage and disengage tests are used to show the variation in blade deflection as a function of a variety of representative operational parameters. In terms of fully characterizing the effects of each important operational parameter, this study is preliminary.

6.1 Helicopter Properties

The typical ship-helicopter-rotor system used in this chapter is based on a typical frigate in beam winds (deck width 12.25 m and deck height 3.92 m above the waterplane); a helicopter body, suspension, and landing gear configuration similar to the CH-149 Cormorant; and a helicopter rotor with the hub and flexibility characteristics of the CH-46 Sea Knight. This combination was selected in order to simulate a typical Canadian system; the rotor was

selected based on rotor properties that are available in the literature [48].

The properties of the helicopter system are given in Table 6.1, and the radially-dependant blade properties given in Reference [48] are approximated as shown in Figures 6.1 through 6.4. The properties were approximated such that the blade could easily be segmented. Ten blade segments per blade were used to model this system, and the blade segment joints are located at radial locations $x = [0.017\ 0.15\ 0.25\ 0.35\ 0.45\ 0.55\ 0.65\ 0.75\ 0.85\ 0.95]R$. All the simulation cases shown in this section were solved using Gear's method in the IMSL Fortran implicit integrator, DIVPAG [103].

The deflections predicted in this section should be considered in conjunction with the definitions for blade sailing given in Section 1.2. A downward blade tip deflection of -1.4 m will cause a fuselage strike on a Sea Knight, and -1.3 m will exceed the limit for linear beam deflections with hinge motion, including the tip deflection from hinge angle, assuming first mode elastic bending. A downward tip deflection of only -0.8 m will bring the blade within 0.58 m of the fuselage, for a blade clearance value [1] of 2, and a deflection of -1.2 m will bring the blade within 0.2 m of the fuselage for a blade clearance value of 3 or 4.

6.2 Blade Response

The response of all three blades in representative conditions with and without ship motion are shown in Figure 6.5. The operating conditions, given in Table 6.2, were selected to represent as closely as possible typical engagement conditions in moderate-to-severe wind and sea conditions, as detailed mainly in Reference [48]. A collective setting of 3° during engage and disengage is part of the typical engage procedure. Engage and disengage take approximately 20 s each. Wind speeds in the range of 15 m/s and ship motion of 4 m significant wave height are typical of upper sea state 5 or lower sea state 6. The individual blades can experience different responses, because the operational conditions for each blade vary with time. This is especially apparent when ship motion is present, since the airwake properties change in time with roll angle.

Table 6.1: Helicopter system properties [48].

property	value	units
number of blades	3	
full rotor speed (NR)	27.65	rad/s
rotor engage time	20	s
rotor hold at full speed	20	s
rotor disengage time	20	s
rotor radius	7.7724	m
blade chord	0.47625	m
flap hinge location	1.7	%R
pitch bearing location	6.5	%R
first flap frequency	1.02	/rev
first torsional frequency	6.05	/rev
flap stop settings	1	deg
effective blade twist at tip	-8.5	deg
stop exension/retraction speed	50	%NR
downward tip deflection for tunnel strike	- 1.4	m
helicopter mass	11000	kg
centre of gravity distance above deck (undeflected suspension)	2.97	m
rotor hub centre distance above centre of gravity	2.13	m
rotor axis tilted from vertical by	0	deg
ship deck width	12.25	m

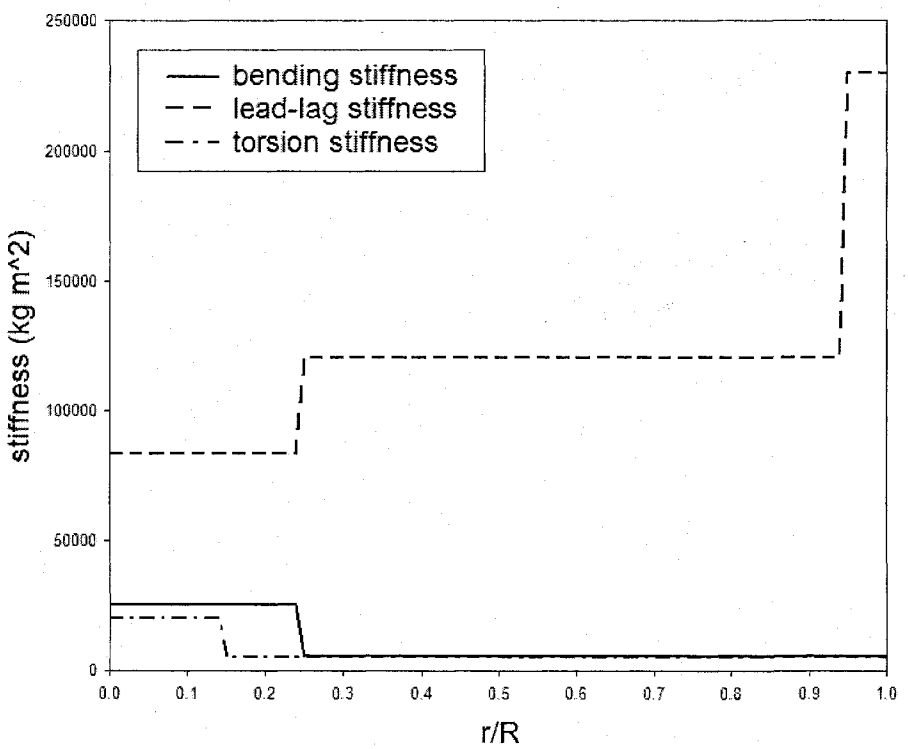

Figure 6.1: CH-46 rotor blade property distributions: stiffness (given with respect to fraction of rotor radius: r/R).

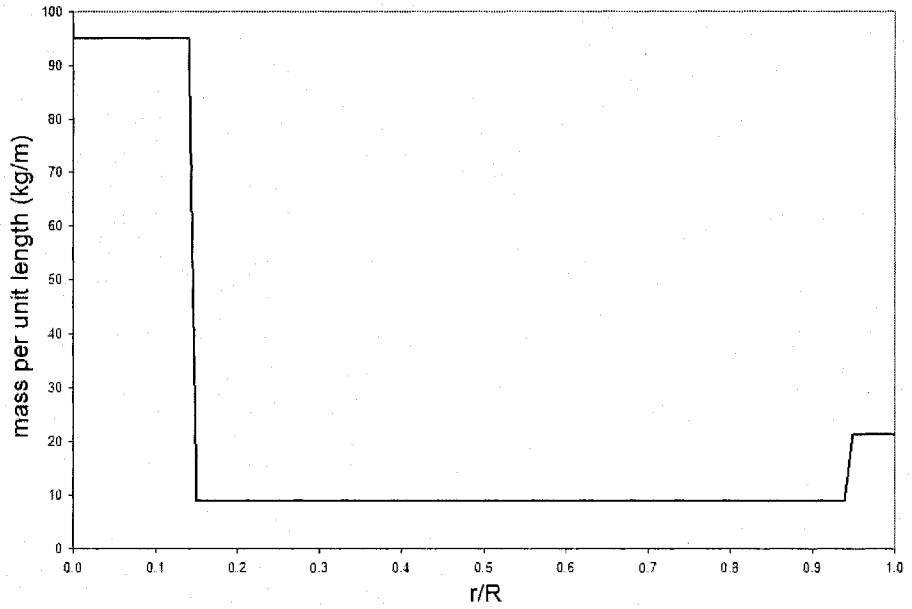

Figure 6.2: CH-46 rotor blade property distributions: mass distribution (given with respect to fraction of rotor radius: r/R).

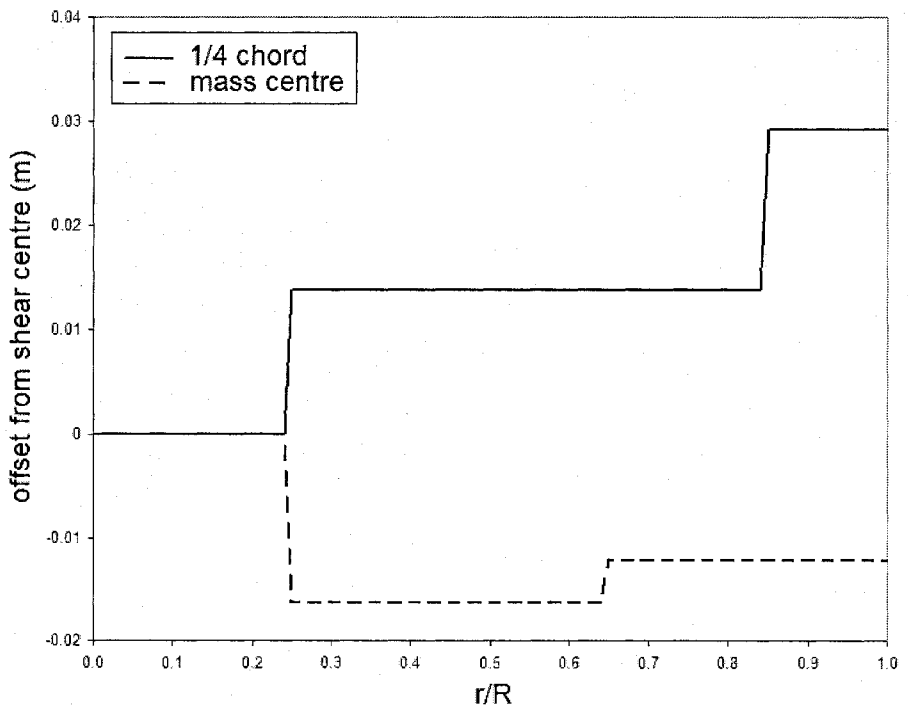

Figure 6.3: CH-46 rotor blade property distributions: inertia and aerodynamic centre offsets (given with respect to fraction of rotor radius: r/R).

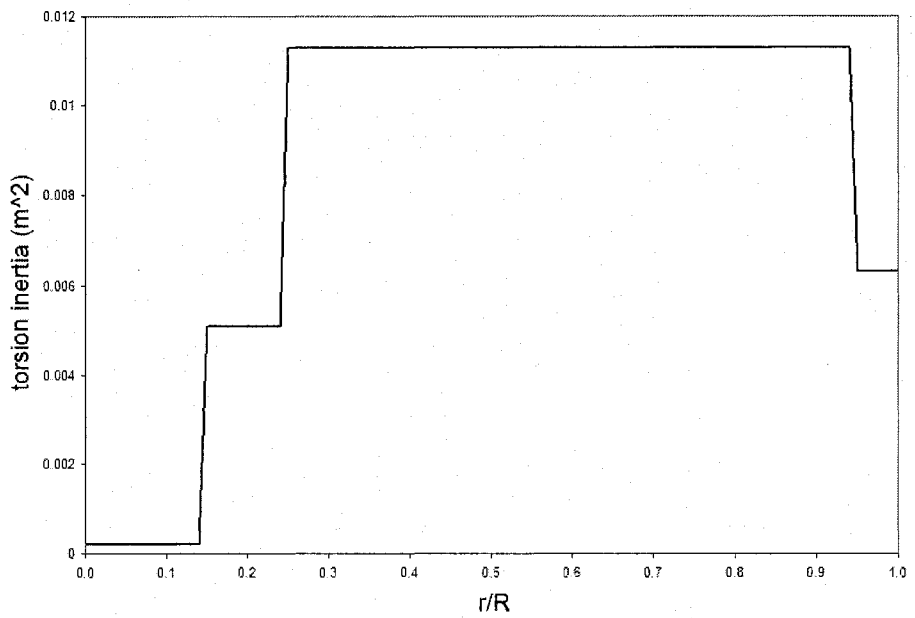

Figure 6.4: CH-46 rotor blade property distributions: torsion inertia (given with respect to fraction of rotor radius: r/R).

Ship motion has the potential to increase the maximum downward blade tip deflection. Comparing Cases 1 and 2, it increased from -0.99 m to -1.15 m for blade 1, and blade 3 achieved the deflection sufficient to cause a fuselage strike.

In order to show the relative effects of changes in operational parameters, a baseline case was used. The baseline response is shown in Figure 6.6, and is based on parameters similar to those selected for Case 1. However, the wind speed was increased to 25 m/s since studies by both Newman and Smith/Keller, as discussed in Section 2.4, used this speed in

Table 6.2: Parameters for the test cases with three blades and suspension active

case number	collective setting deg	ship motion	wind speed m/s	airwake roll angle	turbulence	max tip deflection (blade 1) m
1	3°	no	15	0°	no	-0.99
2	3°	yes (45° waves)	15	variable	no	-1.15

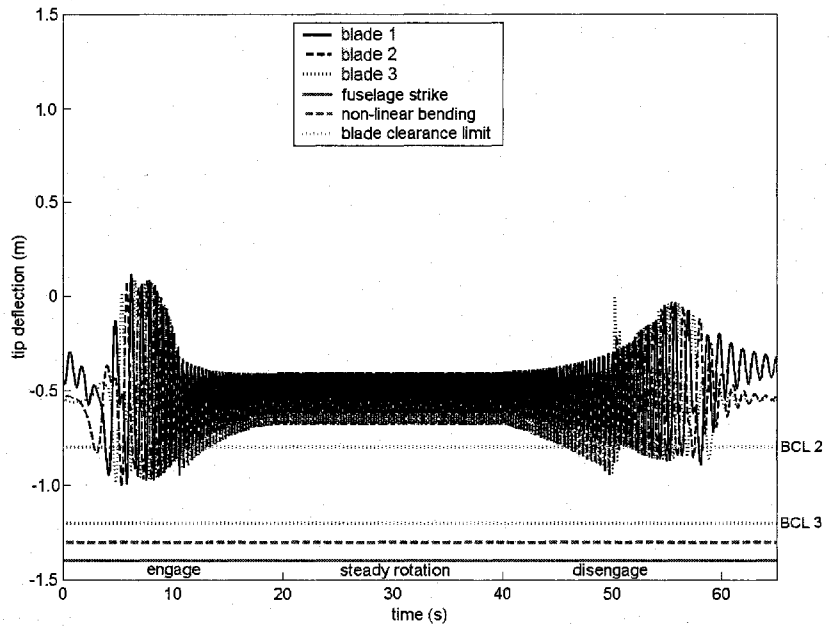

(a) without ship motion (case 1).

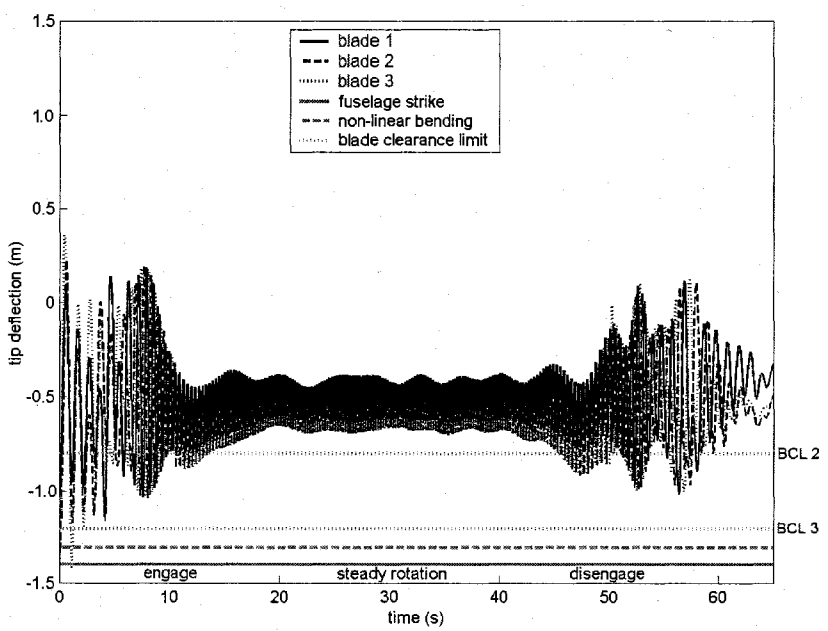

(b) with ship motion (case 2).

Figure 6.5: Typical system response for all 3 blades.

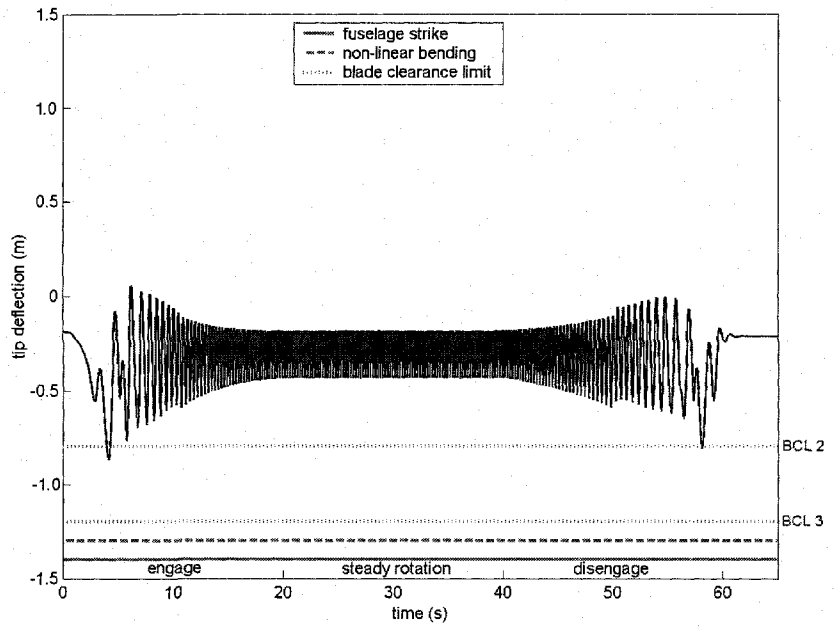

Figure 6.6: Typical system response (baseline).

their simulations. The baseline maximum tip deflection was -0.87 m.

Important system parameters were then varied, according to the properties listed in Table 6.3. All of the test cases were conducted using the model properties listed in Table 6.1, the quasi-steady aerodynamic model, and with all blade flap and torsional degrees of freedom active.

Figure 6.7(a) shows blade behaviour for static ship deck roll of -20°. The upward blade deflection is increased significantly, but the downward deflection is not seriously affected. This trend was observed during examination of the validation experiment results, and is attributed to the airwake shape at static -20° deck roll, which exhibits severe updrafts at the windward deck edge, but no appreciable downdrafts. Figure 6.7(b) shows blade behaviour for static ship deck roll of 20°, which exhibits blade deflections in the tunnel strike range. While a typical engagement is likely to contain only periodic excursions toward ±20°, it is useful to see how the blade might respond to these excursions at any point during a typical engagement profile.

Table 6.3: Parameters for the test cases with one blade active and suspension frozen

case number	collective setting deg	ship motion	wind speed m/s	airwake roll angle	turbulence	max downward tip deflection m
baseline	3°	no	25	0°	no	-0.87
3	3°	no	25	-20°	no	-1.05
5	3°	no	25	20°	no	**-1.40**
6	3°	yes (45° waves)	25	variable	no	-1.26
7	3°	yes (90° waves)	25	variable	no	**-1.38**
8	3°	no	15	0°	no	-0.68
9	3°	no	30	0°	no	-0.99
10	3°	no	25	0°	yes	-0.85
11	0°	no	25	0°	no	**-1.36**

Through Figures 6.8, the effects of ship motion at 45° and 90° relative wave direction respectively are shown. The variation in blade deflection, especially at low rotational speeds, supports the claim that ship motion is a critical component of blade sailing modelling. For Case 6, the ship motion is given in Figure 2.2.

Figure 6.9 shows the relative effect of wind speed on blade tip deflection. As expected, higher wind speeds led to larger blade deflections. The downward-most blade tip excursion increased from -0.68 to -0.99 m as the windspeed was increased from 15 to 30 m/s.

Figure 6.10 shows the effect of spatially- and temporally-correlated turbulence with the Advancing Fourier Series method on blade deflection. The magnitude of blade deflection can be significantly changed at lower rotational speeds, either as an increase or decrease, depending on whether an upward or downward turbulent excursion is occurring. The magnitude of blade deflection is not appreciably affected at higher rotor speeds, since the aerodynamic loads are governed by rotor rotation rather then flow turbulence.

As a final parameter variation, the root collective setting was decreased from 3° to 0°. The resulting tip deflection profile is shown in Figure 6.11. Tip excursions increased

significantly and dangerously approached fuselage strike levels.

Based on the results shown in this study, ship motion and its effect on the airwake can cause blade sailing with deflections in the fuselage strike range (Cases 5 and 7). Fuselage strike can also occur if the pitch angle of the blades is not carefully controlled (Case 11).

The results shown in this study exhibit characteristically lower downward blade deflections than those shown in some previous blade sailing studies. However, the previous studies used the deterministic airwake models as shown in Figure 2.4, which contain similar updraft velocities, but larger downward velocities, compared to those exhibited in the representative airwake profile given in Section 4.3. The results presented here still support some of the conclusions made by previous blade sailing research, especially the idea that largest blade deflections occur in the rotor speed range less than 15% NR. Also, in high wind conditions of 25 - 30 m/s (50 - 60 kn), especially including ship motion, the rotor blades can undergo deflections large enough to cause fuselage strike.

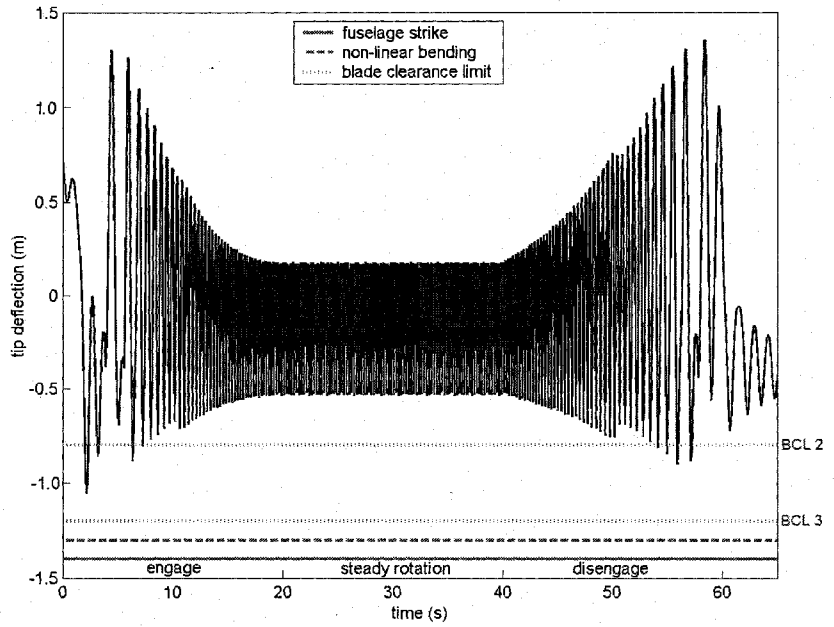

(a) -20° (case 3).

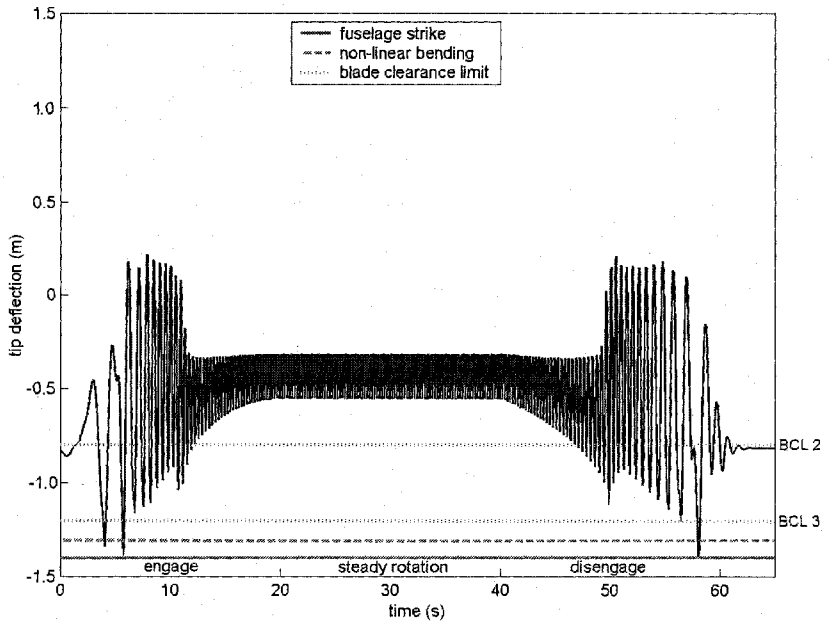

(b) 20° (case 4).

Figure 6.7: Typical system response at static ship roll.

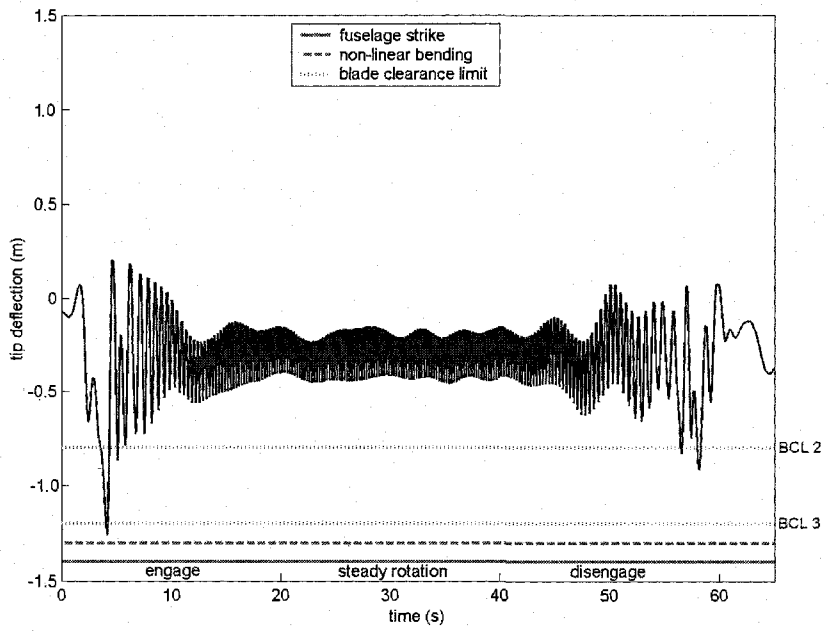

(a) 45° relative wave direction (case 4).

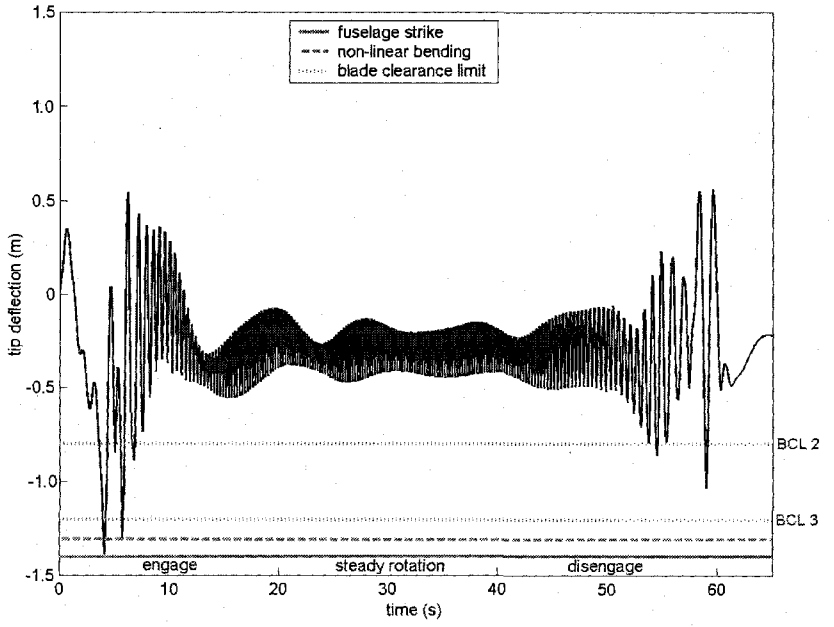

(b) 90° relative wave direction (case 5).

Figure 6.8: Typical system response with ship motion.

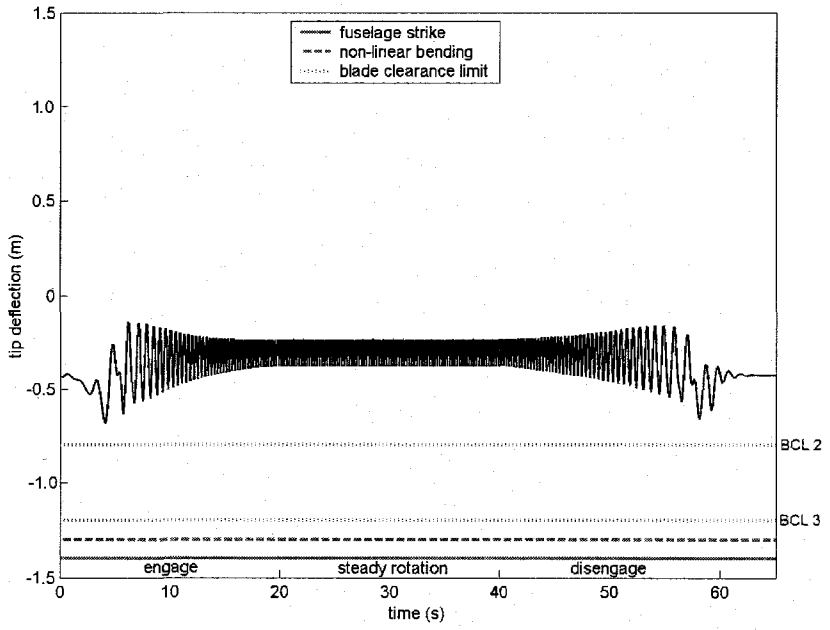

(a) 15 m/s (case 6).

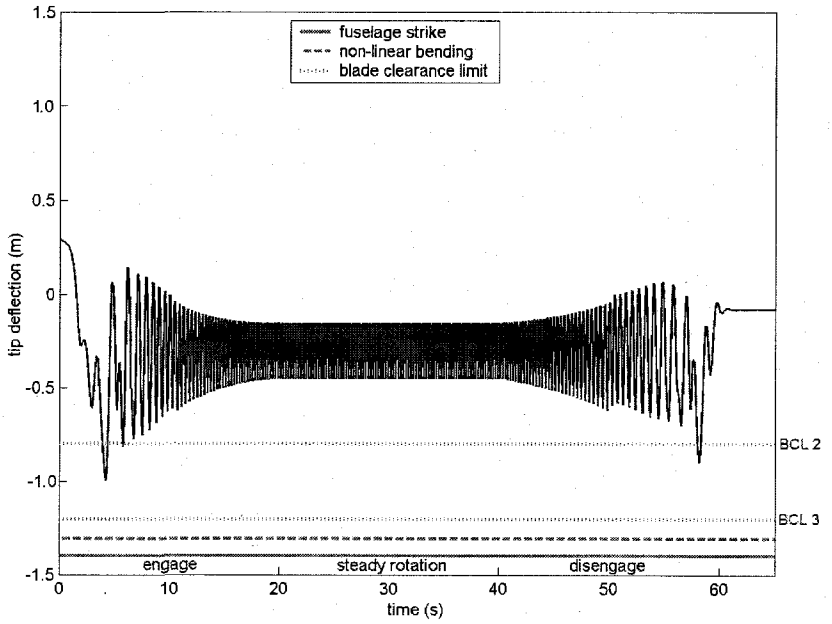

(b) 30 m/s (case 7).

Figure 6.9: Typical system response with varying wind speed.

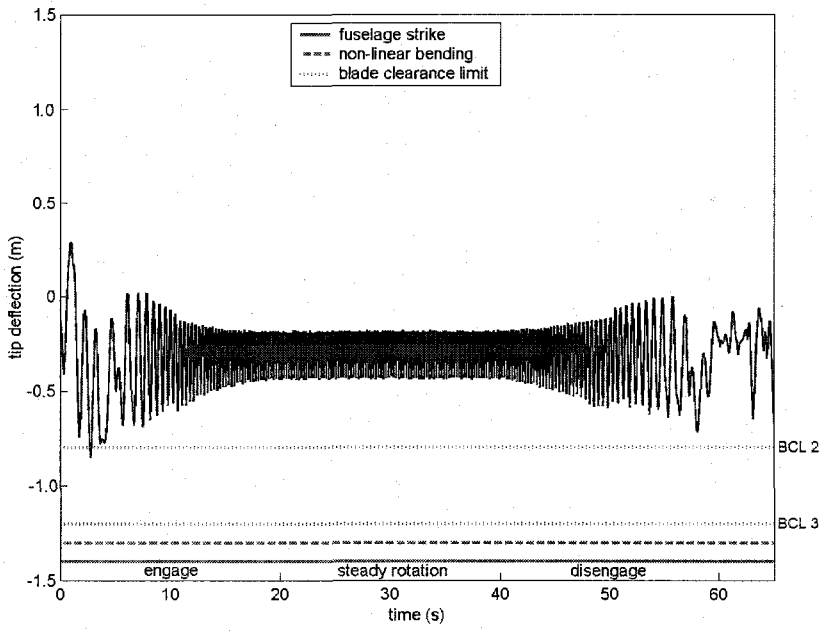

Figure 6.10: Typical system response with turbulence (case 8).

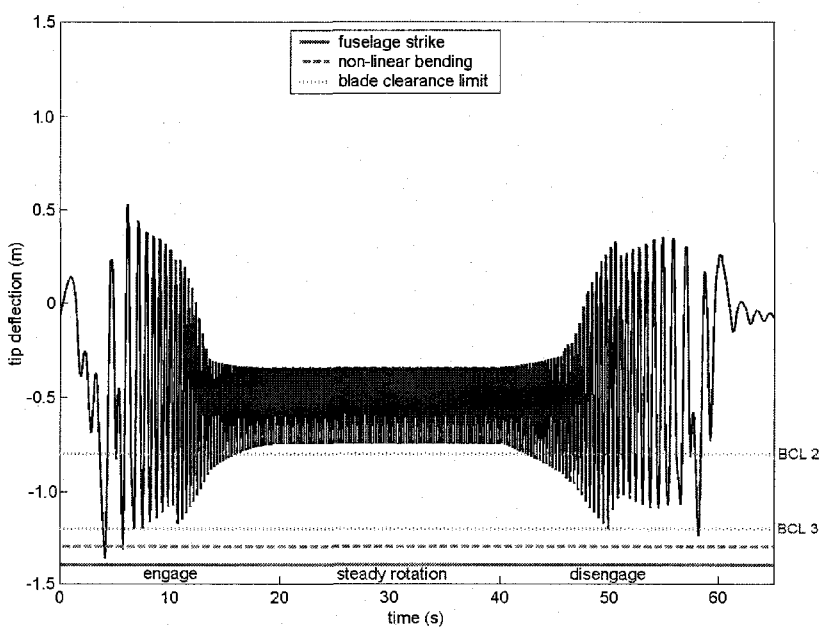

Figure 6.11: Typical system response with 0° root collective (case 9).

Chapter 7

Conclusion

The research encompassed within this thesis has achieved the goals set out at the beginning of the project, which were

1. to study the contributors to the blade sailing phenomenon individually and collectively; and
2. to develop validated modelling tools for this purpose.

These goals have been met through the development of a number of novel models and extensive validation. The important contributions and conclusions from this research are summarized here.

7.1 Contributions

The main contributions of this research fall into three categories: the numerical models themselves, which can be used for the simulation of blade sailing; methods for rigid-body dynamics, which can be applied in other rigid-body modelling applications; and experimental data that was gathered over the course of the research project.

7.1.1 Numerical Tools

A numerical model of the ship-helicopter-rotor system was developed by combining novel and existing models of important system components.

- A rigid-segment dynamic model of the ship-helicopter-rotor system was developed that allows the analyst to vary a wide number of system parameters. Through extensive validation, this model shows that rigid body dynamics can be applied to problems with relatively complicated dynamics undergoing complicated aerodynamic excitement.

- A novel method for simulating spatially- and temporally-correlated turbulence for non-uniform flowfields was developed. This method is called the Advancing Fourier Series (AFS) method.

- These models were combined with existing models for aerodynamic force calculation and ship motion.

The numerical tools have shown good agreement with analytical, published, and experimental data.

7.1.2 Methods in Rigid-body Dynamics

Two rigid-body modelling methods were identified during the development of the dynamic simulation.

- A method for assembling the equations of motion for a blade with a user-defined number of rigid segments by Lagrange's equation was developed. To assemble the equations of motion, the derivatives can be taken using the differentiating rule (Equation 3.37)

$$\frac{\partial}{\partial \phi_{(l_2,n)}}\left(\sum_{i=l_1}^{n_s} G_i\right) = \sum_{i=l_{max}}^{n_s} \frac{\partial G_i}{\partial \phi_{(l_2,n)}}$$

$$\text{where } l_{max} = \begin{cases} \max(l_1, l_2) & \text{if } G_i \text{ contains } \sum_{j=1}^{i} \phi_{(j,n)} \\ l_1 & \text{otherwise} \end{cases}$$

which applies when an unknown number of rigid bodies are connected in series, and the energy expression contain cascading products or sums of system coordinates, $\phi_{(j,n)}$.

- Coupled stiffness properties between rigid segments can be represented using a fully populated rotational stiffness matrix, $[\mathbf{k}_{(i,n)}]$. If the stiffness properties of the equivalent continuous system are known, then the properties of the discrete system can be calculated as (Equation 3.64)

$$[\mathbf{k}_{(i,n)}] = \frac{[\mathbf{k}_b]}{l_{(i,n)}}$$

  where $[\mathbf{k}_b]$ is the continuous stiffness matrix and $l_{(i,n)}$ is the length of the segment.

7.1.3 Experimental Data

A large quantity of experimental data has been collected over the course of this research project, which has led to the development of some novel simulation tools, and to some important conclusions. Three sets of experimental data have been gathered.

- The steady airwake data shows the variations in the time-averaged quantities of the flowfield as a function of space above the ship deck and as a function deck roll angle.
- The unsteady airwake data shows the how the flow correlation characteristics vary with position over the flight deck, considering a variety of correlations spacing distances and directions.
- The validation data consists of a wide variety of validation cases for a model helicopter exposed to combined sailing-like conditions in the wind tunnel and on the motion platform.

7.2 Conclusions

Several important conclusions can be drawn based on the experimental and simulated data gathered in this research.

7.2.1 Experimental Airwake Measurements

Based on experimental results from the airwake experiment, the time-averaged component of the ship airwake in beam winds has some interesting characteristics (Figures 4.3 to 4.9).

- The flow profile is significantly affected by ship roll angle.
- At large positive roll angles, when the ship deck is rolled toward the wind, the flow is approximately parallel to the deck.
- At zero and negative roll angles, positive updrafts appear at the leading edge. They increase in magnitude with negative deck roll angle.
- At negative roll angles, a separation bubble develops near the surface of the deck. This bubble increases in size with negative roll angle, and can encompass up to half of the rotor disc plane at deck roll angles around -20°.
- For small roll angles, the turbulence intensity varies mainly with height. For large negative roll angles, the turbulence intensity tends to increase in the windward direction across the deck.

The coherence results for pairs of points measured at a wide range of probe spacings, probe directions, and positions in the flowfield confirm a number of expected correlation trends in airwake flow (Figures C.9 to C.50).

- Correlation decreases with increasing frequency (eddy size).
- Overall coherence decreases as turbulence content increases.
- The -20° ship deck exhibits lower correlations along the deck than the 0° ship deck. This is an indication of higher turbulence content, smaller eddies, or a shear layer.

The measured auto- and cross-correlations can be reproduced well using von Kármán spectral models, and Taylor's hypothesis for frozen turbulence for spacing distances over which significant correlations exist. The generalized models, described in Section 4.4.4, confirm some expected trends (Figures 4.19 to 4.25).

- The magnitude of the fitted length scale for a given point over the deck remains similar regardless of correlation spacing direction or distance.

- For a deck angle of 0°, the fitted length scale varies mainly with height. For a deck angle of -20°, the fitted length scales tend to decrease in the windward direction across the deck.

7.2.2 Combined Effects at Model Scale

Based on the validation experiment results, the following general trends, but not rules, regarding the magnitude of blade deflection can be stated, bearing in mind that the experimental blades possessed exaggerated flexibility in the flap direction.

For the data collected during experimental Phase 1 (wind tunnel), these conclusions have been drawn (Figures D.5 to D.21).

- Maximum blade deflections occur during droop stop impacts.
- Increases in wind speed increase blade deflections.
- Faster engage/disengage times lead to more erratic blade response and often the larger blade deflections.
- Slower engage/disengage times allow the updrafts to influence blade behaviour over several rotor rotations. This can also lead to large blade deflections.
- Deck inclination away from wind leads to increased updrafts, larger upward blade deflections, and sometimes larger downward blade deflections.
- Increases in blade pitch angle, positive or negative, increase the resultant aerodynamic forces and often the resulting blade deflections.
- Individual blades do not exhibit the same maximum deflections due to their relative azimuthal positions and the different times at which they encounter the up and down drafts in the flow.
- At a deck angle of -20°, maximum upward deflections are increased. Maximum downward deflections are generally similar for low pitch angles, and sometimes decreased for high pitch angles.

For the data collected during experimental Phase 2 (motion platform), these conclusions have been drawn (Figures D.22 to D.23).

- Blade pitch angle does not appreciably affect the frequency response characteristics of the blades.
- Wave approach angle affects ship motion, which has an affect on the magnitude of blade tip deflection.

7.2.3 Numerical Tools

Using the validation experiment, the numerical tools have been shown to capture both the transient and steady-state trends in a complex sailing-like environment. From the comparison of simulated and experimental data, these conclusions regarding airwake and aerodynamics modelling have been drawn.

- The perfectly-correlated turbulence model induces relatively unrealistic large turbulence content and therefore blade deflections.
- The spatially- and temporally-correlated turbulence model using the Advancing Fourier Series method improves the fidelity of the airwake model.
- The inclusion of unsteady aerodynamic effects, through the AMT method, improves the fidelity of the aerodynamics when attached flow is maintained. The accompanying dynamic stall model does not to consistently improve the fidelity of the model.
- The quasi-steady aerodynamics model performs well and consistently at low blade rotation speeds as well as higher speeds.

7.2.4 Blade Sailing

A preliminary study was completed on a typical full-scale helicopter configuration to evaluate the relative importance of the modelled contributors on the magnitude of blade deflections (Figures 6.5 to 6.11). Based on these results, the following conclusions can be drawn.

- Blade azimuthal angle affects the blade response due to the changing nature of the operational conditions. Therefore, some blades may deflect more than others.
- Both representative turbulence and ship motion have the potential to appreciably increase blade deflections at low rotational speeds. Accurate modelling is important for the study of blade sailing.

7.3 Future Work

The work contained in this thesis has many possible extensions. The most obvious is to use the model to examine the sailing behaviour of some specific helicopters in specific environments.

The models could also be further developed to yield a higher fidelity simulation with more simulation options. Concerning airwake modelling, a CFD model interfaced to the dynamics would improve the range of operating conditions over which the blade sailing phenomenon could be studied. Additionally, the advancements made toward the simulation of spatially- and temporally-correlated turbulence modelling could be advanced by studying the following avenues.

- Methods for extending the AFS method along the length of the blade as the blade rotates through space.
- Methods for increasing the speed of the current AFS method.

Additional models could be added to the simulation to improve its fidelity, such as an alternate aerodynamics model, with inflow and a more appropriate dynamic stall model; a more advanced suspension model, allowing for the modelling of complex suspension elements and non-linear tire behaviour; and a pilot model or control system, which could be used to actively change the collective and pitch settings.

The simulation tools also have the potential for being used to study other on-deck phenomena, and could be expanded to simulate blade dynamics of flying helicopters. Some extensions that could provide expanded model applicability are listed.

- The extensional degree of freedom could be added to each blade segment. This could be necessary for composite blades rotating at full speed.
- The capability for the tires to lift or slide off the deck could be added. This would allow flight and landing to be simulated.
- A tail rotor could be added to allow flight and tail rotor tests to be completed.

List of References

[1] D. Carico, "Dynamic interface flight test and simulation limitations," in *Proceedings of the 11th European Rotorcraft Forum*, no. 100, (London, England), pp. 100–1 – 100–20, September 10 - 13 1985.

[2] J. Gere and S. Timoshenko, *Mechanics of Materials.* PWS-Kent Publishing, 3rd ed., 1990.

[3] T. Porteous, "Commercial Chinook - first year of operation," in *Proceedings of the 26th Symposium of the Society of Experimental Test Pilots*, no. 5, pp. 246–256, Sept 1982.

[4] S. Newman, "The safety of shipborne helicopter operations," *Aircraft Engineering and Aerospace Technology*, vol. 76, no. 5, pp. 487–501, 2004.

[5] C. Hofman and R. Fang, "Determination of limitations for helicopter ship-borne operations," in *Proceedings of the 10th European Rotorcraft Forum*, no. 79, (The Hauge, The Netherlands), pp. 79–1 – 79–19, August 28-31 1984.

[6] R. Langlois, A. Tadros, and M. LaRosa, "Investigation of the relationship between helicopter geometrical and inertial parameters and shipboard securing requirements," in *Proceedings of American Helicopter Society 58th Annual Forum*, (Montreal, QC.), American Helicopter Society, June 2002.

[7] J. G. Ginsberg, *Advanced Engineering Dynamics.* Cambridge University Press, 2nd ed., 2005.

[8] D. Kunz, "Survey and comparison of engineering beam theories for helicopter rotor blades," *Journal of Aircraft*, vol. 31, pp. 473–479, May-June 1994.

[9] D. Hodges and E. Dowell, "Nonlinear equations of motion for the elastic bending and torsion of twisted nonuniform rotor blades," Tech. Rep. NASA TN D-7818, NASA, Dec 1974.

[10] D. Hodges, X. Shang, and C. Cesnik, "Finite element solution of nonlinear intrinsic equations for curved composite beams," *Journal of the American Helicopter Society*, pp. 313–321, Oct 1996.

[11] O. A. Bauchau, C. L. Bottasso, and Y. G. Nikishkov, "Modeling rotorcraft dynamics with finite element multibody prodcedures," *Mathematical and Computer Modelling*, vol. 33, pp. 1113–1137, 2001.

[12] R. Huston, "Computer methods in flexible multibody dynamics," *International Journal for Numerical Methods in Engineering*, vol. 32, no. 8, pp. 1657–1668, 1991.

[13] R. Langlois and R. Anderson, "A tutorial presentation of alternative solutions to the flexible beam on a rigid cart problem," *CSME Transactions*, vol. 29, no. 3, 2005.

[14] W. Haering, "Simple discrete lumped parameter models: Insight into large displacement continuous beam models," in *45th AIAA/ASME/ASCE/AHS/ASC Structures, Structural Dynamics and Materials Conference*, no. AIAA-1864, 2004.

[15] Department of the Army, *Aviation unit and aviation intermediate maintenance manual: CH-47D helicopter*, tm 55-1520-240-23-4 ed., Sept 2002.

[16] D. Bastow, G. Howard, and J. P. Whitehead, *Car suspension and handling.* Warrendale, PA, USA: SAE International, 4th ed., 2004.

[17] J. P. Tremblay, "Development and validation of a tire model for a real time simulation of a helicopter traversing and manoeuvring on a ship flight deck," Master's thesis, Carleton University, Ottawa, ON, Canada, 2007.

[18] E. Lewis, ed., *Principles of Naval Architecture.* New Jersey, US: The Society of Naval Architects and Marine Engineers, 2nd ed., 1989.

[19] NATO, "Standardization wave and wind environments and shipboard reporting of sea conditions," Standardization Agreement STANAG 4194, April 1983.

[20] A. Lloyd, *Seakeeping: Ship Behaviour in Rough Weather.* Gosport, UK: A.R.J.M. Lloyd, revised ed., 1998.

[21] K. McTaggart, "Shipmo7: an updated strip theory program for predicting ship motions and sea loads in waves," DREA Technical Memorandum 96/243, Defence Research Establishment Atlantic, 1997.

[22] R. G. Langlois and G. Sopher, "Importance of random frequency spacing in ship motion," in *Proceedings of the 18th Canadian Congress of Applied Mechanics*, (St. John's, Newfoundland, Canada), June, 2001.

[23] R. Phillion and R. Langlois, "Avoiding repetition in ship motion simulation," in *Proceedings of the 2004 CSME Forum*, (London, Ontario, Canada), Canadian Society for Mechanical Engineers, June 1-4, 2004.

[24] H. Teunnissen, "Characteristics of the mean wind and turbulence in the planetary boundary layer," Tech. Rep. UTIAS Review No. 32, University of Toronto Institute for Aerospace Studies, Oct 1970.

[25] ESDU, "Characteristics of atmospheric turbulence near the ground. PART I: definitions and greneral information," Tech. Rep. 74030, Engineering Sciences Data Unit, October 1976.

[26] J. Mann, "The spatial structure of neutral atmospheric surface-layer turbulence," *Journal of Fluid Mechanics*, vol. 273, pp. 141 – 168, 1994.

[27] ESDU, "Characteristics of atmospheric turbulence near the ground. PART II: single point data for strond winds (neutral atmosphere)," Tech. Rep. 85020, Engineering Sciences Data Unit, October 1985.

[28] J. Mann, "Wind field simulation," *Probabilistic Engineering Mechanics*, vol. 13, no. 4, pp. 269 – 282, 1998.

[29] J. Mann, S. Ott, B. H. Jørgensen, and H. P. Frank, "Wasp engineering 2000," Tech. Rep. Risø-R-1356(EN), Risø National Laboratory, Roskilde, Denmark, August 2002.

[30] S. J. Zan and G. F. Syms, "Numerical prediction of rotor loads in an experimentally-determined ship airwake," Tech. Rep. LTR-AA-15, National Research Council Canada - Institute for Aerospace Research, 1995.

[31] J. S. Bendat and A. G. Piersol, *Random Data: Analysis and Measurement Procedures.* John Wiley and Sons, Inc., 3rd ed., 2000.

[32] A. S. Wall, S. J. Zan, R. G. Langlois, and F. F. Afagh, "Modelling helicopter blade sailing: Contributions from ship motion and airwake to blade dynamic response," in *Proceedings of the CASI AERO 2007 Conference*, (Toronto, Ontario, Canada), CASI, Apr 24-26, 2007.

[33] S. J. Zan, "On aerodynamic modelling and simulation of the dynamic interface," in *IMechE Part G: Journal of Aerospace Engineering*, vol. 219, pp. 393 – 410, 2005.

[34] K. R. Cooper, "Wind flow mesurements on the helicopter flight deck of a 120 m frigate," Laboratory Technical Report LTR-LA-259, National Aeronautical Establishment, January 1983.

[35] S. Zan, G. Syms, and B. Cheney, "Analysis of patrol frigate air wakes," in *Proceedings of 15th NATO RTO Meeting on Fluid Dynamics Problems of Vehicles Operating Near or In the Air-Sea Interface*, (Amsterdam, The Netherlands), Research and Technology Oranization, Applied Vehicle Technology, Oct 1998.

[36] R. Lee and S. Zan, "Wind tunnel testing of a helicopter fuselage and rotor in a ship airwake," in *Proceedings of the 29th European Rotorcraft Forum*, (Friedrichshafen, Germany), Sept 2003.

[37] R. Lee and S. Zan, "Unsteady aerodynamic loads on a helicopter fuselage in a ship airwake," in *Proceedings of American Helicopter Society 58th Annual Forum*, (Montreal, QC), American Helicopter Society, June 2002.

[38] L. M. K. Johns and J. V. Healey, "The airwake of a DD-963 class destroyer," *Naval Engineers Journal*, pp. 36–42, May 1989.

[39] J. V. Healey, "Establishing a database for flight in the wakes of structures," *Journal of Aircraft*, vol. 29, pp. 559–564, July-August 1992.

[40] M. Rhoades and J. V. Healey, "Flight deck aerodynamics of a non-aviation ship," *Journal of Aircraft*, vol. 29, pp. 619–626, July-August 1992.

[41] N. H. Wakefield, S. J. Newman, and P. A. Wilson, "Helicopter flight around a ship's superstructure," in *IMechE Part G: Journal of Aerospace Engineering*, vol. 216, pp. 13 – 28, 2002.

[42] G. Syms, "Simulation of simplified-frigate airwakes using a Lattice-Boltzmann method," in *Proceedings of the 5th International Colloquium on Bluff Body Aerodynamics and Application*, (Ottawa, Canada), July 2004.

[43] K. Reddy, R. Toffoletto, and K. Jones, "Numerical simulation of ship airwake," *Computers and Fluids*, vol. 29, pp. 451–465, 2000.

[44] J. Liu and L. Long, "Higher order accurate ship airwake predictions for the helicopter/ship problem," in *Proceedings of American Helicopter Society 54th Annual Forum*, (Washington, D.C.), May 1998.

[45] A. Tadros, S. Zan, and M. Khoury, "Effects of flight deck configurations and conditions on helicopter securing requirements at landing," in *WARSHIP 2003: Airpower at Sea (Royal Institution of Naval Architects)*, (London, UK), June 2003.

[46] C.C.Critzos, H. Heyson, and J. R.W. Boswinkle, "Aerodynamic characteristics of naca 0012 airfoil section at angles of attack from 0° to 180°," *NACA TN 3361*, 1975.

[47] R. Sheldahl and P. Klimas, "Aerodynamic characteristics of seven symmetrical airfoil sections through 180-degree angle of attack for use in aerodynamic analysis of vertical axis wind turbines," tech. rep., Scandia National Laboratories, Springfield, VA, USA, March 1981.

[48] J. Keller, *Analysis and control of the transient aeroelastic response of rotors during shipboard engagement and disengagement operations.* PhD thesis, The Pennsylvania State University, 2001.

[49] J. Leishman, *Principles of Helicopter Aerodynamics.* Cambridge University Press, 2000.

[50] B. van der Wall and J. Leishman, "On the influence of time varying flow velocity on unsteady aerodynamics," *Journal of the American Helicopter Society*, pp. 25–36, Oct 1994.

[51] A. Jose, J. Leishman, and J. Baeder, "Unsteady aerodynamics modeling with time-varying free-stream mach numbers," *Journal of the American Helicopter Society*, pp. 299–318, Oct 1996.

[52] J. Leishman and T. Beddoes, "A semi-empirical model for dynamic stall," *Journal of the American Helicopter Society*, pp. 3–17, July 1989.

[53] J. Leishman and T. Beddoes, "A generalised model for airfoil unsteady aerodynamic behaviour and dynamic stall using the indicial method," in *42nd Annual Forum of the American Helicopter Society*, 1986.

[54] D. A. Peters, M. Hsieh, and A. Torrero, "A state-space airloads theory for flexible airfoils," in *Proceedings of the American Helicopter Society 62nd Annual Forum*, (Phienix, AZ), pp. 1806–1823, May 9-11 2006.

[55] D. A. Peters and W. M. Cao, "Finite state induced flow models part i: Two-dimensional thin airfoil," *Journal of Aircraft*, vol. 32, pp. 313–322, March-April 1995.

[56] D. A. Peters and C. J. He, "Finite state induced flow models part ii: Three-dimensional rotor disk," *Journal of Aircraft*, vol. 32, pp. 323–333, March-April 1995.

[57] S. Newman, "The phenomenon of helicopter rotor blade sailing," *Proceedings of the Institution of Mechanical Engineers Part G*, vol. 213, no. G, pp. 347–363, 1999.

[58] P. F. Leone, "Theoretical and experimental study of the flap droop stop impact transient aero-elastic response of a helicopter rotor blade," *Journal of the American Helicopter Society*, vol. 9, January 1964.

[59] V. Pavlov, S. Mikhailov, and E. Nikolaev, "Approach of coaxial main rotor blades during startup on a shipdeck," *Izvestiya VUZ. Aviatsionnaya ekhnika*, vol. 32, no. 1, pp. 25–28, ??

[60] D. Hurst and S. Newman, "Wind tunnel measurements of a ship induced turbulence and the predicition of helicopter rotor blade response," in *Eleventh European Rotorcraft Forum*, (London, England), Sept 10-13 1985. Paper 99.

[61] D. Hurst and S. Newman, "Wind tunnel measurements of a ship induced turbulence and the predicition of helicopter rotor blade response," *Vertica*, vol. 12, no. 3, pp. 267–278, 1988.

[62] S. Newman, "A theoretical model for predicting the blade sailing behaviour of a semi-rigid rotor helicopter," *Vertica*, vol. 14, no. 4, pp. 531–544, 1990.

[63] S. Newman, "The application of a theoretical blade sailing model to predict the behaviour of articulated helicopter rotors," *Aeronautical Journal*, pp. 233–239, June/July 1992.

[64] S. Newman, "The verification of a theoretical helicopter rotor blade sailing method by means of wind tunnel testing," *Aeronautical Journal*, pp. 41–51, Feb 1995.

[65] M. Jones and S. Newman, "A method of reducing blade sailing through the use of trailing edge flaps," in *Proceedings of the 63rd American Helicopter Society Annual Forum*, (Virginia Beach, VA, USA), pp. 411–422, May 1-3 2007.

[66] W. G. Jr. and E. Smith, "Aeroelastic analysis of transient blade dynamics during shipboard engage/disengage operations," in *Proceedings of the 2nd International AHS Aeromechanics Specialists Meeting*, (Alexandria, VA), pp. 8–91 – 8–114, American Helicopter Society, Oct 1995.

[67] W. Geyer, E. Smith, and J. Keller, "Validation and application of a transient aeroelastic analysis for shipboard engage/disengage operations," in *Proceedings of American Helicopter Society 52nd Annual Forum*, (Washington, D.C.), American Helicopter Society, June 1996.

[68] W. Geyer, E. Smith, and J. Keller, "Aeroelastic analysis of transient blade dynamics during shipboard engage/disengage operations," *Journal of Aircraft*, vol. 35, pp. 445–453, May-June 1998.

[69] J. Keller and E. Smith, "Analysis and control of the transient shipboard engagement behaviour of rotor systems," in *Proceedings of American Helicopter Society 55th Annual Forum*, (Montreal, QC), American Helicopter Society, May 1999.

[70] J. Keller and E. Smith, "Experimental and theoretical correlation of helicopter rotor blade-droop stop impacts," *Journal of Aircraft*, vol. 36, pp. 443–450, March-April 1999.

[71] J. Keller, E. Smith, and C. Knarr, "Experimental/theoretical correlation of analysis for helicopter rotor blade/droop stop impacts," in *38th AIAA/ASME/ASCE/AHS/ASC Structures, Structural Dynamics, and Materials Conference*, 1997.

[72] E. Smith, J. Keller, and H. Kang, "Recent developments in the analytical investigation of shipboard rotorcraft engage and disengage operations," in *Proceedings of 15th NATO RTO Meeting on Fluid Dynamics Problems of Vehicles Operating Near or In the Air-Sea Interface*, (Amsterdam, The Netherlands), Research and Technology Oranization, Applied Vehicle Technology, Oct 1998.

[73] J. Keller and E. Smith, "Active control of gimballed rotors using swashplate actuation during shipboard engagement operations," *Journal of Aircraft*, vol. 40, pp. 726–733, July-August 2003.

[74] C. Bottasso and O. Bauchau, "Multibody modeling of engage and disengage operations of helicopter rotors," *Journal of the American Helicopter Society*, vol. 46, pp. 290–300, Oct 2001.

[75] H. Kang and C. He, "Modeling and simulation of rotor engagement and disengagement during shipboard operations," *Annual Forum Proceedings of the American Helicopter Society*, vol. vol 1, 2004.

[76] A. Wall, R. Langlois, S. Zan, and F. Afagh, "Development of a planar model to investigate the effect of ship motion and wind on non-rotating helicopter blade flapping," in *CCToMM Symposium in CSME Forum*, Canadian Society for Mechancial Engineers, Jun 1-4 2004.

[77] A. Wall, S. Zan, R. Langlois, and F. Afagh, "A numerical model for studying helicopter blade sailing in an unsteady airwake," in *RTO AVT 123 Symposium on "Flow-Induced Unsteady Loads and the Impact on Military Applications"*, (Budapest, Hungary), NATO, April 25 - 29 2005.

[78] A. S. Wall, R. G. Langlois, and F. F. Afagh, "Modelling helicopter blade sailing: Dynamic formulation in the planar case," *Journal of Applied Mechanics*, vol. 74, pp. 1104 – 1113, November 2007.

[79] A. S. Wall, F. F. Afagh, R. G. Langlois, and S. Zan, "Modeling helicopter blade sailing: Dynamic formulation and validation," *In print, Journal of Applied Mechanics*, 2008.

[80] A. Wall, F. Khouli, F. Afagh, and R. Langlois, "Modelling helicopter blade sailing: Model validation using experimental data," in *Proceedings of American Helicopter Society 64th Annual Forum*, (Montréal, QC), 2008.

[81] F. Khouli, F. Afagh, and R. Langlois, "Asymptotically-correct structural modelling of thin-walled anisotropic closed cross-section rotating slender beams," in *International Conference on Advances in Engineering Structures, Mechanics & Construction*, (Waterloo, Ontario, Canada), May 14-17 2006.

[82] F. Khouli, F. F. Afagh, and R. G. Langlois, "Application of the first order generalized-alpha method to the solution of an intrinsic geometrically exact model of rotor blade systems," *Accepted to Journal of Computational and Nonlinear Dynamics*, 2008.

[83] F. Khouli, A. Wall, R. Langlois, and F. Afagh, "Investigation of the active-twist rotor response of various rotor system configurations during shipboard engagement and disengagement operations," in *Proceedings of the 18th International Conference on Adaptive Structures and Technologies*, (Ottawa, ON, Canada), October 3-5 2007.

[84] F. Khouli, A. Wall, R. Langlois, and F. Afagh, "Investigation of the feasibility of a proposed hybrid passive and active control strategy for the transient aeroelastic response of helicopter rotor blades during shipboard engage and disengage operations," in *Proceedings of American Helicopter Society 64th Annual Forum*, (Montréal, QC), 2008.

[85] P. Nikravesh, *Computer-aided Analysis of Mechanical Systems.* New Jersey: Prentice-Hall, Inc., 1988.

[86] S. Chapra and R. Canale, *Numerical Methods for Engineers with Software and Programming Applications.* Boston: McGraw-Hill, 4th ed., 2002.

[87] A. Heck, *Introduction to Maple.* Springer-Verlag, 3rd ed., 2003.

[88] R. Schilling, *Fundamentals of Robotics: Analysis and Control.* New Jersey: Prentice-Hall, Inc., 1990.

[89] T. Kane and D. Levinson, *Dynamics: Theory and Applications.* McGraw-Hill Book Company, 1985.

[90] R. Langlois and R. Anderson, "Multibody dynamics of very flexible damped systems," *Multibody System Dynamics*, vol. 3, pp. 109–136, May 1999.

[91] E. Christensen and S. Lee, "Non-linear finite element modeling of the dynamics of unrestrained flexible structures," *Computers and Structures*, vol. 23, no. 6, pp. 819–829, 1986.

[92] J. Epps and R. Chandra, "The natural frequencies of rotating composite beams with tip sweep," *Journal of the American Helicopter Society*, vol. 41, pp. 29–36, Jan 1996.

[93] A. Bramwell, G. Done, and D. Balmford, *Bramwell's Helicopter Dynamics.* AAIA Education Series, 2nd ed., 2001.

[94] G. D. Padfield, *Helicopter Flight Dynamics: The Theory and Application of Flying Qualities and Simulation Modeling.* AIAA Education Series, 1996.

[95] J. S. Bendat and A. G. Piersol, *Engineering Applications of Correlations and Spectral Analysis.* John Wiley and Sons, Inc., 2nd ed., 1993.

[96] A. Davenport, "The relationship of wind structure to wind loading," in *Proceedings of the Symposium on Wind Effects on Buildings and Structures*, no. Paper 2, (England), 1963.

[97] G. Larose, *The dynamic action of gusty winds on long-span bridges.* PhD thesis, Technical University of Denmark, Department of Civil Engineering, 1997.

[98] L. Kristensen and N. O. Jensen, "Lateral coherence in isotropic turbulence and in the natural wind," *Boundary Laye Meteorology*, vol. 17, pp. 353–373, 1979.

[99] J. Mann, L. Kristensen, and M. S. Courtney, "The great belt coherenc experiment," Tech. Rep. Risø-R-596, Risø National Laboratory, Roskilde, Denmark, August 1991.

[100] ESDU, "Characteristics of atmospheric turbulence near the ground. PART III: variations in space and time for strong winds (neutral atmosphere)," Tech. Rep. 75001, Engineering Sciences Data Unit, October 1975.

[101] C. Wolowicz, J. B. Jr., and W. Gilbert, "Similitude requirements and scaling relationships as applied to model testing," Technical Paper 1435, NASA, 1979.

[102] M. Selig, J. Guglielmo, A. Broeren, and P. Giguere, *Summary of Low-Speed Airfoil Data*, vol. 1. Virginia Beach, Virginia, USA: SoarTech Publications, 1995.

[103] IMSL, *MATH/LIBRARY FORTRAN Subroutines for Mathematical Appications.* Houston, TX: IMSL, Inc, 1989.

[104] R. Burden and J. Faires, *Numerical Analysis.* Brooks Cole, 7th ed., 2001.

[105] J. V. Healey, "The prospects for simulating the helicopter/ship interface," *Naval Engineers Journal*, pp. 45–63, March 1987.

[106] H. Panofsky and J. Dutton, *Atmospheric Turbulence: Models and Methods for Engineering Applications.* John Wiley & Sons, 1984.

[107] J. Mann, "Investigation of atmospheric low-frequency turbulence over the ocean," tech. rep., Risø National Laboratory, Roskilde, Denmark, March 1992.

[108] A. Davenport, "Rationale for determining design wind velocities," in *Journal of the Structural Division*, no. 2475.ST5, American Society of Civil Engineers, May 1960.

[109] P. D. Welch, "The use of fast Fourier transform for the estimation of power spectra: A method based on time averaging over short, modified periodograms," *IEEE Transactions on Audio and Electroacoustics*, vol. Au-15, pp. 70–73, June 1967.

[110] L. M. Fingerston and P. Freymuth, *Fluid Mechanics Measurements*, ch. 4, pp. 99–154. Hemisphere Publishing Co., 1983.

[111] S. Miller and J.-C. Piedbœuf, "Estimation of endpoint position and orientation of a flexible link," in *Knowledge-Based Systems and Robotics Workshop*, (Ottawa, ON, Canada), Nov 14-17 1993.

[112] J. H.W. Haslach and R. Armstrong, *Deformable Bodies and their Material Behaviour.* John Wiley and Sons, Inc., 2004.

Appendix A

Aerodynamic and Airwake Algorithms

A.1 Algorithm for Unsteady Aerodynamics

This appendix defines the execution of the unsteady aerodynamics model used in this research, as described in Section 3.4.5. It is a time-history model that combines the indicial method (AMT) for unsteady attached flow and dynamic stall, and the quasi-steady method for separated flow.

This aerodynamics model evaluates aerodynamic coefficients in blade coordinates. The coefficients C_n and C_c are the force coefficients normal to the chord and parallel to the blade chord, as shown in Figure A.1, and C_m is the moment coefficient about the 3/4 chord axis. The aerodynamic forces normal to the chord, N, parallel to the chord, C, and the aerodynamic moment, M, can be calculated from these coefficients using Equations A.1 through A.3.

$$N = \frac{1}{2}\rho V^2 C_n(\alpha) c d \tag{A.1}$$

$$C = \frac{1}{2}\rho V^2 C_c(\alpha) c d \tag{A.2}$$

and

$$M = \frac{1}{2}\rho V^2 C_m(\alpha) c^2 d \tag{A.3}$$

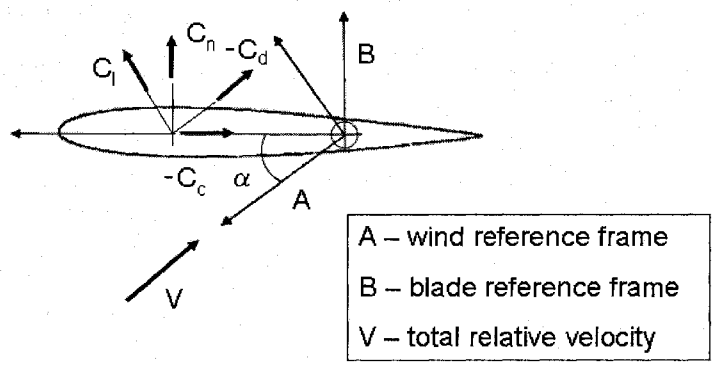

Figure A.1: Coordinate systems in use in aerodynamics model. Relative wind velocity calculated at 3/4 chord; resultant force coefficients applied at 1/4 chord point (the drag coefficient is negative because the coordinate system defines positive forward).

where ρ is the air density, V is the magnitude of the local relative air in the airfoil plane, c is the chord length, and d is the width of the section. The lift, L, and the drag, D, can be calculated using Equations 2.11 and 2.12.

A.1.1 Model Component 1 - Unsteady Attached Flow

The attached flow component of the model is detailed in References [50] and [49]. With this model, the time-varying lift per unit length, ℓ, is given by

$$\ell_l(t) = \frac{1}{2}\rho V(t) c C_{l_\alpha}\left(w_{34}(0)\phi(s) + \int_{s_o}^{s} \frac{dw_{34}(\sigma)}{ds}\phi(s-\sigma)d\sigma\right) = \frac{1}{2}\rho V(t) c C_{l\alpha} w_{34_{\text{eff}}}(t) \quad \text{(A.4)}$$

where $\phi(s)$ represents the indicial response to a unit step input in angle of attack, and the integral is known as Duhamel's integral. The variable s represents the travel of the airfoil through the air in semi-chords, given by

$$s = \frac{2}{c}\int_0^t V dt \quad \text{(A.5)}$$

The effective wind vertical velocity, $w_{34_{\text{eff}}}$, on the airfoil is related to an effective angle

of attack, α_{eff}, by

$$\alpha_{\text{eff}} = \arcsin \frac{w_{34_{\text{eff}}}}{V} \tag{A.6}$$

In Reference [50], the vertical velocity, at instant i, is defined as

$$w_{34_i} = V_i \alpha_i + \dot{h}_i + b\dot{\alpha}_i \left(\frac{1}{2} - a\right) \tag{A.7}$$

where h represents the plunge of the airfoil, $b = c/2$, and a is the centre of rotation with respect to the flow, in fractions of semi-chords measured positive toward the trailing edge from mid-chord. In the modified formulation used in the current research, blade plunge is given as a component of V. Considering this and acknowledging that the angle of attack is not necessarily small, the vertical blade velocity is given by

$$w_{34_i} = V_i \sin \alpha_i + b\dot{\alpha}_i \left(\frac{1}{2} - a\right) \tag{A.8}$$

and the change in vertical velocity over one timestep is given by

$$\Delta w_{34_i} = (V_i - V_{i-1}) \sin \alpha_i + V_i \cos(\alpha_i)(\alpha_i - \alpha_{i-1}) + b\left(\frac{1}{2} - a\right)(\dot{\alpha}_i - \dot{\alpha}_{i-1}) \tag{A.9}$$

Therefore, the deficiency functions from Duhamel's integral are given by [49]

$$X_i = X_{i-1} e^{-b_1 \Delta s_i} + \frac{A_1}{6} \Delta w_{34_i} \left(1 + 4e^{-b_1 \frac{\Delta s_i}{2}} + e^{-b_1 \Delta s_i}\right) \tag{A.10}$$

and

$$Y_i = Y_{i-1} e^{-b_2 \Delta s_i} + \frac{A_2}{6} \Delta w_{34_i} \left(1 + 4e^{-b_2 \frac{\Delta s_i}{2}} + e^{-b_2 \Delta s_i}\right) \tag{A.11}$$

where the coefficients A_1, A_2, b_1, and b_2 given by Jones' approximation [49] are

$$\phi(s) = 1 + A_1 e^{-b_1 s} + A_2 e^{-b_2 s} = 1 - 0.165e^{-0.0455s} - 0.335e^{-0.3s} \tag{A.12}$$

and the value of Δs_i is calculated using backward difference such that

$$\Delta s_i = \frac{(V_{i-1} + V_i)}{2} \frac{\Delta t}{b} \tag{A.13}$$

Finally, the effective vertical velocity is calculated by

$$w_{34_{\text{eff}_i}} = w_{34_i} - X_i - Y_i \tag{A.14}$$

at each timestep, and the effective angle of attack is calculated using Equation A.6. The resulting lift coefficient is calculated by

$$C_l^c = C_{l_\alpha} \alpha_{\text{eff}} \tag{A.15}$$

In order to apply the model in blade coordinates, the lift coefficient is transformed using

$$C_n^c = C_l^c \cos \alpha_{\text{eff}} \tag{A.16}$$

and

$$C_c^c = C_l^c \sin \alpha_{\text{eff}} \tag{A.17}$$

The above lift coefficients account for the circulatory lift, indicated by the superscript c. They are so named because they account for the lift resulting from circulation through potential flow theory. Unsteady loads are also caused by the inertial interaction between the blades and the air. These loads, called non-circulatory and labelled with a superscript nc, are given by

$$C_n^{nc} = \frac{\pi b^2}{V_i^2} \frac{(V_i - V_{i-1})}{\Delta t} \sin \alpha_i + V_i \dot{\alpha}_i \cos \alpha_i \tag{A.18}$$

$$C_m^{nc} = \frac{\pi b^3}{V^2} \left(a \frac{V_i - V_{i-1}}{\Delta t} \sin \alpha_i \right) - V_i \left(\frac{1}{2} - a \right) \dot{\alpha}_i \cos \alpha_i \tag{A.19}$$

Chordwise non-circulatory lift is taken to be 0.

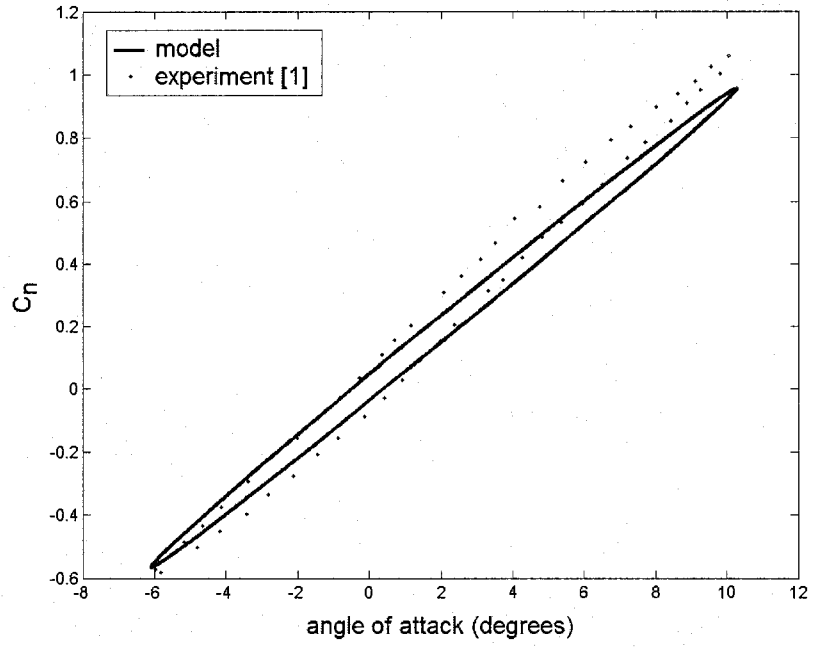

(a) Normal force coefficient

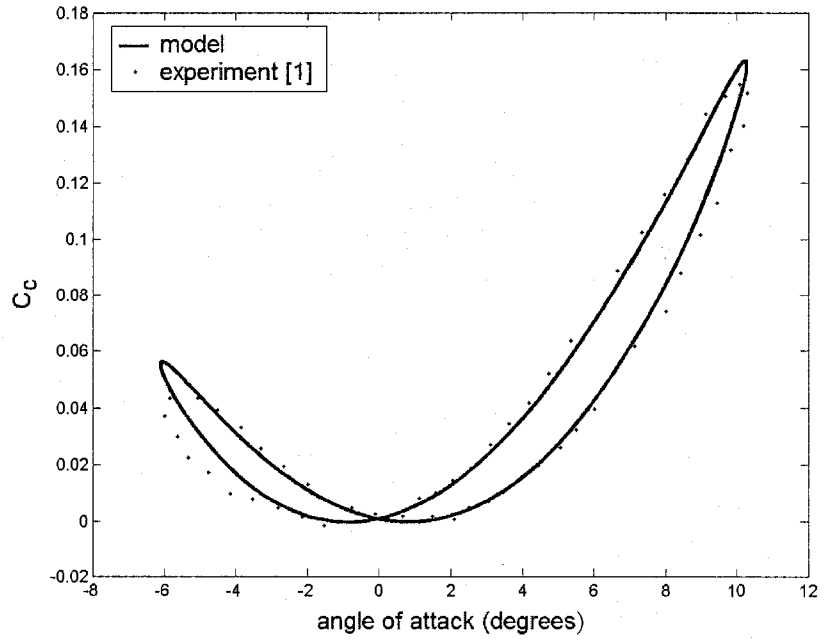

(b) Chordwise force coefficient

Figure A.2: Unsteady aerodynamics model validation results.

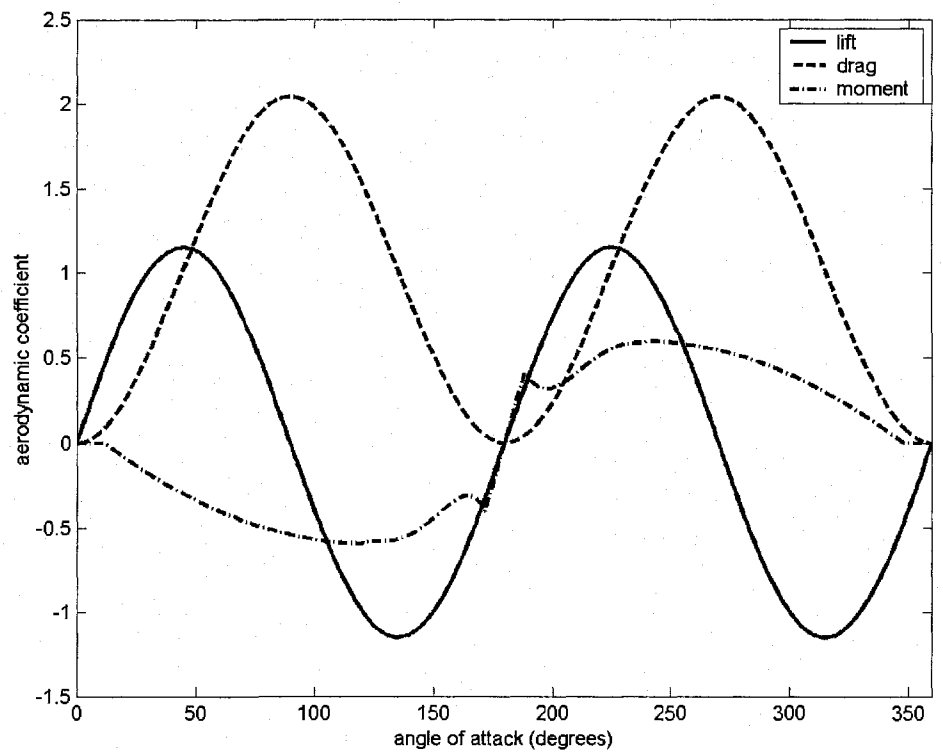

Figure A.3: Separated aerodynamic coefficients for combined unsteady aerodynamics model.

Validation

The unsteady behaviour of the coefficient of lift is validated against experimental results for an airfoil oscillating in steady flow [52]. For this case, the Mach number was 0.383, the reduced frequency, k, was 0.074, and the angle of attack was varied as

$$2.1^\circ + 8.2^\circ \sin \omega t \tag{A.20}$$

The normal and chordwise force coefficients are shown in Figure A.2. The agreement is good.

A.1.2 Model Component 2 - Quasi-steady

If the flow over the airfoil is separated, as indicated by the dynamic stall model, the aerodynamic coefficients are obtained using the quasi-steady lookup method. The coefficients are shown in Figure A.3, and are given by the expressions

$$C_l^q = 1.15 \sin(2\alpha) \tag{A.21}$$

$$C_d^q = 1.02 - 1.02 \cos(2\alpha) \tag{A.22}$$

$$C_m^q = \tag{A.23}$$

$$\begin{cases} 0 & \alpha < 12^\circ \\ 4.69e^{-5}\alpha^2 - 1.17e^{-2}\alpha + 0.133 & 12^\circ \leq \alpha < 120^\circ \\ 4.23e^{-7}\alpha^4 + 2.36e^{-4}\alpha^3 - 4.92e^{-2}\alpha^2 + 4.52\alpha - 155.5 & 120^\circ \leq \alpha < 172^\circ \\ 0.05(\alpha - 180.0) & 172 \leq \alpha < 188^\circ \\ 2.16e^{-7}\alpha^4 - 1.96e^{-4}\alpha^3 + 6.64e^{-2}\alpha^2 - 9.96\alpha + 556.8 & 188^\circ \leq \alpha < 240^\circ \\ -4.69e^{-5}\alpha^2 + 2.20e^{-2}\alpha - 1.98 & 240^\circ \leq \alpha < 348^\circ \\ 0 & 348^\circ \leq \alpha \end{cases}$$

which are modified from those found in Reference [48]

These expressions are the same as those given in Equation 3.5, except that the attached flow effects have been removed. This is because the attached flow generated-loads are accounted for using the AMT method. The coefficients are transformed to blade coordinates using the geometrical angle of attack, α.

A.1.3 Model Component 3 - Dynamic Stall

The dynamic stall model provides an interface between the attached and quasi-steady (separated) model components. Using two criteria, the model indicates whether or not the airfoil has stalled. The first criteria checks for leading edge stall. A corrected quasi-steady normal coefficient, $C_n^{c\prime}$ is calculated as

$$C_{n_i}^{c\prime} = C_{n_i}^{c} - D_{p_i} \tag{A.24}$$

where

$$D_{p_i} = D_{p_{i-1}} e^{\frac{\Delta s_i}{T_p}} + (C_{n_i}^{c} - C_{n_{i-1}}^{c}) e^{\frac{\Delta s_i}{2T_p}} \tag{A.25}$$

The corrected coefficient is then compared to the quasi-steady maximum coefficient.

$$\text{if } C_{n_i}^{c\prime} > C_{l_\alpha} \alpha_a \rightarrow \text{ stall} \tag{A.26}$$

The second criteria checks for trailing edge stall, which is based on a Kirchoff's separation model [52]. The sequence of calculations for the trailing edge stall criteria is well described in Reference [48], and the modified version used in the current model is described here.

The procedure requires the calculation of a corrected stall angle of attack, α_1', which accounts for hysteresis effects. It is given by

$$\alpha_1' = \alpha_1 - \Delta\alpha_1' \tag{A.27}$$

where $\Delta\alpha_1\prime$ is given by

$$\Delta\alpha_1' = \begin{cases} \Delta\alpha_1 (1 - f_{i-1})^{\frac{1}{4}} & \text{if } K_{\alpha_i} < 0 \\ 0 & \text{if } K_{\alpha_i} \geq 0 \end{cases} \tag{A.28}$$

if $\alpha_i \geq 0$, and

$$\Delta\alpha_1' = \begin{cases} \Delta\alpha_1 (1 - f_{i-1})^{\frac{1}{4}} & \text{if } K_{\alpha_i} \geq 0 \\ 0 & \text{if } K_{\alpha_i} < 0 \end{cases} \tag{A.29}$$

if $\alpha_i < 0$ and

$$K_a = \frac{\Delta\alpha}{\Delta t} \tag{A.30}$$

An effective angle of attack, α_f, is given by

$$\alpha_f = \arcsin \frac{C_n'}{C_{l_\alpha}} \tag{A.31}$$

and from this, an effective separation point, f', is given by

$$f' = \begin{cases} 1 - 0.3e^{\frac{|\alpha_f| - \alpha_1'}{S_1}} & \text{if } |\alpha_f| \leq \alpha_1' \\ 0.04 + 0.66e^{\frac{\alpha_1' - |\alpha_f|}{S_2}} & \text{if } |\alpha_f| > \alpha_1' \end{cases} \tag{A.32}$$

The boundary layer lag effects are accounted for using D_{f_i} given by

$$D_{f_i} = D_{f_{i-1}} e^{\frac{-\Delta s_i}{T_f}} + (f_i' - f_{i-1}') e^{\frac{-\Delta s_i}{2T_f}} \tag{A.33}$$

to give a new separation point, f_i'' by

$$f_i'' = f_i' - D_{f_i} \tag{A.34}$$

The criteria for trailing edge stall can then be tested.

$$\text{if } f'' < 0.7 \rightarrow \text{ stall} \tag{A.35}$$

The effective separation point is also used to calculate normal force and moment correction factors, which modify the force coefficients near stall. These are given by

$$f_{n\text{correct}} = \left(\frac{1 + \sqrt{f_i''}}{2} \right)^2 \tag{A.36}$$

$$f_{m\text{correct}} = K_0 + K_1 \left(1 - f_i''\right) + K_2 \sin\left(\pi (f_i'')^{m_1}\right) \tag{A.37}$$

A similar procedure is used to check for flow reattachment. The quasi-steady reattachment/separation point is given by

$$f_{qs} = \begin{cases} 1 - 0.3e^{\frac{|\alpha_i| - \alpha_1}{S_1}} & \text{if } |\alpha_i| \leq \alpha_1 \\ 0.04 + 0.66e^{\frac{\alpha_1 - |\alpha_i|}{S_2}} & \text{if } |\alpha_i| > \alpha_1 \end{cases} \tag{A.38}$$

and then the dynamic reattachment point is given by

$$f_i^r = \begin{cases} f' & K_a > 0 \\ f_{qs} & K_a \leq 0 \end{cases} \tag{A.39}$$

if $\alpha_f \geq 0$ and

$$f_i^r = \begin{cases} f' & K_a \leq 0 \\ f_{qs} & K_a > 0 \end{cases} \tag{A.40}$$

if $\alpha_f < 0$. Correcting for lag effects, the reattachment point becomes

$$f_i^{r\prime\prime} = f_i^{r\prime} - D_{f_i}^r \tag{A.41}$$

where

$$D_{f_i}^r = D_{f_{i-1}}^r e^{\frac{-\Delta s_i}{T_f}} + \delta f_i^{r\prime} e^{\frac{-\Delta s_i}{2T_f}} \tag{A.42}$$

and reattachment occurs

$$\text{if } f_i^{r\prime} > 0.7 \rightarrow \text{ reattachment} \tag{A.43}$$

An additional characteristic of dynamic stall is vortex shedding. The modelling of this phenomenon is based on the idea that a vortex strengthens at the leading edge of a stalling airfoil and is then shed downstream immediately after the stall.

The vortex contributes to the coefficient of lift by

$$C_{l_i}^v = \begin{cases} C_{l_{i-1}}^v e^{\frac{-\Delta s_i}{T_v}} + (C_i^v - C_{i-1}^v) e^{\frac{-\Delta s_i}{2T_v}} & \text{for attached flow} \\ C_{l_{i-1}}^v e^{\frac{-\Delta s_i}{T_v}} & \text{for separated flow} \end{cases} \tag{A.44}$$

where

$$C_i^v = C_{n_i}^c \left(1 - (\frac{1+\sqrt{f''}}{2})^2\right) \tag{A.45}$$

and the moment coefficient by

$$C_{m_i}^v = \begin{cases} -C_P C_{l_i}^v & \text{for forward attached flow} \\ C_P C_{l_i}^v & \text{for reversing attached flow} \\ 0 & \text{for separated flow} \end{cases} \tag{A.46}$$

where

$$C_P = 0.2\left(1 - \cos \pi \frac{t - t_{\text{stall}}}{\tau_v}\right) \tag{A.47}$$

A.1.4 Model Execution

The combined model operates according to the flowchart shown in Figure A.4. The calculation steps are indicated by capital letters in brackets.

The vertical lines on either side of the calculation steps represent important calculation variables. On the left side, six indices that track information about the flow are shown. Some of the indices must be stored because their values at the previous timestep are important for the subsequent calculation. These are labeled "global".

stalltime (global): indicates the time at which stall begins.

revindex (local): indicates if the flow is reversed, that is α within 25° of the chord-line at the trailing edge (1: reversed; 0: default).

teindex (local): indicates if the criteria is met for leading edge attachment (1: attached, 0: stalled)

leindex (local): indicates if the criteria is met for trailing edge attachment (1: attached, 0: stalled)

flying (global): indicates the type of flow at that timestep as

0: stall has occurred and flow is unattached;

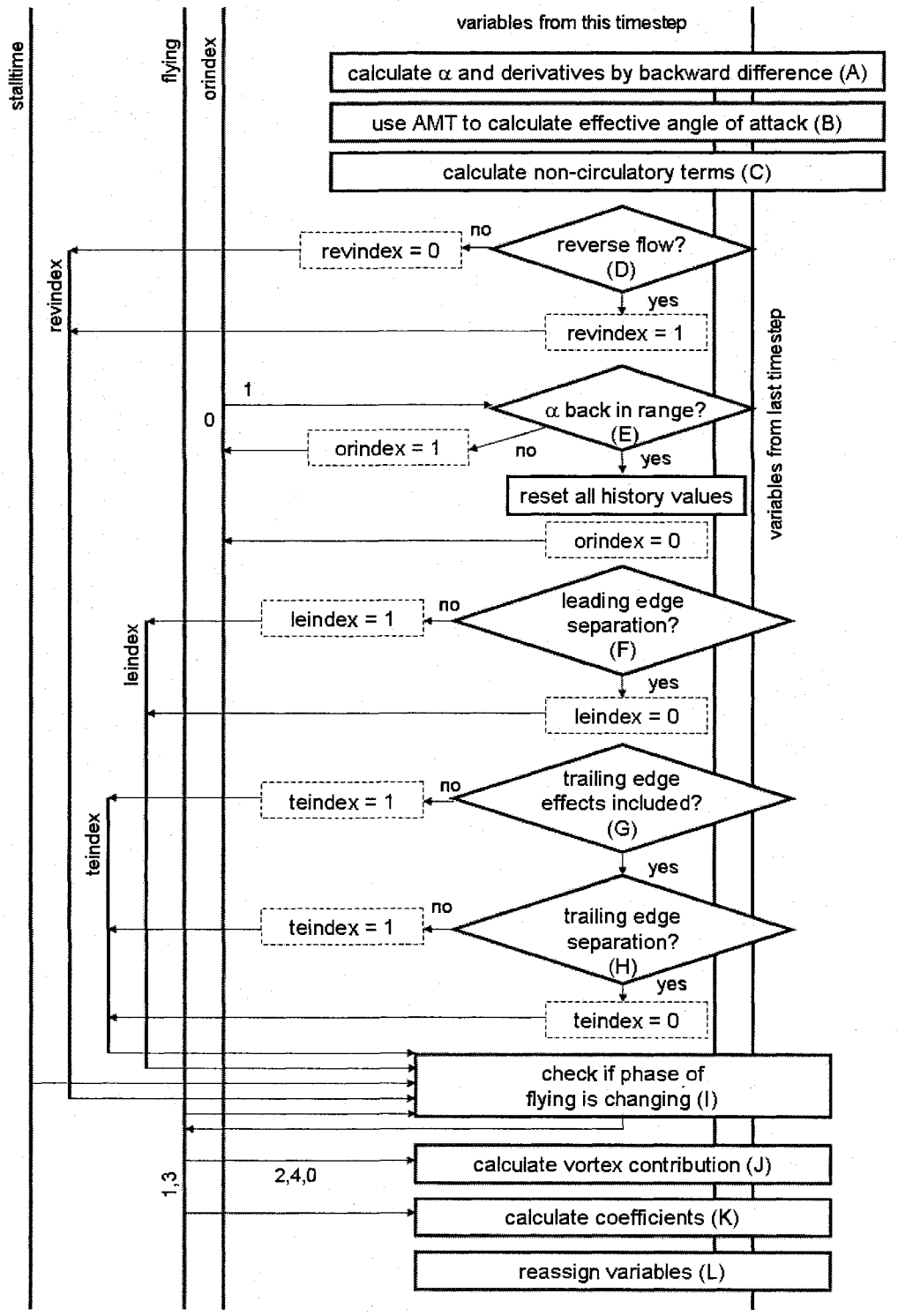

Figure A.4: Flow chart for operation of unsteady aerodynamics function.

1: flow is attached;

2: airfoil is in the process of stalling (vortex is shedding);

3: flow is attached (reverse flow); or

4: airfoil is in the process of stalling (vortex is shedding in reverse flow).

orindex (global): indicates that the angle of attack is well beyond a reasonable attached flow angle therefore history variables need not be stored (1: α beyond 25°, 0: attachment possible). When orindex is 1, the quasi-steady model is always used, unless the airfoil has just stalled and the vortex is still shedding.

The two lines on the right indicate the current and previous values of other variables, as given by the equations in this section. The details of each calculation step are now described.

(A): The resultant velocity, V, angle of attack, α, and the derivatives are calculated using the velocity vector given in blade coordinates as

$$V_i = \sqrt{U(2)_i^2 + U(3)_i^2} \tag{A.48}$$

$$\alpha_i = \arctan\left(\frac{U(3)_i}{-U(2)_i}\right) \tag{A.49}$$

$$\dot{\alpha}_i = \frac{\alpha_i - \alpha_{i-1}}{dt} \tag{A.50}$$

$$\ddot{\alpha}_i = \frac{\dot{\alpha}_i - \dot{\alpha}_{i-1}}{dt} \tag{A.51}$$

and the possible vortex shed time at this time step is calculated as

$$\tau_v = \frac{2b}{V_i} \tag{A.52}$$

(B): The attached flow coefficients are calculated using Equations A.16 and A.17.

(C): The circulatory loads are calculated using Equations A.18 and A.19.

(D): If the flow is reversed, then the angle of attack is corrected such that it is given with respect to the trailing edge rather than the leading edge, and the attached flow calculation can proceed as if the flow were attached and forward.

(E): If the angle of attack is above $\pm 25°$ during the previous time step, check to see if it has come within that angular range this timestep. If not, proceed directly to (K).

(F): Check the leading edge stall criteria using Equation A.26.

(G)/(H): Check the trail edge stall using Equation A.35 and A.43.

(I): At this point, all the conditions of this timestep have been collected. To check if the index flying must be updated this timestep, the following criteria are applied.

- If the flow is attached, "flying" = 1 (or 3), check if stall has occurred. If stall has occurred according to the leading edge or the trailing edge criteria, "flying" = 2 (or 4), the vortex shed time is τ_v, and the time is recorded in "stalltime".
- If the airfoil is stalling, "flying" = 2 (or 4), check if the vortex has finished shedding. If the time that has passed since the onset of stall is greater than the vortex shed time, then "flying" = 0 and "stalltime" is reset to 0.
- If the flow is unattached, "flying" = 0, check if reattachment has occurred.
  - If the flow is forward ("revindex" = 0), both leading and trailing edge conditions allow for attached flow, and the angle of attack is decreasing, then "flying" = 1.
  - If the flow is forward ("revindex" = 1), both leading and trailing edge conditions allow for attached flow, and the angle of attack is decreasing, then "flying" = 3.
  - If the flow remains unattached and the angle of attack exceeds 25°, then the flow is out of range ("orindex" = 1, "revindex" = 0).

(J): If the vortex is shedding ("flying" = 2 or 4), or has just shed ("flying" = 0), then the vortex contributions from Equations A.44 and A.46 are calculated and included.

(K): Calculate the aerodynamic coefficients that are appropriate for the flying conditions.

- if "flying" = 1 or 2

$$C_{n_t} = C_n^c f_{n\text{correct}} + C_l^v + C_n^{nc} \tag{A.53}$$

$$C_{c_t} = C_c^c \sqrt{f_i''}\eta \tag{A.54}$$

$$C_{m_t} = C_n^c \left(\frac{1}{2} + a\right) f_{m\text{correct}} + C_m^v + C_m^{nc} \tag{A.55}$$

- if "flying" = 3 or 4

$$C_{n_t} = C_n^c f_{n\text{correct}} + C_l^v + C_n^{nc} \tag{A.56}$$

$$C_{c_t} = -C_c^c \sqrt{f_i''}\eta \tag{A.57}$$

$$C_{m_t} = -C_n^c \left(\frac{1}{2} + a\right) f_{m\text{correct}} + C_m^v + C_m^{nc} \tag{A.58}$$

- if "flying" = 0

$$C_{n_t} = C_n^q + C_l^v \tag{A.59}$$

$$C_{c_t} = C_c^q \tag{A.60}$$

$$C_{m_t} = C_m^q \tag{A.61}$$

(L): Store the variables that are required at the next time step.

A.2 Algorithm for Airwake Modelling

The algorithms behind the turbulence modelling options specified in Section B.2 are described here.

A.2.1 Perfectly Correlated Turbulence (PCT)

For perfectly correlated turbulence, given by "AEROindex" = 3, two assumptions are made. First, the normalized turbulence spectrum, given by Equation 4.37, is assumed to be the same at every point in the flow field. The spectrum is scaled in magnitude according to the measured turbulence intensity and the local velocity at the point of interest. Second, the root-coherence between any two points in the flow field has a value of 1. The turbulence value is calculated according to the following procedure.

- A scaled frequency vector of the desired range is created.
- The scaled von Kármán auto-spectra are created from the specified spectral parameters ($\alpha\epsilon_u^{2/3}$, L_{uauto}, $\alpha\epsilon_w^{2/3}$ and L_{wauto}), used in Equations 4.24 and 4.25.
- The spectra are scaled to simulation scale in both magnitude and frequency by

$$f = \frac{f_n U_{\text{free}}}{D} \tag{A.62}$$

  and Equation 4.38. The magnitude of the spectra are corrected to reflect the turbulence intensity given by the model developed under airwake experiment A, which is discussed in Chapter 4.
- The values of turbulence at time t are calculated using

$$u(t) = \sum_{j=1}^{n} (A_{u_j} \sin(\omega_{u_j} t + \psi_{u_j})) \tag{A.63}$$

  and

$$w(t) = \sum_{j=1}^{n} (A_{w_j} \sin(\omega_{w_j} t + \psi_{w_j})) \tag{A.64}$$

  where the amplitudes, A_j and frequencies, ω_j are from the simulation-scaled spectra and the phase angles, ϕ_j are generated randomly during the first time step. The frequencies are selected with random frequency spacing.

The quality of the reproduced spectra is shown in Figure A.5. The shape with respect to frequency is reproduced correctly up to 5 Hz, which is the upper limit of the frequency range specified in the input file. The difference in magnitude of the recreated spectra reflects the difference in desired target turbulence intensity, as calculated using Equation 4.38. For this simulation, the windspeed was 1 m/s, the deck width was 1 m, and the points in question were at 0.457 m vertically (Z), and 0.41 m and 1.25 m laterally (Y) in ship coordinates. The desired frequency range was 0 - 5 Hz with 60 frequency components. A sample of horizontal and vertical flow velocity for two points on two adjacent blade segments in the flow field is shown in Figure A.6. Although the signals have slightly different means and turbulence intensities, as per the steady airwake model, the two velocities show no phase offsets.

A modified version of the perfectly correlated model is given by AEROindex = 4. For this model, the turbulent eddies are assumed to convect as per Taylor's frozen turbulence hypothesis across the flight deck. For points in the flowfield a distance of r_Y away from the ship's centreline in the streamwise (Y) direction, the appropriate time shift is calculated by

$$t_{\text{shifted}} = t - \frac{r_Y}{U_{\text{free}}} \tag{A.65}$$

so that the turbulent fluctuations are given by

$$u(t) = \sum_{j=1}^{n} (A_{u_j} \sin(\omega_{u_j} t_{\text{shifted}} + \psi_{u_j})) \tag{A.66}$$

and

$$w(t) = \sum_{j=1}^{n} (A_{w_j} \sin(\omega_{w_j} t_{\text{shifted}} + \psi_{w_j})) \tag{A.67}$$

A sample of horizontal and vertical flow for the same two segments as Figure A.6 are shown in Figure A.7. In this figure, the velocity signals exhibit a relative phase shift, which reflects their relative offset in the lateral (Y) direction.

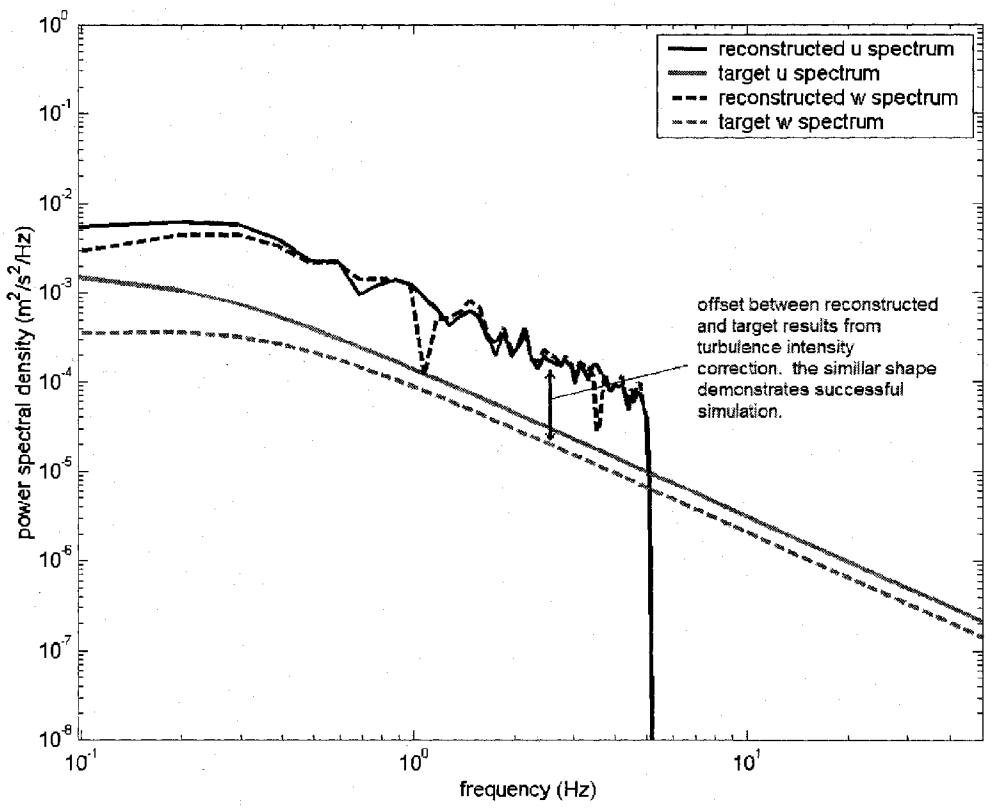

Figure A.5: Target and reconstructed spectra from perfectly correlated turbulence (PCT) model.

A.2.2 Spatially- and Temporally-Correlated (STC) Turbulence

The Advancing Fourier Series (AFS) method is used to simulate spatially- and temporally-correlated (STC) turbulence. The theory, as described in Section 4.4.5, is shown schematically in Figure A.8. For each blade, the AFS method is applied to the outboard-most blade segment, and the inboard segments are assumed perfectly correlated but are scaled for the local turbulence intensity and are shifted via Taylor's hypothesis to compensate for the appropriate streamwise spacing difference. Since the outboard segment has the largest moment arm, the force acting on this segment has the highest impact on blade deflection. It also experiences the highest velocities when advancing. If the wind velocity is very low, the aerodynamic flapping moment on the rotor hub varies as approximately radius cubed. Therefore, this loads on this segment are most important from a modelling point of view.

Verification

The Advancing Fourier Series method was verified against the expected auto- and cross-spectral characteristics for the time-history signal generated at each time step. A sample of the expected and recreated auto- and cross-spectra used to advance the Fourier series coefficients for one blade segment from one point to the next in space and in time are shown in Figure A.9. The agreement is excellent.

Spectral Property Models

The AFS method requires a consistent and complete model for estimating the parameters L_u and L_w for any point in the flowfield. Based on the results described in Section 4.4.4, three different possible parametric models have been proposed.

Model A: uses the fitting parameters from the 0° deck at 35 mm spacing only, but includes all the spacing directions.

Model B: uses the fitting parameters from the 0° deck at 35 mm spacing in the X direction only.

Model C: uses constant fitting parameters ($L_u = 0.162$ m; $L_w = 0.103$ m). These constants were selected as typical values for X spacing of 35 mm as given by pair 43 in Figure C.17.

These models are listed in order of decreasing accuracy and increasing simplicity. They have been compared to examine their respective ability to generate representative spectra across the entire flowfield.

A total of 210 data sets were used to generate the results in Figures C.9 to C.50, and another 106 were used to select the basic correlation distance, described in Section 4.4.2. Coherence functions were calculated for each of these 316 measured data sets and compared with the function calculated using each model. The relative error was calculated using

$$\epsilon_{coh} = \frac{\sqrt{\left(\sum_{i=1}^{N} \left(\gamma_m(i) - \gamma_c(i)\right)^2\right)}}{N} \tag{A.68}$$

where c and m are the calculated and measured root coherences respectively, and N is the number of discrete points where the model coherence is above 0.4. The maximum and mean of errors for all data sets are shown in Table A.1. The original data set shows the error inherent in the original fitting calculations.

Figures A.10 through A.12 show fitting results for a sample of data points using models A through C respectively. The same five pairs are shown in each figure, giving a typical X spacing at mid deck from the fitting data; small X spacing at a streamwise location not used in the fitted data; a larger vertical spacing at a location not used in the fitted data; a typical combined fitting (ZYD) at mid deck for 0° deck; and a typical combined fitting (ZYD) at mid deck for -20° deck. These five points were selected to show a variety of spacing directions, distances, deck angles, and model agreement quality.

As is shown in both the table and the figures, all three models give very good approximations for the coherence, with the errors generated in each model being only slightly larger than those generated' by the original fits.

The horizontal coherence functions fit well, where the largest errors are exhibited close to the deck for pairs involving streamwise spacing. For vertical coherence, the pairs with

Table A.1: Euclidean error for verification points.

model	original	A	B	C
max ϵ_{coh_u}	0.245	0.277	0.270	0.295
max ϵ_{coh_w}	0.251	0.271	0.289	0.282
mean ϵ_{coh_u}	0.057	0.080	0.069	0.094
mean ϵ_{coh_w}	0.067	0.067	0.081	0.082

horizontal spacing agree well in all three models. Pairs with vertical spacing suffer from larger errors for models B and C. This is likely due to a higher degree of coherence in the vertical velocity fluctuations as induced by the ship deck. These are not captured by models based on the fitting parameter for horizontal spacings only. Coherences over the -20° deck are also typically well modelled in all three cases, although these exhibit somewhat larger errors than pairs over the 0° deck.

Based on these results, Model B was selected for use in the simulations that were run as part of the work contained within this thesis. The AFS method could be used with any of these, or some other proposed model for generating representative flow auto- and cross-spectra.

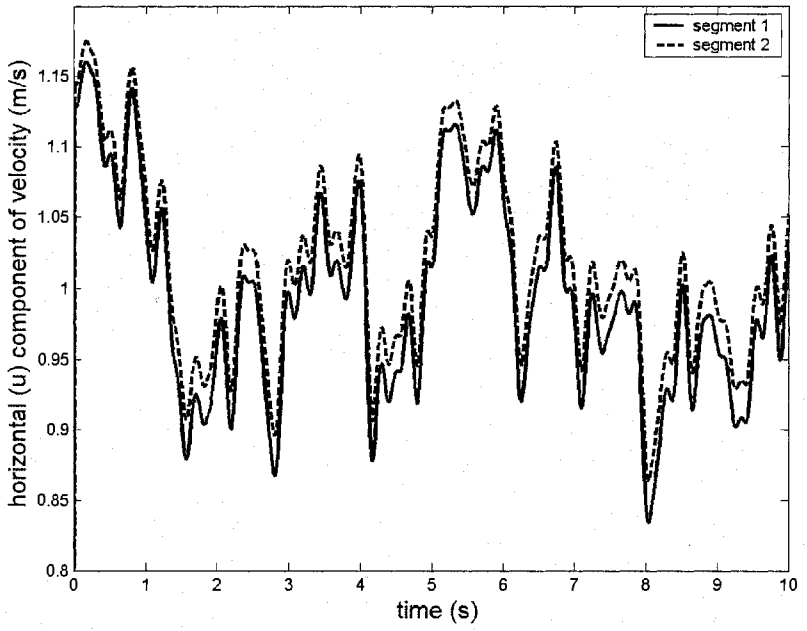

(a) horizontal (Y)

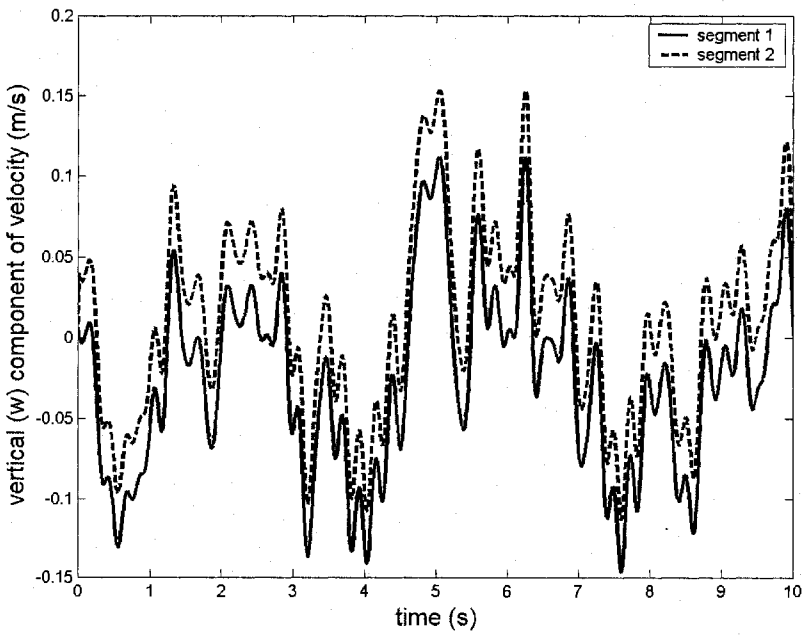

(b) vertical (Z)

Figure A.6: Reconstructed velocity signals without Taylor's hypothesis.

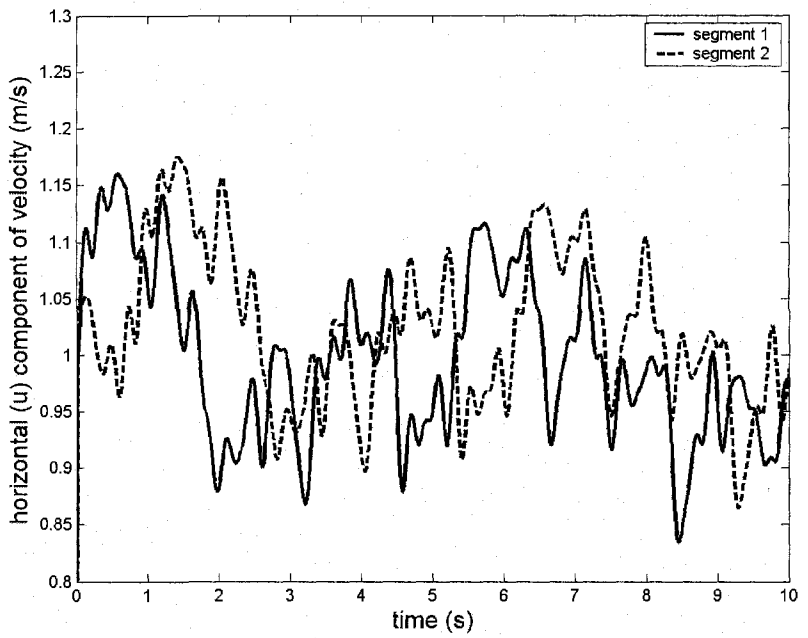

(a) horizontal (Y)

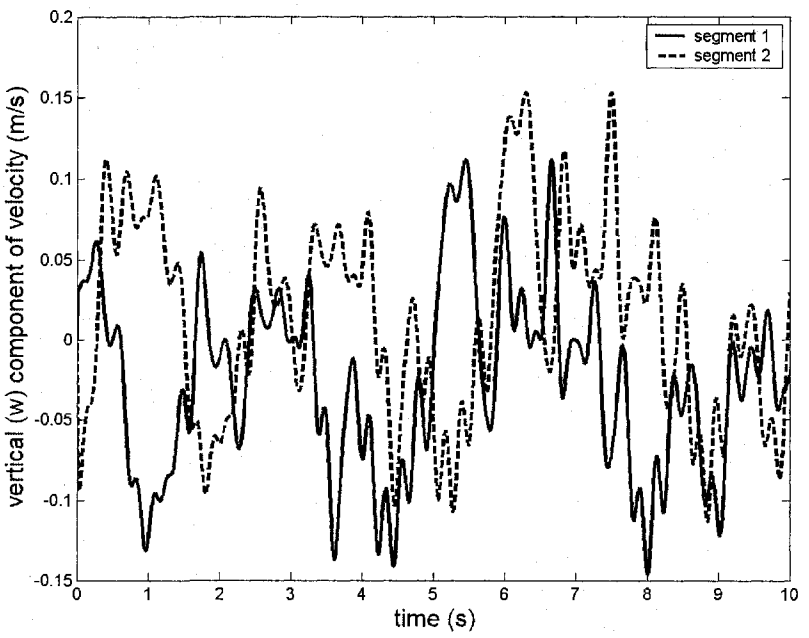

(b) vertical (Z)

Figure A.7: Reconstructed velocity signals with Taylor's hypothesis.

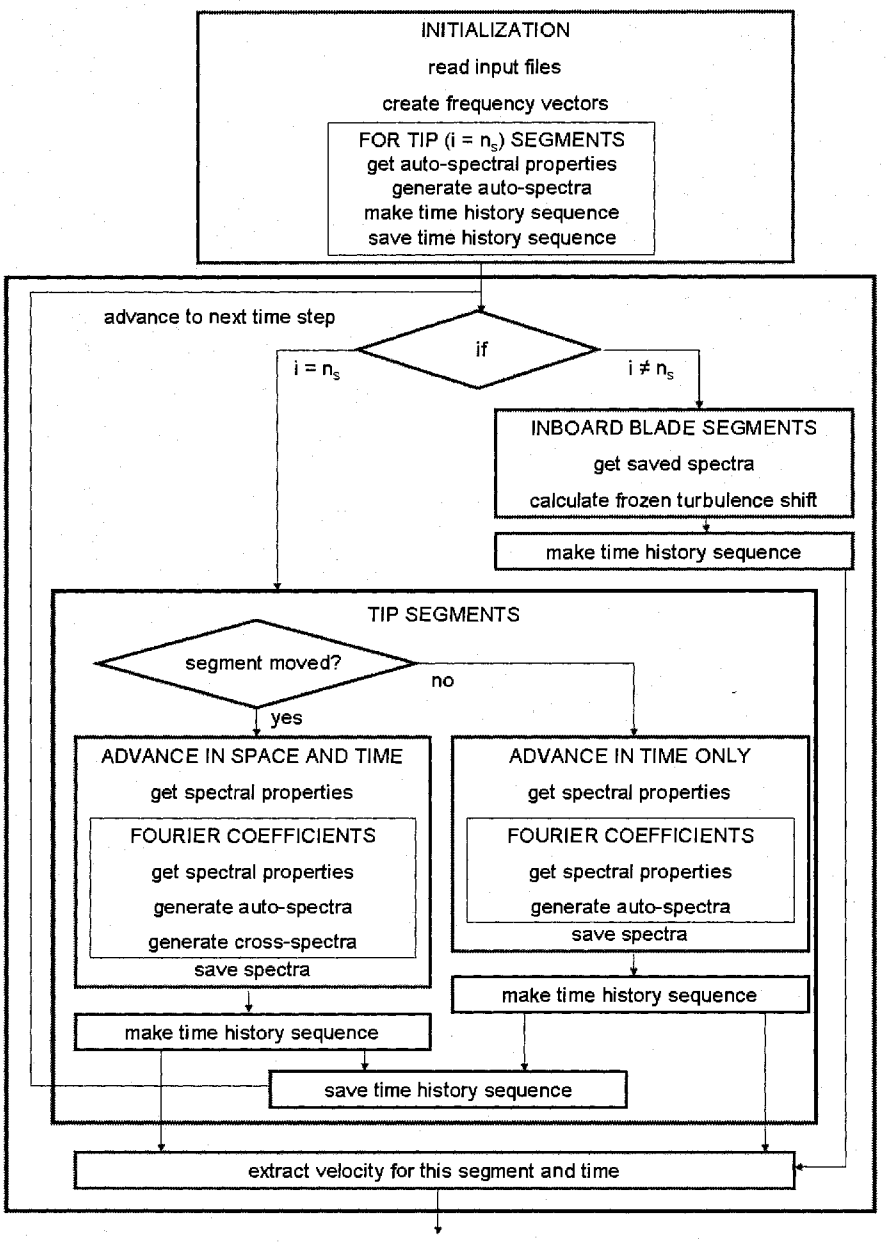

Figure A.8: Flow chart for spatially- and temporally-correlated (STC) turbulence modelling.

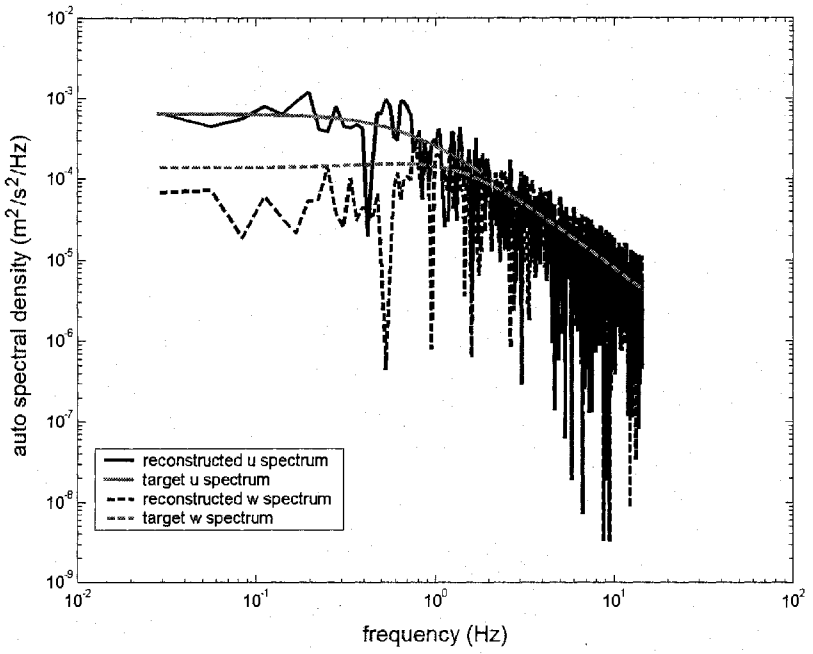

(a) auto-spectra

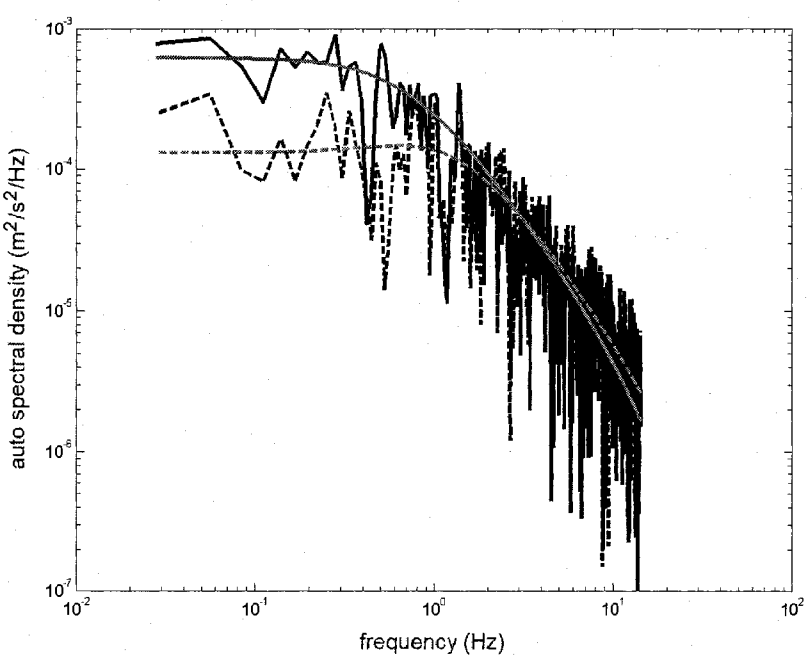

(b) cross-spectra

Figure A.9: Expected and reconstructed auto- and cross-spectra at one point in space and time in the flowfield.

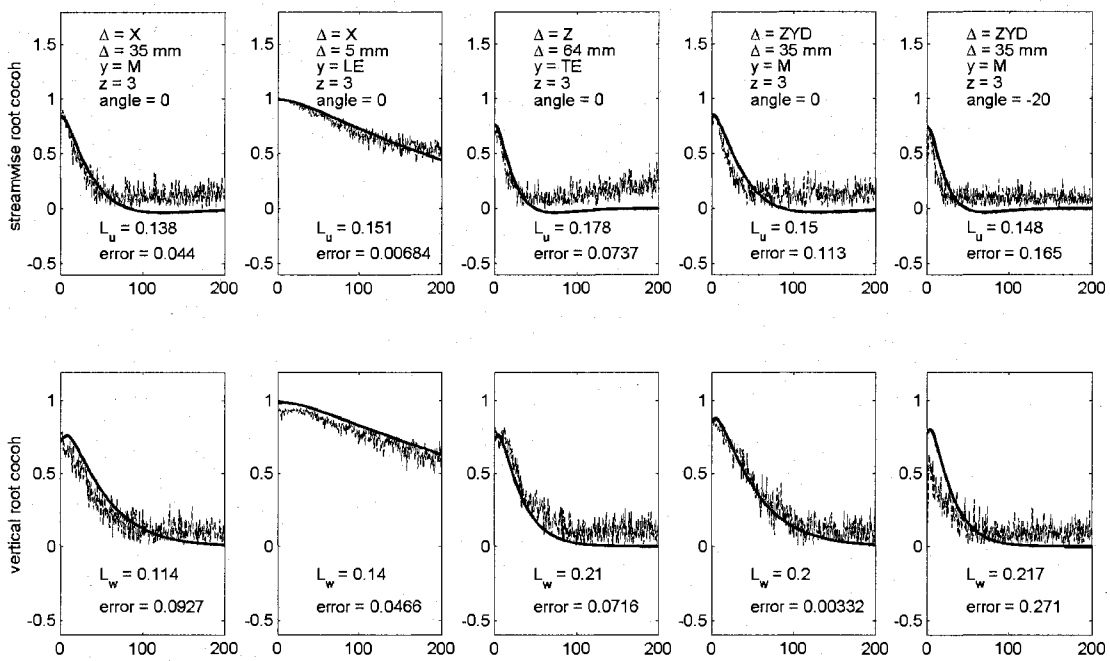

Figure A.10: Fitting parameters for all spacing directions at 35 mm over 0° ship deck (model A).

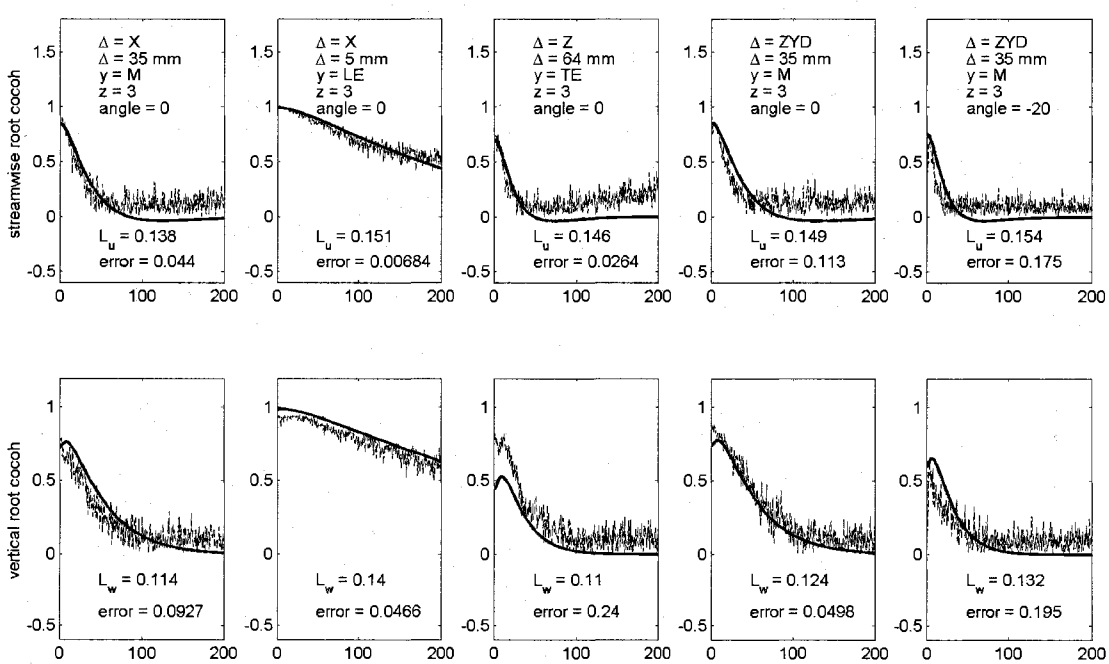

Figure A.11: Fitting parameters for X spacing direction at 35 mm over 0° ship deck (model B).

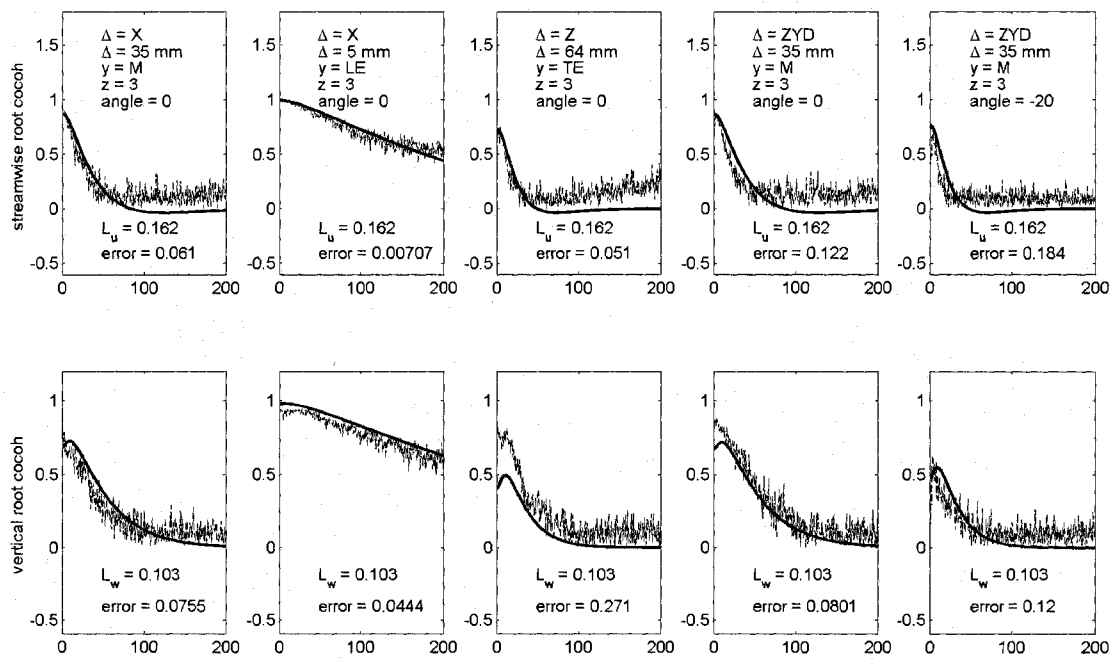

Figure A.12: Fitting parameters for constant fitting parameters ($L_u = 0.162$; $L_w = 0.103$) (model C).

Appendix B

SHREDS Operator's Manual

SHREDS (Shipboard Helicopter Rotor Engage/Disengage Simulation) was developed for the study of the blade sailing phenomenon. This manual provides the details of the structure, files, operating parameters, and variables that are required for the use of the blade sailing simulation program, SHREDS. It is intended to be used in conjunction with the thesis, which describes in detail the theory on which SHREDS is based.

SHREDS operates according to the flowchart shown in Figure B.1, which shows the simulation on the left and an expanded block diagram of "Matrix Calculation" on the right.

B.1 File Structure

The executable simulation file SHREDS.exe is compiled from seven separate files.

SHREDS.for: contains the bulk of the code for SHREDS, which is structured as shown in Figure B.1.

input_aerodynamics.for: contains the subroutines for calculating the instantaneous wind vectors and aerodynamic forces (A).

input_bessel.for: calculates modified Bessel functions of the second kind used by the von Kármán turbulence model. This file is only used by the Advancing Fourier Series method in (A).

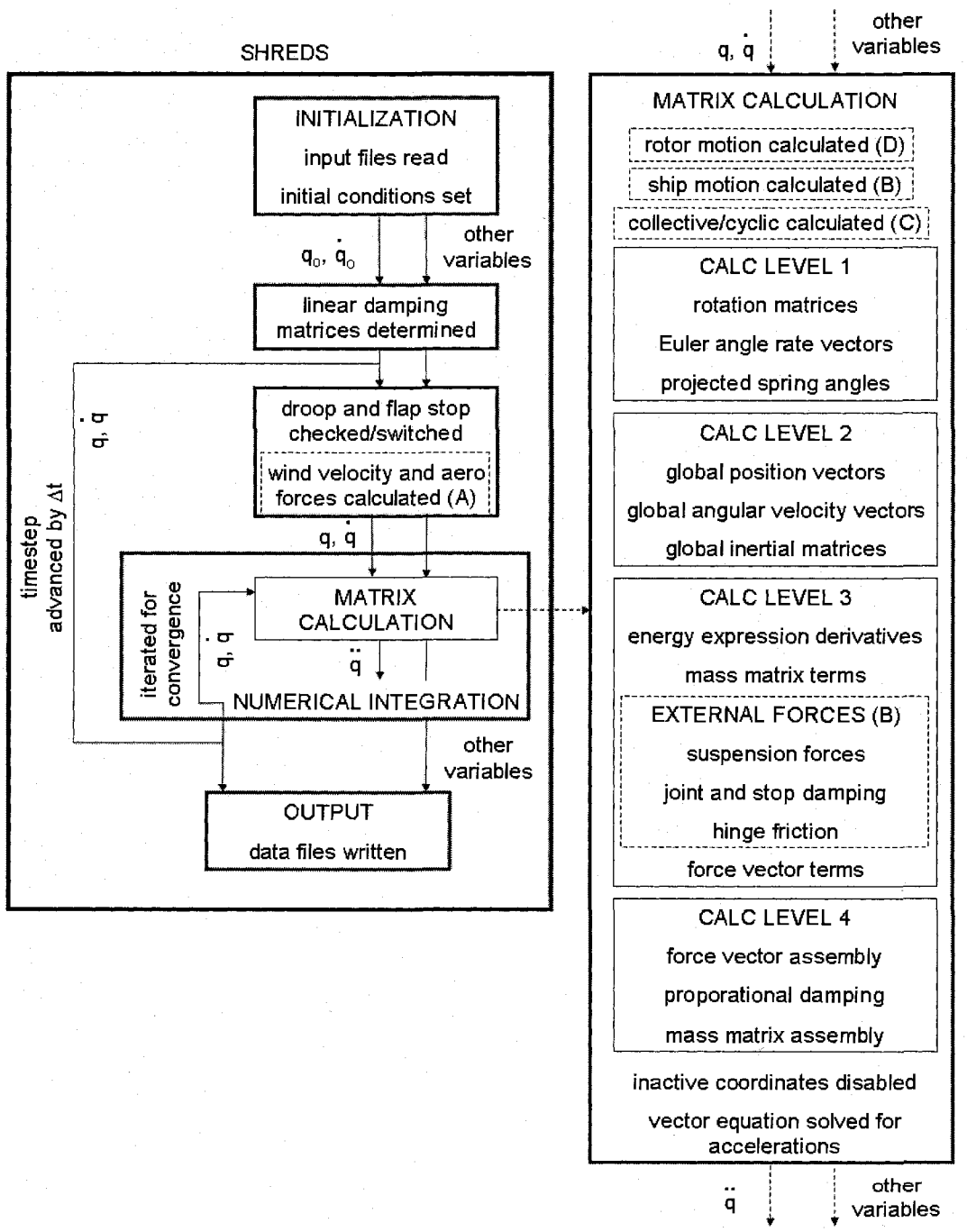

Figure B.1: Operational schematic of SHREDS.

input_forces.for: calculates the force contributions from ship motion, suspension, hinge friction, and damping (B).

input_pitch.for: contains the functionally-defined blade root pitch angle (C).

input_rotor.for: contains the functionally-defined rotor rotation profile (D).

input_vrbs.txt: contains variable and common block definitions.

The executable simulation requires a number of data input files and generates a variety of output files, as described below.

B.1.1 Input Files

A maximum of nine input files are required to operate SHREDS. The files are listed and described here, and the contents of the files are also tabulated. These tables are intended to connect the variable symbols given in the body of the thesis to the variable names given in the input files and in the code itself.

Without exception, the units of this program conform to the kg-m-s metric system. In the spreadsheet for input file generation, as described in Section B.3, the units of each variable are given.

in_SHREDS1.inp: defines the size of the model to be simulated, including the number of blades and segments, the number of suspension points and the output option selected by the analyst. The variables, in order, are given in Table B.1.

in_SHREDS2.inp: defines the main system properties, including the geometrical and dynamic properties of the system. The variables, in order, are given in Table B.2.

in_flightdeck.rsp: defines representative ship motion in six degrees of freedom, giving frequency components with their respective amplitudes and phase angles.

in_int.inp: defines the properties of the numerical integrator. The variables in order are given in Table B.3.

Table B.1: Variables in file "in_SHREDS1.inp".

variable symbol	variable name	variable size	description
n_s	n_s	(1)	number of segments per blade
n_b	n_b	(1)	number of blades
	n_w	(1)	number of suspension elements
	n_d	(1)	number of active degrees of freedom
	OUTPUTindex	(1)	Section B.2

in_rotor.inp: defines the run-up profile properties of the rotor disc. The variables in order are given in Table B.4.

in_aero.inp: defines the aerodynamic properties of the airfoil and aerodynamic force model. The variables are given in order in Table B.5. These properties feed into the model described in Appendix A.1.

in_steady.inp: defines the steady airwake properties, as shown in Figures 4.3 to 4.9, of the airwake flowfield in a grid for interpolation.

in_turb_PC.inp: defines the properties of the perfectly-correlated turbulence model described in Appendix A.2.1.

in_turb_STC.inp: defines the properties of the spatially- and temporally-correlated turbulence model in a grid for interpolation. These properties feed into the model described in Appendix A.2.2.

SHREDS is limited to a certain maximum number of rigid-body elements, since the code was written to allow finite memory space for many of the internal variables. These maximums can be changed in the code, however care must be taken to replace all the variable dimension identifiers in the variables lists. The limits are currently set to

- maximum number of blades (nbmax) = 10;

Table B.2: Variables in file "in_SHREDS2.inp".

variable symbol	variable name	variable size	description
		GENERAL	
g	g	(1)	acceleration due to gravity
ρ	rho	(1)	air density
π	pi	(1)	numerical value of π
		INITIAL MODEL SETUP	
Eqn 3.13	q	(2 ndof)	initial conditions {position, velocity}
	qallow	(ndof)	indicates active (1) and inactive (0) degrees of freedom
	shipallow	(6)	indicates active (1) and inactive (0) ship degrees of freedom
	qlinear_nom	(2 ndof)	operating point for linear matrix calculation {position, velocity}
	qallowdamp	(ndof)	indicates damped (1) and undamped (0) degrees of freedom
		INDICES	
	INTindex	(1)	
	ROTORindex	(1)	
	SHIPMOindex	(1)	
	AEROindex	(1)	
	SWITCHindex	(1)	
	STOPindex	(1)	execution options (Section B.2)
	EIGindex	(1)	
	HINGEindex	(1)	
	DAMPindex	(1)	
	PITCHindex	(1)	
	UNSTEADYindex	(1)	

		STOP PROPERTIES	
ω_{ds}	droopsp	(1)	stop retraction speed (Eqn 3.48)
ω_{fs}	flapsp	(1)	stop retraction speed (Eqn 3.48)
	t_stopswitch	(2)	time for stops to retract/extend
		FORCE PROPERTIES	
	t_shift_sh	(1)	starting time of ship motion time history
	t_ramp	(1)	time of gradual external force application
	tip_force	(1)	validation tool - not used
		SHIP PROPERTIES	
U_{free}	windspeed	(1)	freestream wind speed
	deck	(1)	flight deck width
	deckang	(1)	static deck roll angle (SHIPMOindex = 3)
		DAMPING PROPERTIES	
	perturb	(1)	perturbation for stiffness matrix
	t_lin	(1)	operational time for linear matrices
a	propdamp1	(1)	fraction of mass matrix in damping (Eqn 3.57)
b	propdamp2	(1)	fraction of stiffness matrix in damping (Eqn 3.57)
		HELICOPTER PROPERTIES	
m	m	(1)	helicopter body mass
$[\mathbf{J}_{H_H}]$	Jl	(3,3)	helicopter inertia (Eqn 3.23)
$\{\mathbf{r}_{R_H}\}$	r_r	(3)	position of rotor disc centre
ε_1	epsilon1	(1)	rotor shaft tilt (Eqn 3.9)
ε_2	epsilon2	(1)	rotor shaft tilt (Eqn 3.9)
		BLADE PROPERTIES	
$m_{b(i,n)}$	mb	(n_s,n_b)	blade segment mass
$\left[\mathbf{J}_{b_{(i,n)}B_{(i,n)}}\right]$	Jbl	$(3,3,n_s,n_b)$	segment inertia (Eqn 3.24)
$o_{x(i,n)}$	ox	(n_s,n_b)	structural offset angle (Eqn 3.11)
$o_{y(i,n)}$	oy	(n_s,n_b)	structural offset angle (Eqn 3.11)
$o_{z(i,n)}$	oz	(n_s,n_b)	structural offset angle (Eqn 3.11)

$\left\{\mathbf{r}_{B_{(i,n)}B_{(i-1,n)}}\right\}$	ro	(3,n_s,n_b)	position of blade segment origin
$\left\{\mathbf{r}_{b_{(i,n)}B_{(i-1,n)}}\right\}$	rb	(3,n_s,n_b)	position of segment mass centre
$\left\{\mathbf{r}_{c_{(i,n)}B_{(i-1,n)}}\right\}$	rc	(3,n_s,n_b)	position of segment geometric centre
	chord	(n_s,n_b)	segment chord length
	AEROONindex	(n_s,n_b)	toggles aerodynamic forces (Section B.2)
$\left[k_{(i,n)}(1,1)\right]$	k_txb	(n_s,n_b)	
$\left[k_{(i,n)}(2,2)\right]$	k_tyb	(n_s,n_b)	diagonal stiffness matrix terms (Eqn 3.43)
$\left[k_{(i,n)}(3,3)\right]$	k_tzb	(n_s,n_b)	
$\left[c_{(i,n)}(1,1)\right]$	c_txb	(n_s,n_b)	
$\left[c_{(i,n)}(2,2)\right]$	c_tyb	(n_s,n_b)	diagonal damping matrix terms (Eqn 3.56)
$\left[c_{(i,n)}(3,3)\right]$	c_tzb	(n_s,n_b)	
$\sigma_{o(i,n)}$	or_sigma	(n_b)	starting azimuth angle of each blade
$\left\{\mathbf{r}_{t_{(i,n)}B_{(i-1,n)}}\right\}$	r_t	(3,n_s,n_b)	position of tip (last segment)
$\theta_{2p_{\text{leadlag}}}$	jy2p	(1,n_b)	
$\theta_{1p_{\text{leadlag}}}$	jy1p	(1,n_b)	
$\theta_{1m_{\text{leadlag}}}$	jy1m	(1,n_b)	
$\theta_{2m_{\text{leadlag}}}$	jy2m	(1,n_b)	
$\theta_{2p_{\text{flap}}}$	jz2p	(1,n_b)	
$\theta_{1p_{\text{flap}}}$	jz1p	(1,n_b)	
$\theta_{1m_{\text{flap}}}$	jz1m	(1,n_b)	
$\theta_{2m_{\text{flap}}}$	jz2m	(1,n_b)	defined stop stiffness profile (Eqn 3.48)
$M_{p_{\text{leadlag}}}$	Fy2p	(1,n_b)	
$M_{m_{\text{leadlag}}}$	Fy2m	(1,n_b)	
$M_{p_{\text{flap}}}$	Fz2p	(1,n_b)	
$M_{m_{\text{flap}}}$	Fz2m	(1,n_b)	
$k_{fs_{\text{leadlag}}}$	kyfs	(1,n_b)	
$k_{ds_{\text{leadlag}}}$	kyds	(1,n_b)	
$k_{fs_{\text{flap}}}$	kzfs	(1,n_b)	
$k_{ds_{\text{flap}}}$	kzds	(1,n_b)	

$c_{fs_{\text{leadlag}}}$	cyfs	(1,n_b)	defines stop damping (Eqn 3.55)
$c_{ds_{\text{leadlag}}}$	cyds	(1,n_b)	
$c_{fs_{\text{flap}}}$	czfs	(1,n_b)	
$c_{ds_{\text{flap}}}$	czds	(1,n_b)	
$\mu_{s_{\text{flap}}}$	mus_f_hf	(n_b)	defines hinge friction (Eqn 3.53)
$\mu_{s_{\text{leadlag}}}$	mus_ll_hf	(n_b)	
$\mu_{k_{\text{flap}}}$	muk_f_hf	(n_b)	
$\mu_{k_{\text{leadlag}}}$	muk_ll_hf	(n_b)	
$\varepsilon_{\text{hinge}}$	smalle_hf	(n_b)	
$r_{\text{hinge}_{\text{flap}}}$	pin_f_hf	(n_b)	defines hinge friction (Eqn 3.52)
$r_{\text{hinge}_{\text{leadlag}}}$	pin_ll_hf	(n_b)	
$[k_{(i,n)}(1,2)]$	k_txy	(1,n_b)	coupled stiffness terms (Eqn 3.43)
$[k_{(i,n)}(1,3)]$	k_txz	(1,n_b)	
$[k_{(i,n)}(2,3)]$	k_tyz	(1,n_b)	
$[c_{(i,n)}(1,2)]$	c_txy	(1,n_b)	coupled damping terms
$[c_{(i,n)}(1,3)]$	c_txz	(1,n_b)	
$[c_{(i,n)}(2,3)]$	c_tyz	(1,n_b)	
		SUSPENSION PROPERTIES	
$\{\mathbf{r}_{w_S}\}$	xab_sp	(3,n_w,1)	suspension location in ship frame
$\{\mathbf{r}_{w_H}\}$	xbc_sp	(3,n_w,1)	suspension location in helicopter frame
a_{kx}	a_kx_sp	(3,n_w)	defines suspension and tire stiffness (Eqn 3.50)
b_{kx}	b_kx_sp	(3,n_w)	
a_{ky}	a_ky_sp	(3,n_w)	
b_{ky}	b_ky_sp	(3,n_w)	
a_{kz}	a_kz_sp	(3,n_w)	
b_{kz}	b_kz_sp	(3,n_w)	
a_{cx}	a_cx_sp	(3,n_w)	defined suspension and tire damping (Eqn 3.51)
b_{cx}	b_cx_sp	(3,n_w)	
a_{cy}	a_cy_sp	(3,n_w)	
b_{cy}	b_cy_sp	(3,n_w)	
a_{cz}	a_cz_sp	(3,n_w)	
b_{cz}	b_cz_sp	(3,n_w)	

Table B.3: Variables in file "in_int.inp".

variable symbol	variable name	variable size	description
Δt	dt	(1)	output time step (INT 1,2,3)
	nstep	(1)	number of output time steps (INT 1,2,3)
	tolr	(1)	relative allowable solution tolerance (INTindex = 1,2,3)
	tola	(1)	absolute allowable solution tolerance (INTindex = 1)
	hmin	(1)	minimum internal time step (INTindex = 1)
	hmax	(1)	maximum internal time step (INTindex = 1)
	hstart	(1)	starting internal time step (INTindex = 1)
	nistp	(1)	number of internal timesteps (INTindex = 2)
	mxit	(1)	max iterations per timestep (INTindex = 2)
	param	(20)	properties required by IMSL integrator (INTindex = 3)

Table B.4: Variables in file "in_rotor.inp".

variable symbol	variable name	variable size	description
Ω	rotorsp_r	(1)	maximum rotor speed
t_{r1}	rotortrans_r	(1)	rotor profile time 1
t_{r2}	rotortrans2_r	(1)	rotor profile time 2
t_{r3}	rotortrans_3	(1)	rotor profile time 3
t_{hold}	holdtime_r	(1)	time before profile starts (ROTORindex = 1)

Table B.5: Variables in file "in_aero.inp".

variable symbol	variable name	variable size	description
α_a	alphaa	(1)	quasi-steady stall angle
α_b	alphab	(1)	quasi-steady stall angle (reverse flow)
$C_{l_{\alpha_1}}$	Cl_a1	(1)	lift curve slope, Eqn A.15
$C_{l_{\alpha_2}}$	Cl_a2	(1)	lift curve slope (reverse flow), Eqn A.15
$C_{l_{\alpha_1}}\alpha_a$	Cl_1	(1)	quasi-steady maximum lift coefficient
$C_{l_{\alpha_2}}\alpha_b$	Cl_2	(1)	quasi-steady maximum lift coefficient (reverse flow)
T_p	Tp	(1)	Eqn A.25, [53]
S_1	S1	(1)	Eqn A.32, [53]
S_2	S2	(1)	Eqn A.32, [53]
$\Delta\alpha_1$	dalpha1	(1)	Eqn A.28, [53]
T_f	Tf	(1)	Eqn A.33, [53]
K_0	K0	(1)	Eqn A.37, [53]
K_1	K1	(1)	Eqn A.37, [53]
K_2	K2	(1)	Eqn A.37, [53]
m_1	m_1	(1)	Eqn A.37, [53]
T_v	Tv	(1)	Eqn A.44, [53]
η	eta	(1)	Eqn A.55
A_1	A1	(1)	Eqn A.10, [49]
A_2	A2	(1)	Eqn A.11, [49]
b_1	b1	(1)	Eqn A.10, [49]
b_2	b2	(1)	Eqn A.11, [49]
	teincl	(1)	(1) to include and (0) not to include te influence
	Vmin	(1)	aerodynamic forces are zero below this velocity

- maximum number of blade segments (nsmax) = 20;
- maximum number of suspension elements (nwmax) = 10; and
- maximum number of degrees of freedom (ndmax) = 100.

If these limits are exceeded, the program will not run in its current configuration. They can be changed by modifying the source code.

B.1.2 Output Files

There are four possible output settings, as described in Section B.2. The output option is selected by the analyst using the variable "OUTPUTindex" in the input file "in_SHREDS1.inp". The specific contents of the output files are given here. Each output file contains the simulation time in the first column; the data in the remaining columns is listed.

out_tip.txt: is generated with OUTPUTindex = 0,1,2 and contains

- global displacement of blade tips

given by

$$t\ r_{t_{(1,1)_G}}(1)\ r_{t_{(1,2)_G}}(1)\ \ldots\ r_{t_{(1,n_b)_G}}(1)\ r_{t_{(1,1)_G}}(2)\ \ldots$$
$$r_{t_{(1,n_b)_G}}(2)\ r_{t_{(1,1)_G}}(3)\ \ldots\ r_{t_{(1,n_b)_G}}(3)$$

out_disp.txt: is generated with OUTPUTindex = 0,1,2 and contains

- helicopter body position in global coordinates;
- helicopter body orientation in global coordinates; and
- Euler angles of each segment in the previous coordinate system

given by

$$t\ X_H\ Y_H\ Z_H\ \theta_{H_{roll}}\ \theta_{H_{pitch}}\ \theta_{H_{yaw}}\ \phi_{B(2,1)}\ \phi_{B(3,1)}\ \cdots\ \phi_{B(i,1)}\ \phi_{B(2,2)}\ \cdots$$

$$\phi_{B(i,n_b)}\ \tau_{B(1,1)}\ \tau_{B(2,1)}\ \cdots\ \tau_{B(i,n_b)}\ \psi_{B(1,1)}\ \cdots\ \psi_{B(i,n_b)}$$

out_shipmo.txt: is generated with OUTPUTindex = 0,1,2 and contains

- surge, sway, heave, roll (Euler angle), pitch (Euler angle), yaw (Euler angle); and
- the velocities associated with each in the same order

given by

$$t\ X_S\ Y_S\ Z_S\ \theta_{S_{roll}}\ \theta_{S_{pitch}}\ \theta_{S_{yaw}}\ \dot{X}_S\ \dot{Y}_S\ \dot{Z}_S\ \dot{\theta}_{S_{roll}}\ \dot{\theta}_{S_{pitch}}\ \dot{\theta}_{S_{yaw}}$$

out_sigmas.txt: is generated with OUTPUTindex = 1,2 and contains

- rotor hub azimuth angle (relative to zero), rotor speed, rotor acceleration;
- azimuth angle of each blade in sequence;
- the state of the flap and droop stops (extended or retracted); and
- the time when a stop switch was initiated

given by

$$t\ \sigma\ \dot{\sigma}\ \ddot{\sigma}\ \sigma_{(i,n)}\ \text{stopstate t\_startswitch}$$

out_pitch.txt: is generated with OUTPUTindex = 1,2 and contains

- the root pitch angles of each blade in sequence; and
- the velocities associated with each in the same order

given by

$$t\ \phi_{B(1,1)}\ \phi_{B(1,2)}\ \cdots\ \phi_{B(1,n_b)}\ \dot{\phi}_{B(1,1)}\ \dot{\phi}_{B(1,2)}\ \cdots\ \dot{\phi}_{B(1,n_b)}$$

out_tireforce.txt: is generated with OUTPUTindex = 1,2 and contains

- global forces on the first three suspension elements

given by

$$t\ f_{\text{suspension}k_{1_G}}(1)\ f_{\text{suspension}k_{2_G}}(1)\ f_{\text{suspension}k_{3_G}}(1)$$
$$f_{\text{suspension}k_{1_G}}(2)\ f_{\text{suspension}k_{2_G}}(2)\ f_{\text{suspension}k_{3_G}}(2)$$
$$f_{\text{suspension}k_{1_G}}(3)\ f_{\text{suspension}k_{2_G}}(3)\ f_{\text{suspension}k_{3_G}}(3)$$

out_hinge.txt: is generated with OUTPUTindex = 1,2 and contains

- global forces due to friction at the hinges in sequence

given by

$$t\ f_{\text{hinge}_{1_G}}(1)\ f_{\text{hinge}_{2_G}}(1)\ldots\ f_{\text{hinge}_{n_{b_G}}}(1)\ f_{\text{hinge}_{1_G}}(2)\ f_{\text{hinge}_{2_G}}(2)\ldots$$
$$f_{\text{hinge}_{n_{b_G}}}(2)\ \ldots\ f_{\text{hinge}_{1_G}}(3)\ f_{\text{hinge}_{2_G}}(3)\ f_{\text{hinge}_{n_{b_G}}}(3)$$

out_wind.txt: is generated with OUTPUTindex = 1,2 and contains

- global aerodynamic forces for the blade segments of blade 1 in sequence;
- segment-local aerodynamic moments for the blade segments of blade 1 in sequence;
- positions of aerodynamic force application for the blade segments of blade 1 in sequence in ship coordinates;

- resultant wind velocity for the blade segments in blade coordinates of blade 1 in sequence; and
- angle of attack for the blade segments of blade 1 in sequence

given by

$$t\ f_{a_{(1,1)_G}}(1)\ \ldots\ f_{a_{(n_s,1)_G}}(1)\ f_{a_{(1,1)_G}}(2)\ \ldots\ f_{a_{(n_s,1)_G}}(2)\ f_{a_{(1,1)_G}}(3)\ \ldots\ f_{a_{(n_s,1)_G}}(3)$$

$$M_{a_{(1,1)_{B(1,1)}}}(1)\ \ldots\ M_{a_{(n_s,1)_{B(n_s,1)}}}(1)\ M_{a_{(1,1)_{B(1,1)}}}(2)\ \ldots\ M_{a_{(n_s,1)_{B(n_s,1)}}}(2)$$

$$M_{a_{(1,1)_{B(1,1)}}}(3)\ \ldots\ M_{a_{(n_s,1)_{B(n_s,1)}}}(3)\ r_{a_{(1,1)_S}}(1)\ \ldots\ r_{a_{(n_s,1)_S}}(1)$$

$$r_{a_{(1,1)_S}}(2)\ \ldots\ r_{a_{(n_s,1)_S}}(2)\ r_{a_{(1,1)_S}}(3)\ \ldots\ r_{a_{(n_s,1)_S}}(3)\ V_{a_{(1,1)_{B(1,1)}}}(1)\ \ldots\ V_{a_{(n_s,1)_{B(n_s,1)}}}(1)$$

$$V_{a_{(1,1)_{B(1,1)}}}(2)\ \ldots\ V_{a_{(n_s,1)_{B(n_s,1)}}}(2)\ V_{a_{(1,1)_{B(1,1)}}}(3)\ \ldots\ V_{a_{(n_s,1)_{B(n_s,1)}}}(3)\ \alpha(1,1)\ \ldots\ \alpha(n_s,1)$$

out_vel.txt is generated with OUTPUTindex = 2 and contains

- time derivative of the contents of out_disp.txt

given by

$$t\ \dot{X}_H\ \dot{Y}_H\ Z_H\ \dot{\theta}_{H_{roll}}\ \dot{\theta}_{H_{pitch}}\ \dot{\theta}_{H_{yaw}}\ \dot{\phi}_{B(2,1)}\ \dot{\phi}_{B(3,1)}\ \cdots\ \dot{\phi}_{B(n_s,1)}\ \dot{\phi}_{B(2,2)}\ \cdots$$

$$\dot{\phi}_{B(n_s,n_b)}\ \dot{\tau}_{B(1,1)}\ \dot{\tau}_{B(2,1)}\ \cdots\ \dot{\tau}_{B(n_s,n_b)}\ \dot{\psi}_{B(1,1)}\ \cdots\ \dot{\psi}_{B(n_s,n_b)}$$

out_accel.txt: is generated with OUTPUTindex = 2 and contains

- time derivative of the contents of out_vel.txt

given by

$$t\ \ddot{X}_H\ \ddot{Y}_H\ \ddot{Z}_H\ \ddot{\theta}_{H_{roll}}\ \ddot{\theta}_{H_{pitch}}\ \ddot{\theta}_{H_{yaw}}\ \ddot{\phi}_{B(2,1)}\ \ddot{\phi}_{B(3,1)}\ \cdots\ \ddot{\phi}_{B(n_s,1)}\ \ddot{\phi}_{B(2,2)}\ \cdots$$

$$\ddot{\phi}_{B(n_s,n_b)}\ \ddot{\tau}_{B(1,1)}\ \ddot{\tau}_{B(2,1)}\ \cdots\ \ddot{\tau}_{B(n_s,n_b)}\ \ddot{\psi}_{B(1,1)}\ \cdots\ \ddot{\psi}_{B(n_s,n_b)}$$

out_flying.txt: is generated with OUTPUTindex = 2 and contains

- flying index for the blade segments of blade 1 in sequence;
- vortex shed time for the blade segments of blade 1 in sequence;
- time of stall for the blade segments of blade 1 in sequence; and
- angle of attack for the blade segments of blade 1 in sequence

given by

$$t \text{ flying}(1,1) \ \ldots \ \text{flying}(n_s,1) \ \tau_v(1,1) \ \ldots \ \tau_v(n_s,1)$$

$$t_{\text{stall}}(1,1) \ \ldots \ t_{\text{stall}}(n_s,1) \ \alpha(1,1) \ \ldots \ \alpha(n_s,1)$$

out_wind2.txt: is generated with OUTPUTindex = 2 and contains

- total normal coefficient for the blade segments of blade 1 in sequence;
- total chordwise coefficient for the blade segments of blade 1 in sequence;
- total moment coefficient for the blade segments of blade 1 in sequence; and
- angle of attack for the blade segments of blade 1 in sequence

given by

$$t \ C_{n_t}(1,1) \ \ldots \ C_{n_t}(n_s,1) \ C_{c_t}(1,1) \ \ldots \ C_{c_t}(n_s,1)$$

$$C_{m_t}(1,1) \ \ldots \ C_{m_t}(n_s,1) \ \alpha(1,1) \ \ldots \ \alpha(n_s,1)$$

out_globpostions.txt: is generated with OUTPUTindex = 3 and contains

- global positions of each rigid body in sequence

given by

$$t \ XH \ r_{b_{(1,1)_G}}(1) \ r_{b_{(1,2)_G}}(1) \ \ldots \ r_{b_{(n_s,n_b)_G}}(1) \ YH \ r_{b_{(1,1)_G}}(2) \ \ldots$$

$$r_{b_{(n_s,n_b)_G}}(2)\ ZH\ r_{b_{(1,1)_G}}(3)\ \ldots r_{b_{(n_s,n_b)_G}}(3)$$

out_globorients.txt: is generated with OUTPUTindex = 3 and contains

- global Euler angles of each rigid body in sequence

given by

$$t\ \theta_{H_{roll}}\ \phi_{B(2,1)}\ \phi_{B(3,1)}\ \cdots\ \phi_{B(i,1)}\ \phi_{B(2,2)}\ \cdots$$

$$\phi_{B(n_s,n_b)}\ \theta_{H_{pitch}}\ \tau_{B(1,1)}\ \tau_{B(2,1)}\ \cdots\ \tau_{B(n_s,n_b)}\ \theta_{H_{yaw}}\ \psi_{B(1,1)}\ \cdots\ \psi_{B(n_s,n_b)}$$

out_inputverify.txt: is always generated and contains all input parameters to ensure the inputs have been read in correctly.

out_linear.txt: is always generated and contains the linearized matrices calculated about the operating point.

B.2 Execution Options

There are several different operational modes, which can be controlled using 13 indices. These indices and their respective options are given here.

INTindex: selects the integrator to be used in the propagation of the solution. The options are

1: a Runge-Kutta-Fehlberg fourth/fifth order explicit integrator [86];

2: a simple Newton-Euler implicit integrator [104];

3: the IMSL routine DIVPAG [103]; or

other: error message generated: "selected integration method not supported".

ROTORindex: controls the type of rotor run-up/run-down profile. The options are

0: no rotor rotation;

1: engage using a sine profile and disengage by a linear profile given by

$$\dot{\sigma}(t) = \begin{cases} \Omega\left[-0.5\cos\frac{\pi}{t_{r1}}t + 0.5\right] & t_{\text{hold}} \leq t \leq t_{r1} + t_{\text{hold}} \\ \Omega & t_{r1} + t_{\text{hold}} \leq t \leq t_{r2} + t_{\text{hold}} \\ \Omega\left[\frac{-1}{t_{r3}-t_{r2}}t + \frac{t_{r3}}{t_{r3}-t_{r2}}\right] & t_{r2} + t_{\text{hold}} \leq t \leq t_{r3} + t_{\text{hold}} \\ 0 & t \leq t_{\text{hold}} \text{ or } t > t_{r3} + t_{\text{hold}} \end{cases} \tag{B.1}$$

2: engage by the profile for validation case described in Equation 3.65;

3: turn at constant rotational speed given by

$$\dot{\sigma}(t) = \Omega \tag{B.2}$$

4: engage only using a sine profile given by

$$\dot{\sigma}(t) = \begin{cases} \Omega\left[-0.5\cos\frac{\pi}{t_{r1}}t + 0.5\right] & 0 \leq t \leq t_{r1} \\ \Omega & t > t_{r1} \end{cases} \tag{B.3}$$

or

other: error message generated: "selected rotor run-up profile not supported".

SHIPMOindex: controls the type of ship motion to be included. The options are

0: no ship motion included;

1: representative ship motion with active suspension for ship degrees of freedom indicated with the variable "shipallow";

2: representative ship motion with frozen suspension for ship degrees of freedom indicated with the variable "shipallow";

3: static roll angle for aerodynamics only as defined by the variable "deckang"; or

other: default to 0.

AEROindex: selects the type of wind environment for aerodynamic force calculation. The options are

0: no aerodynamics calculated;

1: uniform flow only;

2: representative mean flow only;

3: perfectly-correlated turbulence with representative mean flow;

4: perfectly-correlated turbulence with Taylor's hypothesis and representative mean flow;

6: spatially- and temporally-correlated turbulence through the Advancing Fourier Series method with representative mean flow; or

other: error message generated: "selected airwake type not supported".

The details of turbulence modelling for AEROindex = 3, 4, and 6 can be found in Appendix A.2.

SWITCHindex: toggles flap and droop stop extension and retraction on and off. The options are

0: stops do not extend or retract;

1: stops can extend and retract; or

other: default to 0.

STOPindex: toggles the inclusion of flap/droop and lead/lag stops on and off. The options are

0: no stops included;

1: allows the application of stops; or

other: default to 0.

If option 1 is selected, then reasonable contact angle values need to be set for both stop sets, even if the applicable stiffnesses are zero, or the degrees of freedom are inactive.

HINGEindex: toggles the inclusion of hinge friction on and off. The options are

0: hinge friction not included;

1: hinge friction included; or

other: default to 0.

EIGindex: controls how the linear matrices for proportional damping are calculated. The options are

0: linear matrices not calculated (no proportional damping);

1: linear matrices are calculated with all force terms included;

2: linear matrices are calculated with linear force terms only included ($\epsilon_{n_{\text{dof}}}$ terms in Equation 3.16); or

other: default to 0.

DAMPindex: toggles the inclusion of proportional damping on and off. The options are

0: proportional damping off;

1: proportional damping on; or

other: default to 0.

PITCHindex: toggles the functional definition of collective and cyclic pitch on and off. The options are

0: cyclic and collective always 0;

1: cyclic and collective defined functionally; or

other: error message generated: "selected collective/cyclic profile not supported".

UNSTEADYindex: controls the method used to calculate aerodynamic forces. The options are

1: uses quasi-steady theory to calculate aerodynamic forces;

2: uses the AMT method to calculate unsteady forces; or

other: error message generated: "unsteady index is out of range".

OUTPUTindex: controls which output files are generated as part of the program. The options are

0: only the tip displacement, degrees of freedom, and ship motion output files are generated;

1: rotor rotation, tire force, wind and aerodynamic force, and hinge force output files are generated in addition to those above.

2: generalized velocity and accelerations, and more aerodynamic information are output;

3: only the global positions and orientation of each rigid body are given (for visualization); or

other: error message generated: "output index is out of range".

AEROONindex: controls whether aerodynamic forces are applied to each blade segment or not. It is defined for each blade segment. The options are

0: aerodynamic forces not calculated for this segment;

1: aerodynamic forces are calculated for this segment; or

other: default to 0.

B.3 Tools

In order to assist the analyst, a set of tools are included with the SHREDS software.

- An Excel spreadsheet, called "InputGenerator.xls", which can be used in combination with MATLAB to generate some of the input files, is provided. This spreadsheet also contains a description of each input property and the corresponding units.

- In the event that the analyst wishes to modify or generate the input files manually, template copies of each input file are included. They are named "*_template.inp" where the star is the input file name. These show the correct format for each input file.

- In order to select appropriate properties for the droop/flap and lead/lag stops, as shown in Figure 3.4, a MATLAB function, which plots the force and energy curves as a function of joint angle, is provided. It is called "springtest.m". This function allows the user to ensure smooth stiffness transition as the stops are impacted.

B.4 System Upgrading and Interfacing

SHREDS is designed so that changes to the external force calculations can be made without modifications to the main simulation engine. To change the calculation of aerodynamic forces, the file "input_aerodynamics.for" must be modified. To change or add other external forces, the file "input_forces.for" must be modified. The global variables defined in "input_vrbs.txt" are now presented such that the force files can be successfully modified. Where the variables correspond to a symbol given in the body of the thesis, this symbol is also given.

The system generalized coordinates are given in Table B.6. The addition of the letter "d" after the variable name indicates a derivative with respect to time. The most important transformation matrices and kinematic vectors are given in Table B.7. The addition of "d" refers again to a time derivative. Additional matrices, derivatives of the ones listed, are also used. A derivative with respect to generalized coordinate A is given by the notation "_A". Table B.8 gives additional variables that are available through the file "input_vrbs.txt".

Table B.6: Generalized coordinates.

variable symbol	variable name	variable size	description
XH	XH	(1)	
YH	YH	(1)	Eqn 3.7
ZH	ZH	(1)	
$\theta_{H_{roll}}$	tXH	(1)	
$\theta_{H_{pitch}}$	tYH	(1)	Eqn 3.8
$\theta_{H_{yaw}}$	tZH	(1)	
ϕ	phi	(n_s,n_b)	
τ	tau	(n_s,n_b)	Eqn 3.10
ψ	psi	(n_s,n_b)	

Table B.7: Kinematic matrices and vectors.

variable symbol	variable name	variable size	description
$[\mathbf{R}_{HG}]$	Rhg	(3,3)	
$[\mathbf{R}_{SG}]$	Rsg	(3,3)	Eqn 3.1
$[\mathbf{R}_{RH}(n)]$	Rrh	$(3,3,1,n_b)$	
$[\mathbf{R}_{B_{(i,n)}B_{(i-1,n)}}]$	R	$(3,3,n_s,n_b)$	
$[\mathbf{R}_{\omega H}]$	Rwh	(3,3)	
$[\mathbf{R}_{\omega R}(n)]$	Rwr	$(3,3,1,n_b)$	Eqn 3.3
$[\mathbf{R}_{\omega B_{(i,n)}}]$	Rw	$(3,3,n_s,n_b)$	
$\{\mathbf{r}_{H_G}\}$	P	(3)	Eqn 3.7
$\{\omega_{H_G}\}$	w	(3)	Eqn 3.29
$[\mathbf{J}_{H_G}]$ from	J	(3,3)	Eqn 3.23
$\left\{\mathbf{r}_{b_{(i,n)_G}}\right\}$	Pb	$(3,n_s,n_b)$	Eqn 3.30
$\left\{\omega_{b_{(i,n)_G}}\right\}$	wb	$(3,n_s,n_b)$	Eqn 3.31
$\left[\mathbf{J}_{b_{(i,n)_G}}\right]$	Jb	$(3,3,n_s,n_b)$	Eqn 3.24

Table B.8: Globally available variables.

variable symbol	variable name	variable size	description
u_1	ONE	(3)	Eqn 3.4
u_2	TWO	(3)	Eqn 3.4
u_3	THE	(3)	Eqn 3.4
$\theta_{x(i,n)}$	jointx	(n_s,n_b)	Eqn 3.45
$\theta_{y(i,n)}$	jointy	(n_s,n_b)	Eqn 3.46
$\theta_{z(i,n)}$	jointz	(n_s,n_b)	Eqn 3.47
$\{\mathbf{f}_{\text{suspension}}\}$	tireforce	(3,n_w)	Eqn 3.50
$r_{t_{(n)_G}}(1)$	Pt_x	(n_b)	
$r_{t_{(n)_G}}(1)$	Pt_y	(n_b)	
$r_{t_{(n)_G}}(1)$	Pt_z	(n_b)	
$r_{b_{(i,n)_G}}(1)$	Pb_x	(ndof)	
$r_{b_{(i,n)_G}}(2)$	Pb_y	(ndof)	Section B.1.2
$r_{b_{(i,n)_G}}(3)$	Pb_z	(ndof)	
$\phi_{B(i,n)_G}$	gphi	(ndof)	
$\tau_{B(i,n)_G}$	gtau	(ndof)	
$\psi_{B(i,n)_G}$	gpsi	(ndof)	
σ_n	sigmas	(n_b)	azimuthal angle of each blade
σ	sigma	(1)	Eqn 3.9
$\dot{\sigma}$	sigmad	(1)	Eqn B.1
$\ddot{\sigma}$	sigmadd	(1)	rotor acceleration
$f_{\text{hinge}_{n_G}}(1)$	hinge_x_vec	(n_b)	
$f_{\text{hinge}_{n_G}}(2)$	hinge_y_vec	(n_b)	Eqn 3.54
$f_{\text{hinge}_{n_G}}(3)$	hinge_z_vec	(n_b)	
	motion_sh	(6,2)	Eqn 3.5
	t_startswitch	(2,n_b)	time stops started retracting/extending

$\{f_a\}$	aeroforce	$(3,n_s,n_b)$	
$\{r_a\}$	aerolocloc	$(3,n_s,n_b)$	
$\{V_a\}$	aerovel	$(3,n_s,n_b)$	out_wind.tex
$\{M_a\}$	aeromom	$(3,n_s,n_b)$	
	aeroforce1	$(3,n_s,n_b)$	
	XH_force	(n_s,n_b)	
	YH_force	(n_s,n_b)	
	ZH_force	(n_s,n_b)	
	tXH_force	(n_s,n_b)	
	tYH_force	(n_s,n_b)	Components of $\{\mathbf{f}\}$, Eqn 3.49
	tZH_force	(n_s,n_b)	
	phi_force	(n_s,n_b)	
	tau_force	(n_s,n_b)	
	psi_force	(n_s,n_b)	
	nsmax	(1)	
	nbmax	(1)	Section B.1.1
	nwmax	(1)	
	ndmax	(1)	
$[\mathbf{M}_{\text{linear}}]$	mass_lin	(n_d,n_d)	
$[\mathbf{K}_{\text{linear}}]$	stiff_lin	(n_d,n_d)	Eqn 3.57
$[\mathbf{C}_{\text{linear}}]$	damp_lin	(n_d,n_d)	
	rotordata	(5)	contains variables in Table B.4

Appendix C

The Airwake Experiment

This appendix is intended to provide the details of the airwake experiment, which was conducted to study the steady and unsteady characteristics of the flow field over a typical frigate in beam wind conditions. The context for this experiment, the conclusions drawn from the data, and the synthesis of the information into numerical models can be found in Chapter 4.

C.1 Background on Atmospheric Boundary Layer

The importance of correctly modelling the wind profile approaching the ship for dynamic interface work has been stressed by S. Zan [35] and J. Val Healey [105]. The atmospheric air flow above the Earth's surface is complex and depends on a wide variety of factors, which include but are not limited to: the surface roughness, moisture content, thermal stability, altitude, pressure gradients, and Coriolis force (apparent velocity due to Earth's rotation) [106]. The behaviour of the atmospheric boundary layer has been extensively studied, drawing heavily on the fundamental equations for fluid flow and thermodynamics, combined with much experimental data that has been collected over many different types of terrain at many different altitudes. The atmospheric boundary layer over the ocean, in which ships and shipboard helicopters operate, is additionally complex, owing to the fact that the wind changes the surface conditions that in turn affect the boundary layer profile.

Frictional effects influence the planetary boundary layer, which extends up to a height

of z_g, called the gradient height, in the range of 300 m over water. The planetary boundary layer can be divided into sections. In the surface boundary layer, the shear stress can be assumed constant. It extends from the earth up to a height in the range of 30 - 60 m. Above the surface boundary layer, which is the only section of interest for blade sailing, a transition region extends up to the free atmosphere.

Many different models for atmospheric boundary layer modelling exist, each considering a different combination of contributing factors. The mean velocity profile has been shown to be adequately described by the Prandtl logarithmic profile, given by

$$U_z = \frac{U^*}{k} \ln \frac{z}{z_o} \tag{C.1}$$

where U_z is the mean velocity at height z above the surface, $U^* = (\tau/\rho)^{1/2}$ is the friction velocity, τ is the shear stress in the boundary layer, ρ is the density of the air, z_o is the eddy size at the surface, an approximate measure of the surface roughness, and also the height at which $U_z = 0$. The proportionality constant, k, is the Kármán constant, and while difficult to measure in the atmosphere, is widely accepted to be 0.4 [107].

Typical over-ocean roughness is given to be in the range 0.001 - 0.01 m [27]. However, the flow over the ocean must be considered to have changing values of z_o, since the surface roughness changes with the wind speed. A relationship between friction velocity and surface roughness is given by [107]

$$z_o = A\frac{{U_*}^2}{g} \tag{C.2}$$

where g is gravity and A, taken to be 0.0144, is the non-dimensional Charnock constant, which is determined experimentally. The change in friction velocity with wind speed (and surface roughness) is captured by the neutral drag coefficient, C_{DN}, which is related to the friction velocity and a reference velocity at 10 m above the ocean surface by

$$C_{DN} = \left(\frac{U^*}{U_{10\mathrm{m}}}\right)^2 \tag{C.3}$$

and can be found using Figure C.1

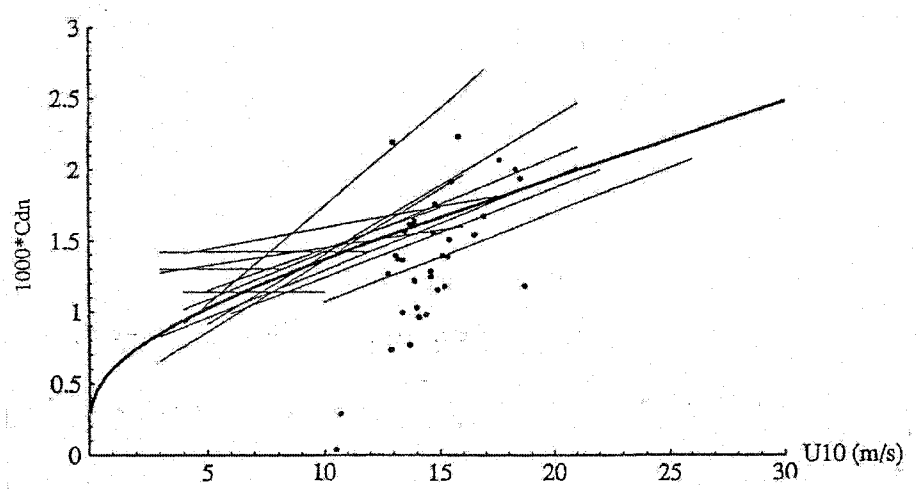

Figure C.1: Atmospheric neutral drag coefficient, C_{DN}, as a function of wind speed at $z = 10$ m. The thick line is from Charnock's relation; the lines are empirical relations; and the dots are measurements [107].

The surface boundary layer can also be represented by the power law [107]. Here,

$$\frac{U}{U_1} = \left(\frac{z}{z_1}\right)^{\alpha} \tag{C.4}$$

where U is the velocity at height z, and U_1 and z_1 are a reference height and velocity. The exponent, α, varies depending on the surface roughness. In a special case of Equation C.4, the gradient height and velocity can be used: $U_1 = U_g$ and $z_1 = z_g$. The characteristics of the atmospheric boundary layer have been extensively studied by Davenport [96, 108]. In these works, specific values for z_g and α, which are based on an impressive collection of experimental data starting from 10 m above the surface, have been proposed. The value of α for rough seas is about 0.11.

For airwakes above frigates, the boundary layer of interest is below 10 m. In this region, the boundary layer is locally influenced by waves, and data on the relevant boundary layer characteristics have not been found. Therefore the log law or power law models are used as an approximation.

Turbulence intensities in the atmospheric boundary layer are dependant on flow velocity

and on surface roughness, and decrease with increasing altitude [27]. For surface roughnesses in the range of 0.01 - 0.001, turbulence intensity ranges from a value of 0.26 to 0.13 at 3 m above the ground and decreases from 0.18 to 0.12 at 10 m above the ground. These values are for a freestream velocity at 10 m above the ground of 20 m/s. The turbulence intensity in the planetary boundary layer can also be expressed by [24]

$$i_u = = \frac{1}{\ln\left(\frac{z}{z_o}\right)} \tag{C.5}$$

$$i_v = = \frac{0.80}{\ln\left(\frac{z}{z_o}\right)} \tag{C.6}$$

$$i_w = = \frac{0.52}{\ln\left(\frac{z}{z_o}\right)} \tag{C.7}$$

which assumes stable atmosphere and a logarithmic mean velocity profile.

The length scales in the atmospheric boundary layer are also given approximately by models such as [100] (in m)

$$^xL_u = 25\frac{z^{0.35}}{z_o^{0.063}} \tag{C.8}$$

$$^xL_w = 0.35z \text{ or } 140 \text{ if smaller} \tag{C.9}$$

when $z \leq 1000z_o^{0.18}$ or by [24] (in ft)

$$^xL_u = 20\sqrt{z} \tag{C.10}$$

$$^xL_w = 0.4z \tag{C.11}$$

C.2 Experimental Design

Ship airwake data was taken during two separate test phases. The first phase, intended to characterize the steady characteristics of the flow field, is referred to as "airwake experiment A". The second phase, intended to characterize the unsteady component of the flow field is referred to as "airwake experiment B".

Table C.1: Frigate deck dimensions and scaling.

deck	width at flight deck (m)	height above the waterplane (m)
tunnel model	0.35	0.112
typical frigate (35:1 of model)	12.25	3.92
Canadian Patrol Frigate	14.7	5.7

Although the goals of the two experimental phases are distinctly different, the test setup, calibration procedure, and equipment are largely the same. The details of the experimental design apply to both experimental phases.

C.2.1 Scaling

The airwake experiment was conducted at a scale of 1:35, which was arrived at by comparing the ship deck models, which were pre-fabricated, to a representative frigate size. Table C.1 gives the approximate size of the ship deck cross sections for the wind tunnel model, the representative frigate, and the Canadian Patrol Frigate.

Due to the fact that the ship deck models in use are sharp-edged bluff bodies, the resulting airwake is relatively insensitive to Reynolds number effects. In the Reynolds number range of the model and full scale, the mean flow characteristics are assumed to be linearly scalable with flow velocity. Healey [35] notes that for this to be true, the local deck Reynolds number should be maintained above $11\text{x}10^3$ for wind tunnel modelling of ships. For a wind speed of 7 m/s at the ship deck height, the local deck Reynolds number is in the range of $2\text{x}10^5$. At full scale, the deck Reynolds number is $7\text{x}10^6$.

Reduced frequency, which captures the relationship between the rotor rotational speed and the frequency of the incoming turbulent vortices, is an important scaling parameter for blade sailing. The reduced frequency, f^* is given by [101]

$$f^* = \frac{fD}{V} \tag{C.12}$$

where f is the frequency of interest. Reduced frequency similarity was maintained through this equation in the airwake experiment.

C.2.2 Equipment

The experiments were conducted in the 5 m diameter Vertical Wind Tunnel Facility at the Aerodynamics Laboratory, National Research Council of Canada. The following equipment was used in both phases of the airwake experiment.

- Vertical Wind Tunnel (NRC; 2 x 3 m insert installed);
- Ship deck shapes at 0°, 5°, 10°, 15° and 20° roll (courtesy Indal Technologies);
- Cross hot-film anemometers (TSI model 1241-20);
- Hot-film circuitry (TSI IFA 100 [Intelligent flow analyzer]);
- Associated wiring and probe holders;
- Digital impeller anemometer (Omega HH30); and
- Horizontal traverse with combined traverse control and data acquisition system (NRC).

Figure C.2 shows a model of the wind tunnel facility and some of the components of the experimental set-up. The wind tunnel working section was 3/4 open jet and is 2 m by 3 m in size. The nominal tunnel velocity was recorded using a digital impeller anemometer mounted in the tunnel freestream. The tests were completed at a nominal wind speed around 9.05 m/s, which was achieved with a fan speed of approximately 150 rpm.

Five different ship deck cross-sectional models were used, for a total of seven ship deck roll angles: -20°, -15°, -10°, -5°, 0, 5°, and 20°. Negative roll angles are achieved when the deck was tilted away from the freestream wind direction; flows at negative rolls angles are characteristically separated and turbulent. Flows at positive roll angles are in contrast attached, and move approximately parallel to the deck. They are less affected by small

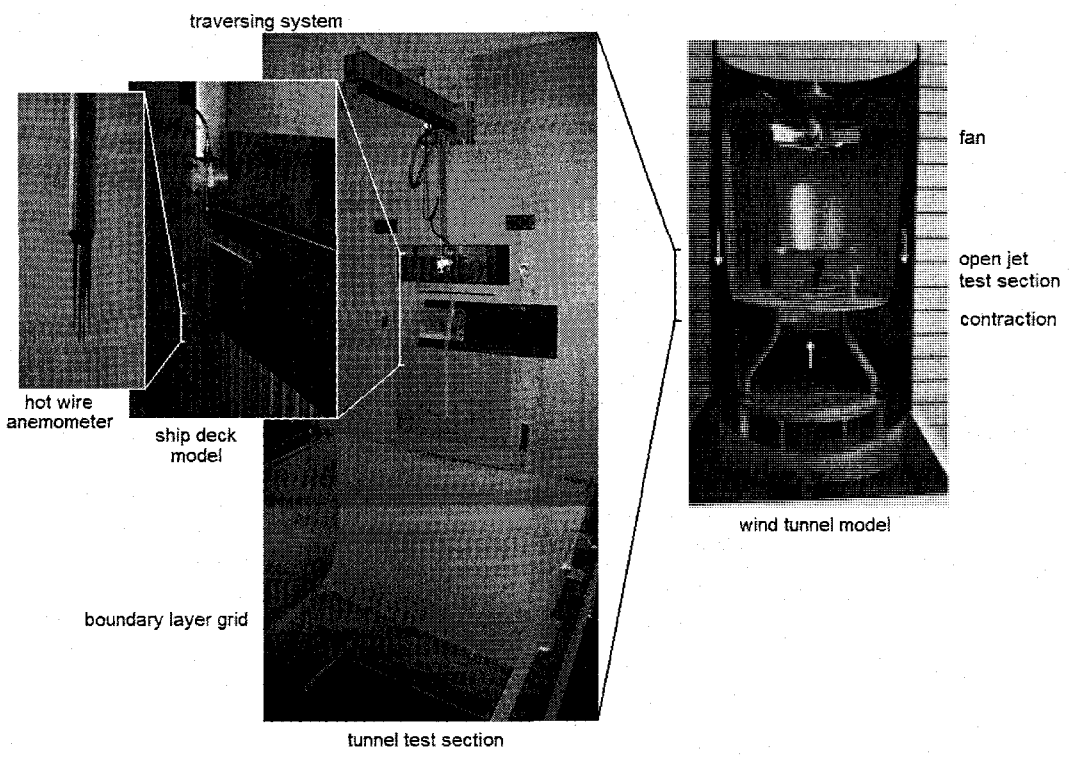

Figure C.2: Vertical tunnel facility and experimental equipment.

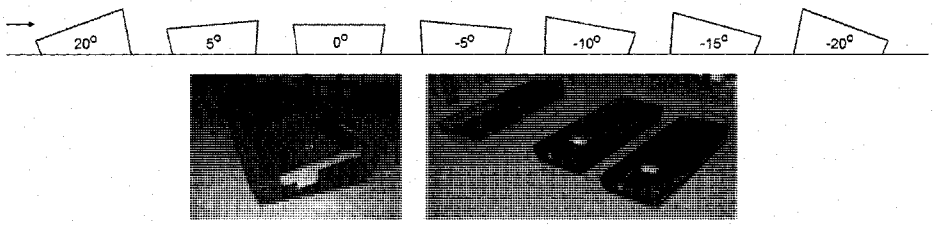

Figure C.3: Ship deck cross-sectional shapes (top); photos of some of the models (bottom).

changes in roll angle. For this reason, fewer positive roll angles were tested. Figure C.3 shows the cross-section of each tested model. Positive roll angles were achieved by reversing the models used for the corresponding negative roll angle.

The deck models were owned by Indal Technologies, having been previously used at the National Research Council of Canada for other research [45]. The models are made of wood and foam, and were constructed to be adjustable such that the relative width and height of the cross-sectional shape can be varied. The models tested in the airwake experiment had a constant height along the deck centreline of 112 mm (3.92 m full scale) and a constant width of 350 mm (12.25 m full scale). The height at the centre of the flight deck remained fixed for models at each roll angle. The maximum roll angle available with the Indal models was 20°, which was deemed to be appropriate, given that sea state 5 can lead to maximum ship roll angles in the range of 20°.

The boundary layer grid, another existing piece of equipment, was used to give a representative mean wind profile approaching the ship decks. It was made of 13 mm metal bars placed at increasing spacing up to a height above the tunnel wall of 645 mm (22.6 m full scale).

C.2.3 Experimental Flow

Figure C.4 shows the mean flow velocity measured in the experimental boundary layer over the course of experiments A and B, compared to the theoretical logarithmic and power laws that are discussed in Section C.1. Using a mean wind speed of 15 m/s and the C_{DN} value from Figure C.1, the resulting surface roughness is $z_o = 6\text{x}10^{-4}$ m. The freestream value

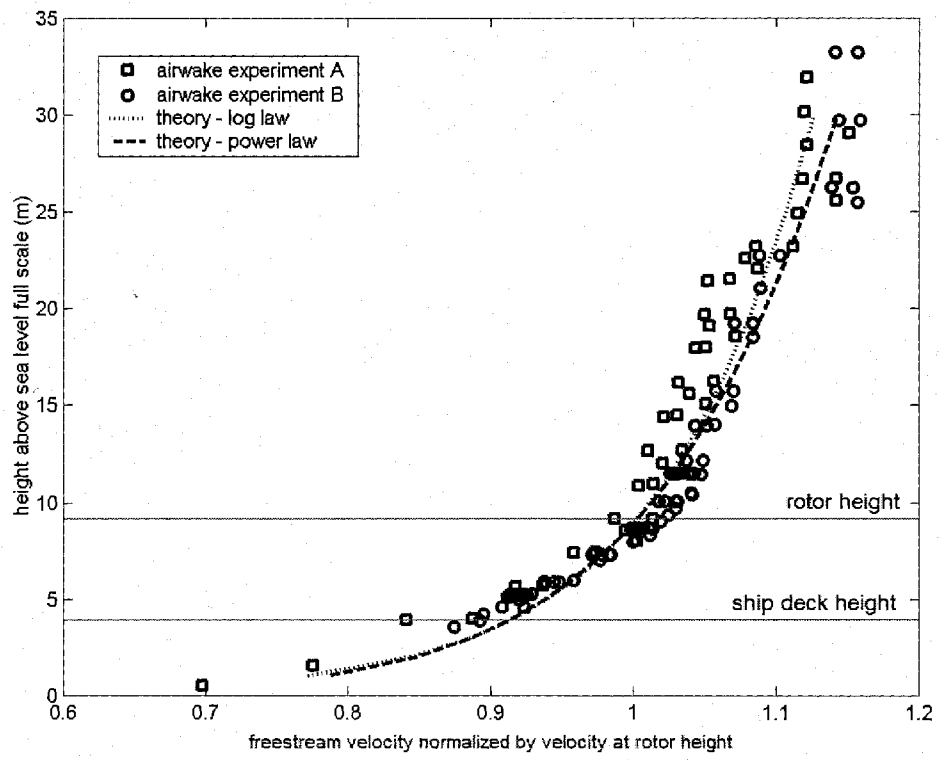

Figure C.4: Wind tunnel boundary layer profile compared to theory.

is always, unless otherwise specified, taken to be the velocity at the typical rotor height, which is at 260 mm (5 m full scale) above the ship deck.

Good agreement is shown between the theoretical boundary layer and the profile given by the boundary layer grid, especially in the region of the rotor disc plane. The scatter in the experimental results is an indication of the velocity measurement uncertainty; this scatter is less than 5% of the freestream value.

The unsteady characteristics of the wind tunnel velocity are also of interest. Figure C.5 shows examples of the spectrum measured in the wind tunnel behind the grid at 169 mm and 289 mm above the ocean at model scale (4.2 m and 10.1 m full scale).

The turbulence intensities measured in the wind tunnel are of the correct order of magnitude, although smaller, than those expected in the atmosphere. This is considered acceptable since the turbulence intensity close to the ground can vary significantly and is

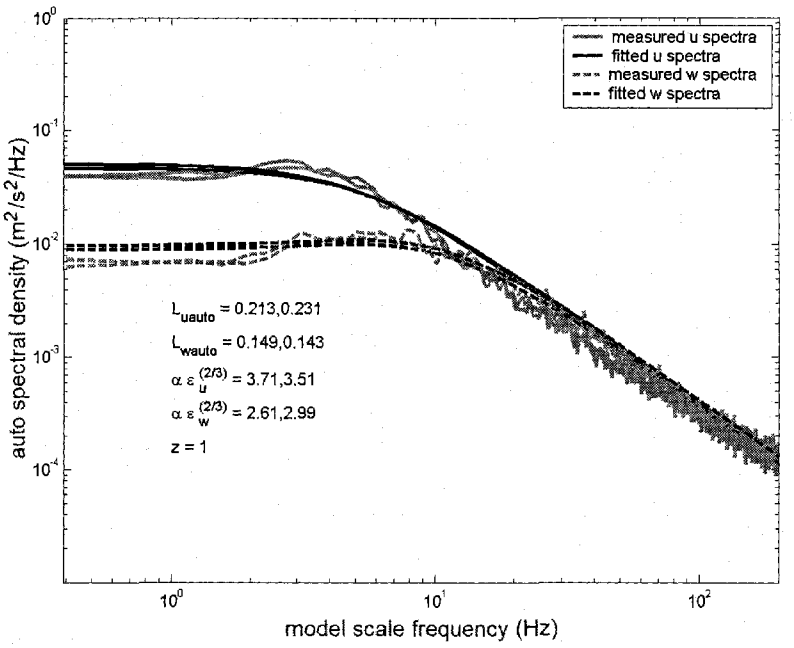

(a) at 169 mm above ocean at model scale (freestream 8.85 m/s)

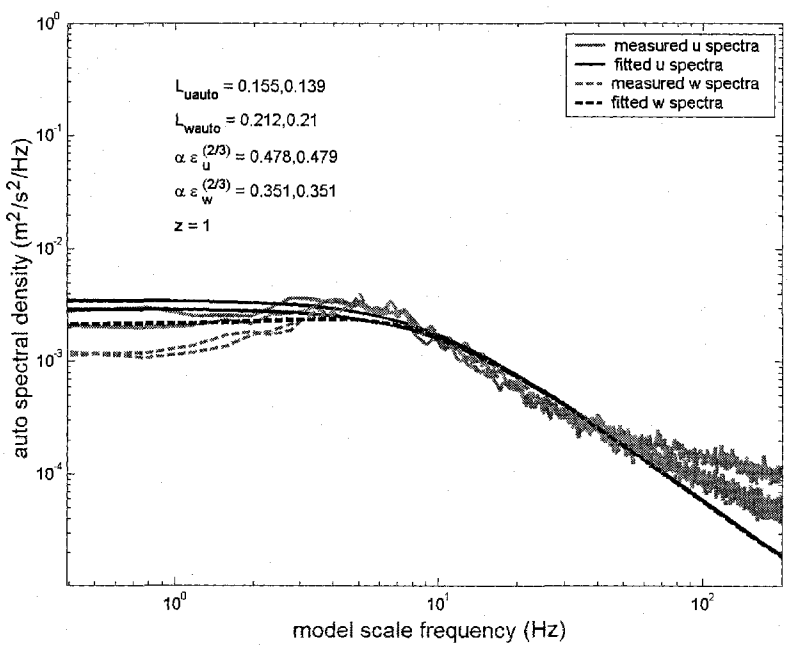

(b) at 289 mm above ocean at model scale (freestream 8.86 m/s)

Figure C.5: Auto-spectra for the measured boundary layer in the wind tunnel (probe spacing is X 63.5 mm).

only approximately given by published models. However, it is likely that true airwake flows will have higher turbulence intensity than the models used in this study.

The length scales in the atmospheric boundary layer as predicted by the models are much larger than those available in the wind tunnel. This is not expected to appreciably affect the results collected in the wind tunnel, since the eddies generated by the deck itself are self-scaling and are expected to be of highest importance from a blade sailing perspective.

C.3 Equipment Calibration

C.3.1 Hot-film Aneomometers

Cross hot-film anemometers were used in both phases of the airwake experiment. For the airwake experiment, the hot films were calibrated in the 3/4 open-jet 1 m by 1 m Pilot Wind Tunnel at the Aerodynamics Laboratory, National Research Council of Canada. They were calibrated using the following procedure.

- The hot films were mounted on the yaw traverse in the wind tunnel at a location with known wind velocity.
- The hot-film system was set up according the the procedure laid out in the manual.
- A total of 1000 data scans were taken at 100 Hz for each speed and yaw angle combination, sweeping first through velocities from 0 to 15 m/s with the probe at 0°, and then through yaw angles ranging from -30° to 30° with the velocity at 8 m/s.
- The voltage readings from each hot film were corrected for ambient temperature and pressure.
- The empirical directional correction factor, k, and fourth-order polynomial fit are determined to calculate velocity from the hot-film voltage signals.
- The reference temperature and density value along with the fitted values are stored in a calibration file.

A sample calibration is shown in Figure C.6, which shows the polynomial fits for effective velocity and the error induced by flow at an angle respectively for probe number 83388, which was used for experimental phase A. Five hot film anemometers were used to take the data in airwake experiments A and B. Each hot film was calibrated using this procedure.

C.3.2 Propellor anemometer

The vane anemometer used to measure the freestream wind tunnel velocity was also calibrated in the Pilot Wind Tunnel facility. The vane anemometer reading was found to be within 1.7% percent of the wind tunnel speed, when compared to the velocity as calculated from a pitot tube.

C.4 Airwake Experiment A

Dates: 14 May - 19 Jun 2004

Goal: Steady statistics of the flow field.

Data Collection: For each point, 1000 samples were taken at 100 Hz, data unfiltered. The A/D converter was a 16 bit ± 10V sample-and-hold multichannel data acquisition card.

Hot-film: Probe #83388.

Temperature: Calibration was completed at 27.8^oC. Tests were completed at a temperature field of $29 - 32^o$C.

Probe position error: Estimated to be ± 0.1 m full scale (3 mm model scale) in the Y (spanwise) direction and ± 0.04 m full scale (1 mm model scale) in the Z (vertical) direction, as discussed in Section C.6.

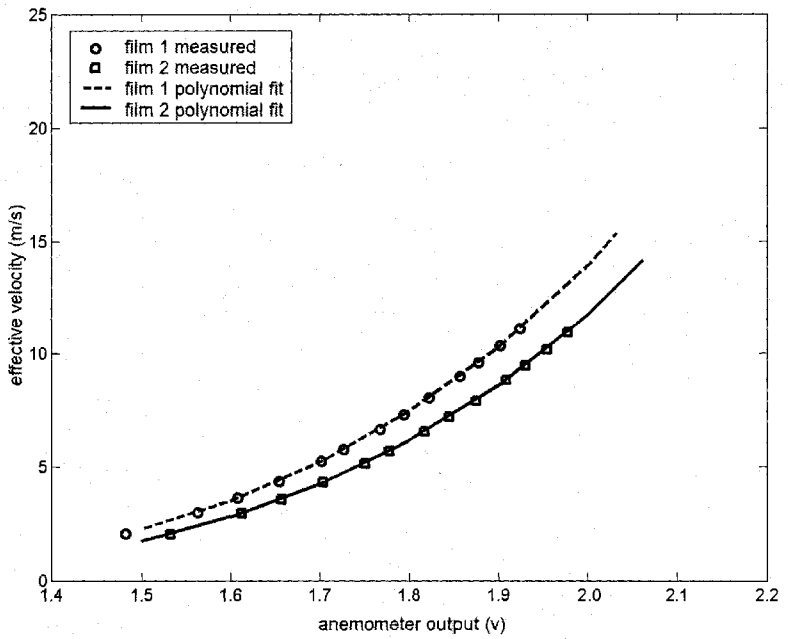

(a) polynomial fit of effective film velocity.

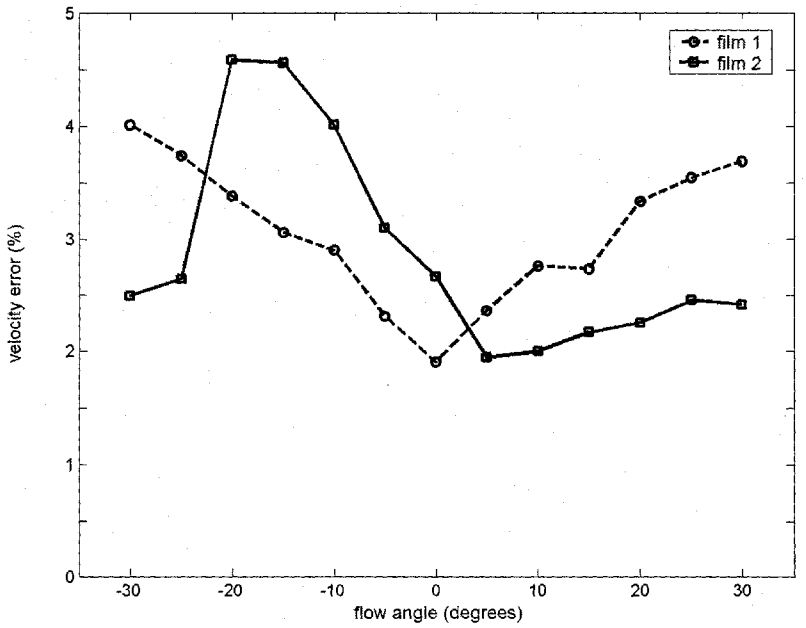

(b) velocity error at varying flow angles.

Figure C.6: Sample hot-film calibration.

C.4.1 Experimental Procedure

Once the probe locations above the ship deck were determined for each run, time history data was collected according to the following procedure.

- The probe and ship deck were manually positioned laterally (in the XY plane).
- Data was taken for each vertical (Z) location using an automated data collection and probe traversing system.
- The nominal wind tunnel speed was recorded.
- The ship deck was re-positioned laterally.

The boundary layer was periodically measured throughout the tests to ensure that the hot-film sensors did not drift out of calibration. The data was reduced according to the following procedure.

- The measurement air density was calculated using

$$\rho = 1.225 \frac{P_{\text{atm}}}{101.325\text{kPa}} \frac{288\text{K}}{T} \tag{C.13}$$

  where atmospheric pressure, P_{atm}, and tunnel temperature, T, are measured using the tunnel instruments.

- The electrical signals from each hot-film were corrected for density and temperature using

$$E = E\sqrt{\frac{T_{\text{ref}} - T_r}{T - T_r}} \left(\frac{\rho_{\text{ref}}}{\rho}\right)^{0.22} \tag{C.14}$$

  where $T_r = 250°$ C is the hot-film temperature, and the reference values, T_{ref} and ρ_{ref}, are part of the hot-film calibration.

- The effective velocity at each film was calculated using the calibration polynomials given by

$$u_{\text{eff}} = p_1 E^4 + p_2 E^3 + p_3 E^2 + p_4 E + p_5 \tag{C.15}$$

where the constants are given by the film calibration.

- The effective velocity signal was then expressed as direction, θ, and magnitude, V, relative to the probe axis using

$$\theta = \frac{\pi}{4} - \arctan \sqrt{\frac{\left| \frac{u^2_{\text{eff}_1}}{u^2_{\text{eff}_2}} - k_1^2 \right|}{1 - \frac{k_2^2 u^2_{\text{eff}_1}}{u^2_{\text{eff}_2}}}} \tag{C.16}$$

and

$$V = \left| \frac{u_{\text{eff}_1}}{\sqrt{\cos^2(\frac{\pi}{4} + \theta) + k_1^2 \sin^2(\frac{\pi}{4} + \theta)}} \right| \tag{C.17}$$

respectively and then corrected for probe misalignment. The effective velocities, u_{eff_1} and u_{eff_2} are for each wire, from Equation C.15.

- The final velocity vector was finally expressed as horizontal and vertical components in global coordinates.

C.4.2 Data and Results

Figure C.7 shows mean velocity vectors at each measurement point for each ship deck roll angle. This is intended to show the density of measurements and also the trends exhibited by the data. The data is then gridded and interpolated to a much finer grid of spacing 3 mm (0.1 m full scale) in horizontal velocity and turbulence intensity, vertical velocity and turbulence intensity. Figures 4.3 to 4.9 show contour plots of these quantities for each deck angle. Flow visualization was also conducted using a smoke wand over the -20° deck.

Results, models and discussion relating to airwake Experiment A can be found in Chapter 4.

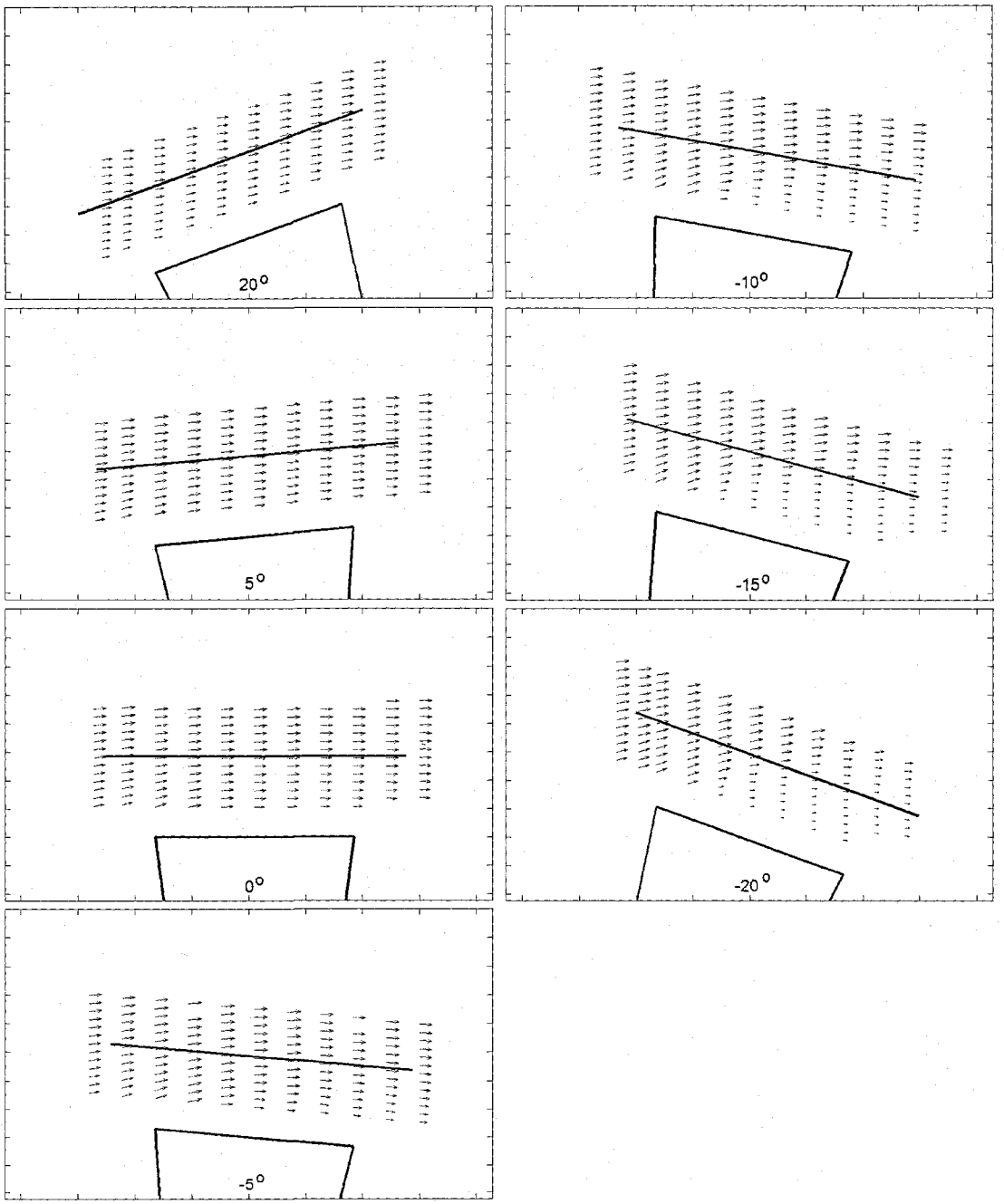

Figure C.7: Measured velocity vectors at measurement locations for the airwake Experiment A.

C.5 Airwake Experiment B

Dates: 23 - 30 Aug, 14 Oct - 20 Jan 2005/6.

Goal: Unsteady statistics of the flow field.

Data Collection: For each point, 90000 samples were taken at 400 Hz and filtered at 200 Hz. The A/D converter was a 16 bit ±10 V sample-and-hold multichannel data acquisition card.

Hot-film: Probes #86172 and #9893.

Temperature: Calibration was completed at 24.0°C. Tests were completed at a temperature of 24 – 26.5°C.

Probe position error: Estimated to be ±0.2 m full scale (6 mm model scale), as discussed in Section C.6.

C.5.1 Experimental Procedure

The procedure used in Experiment B is the same as that used in Experiment A. The data reduction process is an extension of the reduction for Experiment A, in that the spectral and unsteady characteristics are examined as well. The extra steps are summarized here.

- The velocity signals were normalized by the freestream velocity and the frequencies were scaled to maintain reduced frequency similarity.
- The auto- and cross-spectral density functions of each horizontal and vertical velocity component, as defined in ship coordinates, were calculated using Welch's averaged modified periodogram method [109] with non-overlapping Hanning windows of 1024 points each.

C.5.2 Data and Results

The details of the data synthesis for Experiment B are largely discussed in Chapter 4. The coherence and phase angle data collected during Experiment B are shown in Figures C.9

through C.50. Primarily, these figures show the quality of the model fits discussed in Section 4.4.5.

These plots also confirm expected trends in the variation of the coherence throughout the data. Greater spacing between probes leads to lower coherence, as does increased turbulence. This trend can be observed by comparing, for example, the magnitude of coherence measured for a XY probe spacing of 35 mm. Considering the five points above the 0° deck prior to the leading edge (point 11 - 15; Figure C.11), at mid-deck (points 51 - 55; Figure C.19) and after the trailing edge of the deck (points 92 - 96; Figures C.27 and C.28), a decrease in the overall coherence is observed for z locations close to the deck. The correlations further from the deck remain relatively unchanged since they are not significantly influenced by the presence of the ship deck. These coherences can be further compared to the points above the -20° deck (points 132-136, 162-166, and 188-190; Figures C.35-C.36, C.41-C.42, and C.46 respectively). The -20° deck causes higher flow turbulence, which is exhibited by lower overall correlations near the deck.

The phase angle also behaves as expected. Data with increasing spacing in the local streamwise direction exhibit increasing phase angles between the points. They also exhibit mainly linear phase angle versus frequency relationships, which allows the use of Taylor's hypothesis in this situation. The sign of the phase angle depends only on the order in which the points are compared. For these figures, the lowest point in the (z) direction was taken to be the first point. Due to slight probe misalignments and angled local flow, the lowest point is not intuitive for every case shown.

C.6 Sources of Uncertainty

Careful characterization of the s present in this, and indeed any, measurement system is essential for correctly interpreting the data. Sources of experimental uncertainty traditionally fall into three categories: calibration uncertainties, data acquisition uncertainties, and data reduction uncertainties. Each uncertainty can be classified as either bias error or random error. While random errors are a measure of the scatter of data about the true value, bias

errors represent a systematic shift of the data away from the true value. An effort has been made to quantify each uncertainty in order to understand the overall resolution of the experiments that have been completed.

C.6.1 Calibration Uncertainties

Calibration uncertainties result from the calibration process and thus are inherent to all measurements made with the calibration. Calibration uncertainties are all taken to be bias errors.

Calibration standard: Some uncertainties exist as a result of the fact that velocity is a derived quantity, comprised of the fundamental units length and time. Many measurement steps exist between a velocity measurement with hot-films or pressure and its calibration against standards for fundamental magnitudes.

Calibration changes: Uncertainties can be introduced if the properties of the films change. Hot-film probes are sensitive to calibration changes as a result of contamination, although to a lesser degree than hot-wires. This is even more likely during tests in which the probe is often moved in and out of the test set-up.

Calibration assumptions: During calibration, the empirical directional correction factor, k, which determines the extent to which flow along the film affects the reading, is found by minimizing the angular uncertainty. Table C.2 shows the angular uncertainties for angle range between -30° and 30° for each probe used, with one probe repeated three times.

C.6.2 Data Acquisition Uncertainties

These uncertainties come from uncertainties present in the acquisition process itself. These uncertainties are also taken to be bias errors for the purpose of data analysis.

Digitization of analog signal: The 16 bit ±10V A/D converter can resolve up to 0.0003 V. This allows a speed resolution of about 0.008 m/s.

Table C.2: Probe angular uncertainty and associated experiment.

probe #	angular error (%)	directional sensitivity k_1/k_2	experiment
83388	4.6	.22/.28	A
86172 (1)	4.1	.28/.35	boundary layer
85212	2.8	.34/.28	boundary layer
86172 (2)	2.8	.36/.35	boundary layer
8760	3.2	.23/.24	boundary layer
86172 (3)	5.6	.32/.37	B
9893	5.5	.29/.26	B

Temperature effects and drift in internal circuitry: A mathematical correction exists to compensate for differences in the heat transfer from the hot-film when the operating and calibration temperatures differ. This correction is given in Equation C.14. However, the circuitry taking the measurements will also be affected by temperature changes. The magnitude of the uncertainty induced by this is expected to be small.

Background electrical noise: Signal noise at 20, 60, 100, 140, and 180 Hz was observed. Depending on the local turbulence intensity, the noise frequencies may or may not be visible in the resulting spectra. The noise frequencies are narrow enough, though, not to affect the calculated turbulence intensity by more than ± 0.002.

Wind tunnel speed uncertainty: Since all single point statistics are quoted as a percent of the wind tunnel velocity, errors in free stream measurement add some error to the results. The vane anemometer used to measure the tunnel velocity has an accuracy of 1.7%.

Out-of-plane velocity uncertainties: Out of plane turbulence still affects the cross-film readings, even though they cannot be resolved. Velocity uncertainties of up to 8% can be induced for turbulence intensities of 20% [110].

Table C.3: Estimates of spatial error in the global reference frame.

Test #	Vertical (Z) error (±m) full scale : (±mm) model scale	Spanwise (Y) error (±m) full scale : (±mm) model scale
A	0.1:3	0.04:1
B	0.2:6	0.2:6

Probe positioning uncertainties: Probe positioning uncertainties are of significant concern in these tests. Many manual set-up changes were required. Based on the number and complexity of the setup changes and an estimate for the repeatability of each, the spatial error for each test has been estimated. The locations of the data from experiment A are known with much higher precision than those from experiment B. Table C.3 summarizes these.

Time-base uncertainties: Temporal uncertainties occurring in the data acquisition are believed negligible compared to other uncertainties since a sample-and-hold data acquisition card was used, and the sampling rates are not high compared to the computer speeds and system capabilities.

Probe mounting uncertainties: Any angular offset of the probe in the plane of the flowfield will result in an apparent flow angle as read by the sensor. This effect can be corrected provided the offset angle is known. For experiment A, the set-up was significantly more consistent and the angular repeatability is believed to have been on the order of one degree. For experiment B, the angular mounting repeatability may have been higher. While this had minimal effect on the streamwise statistics, it may affect the vertical fluctuations more significantly.

C.6.3 Velocity Uncertainty Quantification

The magnitudes of the uncertainties listed above are summarized in Table C.4. Using the root-sum-square error analysis and a nominal freestream speed of 8.2 m/s, the total

Table C.4: A summary of the velocity measurement errors.

experiment error	(A) magnitude	(A) percent	(B) magnitude	(B) percent
calibration standard		negligible		1.7%
calibration assumptions		up to 4.6%		up to 5.6%
calibration changes		negligible		negligible
tunnel speed error		1.7%		1.7%
digitization	0.008m/s	negligible	0.008m/s	negligible
temperature effects and drift		negligible		negligible
signal noise		negligible		negligible
out of plane turbulence		8%		8%

Table C.5: A summary of the temporal and spatial uncertainties.

experiment error	(A) magnitude	(A) percent	(B) magnitude	(B) percent
spatial error	±3 mm		±6 mm	
temporal error		negligible		negligible
probe mounting error	$\pm 1^o$		$\pm 2^o$	

estimated error is 9.4% for experiment A and 9.9% for experiment B. The two largest sources of uncertainty are calibration uncertainties, which are most pronounced at large angles, and out-of-plane turbulence uncertainties, which are most pronounced near the separation bubble. Using Figures 4.3 through 4.9 it is clear that these two uncertainties are not at their maximum in the same locations in the flow. Additionally, the spatial uncertainty in the probe position contributes to velocity uncertainty when using the model to estimate flow velocity for a given position. These uncertainties could exceed 10% in the shear layer, but are far below 10% across most of the flowfield. Clearly the expected uncertainty in velocity measurements depends on the location in the flowfield, and is expected to be much less than 10% for most spatial locations.

C.6.4 Data Reduction Uncertainties

Data reduction errors take the form of statistical uncertainty [95]. For the steady measurements, uncertainty in the mean and variance are respectively given by

$$\epsilon_{r_{\text{mean}}} = \frac{\sigma_a}{\mu_a\sqrt{N}} \tag{C.18}$$

$$\epsilon_{r_{\text{variance}}} = \sqrt{\frac{2}{N}} \tag{C.19}$$

where the time history record is $a(t)$ and N is the number of samples taken at a spacing of Δt in the time history record.

Since $\frac{\sigma_a}{\mu_a}$ is the calculated turbulence intensity, i_a, at the point where record $a(t)$ was taken, then the uncertainty in the mean estimation is $i_a/\sqrt{N}$. For Experiment A, the uncertainty is $i_a/\sqrt{2000} = i_a 0.022$ which means that the fractional uncertainty in the estimated mean is 2.2% of the turbulence intensity value. For the variance (square of the standard deviation), the uncertainty is 3.16% for all variance estimates.

For the measurements taken in experiment B, the mean uncertainty drops to 0.33% of the turbulence intensity and the variance uncertainty drops to 0.47% since the records taken contained 90 000 points. The random error in auto-spectral estimates is given by [95, 109]

$$\epsilon_{r_{\hat{G}_{\text{aa}}(\text{f})}} = \frac{1}{\sqrt{n_d}} \tag{C.20}$$

when non-overlapping windows are used in the spectral analysis and the n_d is the number of windows. For the data taken in experiment B, 87 windows of 1024 points were used. This corresponds to a PSD magnitude uncertainty of 10.7%. The random error in the cross-spectra depends on the value of the root coherence through

$$\epsilon_{r_{|\hat{G}_{\text{ab}}(\text{f})|}} = \frac{1}{|\hat{\gamma}_{ab}(f)|\sqrt{n_d}} \tag{C.21}$$

For 87 windows, the cross-spectral uncertainty exceeds 25% when the coherence drops below 0.43. Therefore 0.4 shall be considered the critical level for coherence analysis completed in this research.

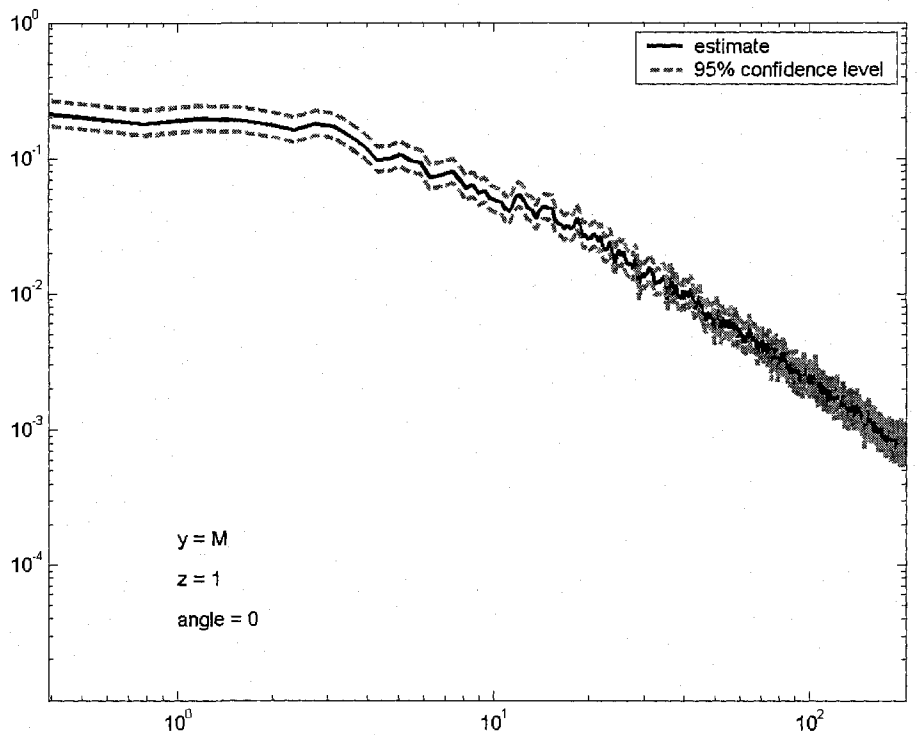

Figure C.8: Auto-spectral estimation within 95% confidence limits.

The random error in the coherence function is given as

$$\epsilon_{r_{\hat{\gamma}^2_{ab}(f)}} = \frac{\sqrt{2}(1-\hat{\gamma}^2_{ab}(f)}{|\hat{\gamma}_{ab}(f)|\sqrt{n_d}} \tag{C.22}$$

The auto-spectral value is predicted to within 95% confidence within the error bars shown in Figure C.8. The magnitudes of these uncertainties are consistent throughout the data.

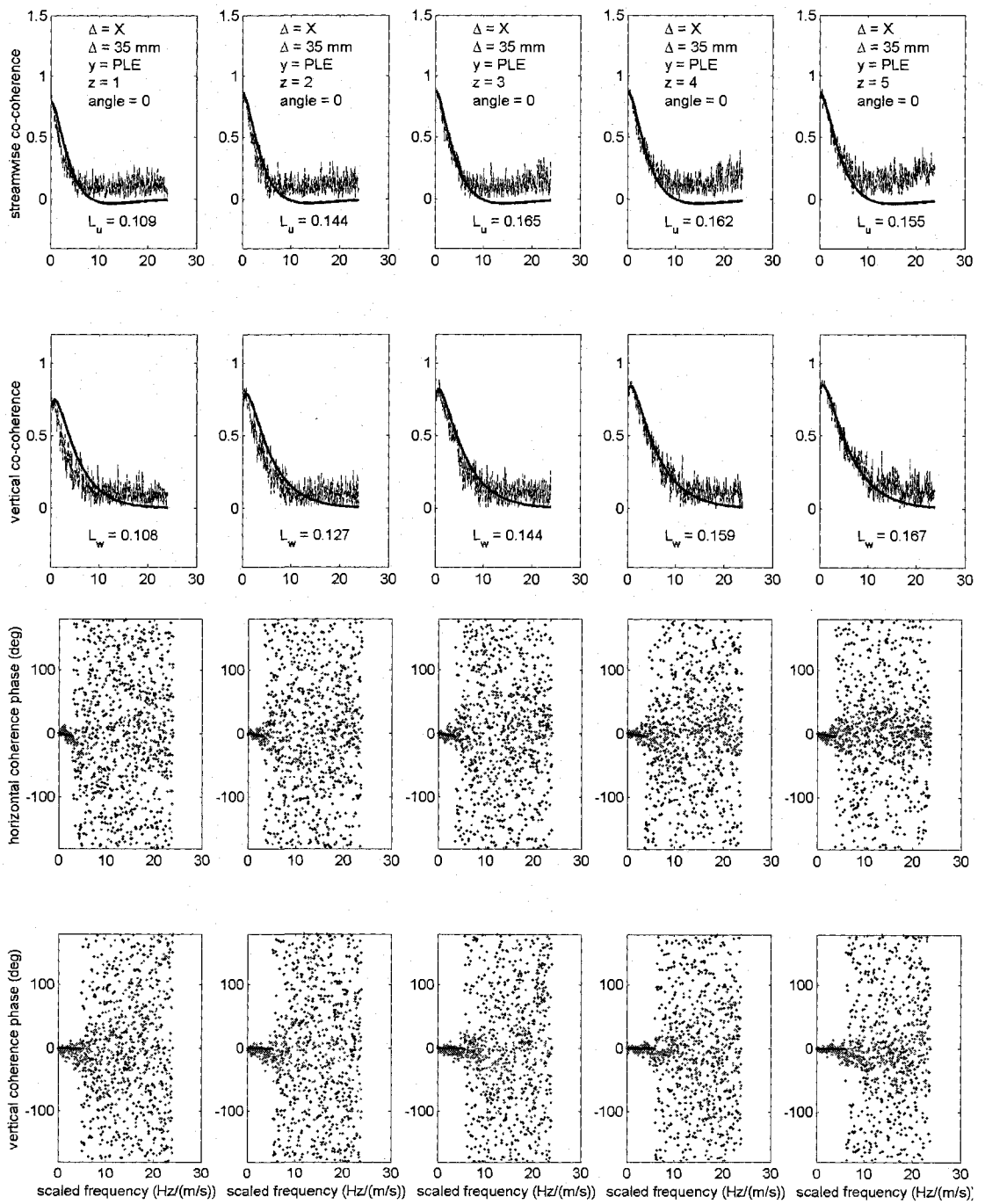

Figure C.9: Root coherence (top) and phase angle (bottom) model agreement (points 1-5).

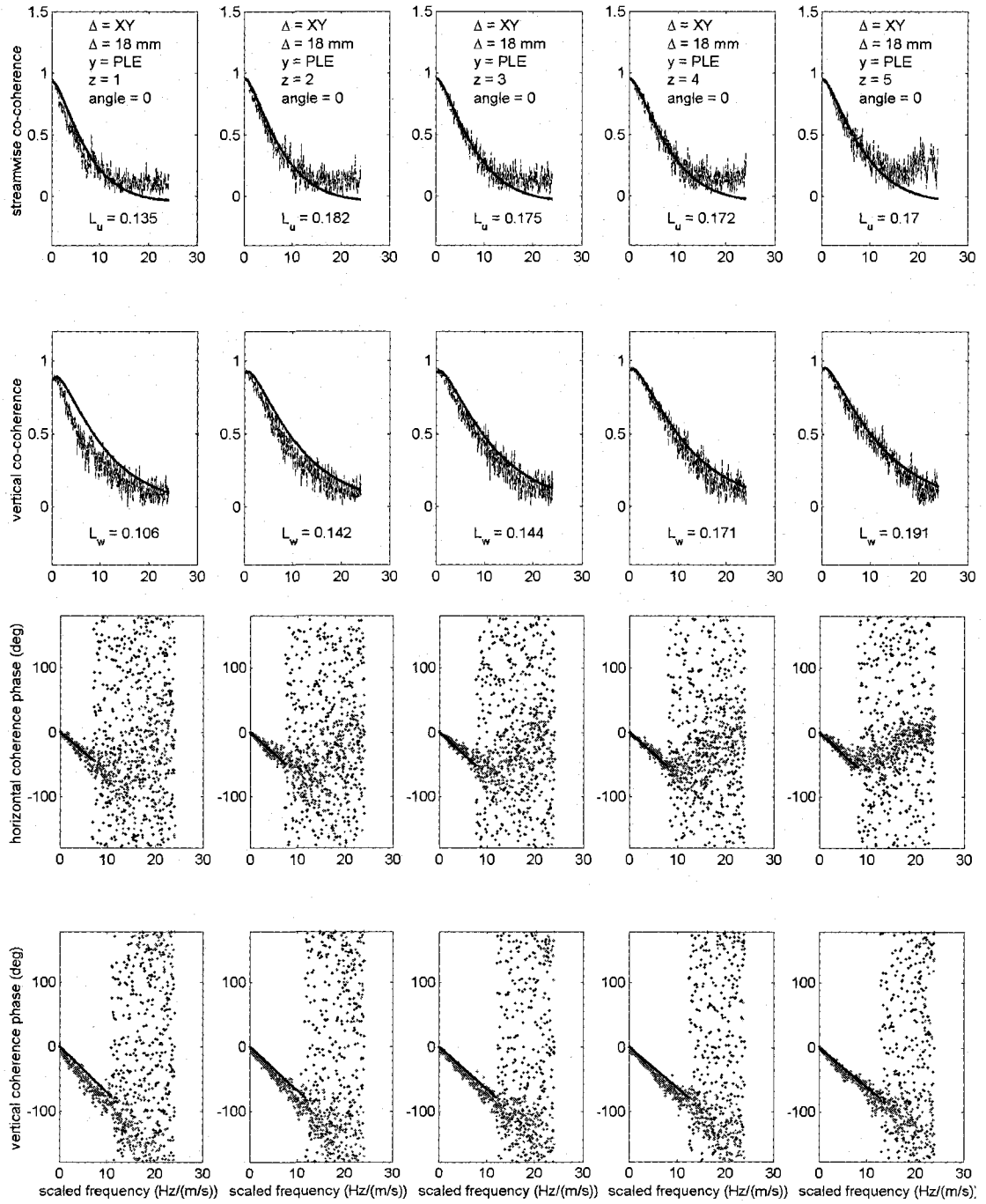

Figure C.10: Root coherence (top) and phase angle (bottom) model agreement (points 6-10).

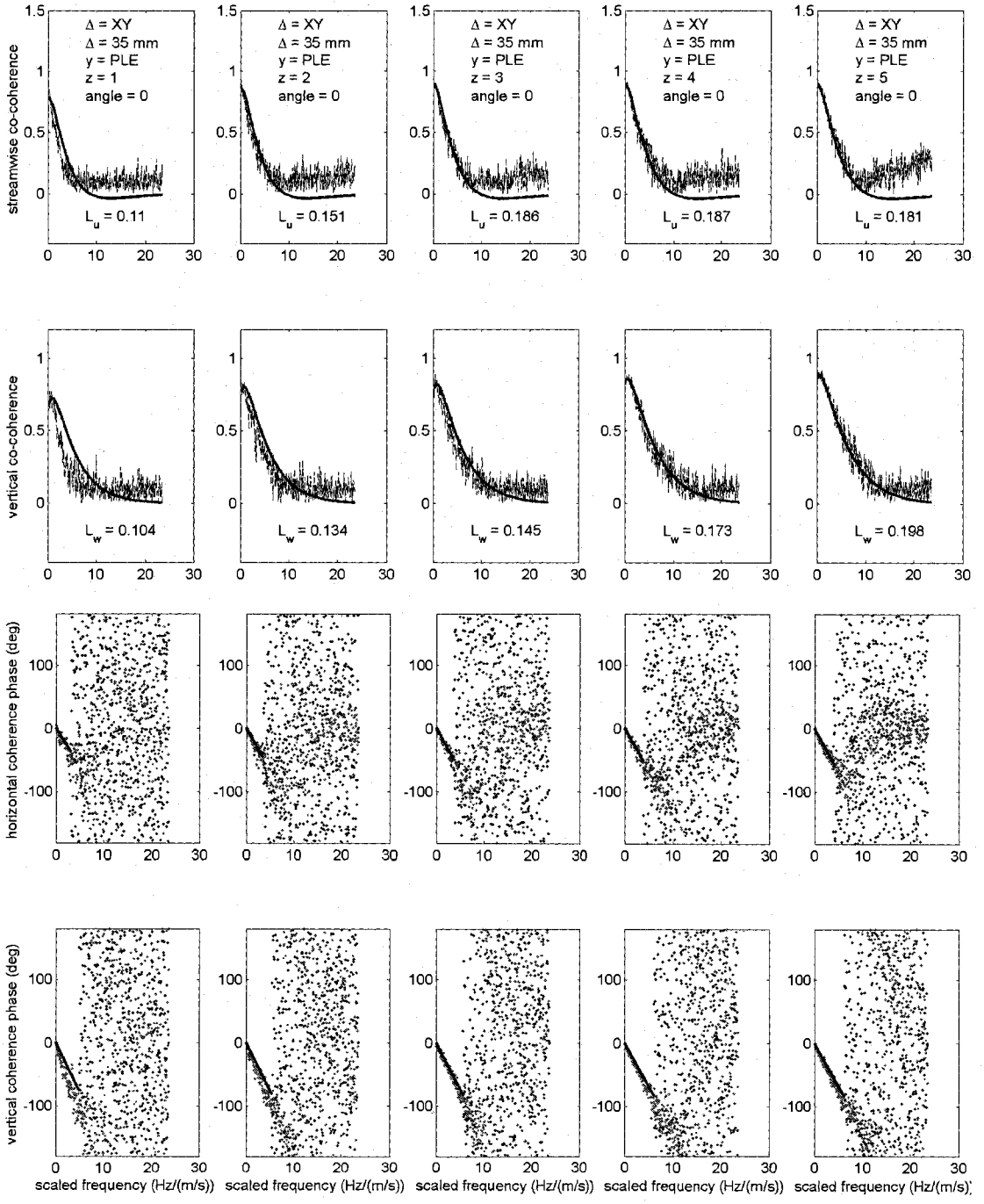

Figure C.11: Root coherence (top) and phase angle (bottom) model agreement (points 11-15).

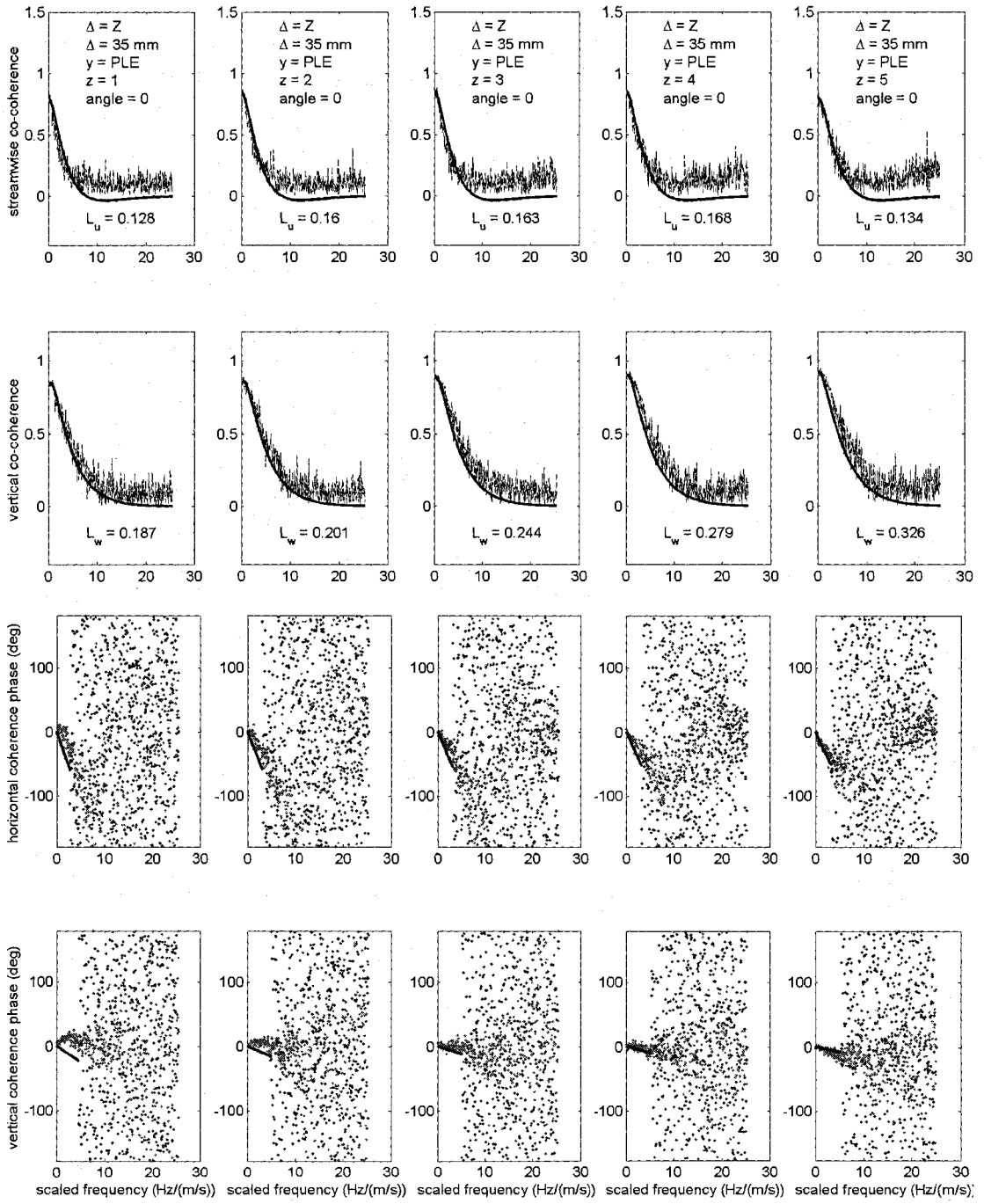

Figure C.12: Root coherence (top) and phase angle (bottom) model agreement (points 16-20).

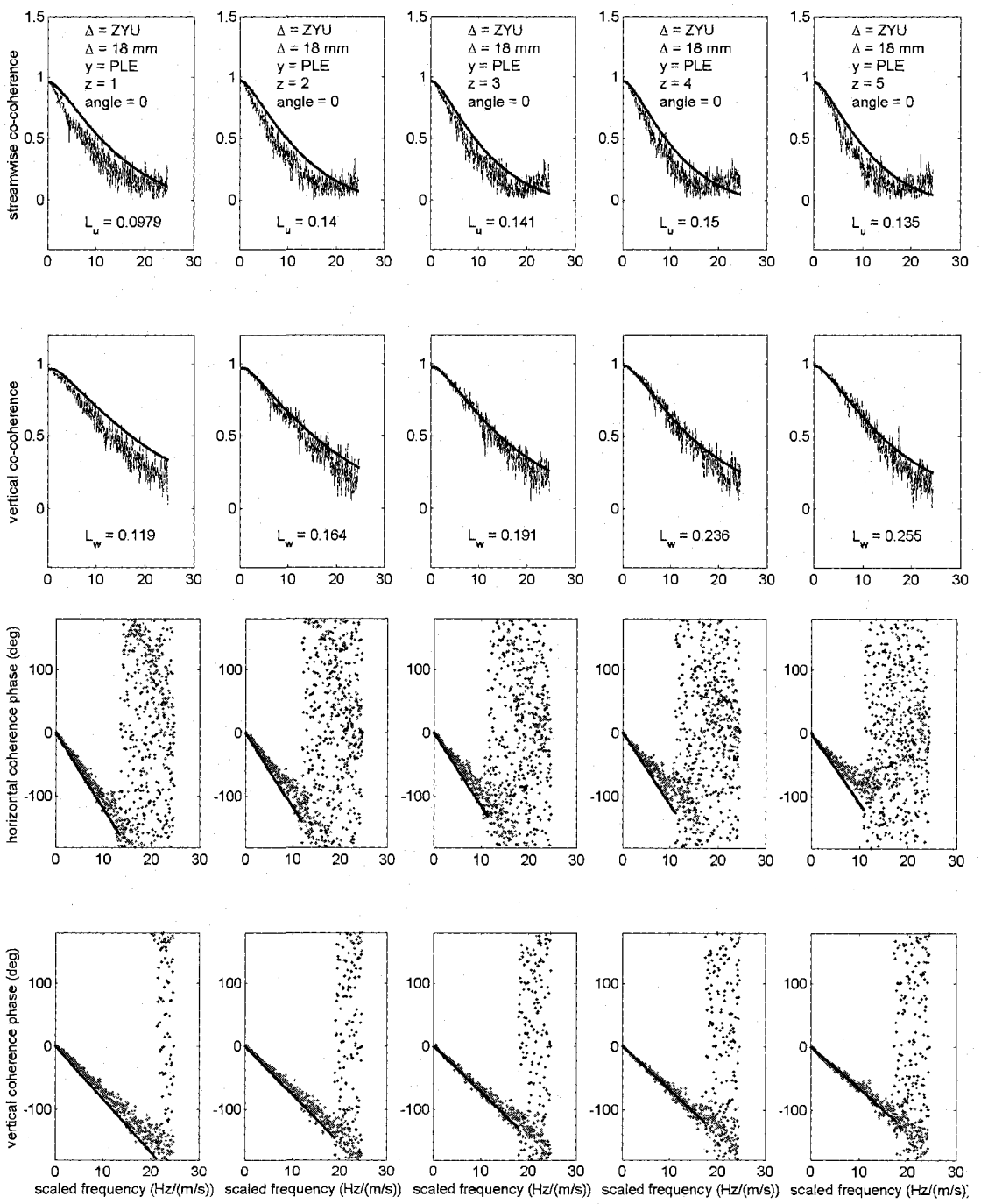

Figure C.13: Root coherence (top) and phase angle (bottom) model agreement (points 21-25).

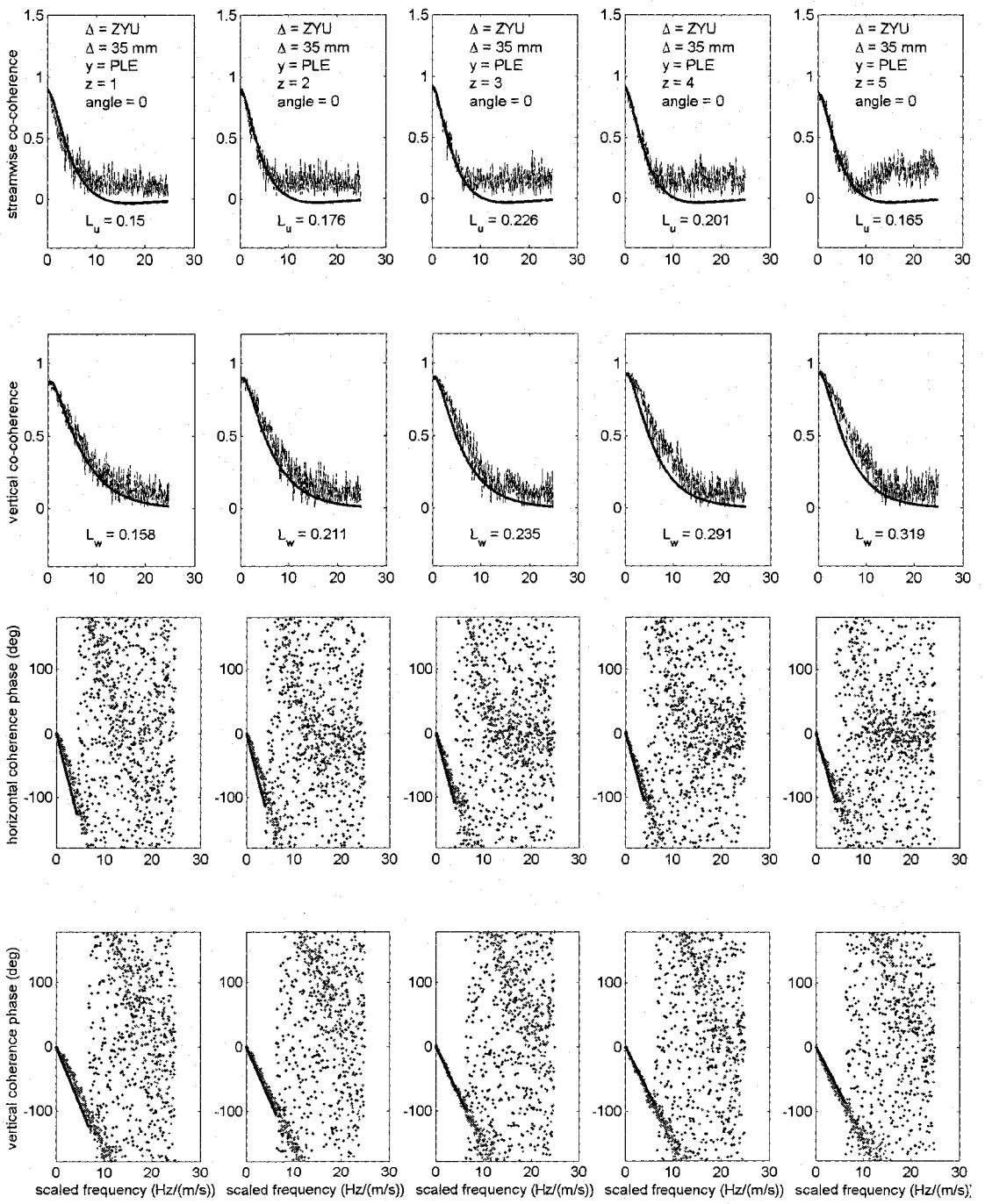

Figure C.14: Root coherence (top) and phase angle (bottom) model agreement (points 26-30).

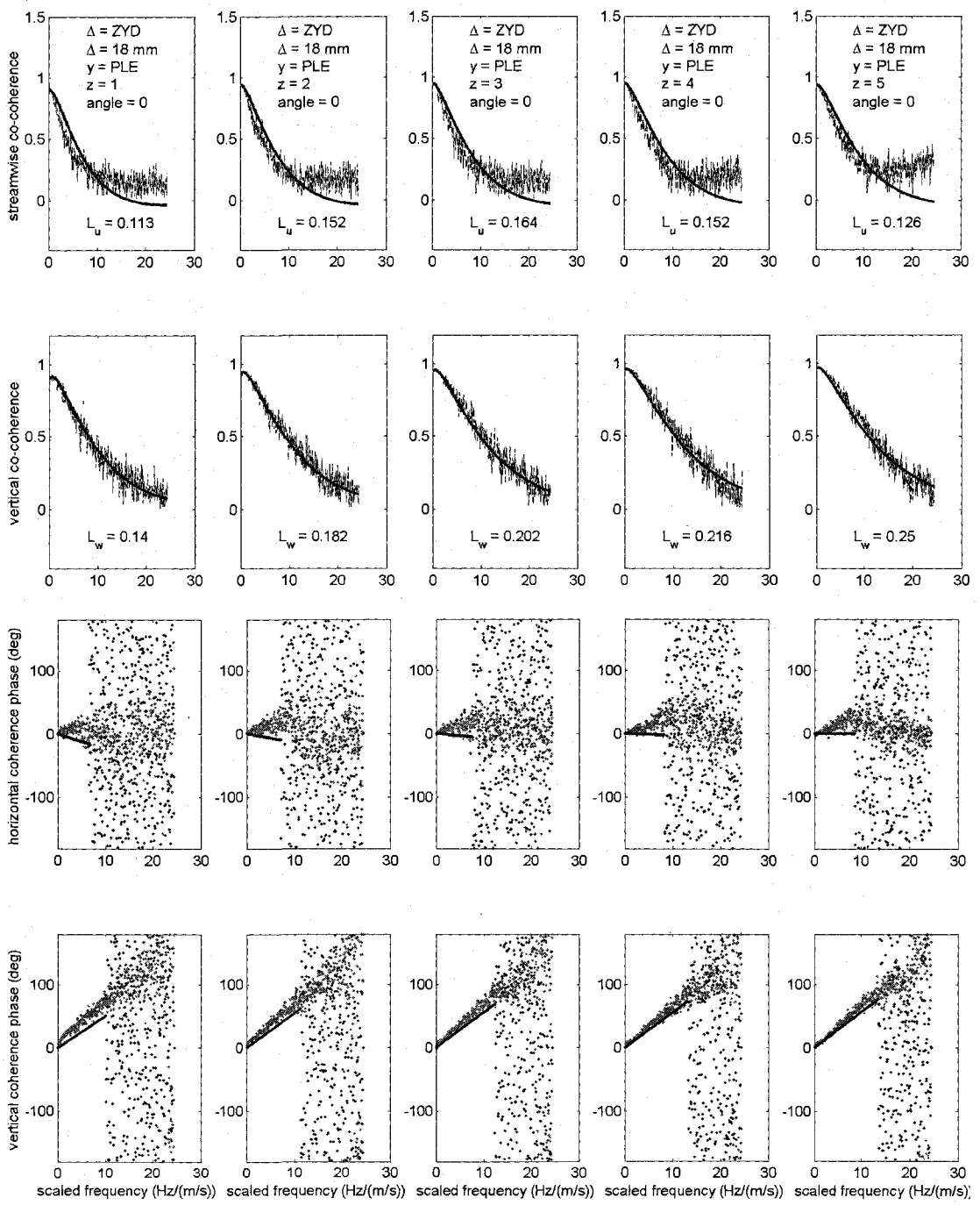

Figure C.15: Root coherence (top) and phase angle (bottom) model agreement (points 31-35).

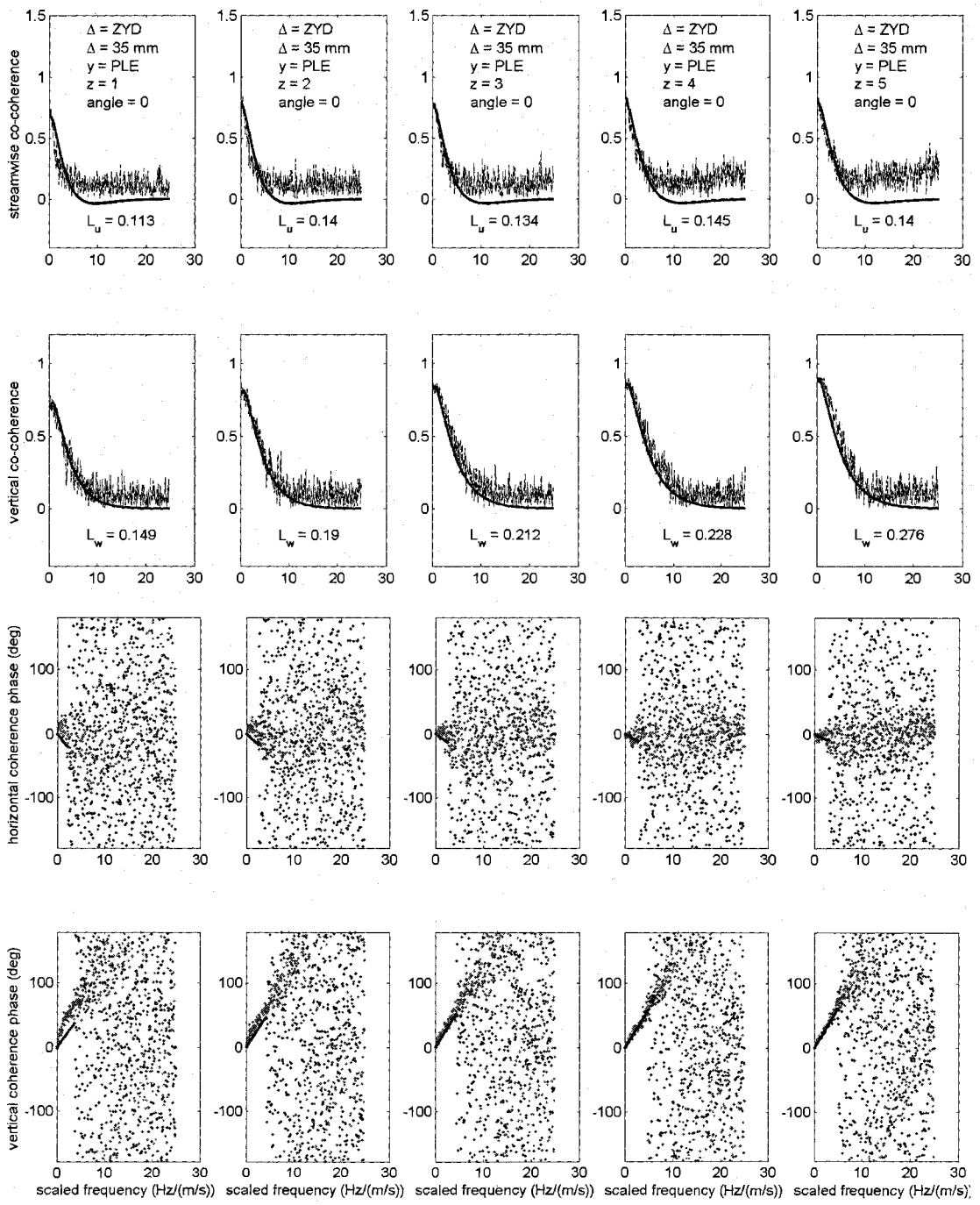

Figure C.16: Root coherence (top) and phase angle (bottom) model agreement (points 36-40).

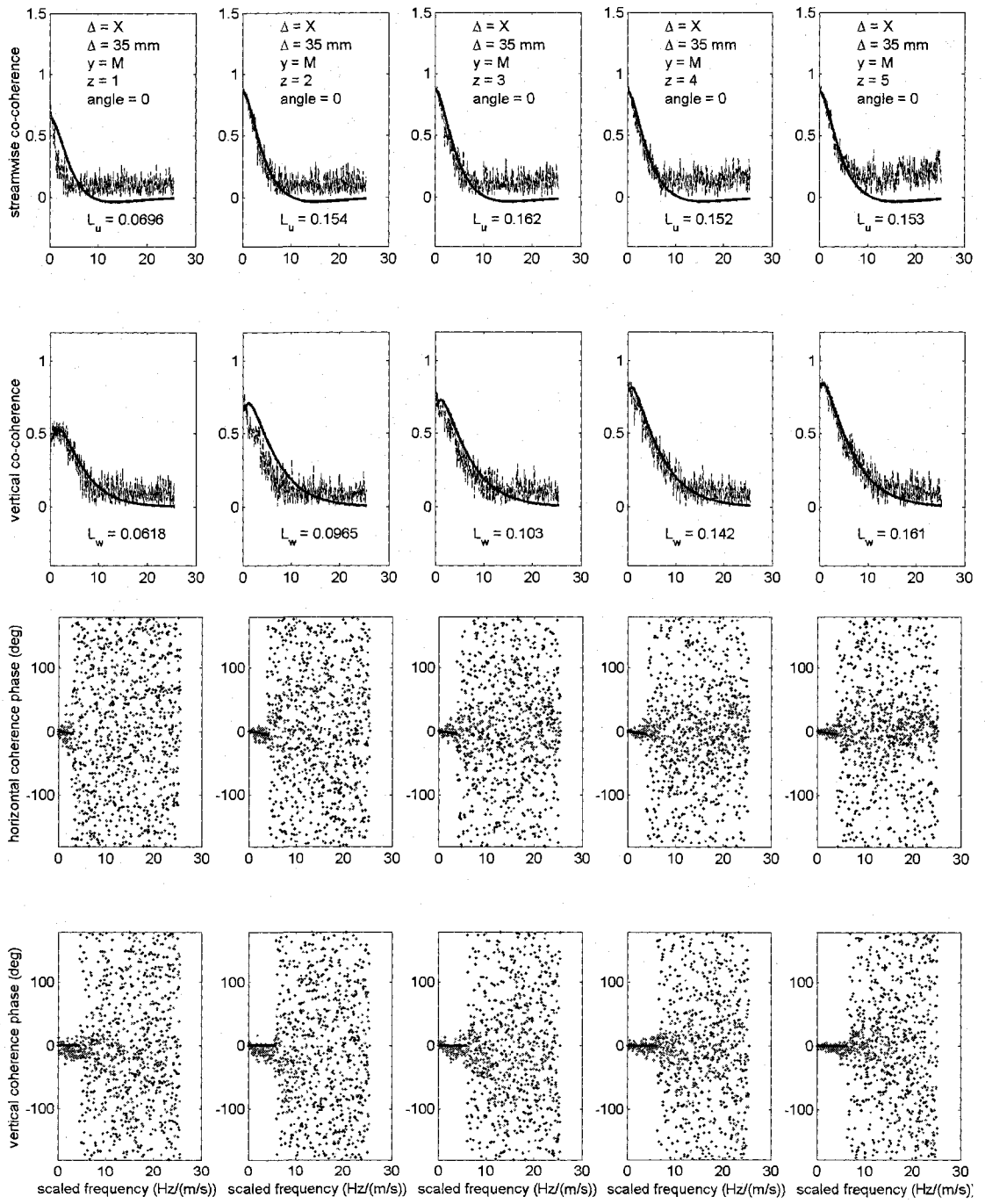

Figure C.17: Root coherence (top) and phase angle (bottom) model agreement (points 41-45).

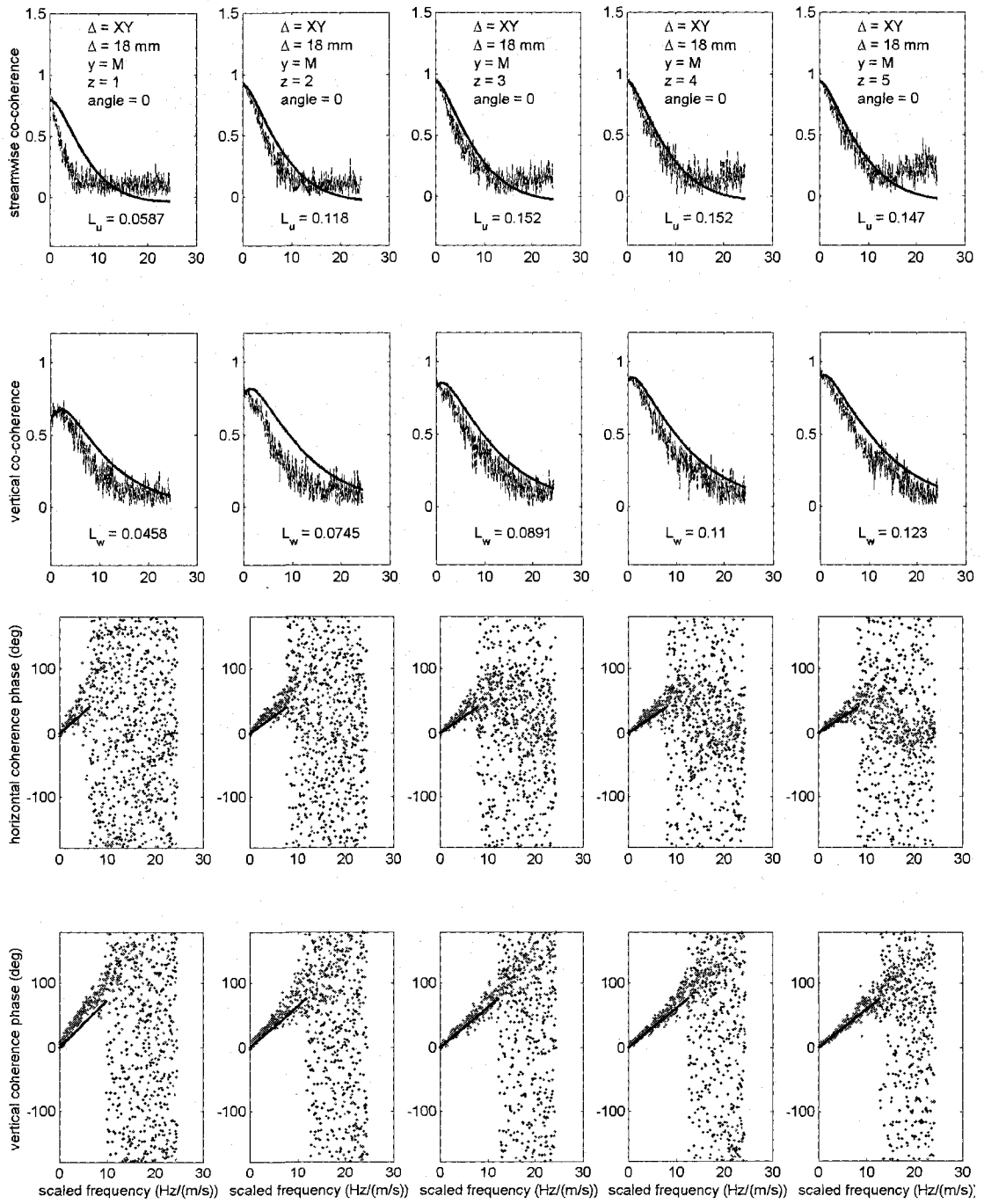

Figure C.18: Root coherence (top) and phase angle (bottom) model agreement (points 46-50).

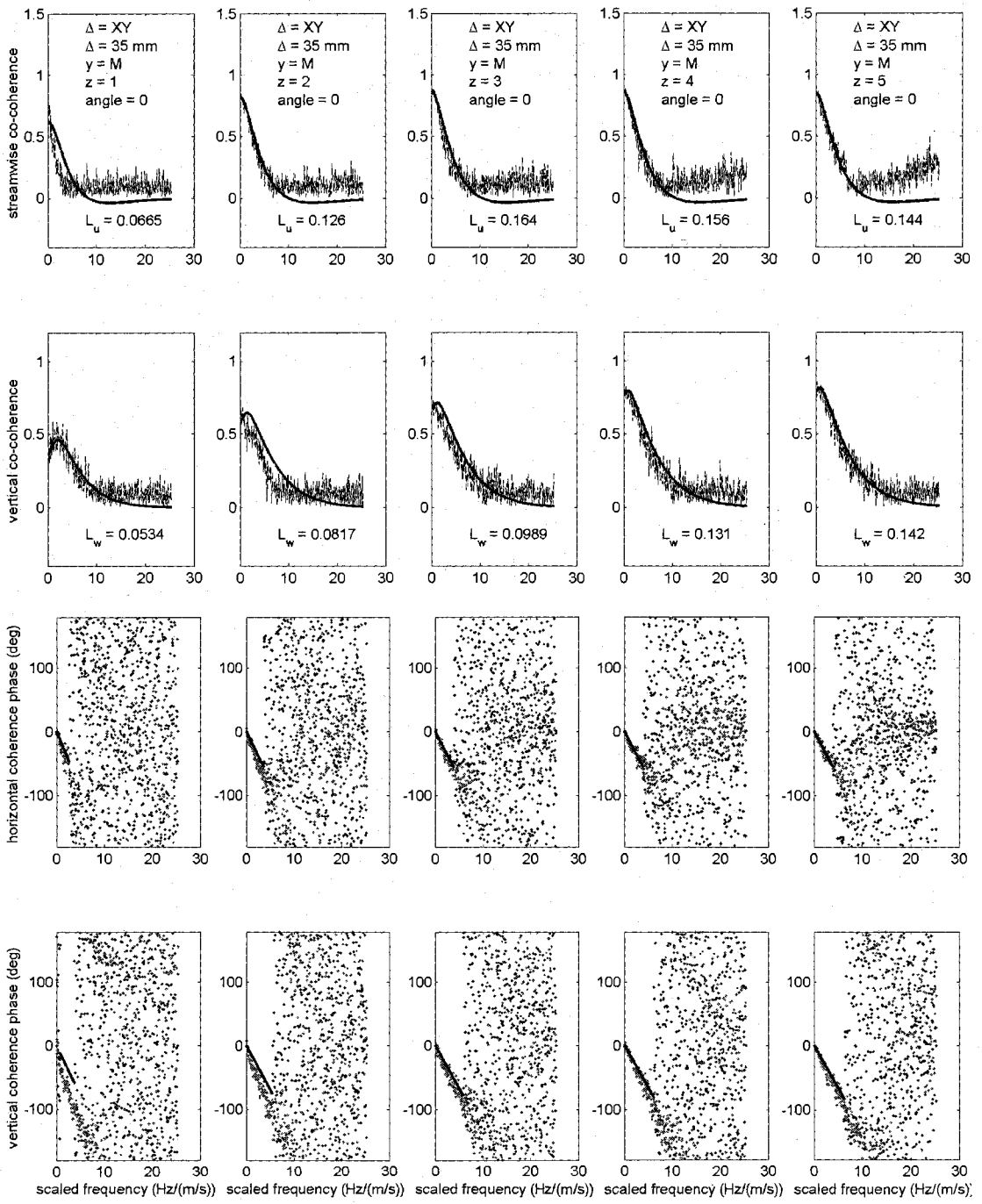

Figure C.19: Root coherence (top) and phase angle (bottom) model agreement (points 51-55).

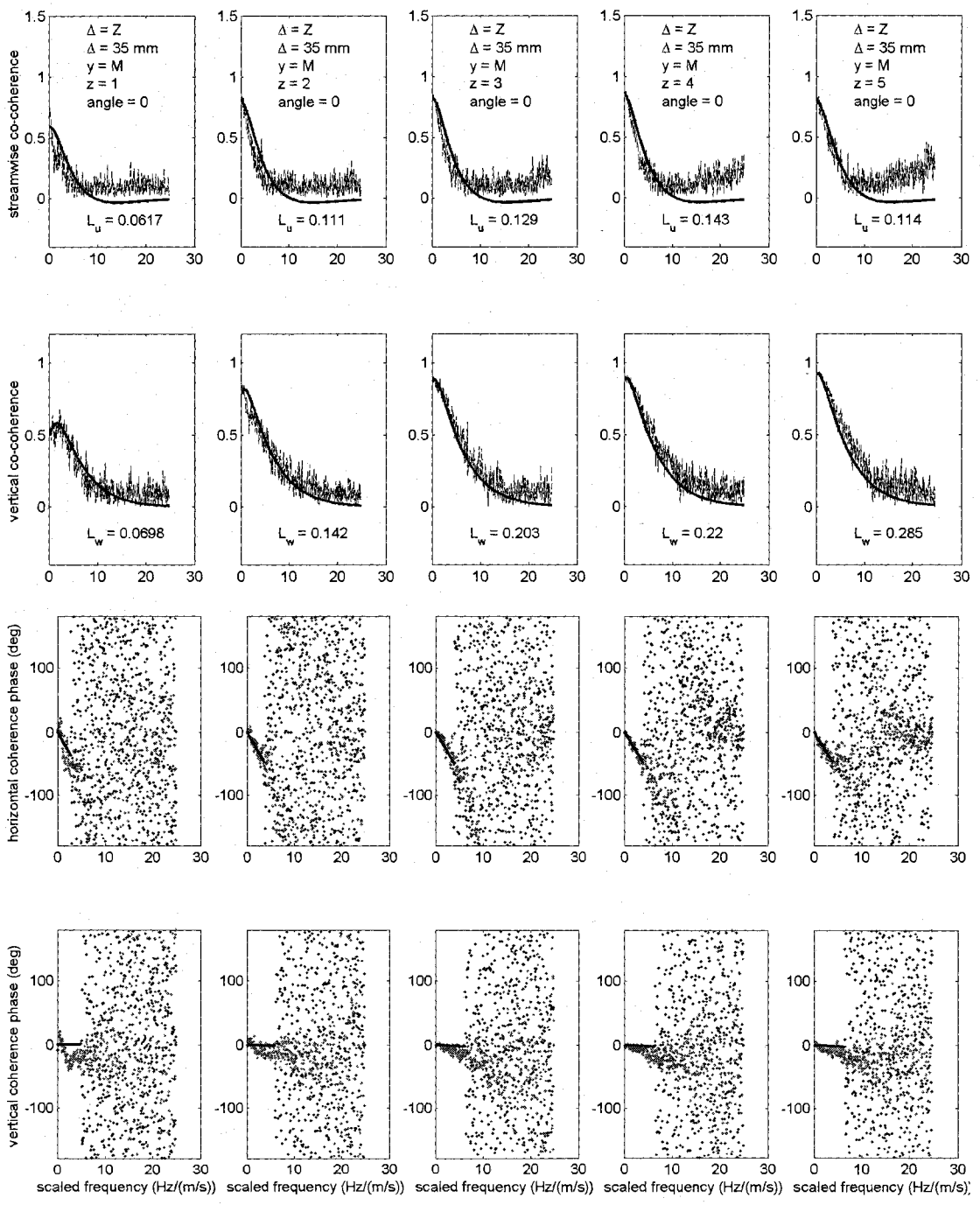

Figure C.20: Root coherence (top) and phase angle (bottom) model agreement (points 56-60).

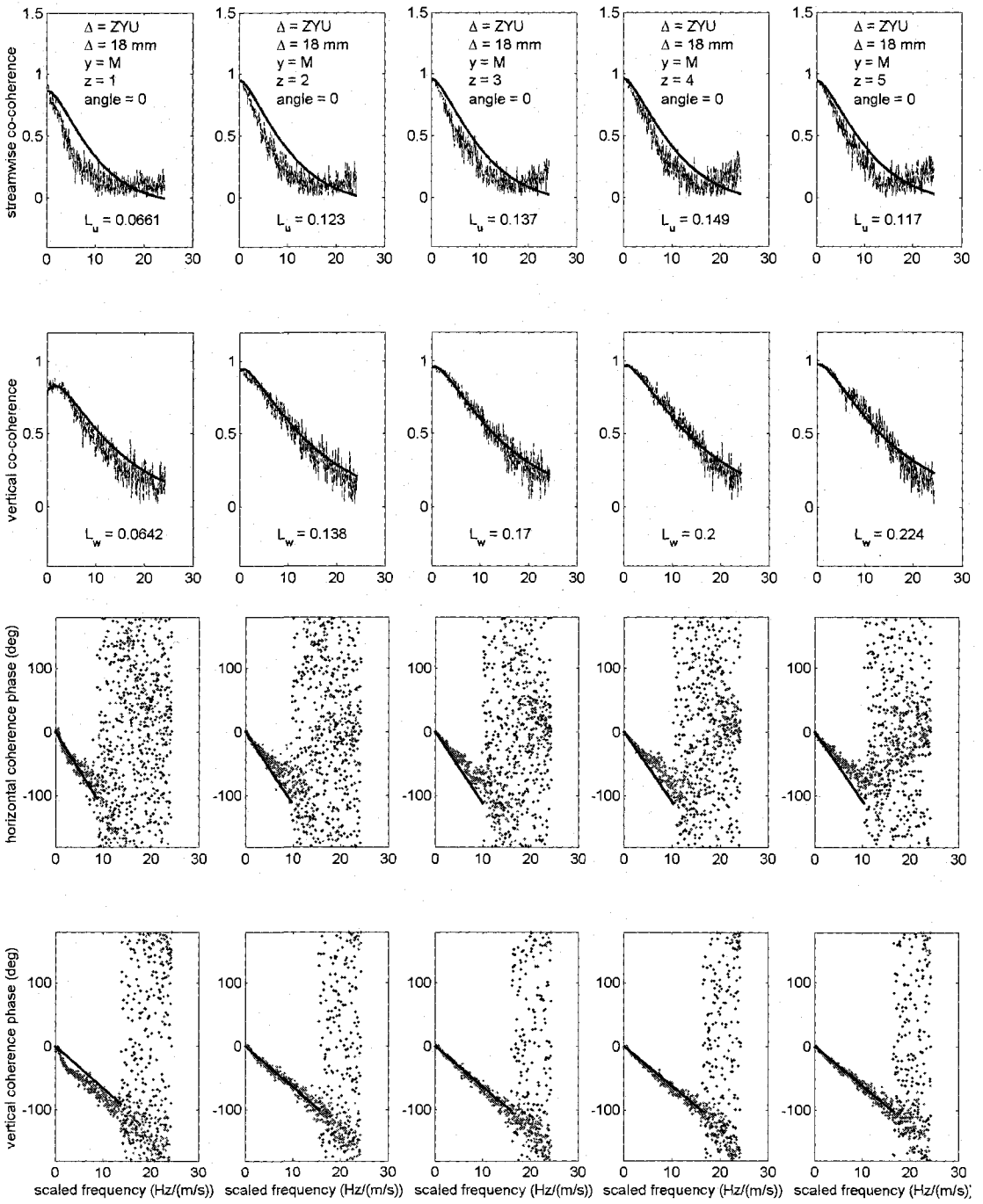

Figure C.21: Root coherence (top) and phase angle (bottom) model agreement (points 61-65).

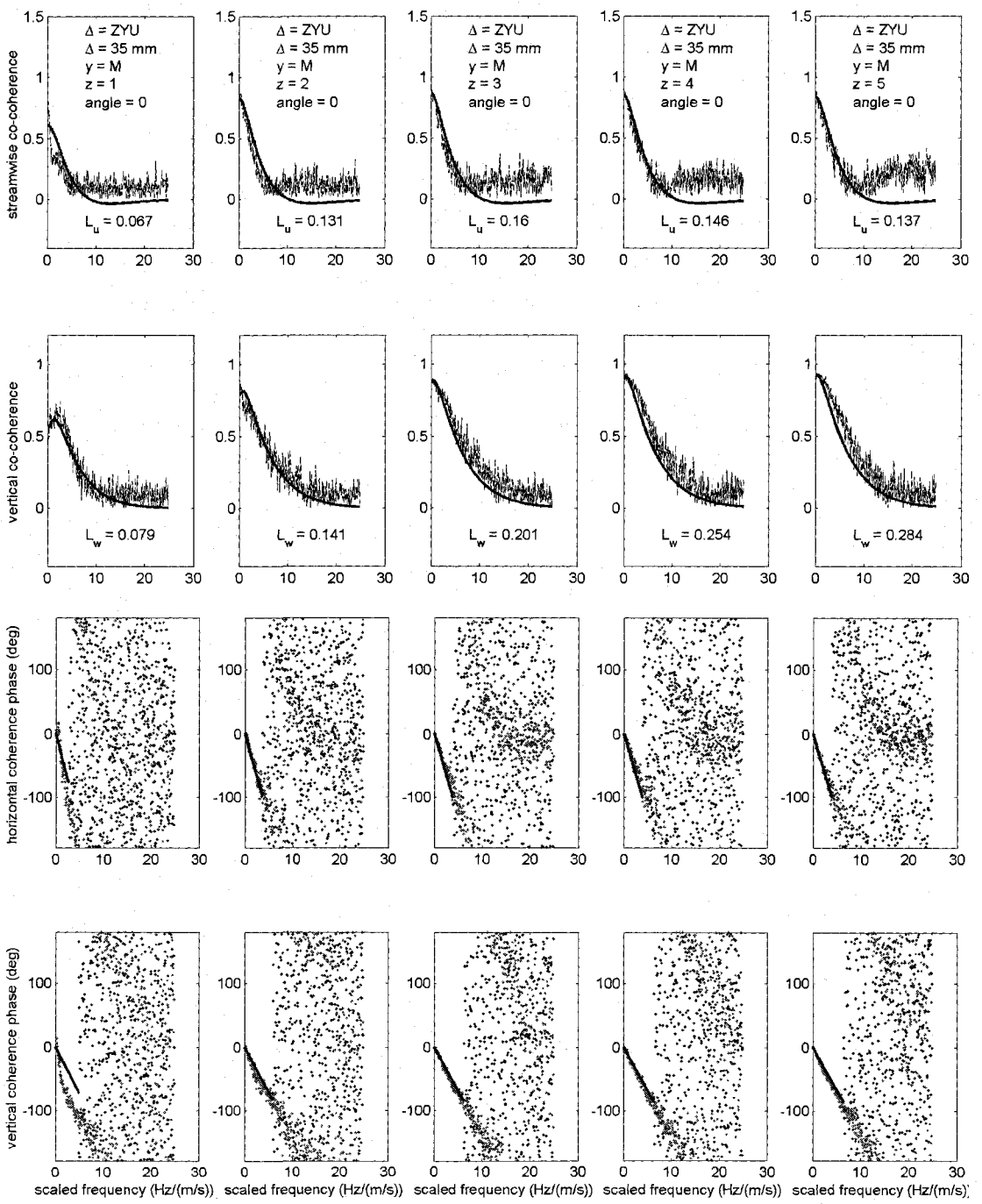

Figure C.22: Root coherence (top) and phase angle (bottom) model agreement (points 66-70).

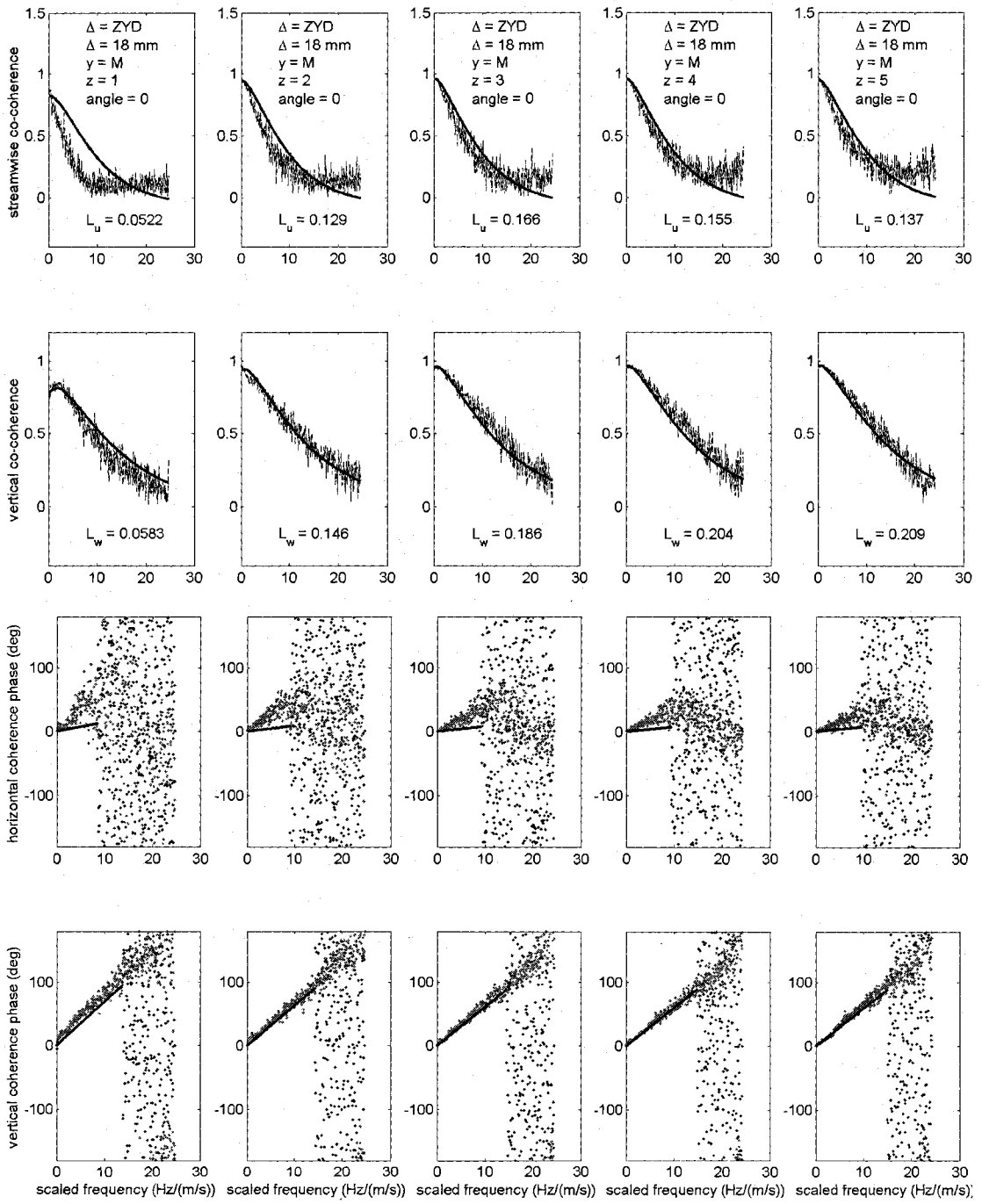

Figure C.23: Root coherence (top) and phase angle (bottom) model agreement (points 71-75).

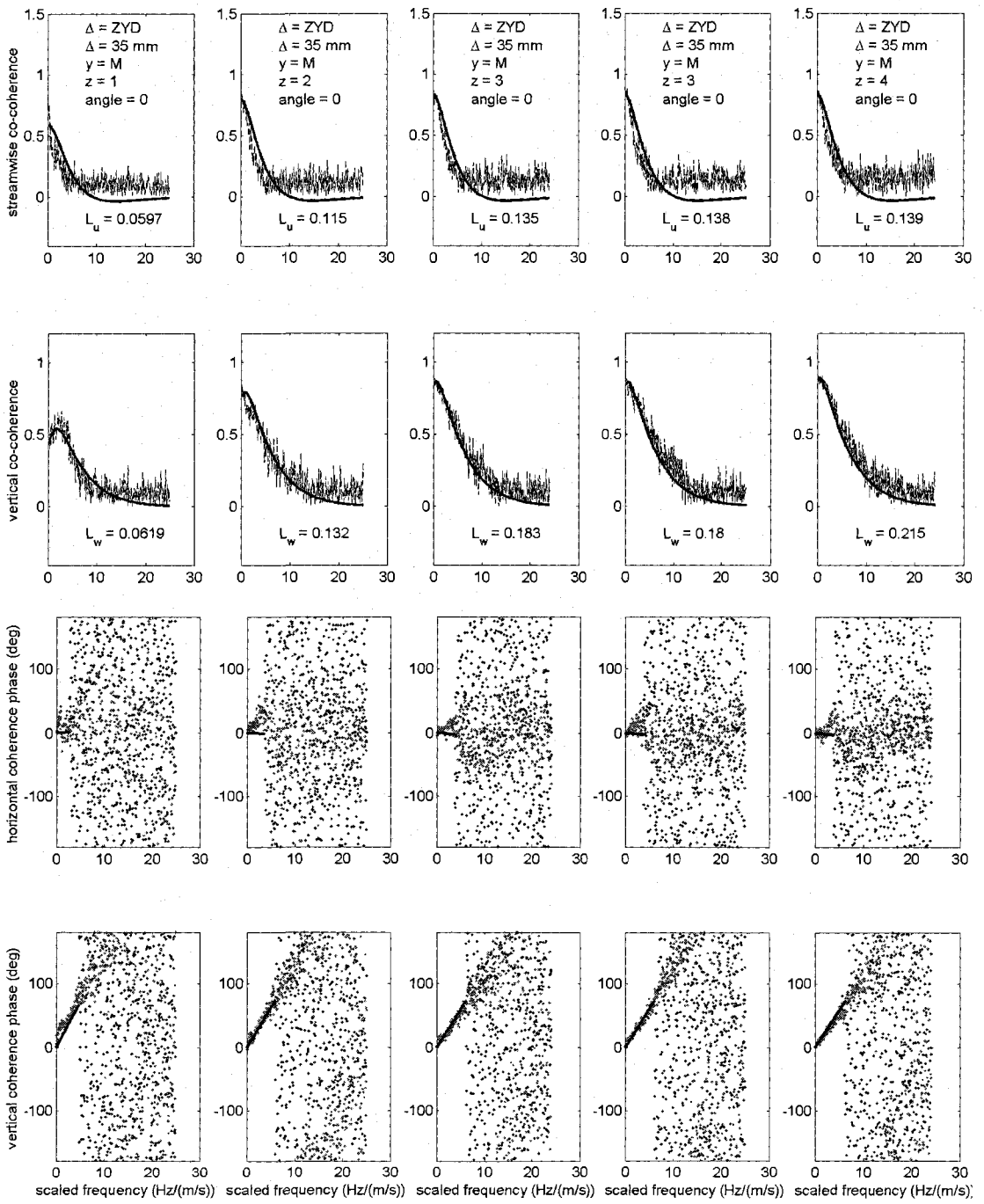

Figure C.24: Root coherence (top) and phase angle (bottom) model agreement (points 76-80).

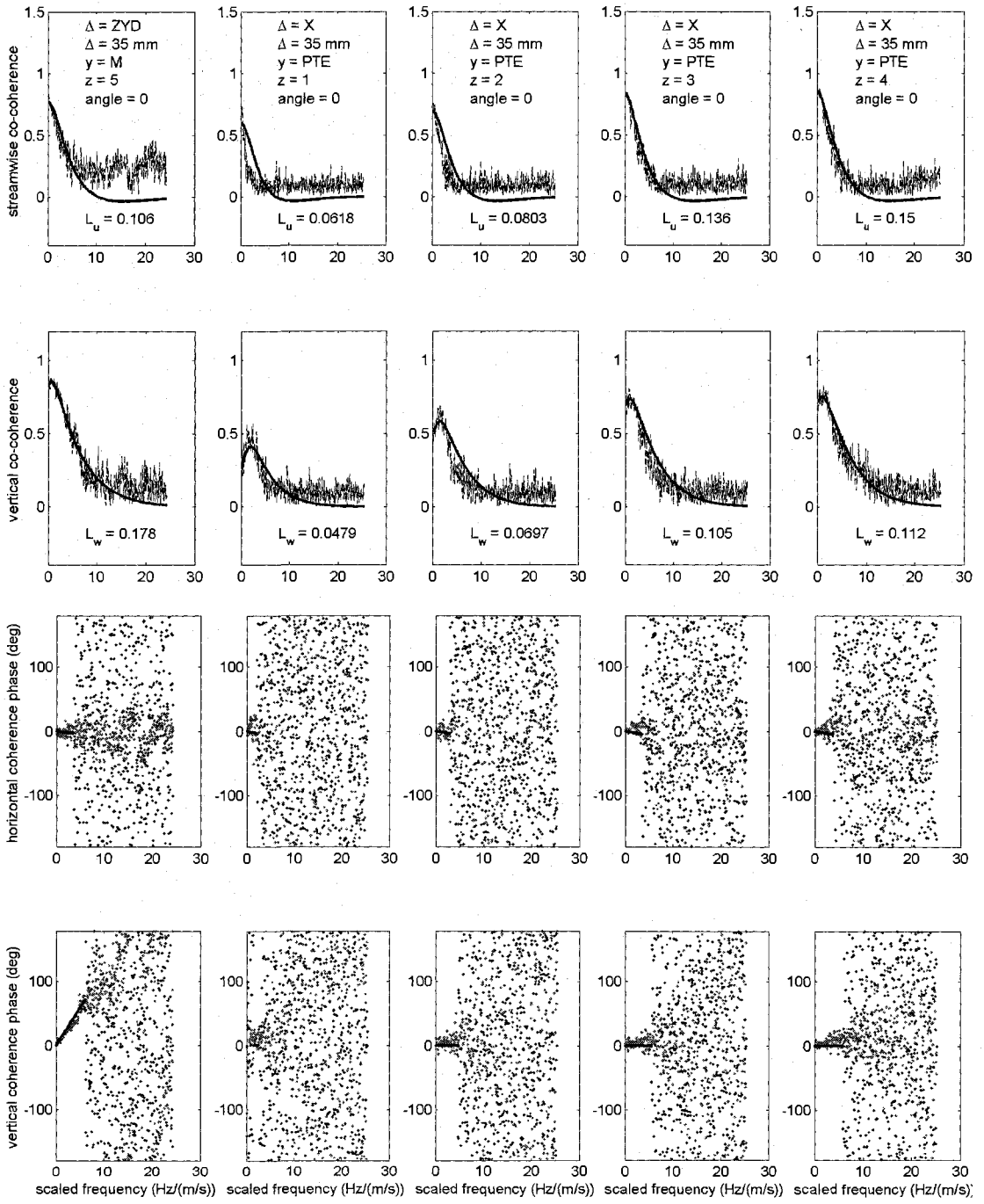

Figure C.25: Root coherence (top) and phase angle (bottom) model agreement (points 81-85).

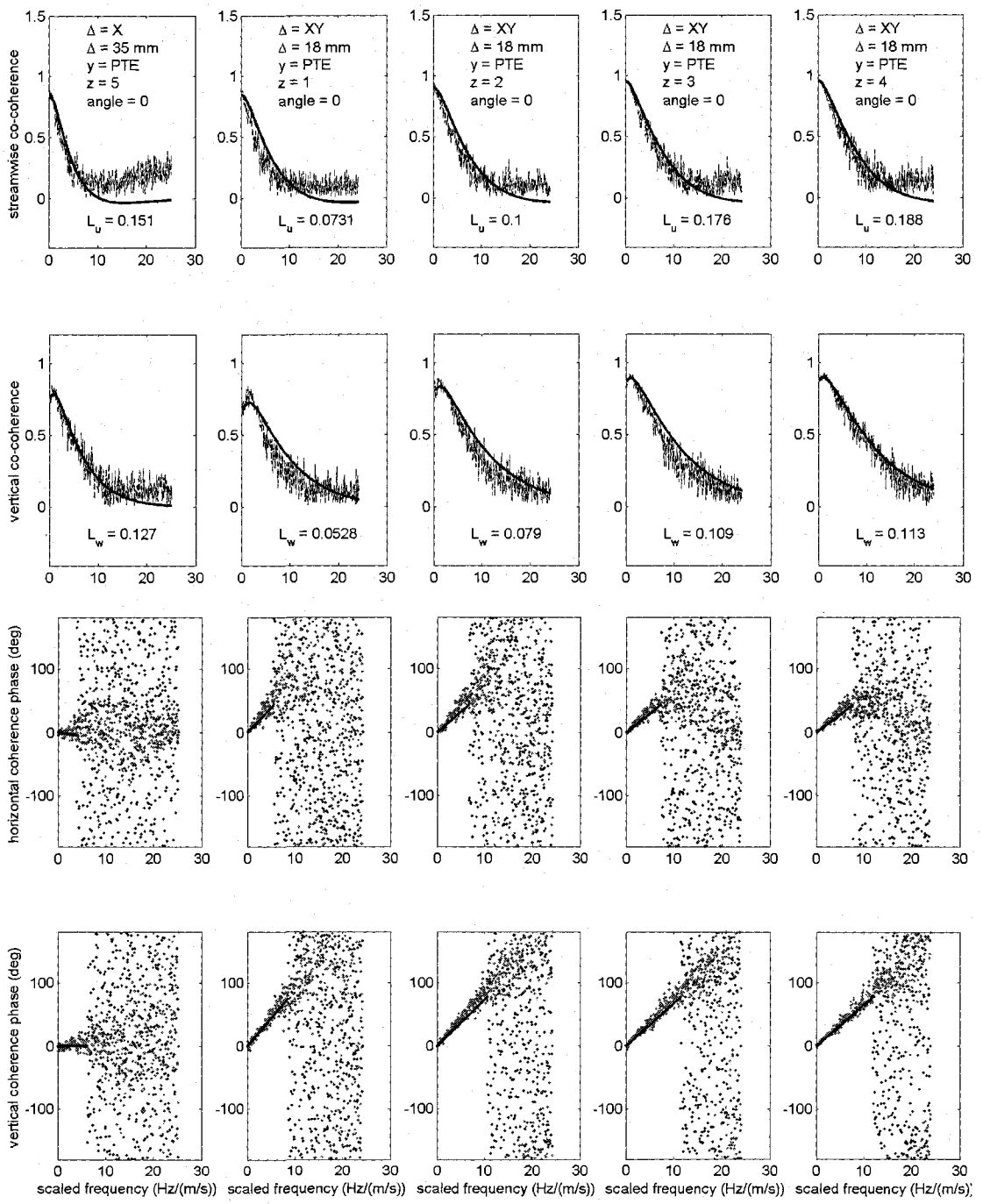

Figure C.26: Root coherence (top) and phase angle (bottom) model agreement (points 86-90).

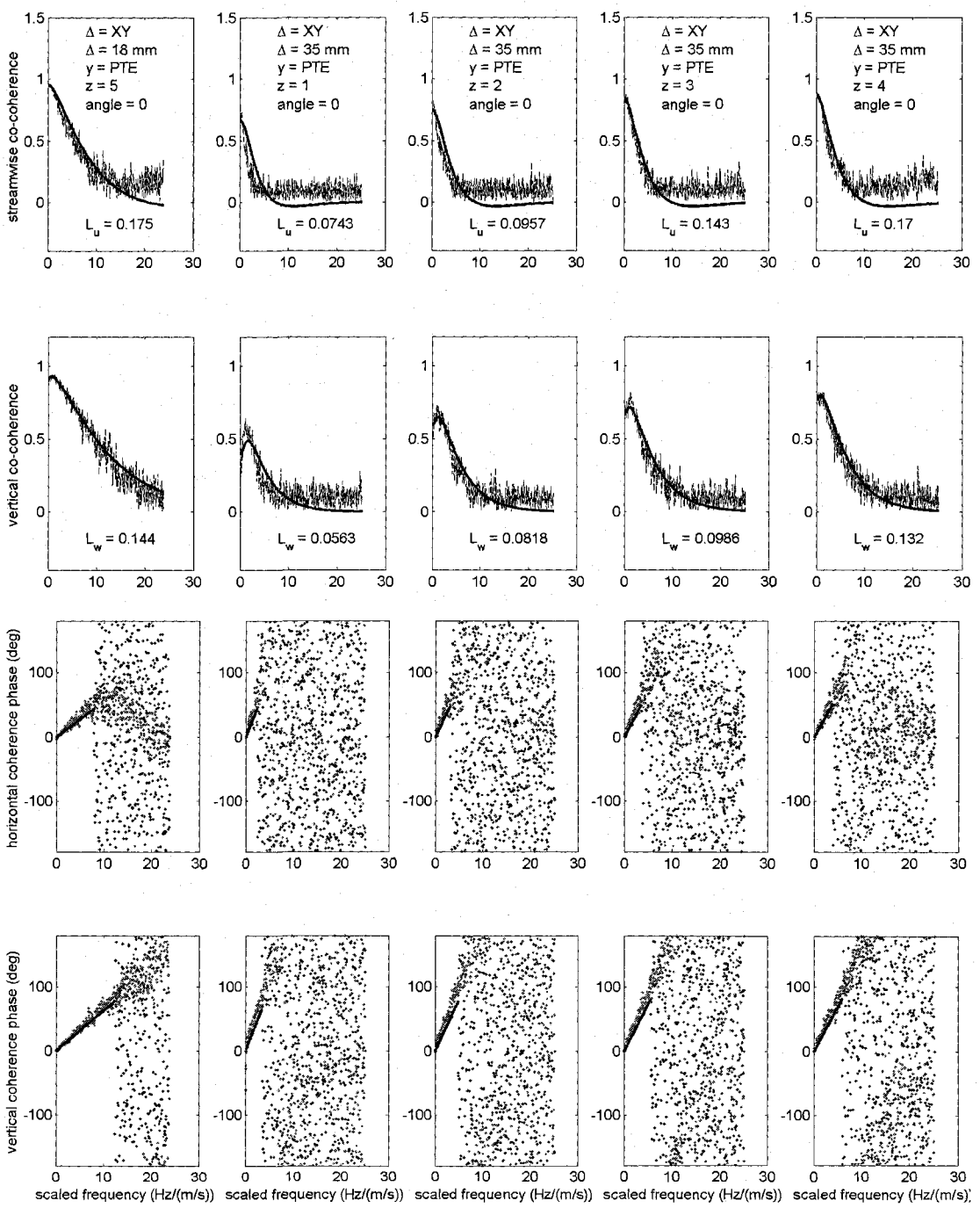

Figure C.27: Root coherence (top) and phase angle (bottom) model agreement (points 91-95).

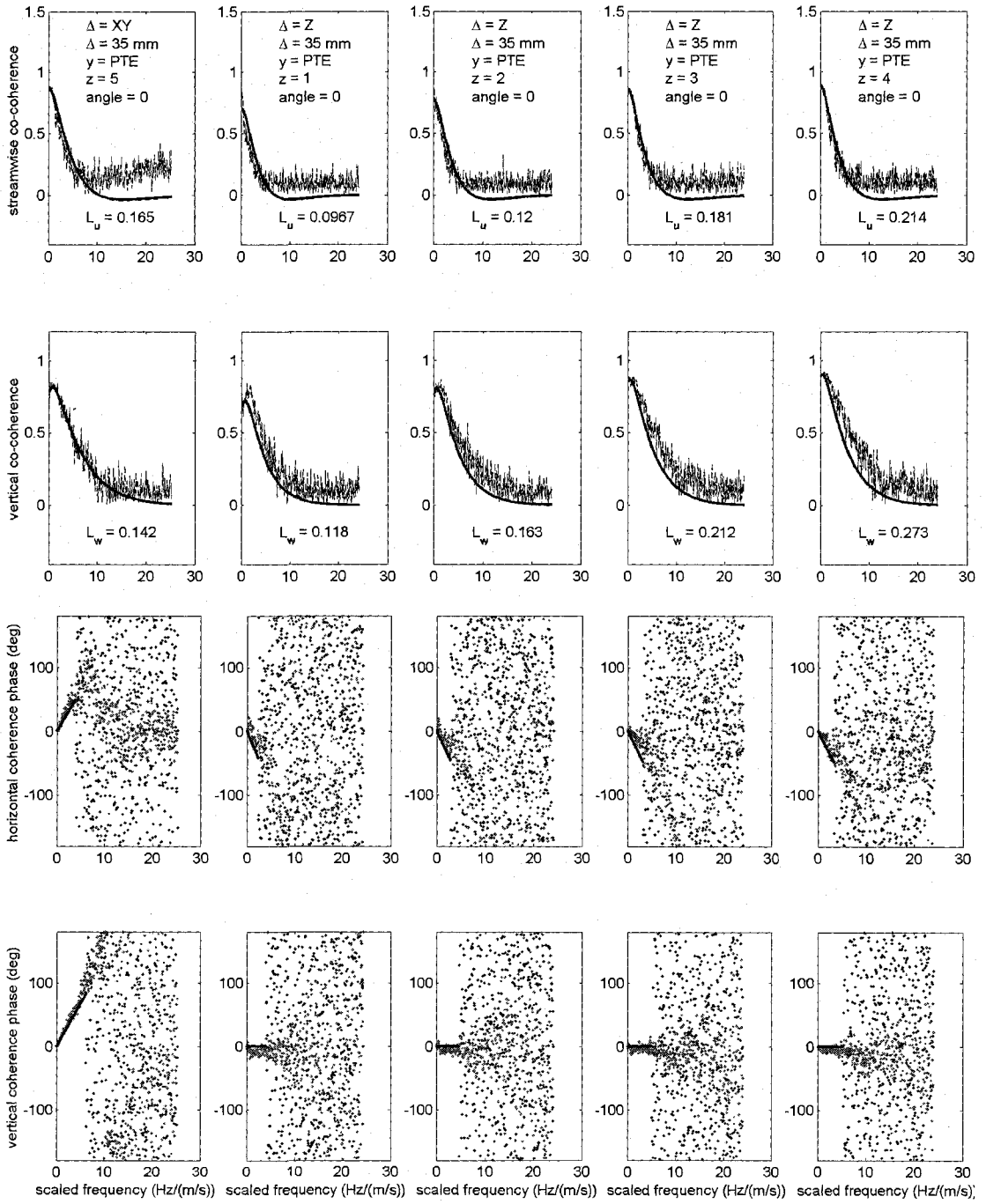

Figure C.28: Root coherence (top) and phase angle (bottom) model agreement (points 96-100).

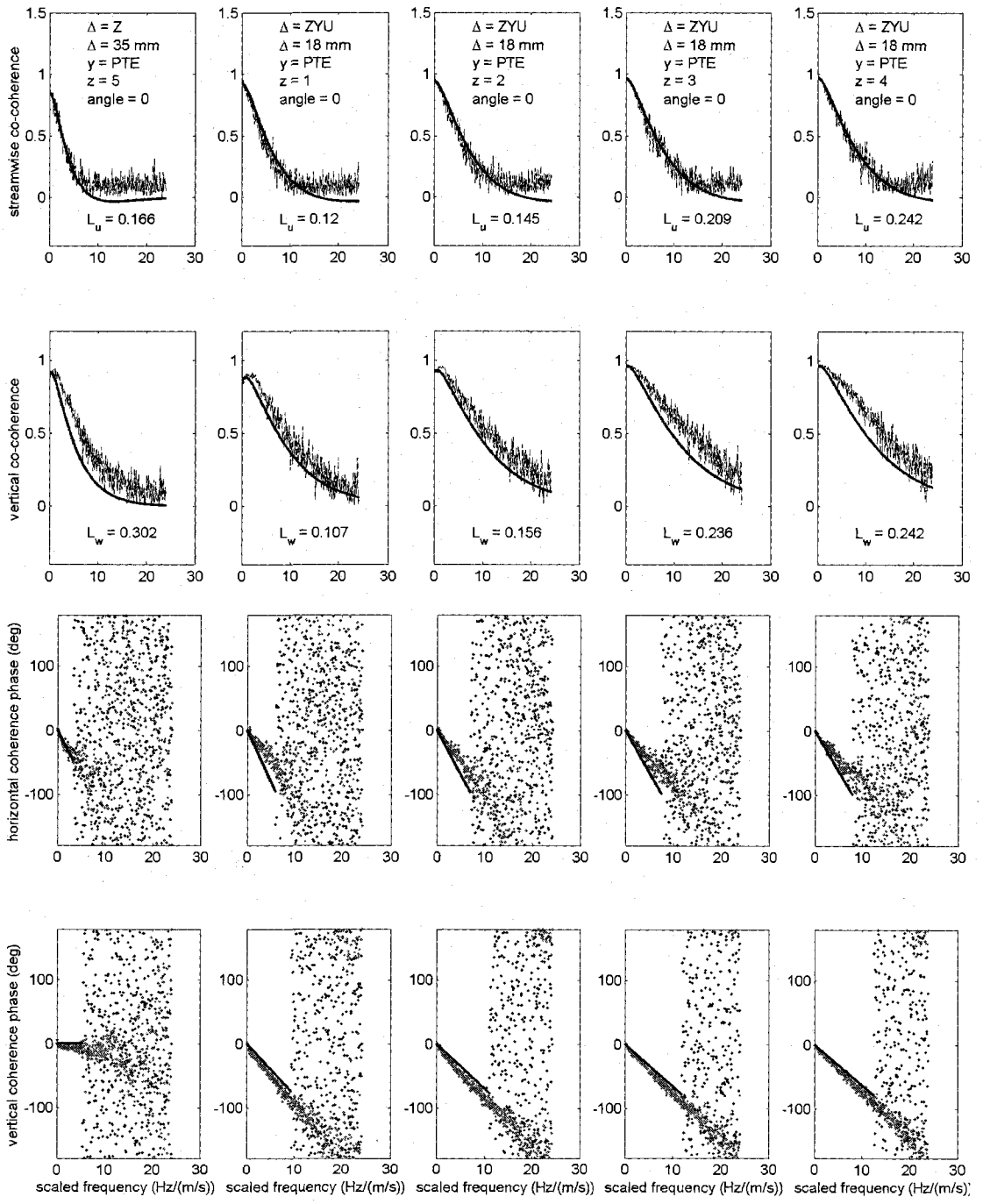

Figure C.29: Root coherence (top) and phase angle (bottom) model agreement (points 101-105).

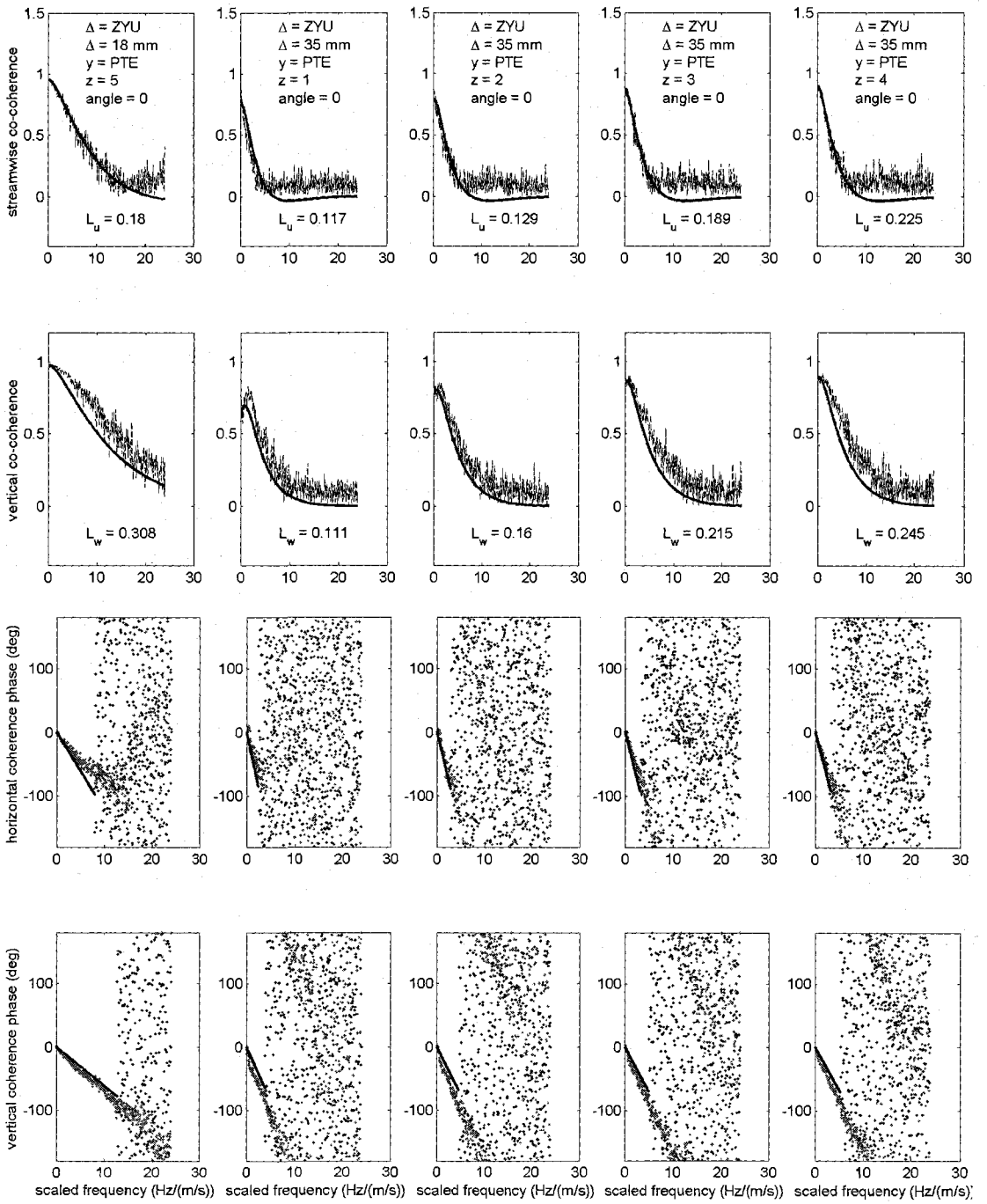

Figure C.30: Root coherence (top) and phase angle (bottom) model agreement (points 106-110).

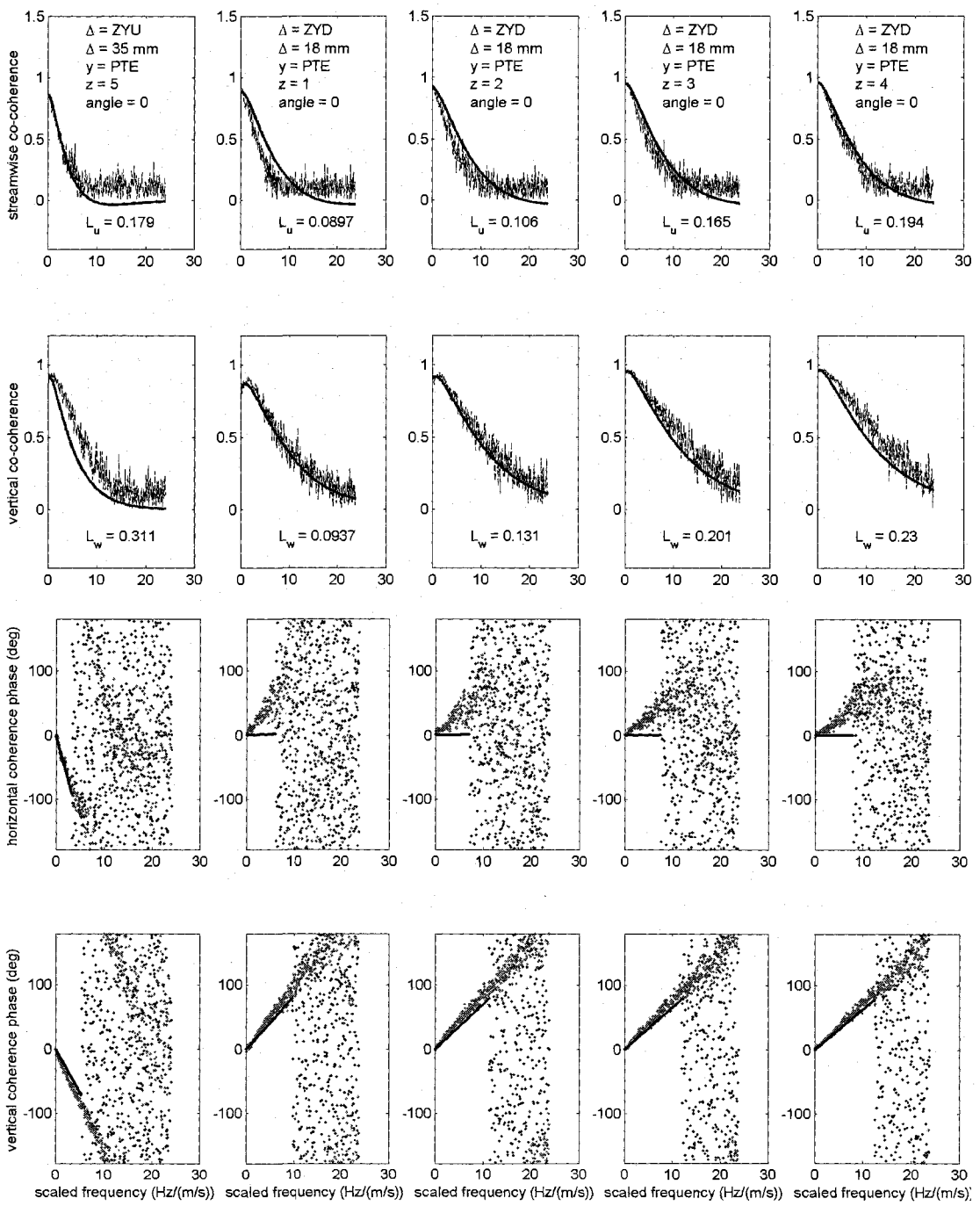

Figure C.31: Root coherence (top) and phase angle (bottom) model agreement (points 111-115).

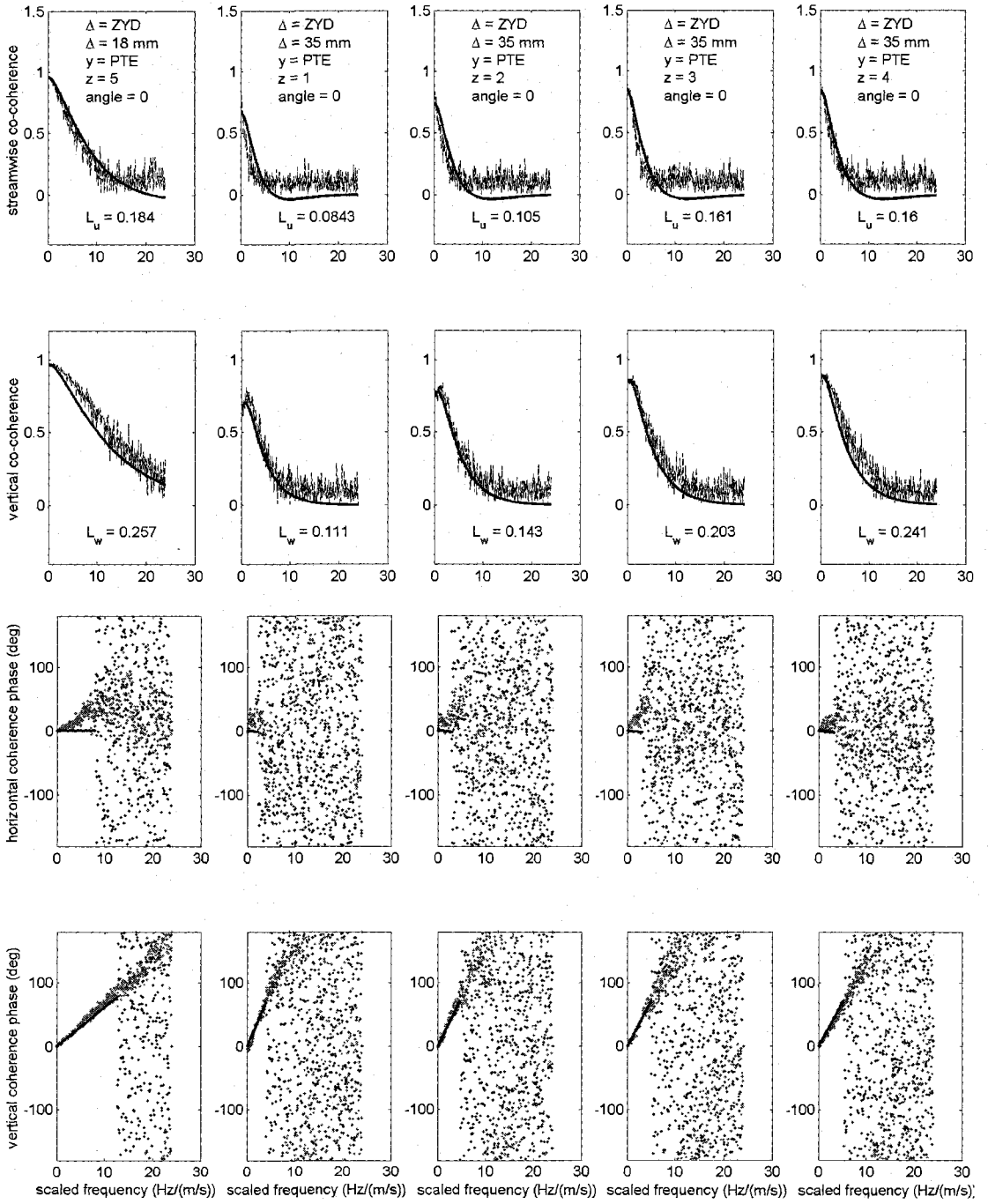

Figure C.32: Root coherence (top) and phase angle (bottom) model agreement (points 116-120).

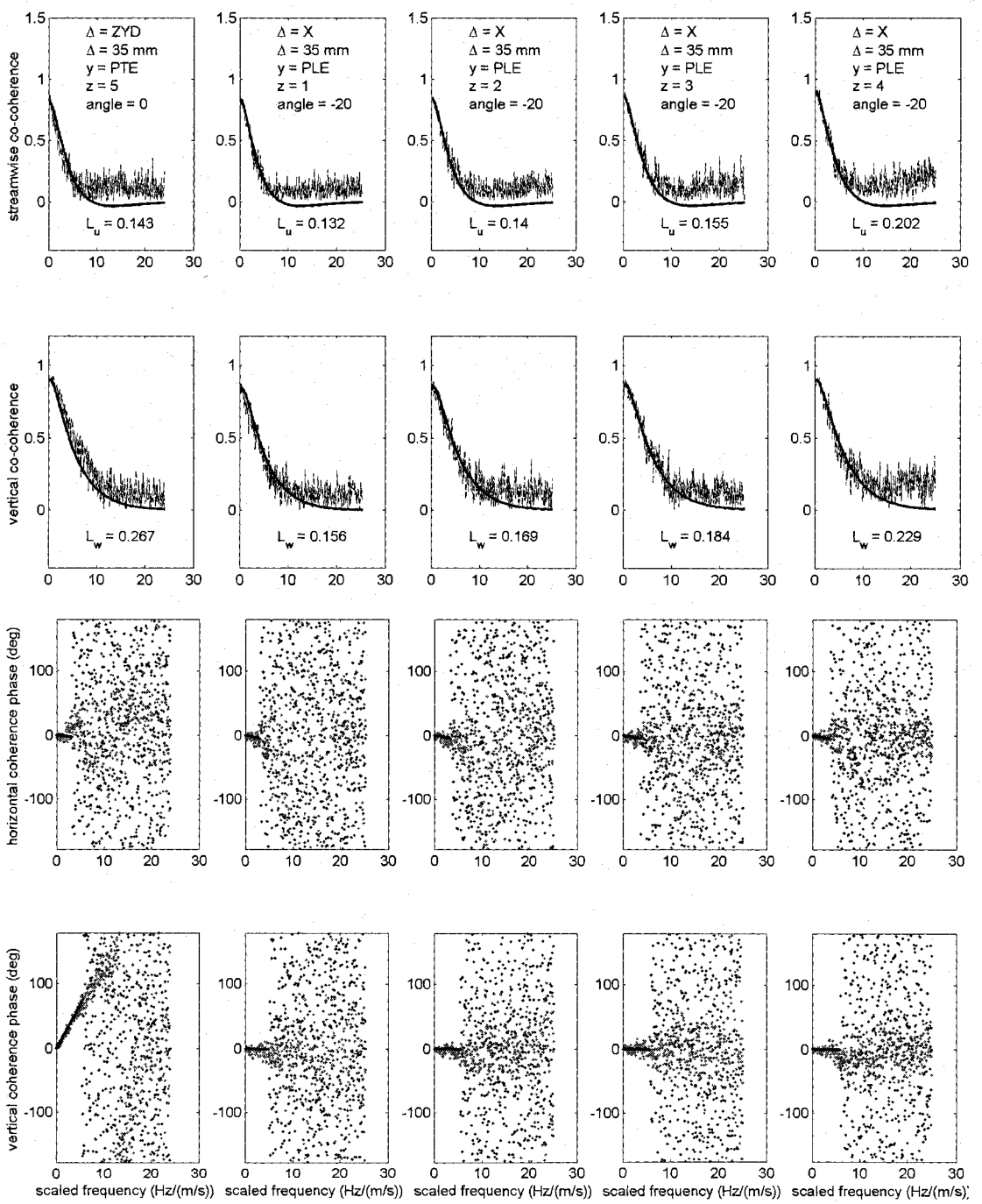

Figure C.33: Root coherence (top) and phase angle (bottom) model agreement (points 121-125).

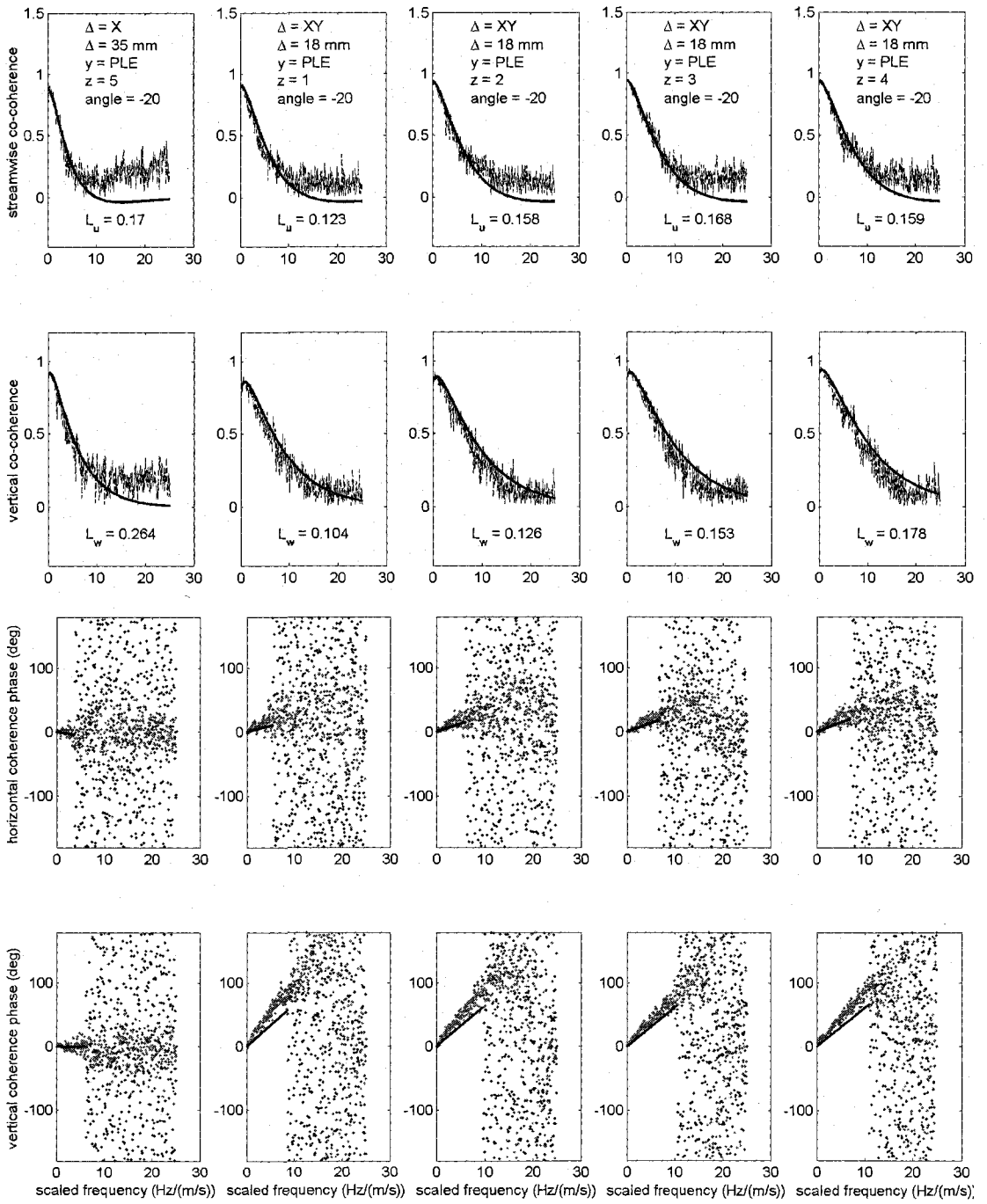

Figure C.34: Root coherence (top) and phase angle (bottom) model agreement (points 126-130).

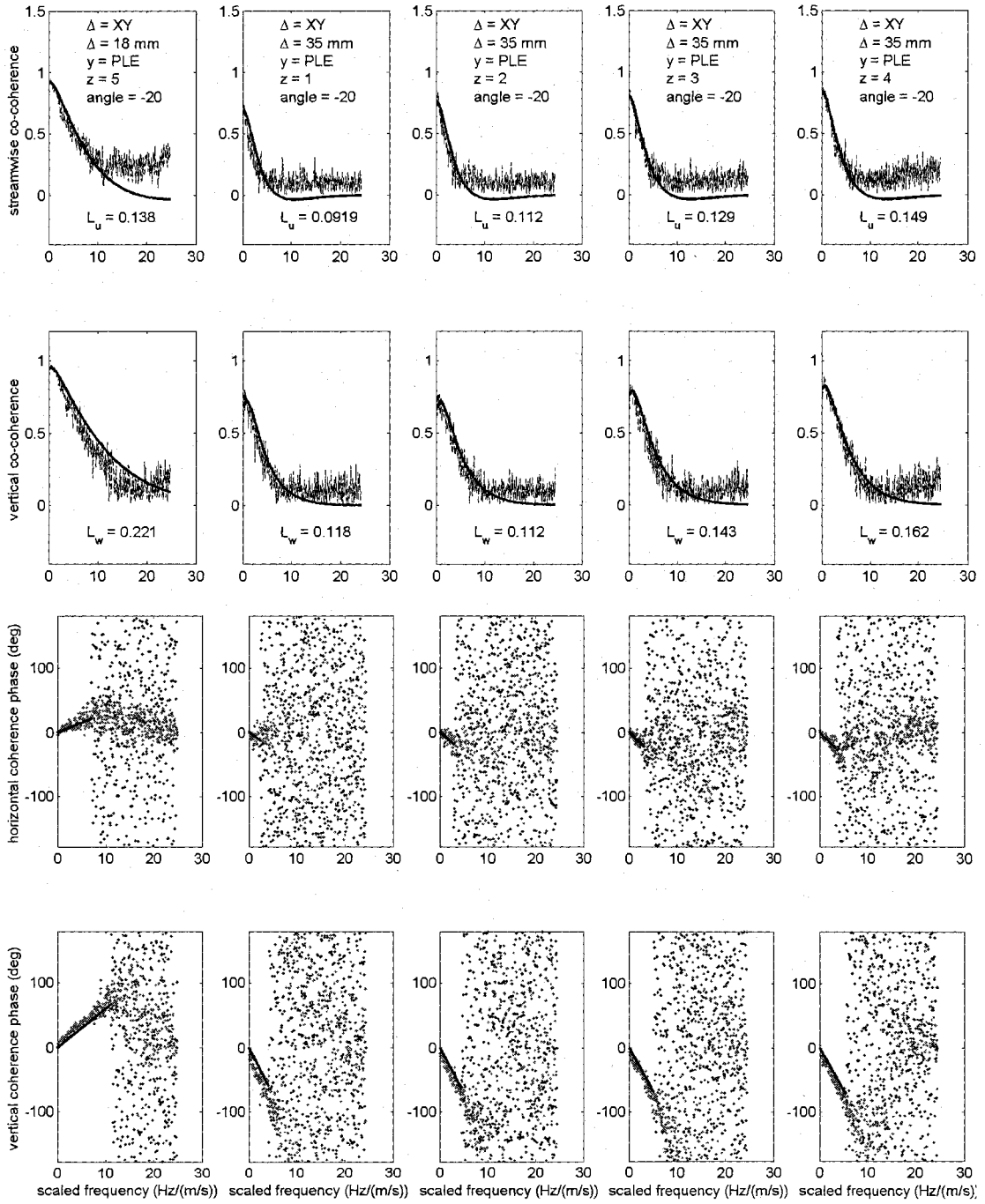

Figure C.35: Root coherence (top) and phase angle (bottom) model agreement (points 131-135).

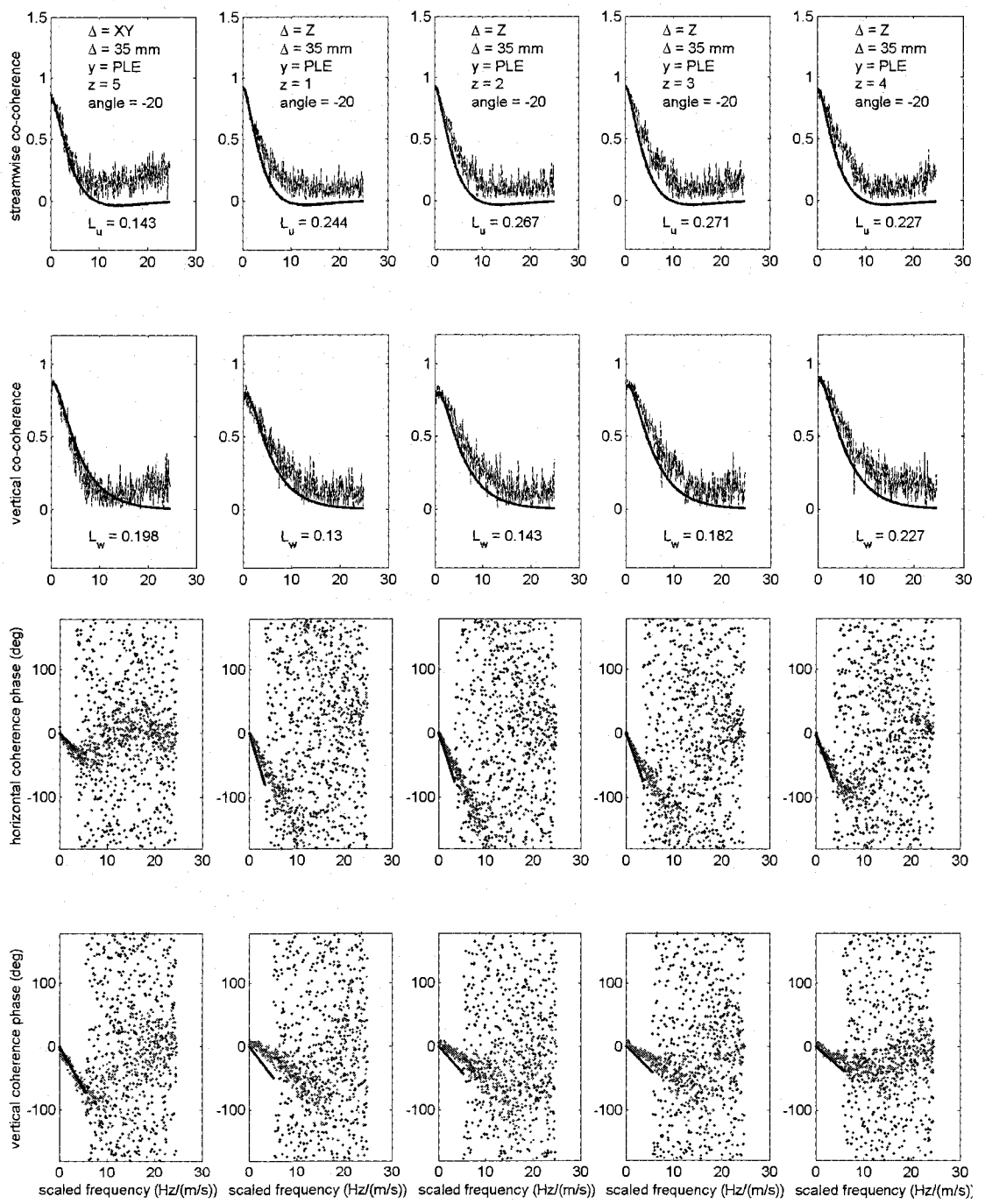

Figure C.36: Root coherence (top) and phase angle (bottom) model agreement (points 136-140).

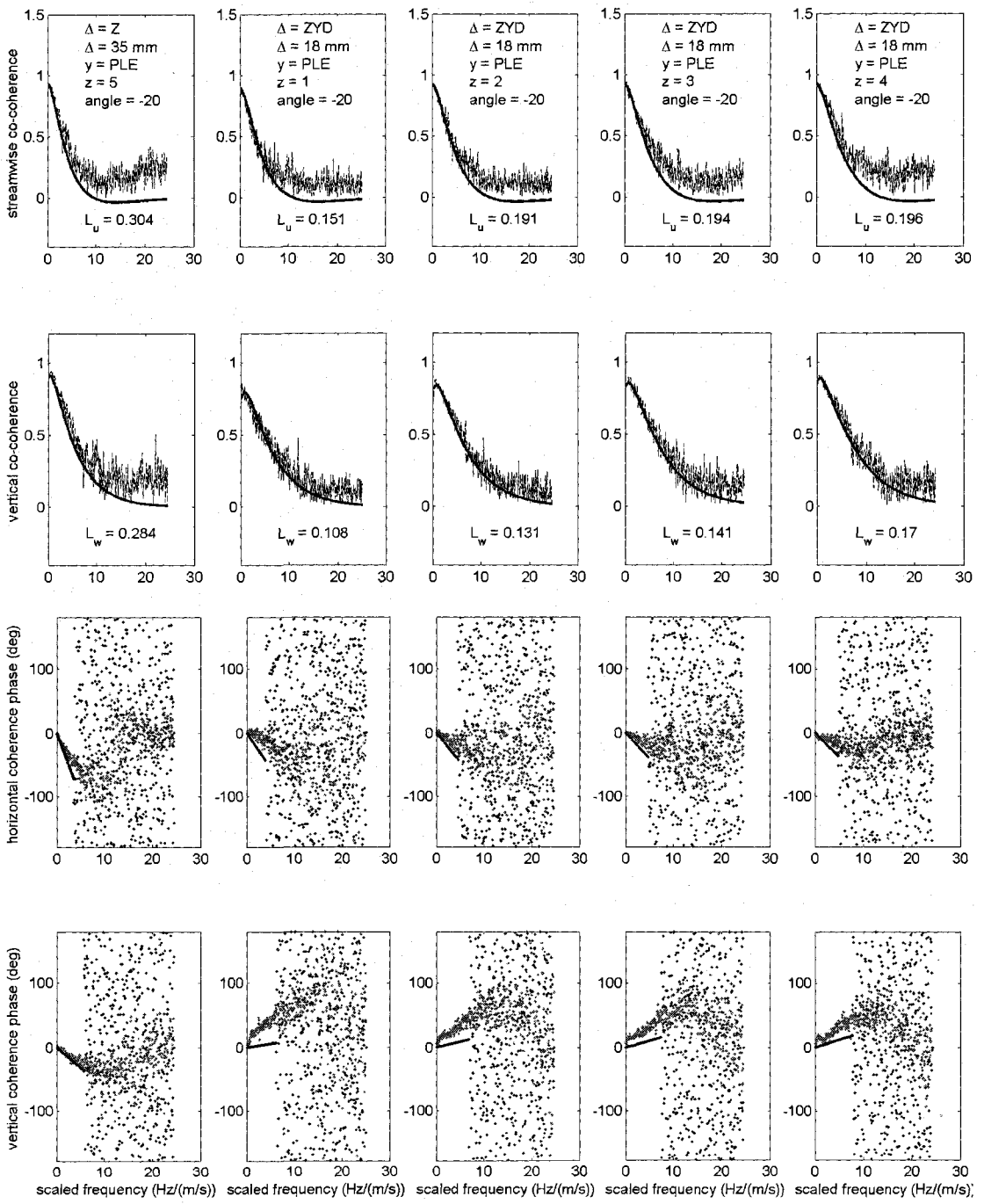

Figure C.37: Root coherence (top) and phase angle (bottom) model agreement (points 141-145).

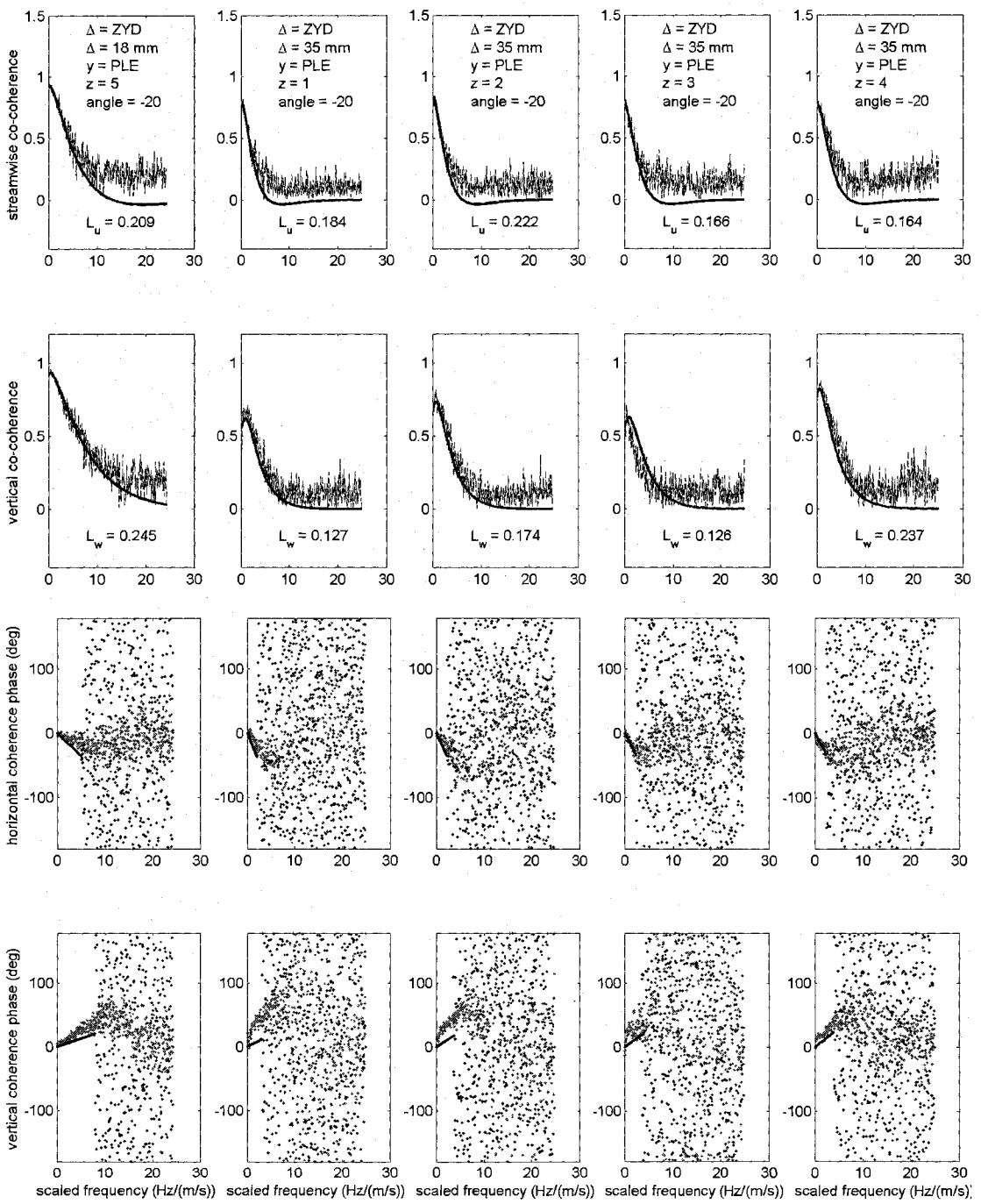

Figure C.38: Root coherence (top) and phase angle (bottom) model agreement (points 146-150).

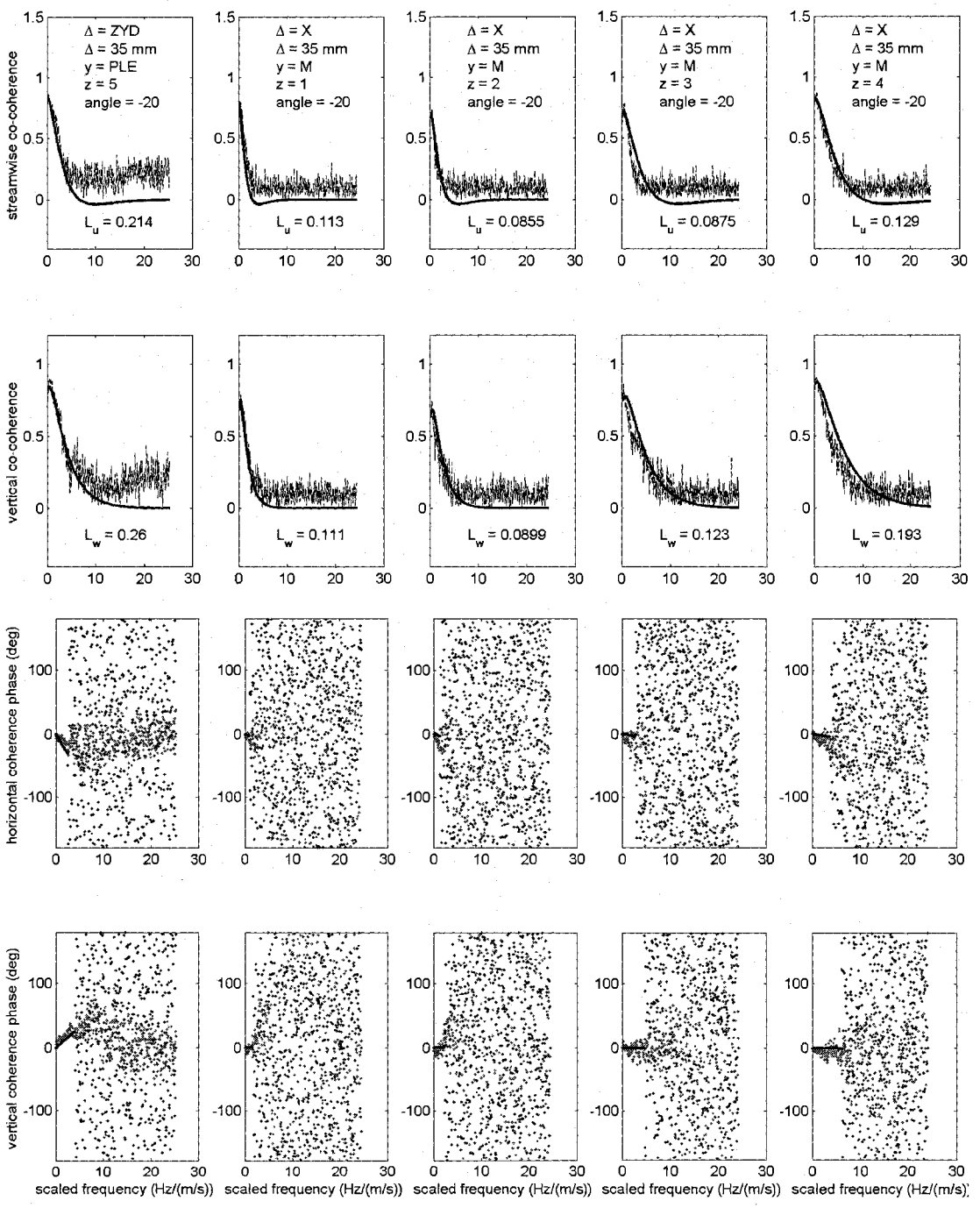

Figure C.39: Root coherence (top) and phase angle (bottom) model agreement (points 151-155).

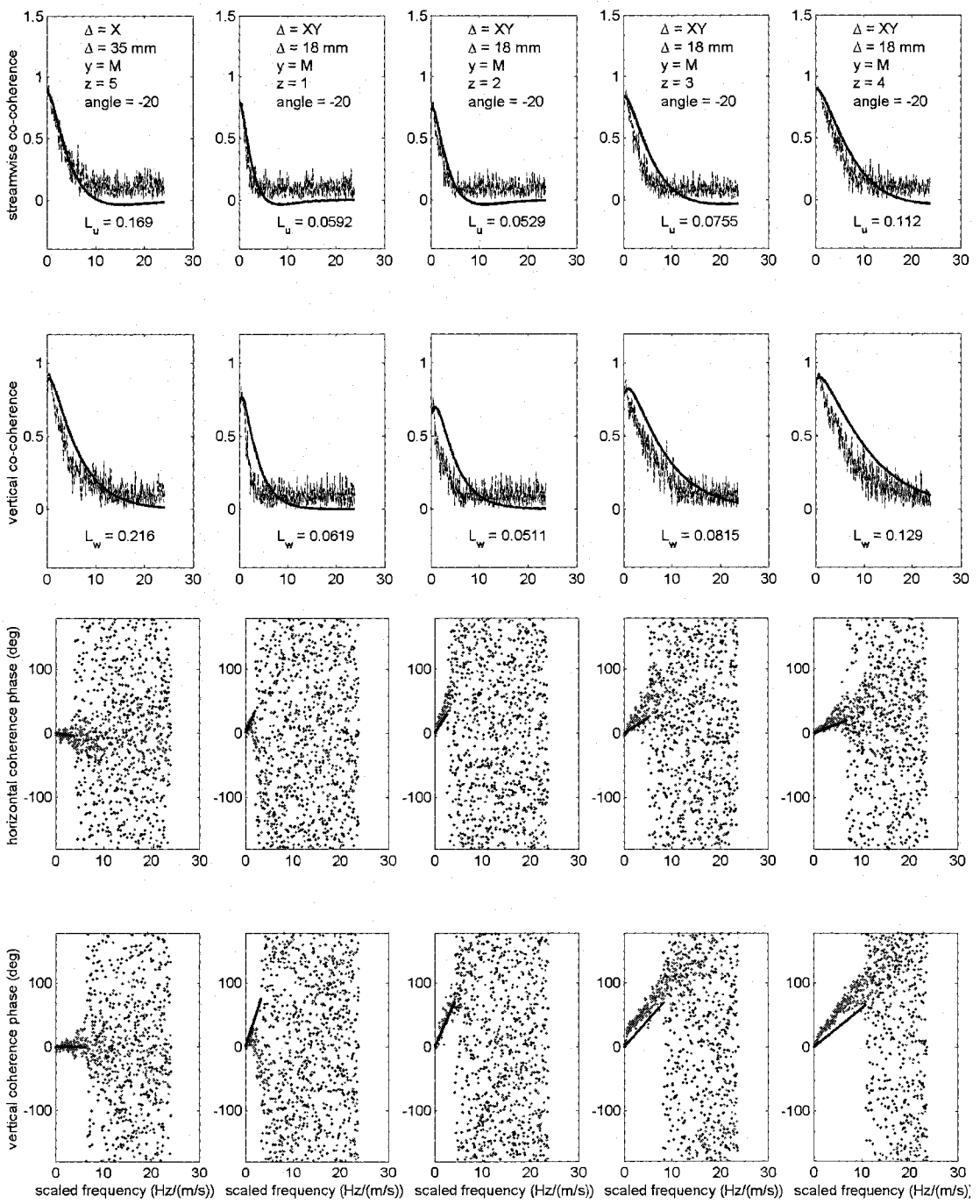

Figure C.40: Root coherence (top) and phase angle (bottom) model agreement (points 156-160).

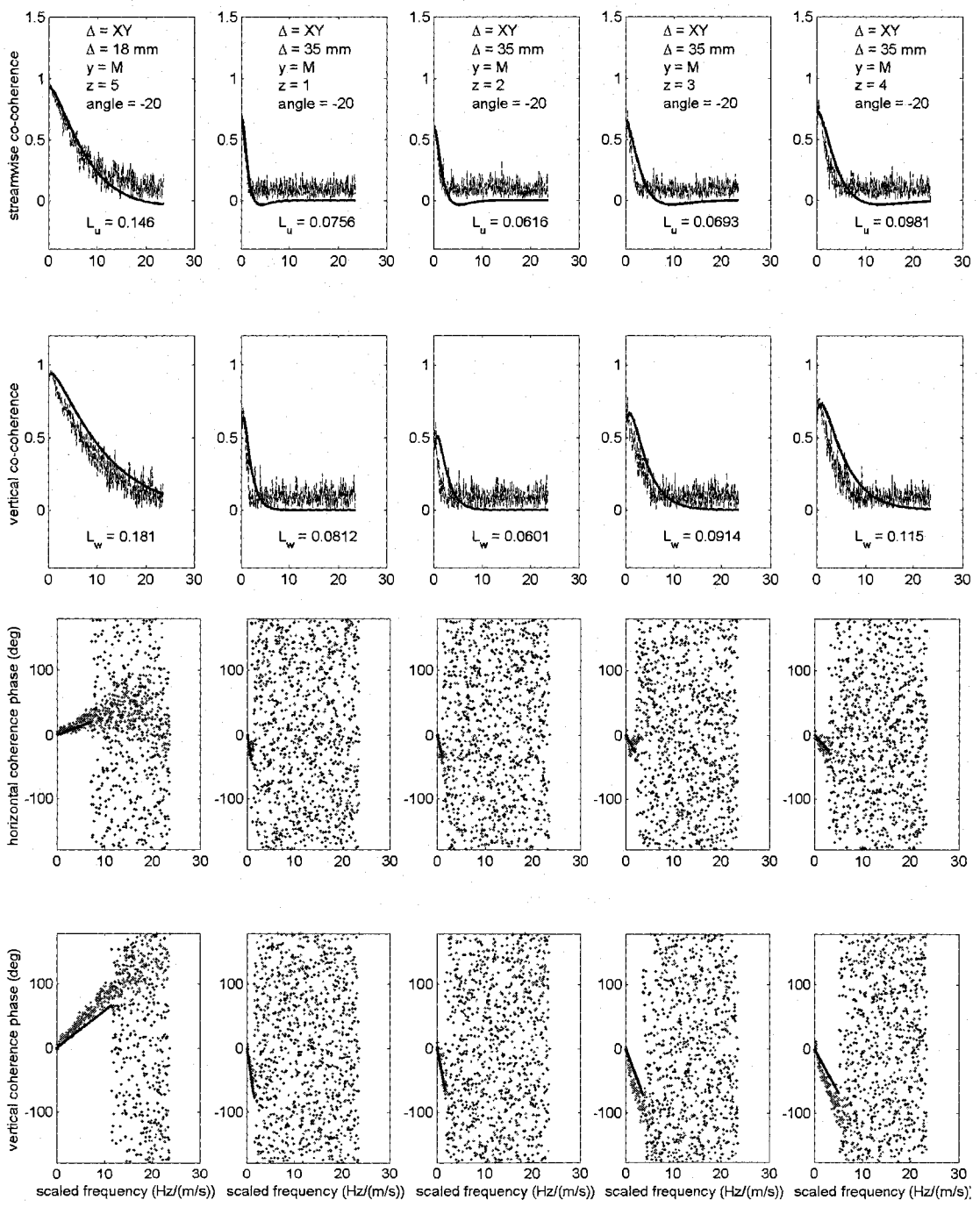

Figure C.41: Root coherence (top) and phase angle (bottom) model agreement (points 161-165).

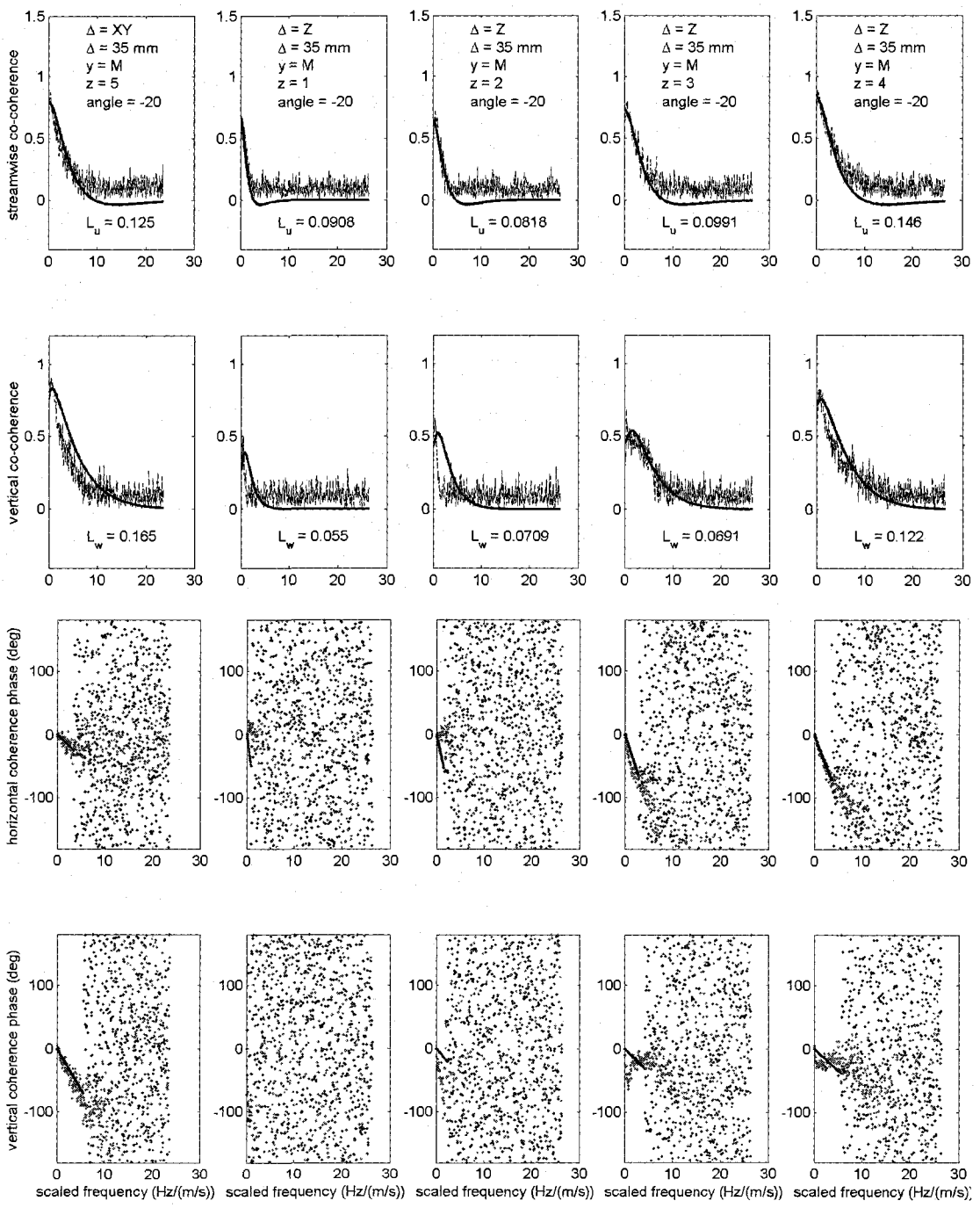

Figure C.42: Root coherence (top) and phase angle (bottom) model agreement (points 166-170).

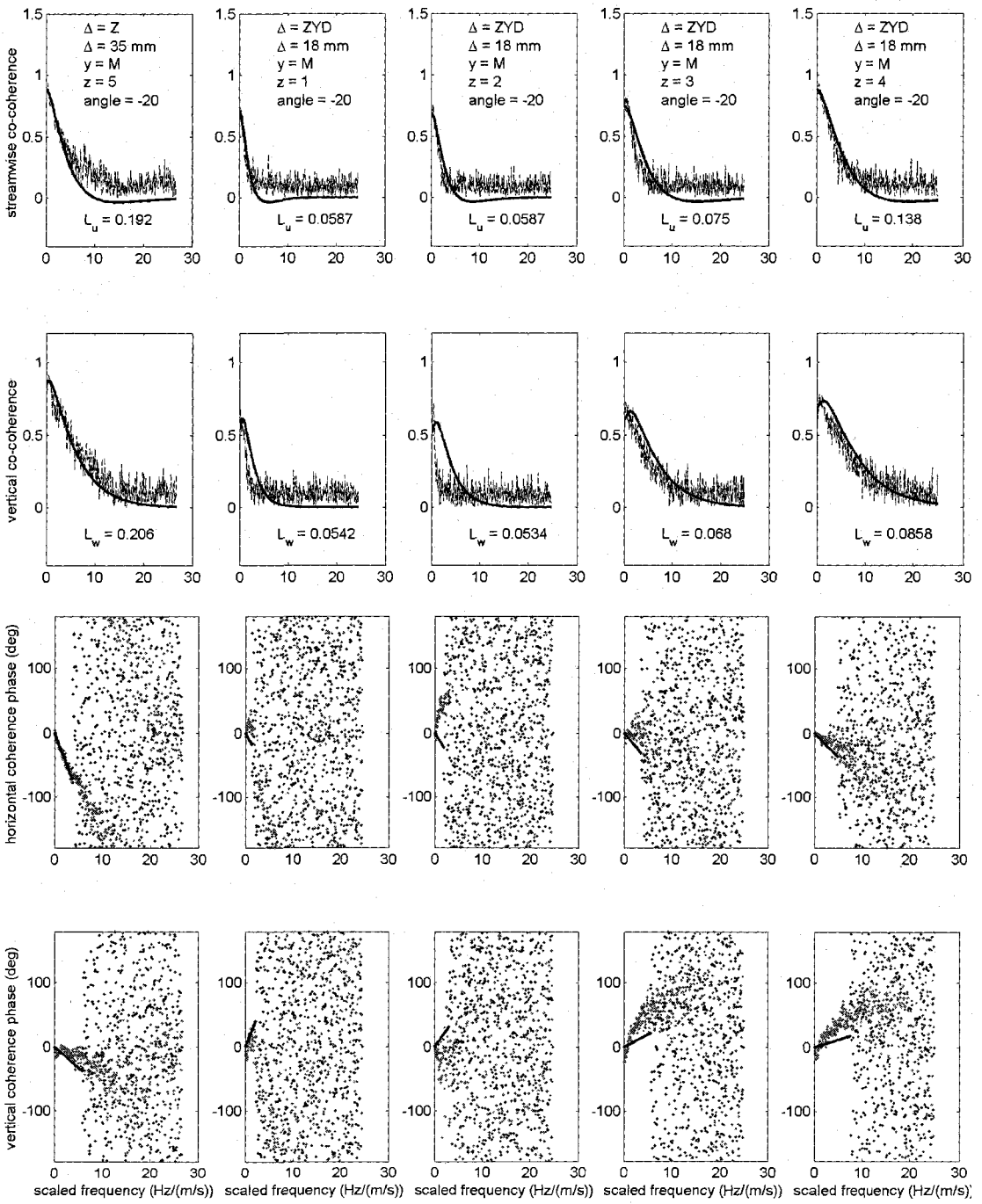

Figure C.43: Root coherence (top) and phase angle (bottom) model agreement (points 171-175).

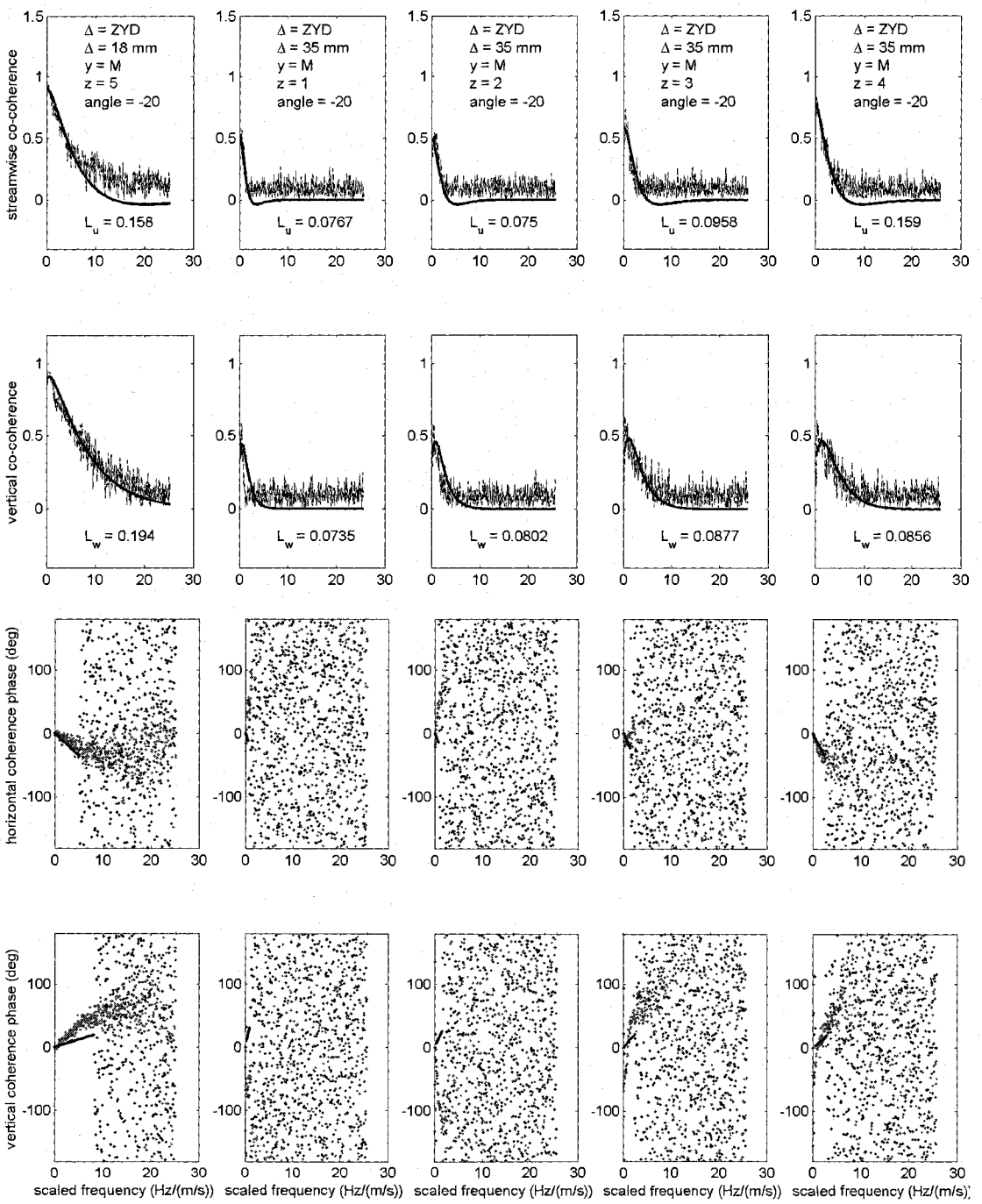

Figure C.44: Root coherence (top) and phase angle (bottom) model agreement (points 176-180).

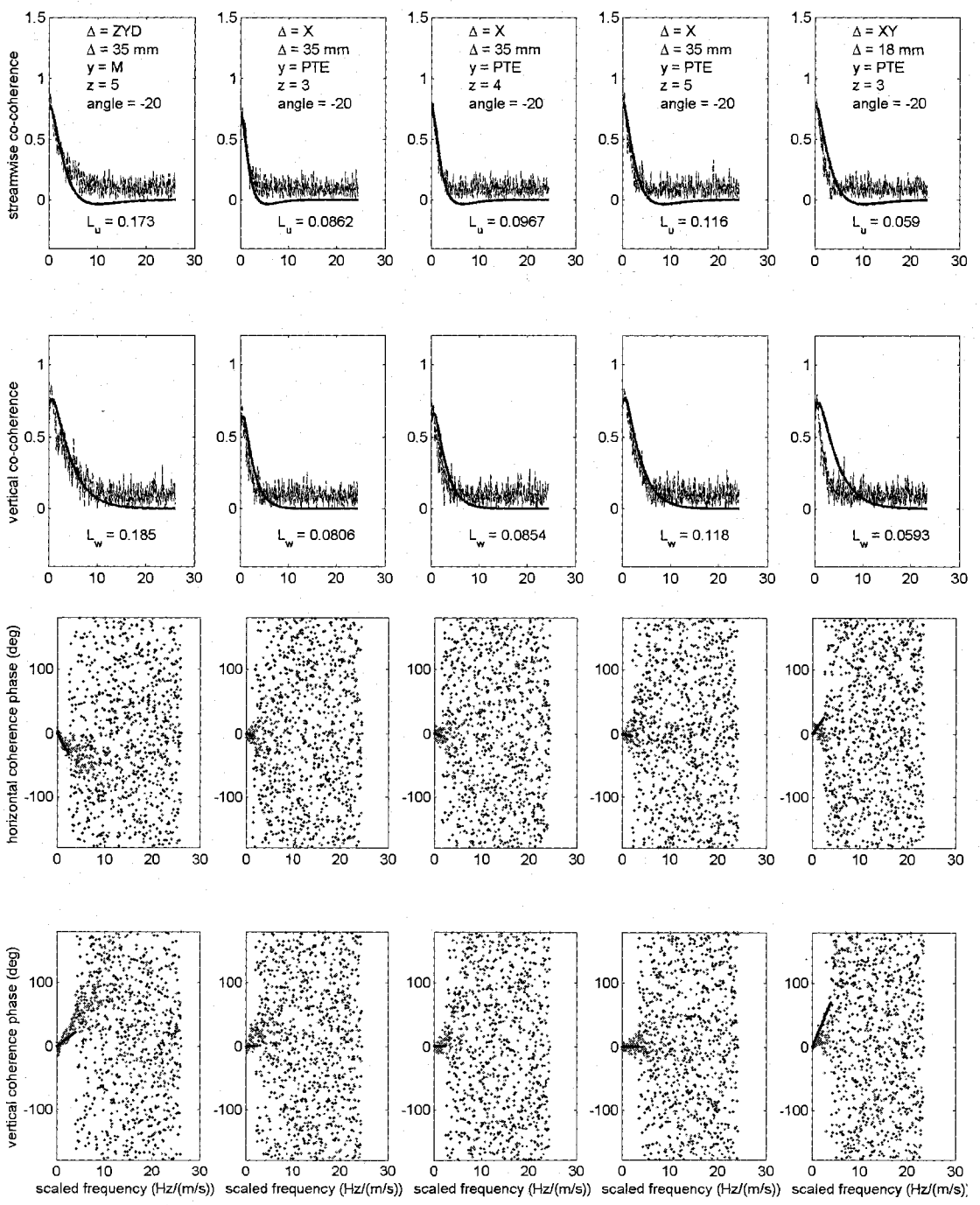

Figure C.45: Root coherence (top) and phase angle (bottom) model agreement (points 181-185).

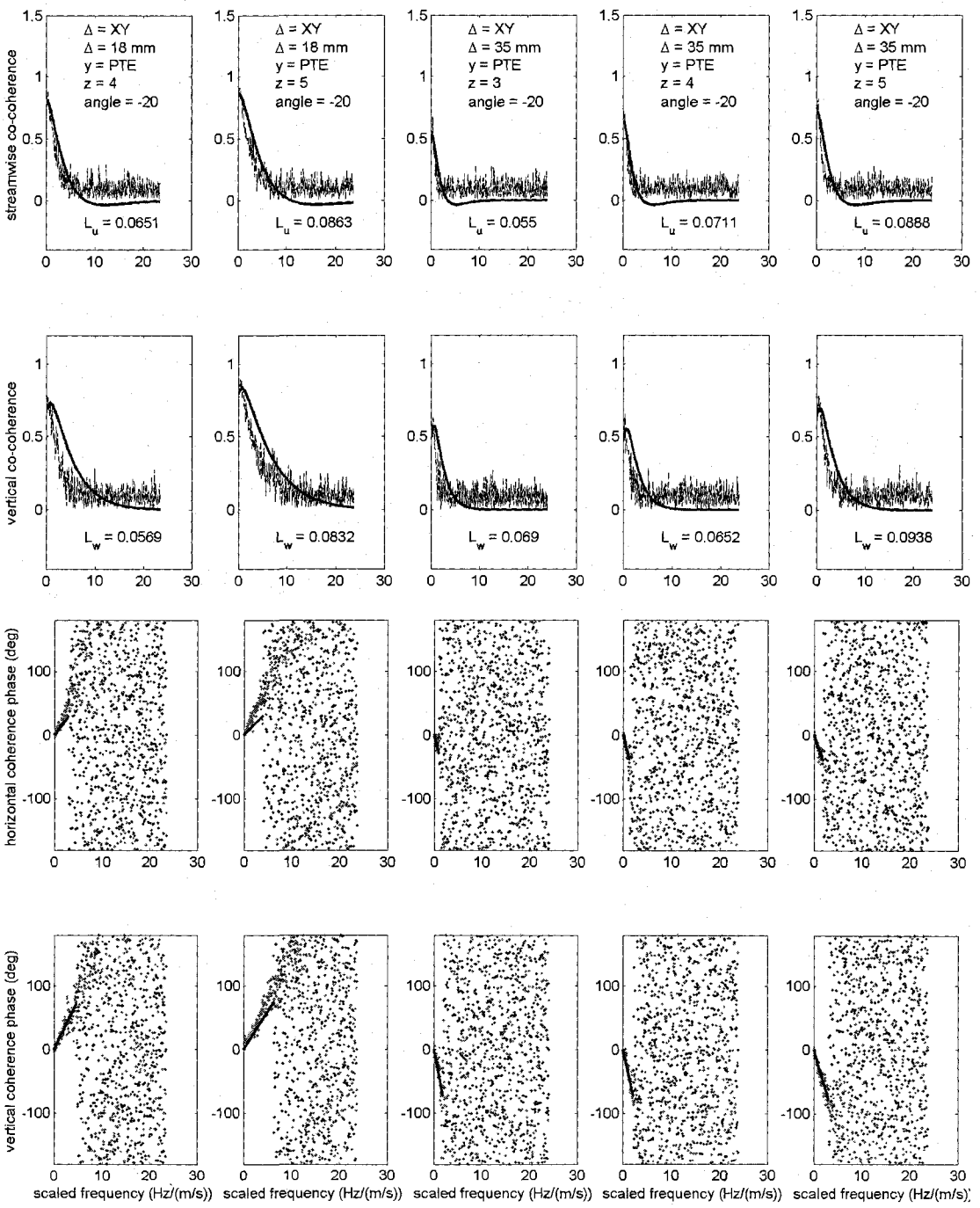

Figure C.46: Root coherence (top) and phase angle (bottom) model agreement (points 186-190).

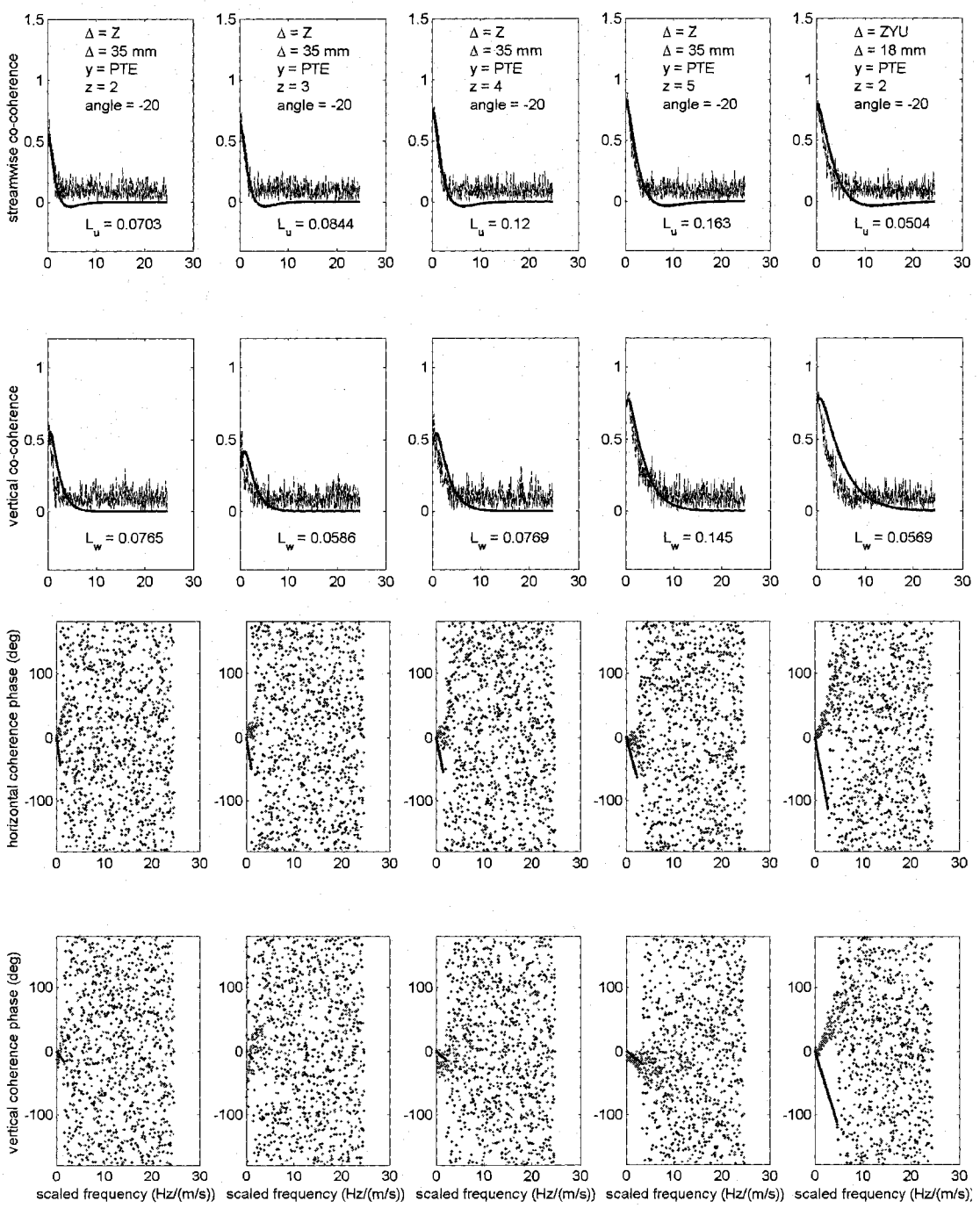

Figure C.47: Root coherence (top) and phase angle (bottom) model agreement (points 191-195).

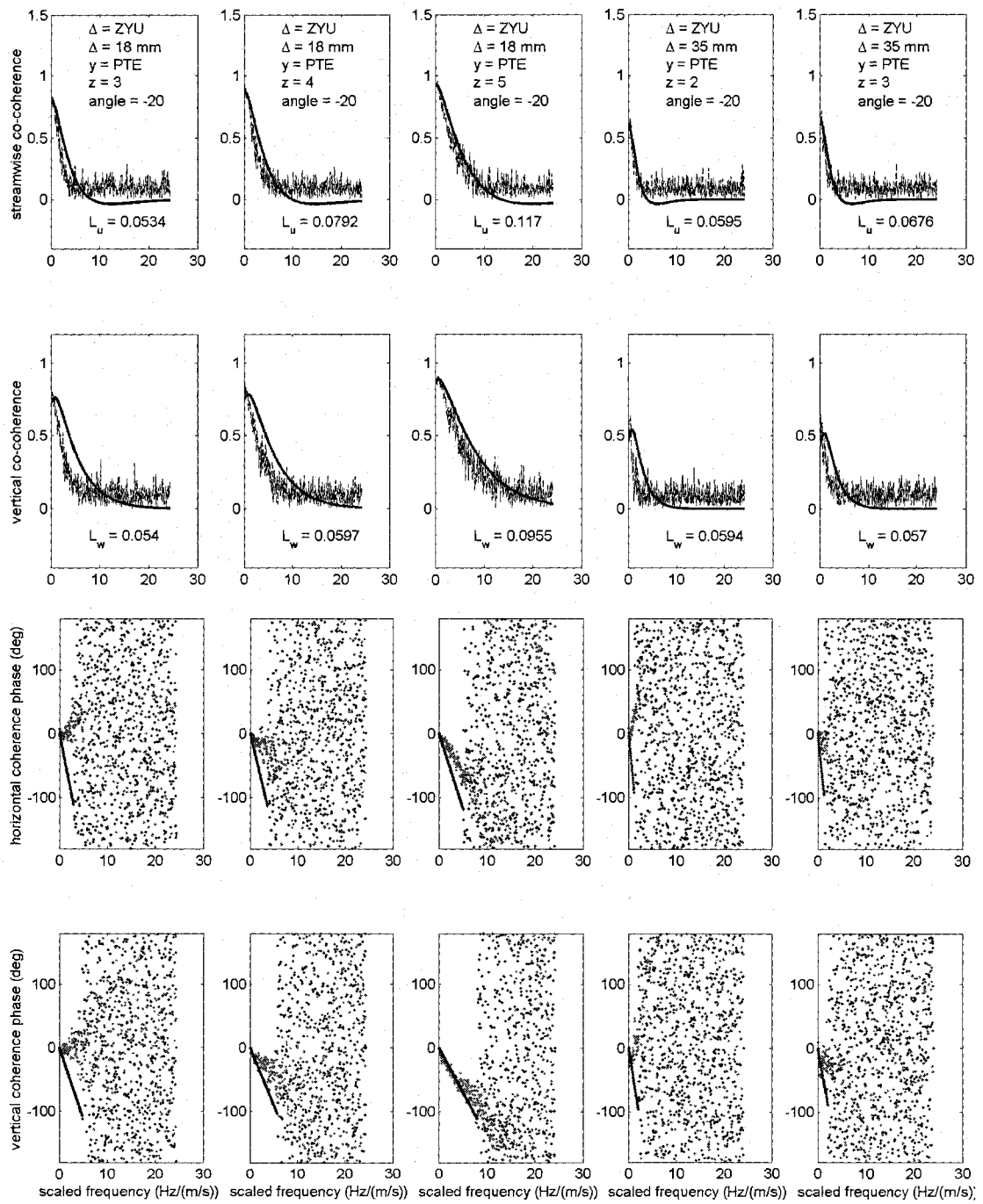

Figure C.48: Root coherence (top) and phase angle (bottom) model agreement (points 196-200).

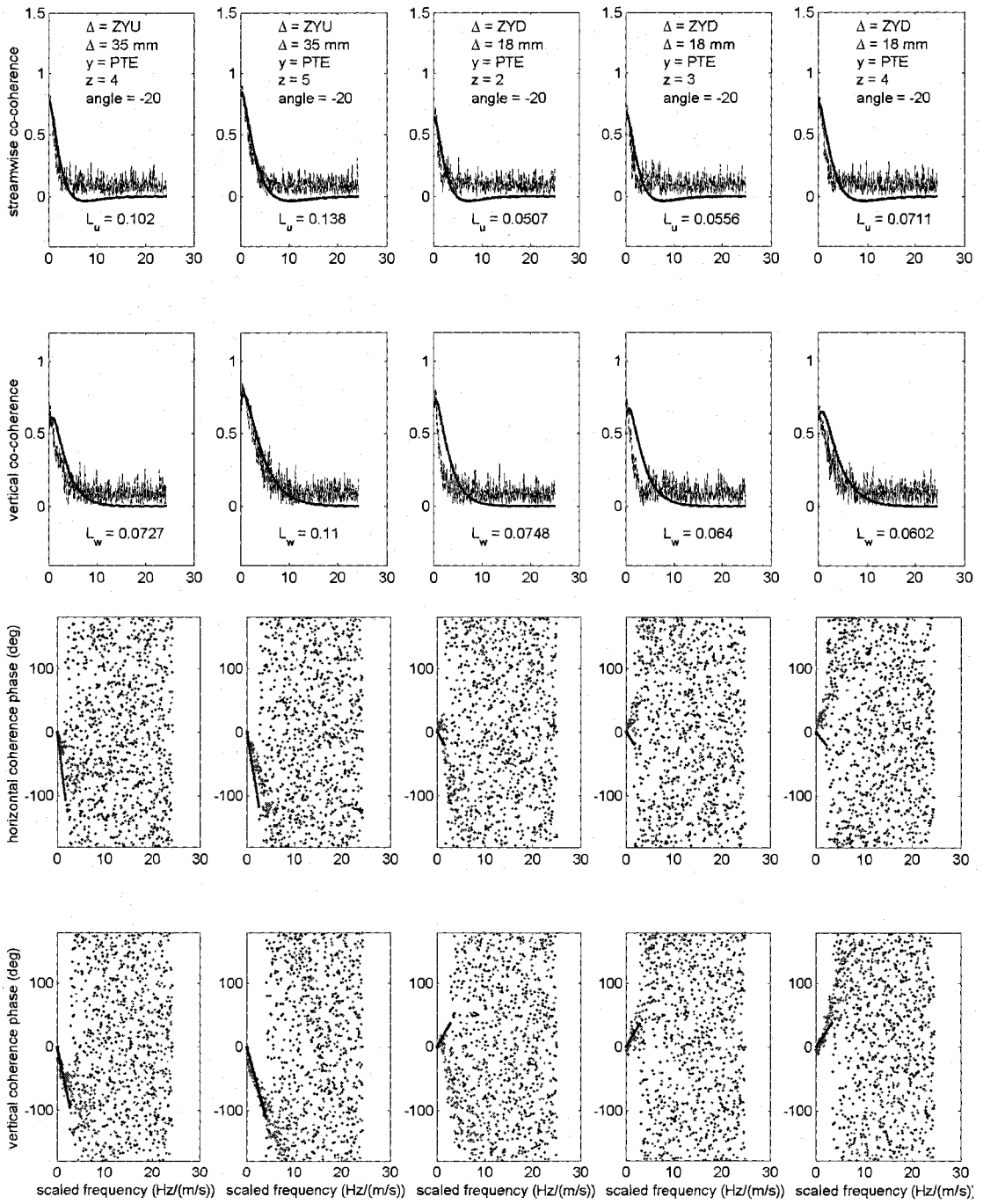

Figure C.49: Root coherence (top) and phase angle (bottom) model agreement (points 201-205).

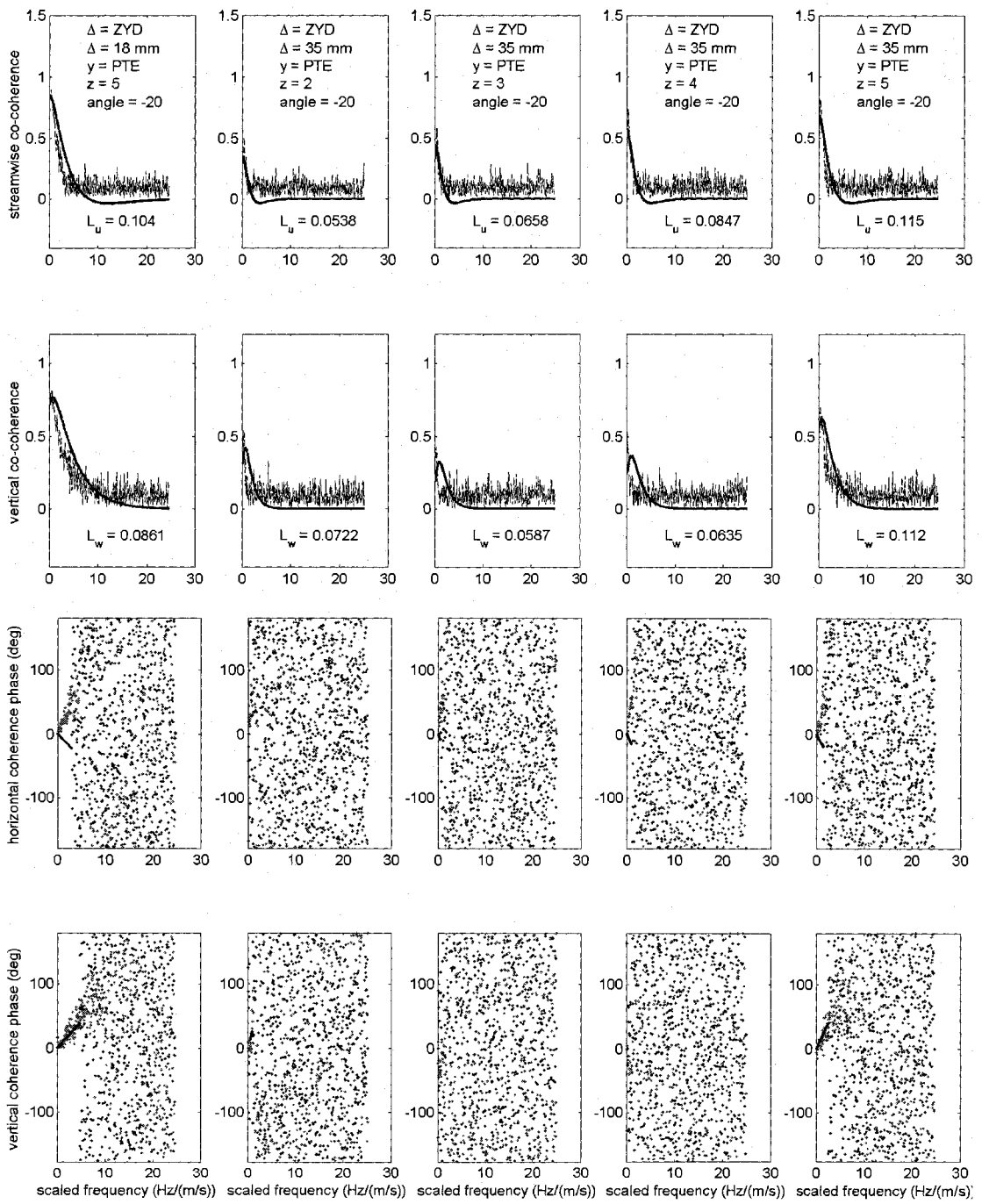

Figure C.50: Root coherence (top) and phase angle (bottom) model agreement (points 206-210).

Appendix D

The Validation Experiment

This appendix contains details of the experimental design, data reduction, and results of the validation experiment, which is described in Chapter 5.

D.1 Experimental Design

In addition to the design scaling and physical model details, which are covered in Chapter 5, some additional experimental design considerations are presented here.

D.1.1 Instrumentation

Time histories of hinge and of elastic blade deflections were the desired results of the validation experiment, including the correlation of these measurements with azimuthal blade position.

A continuous expression for the strain profile along a beam can be obtained by curve-fitting the strain readings from a finite number of gauges, provided the number of gauges is sufficient to capture the number of modes under consideration [111]. This expression can be then used to obtain the deflection profile. The elastic bending of the blade was measured using strain gauges situated at five locations along the blade, as shown in Figure 5.2. The strain gauges were mounted on the top and bottom of the blade in pairs such that all four bridge arms were active to measure bending in the flap direction. This configuration maximizes strain measurement sensitivity in bending, and compensates for temperature,

lead wire resistance, and extensional strain. Parallel grid dual strain 1000 Ω gauges were used. The extensional, torsional, and lead-lag strains were not measured.

The articulated hinge angle was measured using rotational Hall Effect sensors with a range of 0° to 30° and a published accuracy of ±0.1°. The sensor module remained fixed to the rotor hub while the magnet was mounted to the end of the hinge pin and rotated with the blade. These sensors were selected for their small size, large linear output over a small angular range, and excellent accuracy. In addition, the sensors are non-contact and therefore do not cause any resistance to the hinge motion. The sensors exhibit up to an 11 ms time lag between measurement and output. At the highest rotational speed projected for this experiment, this lag corresponds to a hub rotation of 14 degrees. At lower speeds, where large hinge deflections are expected, the azimuthal lag is much less. Since the hinge angle is expected to vary at the rotational frequency of the hub, this offset was considered acceptable for capturing the hinge behaviour.

As with many rotating systems, the collection of data is complicated by the fact that measurement system cannot be hard wired to the non-rotating frame. To solve this problem, wireless voltage nodes were employed. Two devices, one per blade, were used during the experiment. The devices are capable of reading seven analog input voltage channels each. Four of the channels are differential channels, with amplification and filtering. The first four strain gauges were read through these. The commercial software allowed the gauge offset and bridge factor to be preset, such that the software logged strain directly. The other three channels are single ended and were used to measure the fifth strain gauge, the Hall Effect sensor, and the analog azimuth encoder signal respectively. These three channels were logged as digital bits and were therefore filtered and converted to strain, hinge angle, and azimuth angle respectively as part of the data post-processing.

The rotor azimuthal angle was measured using a 1000 counts-per-revolution optical encoder ring and reader. In order to capture meaningful data from the optical encoder, the pulsed signal was converted to an analog signal that varied between 0 and 3 V and was reset with the encoder index pulse. Some supporting circuitry was required to collect and condition the data. DC power of +5 V was supplied to the instrumentation through a slip

ring mounted at the base of the shaft.

The supporting circuitry was contained at the top of the rotor, and was designed to perform the following functions:

- distribution of +5 V DC excitation to all the components of the instrumentation system;
- counting of the encoder pulses, converting them to analog voltage, and resetting the analog voltage at the reference location; and
- dividing of the output of the Hall Effect sensor from 5 to 3 V.

During set-up, the two outboard gauges on one blade were damaged. Data was collected from the working gauges on both blades for all experiments. The sample rate was selected automatically by the wireless nodes and is related to the number of active channels on the node. Blade 2, having five working gauges, was sampled at 452 Hz. Blade 1, having 3 working gauges, was sampled at 520 Hz.

D.1.2 Motor Control

The rotor rotation velocity profile was governed by a brush servo motor that was connected to the rotor through a 3:1 gear box. The rotor motion was controlled to a pre-defined engage/disengage profile of angular velocity that follows a sinusoidal acceleration during engage and a linear deceleration during disengage. Figure D.1 shows the engage/disengage profile that was used. The rotor was engaged over the specified engagement time, t_{r1} s, to the final speed, which was most often 200 RPM at model scale, representing 33% of the scaled normal operating rotor speed. This speed was then held for 30 - t_{r1} s, and disengaged over t_{r1} s.

The motion control system consisted of a universal motion instrument card, motion control card, and a current adjustable amplifier all connected to a single CPU. The virtual instruments provided with the motion control card were used to develop a motor control Graphical User Interface, which allowed easy modification of the engage profile parameters.

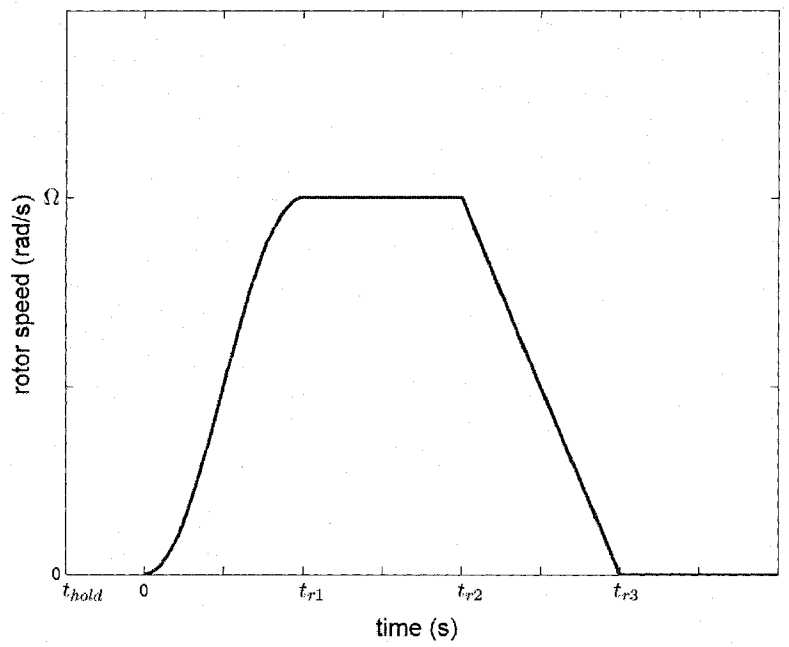

Figure D.1: Experimental rotor engage/disengage profile.

A PID controller was set up with user-defined inputs for position and velocity control. The controller was tuned for velocity control primarily due to the importance of accurately tracing the specified rotor angular velocity profile. The position control was occasionally employed to orient the rotor system at the start of each experimental run.

D.1.3 System Configuration

The first phase of the experiment was composed of components as shown in Figure D.2(a). The wind tunnel was controlled by and the data from tunnel instruments were acquired from the existing tunnel infrastructure computers. The rotor motor parameters were managed by a controller computer, and the motion was triggered by the tunnel data system. The model instrumentation information was transmitted wirelessly to a separate acquisition computer.

The motion platform experiment was set up using similar equipment. In this case, the motor controller was triggered manually instead of remotely with an electronic trigger. A schematic of the system for the motion platform is shown in Figure D.2(b).

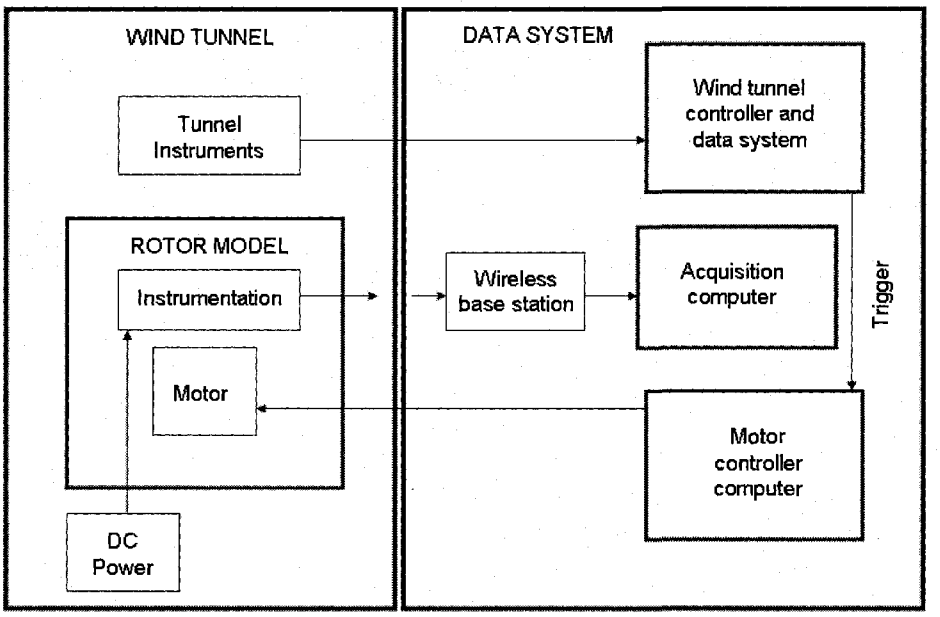

(a) Wind tunnel

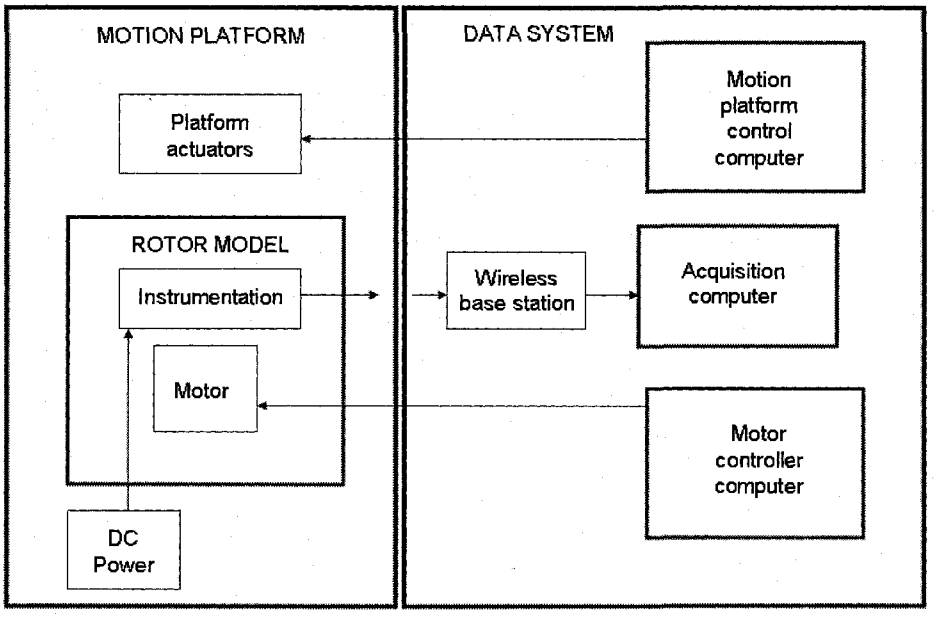

(b) Motion platform

Figure D.2: Schematic of the experimental data and control systems.

D.2 Experimental Execution

For each data set, the wind tunnel or motion platform, and motor parameters were set; the rotor was centred by hand such that the blades started in a consistent configuration, with blade 1 into wind; the wind tunnel or motion platform, and motor system were triggered; and the data was collected automatically and saved manually.

D.3 Data Processing

D.3.1 Calibration

Prior to beginning the experiment, the strain gauges were zeroed by setting the blades on their edges such that gravitational effects did not act in the flap direction. These settings were recorded in the data collection software and used for the duration of the experiment, and their applicability was verified periodically using a known resting blade state. Strain data for the following cases were also recorded to facilitate data reduction and later simulation of the experimental cases:

- blade static deflection due to gravity;
- damping profile of the blade resulting from a drop test; and
- damping profile of the blade and bumpers resulting from a drop test onto the droop stops.

Photographs of the blade deflecting due to gravity were also taken.

Additionally, the following calibrations were completed. The voltage response of the Hall Effect sensors at known hinge angles was recorded and the linearity of the sensors across the hinge angle range was verified. The sensitivity of the Hall Effect sensors to variations in the input voltage was measured, and found to vary between the sensors and with hinge angle. The accuracy of the wirelessly transmitted single-ended channels was found to be within 15 mV.

With respect to the wind tunnel, the boundary layer profile, including turbulence, resulting from the grid was measured using a three-hole Cobra probe. Due to the large wind tunnel blockage of the boundary layer grid and the ship decks, the wind tunnel velocity at the hub location was calibrated for the 0 and -20° ship decks at rotor height using a vane anemometer. These measurements were used to compute the corresponding freestream reference flow velocity at rotor height for use as input into the airwake model. At the beginning of each set of runs, typically every half day, a tare was taken to record the tunnel conditions with wind off. The tare runs are used to correct the tunnel speed information for atmospheric pressure and temperature.

D.3.2 Data Reduction

The reduction and analysis of the experimental data was carried out after the experiment had been completed. The Hall Effect signal was digitally filtered to eliminate frequencies above 35 Hz and was converted to hinge angle using the calibration. The analog signal from the fifth strain gauge was filtered and converted to strain.

The strain gauge data was then processed to give blade deflections. The elastic deflection of the blade and curvature are related by [112]

$$\kappa = \frac{\frac{d^2z}{dx^2}}{\left[1 + \left(\frac{dz}{dx}\right)^2\right]^{\frac{3}{2}}} \tag{D.1}$$

where x is measured along the blade, z is the vertical deflection of the beam from the beam reference line, and the curvature, κ, can be obtained using $\kappa\nu = \epsilon$, which is valid for small strains. Here, ν is the distance from the neutral axis to the strain gauges, and ϵ is the measured bending strain.

After solving for a functional expression for the curvature along the blade at a specific instant, Equation D.1 was converted to first order using a change of variables and then solved numerically for slope with spatial marching. The slope was then directly integrated to find elastic deflection. This procedure was completed for each instantaneous time measurement.

During data reduction, the wind tunnel speed was obtained using the data-point-specific

tunnel static and dynamic pressure, tunnel static offset, and tunnel total temperature combined with calibration data.

D.4 Experimental Challenges

Due to the available equipment, time constraints, and lack of experience, some experimental challenges were encountered during and after data collection. These challenges, their effects on the results, and associated mitigation strategies are briefly described.

D.4.1 Voltage Regulation

The supporting circuitry was missing one important feature: adequate voltage regulation. During testing with the rotating system, the sliding contact in the slip ring was shown to affect the consistency of the voltage supplied to the instrumentation. The impact on the collected data varies. The wireless devices have their own voltage regulators, and so the strain gauges were not affected.

The encoder analog signal was directly affected by variations in supply voltage. While the exact azimuthal position at a given time is uncertain, the reset angle is not, and so the rotor profile could be obtained by curve fitting the reset times. Since the supply voltage to the onboard circuitry was not recorded, the variation in the encoder reset voltage gives some insight into the magnitude of the supply voltage variation. The reset voltage varies by an amount in the order of 0.27 V, which is 5% of the nominal voltage.

The Hall Effect sensor information is most affected by the varying supply voltage. The magnitude of sensor output is affected by the magnitude of voltage input at a rate of $\Delta V_{out} = 0.35\Delta V_{in}$. Therefore the hinge angle uncertainty due to slip ring voltage supply is in the order of 0.095 V, which corresponds to at most 1.2°. Individual inspection of data sets led to greater confidence in the hinge angle measurement in some cases.

This issue is present in both phases of the validation experiment.

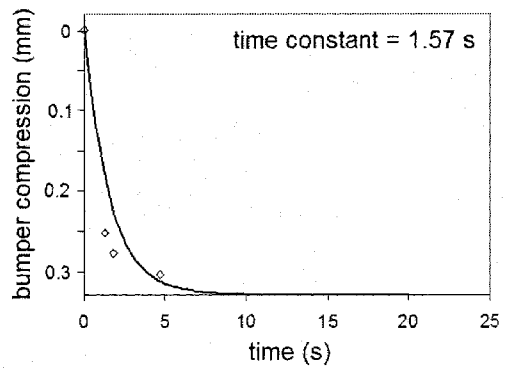

Figure D.3: Time response of neoprene bumpers.

D.4.2 Variable Bumper Stiffness

During data reduction, it became apparent that the neoprene bumpers exhibit a nonlinear flexible behaviour that resembles a first-order system. Due to this property, and the nonlinear stiffness curve shown in Figure 5.4, the stops are not properly modelled using linear assumptions. As a first approximation for the time history of bumper deflection, the response for an applied load of 6.5 N was recorded using a stop watch and dial gauge. The response is shown in Figure D.3.

D.4.3 Wireless Packet Drop

In order to correlate the data collected by each wireless node, the encoder signal was recorded by both. When plotted together, the encoder signals show an inconsistent shift of up to 1.5 rad/s in rotor speed with respect to one another and with the expected rotor speed as prescribed by the motor controller. This discrepancy is believed to result from dropped data packets in the wireless data transmission. As a result, frequency domain analysis of the results will yield only approximate results, and time history comparisons drift over time. Still, displacement values are unaffected, and correlations of the time history of results over short times, such as the engage sequence, are still believed to be valuable.

During Phase 2 of the experiment, the data were logged locally on the wireless nodes and transferred after the run was complete. This method avoids wireless packet drop.

D.4.4 Motor Control Drift

The rotor velocity profile is determined by variable time parameters that are fed into the LabView program that controls the motor. During the wind tunnel experiment, the profile was controlled using LabView's internal clock, which drifts over time. This phase lag does not seriously affect the engage time, since the error accumulates slowly, however it causes some uncertainty as to the time at which the disengage portion of the profile was initiated.

By using the computer CPU clock, this problem was eliminated for the Motion Platform phase of testing.

D.4.5 Strain Gauge Output

During data reduction, the output of strain gauge five was found to drift. During the initial runs, the fifth strain gauge contributes in an expected manner to the overall strain profile along the blade. Subsequent experimental runs exhibit much more erratic behaviour; both are shown in Figure D.4. The first four gauges are not subject to this drift as their calibration information is handled by the wireless nodes. Therefore, the first four gauges were used to calculate blade tip deflection. Since the blade deflection is governed primarily by the first, second, and third flapping modes, four operating gauges are sufficient to resolve the blade deflection.

The outermost two gauges on blade 1 were damaged during manufacturing and model assembly. For this blade, the first three gauges were used to calculate the blade tip deflection. Once again, three operating gauges were deemed to be sufficient to resolve the blade deflection. During the motion platform experiment, a third gauge on blade 1 was damaged. Therefore, blade 2 only is used for comparison for Phase 2 of the validation experiment.

D.5 Results

The true value of the experimental results is realized when comparison with simulation data is performed. However, the direct results of the experiment, blade deflections under varying conditions, are also interesting. As they are discussed, it is important to bear in

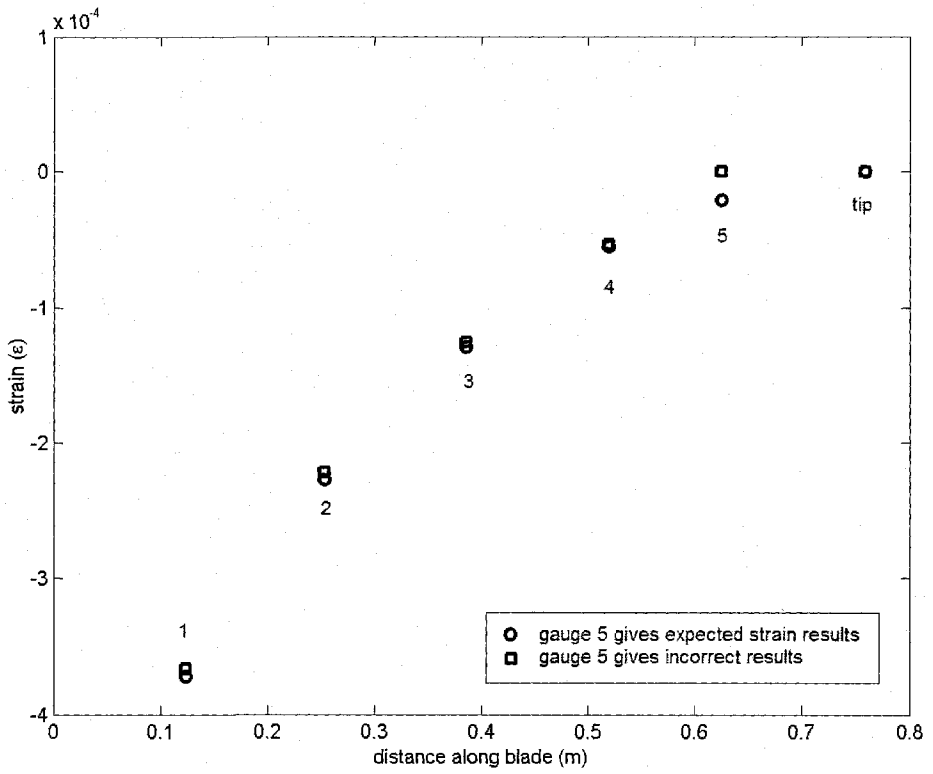

Figure D.4: Strain gauge readings for static gravitational tip deflection to demonstrate inconsistency in gauge 5 (gauge numbers marked).

mind that the magnitudes of the blade deflections have been exaggerated for the purposes of the experiment. The actual magnitudes are not the focus of the results, however the trends offer insight that can be applied more widely.

D.5.1 Phase 1: Wind tunnel

For Figures D.5 to D.21, total vertical blade tip deflection results are shown, given relative to the undeflected rotor disc. For the downward deflection results, the static deflection values are shown as corresponding horizontal lines. The maximum and minimum deflections for the 0 degree deck angle are shown in Figures D.5 to D.10. The blade deflections generally increase with wind speed; this trend is widely observed in the data.

For the operating conditions studied, the engage/disengage time does not appreciably affect blade response. The exception is with the downward deflection during the 2 and 4 s engage/disengage at higher wind speeds. This behaviour can be explained by the speed at which the rotor was disengaged. For fast engage/disengage profiles (2 and 4 s), the rapid changes in aerodynamic loading result largely from the rotor acceleration and deceleration. The blade height from which the blade falls during disengage, which depends on azimuthal angle, is related to the maximum downward deflection. For slower engage times (8, 12 and 15 s), the changes in aerodynamic loading result largely from flow variations in the airwake. For this reason, the blades tend to settle more smoothly onto the droop stops. Still, the blades can encounter the updrafts several times at slow speeds. This effect also yields large blade deflections. However, the tendency for fast-engage cases to experience surprisingly high maximum deflections compared to their slow engaging counterparts, which follow a more predictable trend, is widely observed in the data.

The deflection trends for blades 1 and 2 are not necessarily the same, which is a result of differences in blade azimuthal angle at any given time. Blade 1 always started into wind, and encountered reverse flow and decreasing updrafts for its first half-turn. Blade 2 encountered increasing forward flow and increasing updrafts during its first half-turn. The blades then encountered the updraft flow region 180 degrees out of phase.

Figures D.11 through D.17 show the results for the ship deck at -20 degrees roll angle.

For these results, the magnitude of the updraft at the leading edge of the ship deck is greater than with the 0° deck. As such, data collected for the -20° deck generally exhibit much greater upward blade deflections. However, the downstream blade also experiences some relative updrafts in the -20° deck configuration, and a separated flow region. As a result, downward blade deflections for the -20° deck are not universally greater than those for the flat deck. Generally, the maximum downward deflections are similar for low blade pitch angles, and sometimes decreased for high blade pitch angles.

The blade deflections are shown to increase in severity with both positive and negative pitch angle, as shown in Figures D.18 and D.19. As previously noted, the fast engage time cases (2 and 4 s) typically show very different behaviour from the slow engage time cases (8, 12, and 15 s). Because the fast engage cases are much more sensitive to azimuthal angle, some unpredictability is expected in the blade behaviour. This is demonstrated by the 2 second engage of blade 2 at 8 degree pitch, for which there were two runs at 4 m/s wind speed. The azimuthal position at which disengage starts depends on the engage time for the run, backlash in the motor/gear system, and any position error that accumulates as a result of the velocity-level motor control.

Figures D.20 and D.21 show the relative effects of the ship decks compared to blade deflections without the ship deck installed. At 0° blade pitch, the deck angle appears to affect the magnitude of the upward blade deflections. The results for no deck and the 0° deck are similar, while the deck at -20° shows much higher upward deflections. In contrast, the downward deflections observed with no deck are much reduced compared to those for the deck at 0° and -20°.

D.5.2 Phase 2: Motion Platform

The results of the motion platform experiment also show some interesting trends. Figure 5.17(a), which is used for validation, shows the total root mean square of blade deflection as a function of platform roll frequency and rotor rotation frequency. These results are from experiment Part I.

Parts II and III include six representative ship motion files, which have each been given

a number, as shown in Table 5.5. Figure D.22 shows the maximum upward and downward total blade deflections for representative engage/disengage profiles. Each motion file gives a unique response, depending on the waves encountered during the simulation. Engage times do not appear to appreciably affect the maximum deflections. Pitch angle has the expected effect on upward deflection with large negative pitch angles having the lowest deflection and large positive having the highest. Downward deflections do not show predictable trends, which indicates that more factors, likely the droop stops, are at play. Figure D.23 shows the maximum deflection results for a rotor rotating at slow constant speed during representative ship motion. Here, blade pitch angle appears to have the general effect of lifting the blades.

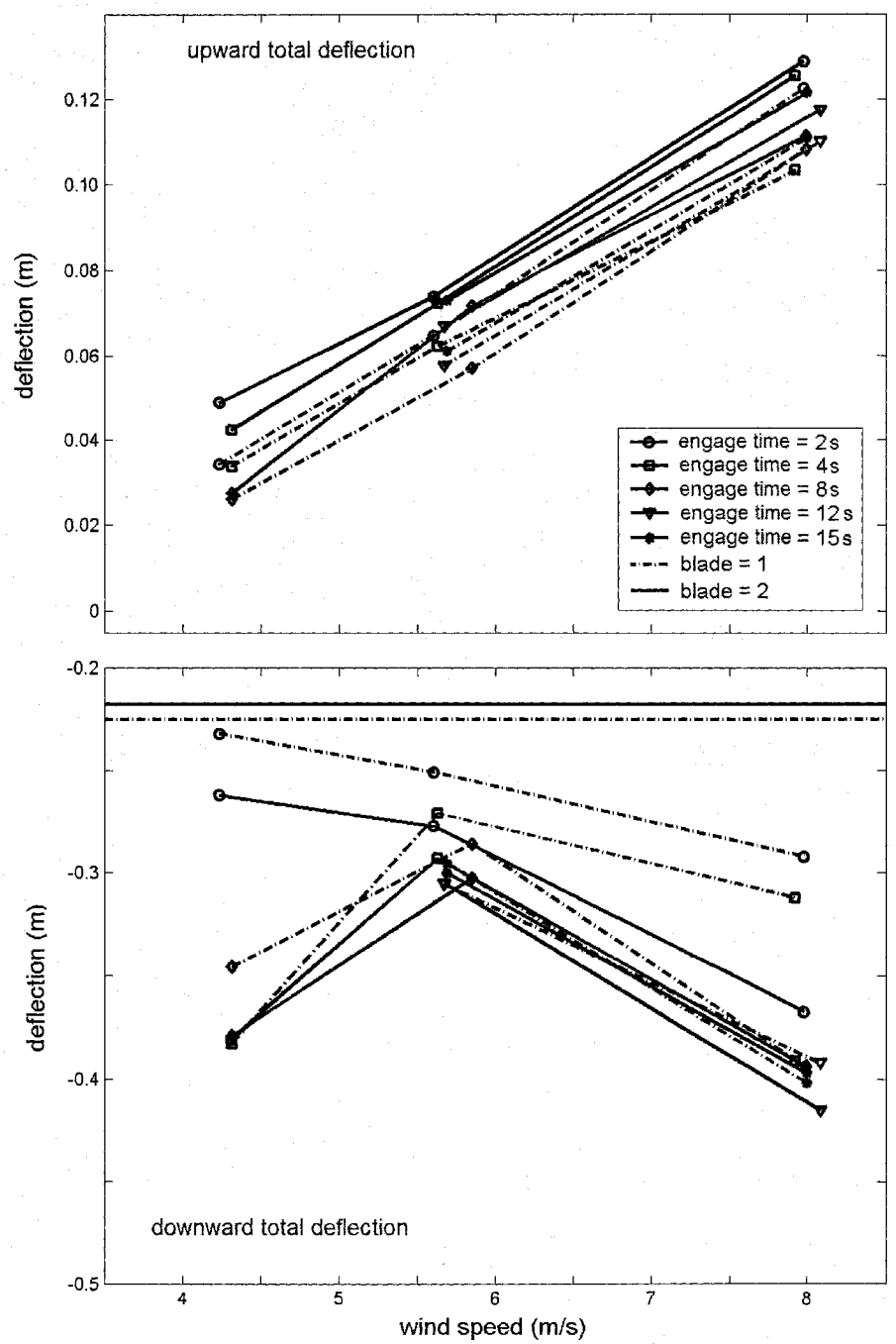

Figure D.5: Blade deflections over the 0° deck for -8° blade pitch.

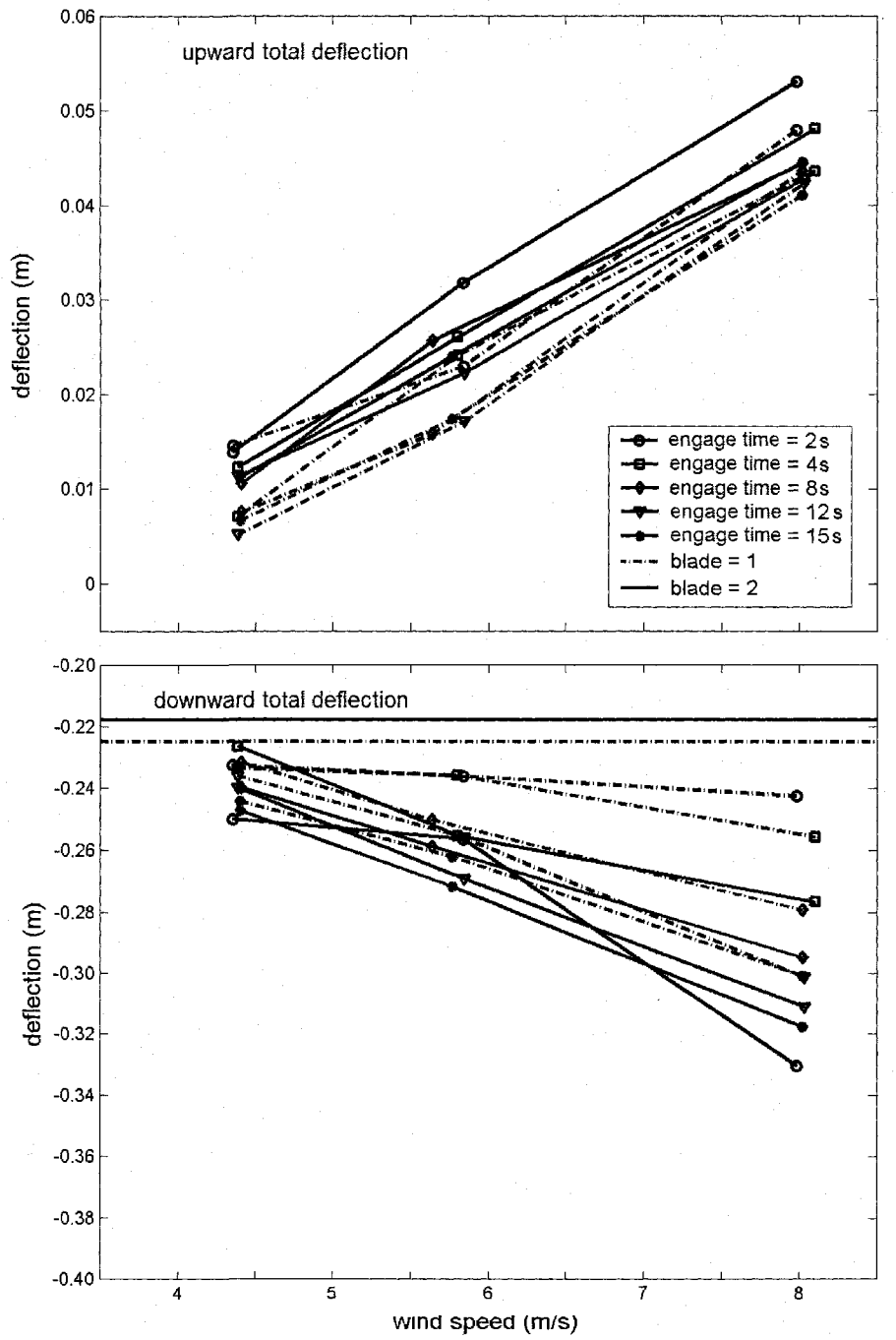

Figure D.6: Blade deflections over the 0° deck for -4° blade pitch.

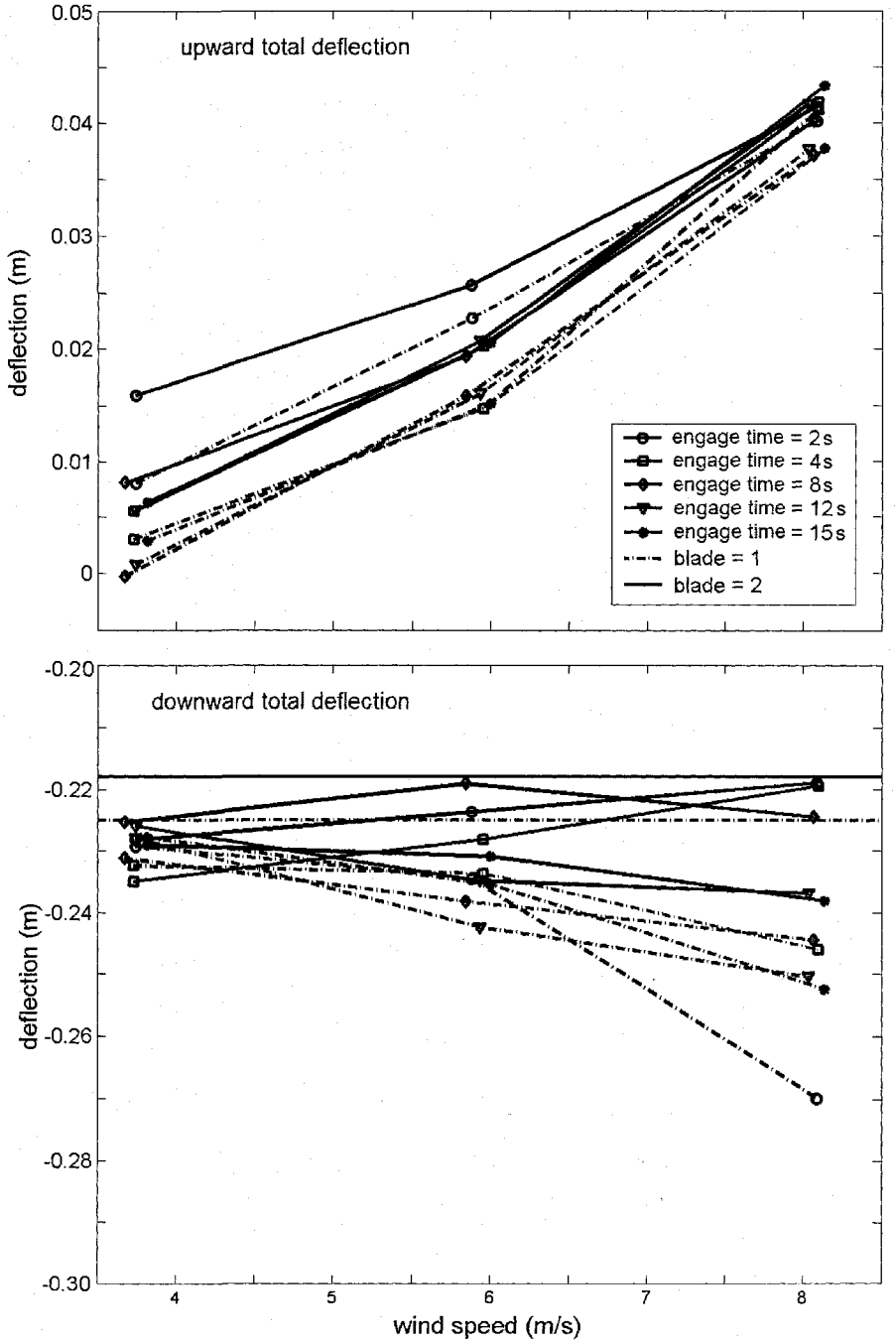

Figure D.7: Blade deflections over the 0° deck for 0° blade pitch.

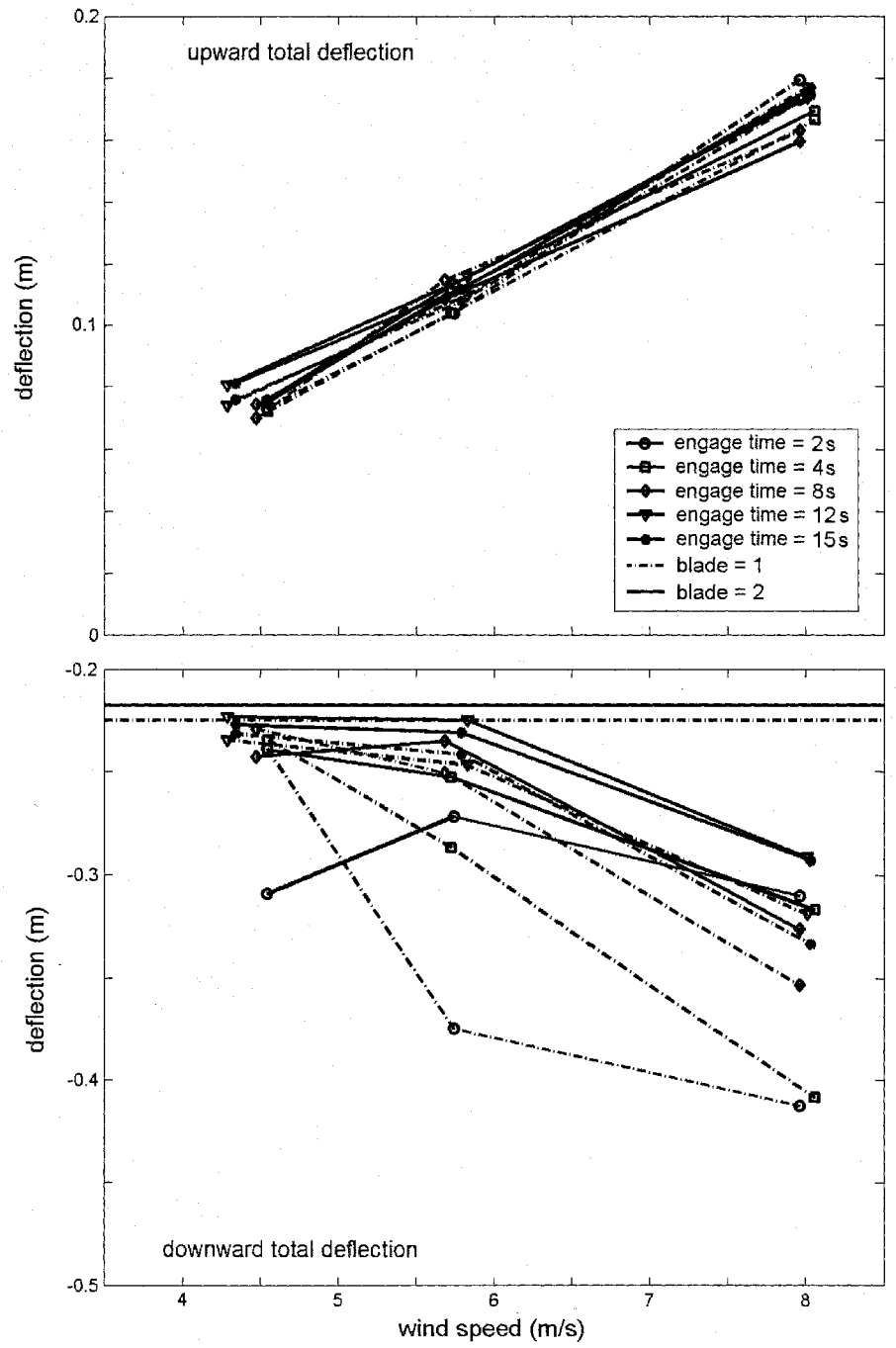

Figure D.8: Blade deflections over the 0° deck for 4° blade pitch.

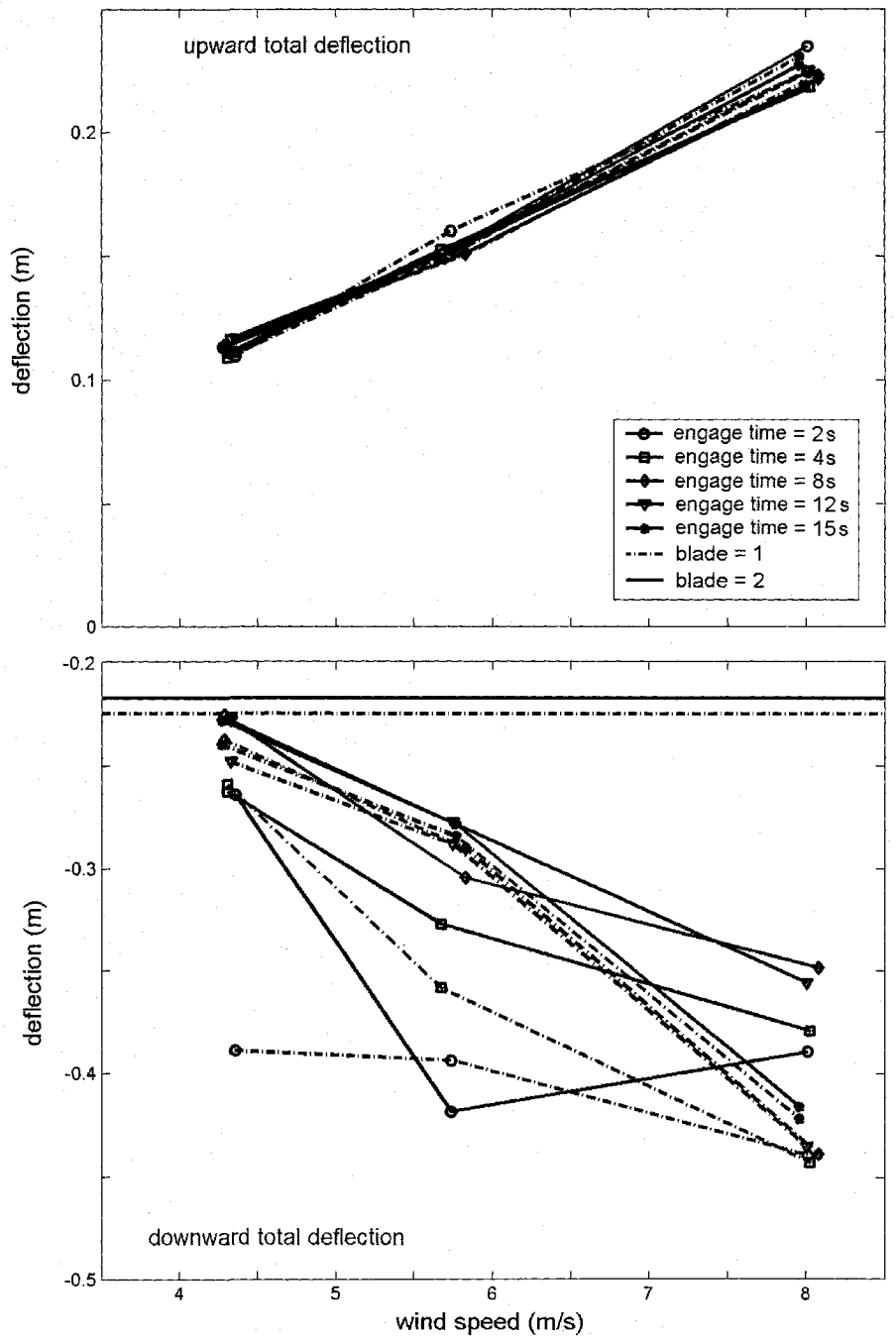

Figure D.9: Blade deflections over the 0° deck for 6° blade pitch.

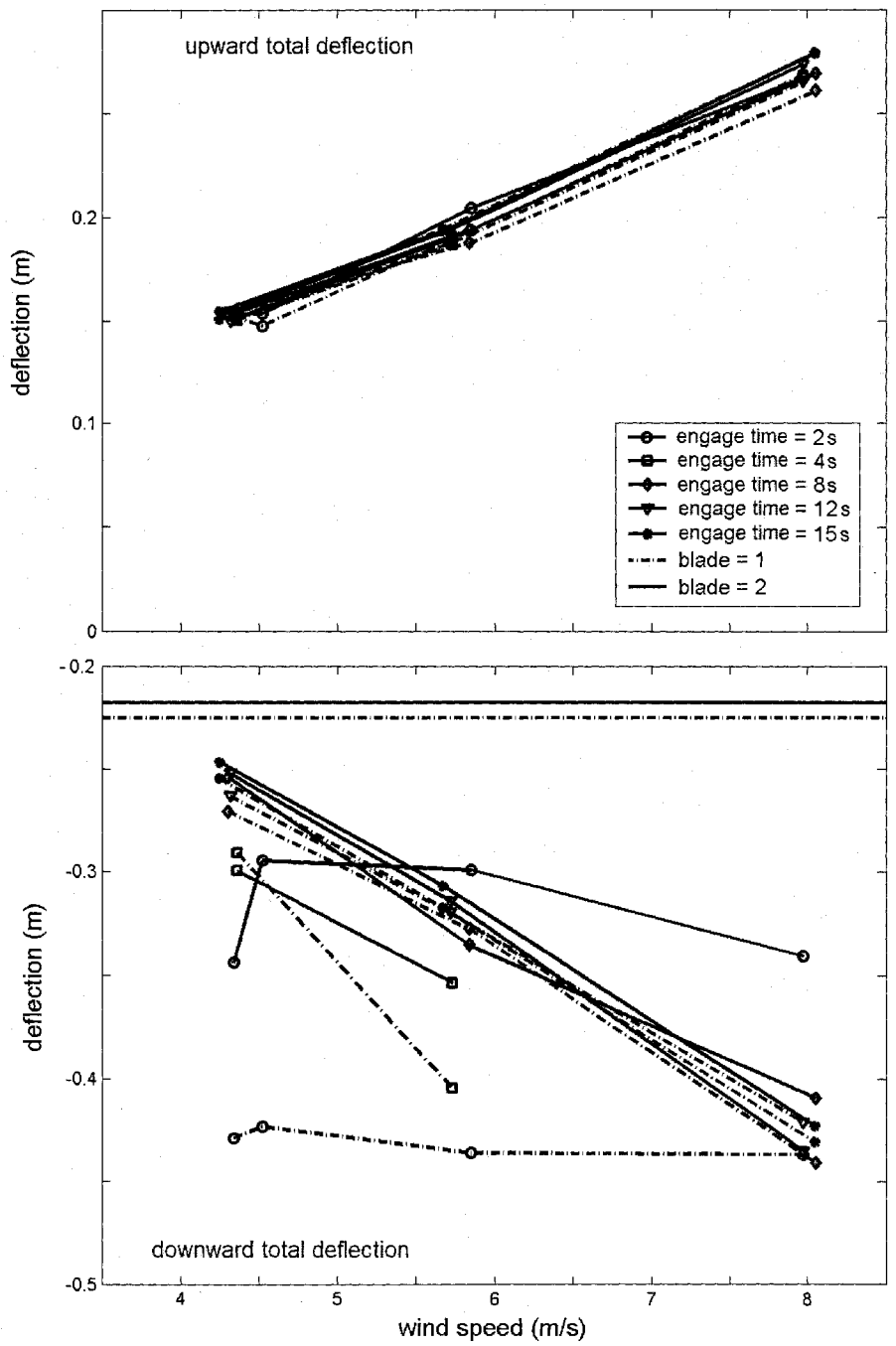

Figure D.10: Blade deflections over the 0° deck for 8° blade pitch.

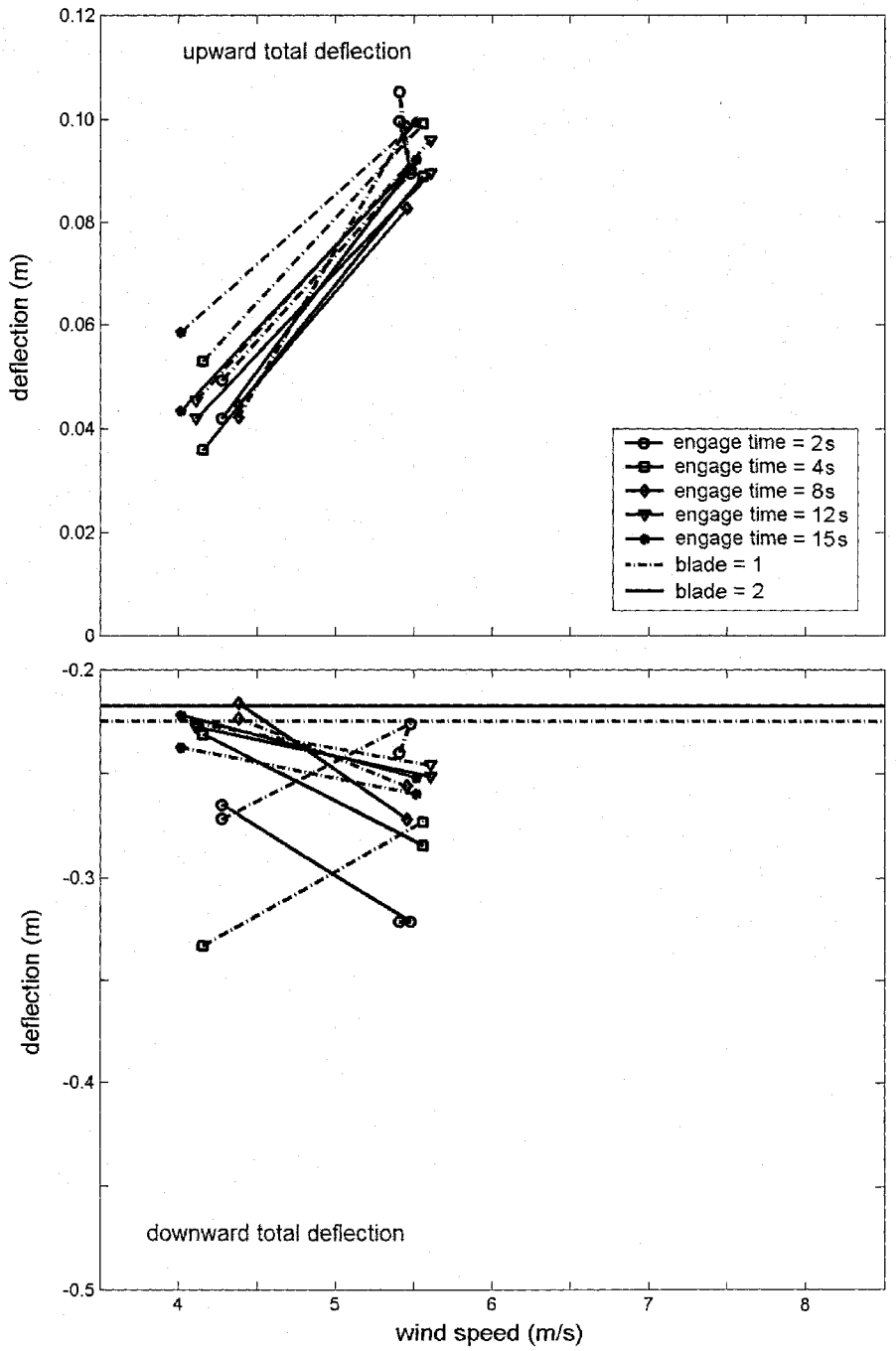

Figure D.11: Blade deflections over the -20° deck for -8° blade pitch.

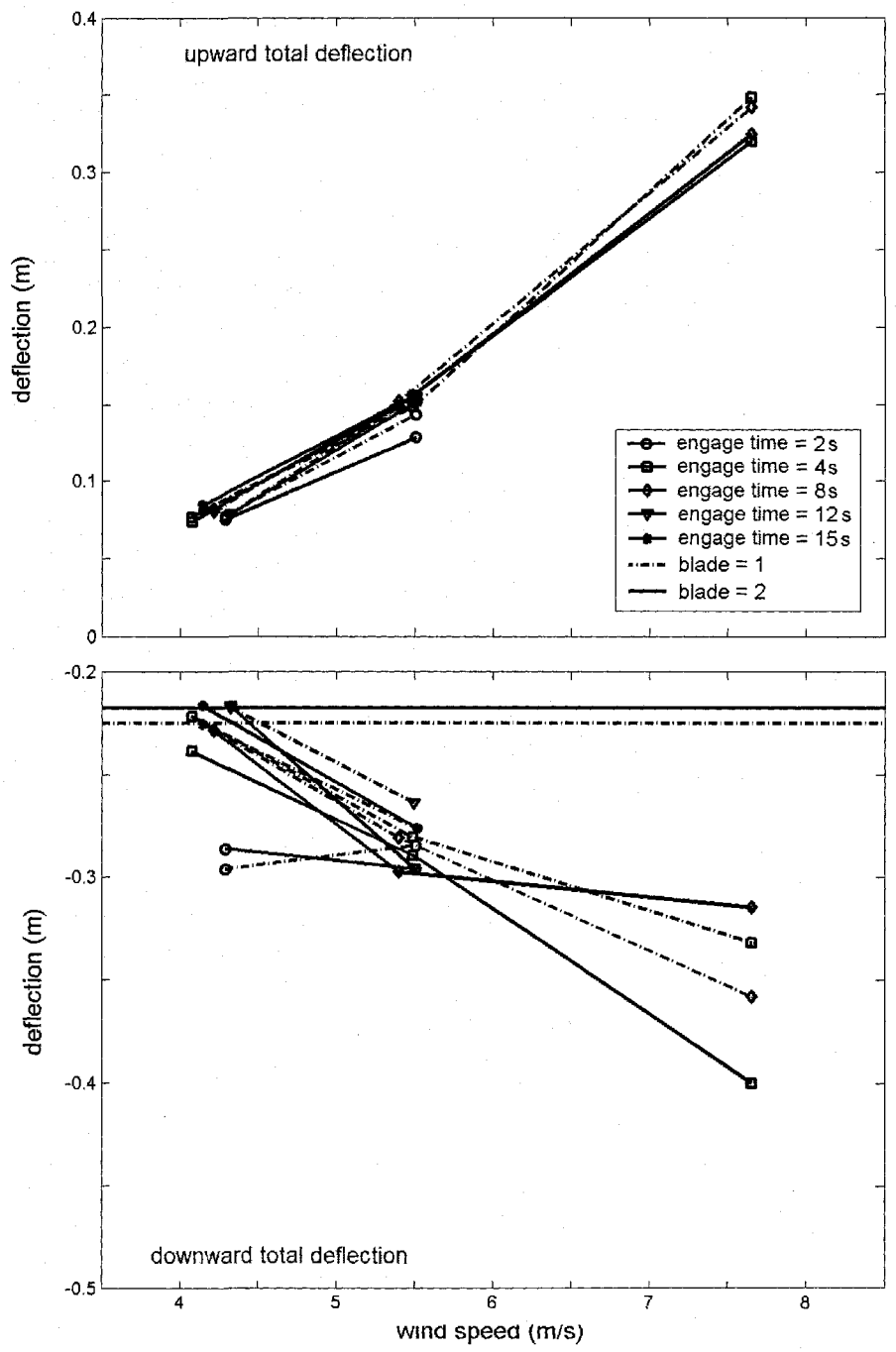

Figure D.12: Blade deflections over the -20° deck for -4° blade pitch.

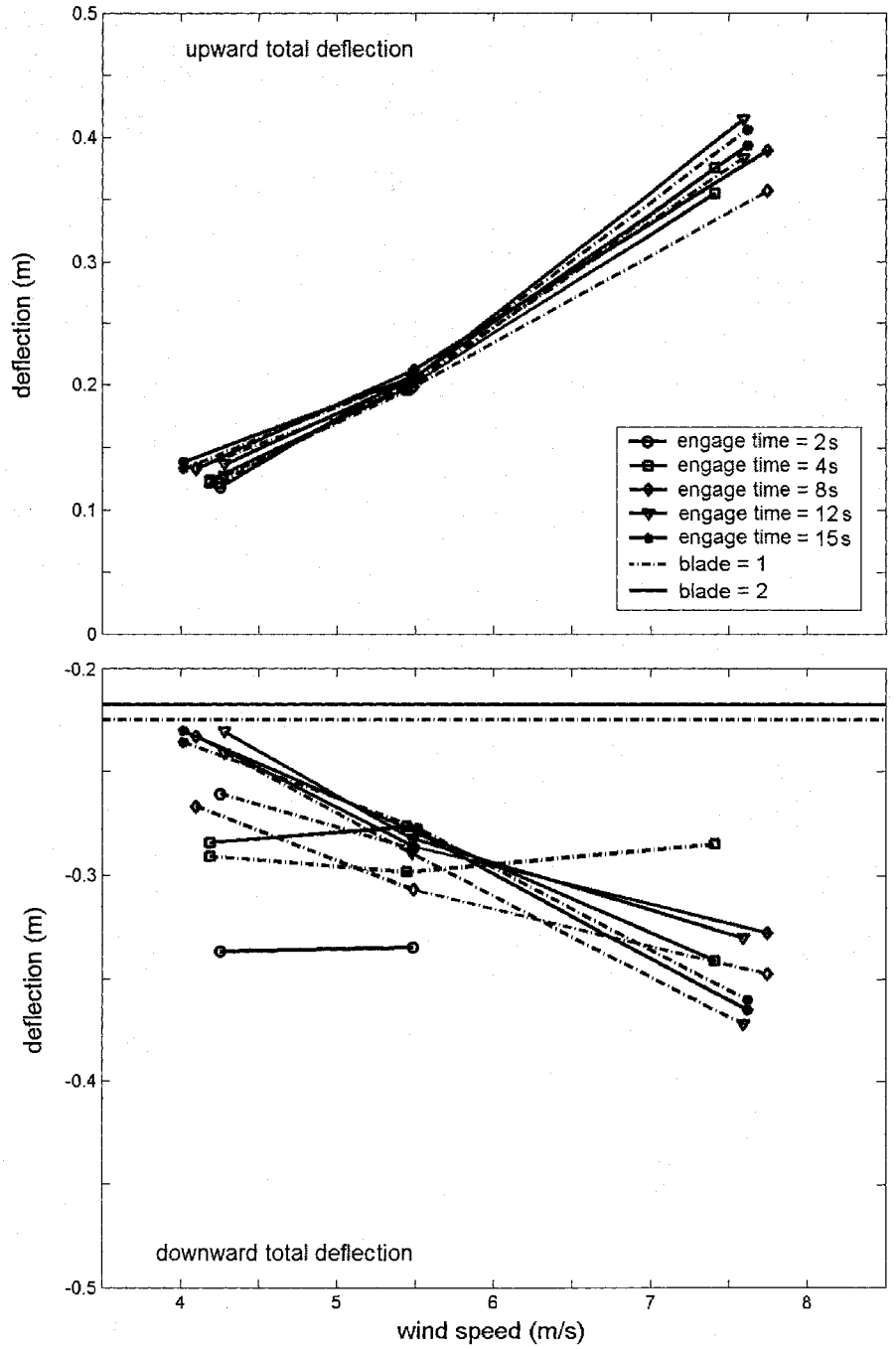

Figure D.13: Blade deflections over the -20° deck for 0° blade pitch.

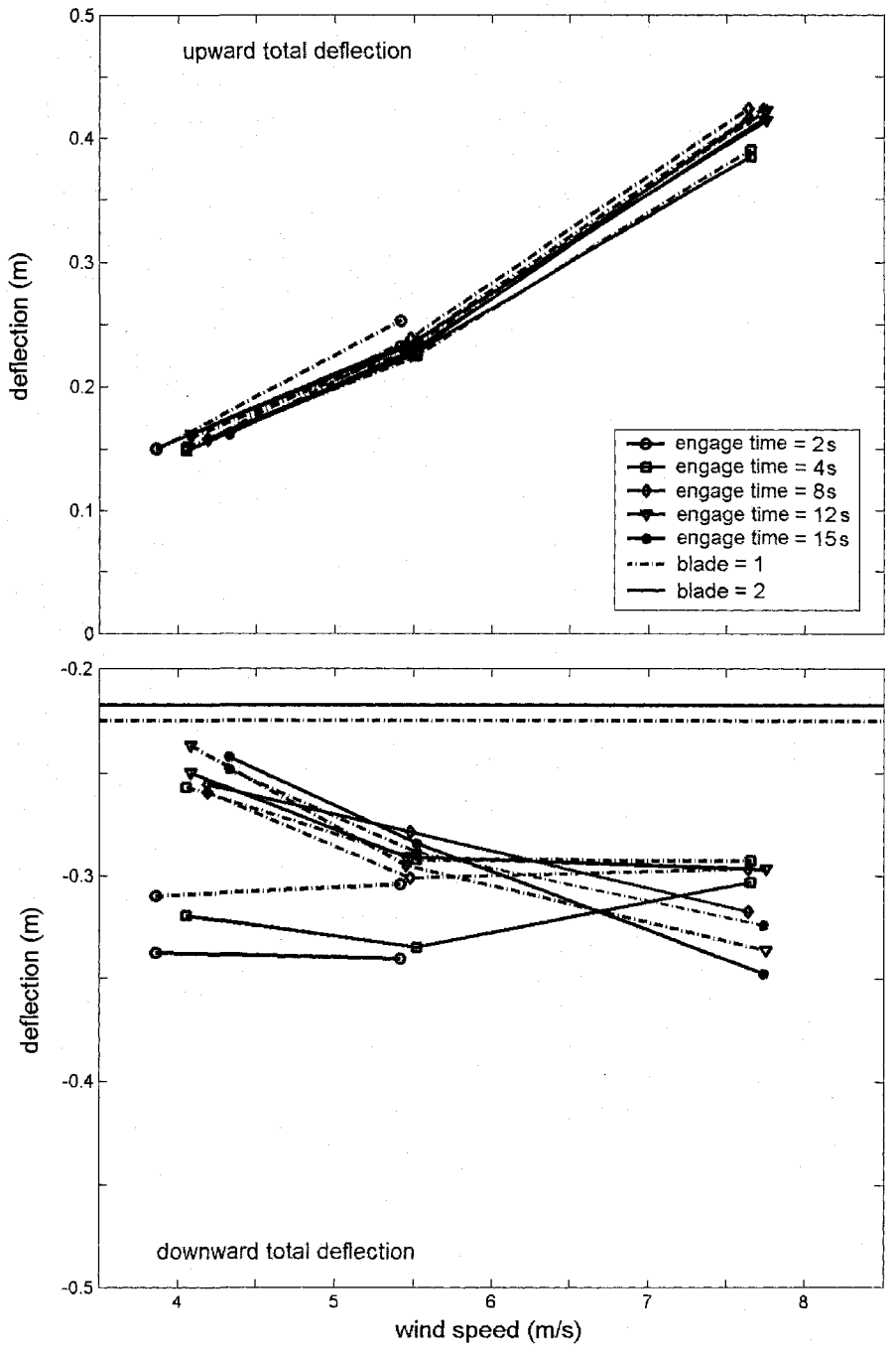

Figure D.14: Blade deflections over the -20° deck for 2° blade pitch.

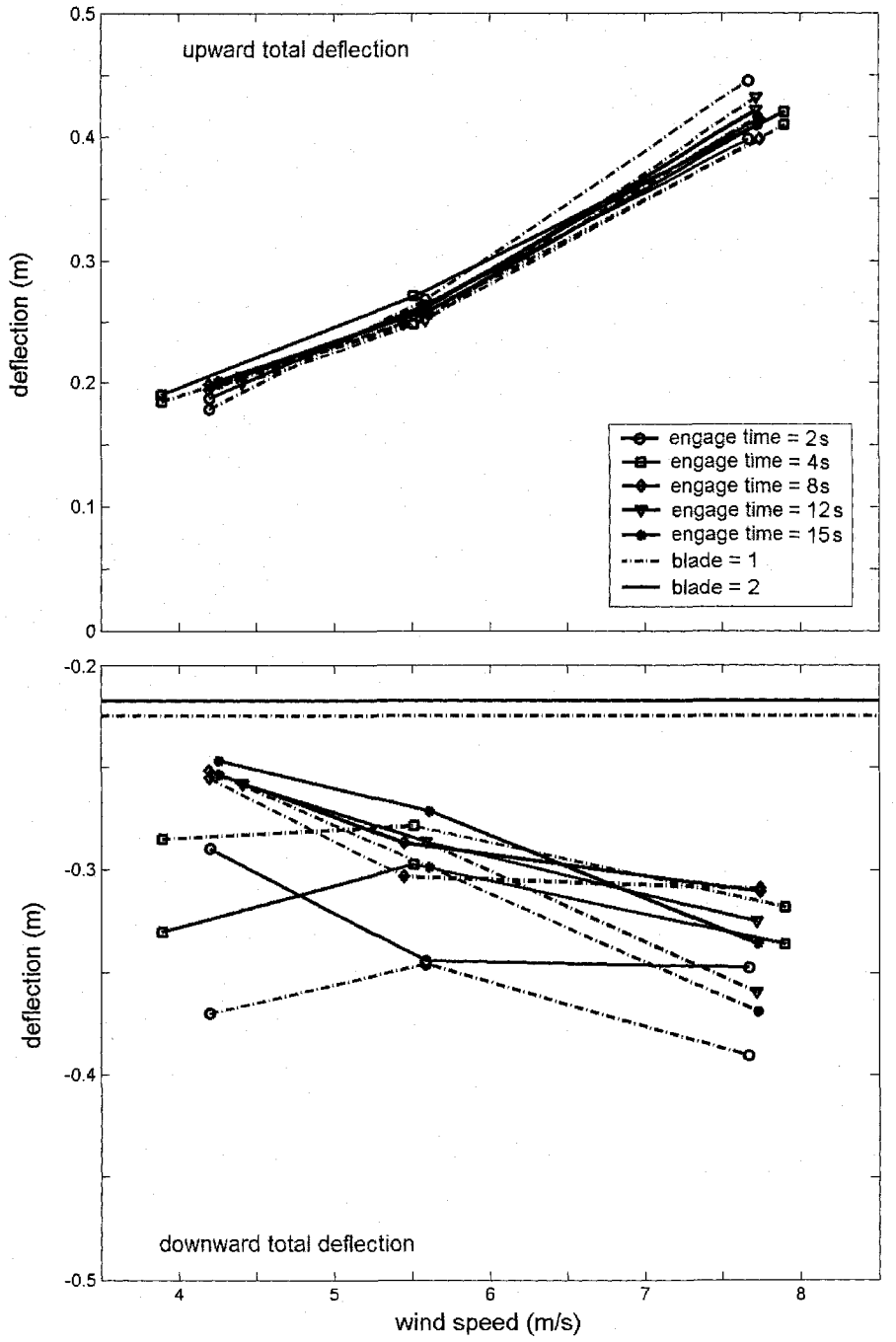

Figure D.15: Blade deflections over the -20° deck for 4° blade pitch.

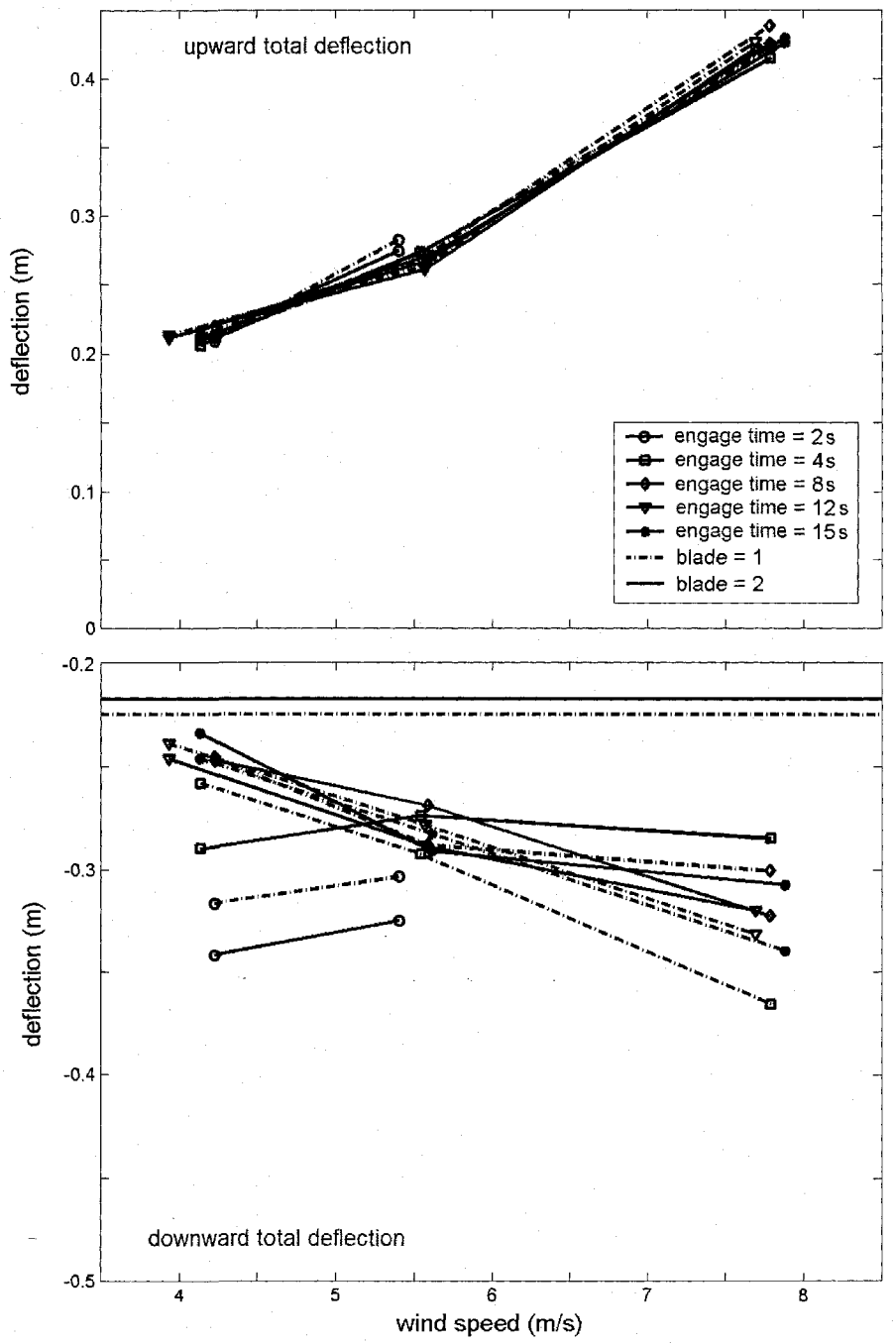

Figure D.16: Blade deflections over the -20° deck for 6° blade pitch.

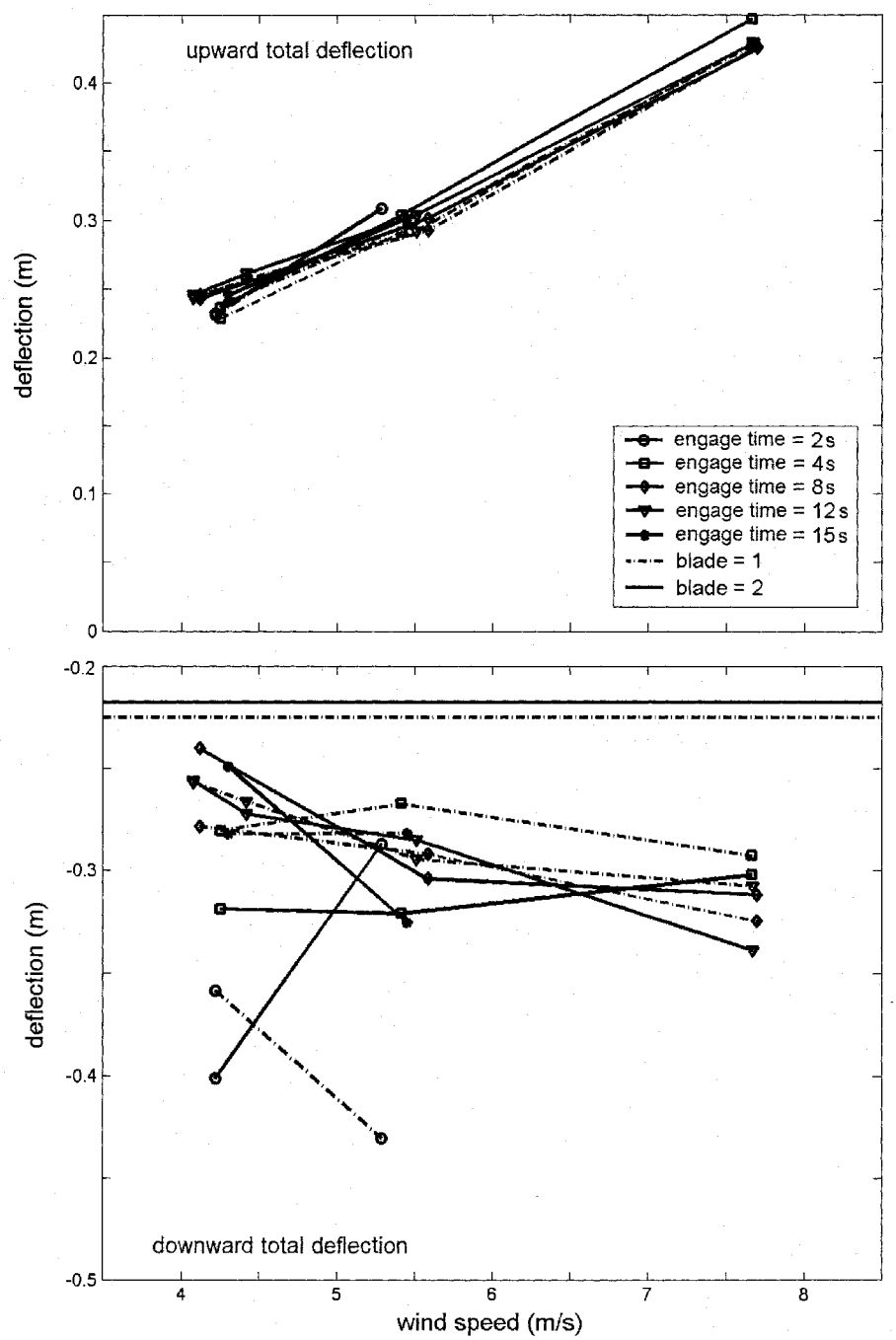

Figure D.17: Blade deflections over the -20° deck for 8° blade pitch.

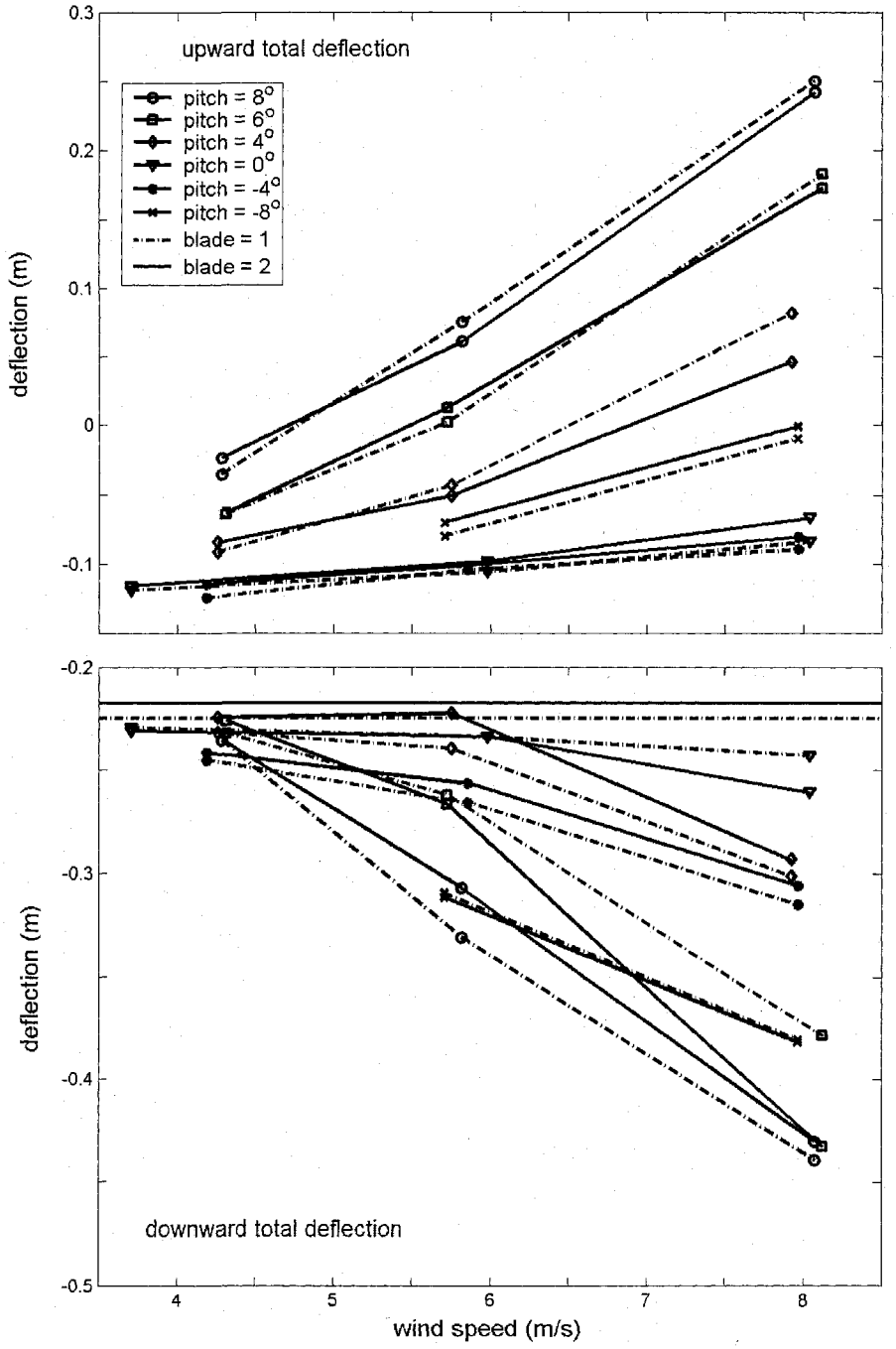

Figure D.18: Blade deflections for a maximum rotor speed of 7 rad/s for 0° ship deck.

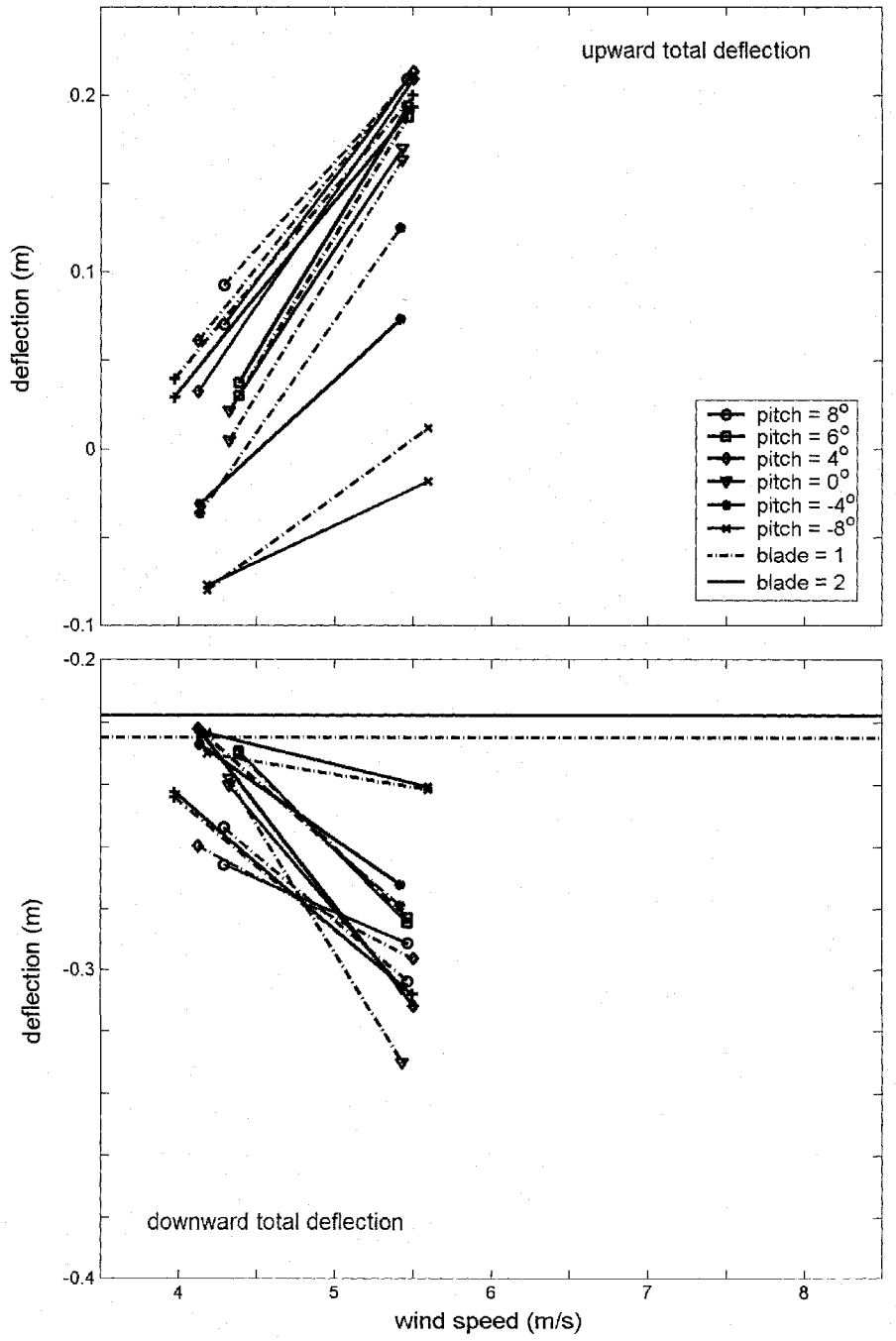

Figure D.19: Blade deflections for a maximum rotor speed of 7 rad/s for -20° ship deck.

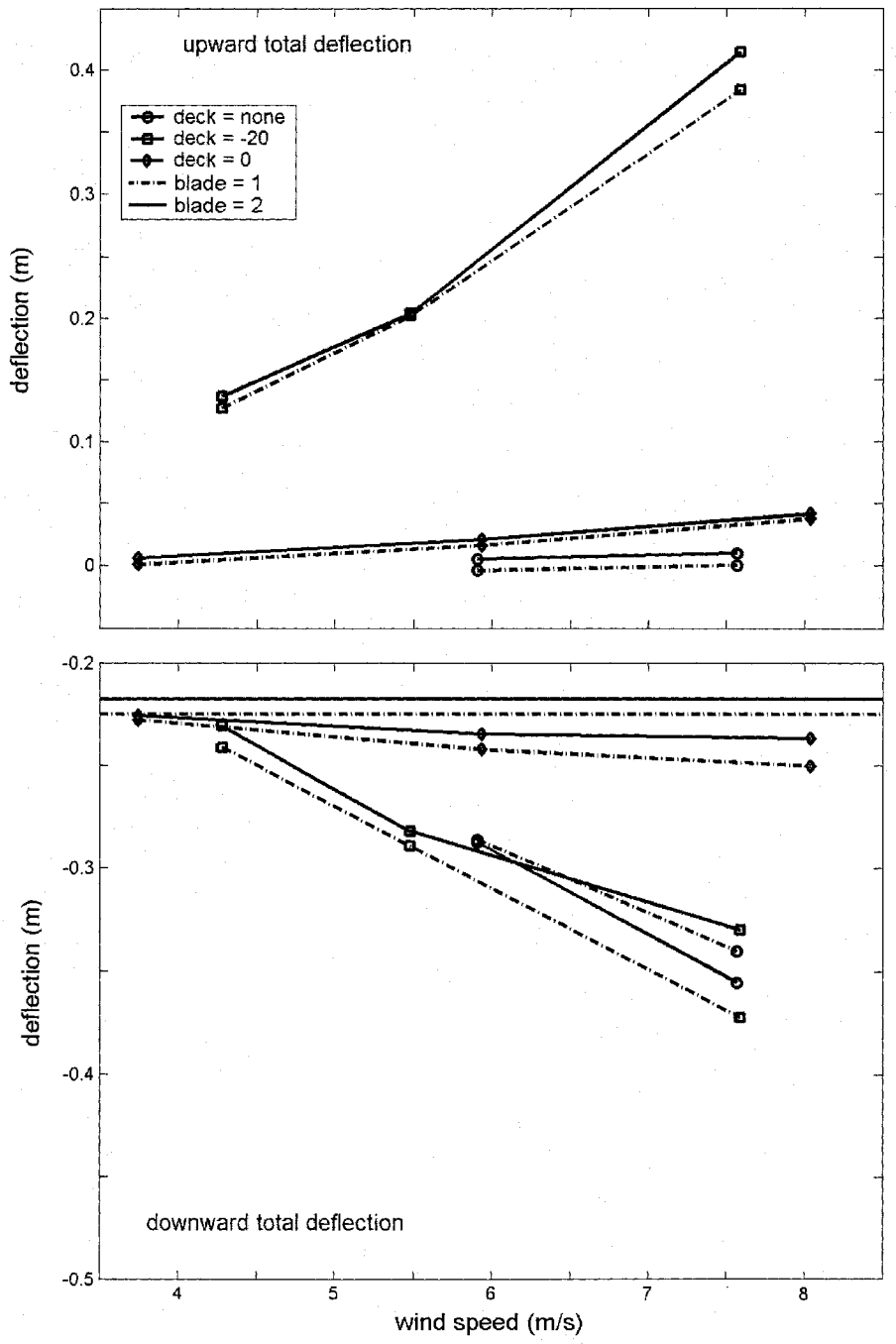

Figure D.20: Blade deflections with and without deck models for 0° blade pitch.

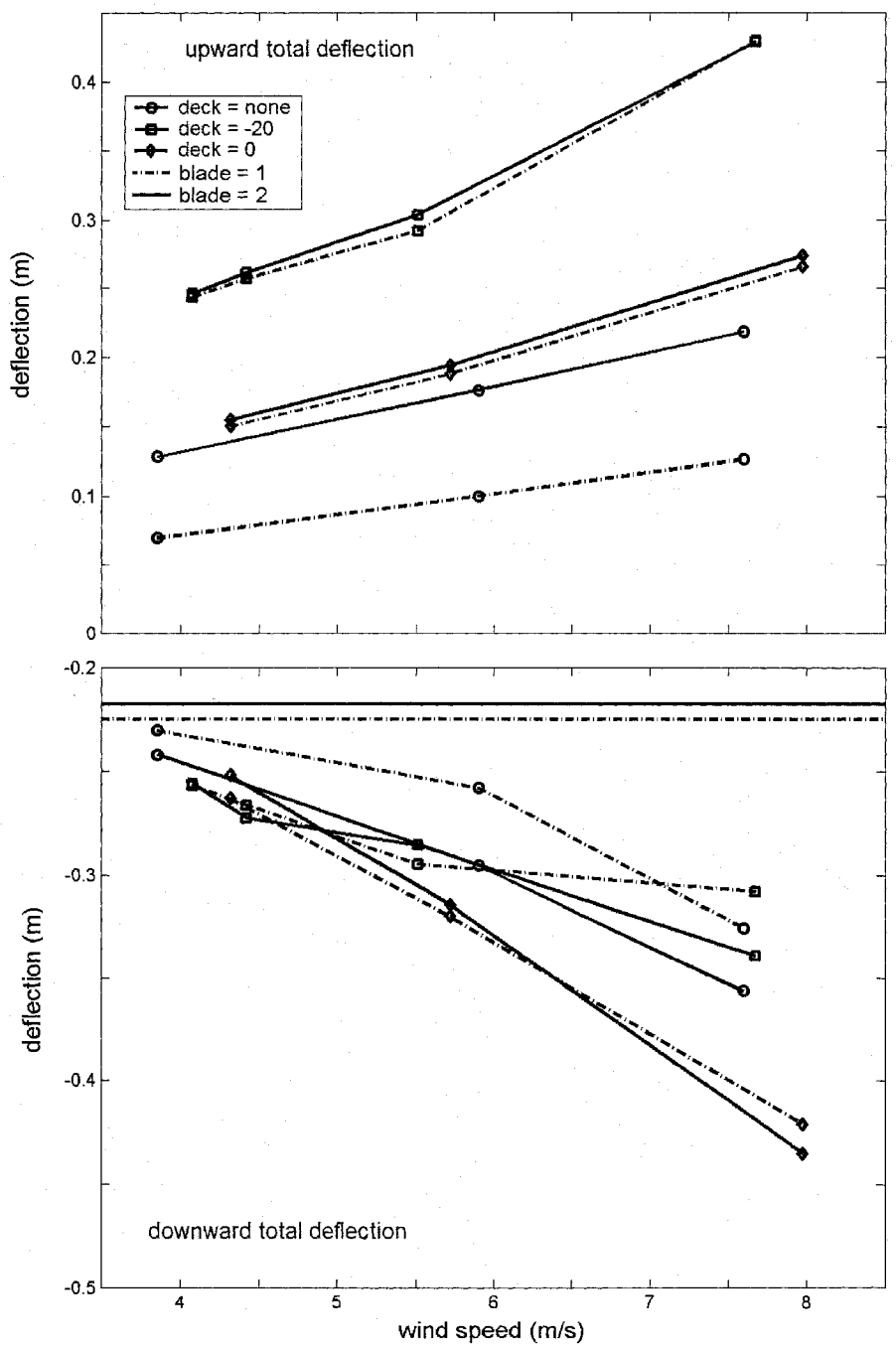

Figure D.21: Blade deflections with and without deck models for 8° blade pitch.

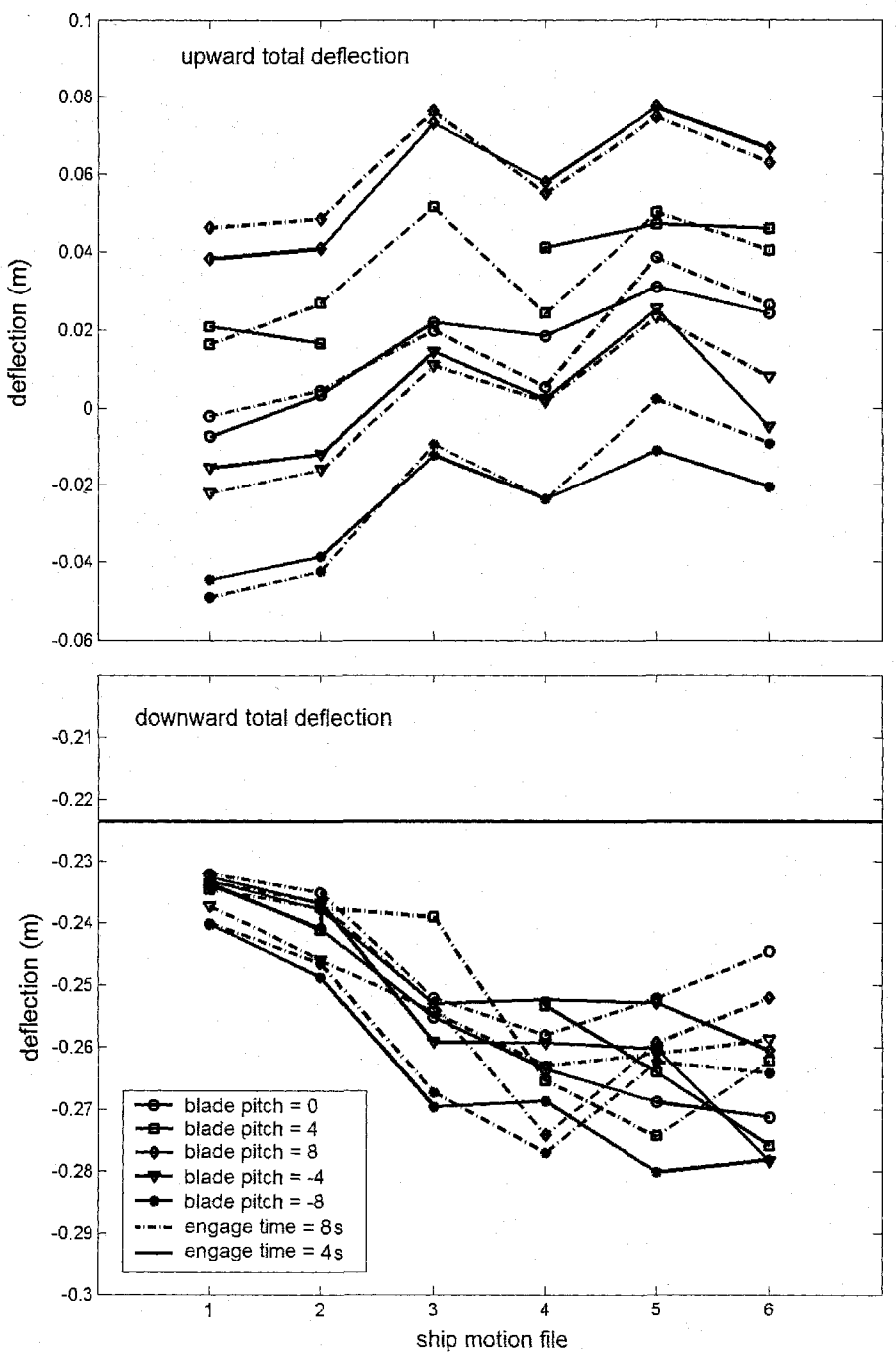

Figure D.22: Blade deflections for motion platform tests with representative ship motion for motion platform test Part II (Section 5.1.4).

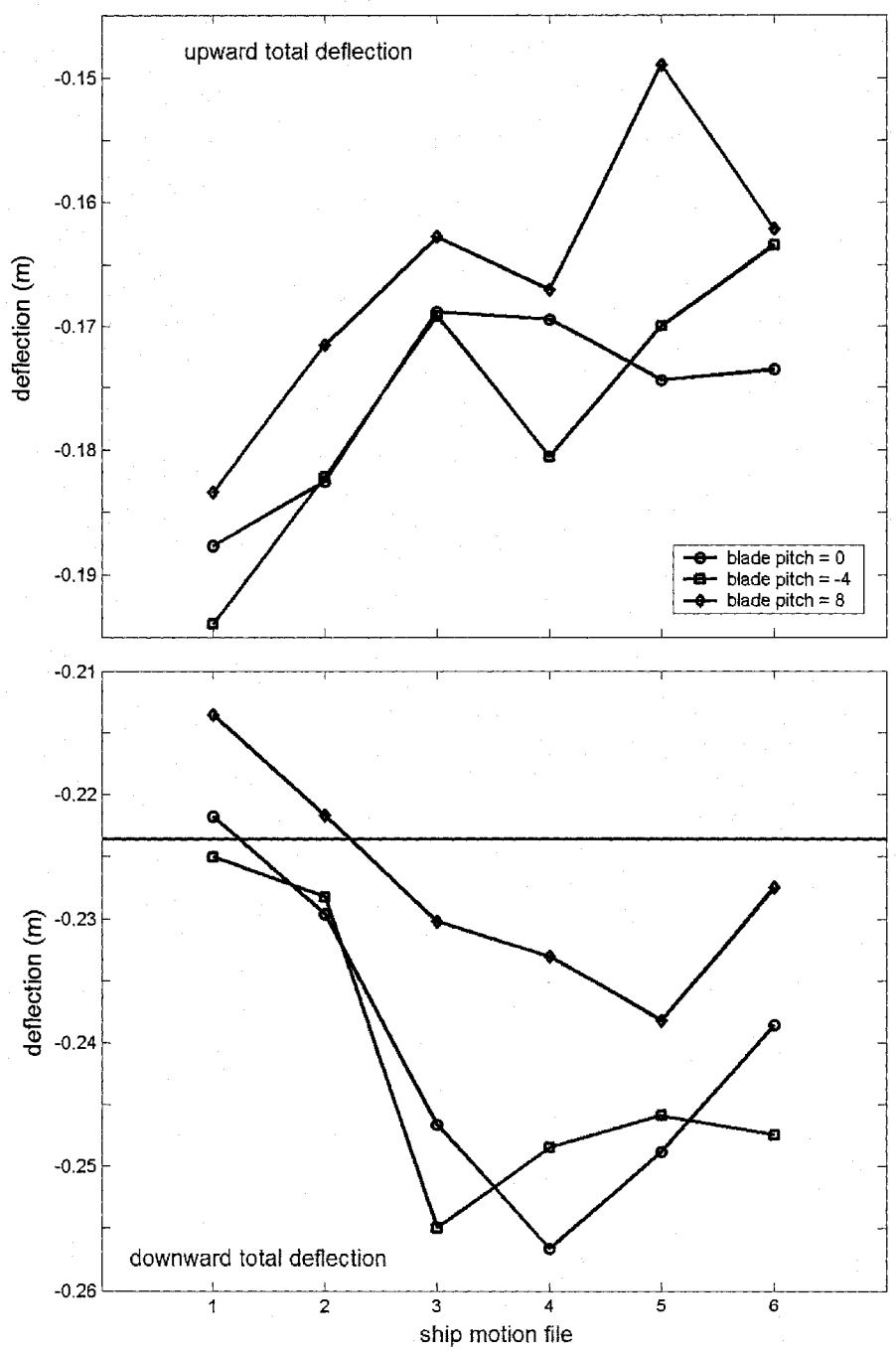

Figure D.23: Blade deflections for motion platform tests with representative ship motion for motion platform test Part III (Section 5.1.4).

Table D.1: Validation cases for 0° ship deck.

case number	wind speed m/s	blade pitch deg
1	4.32	-8
2	5.85	-8
3	8.00	-8
4	4.41	-4
5	5.64	-4
6	8.02	-4
7	3.68	0
8	5.85	0
9	8.07	0
10	4.48	4
11	5.69	4
12	7.97	4
13	4.29	6
14	5.83	6
15	8.08	6
16	4.30	8
17	5.84	8
18	8.06	8

D.6 Wind Tunnel Validation Cases

This section contains the time-history plots that are directly applicable to the validation discussion contained in Section 5.3.3. There are 38 experimental cases for which the rotor engagement time was 8 s. For the 0° ship deck, the 18 cases are listed in Table D.1 and shown in Figures D.24 to D.32. For the -20° ship deck, the 20 cases are listed in Table D.2 and shown in Figures D.33 to D.42.

For each figure, the experimental data is shown by the dashed line ad the simulation equivalent is shown by the solid line.

Table D.2: Validation cases for -20° ship deck.

case number	wind speed m/s	blade pitch deg
1	4.91	-8
2	6.12	-8
3	4.72	-4
4	6.05	-4
5	8.58	-4
6	4.60	0
7	6.16	0
8	8.68	0
9	4.70	2
10	6.14	2
11	8.57	2
12	4.71	4
13	6.10	4
14	8.67	4
15	4.74	6
16	6.27	6
17	8.73	6
18	4.62	8
19	6.26	8
20	8.63	8

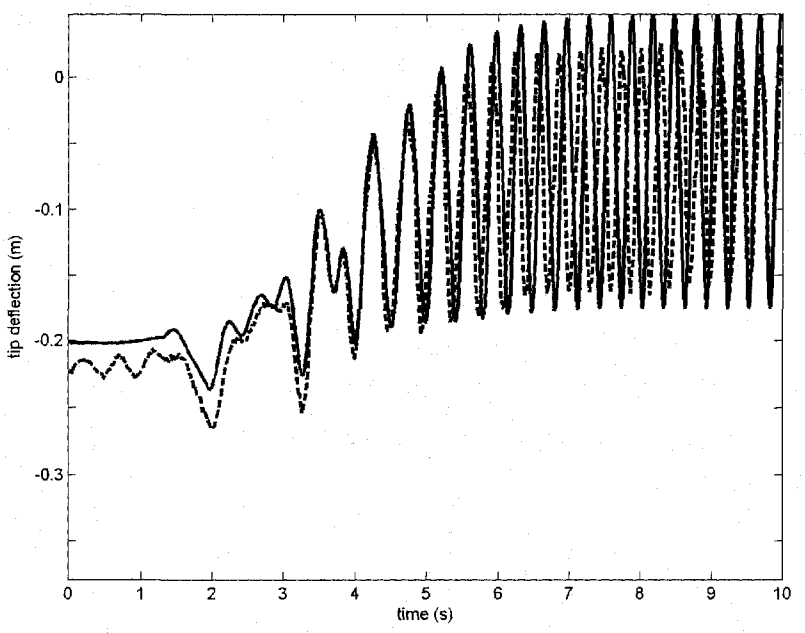

(a) validation case 1

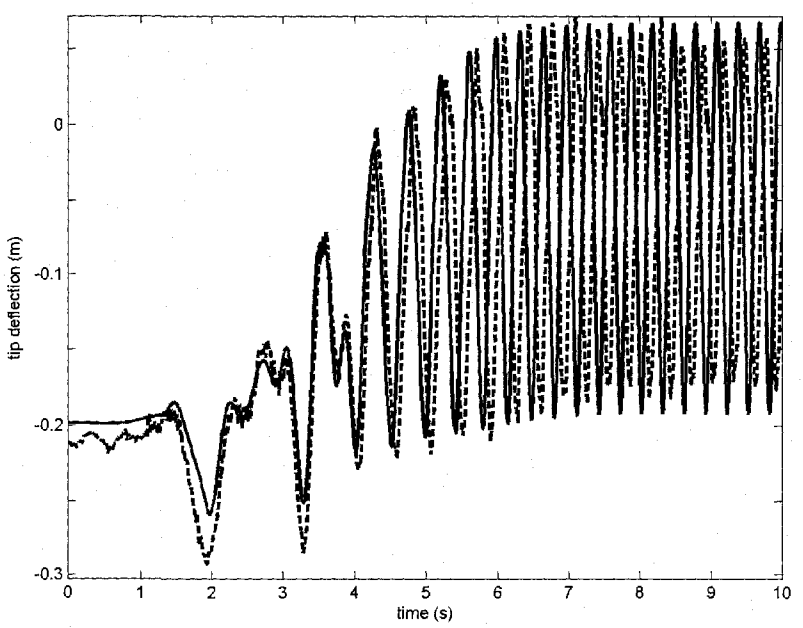

(b) validation case 2

Figure D.24: Time history validation traces for 0° ship deck.

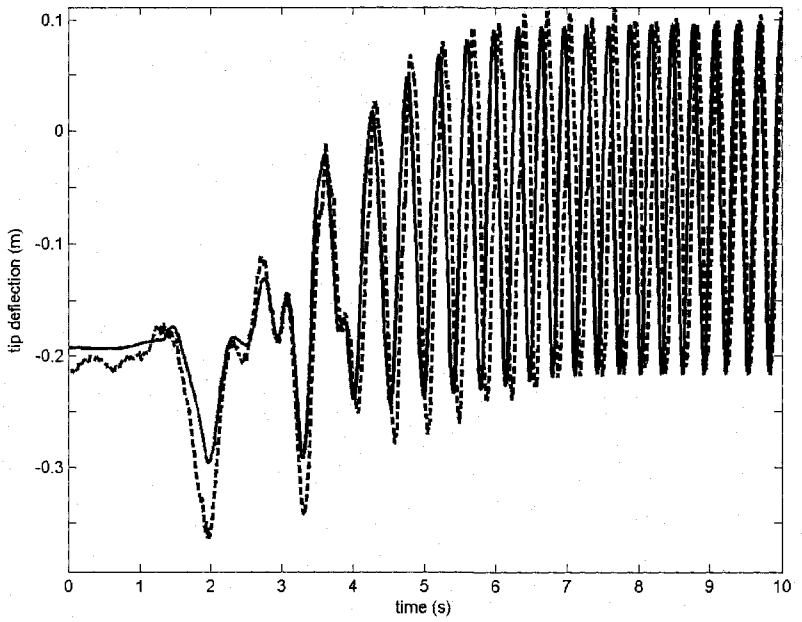

(a) validation case 3

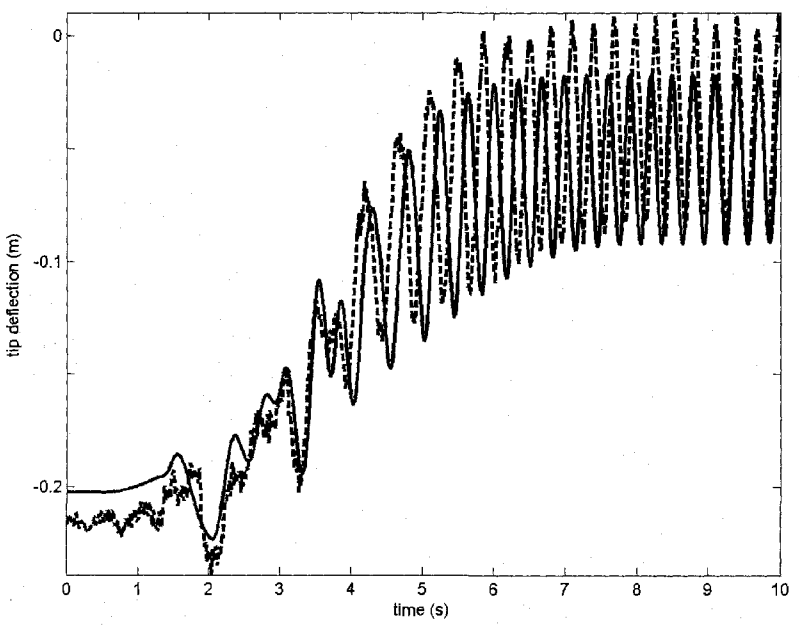

(b) validation case 4

Figure D.25: Time history validation traces for 0° ship deck.

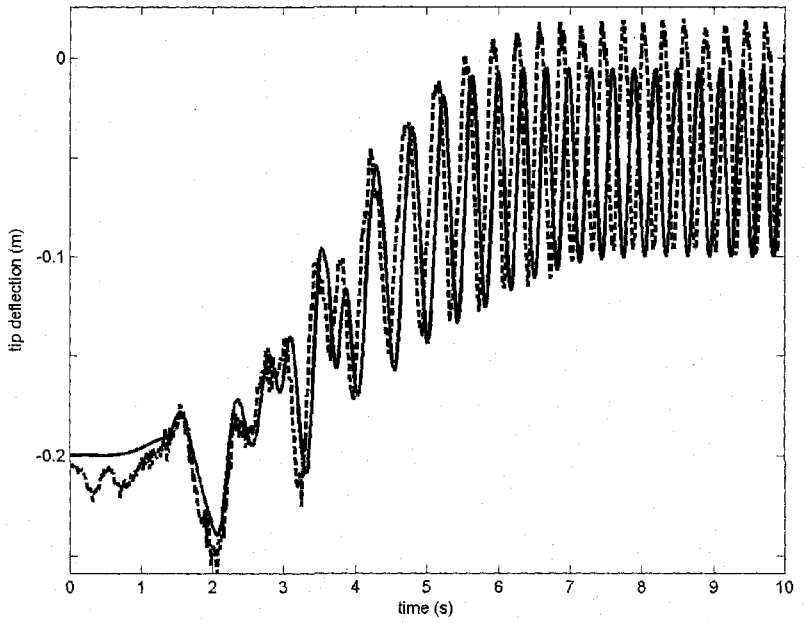

(a) validation case 5

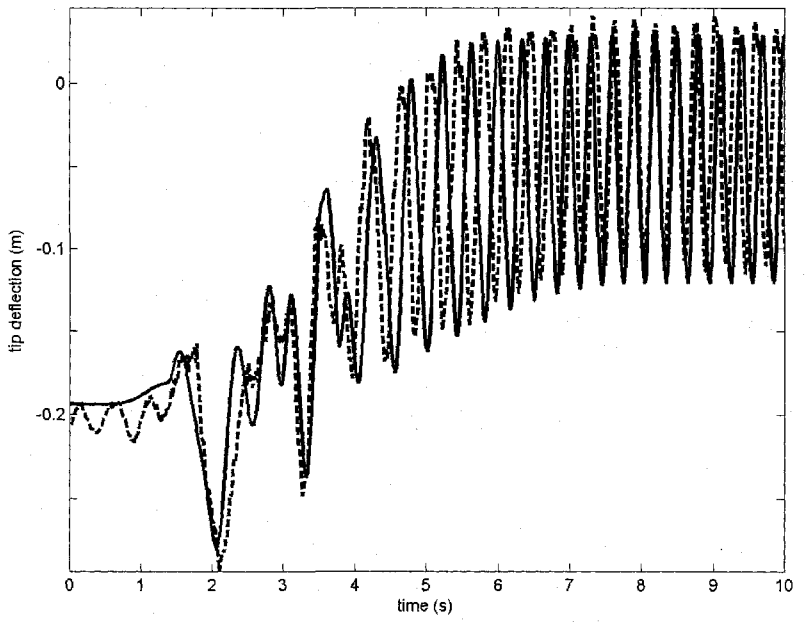

(b) validation case 6

Figure D.26: Time history validation traces for 0° ship deck.

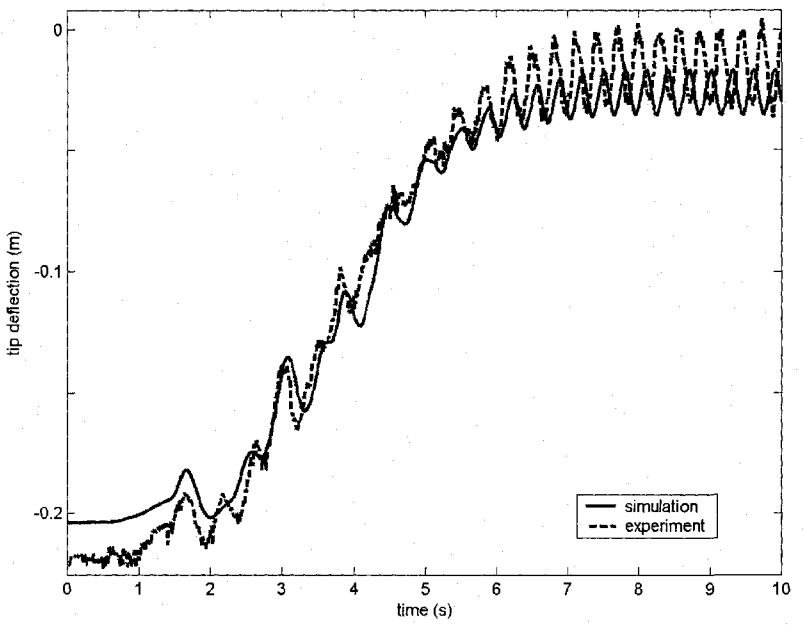

(a) validation case 7

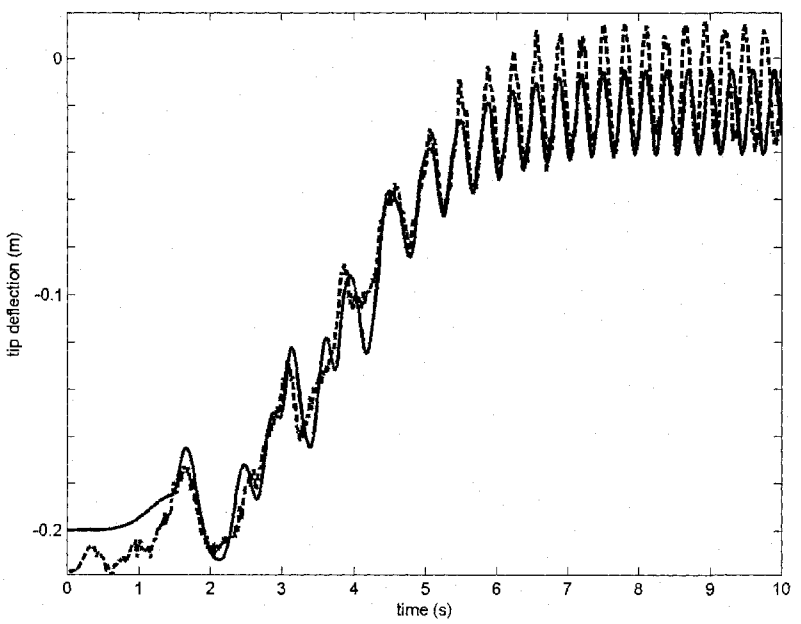

(b) validation case 8

Figure D.27: Time history validation traces for 0° ship deck.

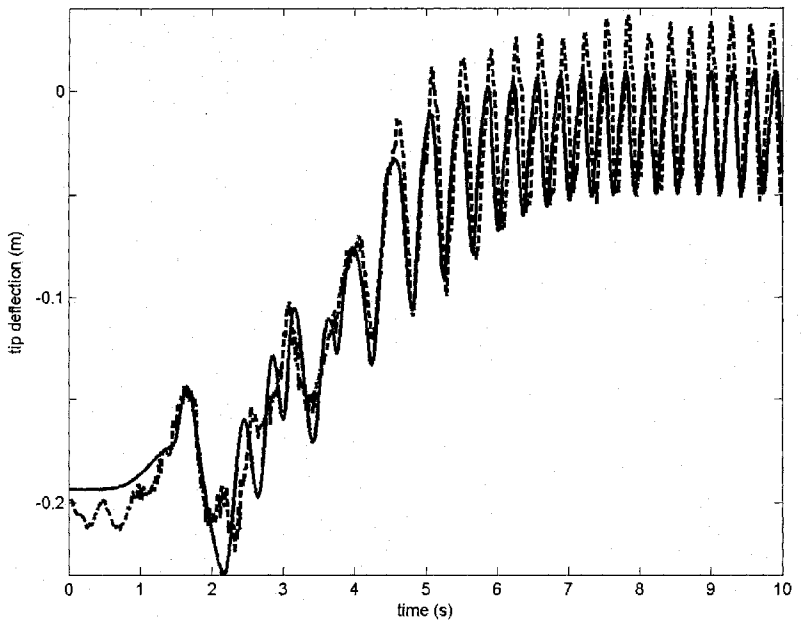

(a) validation case 9

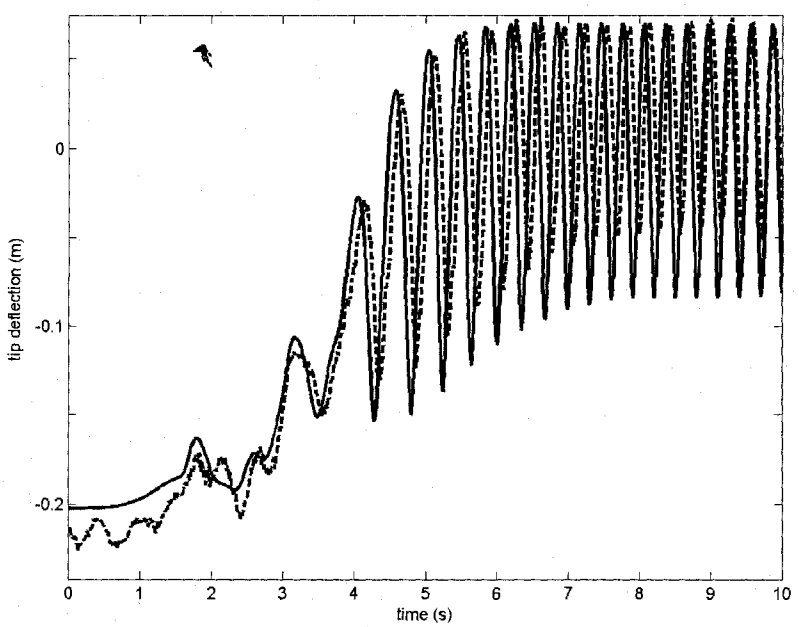

(b) validation case 10

Figure D.28: Time history validation traces for 0° ship deck.

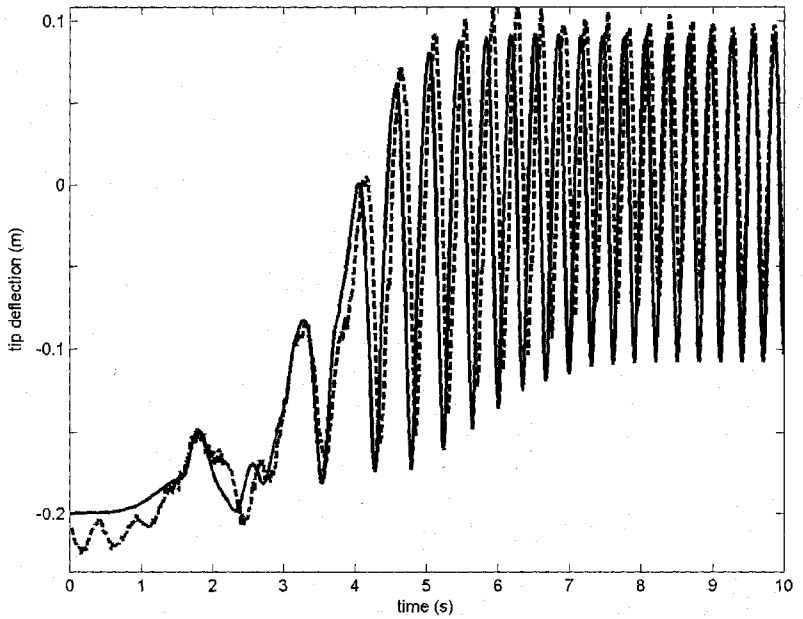

(a) validation case 11

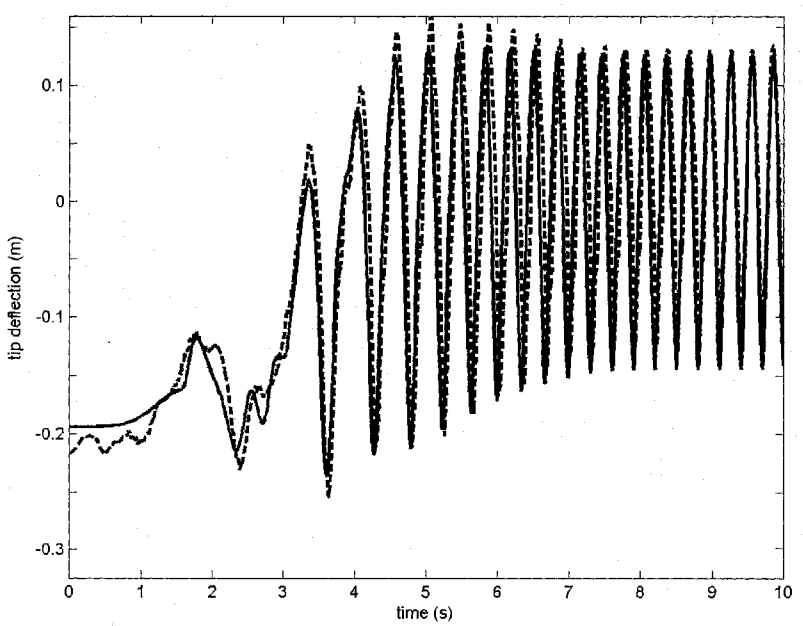

(b) validation case 12

Figure D.29: Time history validation traces for 0° ship deck.

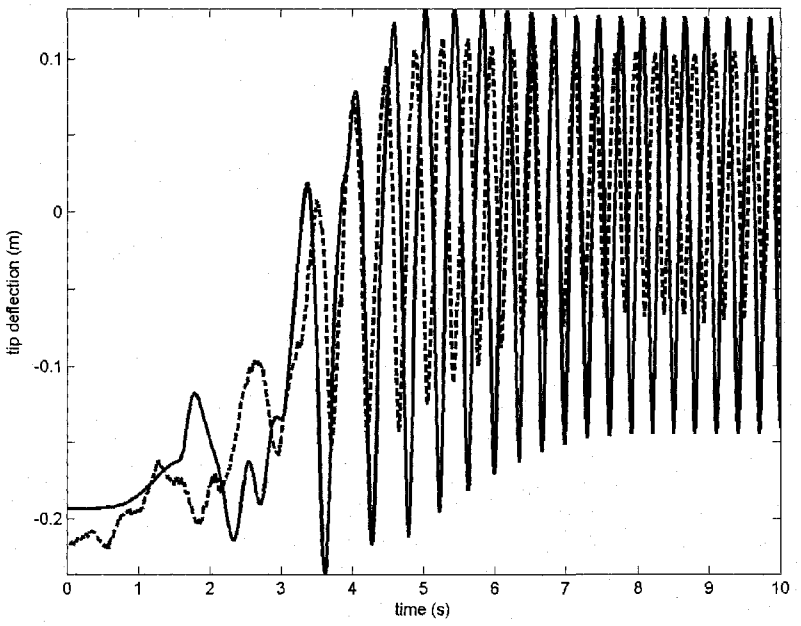

(a) validation case 13

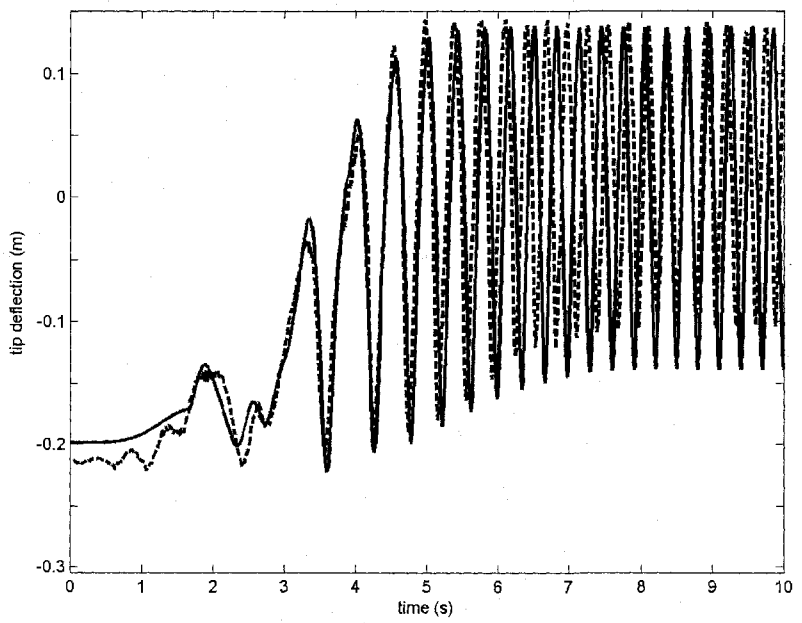

(b) validation case 14

Figure D.30: Time history validation traces for 0° ship deck.

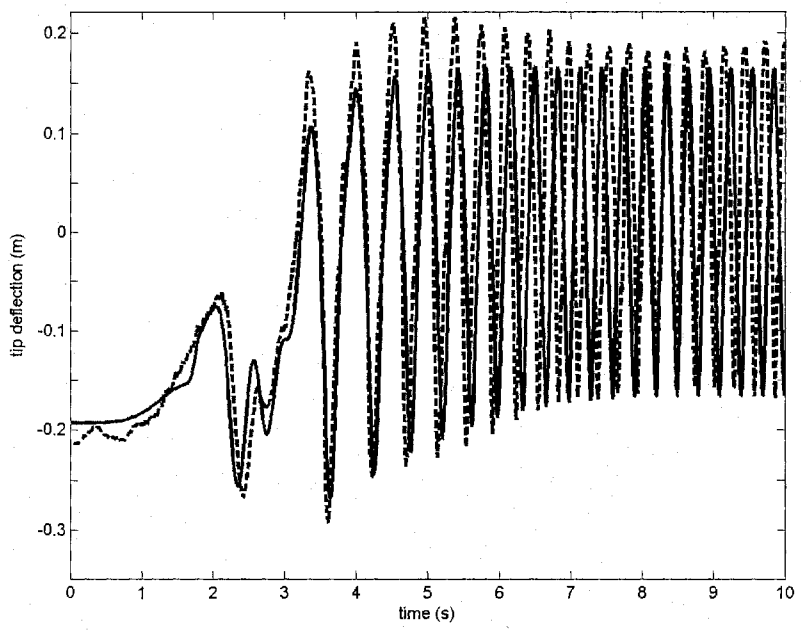

(a) validation case 15

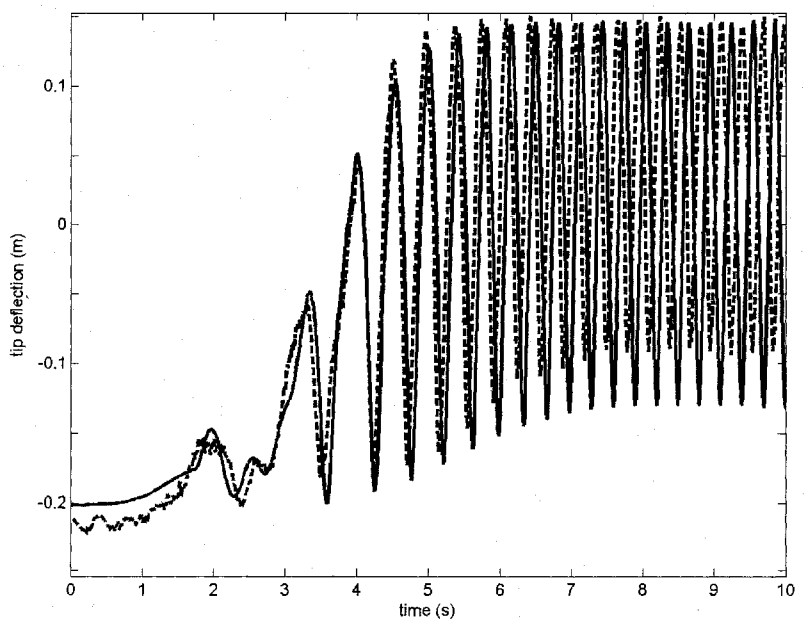

(b) validation case 16

Figure D.31: Time history validation traces for 0° ship deck.

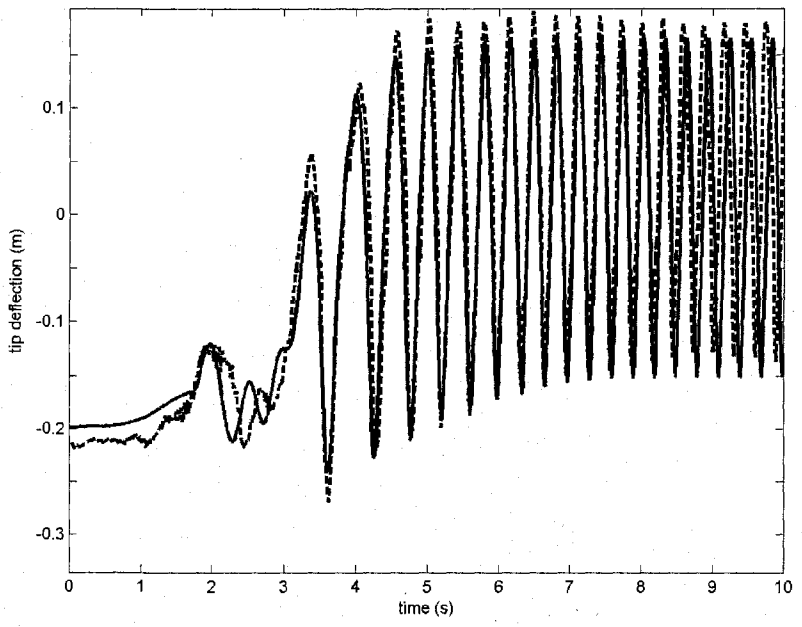

(a) validation case 17

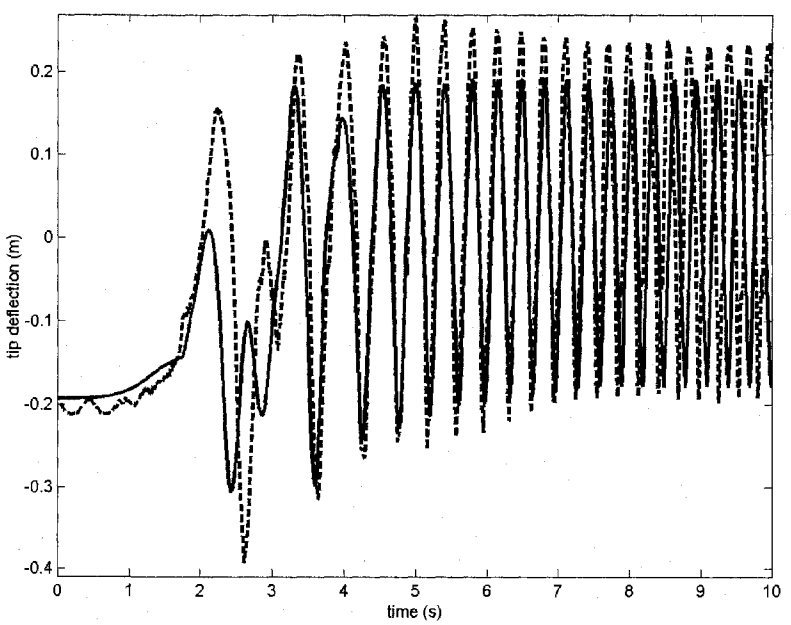

(b) validation case 18

Figure D.32: Time history validation traces for 0° ship deck.

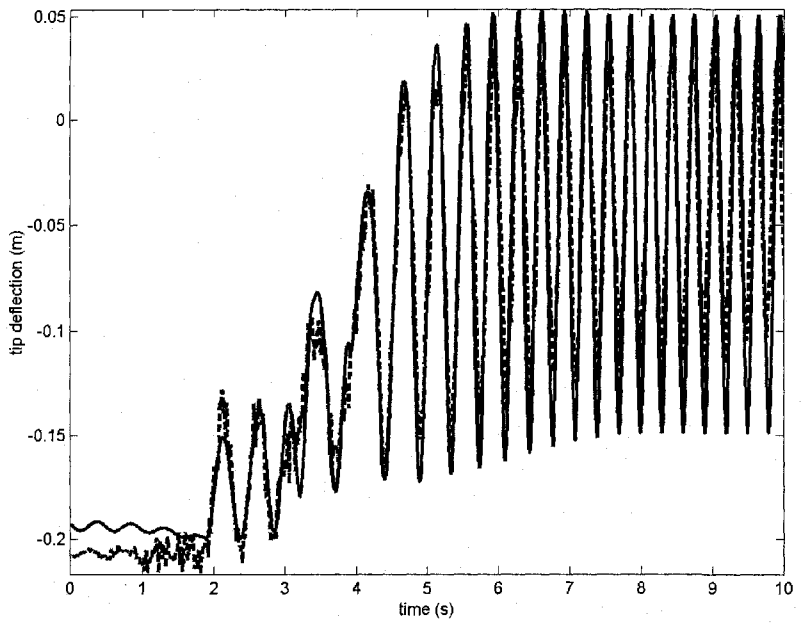

(a) validation case 1

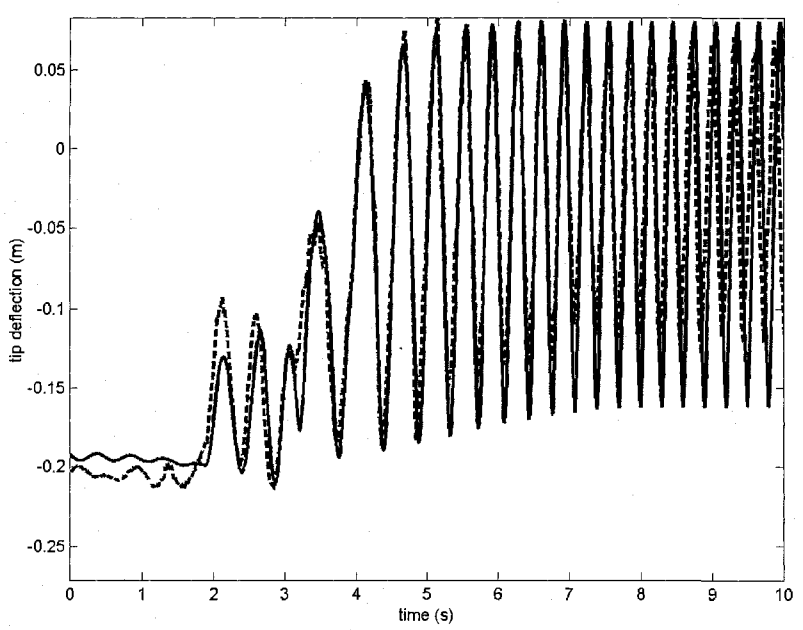

(b) validation case 2

Figure D.33: Time history validation traces for -20° ship deck.

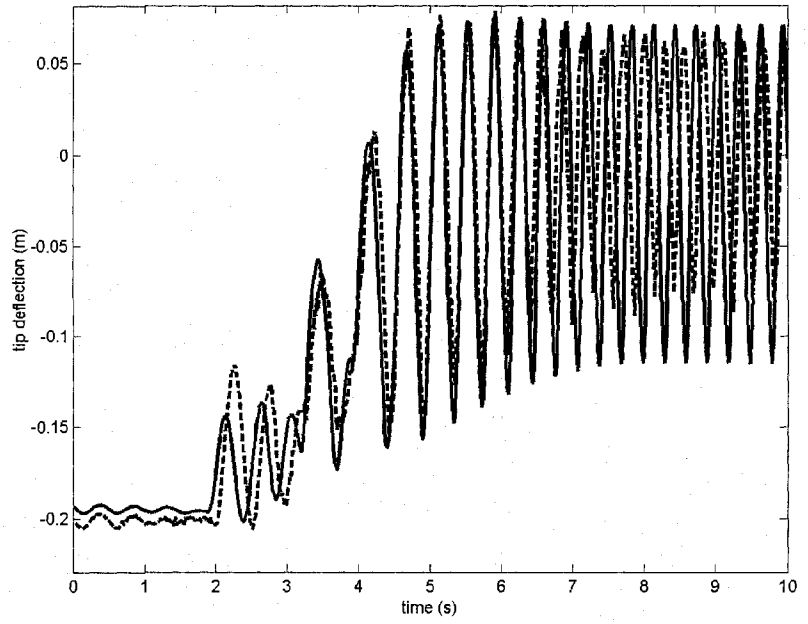

(a) validation case 3

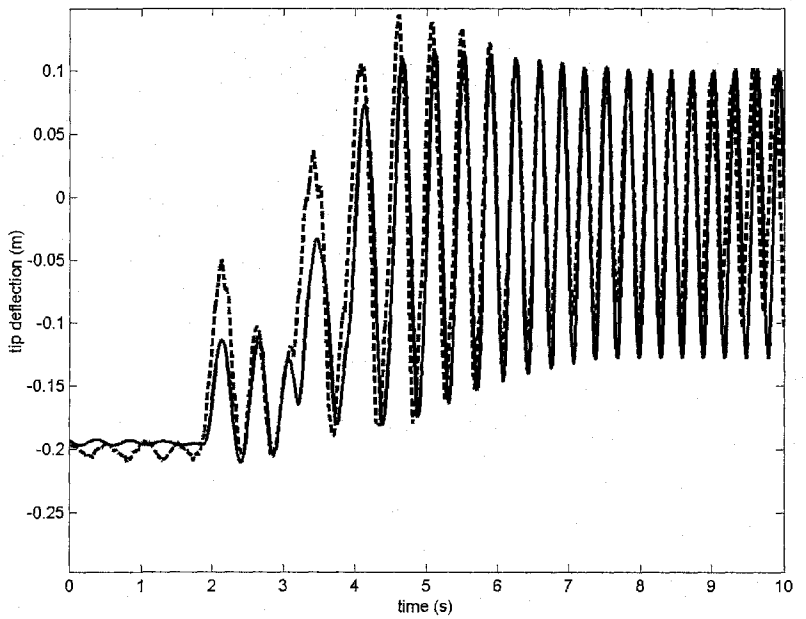

(b) validation case 4

Figure D.34: Time history validation traces for -20° ship deck.

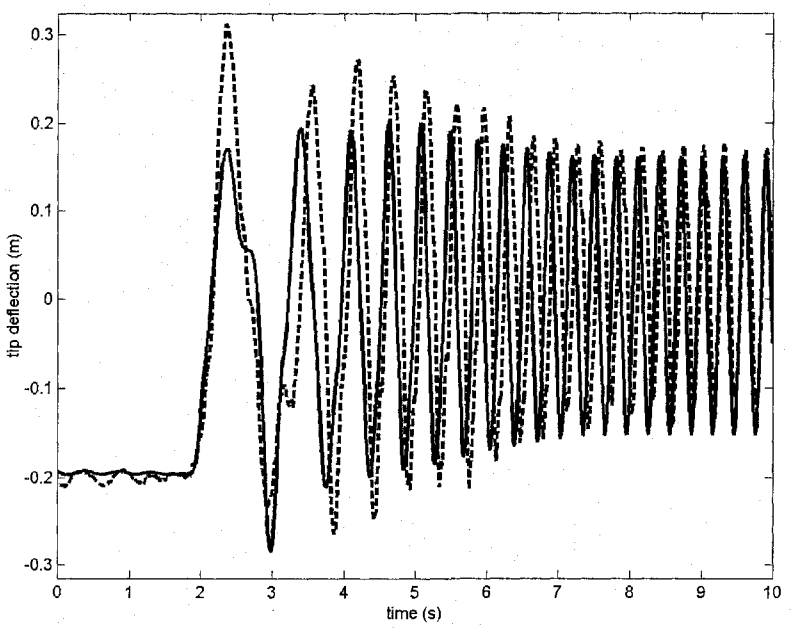

(a) validation case 5

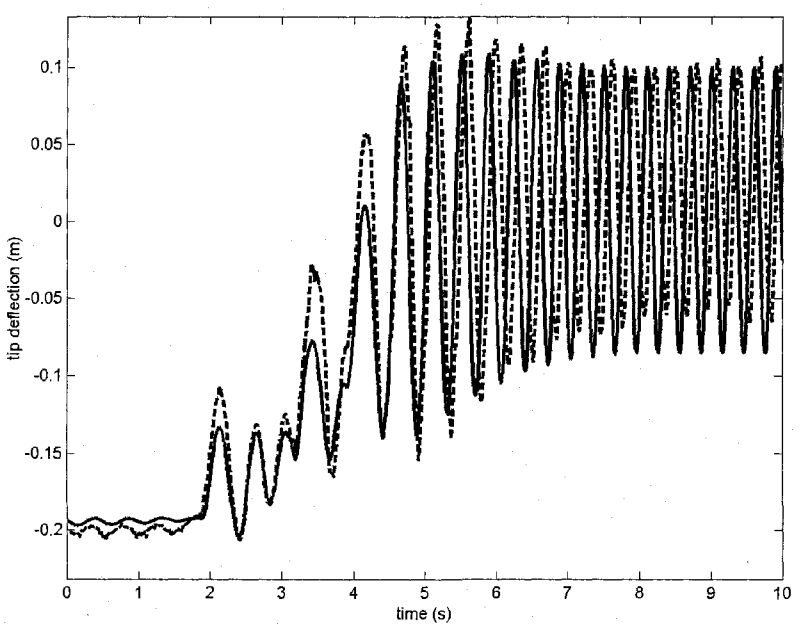

(b) validation case 6

Figure D.35: Time history validation traces for -20° ship deck.

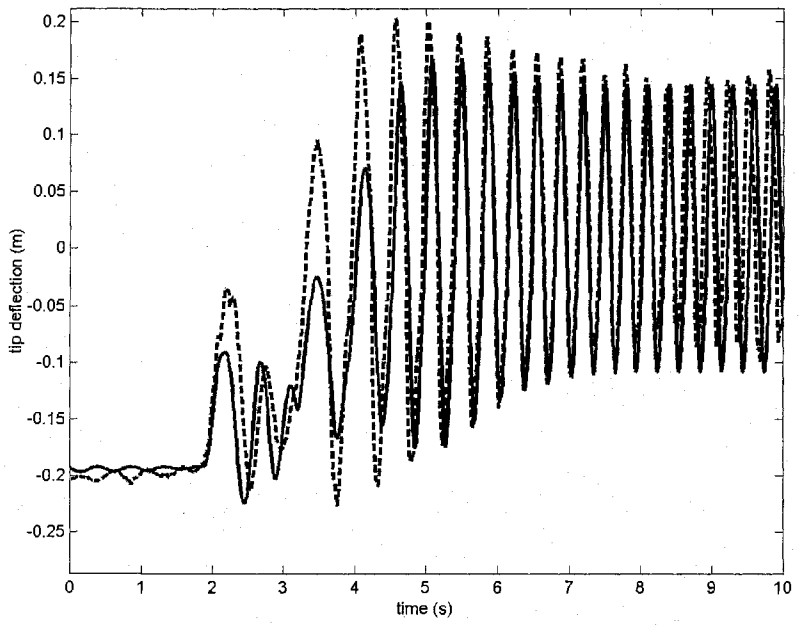

(a) validation case 7

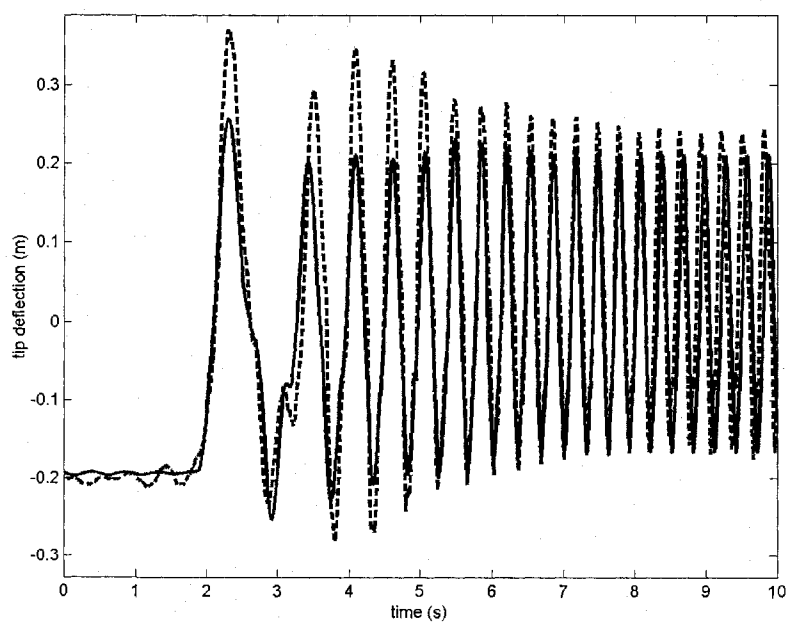

(b) validation case 8

Figure D.36: Time history validation traces for -20° ship deck.

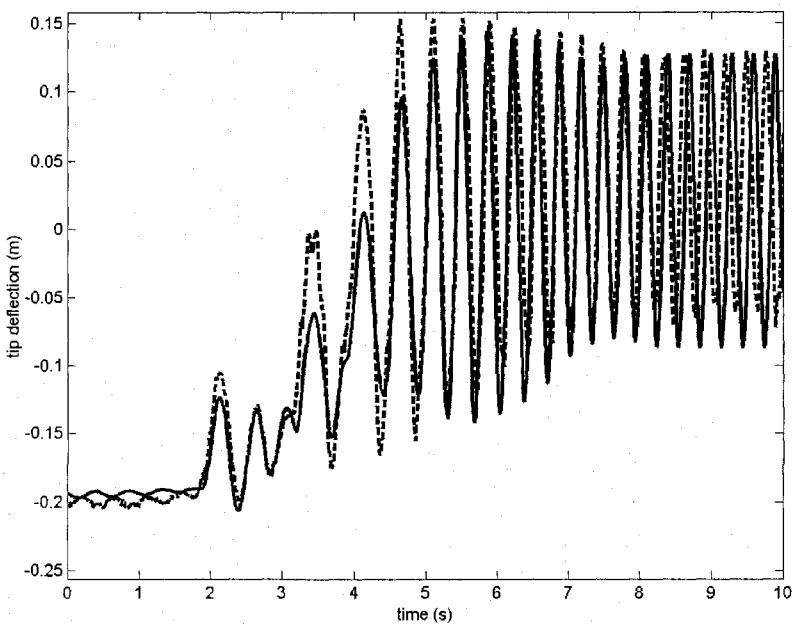

(a) validation case 9

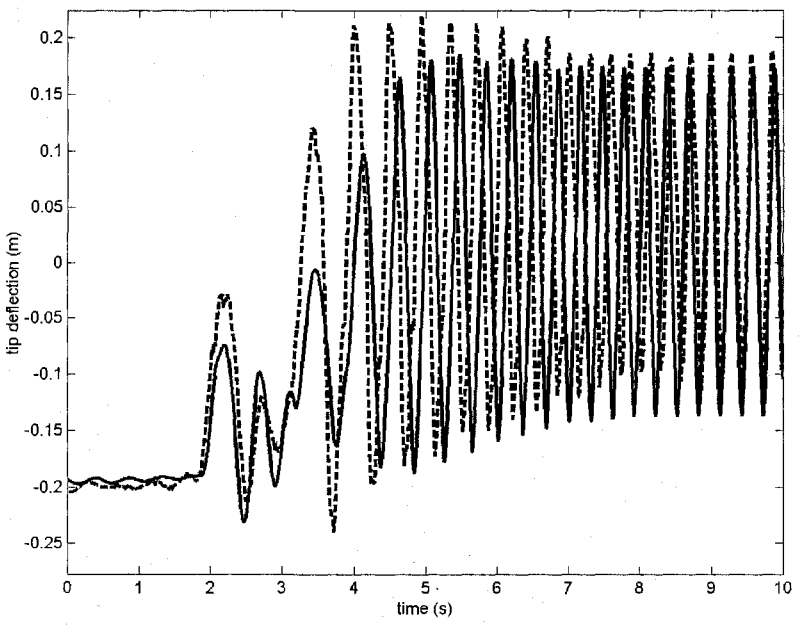

(b) validation case 10

Figure D.37: Time history validation traces for -20° ship deck.

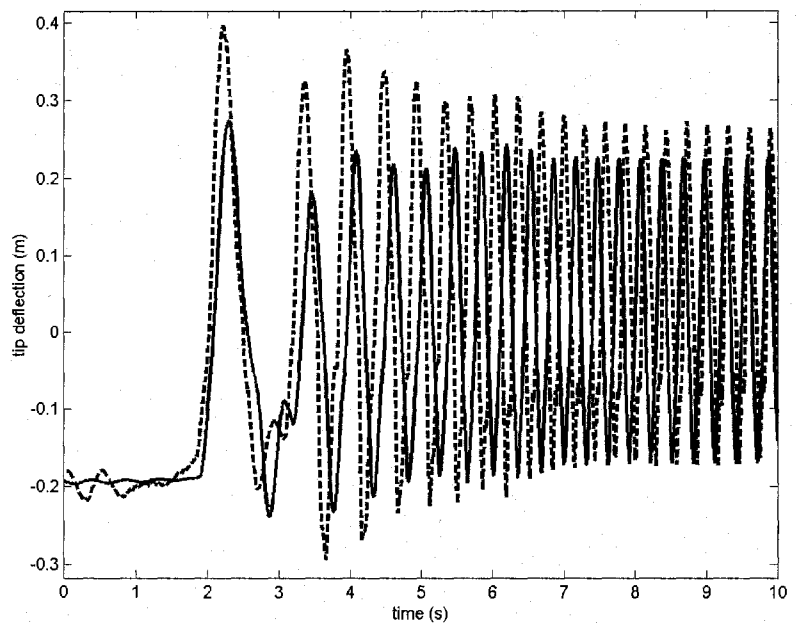

(a) validation case 11

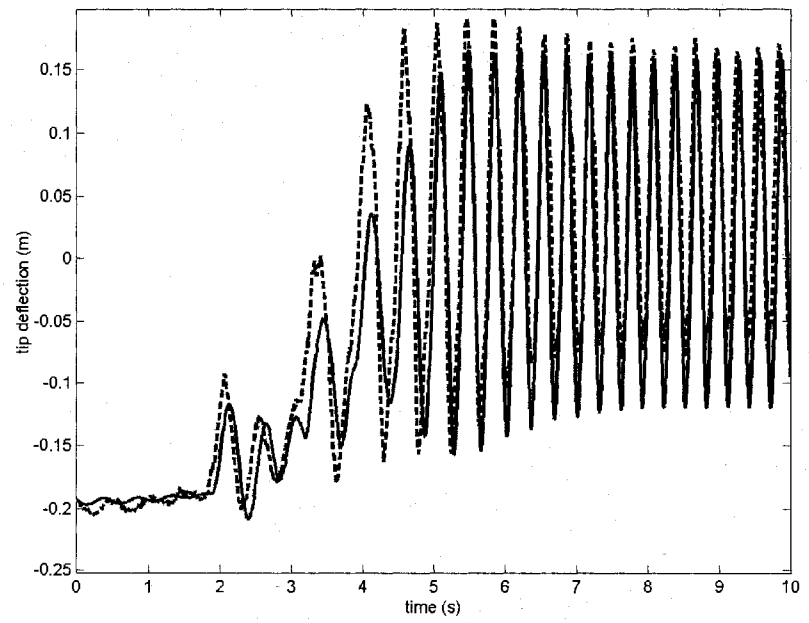

(b) validation case 12

Figure D.38: Time history validation traces for -20° ship deck.

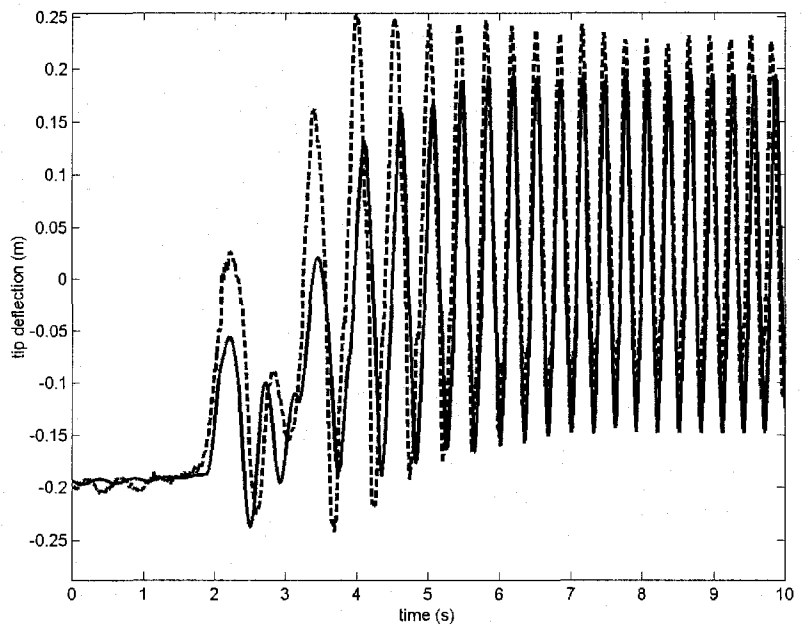

(a) validation case 13

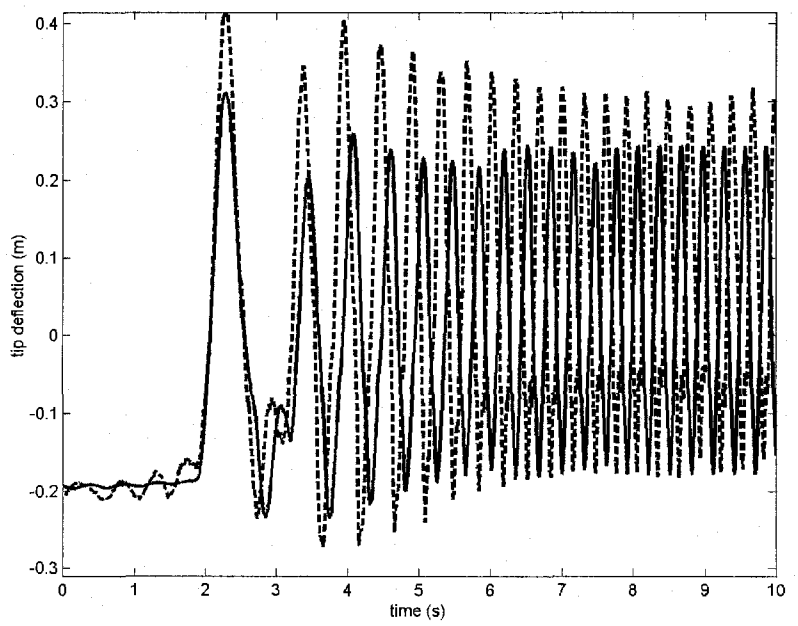

(b) validation case 14

Figure D.39: Time history validation traces for -20° ship deck.

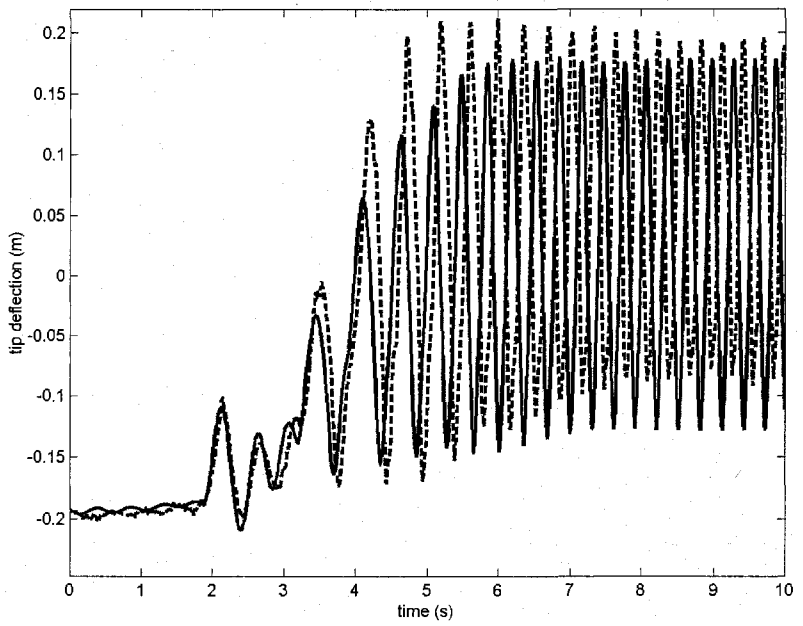

(a) validation case 15

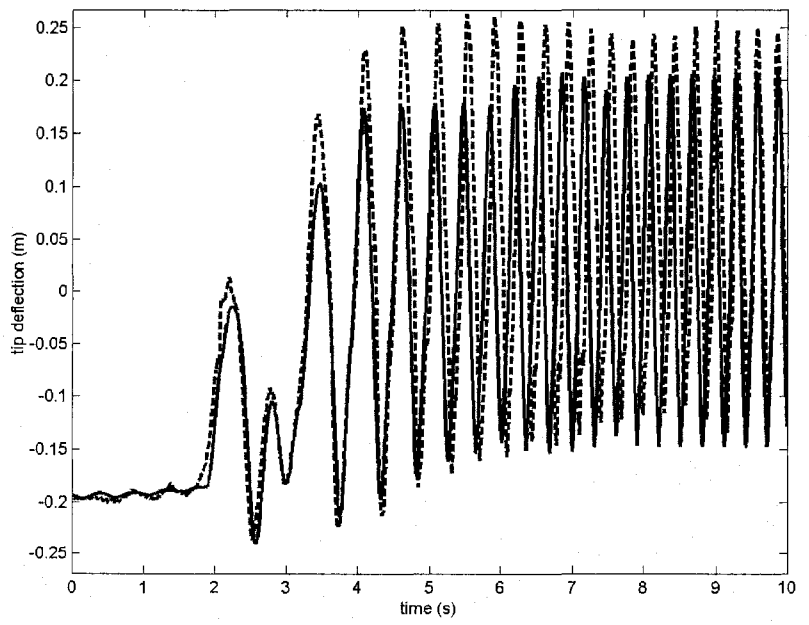

(b) validation case 16

Figure D.40: Time history validation traces for -20° ship deck.

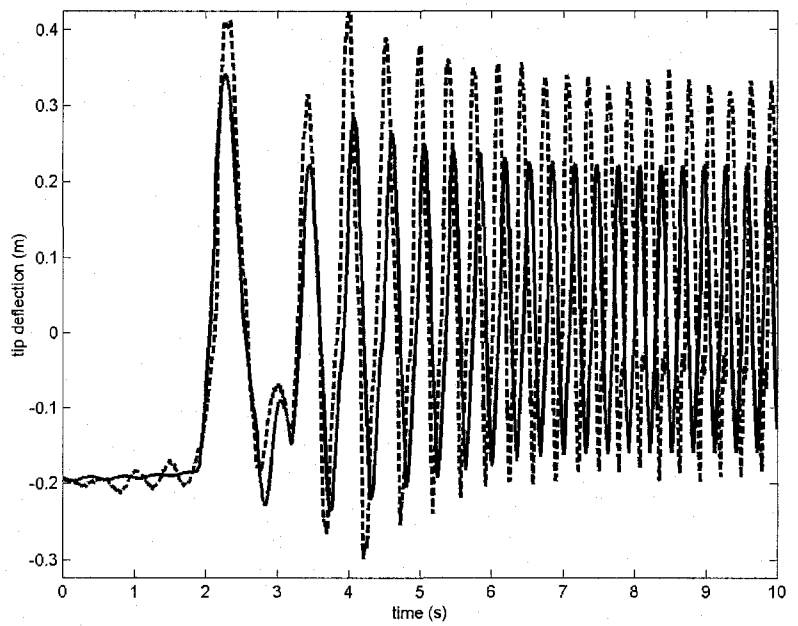

(a) validation case 17

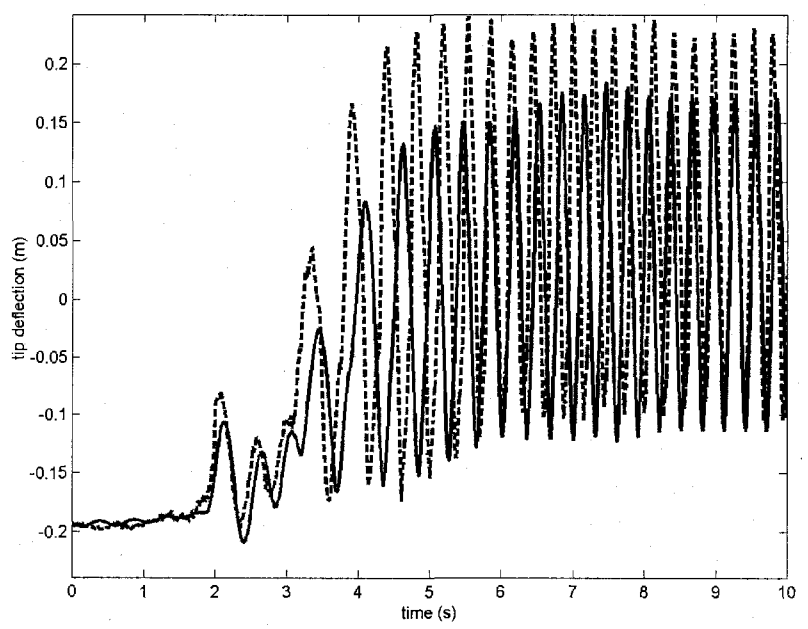

(b) validation case 18

Figure D.41: Time history validation traces for -20° ship deck.

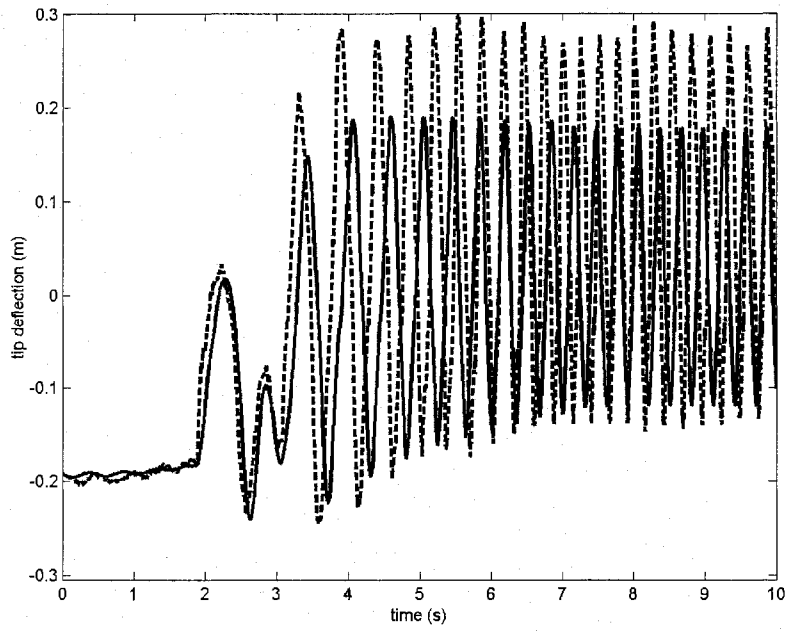

(a) validation case 19

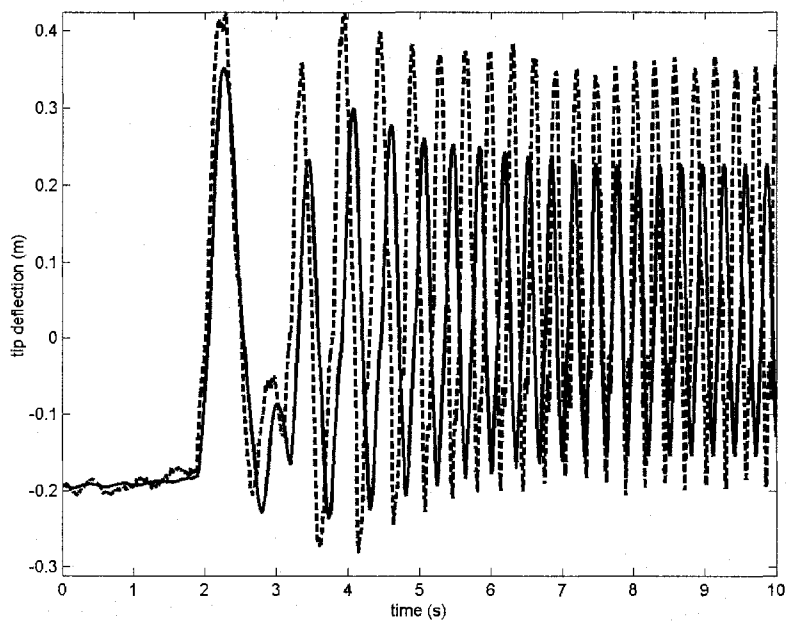

(b) validation case 20

Figure D.42: Time history validation traces for -20° ship deck.